Conference Proceedings of the Society for Experimental Mechanics Series

Tom Proulx *Editor*

Time Dependent Constitutive Behavior and Fracture/Failure Processes, Volume 3

Proceedings of the 2010 Annual Conference on Experimental and Applied Mechanics

SEM Springer

Conference Proceedings of the Society for Experimental Mechanics Series

For other titles published in this series, go to
www.springer.com/series/8922

Tom Proulx
Editor

Time Dependent Constitutive Behavior and Fracture/Failure Processes, Volume 3

Proceedings of the 2010 Annual Conference on Experimental and Applied Mechanics

Springer

Editor
Tom Proulx
Society for Experimental Mechanics, Inc.
7 School Street
Bethel, CT 06801-1405
USA
tom@sem1.com

ISSN 2191-5644 e-ISSN 2191-5652
ISBN 978-1-4419-9498-1 e-ISBN 978-1-4419-9794-4
DOI 10.1007/978-1-4419-9794-4
Springer New York Dordrecht Heidelberg London

Library of Congress Control Number: 2011926997

Preface

Symposium on Time Dependent Constitutive Behavior and Failure/Fracture Processes represents one of six tracks of technical papers presented at the Society for Experimental Mechanics Annual Conference & Exposition on Experimental and Applied Mechanics, held at Indianapolis, Indiana, June 7-10, 2010. The full proceedings also include volumes on: Dynamic Behavior of Materials, Role of Experimental Mechanics on Emerging Energy Systems and Materials, Application of Imaging Techniques to Mechanics of Materials and Structures, Experimental and Applied Mechanics, along with the 11th International Symposium on MEMS and Nanotechnology.

Each collection presents early findings from experimental and computational investigations on an important area within Experimental Mechanics. The current volume on the *Symposium on Time Dependent Constitutive Behavior and Failure/Fracture Processes* includes studies on:

Characterization and modeling of behavior at multiple scales; viscoelasticity, viscoplasticity; transport, chemically and electronically active processes; multiphase and biomaterial systems; thermodynamics; shape memory; mechanics of testing; dynamic rate-dependent behaviors; large deformations; residual stresses; time (rate)-dependent damage and failure; time (rate)-dependent polycrystalline, single crystal and nanocrystalline behaviors; multifunctional materials; mechanics of processing; design methods; environmental interactions; experimental methods and techniques; linear and non-linear time-dependent behavior; time (rate)-dependent composite materials of all types; numerical analysis; physical aging; rheological properties; temperature, pressure, and moisture effects on time dependence; damping.

The papers in the Symposium address constitutive, time (rate)-dependent constitutive and fracture/failure behavior of a broad range of materials systems, including prominent researchers in both applied and experimental mechanics. Solicited papers involve non-negligible time-dependent mechanical response in cases incorporating non-mechanical fields. Papers address modeling and experimental aspects of the subject areas.

The organizers thank the presenters, authors and session chairs for their participation in this symposium.

The Society would like to thank the organizers of the track, H. Jerry Qi, *University of Colorado;* Richard B. Hall, *Air Force Research Laboratory;* Hongbing Lu, *University of North Texas;* Gyaneshwar P. Tandon, *University of Dayton Research Institute;* Bonnie R. Antoun, *Sandia National Laboratories;* Y. Charles Lu, *University of Kentucky* for their efforts.

Bethel, Connecticut

Dr. Thomas Proulx
Society for Experimental Mechanics, Inc

Contents

Proceedings of the SEM Annual Conference
June 7-10, 2010 Indianapolis, Indiana USA

Thermal and Mechanical Characterization of a Healable Polymer

Christian Nielsen[1], Haim Weizman[2] and Sia Nemat-Nasser[1,*]
[1] Center of Excellence for Advanced Materials, Dept of Mechanical and Aerospace Engr,
[2] Dept of Chemistry and Biochemistry,
University of California at San Diego, 9500 Gilman Drive, La Jolla, CA 92093-0416, USA
* sia@ucsd.edu

ABSTRACT

A cross-linked polymer capable of reforming broken bonds is considered a healable polymer. One such polymer, 2MEP4FS, has previously been shown to regain full toughness under ideal fracture and healing conditions. Here, a more purified 2MEP4FS polymer is characterized using thermal and mechanical techniques and compared with the previous 2MEP4FS polymer. Differential scanning calorimetry (DSC) confirms the presence of the thermally reversible Diels-Alder bonds necessary for healing. Dynamic mechanical analysis (DMA) establishes mechanical properties and the glass transition temperature. Fracture tests are conducted using the double cleavage drilled compression (DCDC) geometry. Compression drives symmetric cracks up and down a rectangular column of material with a central through-thickness hole. Correlating the applied stresses and crack lengths with a finite element model, critical stress intensity factors are estimated. The cracks are healed with a thermal treatment and light pressure, and the sample is retested. Over the course of multiple fracture and healing cycles, changes in the critical stress intensity factor are used to establish healing efficiency.

Keywords: polymer, healing, fracture, crack, DSC, DMA, DCDC

EXTENDED ABSTRACT

A healable polymer, 2MEP4FS, is experimentally studied using thermal and mechanical techniques. The polymer was designed by Wudl et al. as a modified version of a previously reported polymer, 2MEP4F [1]. The product of a Diels-Alder reaction between monomers 2MEP and 4FS, 2MEP4FS contains thermally reversible cross-linking bonds that can be reformed after fracture. This healing ability is not found in traditional cross-linked polymers like epoxy.

Testing has previously shown 2MEP4FS capable of complete mechanical recovery after a fracture event [2]. Under ideal conditions, macrocracks were healed and regrown numerous times with no significant changes in the critical stresses required for crack propagation. Some tests even indicated the material was tougher after healing.

Current work seeks to confirm these results for material made from a new batch of monomers synthesized and purified using a different procedure than [2]. Typically, retesting the material would not be necessary, but the new monomers are believed to be more chemically pure. Current batches of 2MEP are observed to be a brighter white color [3]. Regarding 4FS, the previous purification process was determined to be incomplete and a new process was developed. The purity of the new monomers was confirmed using NMR. Monomers from [2] are not available for conclusive chemical characterization and comparison.

Differential scanning calorimetry (DSC) is used to verify the presence of reversible bonds in the current polymer. Several milligrams of cured 2MEP4FS are heated in a sealed pan at a known temperature rate, and the amount of heat energy required is recorded. At the end of the test, when the polymer is at the peak temperature, the sample is removed and quenched in a bath of liquid nitrogen. By rapidly cooling the sample, separated reversible bonds will not be able to reform. Retesting the sample yields an exothermic peak around 80°C, where the bonds have gained sufficient mobility to reconnect.

T. Proulx (ed.), *Time Dependent Constitutive Behavior and Fracture/Failure Processes, Volume 3*, Conference Proceedings of the Society for Experimental Mechanics Series 15, DOI 10.1007/978-1-4419-9794-4_1, © The Society for Experimental Mechanics, Inc. 2011

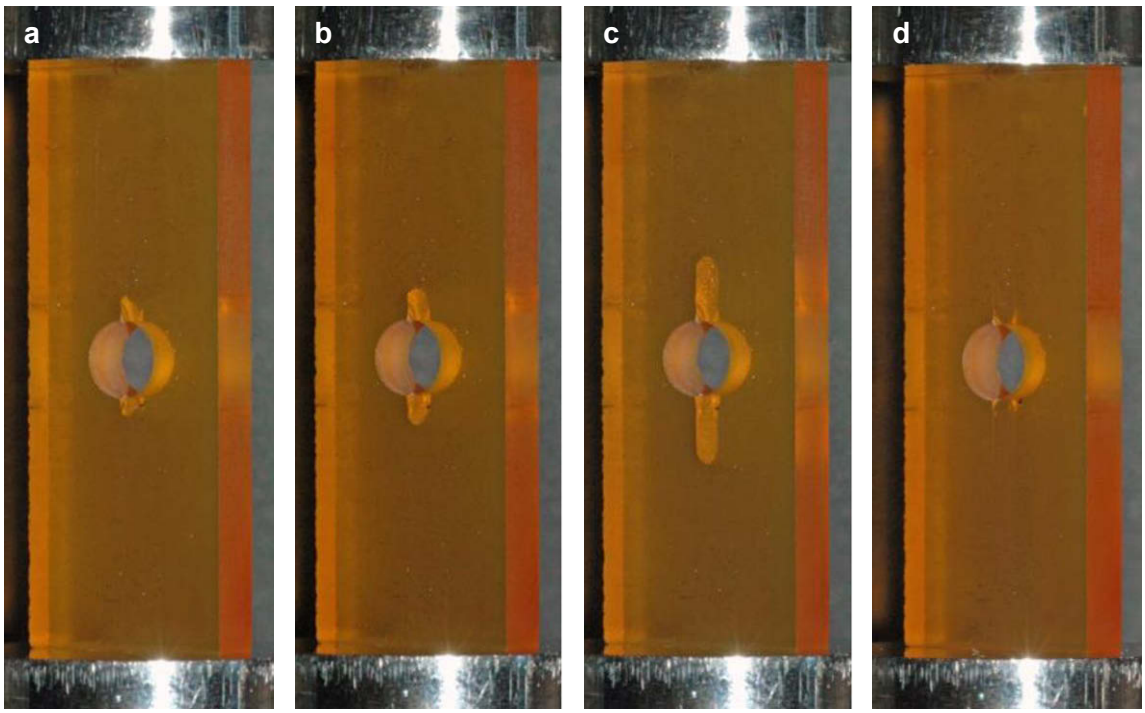

Figure 1. *Crack morphology during a typical DCDC test and healing cycle: (a) the sample is pre-cracked and ready for testing; (b) the cracks start to grow; (c) the test is stopped; and (d) the sample is healed.*

Dynamic mechanical analysis (DMA) gives the complex modulus of the material as a function of temperature, from which the glass transition temperature can be extracted. A single cantilever clamp tests a rectangular block of material using fixed-fixed bending. For a 1 Hz prescribed displacement oscillation, the storage modulus and glass transition temperature are observed to be slightly higher than the results presented in [2].

The healing potential of the current 2MEP4FS polymer is evaluated using the double cleavage drilled compression (DCDC) fracture test [2,4,5]. The test applies uniaxial compression to a column of material with rectangular cross-section and central through-thickness hole. This loading and geometry creates regions of tension at the apex and base of the hole, leading to symmetric mode I cracks. As the applied displacement is increased, these cracks propagate in a stable manner up and down the specimen. Once the cracks have grown to a sufficient length, the DCDC test is stopped and the healing process [2] is initiated. Light lateral pressure is applied to bring the crack faces together and the sample is heated to 85°C. After a period of 30 minutes, the pressure is released and the temperature is increased to 95°C for another 30 minutes. The sample is allowed to slowly cool to room temperature overnight before DCDC fracture testing and healing are repeated (Figure 1).

By correlating the lengths of the cracks during each DCDC test with the measured forces, the fracture toughness of the material is estimated [6]. The crack length and force data are correlated with a set of finite element models, and internal energy, energy release rate and fracture toughness are calculated. After the sample is healed and retested, the healing efficiency is defined by the ratio of the new fracture toughness to the virgin fracture toughness.

The initial series of DCDC tests are conducted using the DMA sample repurposed for DCDC testing. The results are not ideal, with healing efficiencies well below the 100% observed in [2]. The healing pressure, times and temperatures are varied with some improvement. The virgin fracture toughness of the current 2MEP4FS polymer is slightly larger than [2].

The DMA results and estimated DCDC fracture toughness indicate improved monomer purity may increase some material properties. Higher purities should translate to more cross-linking bonds, which would have this effect. More DCDC tests with a larger, dedicated sample are needed to give a better indication of healing potential.

ACKNOWLEDGEMENTS

This work was conducted with the support of Air Force Office of Scientific Research grant FA9550-08-1-0314 to UC San Diego.

REFERENCES

[1] Chen X et al, 'New thermally remendable highly cross-linked polymeric materials', Macromolecules 36(6), 1802-1807, 2003.

[2] Plaisted T et al, 'Quantitative evaluation of fracture, healing and re-healing of a reversibly cross-linked polymer', Acta Materialia 55, 5684-5696, 2007.

[3] Plaisted T, Laboratory tour and conversation, San Diego, California USA, October 29, 2009.

[4] Janssen C, 'Specimen for fracture mechanics studies on glass', 10th International Congress on Glass, Kyoto Japan, Ceramic Society of Japan, 1974.

[5] Plaisted T et al, 'Compression-induced axial crack propagation in DCDC polymer samples: experiments and modeling', International Journal of Fracture 141, 447-457, 2006.

[6] Nielsen C, 'Geometric Effects in DCDC Fracture Experiments', Proceedings of the SEM Annual Conference, Albuquerque, New Mexico USA, 2009.

Proceedings of the SEM Annual Conference
June 7-10, 2010 Indianapolis, Indiana USA

Fracture Behavior of Polymeric Foams Under Mixed-Mode Loading

E.E. Gdoutos

Office of Theoretical and Applied Mechanics of the Academy of Athens
School of Engineering, Democritus University of Thrace
GR-671 00 Xanthi, Greece
egdoutos@civil.duth.gr

ABSTRACT

The present work deals with the crack growth behavior in polymeric foams under mixed-mode loading conditions. Polymeric foams are anisotropic materials and cracks generally propagate under mixed-mode conditions. Due to the anisotropy of the material crack kinking occurs even though the applied load is perpendicular to the crack plane. The strain energy density criterion is used for the determination of the critical load of crack initiation and crack growth path under mixed-mode loading. A stress analysis of the plate is performed by a commercial finite element computer program. Results are obtained for the fracture trajectories for various polymeric foams. The study takes place within the frame of linear elastic fracture mechanics of anisotropic media.

Introduction

Cellular materials have extensively been used in sandwich construction due to their excellent properties, such as high specific modulus and strength, low weight, good thermal insulation and low cost. The mechanical behavior of cellular materials has been studied in [1-4]. It was found that the compressive stress-strain behavior of PVC cellular foams consists of an initial relatively small and stiff elastic regime, an extended stress plateau regime and a final regime in which densification of the material takes place. In the stress plateau regime the cells of the foam collapse, while the average stress remains almost constant during the instability spread through the material. Axial compression produces little lateral spreading resulting to almost zero Poisson's ratio. When all of the cells collapse the material is densified and its stiffness increases. As a consequence of such behavior foams change their volume during plastic compression. This is contrary to dense solids which are incompressible during plastic deformation. On the contrary, the uniaxial stress-strain behavior in tension is nonlinear elastic without any identifiable yield region.
The objective of this work is to study the mixed-mode crack growth behavior in a cross-liked polymeric foam under the commercial name Divinycell H250 with a density of 250 Kg/m^3. The case of a plate with a crack perpendicular to the applied uniaxial stress is analyzed by finite elements. The results of stress analysis are coupled with the strain energy density theory to obtain crack growth trajectories for various values of the angle of orientation of the axes of anisotropy of the material with respect to the loading direction.

Mechanical Characterization of Foam Materials

The study will include many types of fully cross-linked PVC closed-cell foams under the commercial name Divinycell H80, H100, H160, H250 with densities of 80, 100, 160 and 250 kg/m^3, respectively, and balsa wood. Figure 1 shows the stress-strain curves of Divinycell H250 in tension and compression. Note that the uniaxial stress-strain behavior in tension is nonlinear elastic without any identifiable yield region. In uniaxial compression the material is nearly elastic-perfectly plastic in the initial stage of yielding. Mechanical properties of materials studied are shown in Table 1. All Divinycell H80, H100, H160 and H250 materials exhibit axisymmetric anisotropy with much higher stiffness and strength in the cell (3-direction) than the in-plane direction. The ratio of the stiffness in the cell (e-

T. Proulx (ed.), *Time Dependent Constitutive Behavior and Fracture/Failure Processes, Volume 3*, Conference Proceedings of the Society for Experimental Mechanics Series 15, DOI 10.1007/978-1-4419-9794-4_2, © The Society for Experimental Mechanics, Inc. 2011

direction) to the in-plane direction is of the order of 1.5. The anisotropy of balsa wood is more pronounced with the above ratio equal to 42. All materials display different behavior in tension and compression with tensile strengths much higher than corresponding compressive strengths.

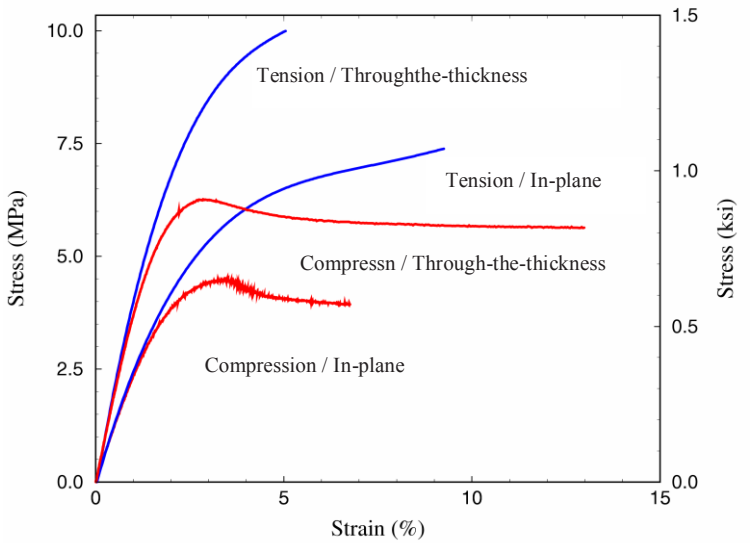

Fig. 1: Stress-strain curves of Divinycell H250 PVC foam, in tension and compression.

Strain Energy Density Criterion

The basic quantity in the strain energy density theory for crack problems is the strain energy density function *dW/dV*, which can be put in the form [5-7]:

$$\frac{dW}{dV} = \frac{S}{r} \tag{1}$$

where S is the strain energy density factor and r is the distance measured from the crack tip.

For plane elastic problems under conditions of plane stress the strain energy density function is given by

$$\frac{dW}{dV} = \frac{1}{2}\left(\sigma_x \varepsilon_x + \sigma_y \varepsilon_y + \tau_{xy}\gamma_{xy}\right) \tag{2}$$

where σ_x, σ_y, τ_{xy} are the stress and ε_x, ε_y, γ_{xy} are the strain components.

The strain energy density factor S is given by [5-7]:

$$S = A_{11}k_1^2 + 2A_{12}k_1k_2 + A_{22}k_2^2 \tag{3}$$

where

$$A_{11}=\frac{1}{4}\left[\alpha_{11}^{'}A^2+\alpha_{22}^{'}C^2+\alpha_{66}^{'}E^2+2\alpha_{12}^{'}AC+2\alpha_{16}^{'}AE+2\alpha_{26}^{'}CE\right] \tag{4a}$$

$$A_{12}=\frac{1}{4}\left[\alpha_{11}^{'}AB+\alpha_{22}^{'}CD+\alpha_{66}^{'}EF+\alpha_{12}^{'}(AD+BC)+\alpha_{16}^{'}(AE+BE)+2\alpha_{26}^{'}(CE+DE)\right] \tag{4b}$$

$$A_{22}=\frac{1}{4}\left[\alpha_{11}^{'}B^2+\alpha_{22}^{'}D^2+\alpha_{66}^{'}F^2+2\alpha_{12}^{'}BD+2\alpha_{16}^{'}BF+2\alpha_{26}^{'}DF\right] \tag{4c}$$

with

$$A=\mathrm{Re}\left[\frac{s_1s_2}{s_1-s_2}\left(\frac{s_2}{z_2}-\frac{s_1}{z_1}\right)\right],\quad B=\mathrm{Re}\left[\frac{1}{s_1-s_2}\left(\frac{s_2^2}{z_2}-\frac{s_1^2}{z_1}\right)\right] \tag{5a}$$

$$C=\mathrm{Re}\left[\frac{1}{s_1-s_2}\left(\frac{s_1}{z_2}-\frac{s_2}{z_1}\right)\right],\quad D=\mathrm{Re}\left[\frac{1}{s_1-s_2}\left(\frac{1}{z_2}-\frac{1}{z_1}\right)\right] \tag{5b}$$

$$E=\mathrm{Re}\left[\frac{s_1s_2}{s_1-s_2}\left(\frac{1}{z_1}-\frac{1}{z_2}\right)\right],\quad F=\mathrm{Re}\left[\frac{1}{s_1-s_2}\left(\frac{s_1}{z_2}-\frac{s_2}{z_2}\right)\right] \tag{5c}$$

and

$$k_1=\frac{K_1}{\sqrt{\pi}}\quad k_2=\frac{K_2}{\sqrt{\pi}}. \tag{6}$$

In the above equations α_{ij} are the compliance coefficients of the anisotropic material relating stress and strain, K_1 and K_2 are the stress intensity factors which dictate the stress field in the neighborhood of the crack tip, $z_1 = x_1 + iy_1$, $z_2 = x_1 - iy_1$ are complex numbers, and the other coefficients are related to the anisotropic behavior of the material [4-6].

Consider a plate with a through-the-thickness crack of length 2a that is subjected to a uniaxial stress σ perpendicular to the crack plane. The axıs x´ of orthotropy of the material makes an angle φ with the crack axis, x (Fig. 1). The compliance coefficients $\alpha_{ij}^{'}$ referred to the system x'y' (Fig. 1) are related to the coefficients a_{ij} refereed to the system xy by the following equations [5-7]

$$\alpha_{11}^{'}=\alpha_{11}\cos^4\varphi+(2\alpha_{12}+\alpha_{66})\sin^2\varphi\cos^2\varphi+\alpha_{22}\sin^4\varphi+(\alpha_{16}\cos^2\varphi+\alpha_{26}\sin^2\varphi)\sin 2\varphi,$$

$$\alpha_{22}^{'}=\alpha_{11}\sin^4\varphi+(2\alpha_{12}+\alpha_{66})\sin^2\varphi\cos^2\varphi+\alpha_{22}\cos^4\varphi-(\alpha_{16}\cos^2\varphi+\alpha_{26}\cos^2\varphi)\sin 2\varphi,$$

$$\alpha_{12}^{'}=\alpha_{12}+(\alpha_{11}+\alpha_{22}-2\alpha_{12}-\alpha_{66})\sin^2\varphi\cos^2\varphi+\frac{1}{2}(\alpha_{26}-\alpha_{16})\sin 2\varphi\cos 2\varphi,$$

$$\alpha_{66}^{'}=\alpha_{66}+4(\alpha_{11}+\alpha_{22}-2\alpha_{12}-\alpha_{66})\sin^2\varphi\cos^2\varphi+2(\alpha_{26}-\alpha_{16})\sin 2\varphi\cos 2\varphi,$$

$$\alpha_{16}' = [\alpha_{22}\sin^2\varphi - \alpha_{11}\cos^2\varphi + \frac{1}{2}(2\alpha_{12}+\alpha_{66})\cos 2\varphi]\sin 2\varphi + \alpha_{16}\cos^2\varphi(\cos^2\varphi - 3\sin^2\varphi)$$
$$+ \alpha_{26}\sin^2\varphi(3\cos^2\varphi - \sin^2\varphi),$$
$$\alpha_{26}' = [\alpha_{22}\sin^2\varphi - \alpha_{11}\sin^2\varphi - \frac{1}{2}(2\alpha_{12}+\alpha_{66})\cos 2\varphi]\sin 2\varphi + \alpha_{16}\sin^2\varphi(3\cos^2\varphi - \sin^2\varphi)$$
$$+ \alpha_{26}\cos^2\varphi(\cos^2\varphi - 3\sin^2\varphi),$$
(7)

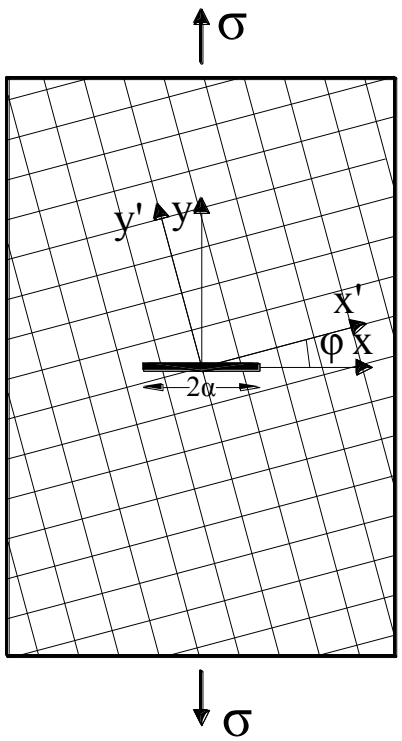

Fig.1 A cracked plate with a crack perpendicular to the applied load at an angle with the direction of the axis of material orthotropy of the material

According to the strain energy density theory unstable crack growth takes place in the radial direction along which S becomes minimum. This condition is mathematically put in the form:

$$\frac{\partial S}{\partial \theta} = 0, \quad \frac{\partial^2 S}{\partial \theta^2} > 0. \tag{8}$$

This equation is used for the determination of the critical angle θ_c of initial crack growth.

Unstable crack growth occurs when $S_{min}(\theta_c)$ takes its critical value S_c which is an intrinsic material parameter, that is,

$$S_{min}(\theta_c) = S_c. \tag{9}$$

Equations (8) and (9) will be used for the determination of the critical quantities at crack instability for the case of Fig. 1.

Results

Results were obtained for an orthogonal plate with a crack perpendicular to the applied uniaxial stress. The axis of material symmetry made an angle φ with respect to the crack axis (Fig. 1). The stress analysis of the plate was performed by the ABACUS computer program. Figs 2 and 3 present the finite element idealization of the specimen in the vicinity of the crack tip. Fig. 4 presents the contours of strain energy density function near the crack tip. Note that due to material orthotropy the contours are not symmetrical, but inclined with respect to the crack axis. Fig. 5 presents the variation of strain energy density function dW/dV along the circumference of a circle centered at the crack tip for φ = 0, 30^0 and 60^0. The values of θ at which dW/dV presents local minima are the critical values of the angle of initial crack growth. Fig. 6 presents the variation of θ_c versus the angle φ of the orientation of the axis of material orthotropic symmetry with respect to the crack axis. Note that the critical angle θ_c increases versus φ reaching a maximum value after which it decreases and becomes zero when the crack is along the axis of material symmetry.

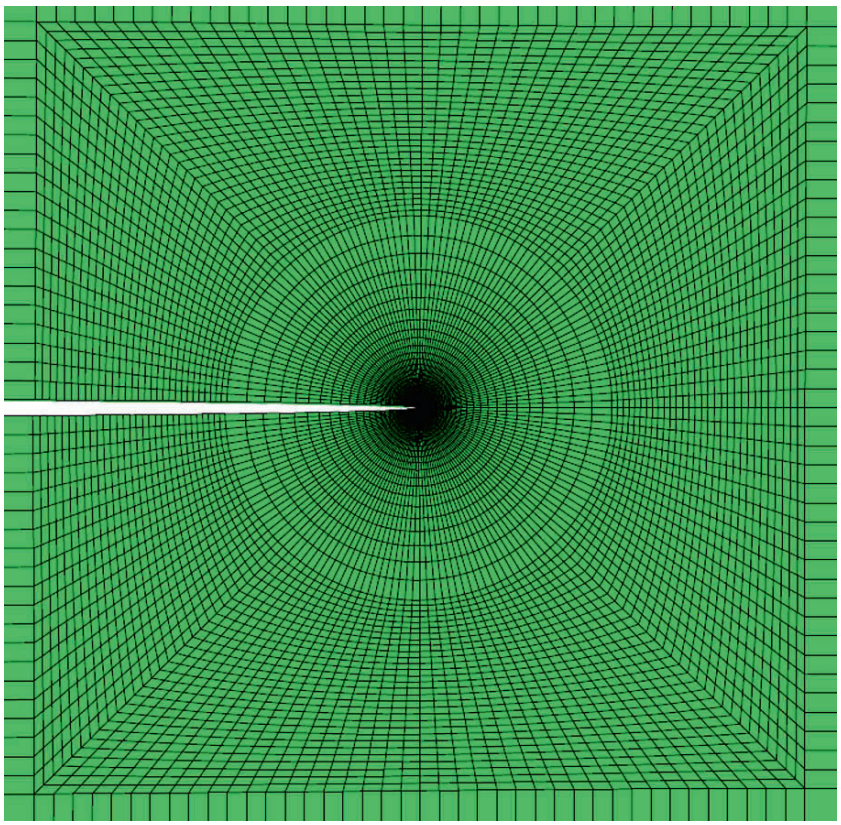

Fig. 2 Finite element mesh near the crack tip

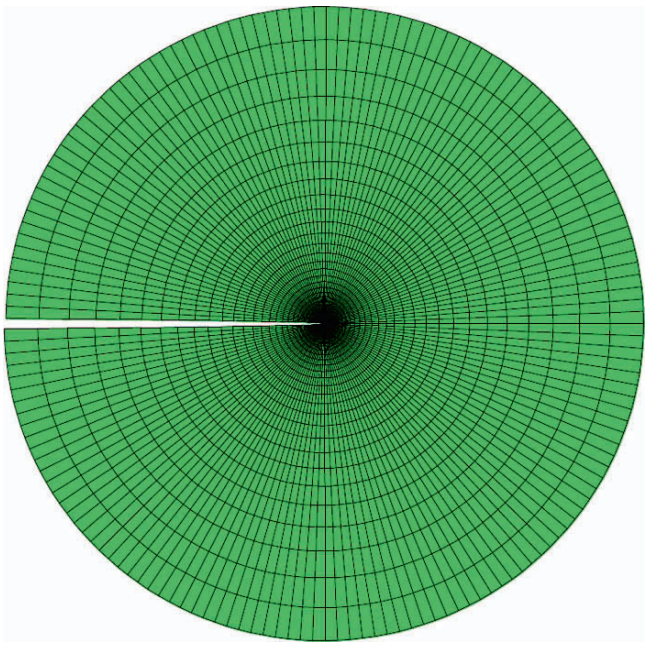

Fig. 3 Detailed mesh

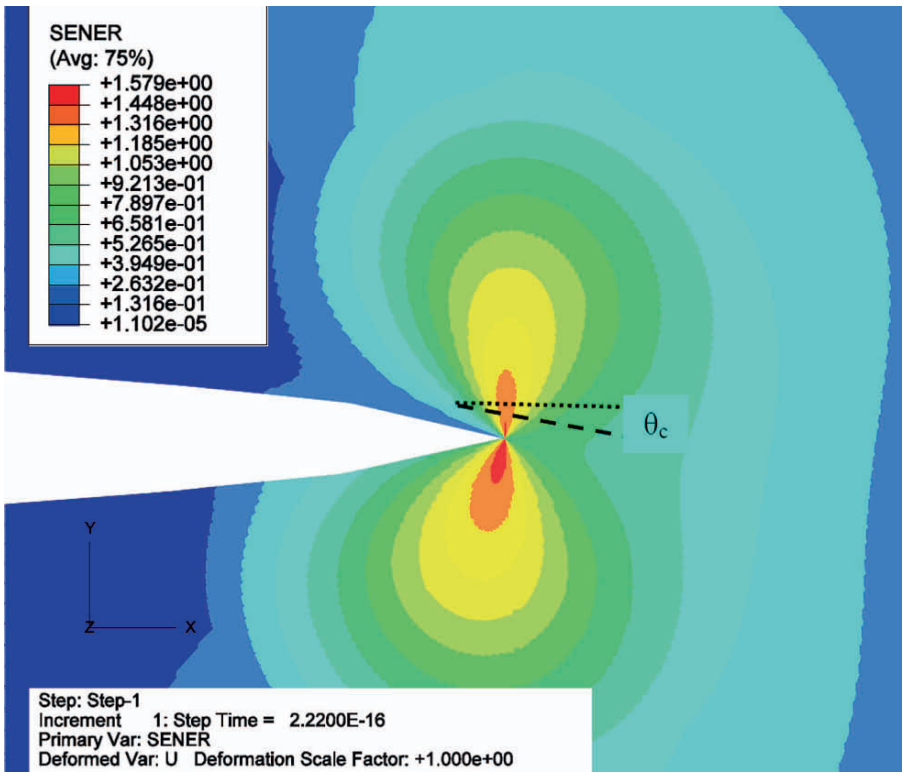

Fig. 4 Contours of strain energy density function near the crack tip for $\varphi = 45^0$

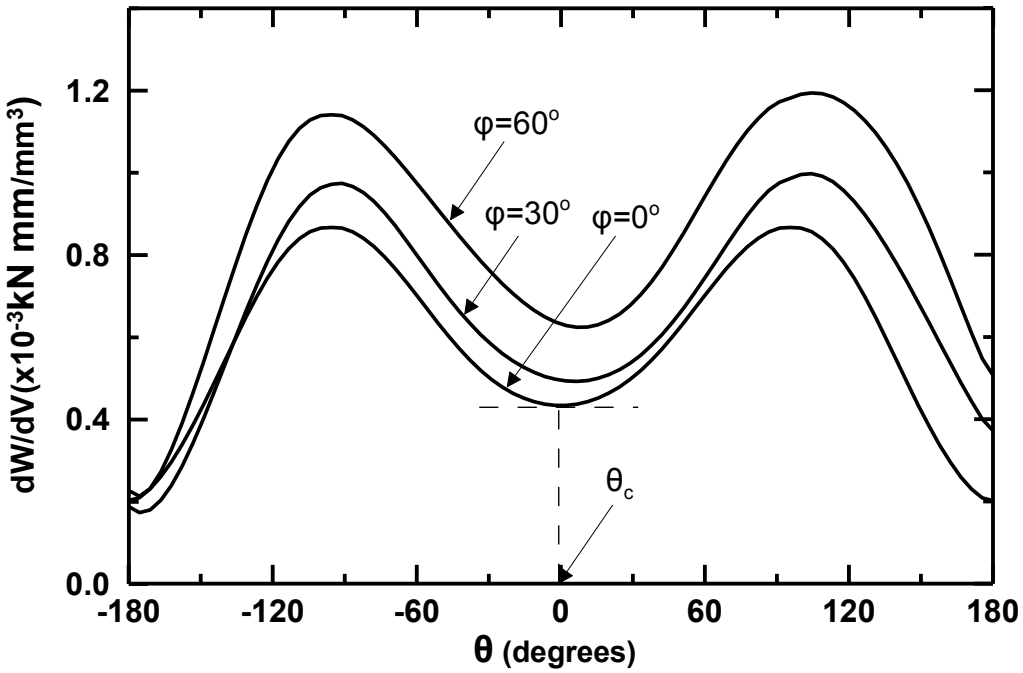

Fig. 5 Variation of strain energy density function dW/dV versus polar angle θ around the circumference of a circle surrounding the crack tip for φ =0, 30^0 and 60^0. Crack grows in the direction of local minimum of strain energy density function

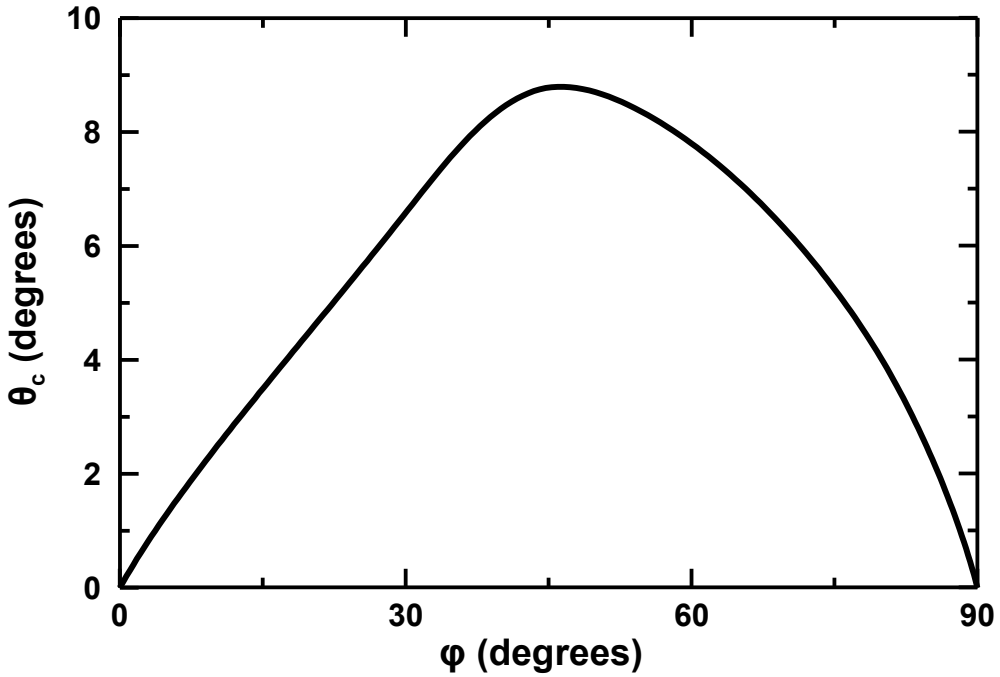

Fig. 6 Critical angle of crack growth θ_c versus angle φ of orientation of axes of material symmetry with respect to the crack axis

Conclusions

The crack growth in polymeric foams which present mechanical anisotropic behavior was studied. The case of a cracked plate subjected to a uniaxial stress perpendicular to the crack plane with the axes of material anisotropy at an angle with respect to the crack plane is analyzed. From the results of stress analysis in conjunction with the strain energy density theory the mixed-mode crack growth behavior of the plate was obtained. Results for the angle of initial crack growth for various orientations of the axes of anisotropy of the material with respect to the loading direction were reported.

References

[1] Gibson L.J. and Ashby, M.F., "Cellular Solids," Cambridge University Press (1997).
[2] Gdoutos, E.E., Daniel, I.M. and Wang, K.-A. "Multiaxial Characterization and Modelling of a PVC Cellular Foam,"J. Therm. Comp. Mat. **14**, 365-373 (2001).
[3] Gdoutos, E.E., Daniel, I.M. and Wang, K.-A., "Failure of Cellular Foams under Multiaxial Loading," Comp Part A, **33**, 163-176 (2002).
[4] Gdoutos E.E. and Abot, J.L., "Indentation of a PVC Cellular Foam," In: *Recent Advances in Experimental Mechanics - In Honor of Isaac M. Daniel,* Kluwer Academic Publishers pp. 55-64 (2002).
[5] Gdoutos, E.E., "Problems of Mixed-Mode Crack Propagation," Martinus Nijhoff Publishers (1984).
[6] Gdoutos, E.E., "Fracture Mechanics Criteria and Applications," Kluwer Academic Publishers (1990).
[7] Gdoutos, E.E., "Fracture Mechanics – An Introduction," Second Edition (2005).

Proceedings of the SEM Annual Conference
June 7-10, 2010 Indianapolis, Indiana USA

Coupled Experimental and Computational Analysis of Fracture Path Selection in PMMA Blocks

C. L. Tsai[1], Y. L. Guan[1], R. C. Batra[1], D. C. Ohanehi[1], J. G. Dillard[2], E. Nicoli[1], D. A. Dillard[1],
[1]Department of Engineering Science and Mechanics
[2]Department of Chemistry
Virginia Polytechnic Institute and State University
Blacksburg, Virginia

Abstract

While developing experimental and computational tools for analyzing crack path selection and failure loci in adhesively bonded joints, we have initially applied these tools for studying crack paths in pre-notched monolithic blocks of polymethyl methacrylate (PMMA), a common material for conducting brittle fracture experiments. Specimen configurations similar to the compact tension specimen but of varying length/width ratios were used to explore the effect of the T-stress on destabilizing the crack from growing straight along its original direction. Asymmetric versions of this geometry were also used to determine the effect of imposed mode mixity on crack path selection. These test configurations provided useful data for checking the robustness of the computational software based on a meshless local Petrov-Galerkin formulation of the boundary-value problem. The PMMA was assumed to be linear elastic, homogeneous and isotropic. A crack was assumed to initiate when the maximum principal tensile stress reached a critical value and propagate in the direction of the eigenvector of this stress. Effects of the mode-mixity on the crack propagation have been studied.

Introduction

Crack trajectories in adhesive bonds and brittle materials under mixed-mode loading are of interest in applications in biomedical implant, microelectronic, transportation, and energy devices and machinery. PMMA (polymethyl methacrylate), a transparent polymer, is the material used in the current study on crack propagation. PMMA has been employed in numerous studies to observe crack trajectories [1-5] in a range of specimen geometries including semi-circular bend (SCB), four-point bend (FPB), Brazilian disc (BD), and diagonally loaded square plate (DLSP). The current work covers a first series of tests to explore crack trajectories under mixed-mode loading of monolithic PMMA specimens.

Using angled-cracked plate specimens, Smith et al. studied the mixed-mode fracture response of PMMA blocks (and brittle materials, in general) and explained crack trajectories in terms of the sign of the T-stress [3]. The T-stress, an important nonsingular term in Williams expansion[6] of stresses near a crack tip, is tangent to the crack, depends on the specimen geometry and loading conditions, and governs the stability of the growing crack. Aliha et al., using four specimen geometries, demonstrated the geometry dependence of the measured fracture toughness, and explained the dependence using the sign of the T-stress [1]. The mode mixity was varied from pure mode I to pure mode II through changes in the angle of the initial crack for various specimens, and the corresponding fracture toughness was computed. The crack trajectories for a series of SCB specimens were very instructive, showing a straight crack for pure mode I (initial crack inclination angle = 0^o) and ending with a crack kink for mode II (initial crack inclination angle = 50^o) [1].

For the current study, experiments were conducted on notched PMMA blocks that were similar to compact tension (CT) specimens, but had varying length/width ratios to explore effects of fracture mode mixity and the T-stress. The findings of these tests can provide an understanding of crack propagation in monolithic and isotropic materials and validate computational models being developed. For the numerical studies, the meshless local Petrov-Garlekin formulation of the boundary-value problem using the symmetric smoothed particle hydrodynamics (SSPH) basis functions for the trial solution was employed. Values of various parameters in the weight (or the test) function were optimized by studying the mode-I fracture problem for which analytical solution is known. Results of the computational studies were used to compute the stress concentration factor (SCF), the stress intensity factor (SIF), and the T-stress for simple tensile deformations of a square plate with a hole at the center.

T. Proulx (ed.), *Time Dependent Constitutive Behavior and Fracture/Failure Processes, Volume 3*, Conference Proceedings of the Society for Experimental Mechanics Series 15, DOI 10.1007/978-1-4419-9794-4_3, © The Society for Experimental Mechanics, Inc. 2011

The same software was used to analyze test configurations, and computed results were compared with the experimental findings. The software was also used to design experimental configurations that will give desired mode-mixity.

Experimental Study Using PMMA

Fracture tests were conducted on CT and modified CT specimens of 12.7 mm thick PMMA sheets. All tests were conducted on an Instron 5800R machine using a 5kN load cell. With one arm of the CT specimen fixed by the pin and the clevis, the other arm of the specimen was displaced downwards by the loading clevis.

CT Specimen Tests

A standard CT specimen (recommended in ASTM D 5045), shown in Fig. 1, has the thickness B=12.7mm (1/2''), w=25.4mm (1'') and a=12.7mm (0.5'') [7]. Tests on the CT specimens were conducted using a crosshead displacement rate of 10 mm/min, as recommended in ASTM D5045. To ensure consistency in K_{Ic} values for all the specimens, sharp initial cracks were necessary. The sharp initial cracks were produced by driving a wedge into the specimens. The initial cracks were made carefully with a razor blade and a wooden hammer after machining the notches. The blade and two shims were inserted in the notch to center the blade and to keep it parallel to the centroidal axis of the notch. Then, gentle hammer blows were applied to the back of the blade, initiating a tiny crack, only a few millimeters in front of the blade, and avoiding a large initial crack, propagating too far into the specimen. A picture of three specimens, prior to the tests, is shown in Fig. 2.

Relationships between the load and the crosshead displacement for three specimens are exhibited in Fig. 3. From these results, the average value of K_{Ic} was determined to be 1.056 ± 0.029 MPa$\sqrt{m}$. As expected, the crack trajectories remained straight.

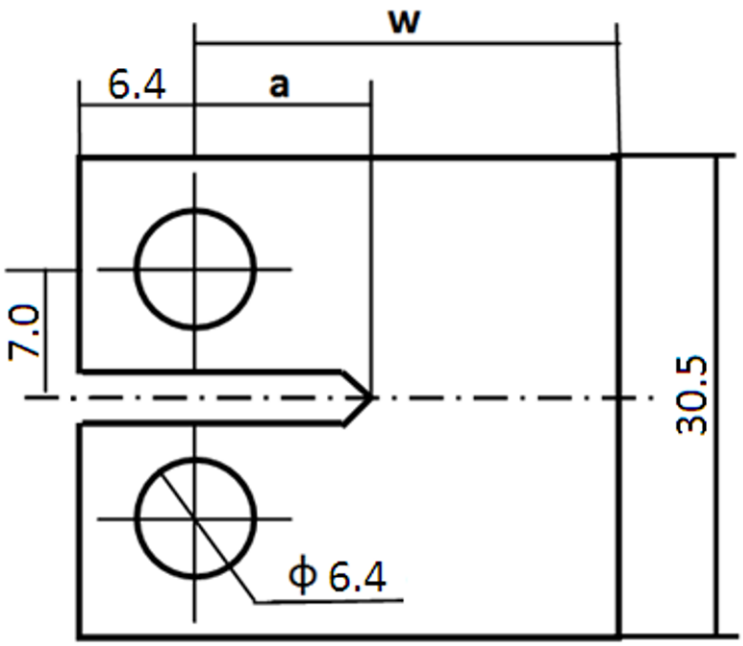

Fig. 1. PMMA CT Specimen with w=25.4mm (1'') and a=12.7mm (0.5''); B, specimen thickness = 12.7mm (0.5''). (All dimensions in mm).

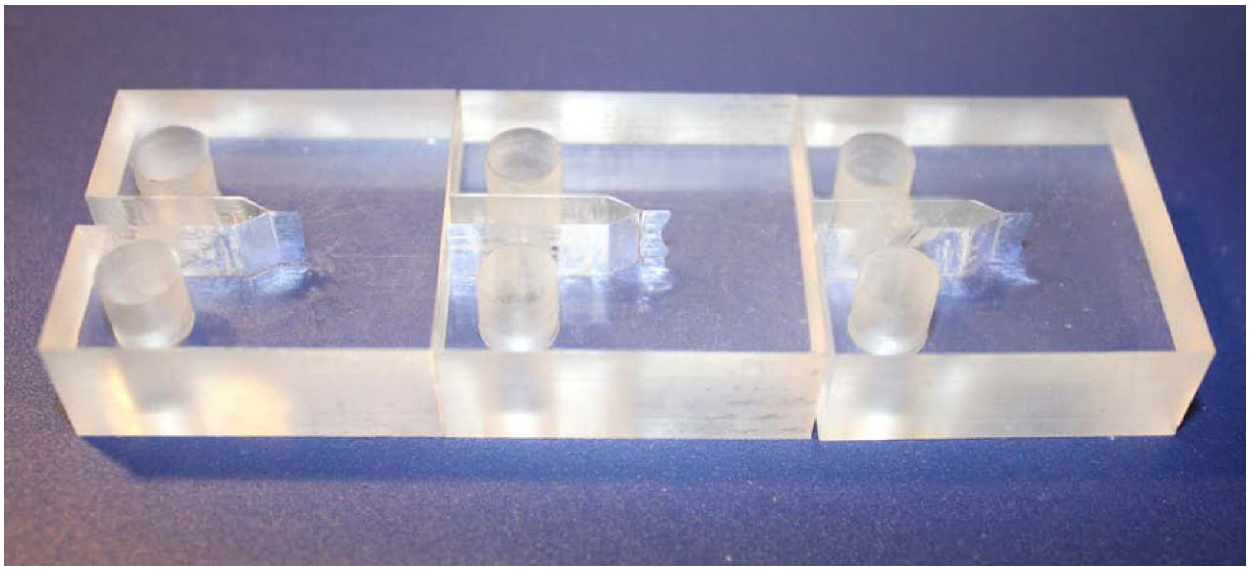

Fig. 2. Notches and Initial Cracks before the Tests.

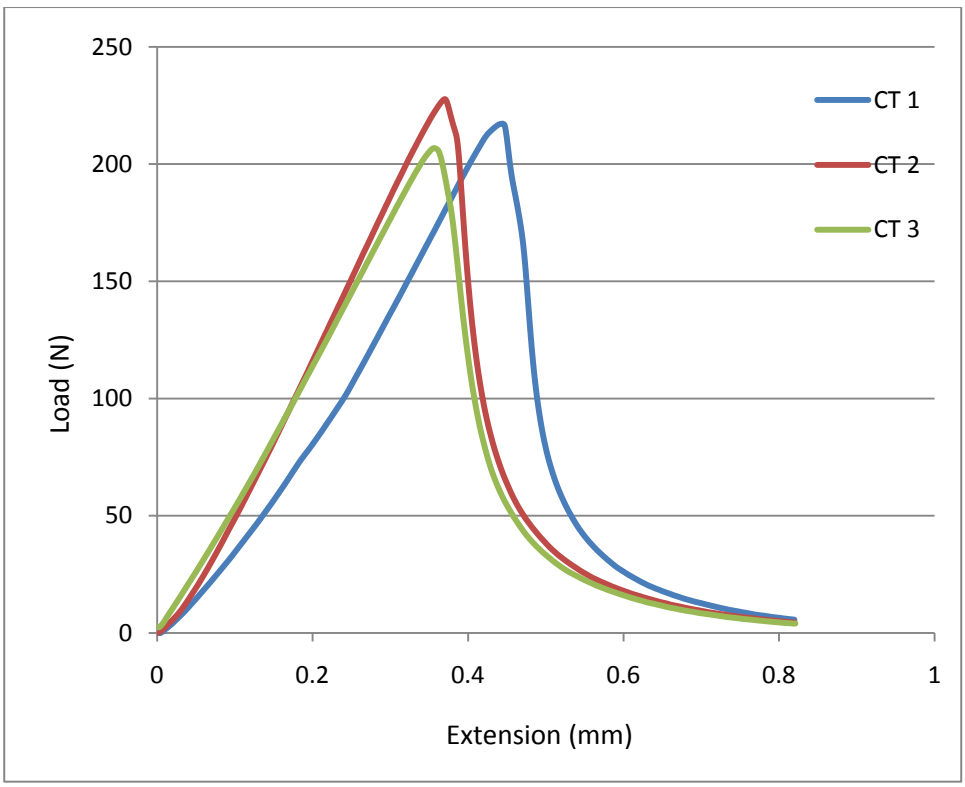

Fig. 3. Load-Extension Curves for the three CT specimens.

Effect of Notch Asymmetry on Crack Path Trajectory

Unlike specimens described above that had a notch placed along the horizontal centroidal axis, specimens with the notch and the starting crack not located along the horizontal centroidal axis("modified" or "asymmetric" CT

specimens) were also tested. The ratio of the specimen height above the notch to that below it is 2 (cf. Fig. 4.), and an unloaded specimen is shown in Figs. 4 and 5. In the asymmetric specimen, the mode mixity initiated as soon as the crack started propagating. Also, the diameter of the holes was reduced to 3.2mm (1/8'') to make room

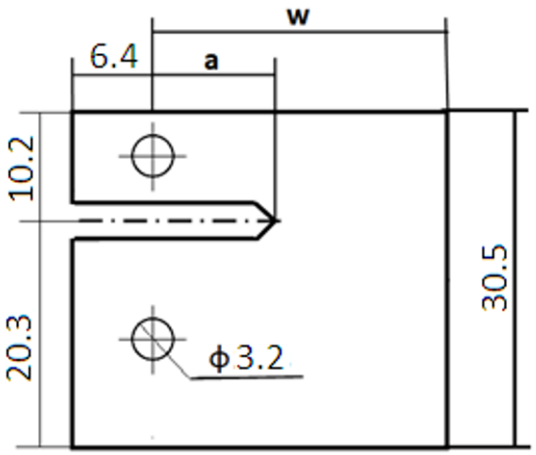

Fig. 4. PMMA asymmetric CT specimens with w=25.4mm (1''), a=12.7mm (0.5''), and the ratio of the specimen height above the notch to that below is 2; B, specimen thickness = 12.7mm (0.5''). (All dimensions in mm).

Fig. 5a. Asymmetric CT specimens with notch and initial crack

for the notch in the narrower arm of the asymmetric geometry. Because of the mode mixity, the crack path was inclined in the direction of the smaller arm (on the top in Fig. 5b). However, the crack path changed direction and became straight (almost perpendicular to the right edge in Fig. 5b) when the crack approached the edge. Additional details on this observation will be discussed in the section on the numerical study and comparisons will be made with the computed results.

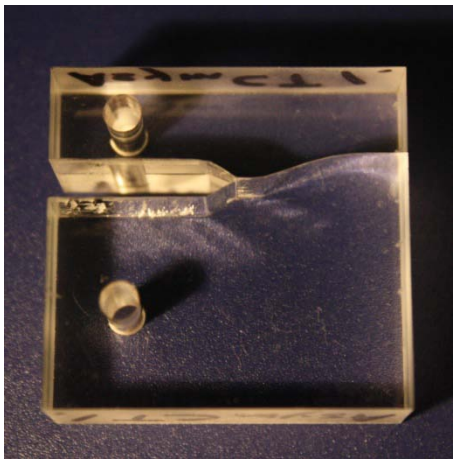

Fig. 5b. Asymmetric CT Specimen with Crack after Test.

Effect of Ratio of Specimen Length / Crack Length on Crack Path Trajectories

The ratio of the specimen length and the initial crack length (w/a) was expected to be important for crack stability. Accordingly, PMMA specimens with different values of w/a were tested. The crack length (a) was varied from 12.7mm (0.5''), to 25.4mm (1''), and 38.1mm (1.5'') while the value of w=101.6 mm (4'') was kept constant; thus w/a equaled 8, 4, and 2.67. The other dimensions were the same as those for the CT specimen. The crack paths are shown in Fig. 6.

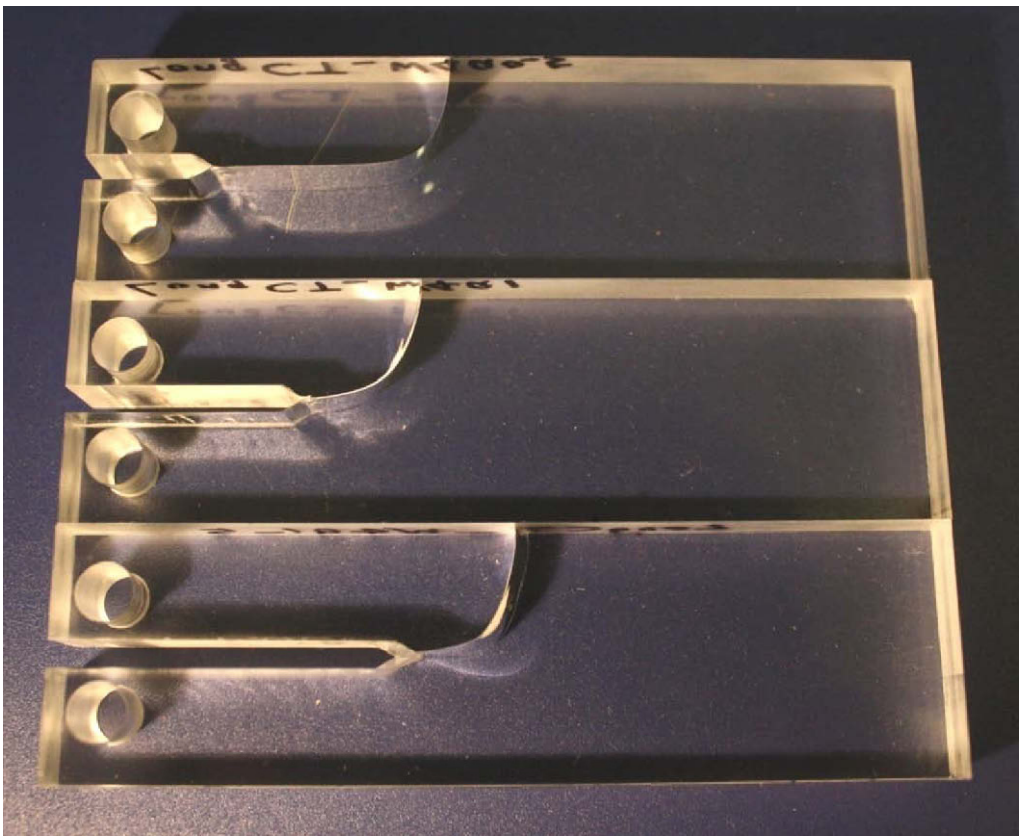

Fig. 6. Trajectories of the crack path of the specimens with different initial crack lengths (From top to bottom: a=12.7mm, 25.4mm, and 38.1mm.)

As the ratio, w/a, was varied from 8, to 4, and 2.67, the crack path became curved and deviated towards one side. The curvatures of the three crack trajectories were almost the same. For specimens with a=25.4mm and 38.1mm, (w/a ≤ 4), the crack curved to one side quickly as soon as propagation started. However, when the initial crack length, a, was 12.7mm (w/a=8), the crack propagated along a straight line for almost 20mm before the deviation started. This suggests that, for small crack lengths, the T-stress is negative and the crack is stable initially. When the crack length increased to some critical value, the T-stress turned positive, destabilizing the crack, and the crack deviated to one side. Additional details will be shown and discussed when test results are compared with those from numerical simulations.

Numerical Studies

Both the finite element (FE) and meshless methods were employed in the numerical studies; the former used the commercial software, ABAQUS™, and the latter our in-house developed computer code.

Finite Element Analysis

The X-FEM (extended finite element method) implemented in ABAQUS™ v.6.9 using 4-node plane strain element, CPE4R, was employed to analyze deformations of the asymmetric CT specimen used in the experimental studies [8, 9]. Assigned boundary conditions simulated as closely as possible those likely to occur in the test configurations. With the loading points shown in Fig. 7a, the following boundary conditions were used in the numerical work.

Load point 1: fixed in x and y directions: u_x= 0, u_y= 0;
Load point 2: fixed in the x-direction and y-displacement prescribed: u_x= 0, u_y= -1 mm.

From tensile tests on PMMA at a strain rate of 0.00014/s and room temperature, Elices and Guinea [10] obtained the following average values: Young's modulus $E = 3000 \pm 30$ MPa, yield limit stress $\sigma_{0.2} = 43.9 \pm 0.7$MPa, rupture stress $\sigma_R = 74.9 \pm 0.2$MPa, and Poisson's ratio $\upsilon = 0.4$; these values were used in our simulations. The maximum principal stress of the damage initiation was set equal to $\sigma_{0.2} = 44$ MPa. Damage evolution was based on fracture energy ($G_{Ic} = G_{IIc} = \frac{{K_{Ic}}^2}{(E/(1-\upsilon^2))} = 312.2\, J/m^2$), linear softening, and mixed mode behavior of power law (α=1) [10]. X-FEM results are show in Figure 7b and will be discussed after meshless methods are introduced.

Analysis of the Problem by the SSPH Method

Meshless methods were introduced in 1970's, and include the Smooth Particle Hydrodynamics (SPH) method [11], Element-Free Galerkin method (EFGM) [12-14], Reproducing Kernel Particle Method (RKPM) [15], Meshless Local Petrov-Galerkin (MLPG) [16], Modified Smoothed Particle Hydrodynamics (MSPH) [17, 18] and Symmetric Smoothed Particle Hydrodynamics (SSPH) [19, 20]. Like the FE and the boundary element methods, meshless methods are used to find an approximate solution of an initial-boundary-value problem with the difference that no element connectivity is needed in a meshless method. Various meshless methods differ in the construction of basis functions for the trial solution.

The EFGM [12-14] has been used to study linear elastic fracture mechanics (LEFM) problems and uses basis functions found by the moving least squares (MLS) method. However, it employs a background mesh to numerically evaluate various integrals appearing in the weak formulation of the problem and thus is not truly meshless. The enriched basis functions [21] are used to capture the stress singularity near a crack-tip without having a very fine distribution of particles (nodes) there. The computational efficiency can be improved by using an appropriate weight or test function [22] and basis functions that better capture singularity of fields near the crack tip [23]. Advantages of the SSPH method are that spatial derivatives of the trial solution are computed without differentiating the basis functions, and the stiffness matrix is symmetric. Our implementation of the SSPH method does not have the enriching terms to capture the stress singularity. We thus use a fine particle distribution around the crack tip. Additional details of the numerical scheme are provided in [24] where results for the CT specimen are also included.

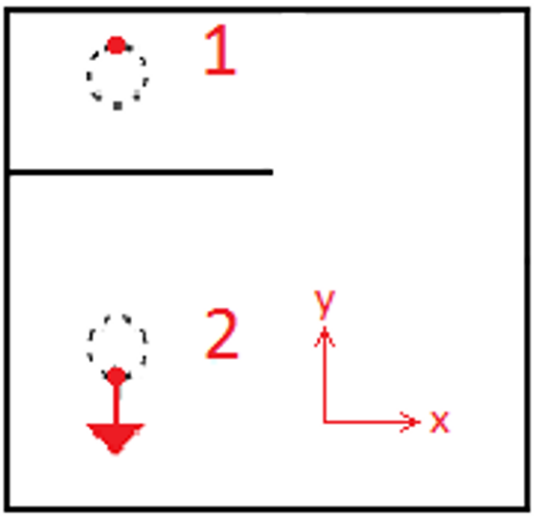

Fig. 7a. Boundary conditions for the asymmetric CT specimen used while analyzing deformations with the commercial software ABAQUS™

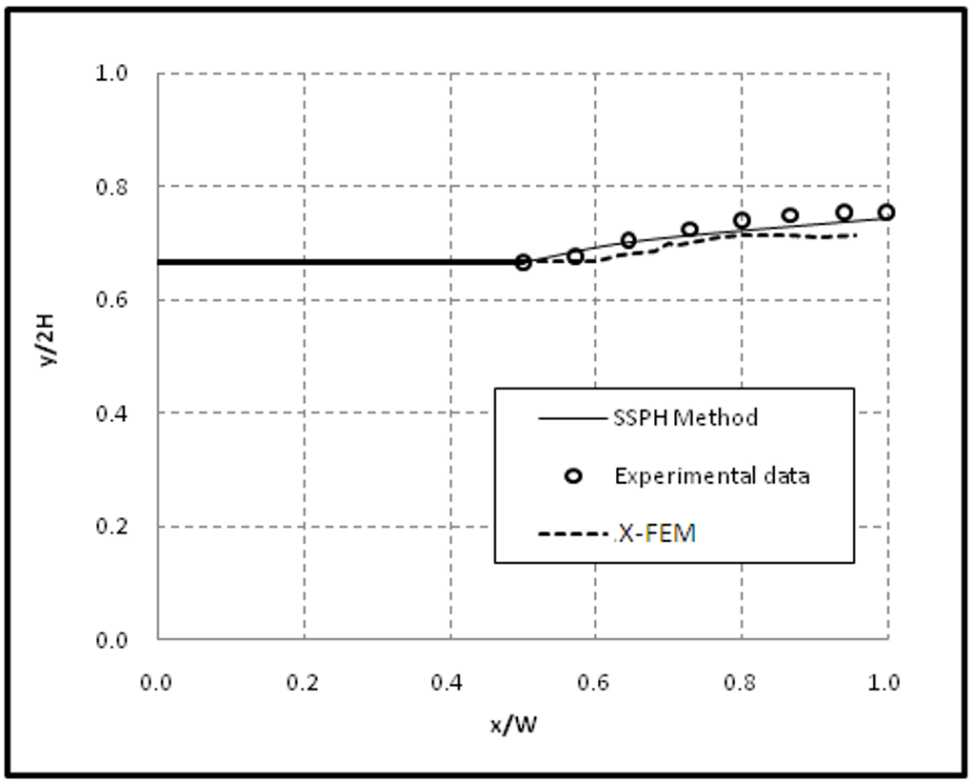

Fig. 7b. Comparison of computed and experimental crack trajectories for an asymmetric CT specimen [The curve denoted by "SSPH Method" will be dicussed in the next section.]

Analysis of deformations of the Double edge notched (DEN) specimen by the SSPH Method

Since the T-stress is expected to play a significant role in the analysis of the crack problem, we first describe results for the mode-I problem obtained by the SSPH method. Deformations of the standard DEN specimen with H=3mm, B=1mm, the crack length ratio (a/B) = 0.2, E = 70GPa and $\nu = 0.3$ have been analyzed. The specimen is subjected to a uniform axial traction S as shown in Fig. 8. Because the specimen geometry and the boundary conditions are symmetric about the x_2-axis, deformations of only the right-half of the specimen are studied. The

analytical expressions for the stress field near the crack-tip are [25]:

$$\begin{bmatrix} \sigma_{11} & \sigma_{12} \\ \sigma_{12} & \sigma_{22} \end{bmatrix} = \frac{K_I}{\sqrt{2\pi r}} \cos(\frac{\theta}{2}) \begin{bmatrix} 1-\sin(\frac{\theta}{2})\sin(\frac{3\theta}{2}) & \sin(\frac{\theta}{2})\sin(\frac{3\theta}{2}) \\ \sin(\frac{\theta}{2})\sin(\frac{3\theta}{2}) & 1+\sin(\frac{\theta}{2})\sin(\frac{3\theta}{2}) \end{bmatrix} + \begin{bmatrix} T & 0 \\ 0 & 0 \end{bmatrix} + O(\sqrt{r}) \quad (1)$$

where (r,θ) are the cylindrical coordinates of a point with the origin located at the crack tip. From Eq. (1), the T-stress along the crack tip, obtained by setting $\theta = 0$, is given by

$$T = \sigma_{11} - \sigma_{22} \quad (2)$$

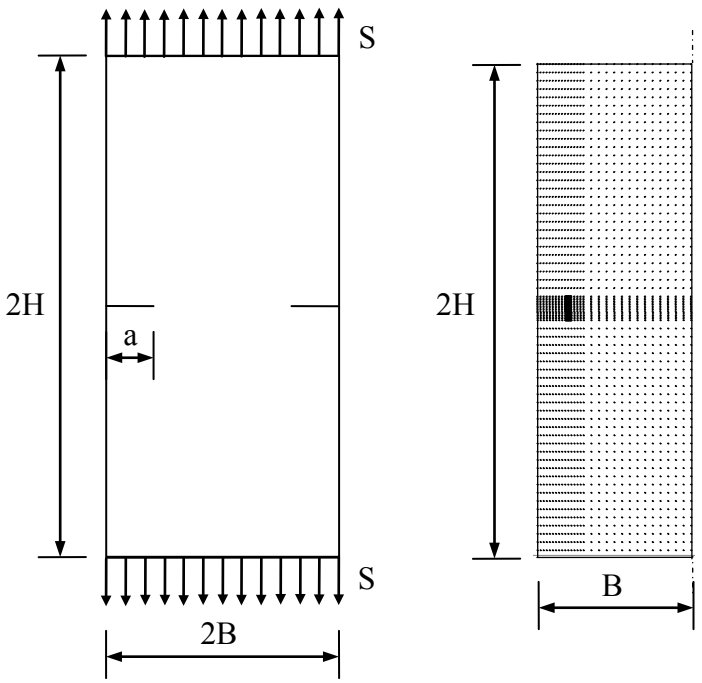

Fig. 8. Double edge notched (DEN) specimen and particles distribution of half model

The computed value, -0.501S, of the T-stress agrees well with of the -0.508S obtained by Kfouri [26].

Analysis of deformations of the Double Cantilever Beam (DCB) specimen by the SSPH Method

The crack trajectories computed by the SSPH method for the DCB specimen shown in Fig. 9 were compared with those found experimentally. Dimensions and material properties for the DCB specimen are: length, $W = 25.4mm$, $2H = 30.5mm$, $a = 12.7mm$, $E = 3.10$ GPa and $\upsilon = 0.35$. A plane strain state of deformation was assumed to prevail in the DCB.

We employed the crack initiation criterion used by Erdogan [27], i.e., a crack initiates when the maximum principal tensile stress reaches a critical value and it propagates in the direction of the eigenvector of this stress. In cylindrical coordinates with the origin at the crack-tip, the stress fields near the crack-tip are [27]

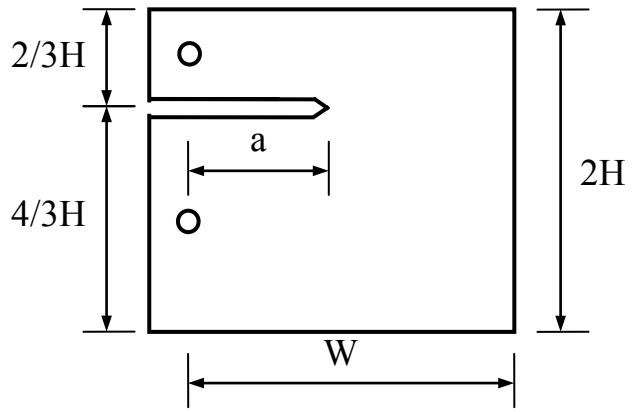

Fig. 9 Double cantilever beam specimen

$$\sigma_{rr}=\frac{1}{\sqrt{2\pi r}}\cos\frac{\theta}{2}\left[K_I\left(1+\sin^2\frac{\theta}{2}\right)+K_{II}\left(\frac{3}{2}\sin\theta-2\tan\frac{\theta}{2}\right)\right]+T\cos^2\theta \tag{3}$$

$$\sigma_{\theta\theta}=\frac{1}{\sqrt{2\pi r}}\cos\frac{\theta}{2}\left[K_I\cos^2\frac{\theta}{2}-\frac{3}{2}K_{II}\sin\theta\right]+T\sin^2\theta \tag{4}$$

$$\sigma_{r\theta}=\frac{1}{\sqrt{2\pi r}}\cos\frac{\theta}{2}\left[K_I\sin\theta+K_{II}(3\cos\theta-1)\right]+T\sin^2\theta \tag{5}$$

where σ_{rr}, $\sigma_{\theta\theta}$ and $\sigma_{r\theta}$ are, respectively, the radial, the circumferential and the shear stresses, K_I and K_{II} are the Mode I and the Mode II stress intensity factors, respectively, and T is the non-singular axial stress. The crack propagation angle θ_0 is found from $\frac{\partial\sigma_{\theta\theta}}{\partial\theta}=0$ or equivalently from

$$\left[K_I\sin\theta_0+K_{II}(3\cos\theta_0-1)\right]-\frac{16T\sqrt{2\pi r_c}}{3}\sin\frac{\theta_0}{2}\cos\theta_0=0 \tag{6}$$

Once the crack initiation criterion has been met, the crack is propagated through the distance 0.02a . Thus the crack propagation analysis may be summarized as follows:

Step1. The displacement, strain and stress fields are determined by using the SSPH method.

Step2. The SIFs are evaluated using the interaction integral based on the results of step1.

Step3. The crack propagation angle θ_0 is determined from Eq. (6).

Step4. The crack is advanced by 0.02a in the direction that makes the angle θ_0 with the horizontal axis.

Step5. Repeat steps1 through 4 until the desired load has been applied on the end faces of the specimen.

In Fig. 7b, we have compared the computed crack path with that found experimentally; and it is clear that the two crack trajectories agree well with each other.

Conclusions

The compact tension PMMA specimens were tested in mode I with a displacement rate of 10 mm/min, and the value of K_{Ic} was found to be 1.056 ± 0.029 MPa$\sqrt{m}$. A set of asymmetric DCB (modified CT) specimens, with the notch and the initial crack not located along the specimen center line, were tested with the goal of investigating crack trajectory deviations due to the mode mixity introduced at the beginning of the crack propagation. Referring to Figs. 4 and 6, the crack first propagated in the lengthwise direction of the specimen, then, briefly, in a transverse direction, followed by the lengthwise direction, and finally nearly perpendicular to the long edge of the specimen. Direction changes in the crack trajectory may be attributed sign switches in the T-stress.

The effect of the specimen length to the initial crack length ratio, w/a, was also studied by testing the modified CT specimens with w/a = 8, 4 and 2.67. For the modified CT specimen with w/a ≤ 4, the crack deviated quickly when propagation started. However, for the specimen with w/a = 8, the crack propagated in a straight line for almost 20 mm before it deviated. These results are in qualitative agreement with those of Aliha and Ayatollahi determined from mixed-mode tests on semi-circular beam specimens of PMMA [1].

Deformations of pre-notched specimens were also analyzed by the X-FEM implemented in the commercial software, ABAQUS™, and the meshless SSPH method implemented in the in-house developed computer software. As should be clear from the results plotted in Fig. 7, the crack path predicted by the SSPH method is in better agreement with that found experimentally than the crack path computed using the X-FEM. However, this needs to be checked for several test configurations before the superiority of the SSPH method over the X-FEM can be ascertained.

Acknowledgements

The authors are grateful for support from the National Science Foundation (NSF/CMMI Award No. 0826143). YG would also like to thank the China Scholarship Council for partial support during this work.

References

1. Aliha, M.R.M., Ayatollahi, M. R., *Geometry effects on fracture behaviour of polymethyl methacrylate.* Materials Science and Engineering A-Structural Material Properties Microstructure and Processing, 2010 **527**(3): p. 526-530.
2. Ayatollahi, M.R., Aliha, M. R. M., Hassani, M. M. , *Mixed mode brittle fracture in PMMA - An experimental study using SCB specimens* Materials Science and Engineering A-Structural Materials Properties Microstructure and Processing, 2006 **417**(1-2): p. 348-356.
3. Smith, D.J., Ayatollahi, M. R., Pavier, M. J., *The role of T-stress in brittle fracture for linear elastic materials under mixed-mode loading.* Fatigue Fract Engng Mater Struct, 2001 **24**: p. 137–150.
4. Mahajan, R.V., and Ravi-Chandar, K., *An experimental investigation of mixed-mode fracture.* International Journal of Fracture, 1989 **41**: p. 235-252.
5. Gomez, F.J., Elices, M., Planas, J., *The cohesive crack concept: application to PMMA at -60 oC.* Engineering Fracture Mechanics, 2005 **72**(8): p. 1268-1285
6. Williams, M.L., *On stress distribution at base of stationary crack.* American Society of Mechanical Engineers -- Transactions -- Journal of Applied Mechanics, 1957 **24**(1): p. 109-114.
7. ASTM, *D5045 - 99(2007)e1 Standard Test Methods for Plane-Strain Fracture Toughness and Strain Energy Release Rate of Plastic Materials*. 2007, ASTM International: West Conshohocken, PA.
8. Hibbitt, K., Sorensen, Inc., *ABAQUS/standard user's manual, v.6.9*. 2009, Pawtucket, Rhode Island.
9. Giner, E., Sukumar, N., Tarancon, J. E., Fuenmayor, F. J., *An ABAQUS implementation of the extended finite element method.* Engineering Fracture Mechancs, 2009 **76**(3): p. 347-368.
10. Elices, M., Guinea, G. V., *The cohesive zone model: advantages, limitations, and challenges.* Engineering Fracture Mechanics, 2002 **69**(2): p. 137-163.
11. Lucy, L.B., *A numerical approach to the testing of the fission hypothesis.* Astron J, 1977 **82**: p. 1013–1024.

12. Belytschko, T., Lu, Y. Y. and Gu, L. , *Element-free Galerkin methods.* International Journal for Numerical Methods in Engineering, 1994 **37**: p. 229-256.
13. Lu, Y.Y.B., T., and Gu, L. , *A new implementation of the element free Galerkin method.* Comp. Meth. Appl. Mech. Engng 1994 **113**: p. 397-414.
14. Lu, Y.Y., Belytschko, T., and Gu, L. , *Crack propagation by element-free Galerkin methods.* Engng Frac. Mech. , 1995 **51**(2): p. 295-315.
15. Liu, W.K., Jun, S., Zhang, Y. F., *Reproducing kernel particle methods.* Int J Num Meth Fl 1995 **20**(1081–1106).
16. Atluri, S.N., and Zhu, T. , *A new meshless local Petrov-Galerkin (MLPG) approach in computational mechanics.* Computational Mechanics 1998 **22**: p. 117-127.
17. Zhang, G.M., Batra, R. C. , *Modified smoothed particle hydrodynamics method and its application to transient problems.* Comput. Mech., 2004 **34**: p. 137–146.
18. Batra, R.C., Zhang, G. M., *Analysis of adiabatic shear bands in elasto-thermo- viscoplastic materials by modified smoothed particle hydrodynamics (MSPH) method.* JComput Phys 2004 **201**: p. 172–190.
19. Batra, R.C., and Zhang, G. M, *SSPH basis functions for meshless methods and comparison of solutions with strong and weak formulations.* Computational Mechanics 2008 **41**: p. 527-545.
20. Zhang, G.M., and Batra, R. C., *Symmetric smoothed particle hydrodynamics (SSPH) method and its application to elastic problems.* Computational Mechanics 2009 **43**: p. 321-340.
21. Fleming, M., Chu, Y., Moran, B., and Belytschko, T. , *Enriched element-free Galerkin methods for crack tip fields.* International Journal for Numerical Methods in Engineering 1997 **40**: p. 1483-1504.
22. Rao, B.N., Rahman, S., *An efficient meshless method for fracture analysis of cracks.* Computational Mechanics 2000 **26**: p. 398-408.
23. Hildebrand, G., *Fracture analysis using an enriched meshless method.* Meccanica DOI 10.1007/s11012-008-9189-4, 2009.
24. Tsai, C.L., Guan, Y. L., Batra, R. C., Ohanehi,D. C., Dillard, J. G., Nicoli, E., Dillard, D. A., *Coupled experimental & computational analysis of fracture of PMMA blocks under mixed mode loading.* Experimental Mechanics, 2010 ([under preparation]).
25. Willams, M.L., *On the stress distribution at the base of a stationary crack*. J Appl Mech 1957 **24**: p. 109-114.
26. Kfouri, A.P., *Some evaluations of elastic T -term using Eshelby's method.* International Journal of Fracture, 1986 **30**(4): p. 301-315.
27. Erdogan, F., and Sih, G. C. , *On the crack extension in constraint effects in plates under plane loading and transverse shear.* Trans. ASME, J. Bas. Engng, 1963 **85 D**: p. 525–527.

Proceedings of the SEM Annual Conference
June 7-10, 2010 Indianapolis, Indiana USA

Procedures for Mixed Mode Fracture Testing of Bonded Beams in a Dual Actuator Load Frame

Edoardo Nicoli and David A. Dillard, Engineering Science & Mechanics Dept.,

Virginia Polytechnic Institute and State University, Blacksburg, VA 24061, enicoli@vt.edu

ABSTRACT

Most of the common methods for conducting fracture tests on adhesively bonded specimens refer to pure mode measures and to traditional load frames, where only one actuator is present. The critical strain energy release rates that characterize mode I, mode II and mixed-mode I/II fracture of bonded adherends can be measured also using a dual actuator load frame in which there are two degrees of freedom. The geometry that is tested is the double cantilever beam (DCB) type. DCB specimens are commonly used in traditional load frames for pure mode I tests but the independent actuators permit testing at different levels of mode-mixity. The focus of this paper is to develop and present evaluations of experimental and analytical aspects for mixed-mode fracture tests performed with the dual actuator load frame. In fact, tests performed with the dual actuator instead of other techniques give new possibilities and simplify the experimental effort, but also introduces different possible issues. New testing procedures have to be implemented; goals of these procedures are to enhance the capabilities of the dual actuator frame maintaining some of the advantages of other techniques already in use with traditional testing and analysis. Moreover, nonlinear geometrical effects during the tests can play a role and are evaluated in this paper.

BACKGROUND

Methods based on fracture mechanics have proved to be useful for design practice and are commonly applied in the characterization of bonded joints. Fracture mechanics is generally used to analyze the correlation among crack growth, material properties, and input test parameters, which include the imposed displacements or loads [1, 2]. The stress intensity factor (K) is commonly applied in fracture study of monolithic materials, while the strain energy release rate (SERR or $\mathcal{G}$) is usually preferred for fracture analysis of bonded joints [3].

The applied SERR can have components associated with each of the three fracture modes. In particular, with mode I, the opening mode, the crack propagates with the opening of its faces normal to the crack plane due to tensile stresses. In mode II, the in-plane shear mode, the crack propagation results from in-plane shear stresses. Finally, in mode III, the out-of-plane shear mode, the crack propagation results from out-of-plane shear stress. The applied strain energy release rate $\mathcal{G}$ is a scalar quantity and it should be noticed that its applied value can be obtained as sum of the components applied in the pure modes.

$$\mathcal{G} = \mathcal{G}_I + \mathcal{G}_{II} + \mathcal{G}_{III} \qquad 1$$

Techniques for partitioning the strain energy release rate in the pure modes components of Equation 1 have been developed by Williams [4], Schapery and Davidson [5] and Hutchinson and Suo [6]. These techniques apply to geometries such as beams and plates subjected to different loading conditions resulting in mixed mode. The techniques describe how to compute the pure mode components of the applied strain energy release rates. Tay [7] and Hashemi [8] addressed mixed mode delamination in fiber composites, developing approaches and physical interpretations that are completely relevant to the fracture in bonded joints and orthotropic materials.

The critical values of SERR, $\mathcal{G}_c$, are typically experimentally measured. These values are also generally depending on the fracture mode that is present at the crack tip, where mode I, mode II, mode III, or combinations of these can cause the crack to propagate. The aspects of fracture in adhesive joints have been investigated by a number of researchers [9-11] who have addressed pure mode and mixed mode fracture using various experimental implementations.

T. Proulx (ed.), *Time Dependent Constitutive Behavior and Fracture/Failure Processes, Volume 3*, Conference Proceedings of the Society for Experimental Mechanics Series 15, DOI 10.1007/978-1-4419-9794-4_4, © The Society for Experimental Mechanics, Inc. 2011

INTRODUCTION

The fracture studies performed with the dual actuator consider the superposition of fracture modes I (opening) and II (in-plane shear), with tests run in pure modes or in mixed-mode conditions. Specimens geometrically identical to the double cantilever beam (DCB) can provide fracture data for mixed-mode fracture conditions when tested by imposing asymmetric loads or displacements to the two beams. The specimen is clamped at the lower end and loads are applied to the debonded (upper) ends of the beams, as illustrated in Figure 1.

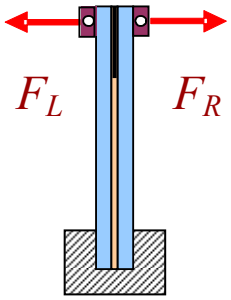

Figure 1: DCB type specimen used in dual actuator load frame

The dual actuator load frame is an instrument that simplifies the experimental effort that is required for collecting data associated with different values of mode-mixity, thus enhancing the possibilities of running tests with different material systems. The dual actuator testing machine illustrated in Figure 2 was built to our specifications before the beginning of the present research by McGaw Technologies Inc. (Fairview Park, OH), with support from the National Science Foundation.

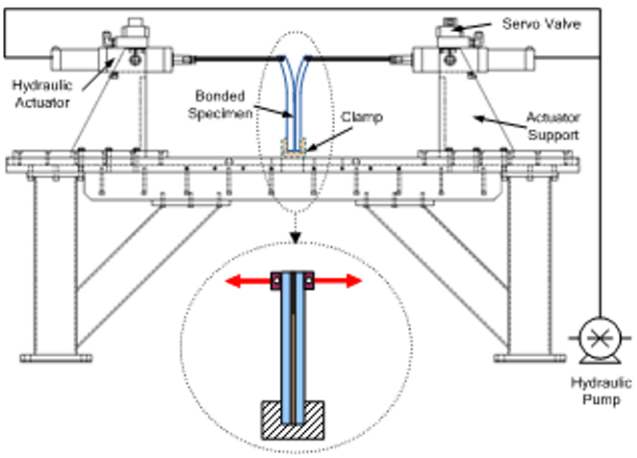

Figure 2: Dual actuator load frame

The dual actuator load frame utilizes two actuators that can impose loads or displacements independently to the ends of the two beams of the bonded specimen. Each actuator has a load cell and a displacement sensor (LVDT) that provides information for quantitative evaluation of specimen behavior. Unless the test is performed in pure mode I, the specimen must be clamped in a vise at the lower end. The loads are applied to the debonded ends of the beams by pins attached to clevises connected to the individual load cells and actuators. A controller drives the two actuators; displacements and forces of the two actuators, as well as time as the test progresses, are collected by a computer equipped with a data acquisition card (DAQ PCI 6229, National Instruments Inc., Austin TX). The crack length values of the specimen are read periodically by the operator running the test. The reading is performed using a magnification lens and facilitated by the white correction fluid and a paper ruler applied on a side of the specimen. The control design allows for imposing different combinations of displacement rates at the two actuators and this results in different levels of in-plane mode mixity with a standard DCB specimen.

The advantages of this testing frame can be summarized in the following points:

- mode mixity is not obtained by a variation of the geometry of the adherends or by the use of other fixtures, but by the imposition of asymmetric loads or displacements; thus, data can be collected from a single specimen type;
- the mode-mixity is infinitely variable between pure mode I and pure mode II;
- the mode mixity can be varied throughout the test without the need of repositioning the specimen.

Papers on experimental results coming from tests performed with the dual actuator load frame have already been presented by Singh et al. [12] and by Nicoli [13]. This paper does not focus on experimental results, but presents some of the specific aspects that are involved in the experimental and analysis procedures when fracture testing is performed with a dual actuator load frame. Parts of this paper include a description of a testing procedure that optimizes the use of the dual actuator and is currently applied and an analytical evaluation of the geometrical nonlinear effects that arise during the test

TESTING PROCEDURE WITH DUAL ACTUATOR LOAD FRAME

The tests performed with the dual actuator are conducted in displacement control to avoid unstable or catastrophic failures of the DCB specimens, but allowing multiple readings of crack length as the debonded part propagates in a controlled fashion. Tests involve imposing different displacement ramps on the two beams and measuring the forces on the left and right actuator. These forces, F_R and F_L in Figure 1, are then combined for evaluating the force F_I, that gives the mode I loading and F_{II} that gives the mode II with Equation 2.

$$F_I = \frac{1}{2}(F_R + F_L)$$
$$F_{II} = \frac{1}{2}(F_R - F_L) \qquad \mathbf{2}$$

F_I and F_{II} are used for evaluating the mode I and mode II components of $\mathcal{G}_c$, which can be calculated as functions of the crack length, the elastic stiffness of the adherends, and the respective forces applied to the two beams of the specimen. These components can be easily computed with the simple beam theory and are equal to Equation 3. I and E are the second moment of area and the elastic modulus of the adherends, respectively, a is the crack length, and b the specimen bond width

$$\mathcal{G}_I = \frac{F_I^2 a^2}{EIb}$$
$$\mathcal{G}_{II} = \frac{3F_{II}^2 a^2}{4EIb} \qquad \mathbf{3}$$

The angle of mode mixity, Ψ, is defined from the ratio between the two components of $\mathcal{G}$. Equation 4 shows this relation.

$$\Psi = ArcTan\sqrt{\frac{\mathcal{G}_{II}}{\mathcal{G}_I}} \qquad \mathbf{4}$$

For the analysis of DCB and other standard test configurations, several improved approaches can be used for analyzing the data. These approaches are more refined than the simple beam theory and include the corrected beam theory (CBT) and the experimental compliance method (ECM) described by Blackman and Kinloch [14, 15]. These techniques address some issues of the tests on DCB specimens adapting the simple beam theory for the geometry of DCB, where the two beams are connected through an adhesive layer. These issues are, for example, the root rotation at the crack tip, shear deformation at the beams, the effects of beam thickness, and inaccuracies in the crack length reading. The CBT evaluates the real elastic stiffness of the beams of the tested DCBs and corrects the crack length reading using a linear fit of the cube root of the compliance vs. crack length plot. The ECM similarly evaluates characteristics of the tested specimens with a differently arranged linear fit of the logarithm of the compliance vs. the logatitm of the crack length. ECM and CBT for DCB specimens are both traditionally based on mode I tests and require experimental data from pure mode I tests, although adaptations of the techniques to pure mode II have also been developed in [16, 17]. One goal of the fracture studies with the dual actuator is usually to test mixed mode conditions, but it is opportune to have each of the specimens partially tested at the same level of mode-mixity. In particular, it is useful to perform a part of pure mode I test in all of the specimens. So, the test procedure was arranged in three separate phases, the first and the latter are run in pure mode I in order to get data points for the CBT and ECM analysis procedures and in the second potion of the test the mixed-mode condition is obtained by imposing different displacement rates on the two beams. Performing the test portions at pure mode I at the beginning and the end of the test gives two advantages. First, the crack growth for short crack length is unstable for fracture modes close to mode II [18], but the first portion of the specimen can give stable data for mode I. Second, for large crack lengths, the presence of the clamping vise at the base of the specimen prevents full debonding of the specimen. Thus, only data from mode I, where clamping is not present, can be collected. The application of the procedure of Figure 3 can be considered beneficial since it tends to

maximize the outcome of information that one can gain from the test of each specimen, consequently increasing the overall efficiency of the testing effort.

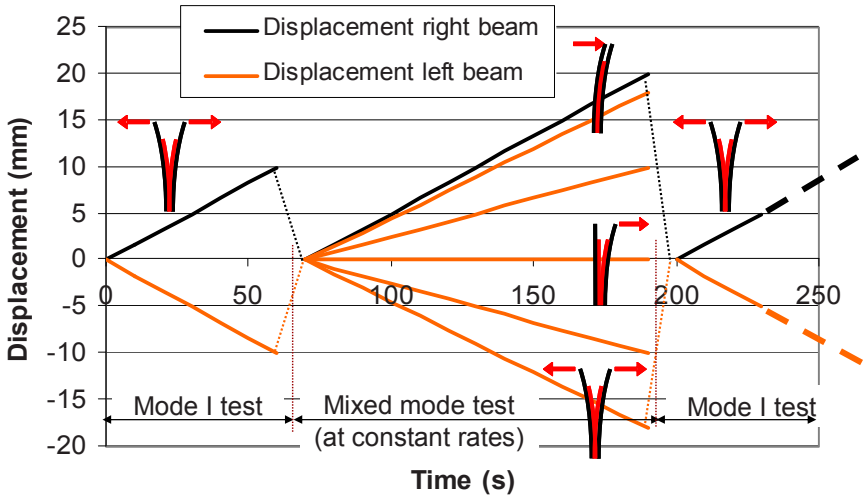

Figure 3: Typical test procedure

The use of CBT is particularly important when natural materials with considerable material properties variation from specimen to specimen are tested. In the calculation of the $\mathcal{G}_c$ components during the mixed mode part of the test, one has not to rely on the elastic modulus listed in tables, but can use the modulus of the specimen obtained in the first and third parts of the test.

NONLINEAR GEOMETRICAL EFFECTS

As previously described, the DCB specimens tested in the dual actuator load frame are clamped at the base and the debonded ends of the two beams are connected to the actuators. The two actuators can rotate around two pinpoints, thus allowing for beam foreshortening and avoiding stresses due to an over-constrained configuration. The geometrical changes that the specimen and load frame encounter during a test are shown in Figure 4.

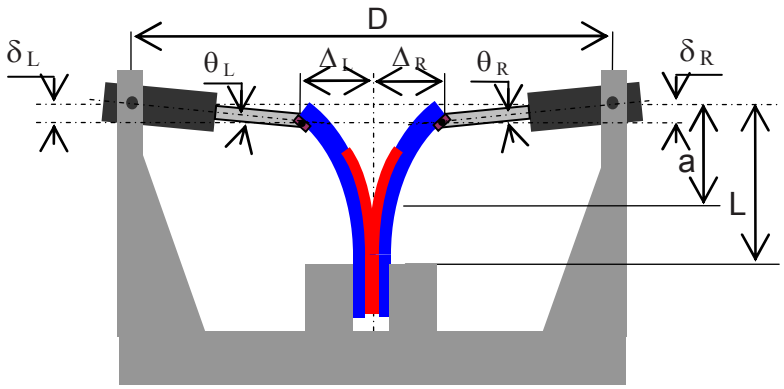

Figure 4: Schematic view of geometry changes during a test on the dual actuator

The DCB specimen consists in two beams bonded together, with a crack that grows during the test and modifies the geometry of the specimen during the test. The evaluations focused on the beam foreshortening (δ), cylinders rotation (θ), illustrated in Figure 4, and the actual moments imposed on the adherends at the crack tip. These three parameters were described as functions of the actuator positions and crack length. The evaluations were carried out for pure mode I and pure mode II and took into account the geometric nonlinear effects in the system. The analysis particularly focused on our dual actuator, where, with reference to Figure 4, D is equal to 1400 mm and L is 220 mm. Also, the maximum displacement of the two actuators, Δ_L and Δ_R, is +/- 50 mm. Figure 5 illustrates that the applied moment decreases not only because of beam foreshortening, but, due to actuator rotation, also because the applied force F has two components F_V and F_H which are generating opposite moments at the crack tip.

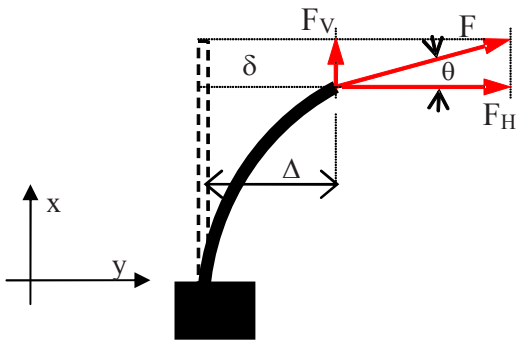

Figure 5: Representation of beam foreshortening and force rotation on a beam tested on a dual actuator load frame.

The beams in the dual actuator are bent with the application of the forces given by the two actuators. The deformed shape can be calculated in each case with the equation

$$\frac{d^2y}{dx^2} = \frac{M(x)}{EI} \qquad \textbf{5}$$

For an imposed force the moment is linearly variable along the beam length, thus the function *y(x)* is not a simple arc, as it would be for an applied moment, but can be obtained via integration of Equation 5. The evaluation of the beam foreshortening can be performed with the following analytical geometry equation

$$\delta = \frac{\int_0^{L^*} \sqrt{(1+(y'(x))^2)}\,dx - L^*}{\sqrt{(1+(y'(L^*))^2)}} \qquad \textbf{6}$$

where L^* is the length of the portion of the DCB specimen that bends during the test. In particular L^* is equal to the crack length in mode I configuration and total beam length above the clamp in mode II. *y(x)* is the equation of the deformed shape of the beams. The equation *y(x)* depends on the imposed displacements at the beam ends and on the crack length. From a geometrical point of view, the beam foreshortening of Equation 6 is a function of the imposed displacement Δ, that influences *y(x)* and thus *y'(x),* and the length of the crack. Graphs of the beam foreshortening as function of the two parameters are shown in Figure 6.

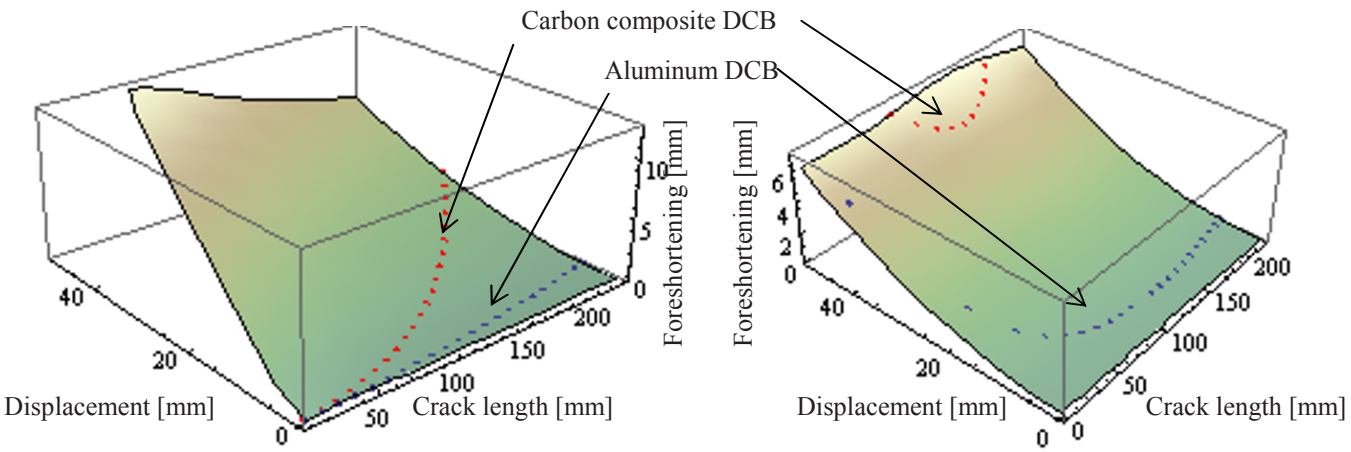

Figure 6: Beam foreshortening as function of imposed displacement and crack length for pure mode I (left) and pure mode II (right)

The graphs show with colored dots also the simulation of data points for two representative geometries: The points indicating lower foreshortening illustrate behavior of aluminum bonded samples (section 25x20 mm, elastic modulus 70 GPa, $\mathcal{G}_{Ic}$ = 5000 J/m^2 and $\mathcal{G}_{IIc}$ = 8000 J/m^2), while the points indicating larger foreshortening describe the behavior of carbon composite bonded samples (section 25x4 mm, elastic modulus 50 GPa, $\mathcal{G}_{Ic}$ = 1000 J/m^2 and $\mathcal{G}_{IIc}$ = 3000 J/m^2). In the two simulations of aluminum and carbon fiber bonded specimens, the crack length

and the imposed displacement are not independent variables, but the first is function of the second and depends on geometry of the specimen and elastic and fracture properties of the adherends.
Another finding of the analysis was the variation of the moment at the crack tip in the two cases of mode I and mode II. This variation results from both beam foreshortening and actuator rotation. The moment variation is important; in fact the real moment present at the crack tip is the element that causes the crack growth. The comparison that was carried out and is shown in Figure 7 is the ratio between the real moment at the crack tip and the nominal one that is simply the product of the force *F* measured at the load cell and the crack length, without effect of beam foreshortening.

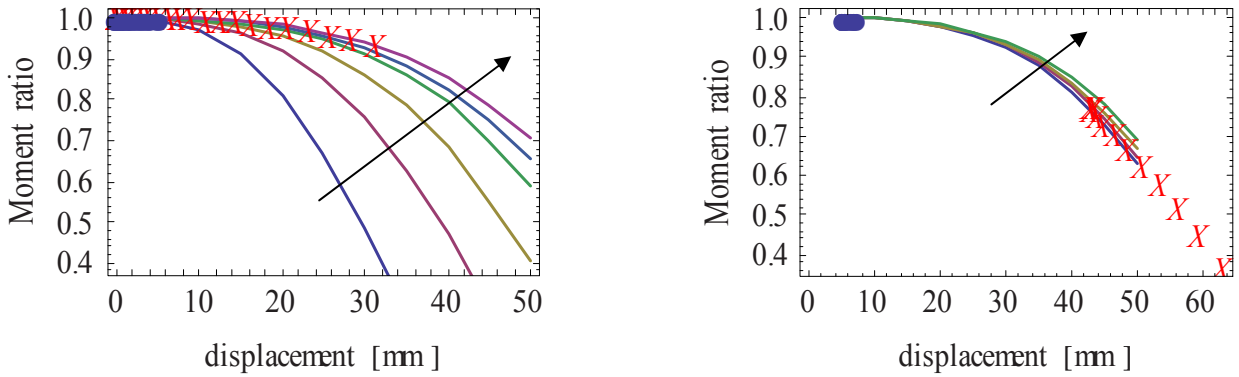

Figure 7: Variation of moment at the crack tip from the nominal value (left pure mode I, right pure mode II) The different curves represent different crack lengths; the arrow indicates increasing crack length.

Also in the case of Figure 7, the graphs illustrate curves coming from geometrical analysis and data points the data from the simulations; in particular dots indicate points from aluminum DCBs and Xs indicate points from carbon composite DCBs. The outcome of the analysis is that for the stiffer aluminum specimens the moment variation is less than 1% in both mode I and mode II, while for the more compliant carbon composite specimens the moment is reduced of 7% in mode I tests and around 40% in mode II tests, for the maximum possible displacement of 50 mm. For metallic specimens the issue is likely to be insignificant, while some care has to be taken in analyzing specimens where the imposed displacement gets large. Having this aspect been evaluated with this analysis, when analyzing the fracture data one could consider a correction factor, returning the real applied moment and thus the real forces F_I and F_{II} as function of imposed displacement and crack length. The forces F_I and F_{II} are in fact important when evaluating the components of $\mathcal{G}_c$,as illustrated in Equations 3.

CONCLUSIONS

The dual actuator test frame simplifies the experimental effort required for mixed-mode characterization of adhesively bonded and laminated beam specimens, since a single geometry type of specimen can be used for spanning from pure mode I to pure mode II loading conditions. The dual actuator introduces the possibility of easily applying different levels of mode mixity on a single specimen, thus allowing to applying some of the positive outcomes of traditional data analysis techniques such as the corrected beam theory (CBT) and the experimental compliance method (ECM) also in mixed mode tests. Especially the results of CBT can be useful also in mixed mode testing and a procedure for increasing the efficiency of each test has been proposed.
The construction characteristics of the testing frame introduce some nonlinear effects such as adherend foreshortening and the force rotation during the test. These variations were analytically evaluated. In particular two representative cases were shown. It has to be pointed out that a problems such as the beam foreshortening is common to most of the techniques that measures fracture properties with DCB type specimens. For the dual actuator load frame it was shown that the nonlinear geometrical effects can be accounted for a 1% variability of the results when testing relatively stiff materials, such as bonded metals, while can have higher influence in relatively compliant specimens, such as DCBs obtained from thin layers of carbon fiber composites. Graphs obtained in this paper can be used in testing practice with the dual actuator as correction factors for the mentioned nonlinear effects.

ACKNOWLEDGMENTS

The authors would like to acknowledge the support of the National Science Foundation under contract DMR-0415840 for constructing the dual actuator load frame. The financial support of the Wood Based Composites Center at Virginia Tech is gratefully acknowledged for funding EN.

REFERENCES

1. Kundu, T., *Fundamentals of fracture mechanics*. 2008, Boca Raton, FL: CRC Press. 286.
2. Miannay, D.P., *Fracture mechanics*. Vol. xviii, 337 p. 1998, New York: Springer.
3. *Adhesion science and engineering*. 1st ed, ed. A.V. Pocius, D.A. Dillard, and M.K. Chaudhury. 2002, Amsterdam ; Boston: Elsevier.
4. Williams, J.G., *On the calculation of energy release rates for cracked laminates.* International Journal of Fracture, 1988. **36**(2): p. 101-119.
5. Schapery, R.A. and B.D. Davidson, *Prediction of Energy Release Rate for Mixed-Mode Delamination Using Classical Plate Theory.* Applied Mechanics Reviews, 1990. **43**(5S): p. S281-S287.
6. Hutchinson, J.W., Z. Suo, and Y.W. Theodore, *Mixed Mode Cracking in Layered Materials*, in *Advances in Applied Mechanics*. 1991, Elsevier. p. 63-191.
7. Tay, T.E., J.F. Williams, and R. Jones, *Characterization of pure and mixed-mode fracture in composite laminates.* Theoretical and Applied Fracture Mechanics, 1987. **7**(2): p. 115-123.
8. Hashemi, S., A.J. Kinloch, and J.G. Williams, *The Analysis of Interlaminar Fracture in Uniaxial Fibre-Polymer Composites.* Proceedings of the Royal Society of London. Series A, Mathematical and Physical Sciences, 1990. **427**(1872): p. 173-199.
9. Choupani, N., *Interfacial mixed-mode fracture characterization of adhesively bonded joints.* International Journal of Adhesion and Adhesives, 2008. **28**(6): p. 267-282.
10. Fernlund, G. and J.K. Spelt, *Mixed-mode fracture characterization of adhesive joints.* Composites Science and Technology, 1994. **50**(4): p. 441-449.
11. Crews, J.H. and J.R. Reeder, *A Mixed-Mode Bending Apparatus for Delamination Testing*. 1998, NASA Langley Technical Report Server.
12. Singh, H.K., et al., *Mixed mode fracture testing of adhesively bonded wood specimens using a dual actuator load frame.* Holzforschung. [in press]
13. Nicoli, E., et al., *Mixed mode fracture testing of adhesively bonded specimens using a dual-actuator load frame*, in *International Conference on Fracture*. 2009: Ottawa, Canada.
14. Blackman, B., et al., *The calculation of adhesive fracture energies from double-cantilever beam test specimens.* Journal of Materials Science Letters, 1991. **10**(5): p. 253-256.
15. Brunner, A.J., B.R.K. Blackman, and P. Davies, *Mode I delamination*, in *European Structural Integrity Society*, D.R. Moore, A. Pavan, and J.G. Williams, Editors. 2001, Elsevier. p. 277-305.
16. Blackman, B.R.K., A.J. Brunner, and J.G. Williams, *Mode II fracture testing of composites: a new look at an old problem.* Engineering Fracture Mechanics, 2006. **73**(16): p. 2443-2455.
17. Blackman, B.R.K., A.J. Kinloch, and M. Paraschi, *The determination of the mode II adhesive fracture resistance, GIIC, of structural adhesive joints: an effective crack length approach.* Engineering Fracture Mechanics, 2005. **72**(6): p. 877-897.
18. Carlsson, L.A., J.W. Gillespie, and R.B. Pipes, *On the analysis and design of the end notched flexure (ENF) specimen for mode II testing.* Journal of Composite Materials, 1986. **20**(6): p. 594-604.

Proceedings of the SEM Annual Conference
June 7-10, 2010 Indianapolis, Indiana USA

LINEAR VISCOELASTIC BEHAVIOR OF POLY(ETHYLENE THEREPHTALATE) ABOVE T_g

AMORPHOUS VISCO-ELASTIC PROPERTY V_S CRYSTALLINITY:

EXPERIMENTAL AND MICROMECHANICAL MODELING

Fahmi Bédoui

Université de Technologie de Compiègne, Laboratoire Roberval UMR-CNRS 6253,

Compiègne, France.

E-mail : Fahmi.bedoui@utc.fr ; Tel : +33 3 44 23 45 28 ; Fax : +33 3 44 23 49 84

Abstract

Linear viscoelastic behavior of amorphous and semi-crystalline Poly(ethylene teraphtalate), PET, was experimentally investigated. Micromechanics models were used to predict the elastic and plastic behavior of semi-crystalline polymers successfully, however the viscoelastic behavior still difficult to be predicted with such models. Difficulties lie on the used numerical methods and also on the understanding of the properties of the amorphous phase. In this paper we tried to first simplify the Laplace Carson-based method by using a pseudo-elastic method that ovoid the numerical difficulties encountered before. The time-dependant problem is so replaced by a frequency-dependant set of elastic equations. To validate the new approach, Poly(ethylene threphtalate) (PET) with different crystallinity fraction (X_c) were prepared and characterized. Based on our experimental results (properties of the amorphous PET and semi-crystalline polymers) micromechanical model were used to first predict the viscoelastic properties of the semi-crystalline polymers and also to predict the changes on the viscoelastic properties of the amorphous phase when the crystallinity fraction increases. Good agreement between the predicted and experimental results of the low crystallinty fraction sample (X_c=17%). However for high crystallinity (Xc=24% and Xc=35%) prediction based on the identified amorphous phase as an input for the micromechanical properties failed to fit the viscoelastic behavior of the semi-crystalline polymer. Based on the dynamic mechanical analysis (DMA) experimental data, changes on the glass transition temperature of the amorphous phase were observed, which could confirm the change of the viscoelastic properties of the amorphous phase upon crystallization. This result confirms the effect of confinement due to the presence of the crystalline phase on the prediction of the viscolelastic behavior of semi-crystalline polymer using micromechanical models.

Mechanical

Keywords: Semi-crystalline polymer, Amoprhous phase, Confinement, Viscoelasticity, Micromechanical modeling.

Introduction

Micromechanics models were used for composite materials and recently for semi-crystalline polymers. Micromechanics models were thoroughly used to predict the plastic behavior of semi-crystalline polymers [1-6]. Recently the prediction of the elastic behavior was subject to an intense interest either to estimate macroscopic properties[7-10] or try to shed light on some paradoxes behavior of polyolefin

T. Proulx (ed.), *Time Dependent Constitutive Behavior and Fracture/Failure Processes, Volume 3*, Conference Proceedings of the Society for Experimental Mechanics Series 15, DOI 10.1007/978-1-4419-9794-4_5, © The Society for Experimental Mechanics, Inc. 2011

polymers [11]. However difficulties on applying micromechanics to predict viscoelastic behavior of semi-crystalline polymer still not overcome. Unlike elasticity, viscoelastic behavior assumes an evolution of the mechanical properties (Young's modulus e. g.) Vs. time. This dependence could not be taken on account using standard micromechanical model. Numerical techniques were introduced to solve this issue. For composite materials Schapery [12] proposes to use the collocation method coupled with Laplace-Carson inversion transformation technique. In a recent study Brener et al. [13] used the collocation method constraints conditions to predict composite material behavior. The same concept on constraints coupled with the collocation method were used for semi-crystalline polymer shows the limit of the micromechanics model to fit the viscoelastic behavior of semi-crystalline polymer[14]. The confinement of the amorphous phase that was not taken on account was suspected to be the origin of the differences between the experimental data and the model prediction.

In this paper based on different approach to represent the viscoelastic properties the effect of the confinement on the mechanical properties of the amorphous phase was studied. Based on the hypothesis of the modeling the results will be correlated with the literature results.

Materials and methods

2 mm thickness PET Extruded plate from ISOSUD was used in this study. Samples were cut and annealed at T=110 ℃ for different period of time. Three crystallinty fractions were prepared (17, 24 and 35%) DSC run were carried out to determine the glass transition temperature and the crystallinity of each sample. DMA tests using a METRAVIB DMA 150 machine were carried out at 90℃. above the glass transition temperature of the amorphous PET is about 80℃. DMA experiments were carried out over four decades; from 0.01 to 100 Hz (Figure 1)

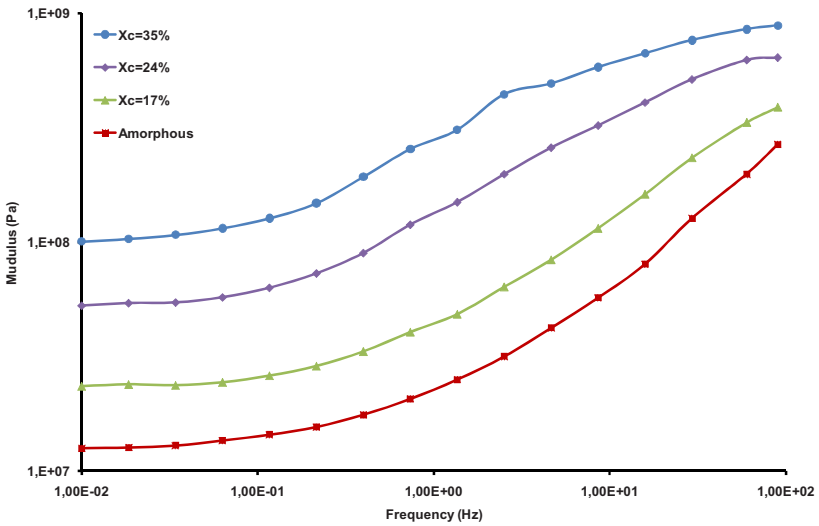

Figure 1: Dynamic modulus for amorphous and semi-crystalline polymers.

Modeling

In a previous papers [8, 11, 14] we used micromechanics models to predict elastic AND viscoelastic properties of semi-crystalline polymers (PP, PE and PET). For elasticity the differential scheme appears the well adapted to predict the elastic properties of such material. However the viscoelsatic properties prediction presents some numerical difficulties due to the collocation method. In order to overcome those difficulties caused by the use using the Laplace-Carson and the collocation method to replace the time dependant problem to pseudo-elastic one, we propose to consider as the viscoelastic properties the complex modulus E* instead of the loss and elastic ones (E' and E" respectively). Coupled with the bulk modulus derived from the PVT diagram, that we suppose constant at a chosen temperature, we replace the time dependant problem by a frequency-dependant elastic one. The new problem consists on a set of elastic equation for each considered frequency (in this study we covered four decades (0.01 to 100 Hz). As we have an elastic problem, the differential scheme will be used to

predict the mechanical properties of PET for different crystallinty fractions. The crystalline phase will be considered as the filler with a shape ratio of 2-2-1. These values are the results of previous work [8, 14].

Discussions

The amorphous phase will be considered as isotropic viscoelastic (figure 1) and the crystalline phase as elastic anisotropic[8]. Applying the described procedure for the semi-crystalline polymer, an acceptable agreement between prediction and experimental data was found for the low crystalline fraction (Xc=17%) as presented in figure 2. and based on the experimental data of the amorphous phase (figure 1) and the crystalline phase

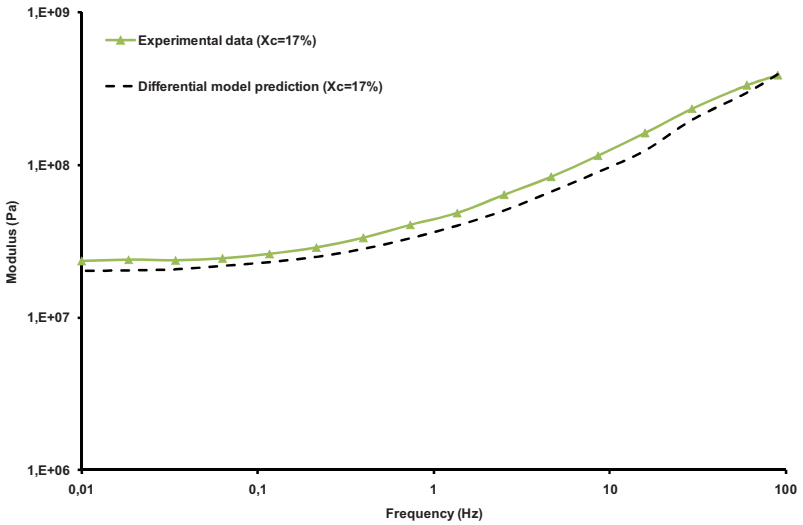

Figure 2: Viscoelastic modulus prediction for Xc=17% using differential model.

Fair predictions however were found for the higher crystalline fraction (Xc=24% and 35%). The same limitations of the modeling were encountered for PET below Tg[14] and also in the case of amorphous PET filled with glass beads. In both cases, even though the length scale is not the same, the confinement of the amorphous phase due to the presence of crystalline lamellae in the case of semi-crystalline polymers and the glass beads in the composite materials, is suspected to be at the origin of the differences between the experimental data and the model prediction. The confinement effect concept and its effect on the mechanical properties of the amorphous phase were introduced to fit the elastic properties of PET using bi-layered representation[10].

A representation of Tan(delta), representative of the glass transition of the amorphous phase, shows clearly that for high crystallinity (24% and 35 % in our case) two peaks could be considered Moreover a shift of the main peak is seen (figure 3).

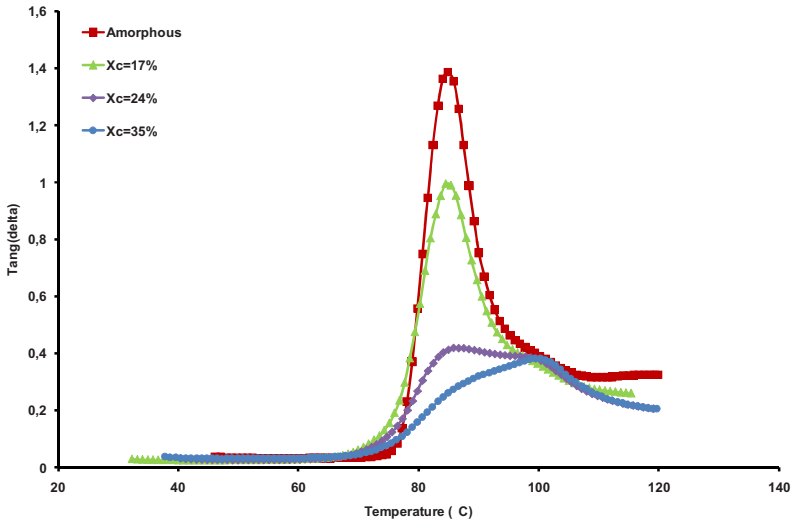

Figure 3: Tan(delta) for amorphous and semi-crystalline polymers.

This two aspects could lead to the conclusion that the glass transition temperature rate increased with increasing cristallinity which is confirmed by Illers and Breuer [15]. Using the Differential scheme, an estimation of what should be the amorphous phase modulus was conducted (Figure 4)

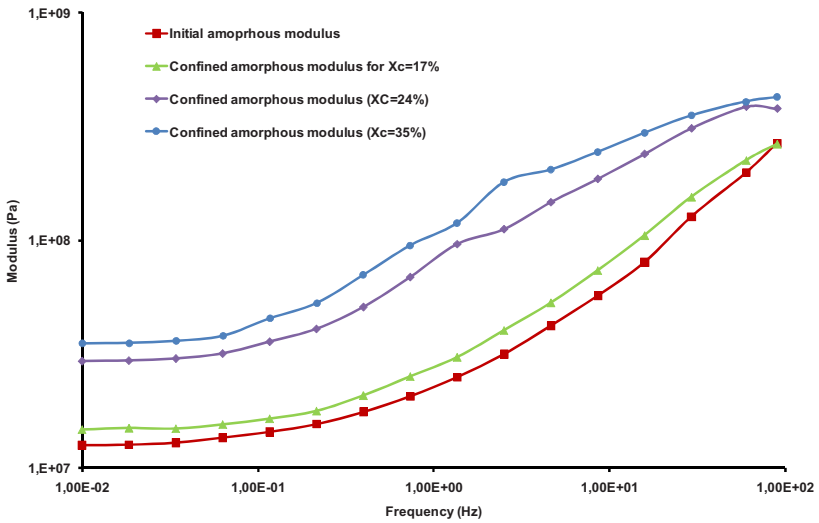

Figure 4: Confined amourphous-phase's moudulus for semi-crystalline polymers compared to the original amorphous polymer.

Conclusion

This study shed some light on the confinement effect which the amorphous phase is subject to due to the increase of the crystallinty fraction. This effect is limited for low crystallinity (Xc=17%) and increased for higher crystallinty (Xc=24 and 35%). This effect was not taken on account in micromechanics models which could be the reason for the fair capability of such models to predict the macroscopic mechanical properties of semi-crystalline polymers such PET. The new approach based on a frequency dependant problem helped overcoming the difficulties encountred in previous work using the Laplace-carson method coupled with collocation method.

Acknowledgment

The author acknowledges the financial support of the Mechanical Engineering Department of the Université de Technologie de Compiègne for this study, under the contract N°M117L.

Conclusion

1. Lee, B.J., et al., *Simulation of large strain plastic deformation and texture evolution in high density polyethylene.* Polymer, 1993. **34**(17): p. 3555-3575.
2. Lee, B.J., D.M. Parks, and S. Ahzi, *Micromechanical modeling of large plastic deformation and texture evolution in semi-crystalline polymers.* Journal of the Mechanics and Physics of Solids, 1993. **41**(10): p. 1651-1687.
3. G'Sell, C. and A. Dahoun, *Evolution of microstructure in semi-crystalline polymers under large plastic deformation.* Materials Science and Engineering: A, 1994. **175**(1-2): p. 183-199.
4. Dahoun, A., et al., *Plastic behavior and deformation textures of poly(etherether ketone) under uniaxial tension and simple shear*. 1995. p. 317-330.
5. van Dommelen, J.A.W., et al., *Micromechanical modeling of the elasto-viscoplastic behavior of semi-crystalline polymers.* Journal of the Mechanics and Physics of Solids, 2003. **51**(3): p. 519-541.
6. van Dommelen, J.A.W., et al., *Micromechanical modeling of intraspherulitic deformation of semicrystalline polymers.* Polymer, 2003. **44**(19): p. 6089-6101.
7. Ahzi, S., D.M. Parks, and A.S. Argon, *Estimates of the overall elastic properties in semi-crystalline polymers.* American Society of Mechanical Engineers, Applied Mechanics Division, AMD 1995. **203** p. 31-40.
8. Bédoui, F., et al., *Micromechanical modeling of isotropic elastic behavior of semicrystalline polymers.* Acta Materialia, 2006. **54**(6): p. 1513-1523.
9. Guan, X. and R. Pitchumani, *A micromechanical model for the elastic properties of semicrystalline thermoplastic polymers.* Polymer Engineering and Science, 2004. **44**(3): p. 433-451.
10. Gueguen, O., et al., *A new three-phase model to estimate the effective elastic properties of semi-crystalline polymers: Application to PET.* Mechanics of Materials, 2010. **42**(1): p. 1-10.
11. Bédoui, F., J. Diani, and G. Régnier, *Micromechanical modeling of elastic properties in polyolefins.* Polymer, 2004. **45**(7): p. 2433-2442.
12. Schapery, R.A., *On the characterization of nonlinear viscoelastic materials*. 1967. p. 295-310.
13. Rekik, A. and R. Brenner. 2007, AFM, Maison de la Mécanique, 39/41 rue Louis Blanc - 92400 Courbevoie.
14. Diani, J., F. Bédoui, and G. Régnier, *On the relevance of the micromechanics approach for predicting the linear viscoelastic behavior of semi-crystalline poly(ethylene)terephtalates (PET).* Materials Science and Engineering: A, 2008. **475**(1-2): p. 229-234.
15. Illers, K.H. and H. Breuer, *Molecular motions in polyethylene terephthalate.* Journal of Colloid Science, 1963. **18**(1): p. 1-31.

Proceedings of the SEM Annual Conference
June 7-10, 2010 Indianapolis, Indiana USA

Experimental Study of Voids in High Strength Aluminum Alloys

Helena Jin, Wei-Yang Lu, John Korellis
Mechanics of Materials Department
Sandia National Laboratories
Livermore, California 94550
hjin@sandia.gov

Sam McFadden
Anamet Inc.,
Hayward, California, 94545

The ductile failure in metals has long been associated with void nucleation, growth and coalescence. Many micromechanics-based damage models were developed to study the effects of the voids sizes, shape and orientation to the nucleation, growth and coalescence of voids [1-2]. However, the experimental methods to quantitatively validate these models were lacking. In this work, the ductility and the microstructural characteristics of the voids in high strength aluminum is investigated. The particular material interested in this work is high strength rolled Aluminum 7075-T7351.

Both smooth tension and notched tension specimens were designed to study the mechanical properties along different orientations. The smooth tension specimens are designed along the longitudinal (LA) and short transverse (ST) directions to study the mechanical properties in different orientations. The specimens are cylindrical with gage length of 1.0 inch and diameter of 0.25 inch. The stress versus strain curves for the tension specimens are shown in Figure 1. It clearly shows the anisotropy in the mechanical properties, especially ductility. This material has much higher ductility in longitudinal (rolling) direction than the short transverse direction.

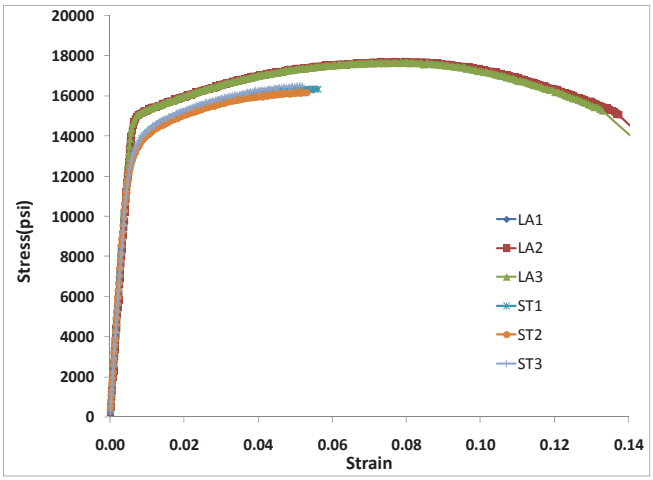

Figure1. Stress versus strain curves along longitudinal and short transverse directions

Notched tension specimens with four different radii of R1 = 0.039 inch, R2 =0.078 inch, R3=0.195 inch, R4 =0.390 inch were designed to introduce different levels of stress concentration. It has been known that the geometry of the notch affects the stress triaxiality which promotes the voids growth [3]. The load versus displacement curves of the notched tension specimens with R2, R4 are shown in Figure 2 (a) and (b). The data also clearly shows the anisotropy of ductility in these two orientations.

T. Proulx (ed.), *Time Dependent Constitutive Behavior and Fracture/Failure Processes, Volume 3*, Conference Proceedings of the Society for Experimental Mechanics Series 15, DOI 10.1007/978-1-4419-9794-4_6, © The Society for Experimental Mechanics, Inc. 2011

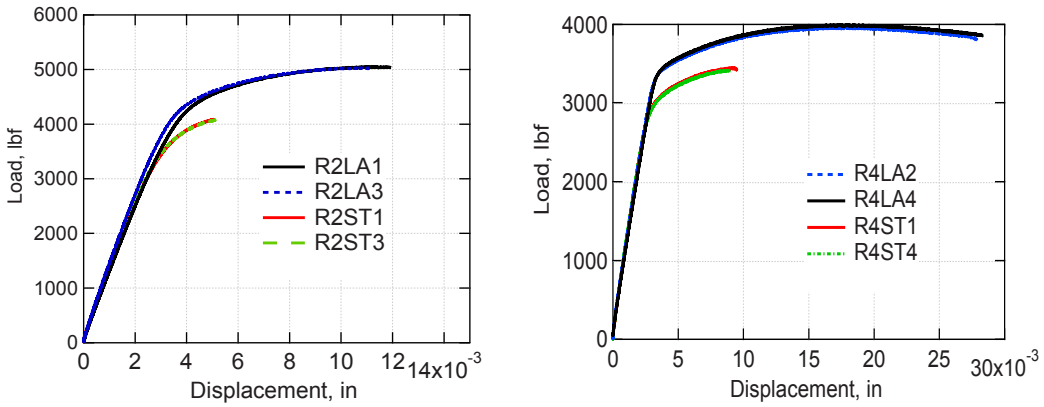

Figure2. Load versus displacement curves along longitudinal and short transverse directions for notch radii (a) R2 and (b) R4

The smooth tension specimen was loaded till failure. The fractured specimen was then sectioned perpendicular to the loading direction to microscopically study the voids size, shape. These cross sections were cut as close as possible to the failure surface. The cross section surface was then mechanically polished till 1 micron finish. Figure 3 (a) shows the optical image of an area on the cross section and (b) shows the AFM scanned image of the voids. Both images clearly showed the voids and the size of the voids ranges about 5 to 10 micrometers.

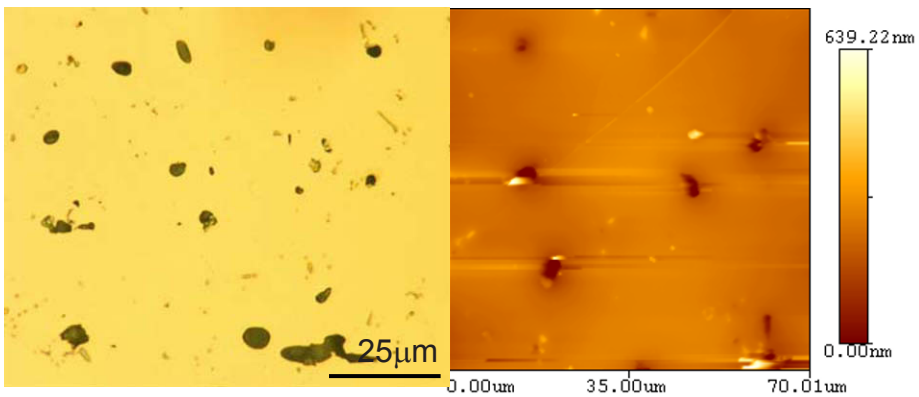

Figure 3. (a) Optical image of the cross section with voids; (b) AFM scanned image of the voids

[1]. Foulk, III, J.W.; Johnson, G.C., Klein, P. A.; Ritchie, R.O., “On the toughening of brittle materials by grain bridging: Promoting intergranular fracture through grain angle, strength and toughness”, Journal of the Mechanics and Physics of Solids, v56, n6, p2381-2400, 2008;
[2]. Weinberg, K.; Mota, A.; Ortiz, M., “A varitional constitutive model for porous metal plasticity”, Computational Mechanics, v37, n2, p142-152, 2006;
[3]. Lu, W.Y., Horstemeyer, M. F., Korellis, J. S., Grishabar, R.B., Mosher, D., “High temperature sensitivity of notched AISI 304L stainless steel tests”, Theoretical and Applied Fracture Mechanics, v. 30, P139-152,1998.

Acknowledgement: Sandia is a multiprogram laboratory operated by Sandia Corporation, a Lockheed Martin Company, for the United States Department of Energy under contract DE-AC04-94-AL85000.

Proceedings of the SEM Annual Conference
June 7-10, 2010 Indianapolis, Indiana USA

Local Strain Accommodation in Polycrystalline Ni-Base Superalloys

Jennifer Walley, The Ohio State University, 477 Watts Hall, 2041 College Rd. Columbus, OH 43210, walley.7@osu.edu

Robert Wheeler, UES, Inc. 4401 North Dayton-Xenia Rd, Dayton, OH 45432

Michael D. Uchic, Air Force Research Laboratory, Materials & Manufacturing Directorate, AFRL/RXLM, Wright Patterson AFB, OH 45433

Michael J. Mills, The Ohio State University

ABSTRACT

To exploit new hybrid nickel-based superalloys, physics-based computational models are needed to predict material properties and describe material behavior during exposure to complex life cycles. Such models will allow an iterative assessment of microstructural morphology as related to mechanical properties prior to production of large-scale test specimens or components, thereby reducing development time and cost. Development of these models is currently hindered by a gap in the understanding of local deformation behavior at the intra- and intergranular level. A new in-situ experimental methodology is being developed to characterize local strain heterogeneities in nickel-based superalloys that have a relatively fine grain size (d_{ave}<50μm). Initial work has been performed on Rene 104 that was heat treated to produce two sets of samples with a similar grain size but different γ' distributions and grain boundary morphologies. One sample set had planar boundaries and a bimodal γ' distribution, the other set had serrated boundaries and a trimodal γ' distribution. Progress has been made towards implementation of a suitable speckle pattern for digital image correlation (DIC). Quasi-isostatic room temperature tensile tests were performed in a scanning electron microscope, with images acquired at regular strain intervals. This preliminary data was qualitatively analyzed using Correlated Solutions VIC-2D software. The data for the serrated boundaries indicates that there are indeed interesting strain heterogeneities being developed that are related to grain orientations, boundary relationships to the tensile axis and other boundaries.

INTRODUCTION

With existing nickel-based superalloys it will be difficult to achieve the performance requirements of future turbine disc designs. This is due to conflicting property requirements at the bore (center) and rim of the disc. At the bore, strength and fatigue resistance are optimized with a fine-grained microstructure, while at the rim damage-tolerance and creep resistance are optimized with a coarse-grained microstructure [1]. For existing alloys and processing methods, these competing design requirements are extremely difficult to achieve using a single alloy composition and microstructure.

T. Proulx (ed.), *Time Dependent Constitutive Behavior and Fracture/Failure Processes, Volume 3*, Conference Proceedings of the Society for Experimental Mechanics Series 15, DOI 10.1007/978-1-4419-9794-4_7, © The Society for Experimental Mechanics, Inc. 2011

One method to address this problem is to develop hybrid superalloys that are both compositionally and microstructurally adaptable, that can tailored to meet the different temperature and stress demands required in different regions of the component [2, 3]. To exploit these new hybrid systems, physics-based computational methods are needed to predict material properties in the gradient regions, and describe material behavior during exposure to complex life cycles.

Currently, development of physics-based deformation models for high-temperature alloys systems is hindered by the type of validation data that can be provided via traditional testing techniques. Traditional tensile and creep tests determine averaged bulk properties, but provide limited insight into local deformation behavior. Even with post-testing microstructural evaluation, only a limited understanding can be gleaned relative to how local strain accommodation is controlled by variations in the microstructure. This makes it difficult to apply the experimental data collected to computational models of both traditional and hybrid alloys. Therefore, novel experimental techniques are required to characterize the local deformation fields produced during creep of these materials.

This paper highlights progress made towards the development and utilization of an in-situ, elevated-temperature tensile frame that operates inside of a scanning electron microscope to characterize the local deformation behavior in Ni-based superalloys. This work includes characterizing the microstructure of samples prior to testing, development of a speckle patterning technique for digital image correlation analysis of deformation fields, set-up of the test frame and preliminary results.

EXPERIMENTAL PROCEDURES

1.1 Materials

Prior to testing any hybrid alloys, in-situ testing procedures are being developed using a traditional Ni-based superalloy. The alloy selected was the γ' strengthened alloy Rene 104 (15wt% Cr,18.2% Co, 3.8%Mo, 1.9%W, 1.4%Nb, 3.5%Al, 3.5%Ti, 2.7%Ta, 0.03%C, 0.03%B, 0.05%Zr, bal Ni) [4]. Samples of Rene 104 were heat treated to produce samples with two different microstructures. The first heat treatment produced a "standard" microstructure consisting of relatively planar grain boundaries, while the second heat treatment produced a microstructure consisting of a serrated grain boundary structure, as shown in Figure 1 [5, 6]. Previous work has indicated that serrated boundaries have beneficial effects on fatigue crack growth resistance [6].

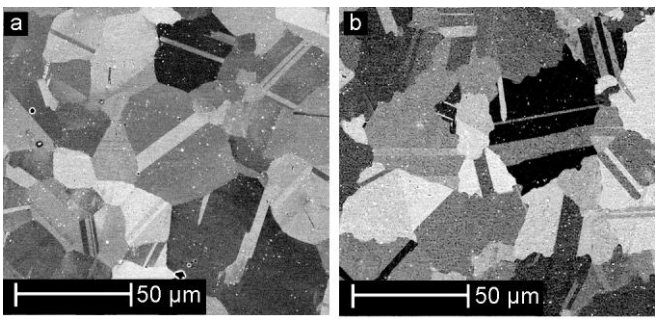

Figure 1. SEM backscatter electron images of the (a) standard heat treatment produces planar grain boundaries, (b) while the second heat treatment produces a serrated boundary structure.

1.2 Sample preparation

Following heat treatment, samples were electrical discharge machined to have a gage length of 1.78 cm, and nominal rectangular cross-section of 0.31 cm by 0.081 cm. Tensile samples were prepared for scanning electron microscopy (SEM) analysis using conventional polishing techniques, culminating with a final vibratory polish using 0.02 µm colloidal silica. Once polished, four microhardness indents were placed at the corners of a 0.01 cm^2 square centered in the middle of the gage section. These hardness indents indicate the location of the speckle pattern needed for in-situ testing, and assist in post-experiment registration of microstructural data with the local displacement maps. Other samples were prepared for γ' particle morphology and distribution analysis. These samples were cut parallel and perpendicular to the tensile loading direction and were mounted and polished similar to tensile samples. For these metallographic samples, after final polishing step the γ' particles were revealed using a selective etchant (2ml HF, 30ml HNO_3, and 50ml lactic acid).

1.2.1 *Characterization techniques*

Electron backscatter diffraction (EBSD) mapping was used to characterize grain size and grain orientation with respect to the tensile axis. EBSD was conducted on an FEI ESEM XL-30 SEM using EDAX TSL orientation image mapping system. Grains were defined as containing at least 5 data points, with less than 5° misorientation between adjacent data points. Twin boundaries of Σ3 orientation were not included in grain area calculations. Grain size distributions were determined using techniques developed by Payton for converting 2-dimensional grain information into 3-dimensional grain information [7]. Analysis of grain size distributions were conducted for each processing type using at least 2000 grains, ASTM standard E112 recommends at least 250 grains be counted to determine mean and standard deviation [8].

SEM images for particle analysis were conducted in an FEI Sirion XL-30 FEG-SEM nominally set at 15keV using ultra-high resolution, backscatter imaging mode. Particle size distributions were determined using image analysis techniques following procedures developed by Payton et al. [7, 9]. An average particle area was determined and linear particle size was calculated by converting area to cube length.

1.2.2 *Speckle patterning*

Correlated Solutions Inc. VIC-2D digital image correlation (DIC) software was used to analyze local deformation fields. In order to characterize intragranular deformation of the Rene 104 microstructure, digital images needed to be acquired at 1500x magnification, which necessitated the use of an SEM. Therefore, the speckle pattern needed for DIC had to be applicable for electron imaging. The DIC software produces optimum accuracy when the minimum speckle size is at least three pixels, and a greater number of speckles per grain produces a more detailed characterization of the strain distribution within each grain [10, 11]. Based on the typical pixel size of SEM images taken at the required magnification and limiting the image acquisition time to less than a minute in time, a random pattern was generated using square speckles with a size range between 0.25 and 0.6 μm.

Electron beam lithography was used to fabricate the desired pattern. This technique uses a focused scanning electron beam to locally expose photo-resist on the sample surface, which results in the point-by-point construction of the desired pattern [12]. Once exposed, the resist is developed and metal or dielectric can be deposited onto the sample surface. After deposition the developed resist is lifted off to reveal the pattern. Following standard clean-room procedures, 4 A PMMA resist was spin coated onto the sample surface. Once coated, the sample was exposed at 50 keV with a dose of 800 uC/cm^2 using a Vistec EBPG 5000 electron beam lithography machine. The resist was then developed in a 9:1 mixture of methyl isobutyl ketone and isopropyl alcohol. The location of the speckle pattern on the sample surface was determined by the microhardness indents placed on the surface before EBSD analysis, as shown in Figure 2. A Denton 502A evaporator was utilized to deposit 10nm of titanium followed by 140nm of gold onto the surface. Once coated the developed resist was lifted off the sample using an acetone bath, leaving a pattern of gold speckles on the sample surface, Figure 3.

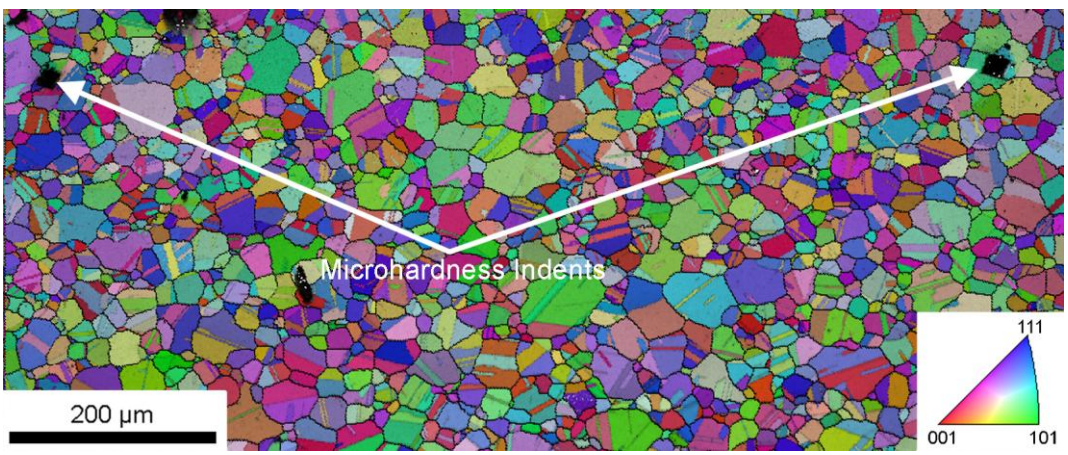

Figure 2. EBSD map of the standard heat treated microstructure showing the location of the microhardness indents used for applying the speckle pattern. In this image each color represents a particular crystal orientation as indicated by the inserted inverse pole figure.

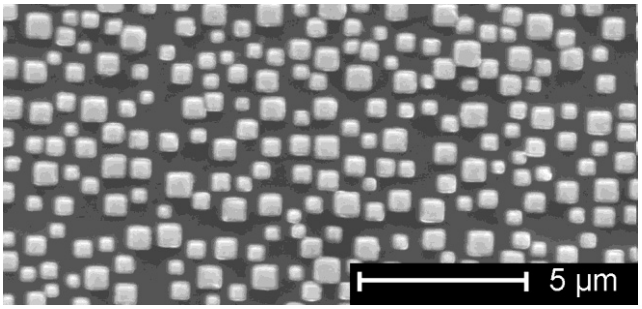

Figure 3. SEM secondary electron image of the Au speckle pattern created by e-beam lithography

1.3 Experimental test set-up

An Ernest Fullam® in-situ tensile stage was employed for this study. The stage is able to apply loads up to 4448 N, heat the specimen to temperatures up to 1200°C, provide measurements of load and crosshead displacement, and allows for EBSD acquisition while the sample is mounted in the test frame. The data acquisition system provided with the test frame was used to acquire load and displacement data every 30 seconds. Initial tensile testing was conducted at room temperature, and the total strain accumulated during each test was approximately 5% at a strain rate of $5x10^{-5}$ s^{-1}. Secondary electron images were collected at approximately 0.2% strain intervals. SEM operating parameters were as follows: 20kV accelerating voltage, dwell time of 10µsec, and an image size of 2048x1768 pixels, which corresponds to an image acquisition time of 37sec. Images were taken at 1000 and 1500x magnification at resolution of 6.7 or 10 pixels/µm.

Elevated temperature image acquisition capabilities of the SEM were tested by imaging a specimen which was incrementally heated to 600°C. At 100°C intervals the sample was held at temperature for 3 to 5 minutes before backscatter and secondary images were acquired using the same SEM operating parameters as discussed previously.

Correlated Solutions VIC-2D software was selected for conducting digital image correlation techniques for determining local strain distributions. Analysis was conducted using 35x35 pixel subset size and spacing between subset centers of 5 pixels. No distortion corrections were conducted for strain analysis, thus, the data presented in this paper is qualitative in nature.

RESULTS

1.4 Microstructural characterization

1.4.1 Grain size

The standard heat treatment produced an average 3-D grain size of 415 μm^2, while the serrated heat treatment produced and average 3-D grain size of 371 μm^2. The distribution of grain sizes is presented in Figure 4. The grain size distributions of these two processing types are very similar, indicating that the major difference between processing types are their boundary morphologies, as seen in Figure 1. The boundary serrations still need to be characterized in accordance with work by Mourer et al. [6].

1.4.2 γ' morphology and distribution

The standard heat treatment produced a bimodal γ' distribution consisting of spherical tertiary γ' precipitates that are typically less than 20 nm (true distribution undetermined), and cuboidal secondary γ' precipitates that are 160 ± 30 nm in width, Figure 5. The serrated heat treatment produced a trimodal γ' distribution with small spherical secondary γ' 86 ±18nm, large dendritic shaped γ' in the grain interiors, and globual γ' along the grain boundaries Figure 5.

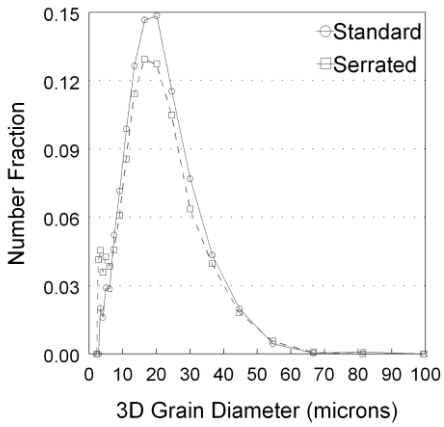

Figure 4. Grain size distributions for both the standard and serrated Rene 104 microstructures

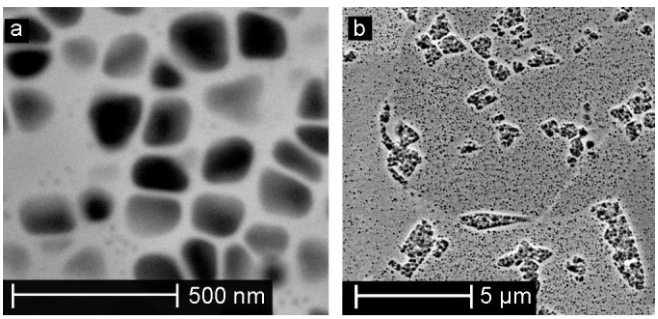

Figure 5. SEM backscatter images of the (a) bimodal γ' distribution of the standard microstructure as compared to the (b) trimodal γ' distribution of the serrated microstructure.

1.5 High temperature imaging

SEM imaging at incremental temperatures indicates that backscatter imaging in this microscope is only possible to about 300°C, above which thermal radiation causes excessive signal noise ratios – an effect which is consistent with other studies [13, 14]. Secondary images showed minimal visible degradation in quality up to 600°C, though specimen cleanliness is important consideration. Organic deposits on the sample surface (dirt, acetone, etc.) charge more readily at elevate temperature and obscure the true sample features. This experiment indicates that for elevated temperature testing above 300°C the speckle pattern for DIC must produce good secondary imaging contrast.

1.6 In-situ strain mapping

Bulk measurements of load and displacement were used to calculate the engineering stress and strain curve, which is shown in Figure 6. Here, sample displacement was obtained by measuring the cross-head displacement, and system compliance (i.e. elastic deflection of the load train) was not accounted for, thus, the stress-strain curves in Figure 6 are not accurate in the elastic regime. Nonetheless, the raw data shows that the serrated samples have higher yield strength then the standard samples by 10%.

Local strain data of the serrated sample, as calculated with the VIC-2D software, is presented for different bulk strain levels in Figure 7. The figure also shows the initial EBSD microstructure overlaid with the speckle pattern in the initial image, and the initial EBSD microstructural boundaries overlaid with the strain fields. None of the local strain levels at the end of the test are at or above the bulk strain levels calculated from crosshead displacement, indicating three possible problems: (a) the load cell is compliant and contributing to the cross-head displacement readings, (b) the sample slipped in the grips during testing, and or (b) spatial and drift distortions in the SEM images are high enough to cause inaccuracy in the quantitative assessment of local strain measurements [15, 16].

Qualitatively, the local strain field maps indicates that some of the grain triple points act as strain localization sites, while other triple points show no appreciable strain build-up. The calculated Schmid factors for the grains oriented for {111}<110> slip under tensile loading along the horizontal axis indicates that due to the high symmetry of the face centered cubic system very few grains are oriented for hard slip, with low Schmid factors. This is indicated by grains that are blue or green in color in Figure 8 (b). With this limited data set, it is seen that most regions of no deformation occur at triple points, or boundaries between favorably and unfavorably oriented grains. There does not appear to be as definitive relationship between areas of maximum strain, but grain boundaries appear to play a dominant role. A more detailed analysis of grain orientations is needed to determine correlations between strain field characteristics and local microstructure.

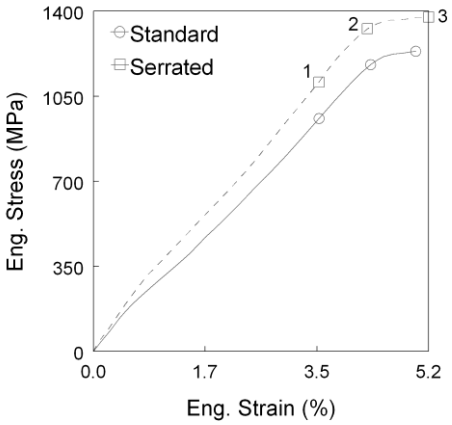

Figure 6. Bulk stress-strain data for standard and serrated heat treated samples

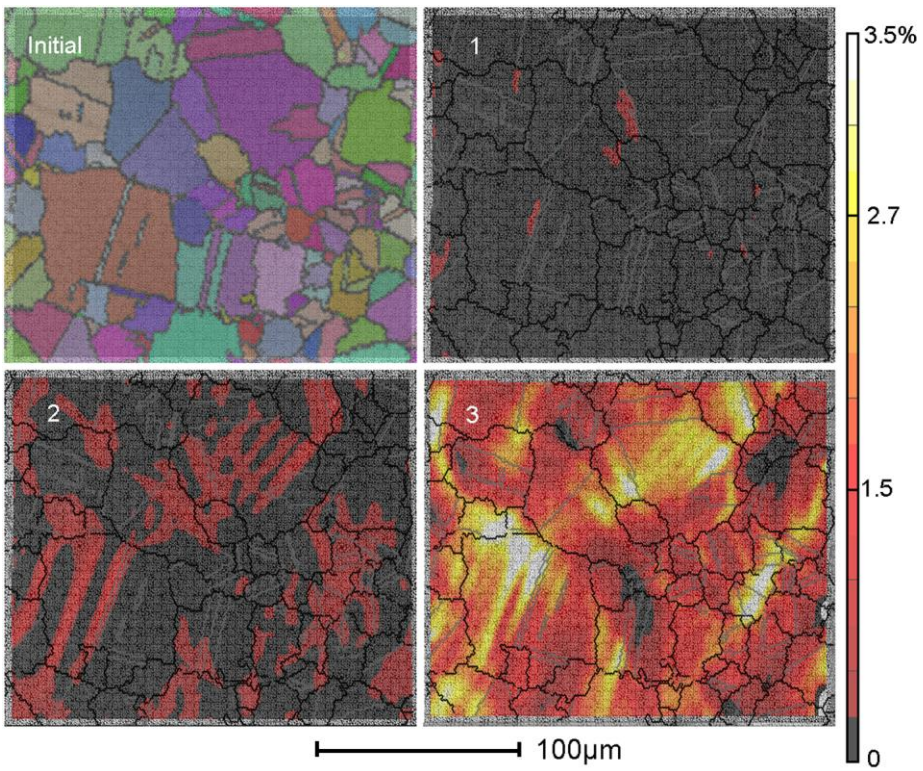

Figure 7. Local strain maps overlaid with the initial EBSD grain information (e_{xx}) at selected points along the stress-strain curve shown in Figure 6. bulk strain levels (as indicated in Figure 6). The loading direction is along the x-axis

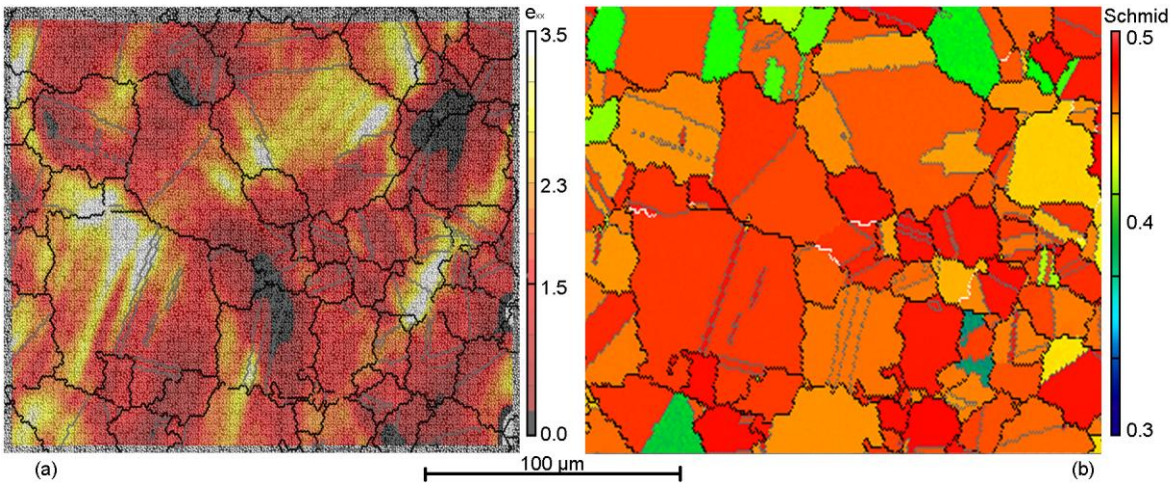

Figure 8 (a) Final strain distribution as compared with the (b) Schmid factor for {111}<110> slip. Blue and green grains are those that have low Schmid factors for octahedral slip

CONCLUSIONS

The ambient temperature data shows there are strain heterogeneities observed in this alloy at the grain size level that cannot be directly linked to Schmid factors. There appears to be a relationship between the extreme strain values and proximity to grain boundaries and grain boundary triple points, this is consistent with another ambient temperature study on a similar nickel based superalloy [17]. Future work includes set-up of the resistance heating equipment for conducting high temperature experiments, 600-800°C. For these high temperature conditions slip by {111} <112> partial dislocations should be predominate.

This study also indicates that the lithography pattern created was too dense to facilitate imaging at low enough magnifications to have a statistically significant representation of grain orientations and grain boundary triple points. At lower magnifications the discreet pattern was not longer recognizable and interference fringes are produced. The lithography pattern needs to be optimized to allow for SEM images at desired magnifications and testing temperatures. In addition, we would like to develop procedures for depositing hafnia speckle patterns, in order to have a pattern that is compatible with high-temperature testing between 600 and 800°C, as other studies have shown that gold and platinum speckles exhibit transient behavior on the surface of Ni-based superalloys at temperatures above 500°C [18]. Another needed modification is the placement of special markers (numbers, different shapes, etc) to help the researcher manually overlay the strain images with EBSD grain images taken after testing. Also, a series of lines parallel and/or perpendicular to the tensile axis needs to be added if grain boundary sliding contributions are to be examined [19].

Following calibration of the equipment for high temperature testing using conventional nickel based superalloys, the system will be utilized to probe heterogeneities in hybrid nickel based superalloys. Testing will be conducted on two different hybrid alloys, a dual heat treatment turbine disc and a bonded turbine disc [3, 4]. The dual heat treatment disc has a very shallow microstructural gradient, while the bonded disc has a very sharp microstructural gradient. This full field in-situ technique should help facilitate better understanding and in turn modeling of deformation behavior in these gradients in microstructures.

ACKNOWLEDGEMENTS

This work is funded by the Air Force Research Laboratory (AFRL) STW-21 program. The author would like to thank Aimee Bross of the Ohio State University Nanotechnology Center for her invaluable assistance with development on the lithography techniques for the speckle patterning. The support received from the Materials & Manufacturing Directorate of the Air Force Research Laboratory has been instrumental for the development of the in-situ tensile frame.

REFERENCES

1. J. Gayda, et al., *The Effect of Dual Microstructure Heat Treatment on an Advanced Nickel-Base Disk Alloy*, in Superalloys, pp.323-329, (2004).
2. D. P. Mourer, et al., *Dual Alloy Disk Development*, in Superalloys, pp.637-643, (1996).
3. D. P. Mourer and J. L. Williams, *Dual Heat Treat Process Development for Advanced Disk Applications* in Superalloys, pp.401-407, (2004).
4. R. C. Reed, *The Superalloys: Fundamentals and Applications*, Cambridge University Press, (2006).
5. H. L. Danflou, et al., *Mechanisms of Formation of Serrated Grain Boundaries in Nickel Base Superalloys*, in Superalloys 1996, pp.119-127, (1996).
6. H. L. Danflou, et al., *Formation of Serrated Grain Boundaries and Their Effect on the Mechanical Properties in a P/M Base Superalloy*, in Superalloys 1992, pp.63-72, (1992).
7. E. J. Payton, *Characterization and Modeling of Grain Coarsening in Powder Metallurgical Nickel-Based Superalloys*, PhD Thesis, The Ohio State University, (2009)
8. ASTM committee E04.08, *ASTM E112-Standard Test Methods for Determining Average Grain Size*, in ASTM Standards, pp.1-26, (1996).
9. E. J. Payton, et al., *Semi-automated Characterization of the gamma prime phase in Ni-based superalloys via high-resolution backscatter imaging*, in Mat. Sci. and Eng. A, **Vol. 527** pp. 2684-92, (2009)
10. W. A. Scrivens, et al., *Development of Patterns for Digital Image Correlation Measurements at Reduced Length Scales*, in Experimental Mechanics, **Vol. 47** (1), pp. 63-77, (2007)
11. M. A. Sutton, et al., *Image Correlation for Shape, Motion and Deformation Measurements*, Springer, (2009).
12. C. Zheng, *Nanofabrication: Principles, Capabilities and Limits*, Springer Inc., (2008).
13. I. M. Fielden, *Investigation of Microsctural Evolution by Real-Time SEM of High-Temperature Specimens*, Sheffield Hallam University (2005)
14. G. G. E. Seward, et al., *High-temperature electron backscatter diffraction and scanning electron microscopy imaging techniques: In-situ investigations of dynamic processes*, in Scanning, **Vol. 24** pp. 232-240, (2002)
15. M. A. Sutton, et al., *Scanning Electron Microscopy for Quantitative Small and Large Deformation Measurements - Part II: Experimental Validation for Magnifications from 200 to 10,000*, in Experimental Mechanics, **Vol. 47** (6), pp. 789-804, (2007)
16. M. A. Sutton, et al., *Scanning Electron Microscopy for Quantitative Small and Large Deformation Measurements - Part I: SEM Imaging at Magnifications from 200 to 10,000*, in Experimental Mechanics, **Vol. 47** (6), pp. 775-787, (2007)
17. M. A. Tschopp, et al., *Microstructure-Dependent Local Stain Behavior in Polycrystals Through In-Situ Scanning Electron Microscope Tensile Experiments*, in Met. Mat. Trans. A, **Vol. 40A** pp. 2363-68, (2009)
18. A. Soula, et al., *Grain boundary and intragranular deformations during high temperature creep of PM Ni-based superalloys*, in Superalloys 2008, pp.387-93, (2008).
19. R. C. Gifkins, *The Measurement of Grain-Boundary Sliding in Polycrystalline Specimens*, in Metal Sci. J., **Vol. 7** pp. 15-19, (1973)

Proceedings of the SEM Annual Conference
June 7-10, 2010 Indianapolis, Indiana USA

Coupled Thermal-Mechanical Experiments for Validation of Pressurized, High Temperature Systems

Bonnie R. Antoun[1], J. Franklin Dempsey[2], Gerald W. Wellman[2], William M. Scherzinger[2], Kevin Connelly[1], Vicente J. Romero[2]
[1]Sandia National Laboratories, Livermore, CA 94551-0969, USA
[2]Sandia National Laboratories, Albuquerque, NM 87185, USA

High fidelity finite element modeling of coupled thermal-mechanical failure processes in complex systems requires, as a precursor, high quality experimentation on several levels. The materials must be characterized such that the entire range of loading parameters is encompassed. Meaningful validation experiments must be developed that allow for the steady, incremental ascension of validation towards system level complexity and, eventually, predictability. This paper describes a combined experimental/modeling effort towards validating failure in pressurized, high temperature systems.

Instrumented, fully coupled thermal-mechanical experiments were conducted to provide validation data for finite element simulations of failure in pressurized, high temperature systems. The design and implementation of the experimental methodology is described in another paper of this conference [1]. Experimental coupling was accomplished on tubular 304L stainless steel specimens by imparting mechanical loading by internal pressurization and thermal loading by side radiant heating. Additionally, mechanical characterization experiments of the 304L stainless steel tube material was completed for development of a thermal elastic-plastic material constitutive model used in the finite element simulations of the validation experiments.

The tubular 304L stainless steel material was characterized in tension at a strain rate of 0.001/s from room temperature to 800°C. The tensile behavior was found to differ substantially from 304L bar stock material characterized in a prior study, with the plasticity characteristics and strain to failure differing at every test temperature. This data, shown in Figure 1, emphasizes the importance of characterizing material of the exact form that will be used in the validation experiment.

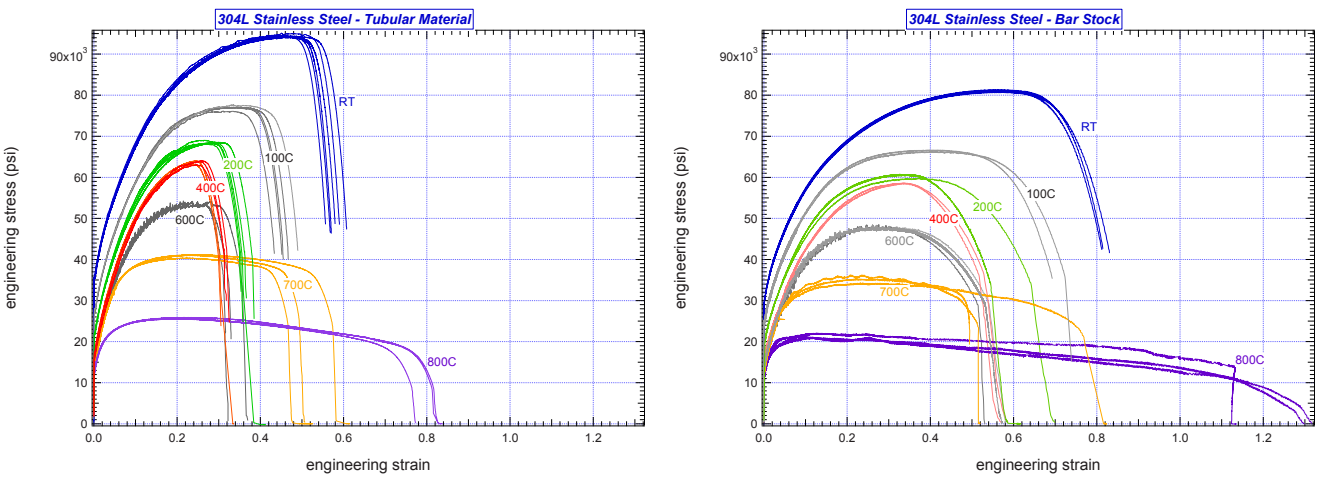

Fig. 1. Comparison of 304L stainless steel tensile behavior with material form

T. Proulx (ed.), *Time Dependent Constitutive Behavior and Fracture/Failure Processes, Volume 3*, Conference Proceedings of the Society for Experimental Mechanics Series 15, DOI 10.1007/978-1-4419-9794-4_8, © The Society for Experimental Mechanics, Inc. 2011

The first generation validation specimen, shown in Figure 2, was machined from the 89 mm (3.5 in.) diameter tube with a wall thickness of 6.35 mm (0.25 in.). Specimens had an overall length of 355 mm (14 in.) and a reduced gage section with a wall thickness of 1.27 mm (0.05 in.). Specimens were instrumented with an array of thermocouples and validation experiments were conducted with various ramp rates of the thermal and mechanical (pressurization and axial load) loads. Figure 3 shows the thermal response of a specimen during the experiment. Pressure was ramped at a rate of 72 psi/min. from 40psi, and temperature at 32 degrees/minute from room temperature. A compressive axial load was ramped to compensate for the pressurization loading the fixtures. Specimen failure occurred after 1188 seconds, at a pressure of 1498 psi. A photograph of the failed specimen is shown in Figure 4. The loading inputs and measured thermal response were used in coupled finite element analyses to predict failure; the predictions were extremely close at 1213 seconds and 1533 psi. The next generation of validation experiments uses a similar geometry with additional complexity of a secondary reduced section.

Fig. 2. Validation specimen in fixtures

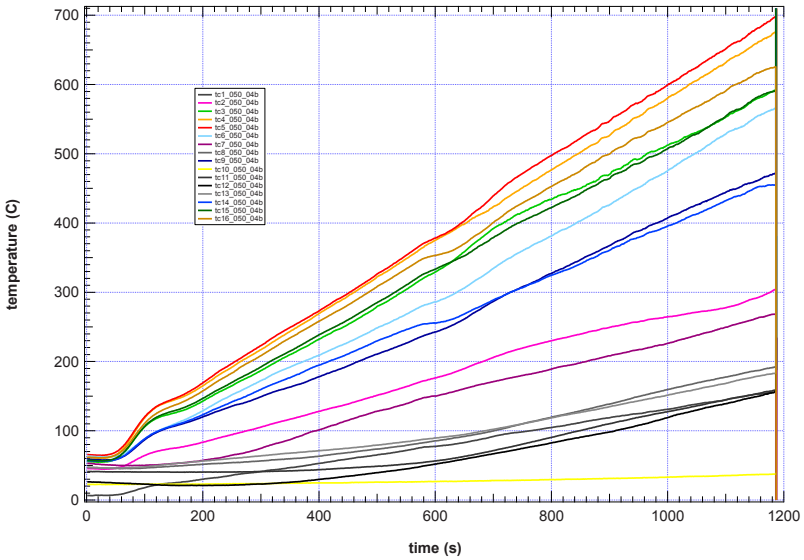

Fig. 3. Measured thermal response of specimen

Fig. 4. Failed validation specimen

ACKNOWLEDGEMENTS

Sandia is a multiprogram laboratory operated by Sandia Corporation, a Lockheed Martin Company, for the United States Department of Energy under Contract DE-ACO4-94AL85000.

REFERENCES

1. Antoun, B. R., Dempsey, J. F., Wellman, G. W., Scherzinger, W. M., and Connelly, K., "Design and Implementation of Coupled Thermomechanical Failure Experiments," *Proceedings of the 2010 SEM Annual Conference and Exposition on Experimental and Applied Mechanics*, Indianapolis, Indiana, June 7-10, 2010.

Proceedings of the SEM Annual Conference
June 7-10, 2010 Indianapolis, Indiana USA

Predictive Simulation of a Validation Forging Using a Recrystallization Model *

Arthur A. Brown[#+], Bonnie R. Antoun[+], Michael L. Chiesa[+], Stephen B. Margolis[+], Devin O'Connor[+], Jason M. Simmons[++], Douglas J. Bammann[++], Chris San Marchi[+], Nancy Y.C. Yang[+]

[#]aabrown@sandia.gov, P.O. Box 969, MS9042
[+]Sandia National Laboratories, Livermore, CA 94551

[++]Department of Computational Manufacturing and Design
Mississippi State University, Mississippi State, MS 39762

ABSTRACT

Recrystallization is the process by which a strained microstructure is replaced by a strain-free set of grains through nucleation and growth. A constitutive model for recrystallization has been developed within the framework of an existing dislocation-based rate and temperature-dependent plasticity model. The theory includes an isotropic hardening variable to represent the statistically stored dislocation density, a scalar misorientation variable related to the spacing between geometrically necessary boundaries, and a variable that tracks the recrystallized volume fraction. The theory has been implemented and tested in a finite element code. Material parameters were fit to data from monotonic compression tests on 304L steel for a wide range of temperatures and strain rates. The model is then validated by using the same parameter set in predictive simulations of experiments in which wedge forgings were produced at elevated temperatures. From the forgings, tensile specimens were machined and tested. Model predictions of the final yield strengths compare well to the experimental results.

1. Introduction

During high temperature manufacturing processes, metals undergo microstructural changes that can greatly affect material properties and residual stresses. Some of the physical mechanisms that influence the strength of a material are strain hardening, recovery, recrystallization, and grain growth [1,2]. If the deformation conditions such as temperature and strain rate are not controlled properly during forging, welding, rolling, or other processes, the final part may have inadequate strength or residual stresses that could be detrimental to the life of the part [3]. In order to be able to optimize manufacturing processes using computational capabilities, it is necessary to have a physically-based constitutive model that captures the dominant strengthening and softening mechanisms. Such a model with predictive capabilities can be used in an optimization scheme to reduce the number of design iterations required to produce a part that meets all strength and microstructural requirements.

Recrystallization is a complex, inhomogeneous process in which nucleation and growth of new strain-free grains replace the worked microstructure of a strained material [4,5]. Recrystallization is due to the motion of grain and subgrain boundaries. As the boundaries move, they sweep away the dislocation structure, leaving a strain-free material with a very low dislocation density. The nucleation of a new recrystallized grain is believed to be due to

* This work was performed at Sandia National Laboratories. Sandia is a multiprogram laboratory operated by Sandia Corporation, a Lockheed Martin Company, for the United States Department of Energy under contract DEAC04-94AL85000.

T. Proulx (ed.), *Time Dependent Constitutive Behavior and Fracture/Failure Processes, Volume 3*, Conference Proceedings of the Society for Experimental Mechanics Series 15, DOI 10.1007/978-1-4419-9794-4_9, © The Society for Experimental Mechanics, Inc. 2011

the growth of an existing deformation-induced subgrain [6]. At elevated temperatures, a subgrain with a lower level of stored energy will preferentially expand at the expense of neighboring subgrains. The driving force for recrystallization is the difference in energy between the deformed and recrystallized state [7]. If the expanding subgrain reaches a critical size, it becomes a stable recrystallized grain.

In the current work, no critical criterion was utilized to initiate recrystallization. Rather, the kinetics of recrystallization are modeled based on the mobility of grain and subgrain boundaries under the driving force provided by the stored energy in the dislocation structure. The internal state variable theory is capable of modeling both static as well as dynamic recrystallization [8], although a simplified version is presented here since we are primarily concerned with static recrystallization for high-rate forgings. The paper is organized as follows: first, the constitutive model will be described. Next, results from parameter optimization will be presented. Finally, a comparison between model predictions and experimental results will be provided.

2. Constitutive Model

A treatment of the kinematics and thermodynamics of the model used here will be published in a future work. Here, for simplicity,we will give a condensed treatment in which we provide the set of equations for the constitutive model for the simplified case of uniaxial stress.

For uniaxial stress, let σ represent the only non-vanishing component of the Cauchy stress tensor and ε represent the axial component of the Eulerian strain tensor. After making approximations for small elastic strains, it can be shown that the model reduces to the following set of equations, written here in the current configuration:

$$\dot{\sigma} = E\left(\dot{\varepsilon} - \dot{\varepsilon}^{p}\right) \tag{1}$$

$$\dot{\varepsilon}^{p} = f(\theta)\left(\sinh\left[\left\langle \frac{\sigma}{\kappa + Y(\theta)} - 1 \right\rangle\right]\right)^{n(\theta)} \tag{2}$$

$$\kappa = \kappa_{1-X}\left(1 - X\right) \tag{3}$$

$$\dot{X} = \frac{1}{\mu\theta} e^{-\frac{c_\theta}{\theta}} \left(1 - e^{-B\bar{\zeta}_{1-X}^{m}}\right)\left[c_{\bar{\kappa}}\bar{\kappa}_{1-X}^{2} + c_{\bar{\zeta}}\bar{\zeta}_{1-X}^{2}\right] X^{a}\left(1 - X\right)^{b} \tag{4}$$

$$\dot{\kappa}_{1-X} = \left[H(\theta) - R_{d}(\theta)\kappa_{1-X}\right]\left|\dot{\varepsilon}^{p}\right| \tag{5}$$

$$\dot{\zeta}_{1-X} = h_{\zeta}\zeta_{1-X}^{1-1/r}\left|\dot{\varepsilon}^{p}\right| \tag{6}$$

Equations (1) and (2) provide the elasticity relation and the flow rule for the plastic strain rate. Equation (3) averages the isotropic hardening variable, κ, between the unrecrystallized and recrystallized volume fractions, where the isotropic hardening variable in the recrystallized volume fraction is assumed to be zero. Equation (4) describes the kinetics of recrystallization through a variable, *X*, that represents the volume fraction of recrystallized material. Equation (5) is the evolution equation for the isotropic hardening variable in the unrecrystallized volume fraction, which has a hardening minus recovery format based on [9]. The last equation, based on [10], tracks a misorientation variable, ζ_{1-X}, in the unrecrystallized volume fraction. ζ_{1-X} is inversely related to the average spacing between geometrically necessary boundaries. The stored energy due to the dislocation structure, represented by κ_{1-X} and ζ_{1-X}, drives the recrystallization kinetics. The mobility of subgrain boundary motion increases with misorientation angle, which increases as the spacing between geometrically necessary boundaries decreases.

The model in this form is only valid for static recrystallization, where the isotropic hardening variable in the recrystallized volume fraction is assumed to be zero. For dynamic recrystallization, the recrystallized material will continue to harden with increased strain. For a treatment of the model form capable of both static and dynamic recrystallization, see [8].

3. Model Performance

Material parameters were fit to data from monotonic compression tests on 304L steel for a wide range of temperatures and strain rates. Three types of test data were included in the set used for parameter optimization. Stress-strain data from single-stage compression at constant strain rate and temperature is shown in Figure 1. It should be noted that although the nominal temperature is held constant, the specimen will heat somewhat due to plastic dissipation. This effect is neglected in the work presented here, but will be included in future work. Figure 2 shows stress-strain data from two-stage compression tests in which the first stage was performed at elevated temperature, followed by a quench after approximately five seconds, and then the second stage was done at room temperature. Figure 3 contains recrystallized volume fraction data from single-stage compressions tests followed by various hold times before quenching. The data was determined from microstructure from etched samples of the compression specimens.

Sixteen parameters were optimized. The results from the parameter optimization for the three types of data are shown in Figures 1 through 3. The model captures the material response quite well over the full range of temperatures and strain rates.

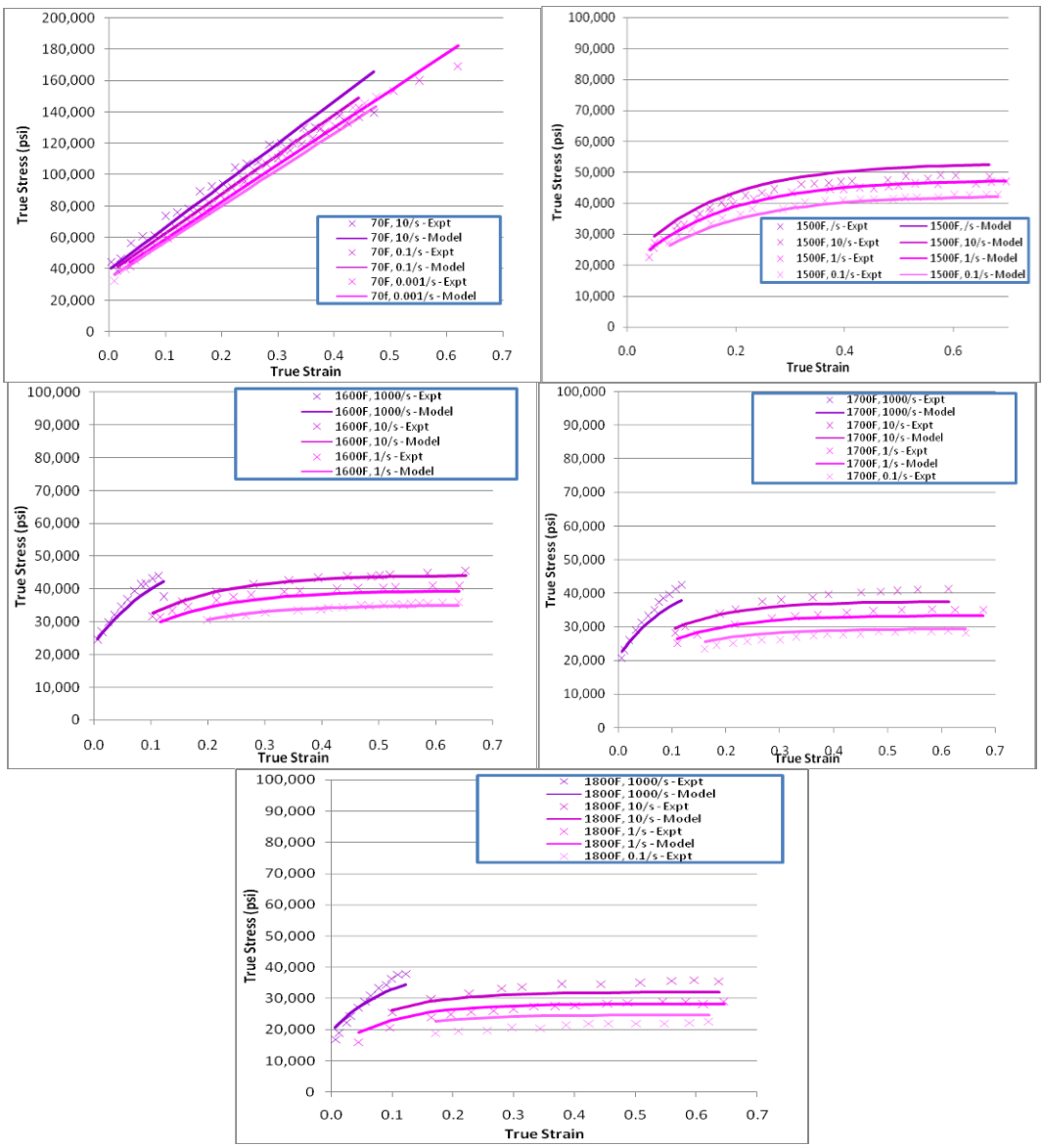

Figure 1. Stress-strain data from single-stage compression tests.

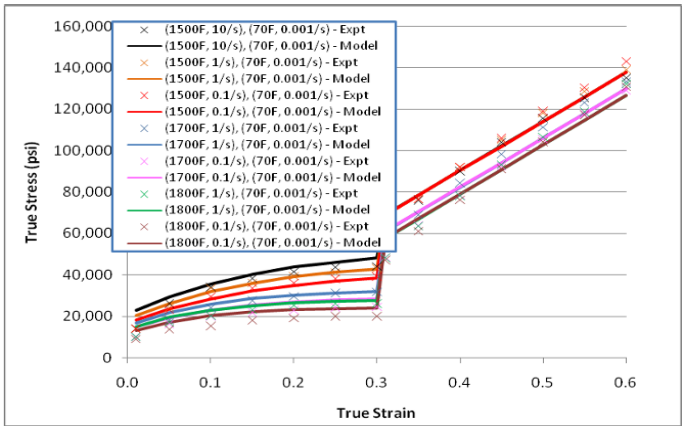

Figure 2. Stress-strain data from two-stage compression tests.

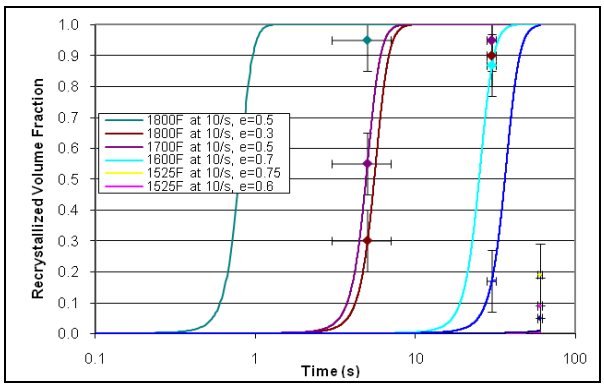

Figure 3. Recrystallized volume fraction data from compress-and-hold tests.

4. Validation

The theory has been implemented and tested in Adagio, Sandia's implicit mechanics code [11]. The model is then validated by using the same parameter set in predictive simulations of experiments in which 304L stainless steel wedges were forged with a HERF machine at Precision Metal Products, Inc. The wedge was held at 1600F, compressed to a final height of one inch by a platen traveling at a rate of approximately 20 ft/s, and then quenched to room temperature. From the flattened forgings, tensile specimens were machined and tested. Figure 4 shows the wedge specimen dimensions.

In the simulation, we assumed a coefficient of friction of 0.1 between the wedge and the platens. Figures 5 and 6 show the evolution of plastic strain and recrystallized volume fraction as the wedge is compressed between the two platens and then held at temperature for 20 seconds. Figure 7 compares the model predictions of the final yield strengths to the initial yield strengths found experimentally. Due to uncertainty in how long the wedge was held at temperature before it was quenched, results are shown for three different hold times.

The model does a fairly good job of predicting the final strength, although it slightly underpredicts the peak strength. This may be due to the fact that the model parameters were determined using compression data, whereas the validation data is from tension tests; stainless steel 304L has a lower yield strength in compression [12]. There is uncertainty in the simulation predictions due to the fact that we do not know for sure how long the wedge was held at temperature before it was quenched. For this reason, we show the results for hold times of 10, 15, and 20 seconds. The most accurate predictions are seen at a hold time of 10 seconds, but the most

accurate profile shape is at 15 seconds. At 15 and 20 seconds, the right side of the wedge has started recrystallizing, which decreases the final yield strength.

Future work includes performing uncertainty quantification on the most important simulation parameters, doing mesh and time step convergence studies, and including the effects of conduction and heat generation due to plastic dissipation in coupled thermal-mechanical simulations.

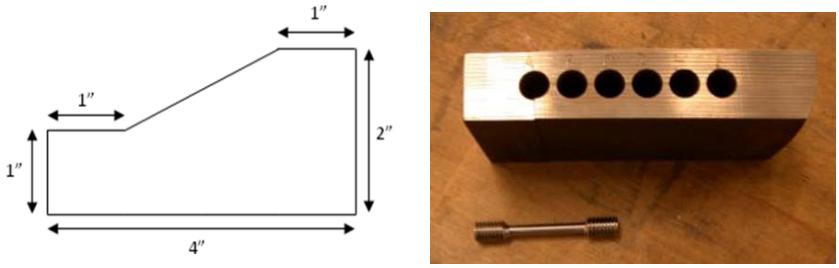

Figure 4. Wedge specimen dimension and machined tensile specimens.

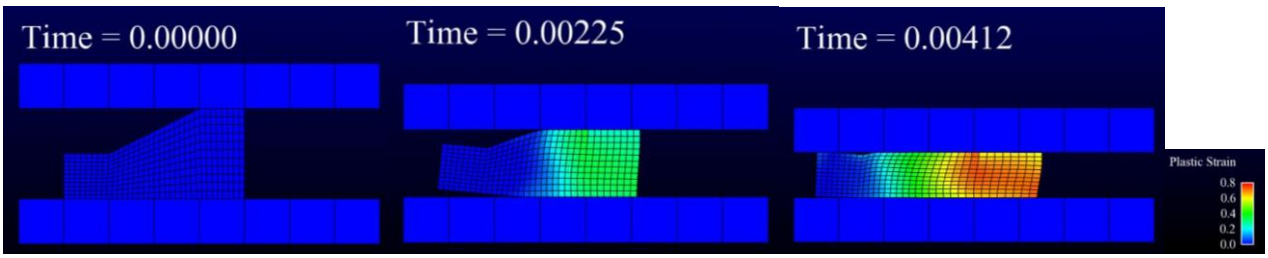

Figure 5. Evolution of plastic strain as the wedge is compressed between the two platens.

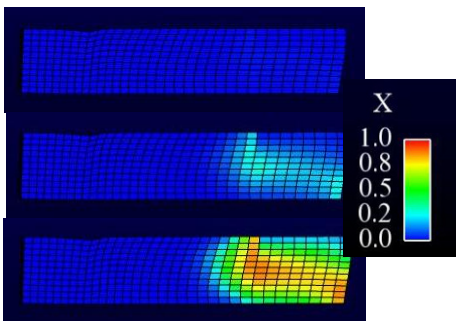

Figure 6. Recrystallized volume fraction at 10, 15, and 20 seconds hold time.

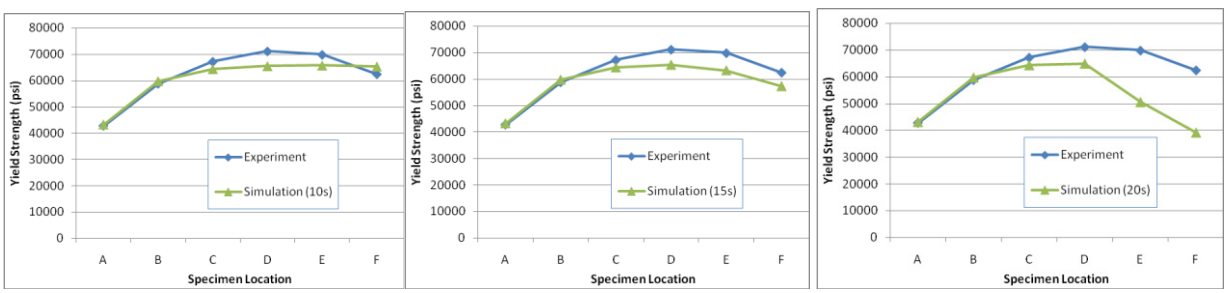

Figure 7. Comparisons between predictions and experimental results.

References

[1] Kocks,U. F., Argon, A. S., Ashby, M. F. The Thermodynamics and Kinetics of Slip. Prog. Mater. Sci. 19, 1-291, 1975.
[2] Doherty, R.D., Hughes, D.A., Humphreys, F.J., Jonas, J.J., Jensen, D.J., Kassner, M.E., King, W.E., McNelley, T.R., McQueen, H.J., Rollett, A.D. Current issues in recrystallization: a review. Mater. Sci. Eng. A238, 219–274, 1997.
[3] Chiesa, M. L., Brown, A. A., Antoun, B. R., Ostien, J. T., Regueiro, R. A., Bammann, D. J., Yang, N. Y. Prediction of final material state in multi-stage forging processes. *AIP Conference Proceedings,* no.712, pt.1, 510-515, 2004.
[4] Haessner, F. (Ed.), Recrystallization of Metallic Materials, 2nd ed., Rieder-Verlag, Stuttgart, 1978.
[5] Humphreys, F. J., Hatherly, M. Recrystallization and Related Annealing Phenomena, Pergamon Press, Oxford, 1995.
[6] Holm, E. A., Miodownik, M. A., Rollett, A. D. On abnormal subgrain growth and the origin of recrystallization nuclei. Acta Mater. 51, 2701–2716, 2003.
[7] Doherty, R. D. Primary recrystallization. In: Cahn, R.W. et al., (Eds.), Encyclopedia of Materials: Science and Technology. Elsevier, pp. 7847–7850, 2005.
[8] Brown, A.A., Bammann, D. J., Chiesa, M. L., Winters, W.S., Ortega, A.R., Antoun, B. R., Yang, N.Y. Modeling static and dynamic recrystallization in FCC metals. In Anisotropy, Texture, Dislocations and Multiscale Modeling in Finite Plasticity & Viscoplasticity, and Metal Forming - Proceedings of PLASTICITY '06: The Twelfth International Symposium on Plasticity and its Current Applications, 2006.
[9] Kocks, U. F., Mecking, H. A Mechanism for static and dynamic recovery. In: Haasen, P., Gerold, V., Kostorz, G. (Eds.), Strength of Metals and Alloys. Pergamon Press, Oxford, pp. 345–350, 1979.
[10] Kok, S., Beaudoin, A. J., Tortorelli, D. A. On the development of stage IV hardening using a model based on the mechanical threshold. Acta Mater. 50 (7), 1653-1667, 2001.
[11] SIERRA Solid Mechanics Team. Adagio 4.14 User's Guide. Sandia Report 2009-7410, 2009.
[12] Qu, S., Huang, C.X., Gao, Y.L., Yang, G., Wu, S.D., Zang, Q.S., Zhang, Z.F. Tensile and compressive properties of AISI 204L stainless steel subjected to equal channel angular pressing. Matls. Sci. and Eng. A. 475, 207-216, 2008.

Proceedings of the SEM Annual Conference
June 7-10, 2010 Indianapolis, Indiana USA

Characterization of Liquefied Natural Gas Tanker Steel from Cryogenic to Fire Temperatures

Bonnie R. Antoun[1], Kevin Connelly[1], Gerald W. Wellman[2], J. Franklin Dempsey[2], Robert J. Kalan[2]
[1]Sandia National Laboratories, Livermore, CA 94551-0969, USA
[2]Sandia National Laboratories, Albuquerque, NM 87185, USA

The increased demand for Liquefied Natural Gas (LNG) as a fuel source in the U.S. has prompted a study to improve our capability to predict cascading damage to LNG tankers from cryogenic spills and subsequent fire. To support this large modeling and simulation effort, a suite of experiments were conducted on two tanker steels, ABS Grade A steel and ABS Grade EH steel. A thorough and complete understanding of the mechanical behavior of the tanker steels was developed that was heretofore unavailable for the span of temperatures of interest encompassing cryogenic to fire temperatures. This was accomplished by conducting several types of experiments, including tension, notched tension and Charpy impact tests at fourteen temperatures over the range of -191 ºC to 800 ºC.

The large range of test temperatures required the use of different specimen geometries, test frames and experimental techniques. For instance, tensile characterization for cold temperatures, room temperature to -191 ºC, were conducted on an MTS 880 20 Kip test frame using a 3.18 mm (0.125 in.) diameter tensile specimen inside an environmental chamber. Gaseous liquid nitrogen (LN) was used to cool the chamber and specimens and strain was measured with a 12.7 mm (0.5 in.) extensometer for temperatures as low as -140 ºC. LN in its liquid state was used to cool submerged specimens and strain gages were used to measure strain below -140 ºC. A photograph during cold temperature testing is shown in Figure 1.

Fig. 1. Cold temperature test setup

Tensile characterization at elevated temperatures to 800 ºC were conducted on an MTS A/T 50 Kip test frame using 8.9 mm (0.35 in.) diameter specimens heated within a three zone high temperature split tube furnace. Strain was measured with a 23 mm (0.9 in.) extensometer fitted with long alumina rods that directly contacted the specimens but allowed the extensometer to remain outside the furnace. A photograph during elevated temperature tensile testing is shown in Figure 2.

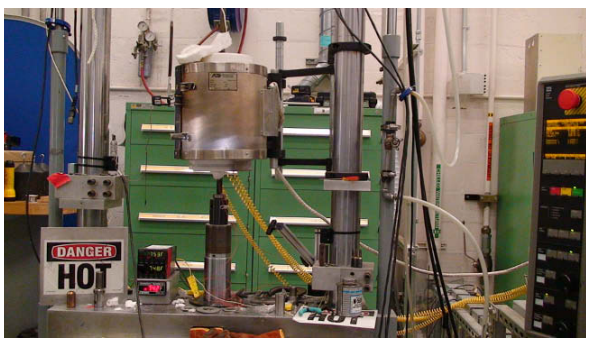

Fig. 2. Elevated temperature test setup

The Charpy impact test results are shown in Figure 3; the ductile-brittle transition temperature was measured at about -50 ºC for both steels. A comparison between the room temperature tensile behaviors of the two ABS steels is shown in Figure 4. Also shown is the measured variation in the Grade A steel from two locations in the same large plate of material, locations are denoted as plate A and plate B. Upper and lower yield points were observed in both steels, this phenomenon occurred at every temperature from the coldest temperature through 300 ºC, except 100 ºC. The tensile behavior of the ABS Grade A material as a function of temperature is shown in Figures 5 and 6. Serrated flow was observed at room temperature through 400 ºC, except again at 100 ºC. These serrations are attributed to dynamic strain aging. Also noteworthy is the increase in flow stress that occurs from room temperature through to between 300 ºC and 400 ºC. This increase is typical in materials that exhibit dynamic strain aging.

T. Proulx (ed.), *Time Dependent Constitutive Behavior and Fracture/Failure Processes, Volume 3*, Conference Proceedings of the Society for Experimental Mechanics Series 15, DOI 10.1007/978-1-4419-9794-4_10, © The Society for Experimental Mechanics, Inc. 2011

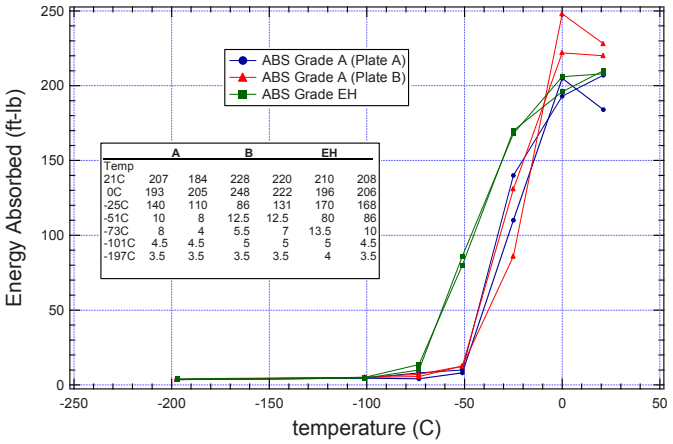

Fig. 3. Charpy impact test results

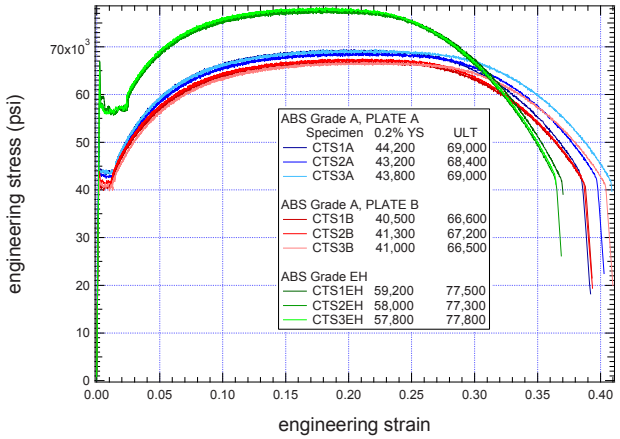

Fig. 4. Room temperature tensile behavior

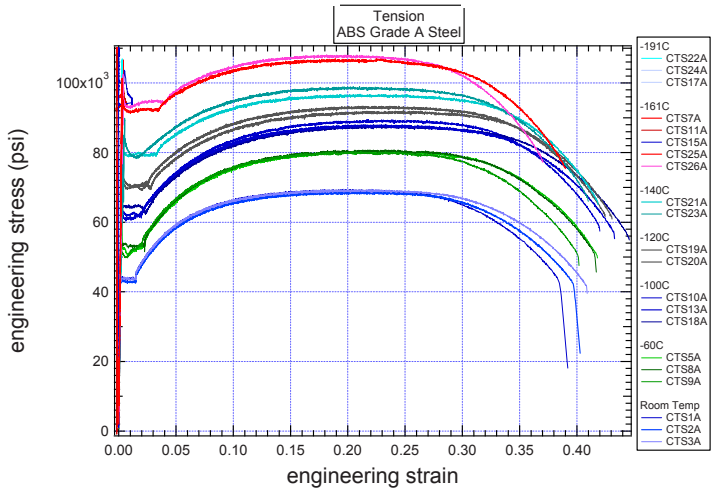

Fig. 5. Cold temperature tensile behavior of ABS Grade A steel

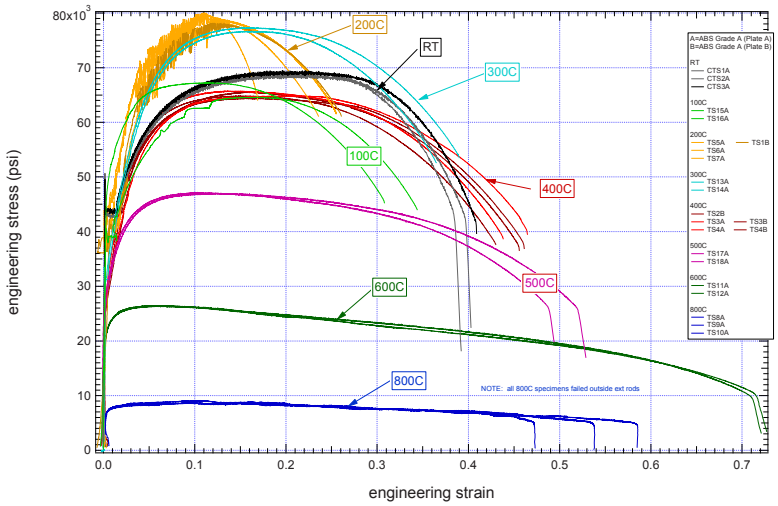

Fig. 6. Elevated temperature tensile behavior of ABS Grade A steel

ACKNOWLEDGEMENTS

Sandia is a multiprogram laboratory operated by Sandia Corporation, a Lockheed Martin Company, for the United States Department of Energy under Contract DE-ACO4-94AL85000.

Proceedings of the SEM Annual Conference
June 7-10, 2010 Indianapolis, Indiana USA

Nonlocal Microdamage Constitutive Model for High Energy Impacts

Rashid K. Abu Al-Rub[1] and Anthony N. Palazotto[2]

[1]Zachry Department of Civil Engineering, Texas A&M University, College Station, TX 77843, USA, E-mail: rabualrub@civil.tamu.edu
[2]Department of Aeronautics and Astronautics, Air Force Institute of Technology, WPAFB, OH 45433-7765, USA

ABSTRACT
During highly dynamic and ballistic loading processes, large inelastic deformation associated with high strain rates leads, for a broad class of heterogeneous materials, to degradation and failure by localized damage and fracture. However, as soon as material failure dominates a deformation process, the material increasingly displays strain softening and the finite element predictions of ballistic response are considerably affected by the mesh size. This gives rise to non-physical description of the ballistic behavior and mesh-dependent ballistic limit velocities that may mislead the design of ballistic-resistant materials. This study is concerned with the development and numerical implementation of a novel coupled thermo-hypoelasto-viscoplastic and thermo-viscodamage constitutive model within the laws of thermodynamics in which an intrinsic material length scale parameter is incorporated through the nonlocal gradient-dependent damage approach. It is shown through simulating plugging failure in ballistic penetration of high-strength steel targets by blunt projectiles that the length scale parameter plays the role of a localization limiter allowing one to obtain meaningful values for the ballistic limit velocity independent of the finite element mesh density. Therefore, the proposed nonlocal damage model leads to an improvement in the modeling and numerical simulation of high velocity impact related problems.

INTRODUCTION
In light of the increasing requirements for lightweight vehicular and personal protection systems in many industries (e.g. military, defense, and space), low-density advanced composite materials are highly desirable. Examples of those materials are metallic alloys, ceramics, and polymers with heterogeneous microstructures reinforced with hard, stiff, and/or soft particles (inclusions) at decreasing microstructural length scales that range in size from few nanometers (e.g. carbon nanotubes) to few microns (e.g. ceramic or metallic oxide particles). The focus of this study is on the use of those materials to increase the ballistic performance of structural systems under high impact damage loading conditions. Therefore, it is imperative to develop very effective constitutive and computational models that can be used in guiding the design processes of those advanced materials under ballistic loading conditions. The development of such models is also motivated by the large time and money cost of conducting ballistic experiments on such advanced materials such that physically-based and effective theoretical and computational models, as an adjunct to experimental work, can save a lot of this cost and also provide important insights about their ballistic behaviors that are not accessible by experimental routs. Moreover, the accuracy and computational effectiveness of these models are crucial for designing better materials. Therefore, the focus of this paper is on the development of these modeling techniques that specifically address one main important issue: the finite element mesh-dependent ballistic limit velocity predictions. Mesh sensitivity is one of the most critical problems of numerical codes, especially for the analysis of damage localization and failure. As the perforation analysis of a steel plate by a projectile is the most typical impact problem, it is very important to understand the variation of fracture mechanism of projectiles and target plates according to the change of mesh density. This issue cannot be addressed sufficiently when using the classical (local) plasticity or viscoplasticity (rate-dependent plasticity) and damage or viscodamage (rate-dependent damage) theories due to the absence of explicit intrinsic material length scale measures in their constitutive equations. Recently, Abu Al-Rub and co-authors [1-4] successfully used the nonlocal damage theory to solve the mesh-sensitivity problem. Explicit (via the nonlocal gradient-dependent theory) and implicit (via the viscosity) intrinsic length scales of material are introduced as a remedy of the mesh sensitivity problem where those length scales act as localization

T. Proulx (ed.), *Time Dependent Constitutive Behavior and Fracture/Failure Processes, Volume 3*, Conference Proceedings of the Society for Experimental Mechanics Series 15, DOI 10.1007/978-1-4419-9794-4_11, © The Society for Experimental Mechanics, Inc. 2011

limiters. This framework is also used here to solve the high energy impact of steel targets by blunt deformable projectiles. The enhanced nonlocal gradient-dependent theory formulates a constitutive framework on the continuum level that is used to bridge the gap between the micromechanical theories and the classical (local) continuum theories. They are successful in explaining the size effects encountered at the micron scale and in preserving the well-posedeness of the initial boundary value problem governing the solution of material instability triggering strain localization. Moreover, viscosity (rate dependency) allows the spatial difference operator in the governing equations to retain its hyperbolicity and the initial boundary value problem is well-posed. Model capabilities are preliminarily illustrated for the dynamic localization of inelastic flow in adiabatic shear bands and the perforation of Weldox 460E steel plates with by a deformable blunt projectile at various high impact speeds.

NONLOCAL MICRODAMAGE CONSTITUTIVE MODEL

The micro-damage model used to predict material behavior under dynamic loading conditions was earlier presented in [1]. Thus, only the main equations will be given in the following. The model is based on the nonlocal gradient-dependent theory. It includes the von Mises yield criterion, the non-associated flow rules, isotropic and anisotropic strain hardening, strain rate hardening, softening due to adiabatic heating and anisotropic damage evolution, and finally a path dependent equation of state. The stress-strain rate relationship in the spatial and damaged configuration is given by

$$\overset{\nabla}{\boldsymbol{\tau}} = \mathbb{C} : \left(\boldsymbol{d} - \boldsymbol{d}^{vp} - \boldsymbol{d}^{vd} \right) - \boldsymbol{A} : \overset{\nabla}{\boldsymbol{\phi}} - \boldsymbol{\beta} \dot{T} , \quad \mathbb{C} = \widehat{\boldsymbol{M}}^{-1} : \overline{\mathbb{C}} : \widehat{\boldsymbol{M}}^{-1}, \quad \widehat{\boldsymbol{M}} = 2 \left[\left(\mathbf{1} - \widehat{\boldsymbol{\phi}} \right) \otimes \mathbf{1} + \mathbf{1} \otimes \left(\mathbf{1} - \widehat{\boldsymbol{\phi}} \right) \right]^{-1} \tag{1}$$

where $\overset{\nabla}{}$ indicates co-rotational objective derivative, $\boldsymbol{\tau}$ is the corotational rate of Kirchhoff stress tensor, $\boldsymbol{d}$ is the total rate of deformation, $\overline{\mathbb{C}}$ and $\mathbb{C}$ are the forth-order undamaged and damaged elasticity tensors, respectively, $\dot{T}$ is the rate of absolute temperature, $\boldsymbol{\beta}$ is the damaged thermal expansion coefficient, and $\mathbf{1}$ is the second-order identity tensor. $\overline{\mathbb{C}}$ and $\boldsymbol{A}$ are given by the following relations:

$$\overline{\mathbb{C}} = K^e \mathbf{1} \otimes \mathbf{1} + 2G^e \mathbf{I}^{dev}, \quad \boldsymbol{A} = \frac{\partial \widehat{\boldsymbol{M}}^{-1}}{\partial \widehat{\boldsymbol{\phi}}} : \widehat{\boldsymbol{M}} : \boldsymbol{\tau} + \mathbb{C} : \widehat{\boldsymbol{M}} : \frac{\partial \widehat{\boldsymbol{M}}^{-1}}{\partial \widehat{\boldsymbol{\phi}}} : \mathbb{C}^{-1} : \left(\boldsymbol{\tau} + \boldsymbol{\beta} \Delta T \right) \tag{2}$$

where K^e is the bulk modulus and G^e is the shear modulus. The viscoplastic rate of deformation, $\boldsymbol{d}^{vp}$, the viscodamage rate of deformation, $\boldsymbol{d}^{vd}$, and the nonlocal second-order damage tensor, $\widehat{\boldsymbol{\phi}}$, are give as follows:

$$\boldsymbol{d}^{vp} = \dot{\lambda}^{vp} \frac{\partial f}{\partial \boldsymbol{\tau}}, \; \boldsymbol{d}^{vd} = \dot{\lambda}^{vd} \frac{\partial g}{\partial \boldsymbol{\tau}}, \; \overset{\nabla}{\boldsymbol{\phi}} = \dot{\lambda}^{vp} \frac{\partial f}{\partial \boldsymbol{Y}} + \dot{\lambda}^{vd} \frac{\partial g}{\partial \boldsymbol{Y}} \tag{3}$$

The potentials f and g are the nonlocal viscoplastic and viscodamage conditions given, respectively, by

$$f = \sqrt{\tfrac{3}{2} \left(\overline{\boldsymbol{\tau}}' - \overline{\widehat{\boldsymbol{X}}} \right) : \left(\overline{\boldsymbol{\tau}}' - \overline{\widehat{\boldsymbol{X}}} \right)} - \left[\overline{Y}_{yp} + \overline{\widehat{R}} \right] \left[1 + (\eta^{vp} \dot{\overline{p}})^{1/m_1} \right] \left[1 - \left(T / T_m \right)^n \right] \leq 0 \tag{4}$$

$$g = \sqrt{\left(\widehat{\boldsymbol{Y}} - \widehat{\boldsymbol{H}} \right) : \left(\widehat{\boldsymbol{Y}} - \widehat{\boldsymbol{H}} \right)} - \left[l + \widehat{K} \right] \left[1 + (\eta^{vd} \dot{\widehat{r}})^{1/m_2} \right] \left[1 - \left(T / T_m \right)^n \right] \leq 0 \tag{5}$$

where $\overline{\boldsymbol{\tau}}'$ is the effective deviatoric stress tensor, $\overline{Y}_{yp}$ is the initial yield strength (at zero absolute temperature, zero plastic strain, and static strain rate), T_m is the melting temperature, $\overline{\widehat{R}}$ is the nonlocal isotropic hardening stress, $\overline{\widehat{\boldsymbol{X}}}$ is the nonlocal anisotropic hardening stress, $\dot{\overline{p}} = \sqrt{\frac{2}{3} \overline{d}_{ij}^{vp} \overline{d}_{ij}^{vp}}$ is the rate of the effective accumulative viscoplastic strain, m and n are material constants, η^v is the relaxation time, the non-local damage forces $\widehat{\boldsymbol{Y}}$

and $\widehat{K}$ are, respectively, characterizing the viscodamage evolution and the viscodamage isotropic hardening forces, l is the initial damage threshold, and $\widehat{r}$ is the nonlocal damage accumulation.

The nonlocal evolution equation for the isotropic and kinematic hardening in the undamaged configuration, are given as:

$$\dot{\overline{R}} = \dot{\overline{R}} + \tfrac{1}{2}\ell_1^2\nabla^2\dot{\overline{R}} \quad \text{with} \quad \dot{\overline{R}} = \frac{a_1\dot{\lambda}^{vp}}{\left(1-\widehat{r}\right)^2}\left(1-k_1\overline{\widehat{R}}\right) \tag{6}$$

$$\overset{\nabla}{\overline{\boldsymbol{X}}} = \overset{\nabla}{\boldsymbol{X}} + \tfrac{1}{2}\ell_2^2\nabla^2\overset{\nabla}{\boldsymbol{X}} \quad \text{with} \quad \overset{\nabla}{\overline{X}}_{ij} = a_2\dot{\lambda}^{vp}\widehat{\boldsymbol{M}} : \widehat{\boldsymbol{M}} : \left(\frac{\partial f}{\partial \overline{\boldsymbol{\tau}}} - k_2\overline{\widehat{\boldsymbol{X}}}\right) \tag{7}$$

The evolution equations for the nonlocal viscodamage isotropic and kinematic hardening functions are given by

$$\dot{\overline{K}} = \dot{K} + \tfrac{1}{2}\ell_3^2\nabla^2\dot{K} \quad \text{with} \quad \dot{K} = a_3\dot{\lambda}^{vd}\left(1-h_1\widehat{K}\right) \tag{8}$$

$$\overset{\nabla}{\overline{\boldsymbol{H}}} = \overset{\nabla}{\boldsymbol{H}} + \tfrac{1}{2}\ell_4^2\nabla^2\overset{\nabla}{\boldsymbol{H}} \quad \text{with} \quad \overset{\nabla}{\boldsymbol{H}} = a_4\dot{\lambda}^{vd}\left(\frac{\partial g}{\partial \boldsymbol{Y}} - h_2\widehat{\boldsymbol{H}}\right) \tag{9}$$

The nonlocal strain energy release rate is given by

$$\widehat{\boldsymbol{Y}} = \frac{\left(1+a_5\right)}{2}\left(\boldsymbol{\tau}-\boldsymbol{\beta}\Delta T\right) : \widehat{\boldsymbol{M}} : \frac{\partial \widehat{\boldsymbol{M}}^{-1}}{\partial \widehat{\boldsymbol{\phi}}} : \mathbb{C}^{-1} : \left(\boldsymbol{\tau}+\boldsymbol{\beta}\Delta T\right) \tag{10}$$

where ℓ_i (i=1-4) are material length scale parameters which should be obtained from gradient-dominant experiments (e.g. indentation tests, bending tests, or torsion tests) [5]. k_i, h_i, and a_i are material constants that can be identified from conventional tests (e.g. uniaxial tension test). In this study, the material length scales ℓ_i (i=1-4) are assumed equal and physically interpreted as the average free-path for dislocations, such that the following expression has been derived in [6] based on dislocation mechanics arguments:

$$\dot{\ell} = \ell\,\nu_o \exp\left[-\left(U_o/k_B T\right)\left\{1-\left(\overline{\tau}^*/\overline{\tau}_o^*\right)^p\right\}^q\right] \tag{11}$$

where ν_o is the fundamental vibration frequency of the dislocation, $p=1$ and $q=2$ are material constants defining the shape of the short-range obstacle, k_B is the Boltzmann's constant, U_o is the referential activation energy at zero absolute temperature, $\overline{\tau}^*$ is the undamaged thermal stress from Eq. (4), which is a function of strain $\overline{p}$, strain rate $\dot{\overline{p}}$, and temperature T,

$$\overline{\tau}^* = [\overline{Y}_{yp} + \overline{\widehat{R}}][1+(\eta^{vp}\dot{\overline{\widehat{p}}})^{1/m_1}][1-\left(T/T_m\right)^n] \tag{12}$$

and $\overline{\tau}_o^*$ is the referential thermal stress for the intact material at which dislocations can overcome the obstacles without the assistance of thermal activation. Furthermore, ℓ has the following expression [7]:

$$\ell = \frac{d\,D}{D + d\left[1-\exp(-a_1\overline{p})\right]} \tag{13}$$

where d is the mean grain size or mean particle (inclusion) size, D is the mean inter-particle spacing in particle reinforced composites or other characteristic size, p is the effective plastic strain, and a_1 is the strain-hardening rate (see Eq.$(6)_2$). This equation shows that ℓ decreases with the effective plastic strain, increases with the grain size or inclusion size, decreases with the ratio of D/d, and decreases with the strain-hardening rate. It also shows that ℓ decreases from an initial value $\ell = d$ at yielding to a final value $\ell \to 0$ which corresponds to the classical local plasticity or damage limit at very large values of D, d, or p.

The thermodynamic pressure stress P for a shock compressed solid is given as follows:

$$P = (1-\gamma) c_v T^{ig} \varepsilon\,, \quad T^{ig} = T_r \exp\left[(\eta - \eta_r)/c_v\right]\left[1+\varepsilon\right]^{(\gamma-1)} \exp\left[(\gamma-1)\left(1/(1+\varepsilon)-1\right)\right] \tag{14}$$

which gives the equation of state necessary for high-impact loading. The equation of state accounts for compressibility effects (changes in density) and irreversible thermodynamic processes. $\gamma = c_p/c_v$ is the ratio of the specific heats, where c_p and c_v are the specific heats at constant pressure and constant volume, respectively. ε is the nominal volumetric strain, and T^{ig} is chosen to have the form of ideal gas temperature with T_r is the room temperature, η is the entropy, and η_r is the reference entropy. The increase in temperature is calculated using the following heat equation:

$$\rho_o c_p \dot{T} = \Upsilon \boldsymbol{\tau}' : \left(\boldsymbol{d}^{vp} + \boldsymbol{d}^{vd}\right) - J^e P(\boldsymbol{d}^e : \mathbf{1}) - T\boldsymbol{\beta} : \boldsymbol{d}^e \tag{15}$$

where ρ_o is the reference density and Υ is the heat fraction.

In this development we base the failure criterion on the nonlocal evolution of the accumulated micro-damage internal state variable, $\widehat{\boldsymbol{\phi}}$, and the equation of state for the thermodynamic pressure. It implies that for

$$\left\|\widehat{\phi}\right\| = \sqrt{\widehat{\phi}_{ij}\widehat{\phi}_{ij}} \geq \left\|\phi\right\|_c \quad \text{and/or} \quad P \geq P_{cutoff} \tag{16}$$

the material loses its carrying capacity, where $\|\phi\|_c$ is the critical damage when catastrophic failure in the material takes place and P_{cutoff} is the pressure cutoff value when tensile failure or compressive failure occurs.

The proposed model is implemented in the well-known commercial finite element program ABAQUS/Explicit [9] via the user material subroutine VUMAT. Now we conduct a numerical simulation of the experimental tests presented in [8] for a blunt projectile made of hardened Arne tool steel impacting a 12mm thick circular plate made of Weldox 460 E steel. The circular target plate of 500 mm diameter is examined here for different projectile velocities. For simplicity, the projectile is modeled as a bilinear elastic-plastic strain rate-independent von Mises material with isotropic hardening. The nominal length and diameter of the hardened projectile are 80 mm and 20 mm, respectively. The target plate is fully clamped at the edge boundary, while the projectile is given an initial velocity for all simulations. The experimental results in [8] indicated the problem involving shear localization and plugging for blunt projectiles. The numerical solution using the present model is mesh size independent and converges monotonically towards a limit solution when the number of elements over the target thickness becomes sufficiently large. The proposed model can predict the shear localization behavior with no finite element mesh dependency.

The plot of the initial configuration of one of the FE analysis is shown in Fig. 1. Due to symmetry and in order to reduce the simulation time, an axisymmetric problem is solved, where a four-node 2D axisymmetric element with one integration point and a stiffness based on hourglass control is used, and the mesh is somewhat coarsened towards the boundary.

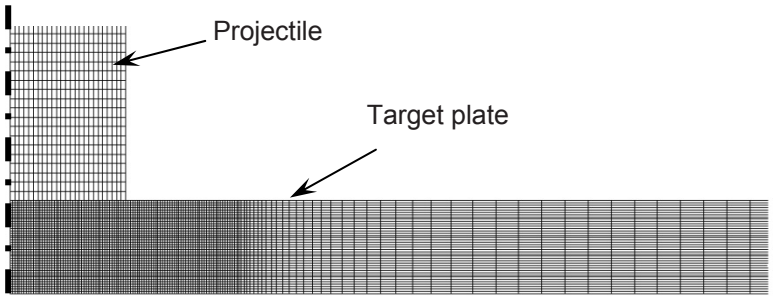

Fig. 1. Finite element mesh plot of the axisymmetric initial configuration just before impact.

Two- and three-dimensional simulations are presented in Figs. 2 and 3. This is done in order to make sure that both types of simulations yield the same results and no dependence on the type of analysis is encountered. Numerical plots showing perforation of the target plate by a blunt projectile at impact velocity close to the ballistic limit of 200m/s are shown in Figs. 2 and 3. The contours of accumulated viscoinelastic strain are plotted on the deformed mesh. It can be seen that limited inelastic deformation occurs outside the localized shear zone. These plots clearly demonstrate that the numerical model qualitatively captures the overall physical behavior of the target during penetration and perforation as compared to the experimental results in Fig. 1. Moreover, the 2-D and 3-D simulations agree very well. Notice also that in these plots, only a part of the complete target plate is shown. High-speed camera images showing perforation of the target plate at impact velocities close to the ballistic limit are shown in Fig. 4, where the numerical simulations are in very well agreement with the simulations.

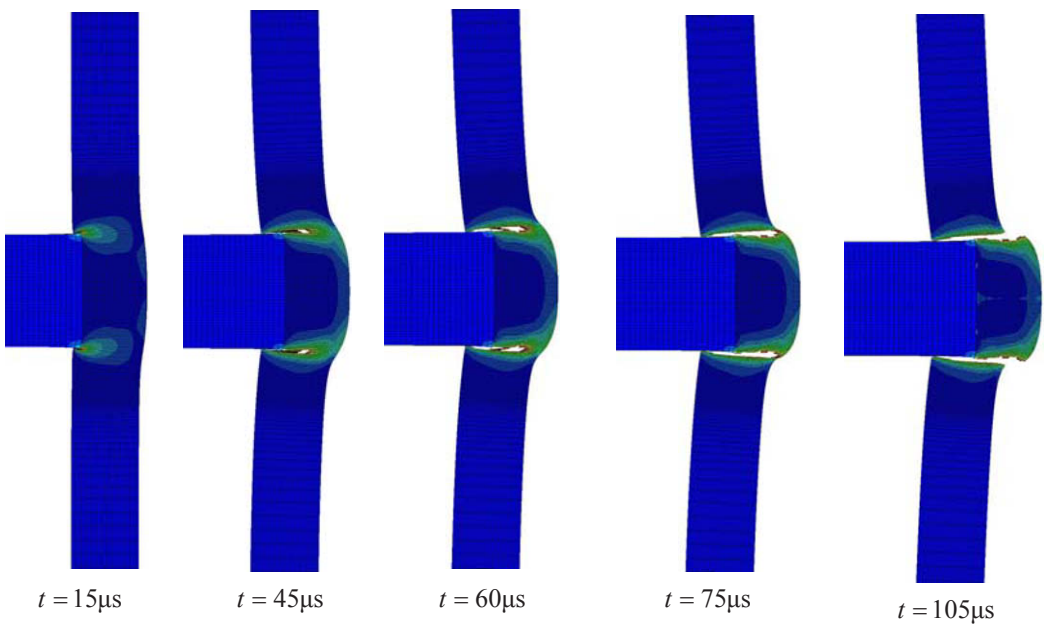

Fig. 2. Two-dimensional numerical simulation of perforation of the target plate by a blunt projectile of initial impact velocity of 200 m/s plotted as contours of accumulated viscoinelastic strain at different times.

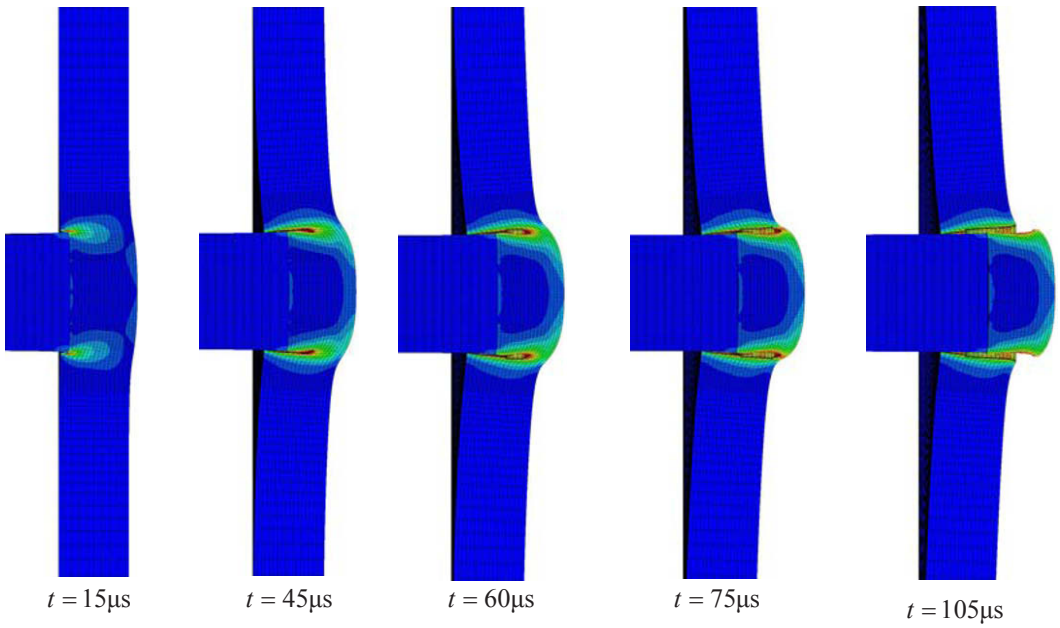

Fig. 3. Three-dimensional numerical simulation of perforation of the target plate by a blunt projectile of initial impact velocity of 200 m/s plotted as contours of accumulated viscoinelastic strain at different times.

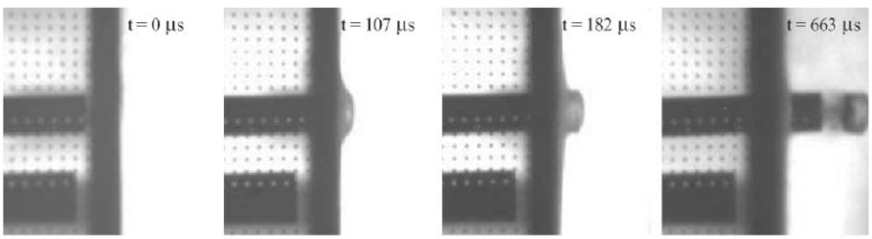

Fig. 4. High-speed camera images showing perforation of the target plate at impact velocities close to the ballistic limits with a blunt projectile; after [8].

Figs. 5(a) and 5(b) shows the impact versus the predicted residual velocity curves for various number of elements through the plate thickness when compared to the experimental data in [8]. Fig. 5(a) shows the current model predictions when assuming a zero length scale $\ell = 0$ (i.e. local damage), while Fig. 5(b) shows the predictions with the nonlocal damage model. It is very clear that mesh sensitivity is most distinct close to the ballistic limit such that the predicted ballistic limit velocity (i.e. at zero residual velocity) when assuming $\ell = 0$ is mesh sensitive. At higher impact velocities, the results are far less affected by the mesh size. However, this mesh sensitivity is alleviated to a great extent when using $\ell \neq 0$ (i.e. nonlocal damage). Also, it is seen from Fig. 5(a) that the ballistic limit velocity decreases as the number of elements through the thickness increases. Therefore, when conducting the ballistic failure simulations using a local damage model, one does not know which mesh density will yield meaningful values for the ballistic limit velocity, which may mislead the design of ballistic protective systems. The proposed nonlocal damage model successfully predicts meaningful values for the ballistic limit; of course, when mesh of sufficient density is used. Also, the nonlocal theory can be used in reducing the computational time by using coarser meshes.

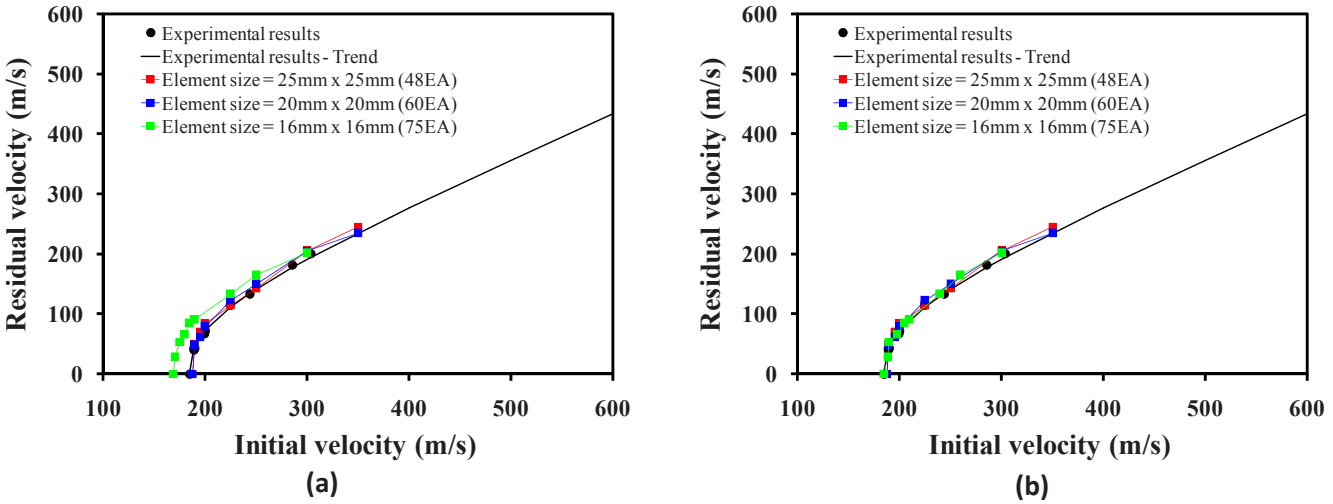

Figure 5. Mesh sensitivity study of the blunt residual velocity versus its initial impact velocity impacting a 12mm thick target when using (a) local damage ($\ell = 0$) and (b) nonlocal damage ($\ell = 7.3\mu m$). Experimental data are after [8].

CONCLUSIONS

A coupled thermo-hypoelasto-viscoplastic and nonlocal gradient-dependent thermo-viscodamage continuum model is utilized in this paper for simulating the ballistic behavior of heterogeneous materials with length scale effects. It is concluded in this paper that an explicit material length scale parameter should be incorporated into the local theories of viscoplasticity and viscodamage in order to predict meaningful values for the ballistic limit velocities independent of the finite element mesh density. Although the presented constitutive equations incorporate length scale parameters implicitly through the viscosity, they are insufficient in predicting mesh objective results of the ballistic behavior of high-strength steel targets impacted by blunt projectiles in which shear plugging due to plastic and damage localization is the dominant mode of failure. This mesh sensitivity is more significant at impact velocities close to the ballistic limit velocity and increases as the target thickness increases. This is attributed to the larger plastic and damage localization as the target thickness increases. Hence, in case of absence of experimental data to check the ballistic results from a specific mesh density, one cannot know if the local model underestimates (conservative) or overestimates (unconservative) the value of the ballistic limit velocity. However, an explicit length scale parameter through the nonlocal damage theory sufficiently alleviates the mesh sensitivity of the ballistic limit velocity allowing one to precisely determine the ballistic limit velocities and describe the overall physical ballistic behavior of targets using numerical simulations. Moreover, it can be concluded that the ballistic limit prediction from the nonlocal theory is a slightly conservative one since it takes into consideration the current damage at a specific point as well as the effect of the surrounding damaged region at that point. Therefore, this desirable feature provided by the nonlocal theory does lead to an improvement in the modeling and numerical simulation of high velocity impact related problems such that numerical simulations could be used in the design process of protective systems against high speed impacts and in providing physical understanding of the ballistic and penetration problem.

ACKNOWLEDGMENT

The work reported in this paper is supported by a grant from the U.S. Army Research Office, and by the Air Force Institute of Technology. These supports are gratefully acknowledged

REFERENCES

[1] Abu Al-Rub, R.K., Voyiadjis, G.Z. “A Finite Strain Plastic-Damage Model for High Velocity Impacts using Combined Viscosity and Gradient Localization Limiters,: Part I-Theoretical Formulation,” International Journal of Damage Mechanics, 15(4), 293-334, 2006.

[2] Voyiadjis, G.Z., Abu Al-Rub, R.K. “A Finite Strain Plastic-Damage Model for High Velocity Impacts using Combined Viscosity and Gradient Localization Limiters, Part II: Numerical Aspects and Simulations,” International Journal of Damage Mechanics, 15(4), 335–373, 2006.
[3] Voyiadjis, G.Z., Abu Al-Rub, R.K., and Palazotto, A.N. “Constitutive Modeling and Simulation of Perforation of Steel Plates by Blunt Projectile,” AIAA Journal, 46(2), 304-316, 2008.
[4] Abu Al-Rub, R.K., Kim, S.-M. “Predicting Mesh-Independent Ballistic Limits for Heterogeneous Targets by a Nonlocal Damage Computational Framework,” Composites: Part B, 40(6), 495-510, 2009.
[5] Abu Al-Rub, R.K. and Voyiadjis, G.Z. “Analytical and Experimental Determination of the Material Intrinsic Length Scale of Strain Gradient Plasticity Theory from Micro- and Nano-Indentation Experiments,” International Journal of Plasticity, 20(6), 1139-1182, 2004.
[6] Abu Al-Rub, R.K., and Voyiadjis, G.Z. “Determination of the Material Intrinsic Length Scale of Gradient Plasticity Theory,” International Journal of Multiscale Computational Engineering, 2, 377-400, 2004.
[7] Voyiadjis, G.Z., Abu Al-Rub, R.K. “Gradient Plasticity Theory with a Variable Length Scale Parameter,” International Journal of Solids and Structures, 42, 3998-4029, 2005.
[8] Børvik, T., Langseth, M., Hopperstad, O.S., Malo, K.A. "Effect of Target Thickness in Blunt Projectile Penetration of Weldox 460E Steel Plates." Int. J. Impact Eng., 28, 413-464, 2003.
[9] ABAQUS. User Manual, Version 6.5, Hibbit, Karlsson and Sorensen, Inc, 2005.

Proceedings of the SEM Annual Conference
June 7-10, 2010 Indianapolis, Indiana USA

Impact Testing and Dynamic Behavior of Materials

Prof. Lothar W. Meyer, Dr. Norman Herzig, Frank Pursche, Dr. Shawky Abdel-Malek

Nordmetall GmbH, Hauptstrasse 16, D-09221 Adorf/Erzgebirge, Germany
lothar.meyer@nordmetall.net, norman.herzig@nordmetall.net

ABSTRACT

This paper gives an overview of different testing facilities and the mechanical material behavior including monoaxial and multi axial testing under high rate loading . Special emphasis is laid on difficult loading conditions and loading states such high temperature and high strain loading (ϑ>1200°C, φ>1) and multiaxial impact tests. The impact behavior of selected materials is shown and compared under different loading conditions. Furthermore, a distinction is made between virgin and manufactured material behavior (e.g. welding) or pre-damaged materials. Specifically, if the influence of the manufacturing history is investigated, under certain loading states the impact material properties show a dramatic difference compared to the virgin state of the material. Some examples of different material behavior under the conditions previously described are given.

INTRODUCTION

It is well known, that the material behavior of construction materials is dependent on strain, strain rate and temperature. Moreover, the knowledge of the dynamic behavior of materials is of interest, if processes like cutting or forming operations are investigated. For many engineering applications, the mechanical impact behavior of materials and components also plays an essential role.

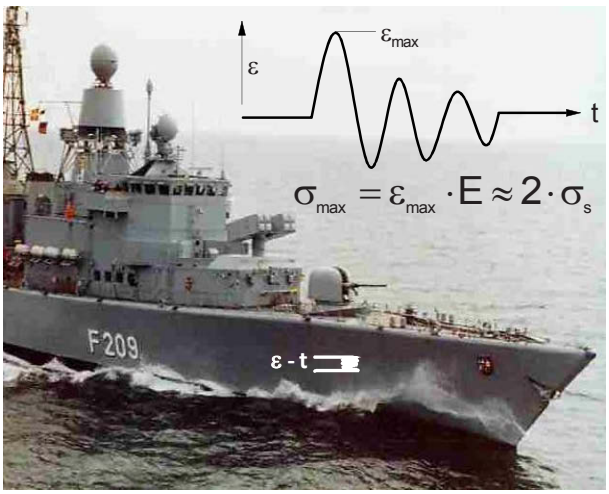

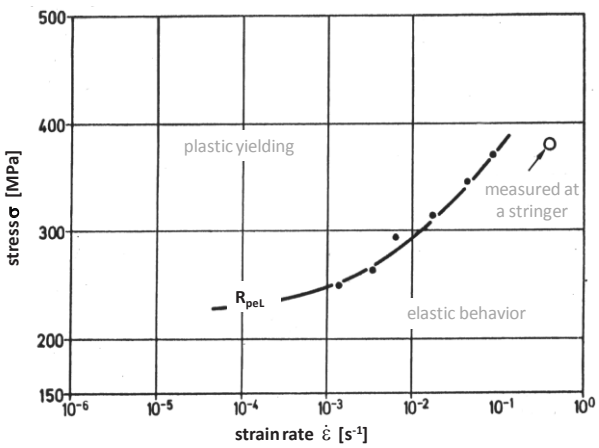

Figure 1: Dynamic loading of a canon shot on a Navy ship structure .

For example, consider a deployed naval ship operating in rough sea conditions, the loading of this ship`s structure by a canon fire can be described as a time dependent strain loading (Figure 1). In reality, the loading is measured by strain gages. If the amplitude of the strain-time signal is multiplied with Young's modulus (Hooke's law), one may find a stress value significantly exceeding the material flow stress as known from quasistatic and standardized experiments. Hence, if the assumption is valid the ship must be deformed plastically. However, , an examination of the strain-time signal shows a complete return to its initial state, which clarifies, that the whole event was purely elastic. Investigations under dynamic tensile loading using a universal hydraulic testing machine show that the large strain rate sensitivity of the flow stress of the ship building steel , during the impact by canon

T. Proulx (ed.), *Time Dependent Constitutive Behavior and Fracture/Failure Processes, Volume 3*, Conference Proceedings of the Society for Experimental Mechanics Series 15, DOI 10.1007/978-1-4419-9794-4_12, © The Society for Experimental Mechanics, Inc. 2011

firing, is enhancing the flow stress above that (elastic) value, what was measured on the stringer at the high strain rate. Thus, the ship is not being deformed plastically during maneuver operations or its deployment.

However, the knowledge of the material behavior under loading conditions matching the intended use is of special importance in design and construction. Thereby, the material behavior must be known over a wide range of strains, strain rates and temperatures. A variety of different experimental techniques exist to determine the dynamic behavior of materials under defined loading conditions and loading states.

IMPACT TESTING CAPABILITIES

Of the experimental work on impact material behavior described in the literature, mostly Hopkinson bar testing is mentioned. However, a variety of different experimental techniques exist to determine the dynamic behavior of materials under defined loading conditions and loading states.
For the characterization of the mechanical behavior of materials investigations over a wide range of strains, strain rates and temperatures are required. Additionally, different loading types may lead to different material behavior even if only monoaxial loading is mentioned and must be considered in material investigations and constitutive modeling. In Figure 2 a summary of different loading types under monoaxial and multiaxial loading is given.

loading type / strain rate [s^{-1}]		10^{-3}	10^{-2}	10^{-1}	10^{0}	10^{1}	10^{2}	10^{3}	10^{4}	10^{5}	temperature [°C]
uniaxial stress / strain	tension	■	■	■	■		■	■			-190 … 1250
	compression	■	■	■	■		■	■	■		-190 … 1250
	torsion	■	■	■	■		■				-190 … 1100
	bending	■	■	■	■		■				-190 … RT
	shear	■	■	■	■	■	■				RT
biaxial stress / strain	servohydraulic (tension, compression + torsion, TU Chemnitz)	■	■	■	■						-190 … 400
	drop weight (compression + shear)						■	■	■	■	-190 … 1200
	gas gun (compression + shear)							■	■	■	RT
	drop weight – blast simulator				■	■	■				RT
	hopkinson (tension + torsion)					■	■				RT
	charpy Impact test						■	■			-190 … 600
	biaxial drop weight (tension + tension by)					■	■				RT
	fracture toughness K [$Nmm^{-2/3}$ s^{-1}]			■	■	■	■	■		■	-190 … 400
triaxial	gas gun – penetration simulator							■	■	■	RT
	flyer plate (IPCP Moskau)									■	-190 … 600
	compression and hydrostatic compression (TU Chemnitz)	■	■	■	■		■				RT
	servohydraulic (tension, compr. + torsion + hydrost. compr.)	■	■	■	■						RT
	tension + tension + tension	■	■	■	■		■	■	■		-190 … 600

Figure 2: Testing capabilities needed for impact dynamic material characterization. Testing facilities in blue are available at Nordmetall GmbH.

For dynamic impact testing of materials only a small amount of universal testing machines in comparison to quasistatic loading are available. Especially, accurate force-time measurements are a great challenge for such type of machines. Due to the large mass which have to be accelerated during testing, the force-time signals often show large ringing and lead to increased uncertainties in the determination of the real material behavior. However, different special designed devices for certain applications of dynamic testing of materials exist, e.g. Hopkinson bars for compression and tensile testing, rotating wheels for tensile loading or drop weight towers for compression or flexure loading.

For modeling of the constitutive behavior of materials uniaxial data are mostly sufficient for the application of simple phenomenological equations and for the description of flow stress and strain hardening behavior (e.g. Johnson-Cook [1], Zerilli-Armstrong [2]). If failure is going to be considered uniaxial experiments are not sufficient for the characterization of the material behavior. Both flow stress and failure are significantly influenced by strain, strain rate and temperature. Therefore, the material must be investigated using a broad range of loading conditions. In addition, compared to flow stress behavior, failure is largely influenced by stress state (especially stress triaxiality). Hence, multiaxial testing by using stress concentrators like notches (Charpy impact test) or cracks (fracture toughness) are necessary. Additionally, complex and defined stress states e.g. observed during forming processes have to be considered using combined loading states, e.g. multiaxial tensile testing superimposed by hydrostatic pressure, whereby all the tests have to be performed at high loading rates (Figure 2).

Additionally, most of the materials studied under impact dynamic loading are not loaded monoaxially in later use. Most applications are characterized by a complex geometry which normally leads to a complex loading state showing stress concentrations and high stress triaxialities. To investigate the impact component behavior , high quality dynamic measurement data (especially for force and deformation measurements) is required. Additionally, a large amount of impact energy is needed for the dynamic deformation of components. This has lead to the design and development of new testing facilities which are capable of meeting the new demands of dynamic component testing.

The following chapters demonstrate how special emphasis is put on high strain, high strain rate and high temperature testing using high speed torsion loading and multiaxial material and component testing using high energy mechanical testing devices for tensile and compression/flexure loading.

HIGH SPEED TORSION TESTING

The parameter identification of constitutive equations nowadays used in finite element analysis of forming or cutting processes are mostly based on monoaxial experimental data from high rate and in some cases high temperature compression or tensile tests. Thereby, the strain reached in tensile or compressive deformation of materials is limited and does not match real forming or cutting process, where plastic strains larger than $\varphi = 2$ or 3 can be observed (e.g. [3], [4]). Especially the stress softening behavior due to recrystallization processes during deformation cannot be measured by compression or tensile tests.

Using torsion loading this mismatch can be overcome, because no geometrical instability or friction effects lead to limited plastic deformation of the material , only the deformation capability of the material itself. Performing torsion tests to reach high plastic strains is familiar in material testing and characterization. To ensure a good predictability of material behavior in real engineering processes like rolling or turning the material behavior has to be known at high strain rates and high temperatures. To solve this challenge a new universal torsion testing machine was designed in cooperation between Nordmetall GmbH and Chemnitz University of Technology (Figure 3). The machine can be used for quasistatic tests by using an electrical drive for loading the specimens as well as for impact dynamic tests using an integrated flywheel construction.

For quasistatic tests the specimens are fixed at both ends. Using a high power electrical drive, the specimen is loaded until failure of the material occurs. The torque during deformation is measured using a calibrated and adjusted load cell. The deformation is measured either by strain gages applied directly on the specimen and/or by an incremental gage of the machine. Dynamically, the force measurement is based on the principles of one dimensional wave propagation effect and the Hopkinson principle. Thereby, the specimen is fixed directly on the Hopkinson bar instrumented with strain gages. The lower end of the specimen stands free. To ensure an impact loading of the specimen a rotating wheel is accelerated by an electrical drive until a desired velocity is reached. Using a specially designed clutch device, the rotation is launched to the lower end of the specimen and the material is loaded by an impact torsion load. Due to the high mass of the flywheel and its rotation the stored energy is sufficient to deform the specimen until fracture. Thereby, shear rates of approximately 300 s^{-1} can be reached, whereby a high signal quality of the load measurement can be assured. For both experimental setups, an inductive heating system can be integrated into the process and high temperature investigations up to 1300°C can be performed. Hence, high strain, high strain rate, and high temperature material behavior matching real cutting or forming processes can be obtained.

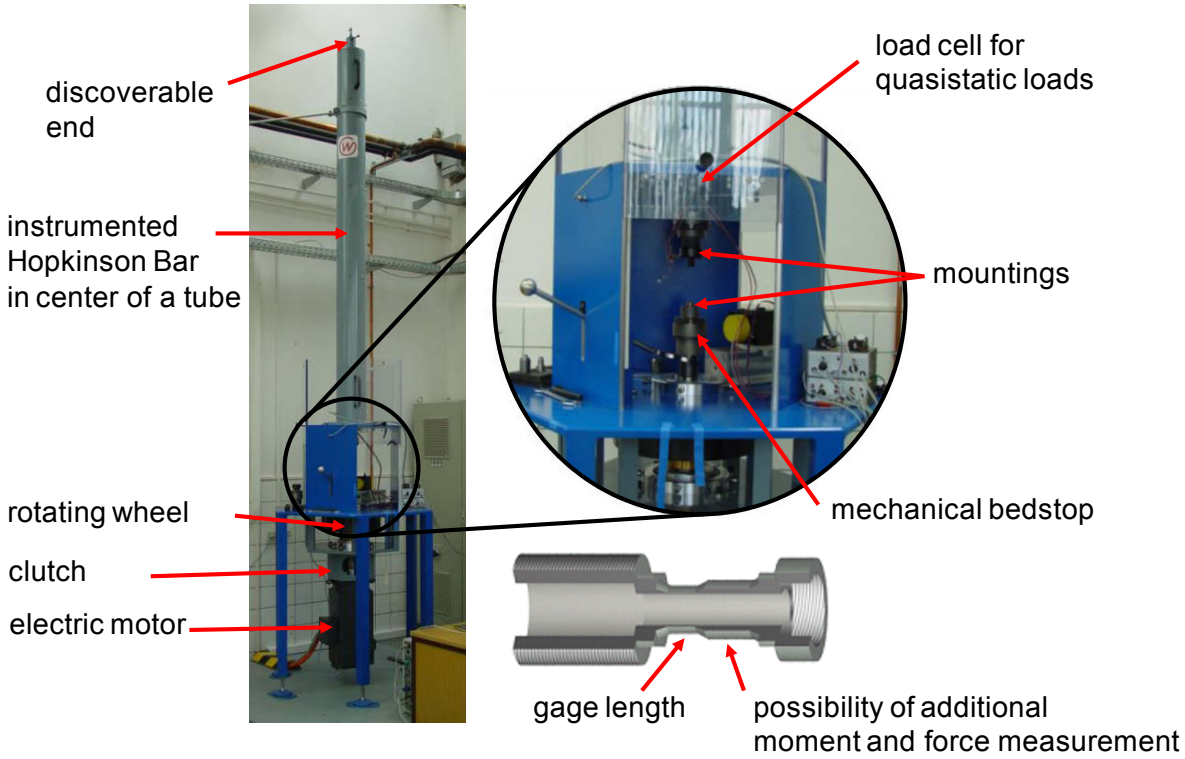

Figure 3: Combined static and impact dynamic universal testing machine.

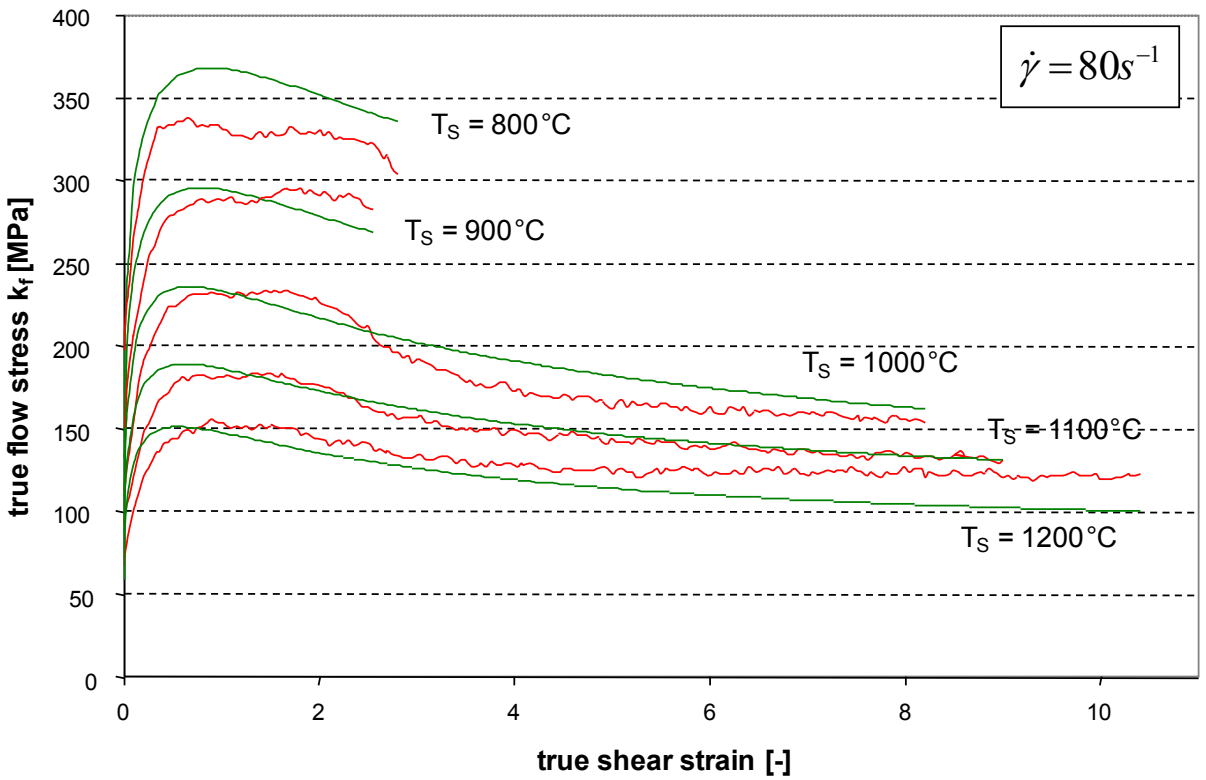

Figure 4: Flow stress evolution of a low alloyed steel at high strains, high shear rate and high temperatures: Comparison of experimental data and modeled data using Hensel-Spittel approach [3].

In Figure 4 an example for the behavior of a low alloyed steel at high strain rate and high temperature torsion loading is shown. It can be seen that the plastic deformability of the material is increased significantly from φ=2 at 800°C to φ=10 at 1200°C. From the experimental data the transition from elastic to elastic-plastic behavior as well as strain hardening behavior can be evaluated. One of the great advantages of the torsion test is shown in Figure 4. After reaching a stress maximum, the onset of recrystallization in conjunction with decreasing measured flow stresses can be found. Thus showing that the onset of softening is strongly dependent on strain, strain rate and temperature.

Additionally, from Figure 4 a comparison between experimental measured and modeled data using Hensel-Spittel (eq. 1, [5]) approach can be evaluated as described in their publication.

$$k_f = A \cdot e^{m_1 T} \cdot T \cdot \varphi^{m_2} \cdot e^{m_4/\varphi} \cdot (1+\varphi)^{m_5 T} \cdot e^{m_7 \varphi} \cdot \dot{\varphi}^{m_3} \dot{\varphi}^{m_8 T} \qquad (1)$$

It can be seen, that experimental and modeled data show a good agreement over the whole range of plastic strains and temperatures. Even the flow stress decrease due to recrystallisation processes can be predicted using Hensel-Spittel approach. Based on these data, a good prediction of the process behavior e.g. in rolling processes using finite element analysis can be expected. It should be emphasised, that most of the common constitutive equations used in finite element simulations like Johnson-Cook or Zerilli-Armstrong cannot predict dynamic recrystallisation phenomena. Hence, not only experimental data are required that matches real process behavior but also equations used for the constitutive description of the material behavior under such conditions must fulfill these requirements.

HIGH SPEED MULTIAXIAL TESTING

Until now only monoaxial material behavior of a virgin material was investigated and discussed. In real engineering applications mostly multiaxial loading occurs. Additionally, materials used in technical products and components normally pass through a variety of different manufacturing steps including forming, as well as cutting and joining technologies. Furthermore, the material or component behavior might be changed during its life cycle use. This may be caused by alteration or fatigue processes, especially in automotive and automobile industry, processes like welding or glueing play a key role in manufacturing today`s innovative products. Howeverless is known about the dynamic behavior of components under a multiaxial dynamic loading.

A new experimental test setup was designed and built at Nordmetall GmbH (www.nordmetall.net) to investigate the material behavior under a multiaxial dynamic loading condition and to include the influence of manufacturing history (welding etc.) and pre-damaging due to fatigue in life cycle use compared to virgin material properties. Special focus is laid on a critical biaxial tensile-tensile stress state, which might occur for example under blast loading of structures and vehicles or even under crash conditions. Normally, component testing under such conditions for automotive applications is performed at high impact velocities (10-20 m/s) that are obtained by a drop weight device having large drop heights. Thereby, high quality force-time measurements during deformation can not be obtained. This is because the large ringing of the signals that are superimposed on the output signal cannot be filtered out. Therefore we enhanced the weight and reduced the drop height and the impact velocity and get undisturbed signals. The falling weight of 4t provides sufficient energy during the test to deform most of the materials to fracture.

The test setup used for dynamic biaxial tensile-tensile loading of steel plates is shown in Figure 5. The plate is fixed on the top of a steel tube and impacted by a semi-spherical punch on the top site. During deformation the deflection is measured by an incremental gage. The force-time characteristic is measured directly on the punch. A high speed deformation field measuring system technique was applied in order to measure the real deformation behavior of the steel plate during impact loading. Thereby, the three dimensional local deformation field at the bottom of the steel plate is measured during the entire process, from onset of plastic flow to fracture.

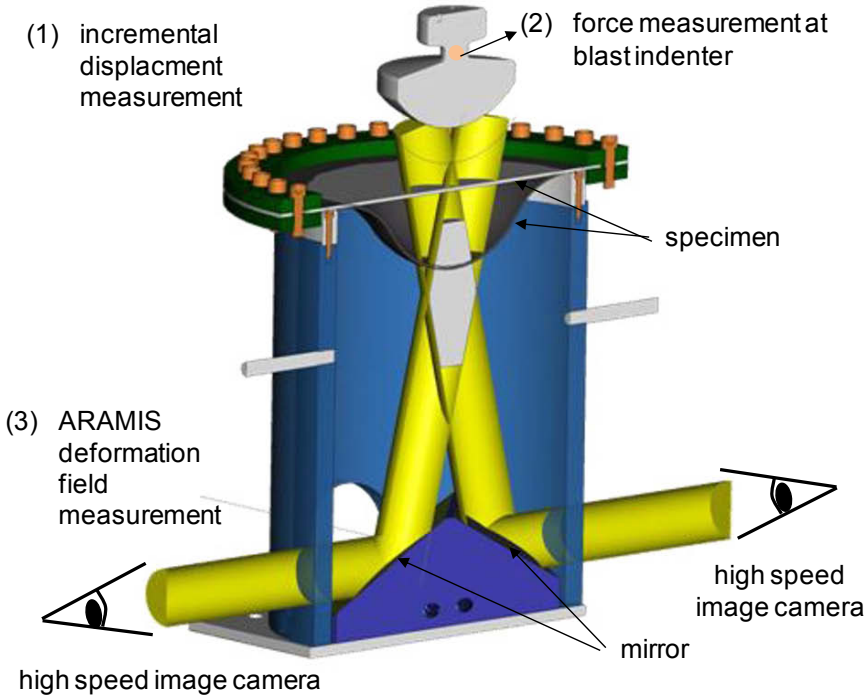

Figure 5: Experimental test setup for high speed biaxial tensile-tensile-tests of steel plates including high speed deformation field measuring system.

For the tests, three different states of the steel plates (plain, pre-notched and cracked, welded stringer) of the same thicknesses and two different materials were used. The results of the dynamic biaxial tensile-tensile tests are summarized in Figure 6 and Figure 7.

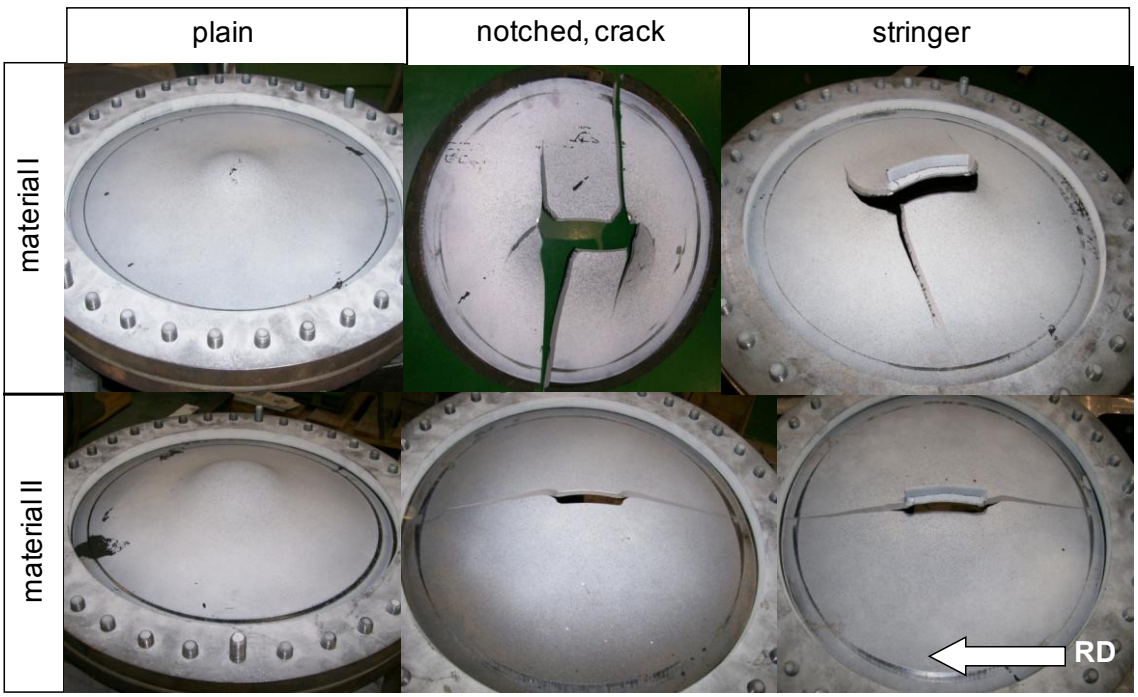

Figure 6: Failure characteristics for two different materials at different pre-treatment states after biaxial testing.

Shown in Figure 6 are the recovered biaxially loaded specimens. For both materials no failure was observed for the plain steel plate. All the energy provided by the falling weight was absorbed by the material as plastic deformation. If the material is pre-damaged, either by a mechanical or a metallurgical notch (1mm deep fatigue crack or welded stringer), both materials fail during biaxial tensile-tensile loading. For material II a straight crack propagated through the whole specimen, whereas for material I branching occured during crack propagation. If the measured force-time signals are compared (Figure 7), one finds the highest strength for material I, if the material is tested in this virgin state (plain condition). If pre-damaging of material I occurs, the measured maximum forces are decreased dramatically. Only a sixth to a seventh of the initial maximum load can be sustained until the material fails. For material II a similar decrease of the maximum load was observed. However, although material II is weaker in plain condition, it can be observed that the smaller influence of mechanical or metallurgical notches of material II leads to a better performance compared to material I.

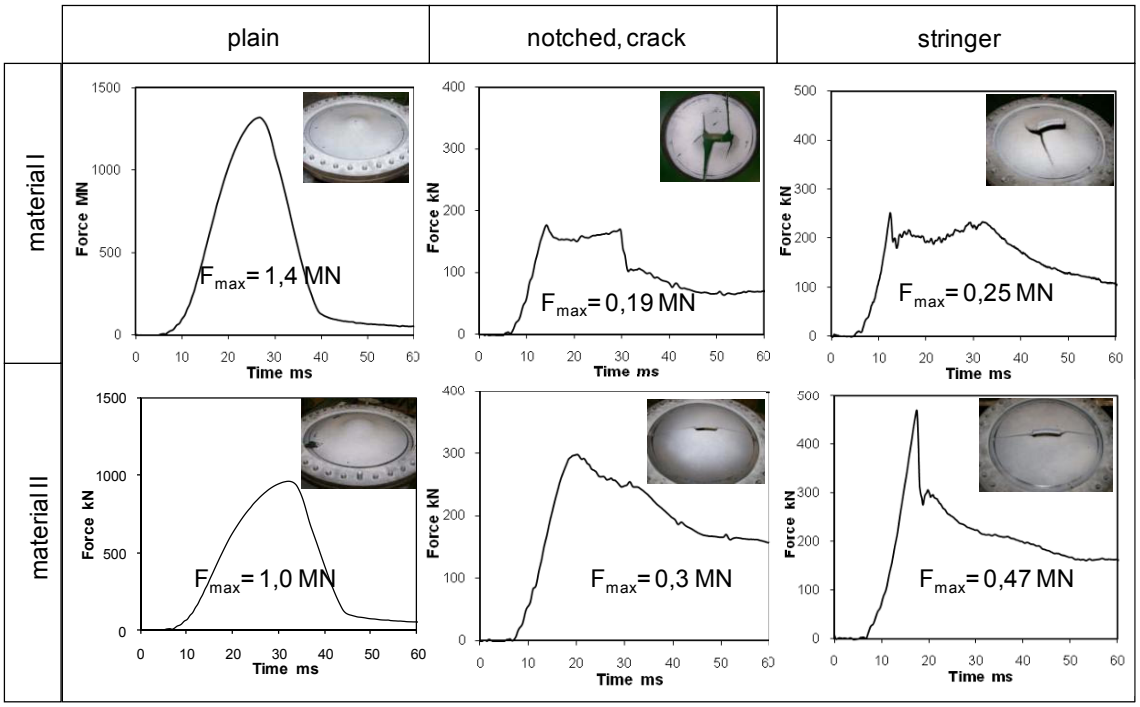

Figure 7: Force-time behavior of two different materials with different stress-states at dynamic biaxial loading.

Until now, material behavior is mostly considered in its virgin and un-damaged condition. To ensure a high level of reliability and safety of engineering products and systems the influence of manufacturing processes and their influence on the final mechanical properties of engineering materials have to be considered as well.

HIGH SPEED TENSILE TESTING USING A FLYWHEEL WITH A HIGH STORED ENERGY

Based on the experience obtained from drop weight tests with high stored energy, the principle was transferred to a new flywheel device. This rotating wheel with a comparably low velocity but a high stored energy due to a 10 t mass flywheel can impact specimen with a maximum velocity of 12 m/s. This new innovative testing machine at Nordmetall GmbH enables dynamic investigations of large engineering components ensuring that a high quality measurement of the force-time signal is obtained. A schematic picture of the machine is shown in Figure 8. The functionality follows the principles of commonly known rotating wheel devices (e.g. [6]), but provides a high amount of energy for the dynamic deformation of high strength and/or high deformable and/or large parts and specimens. Hence, a new quality of material and component input data for finite element analysis as well as for the experimental verification of numerical results can be expected.

Figure 8: Rotating wheel device of Nordmetall GmbH with a high amount of stored energy of 110KJ by a 10 t flywheel (Ø2 m) for dynamic component testing of engineering materials.

CONCLUSIONS

This paper a short contains a short overview about different testing facilities and the material behavior including monoaxial and multiaxial testing under high rate loading. Specifically the overview concerns discussions of difficult loading conditions and loading states such as high temperature and high strain loading (ϑ>1200°C, φ>1) and multiaxial impact tests. Special emphasis was laid on the influence of the manufacturing history of a material on the dynamic properties under biaxial tensile-tensile loading. A dramatically decrease of the deformability and loading capacity was observed, if the material being tested contains a pre-damaged state by a metallurgical or mechanical notch.

REFERENCES

[1] Johnson, G.R.; Cook, W.H.: A constitutive model and data for metals subjected to large strains, large strain rates and high temperatures. Proc. 7th Int. Symp. On Ballistics, 1983, 541-547, The Hague, Netherlands.

[2] Zerilli, F.J.; Armstrong, R.W.: Dislocation-mechanics-based constitutive relations for material dynamics. Journal of Applied Physics **61** (1987), 5, 1816-1825.

[3] Halle, T; Meyer L. W: Influence of different material models on the result of numerical high speed cutting simulations. 1st International Conference on High Speed Forming, Dortmund 2004 (Ed. Kleiner), 133-142.

[4] Meyer, L.W.; Kuprin, C.; Halle, T.: High rate material behavior at hot forming conditions. Mechanics of Time-Dependent Materials **13** (2009), 1, 49-62 .

[5] Spittel, M.; Neubauer, S.: Betrachtungen zur mathematischen Fließkurvenmodellierung. Neue Hütte **28** (1983) 1, 21-25

[6] Meyer, L. W.: Werkstoffverhalten hochfester Stähle unter einsinnig dynamischer Belastung. PhD 1982, Dortmund University of Technology, Germany .

Proceedings of the SEM Annual Conference
June 7-10, 2010 Indianapolis, Indiana USA

Development of an internal state variable model to describe the mechanical behavior of amorphous polymer and its application to impact testing

J.L. Bouvard, D. Ward, E.B. Marin, D. Bammann, M.F. Horstemeyer
Center for Advance Vehicular Systems
Mississippi State University, Mississippi State, MS 39762

ABSTRACT

The use of lighter and impact resistant materials, such as polymers, in vehicular systems is an important motivation for the automotive industry as these materials would make vehicles more fuel-efficient without compromising safety standards. In general, polymers exhibit a rich variety of material behavior originating from their particular microstructural (long molecular chains) behavior that is strongly temperature, pressure, and time dependent. To capture such intricate behavior, a number of polymer constitutive models have been proposed and implemented into finite element codes in an effort to solve complex engineering problems (see [1] for a review of these models). However, developing improved constitutive models for polymers that are physically-based is always a challenging area that has important implications for the design of polymeric structural components.

The work describes the development of a material model for amorphous polymers based on a thermodynamic approach with internal state variables. The modeling approach follows current methodologies used for metals [2], and departs from spring-dashpot based models generally used to predict the mechanical behavior of polymers. To select the internal state variables, we used a hierarchical multiscale approach for bridging mechanisms from the molecular scale to the continuum scale. At this point of the work, we emphasize that molecular dynamics simulations results are mainly used as qualitative information for the continuum model. The continuum constitutive model applied a formalism using a three-dimensional large deformation kinematics and thermodynamics framework. The model predictions are then compared to compression, tensile and impact test data for a thermoplastic polycarbonate deformed at RT and at different strain rates.

Figure 1 presents the comparison between the model prediction and the experimental data for uniaxial compression at RT and different strain rates. All the curves show the expected features of the mechanical response for PC at temperatures below the glass transition: an initial linear elastic response followed by a non-linear transition curve to global yield, then strain softening and subsequent strain hardening. The model predicts well the mechanical behavior for both loading and unloading.

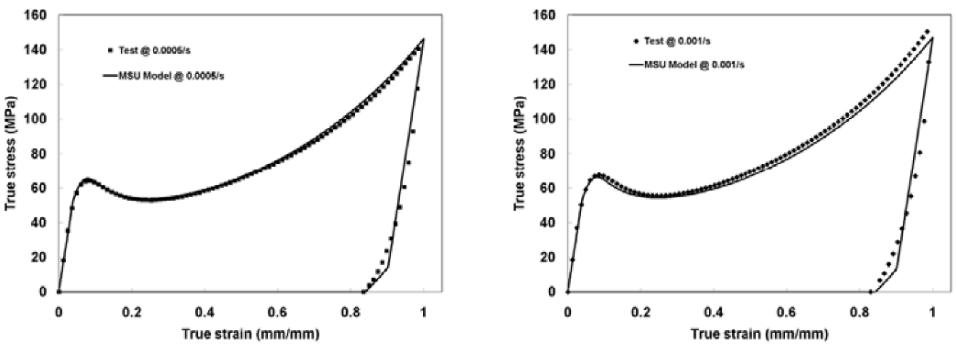

(a) (b)

Figure 1: Comparison between model prediction and experimental data of PC in uniaxial compression at RT for

different strain rates: (a) 0.0005/s, and (b) 0.001/s.

Figure 2 displays the model predictions on tensile tests at 0.0005/s and 0.01/s. We can notice that the numerical simulations predict qualitatively the test results for the different regimes. However, the model seems to underestimate the yield peak and the softening/hardening response.

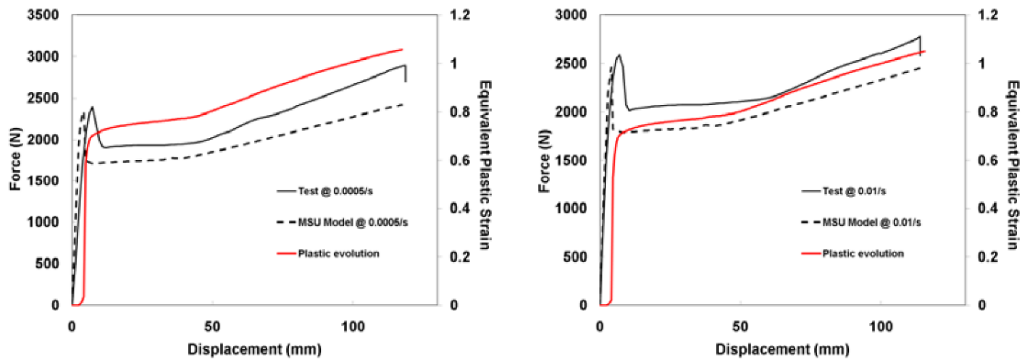

(a) (b)

Figure 2: Comparison between model prediction and experimental data of PC in uniaxial tension at RT for different strain rates: (a) 0.0005/s, and (b) 0.01/s.

Figure 3(a) displays a comparison of the force-displacement curve between the model prediction and the impact test for a velocity of 3 mm/s. Figure 3(b) displays the stress contour at the maximum of deflection. As depicted in the figure, the numerical simulation result is in good agreement with the test data.

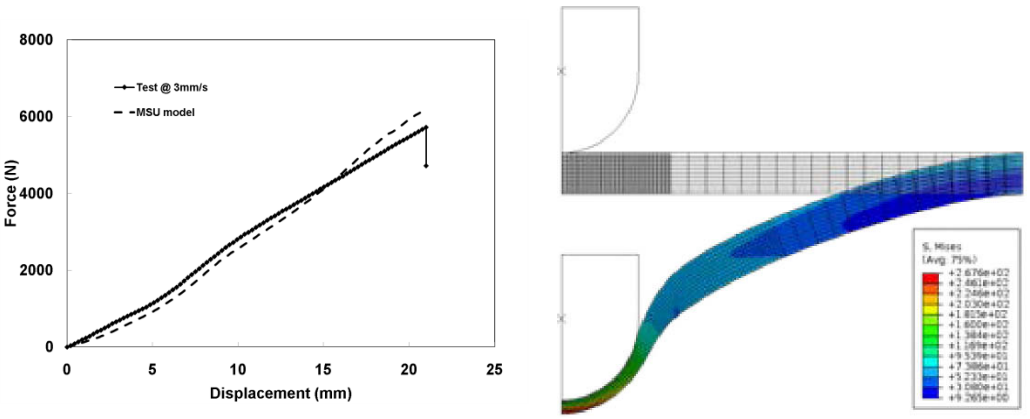

Figure 3: (a) Comparison between model prediction and experimental data for impact at 3 mm /s; (b) Stress contour at the maximum of deflection

Acknowledgements

The authors would also like to thank the Center for Advanced Vehicular Systems (CAVS) at Mississippi State University and American Chemistry Council for their support.

References

[1] Bouvard, J.L., Ward, D.K., Hossain, D., Nouranian, S., Marin, E.B., and Horstemeyer, M.F., 2009, Review of hierarchical multiscale modeling to describe the mechanical behavior of amorphous polymers, JEMT, DOI: 10.1115/1.3183779.

[2] Bamman, D.J., Chiesa, M.L., and Johnson, G.C., 1996, Modeling Large Deformation and Failure in Manufacturing Processes, In: Tatsumi, T., Wanatabe, E., and Kambe, T. (Eds), Theoretical and Applied Mechanics, Elsevier Science, 359-376.

Proceedings of the SEM Annual Conference
June 7-10, 2010 Indianapolis, Indiana USA

Examination of Validity for Viscoelastic Split Hopkinson Pressure Bar Method

T. TAMAOGI[1], Y. SOGABE[2]
[1]Depertment of Mechanical Engineering, Maizuru National College of Technology, 234 Shiroya, Maizuru, Kyoto, 625-8511, JAPAN, E-mail: takatamajp@yahoo.co.jp
[2]Depertment of Mechanical Engineering, Ehime University, 3 Bunkyo-cho, Matsuyama, Ehime, 790-8577, JAPAN

ABSTRACT: The examination of the accuracy for a split Hopkinson pressure bar method with viscoelastic input and output bars (viscoelastic SHPB method), which is one of the methods of evaluating the dynamic properties for viscoelstic materials, is executed. The key-point for accurately determining the dynamic properties of low impedance materials lies in how to measure the moderate size of reflected and transmitted waves. Moreover, the loading at both ends of the specimen should be equal each other in this method. Polymethyl methacrylate (PMMA) bars are used as the input and output bars. The viscoelastic properties of PMMA are approximated to a 3-element solid model in advance through preliminary wave propagation experiments. The same model is used as the mechanical properties of specimens, and the value of the instantaneous modulus is changed. The shape of waves at the boundary and the gage position of the input and output bars as well as the specimen are analyzed using the Elementary theory. The stress distribution in the specimen is also examined. It is found that the dynamic properties of viscoelastic materials can be evaluated with good precision by viscoelastic SHPB method when the ratio of the input / output bars and the specimen of mechanical impedance is about 10-20%. Then, the viscoelastic SHPB tests are actually performed. The complex compliance of the specimens which represent the characteristics of materials is obtained. The dynamic properties of the specimen satisfied the condition obtained by the previously mentioned analysis can be evaluated with high accuracy.

1. INTRODUCTION

The history of split Hopkinson pressure bar method (SHPB method) is very old. It was developed to examine the impact plasticity of metallic materials by Kolsky in 1949 [1]. The SHPB method consists of holding a thin cylindrical specimen of a test material between input and output bars made of elastic metal. The applications to polymers or composite materials have been extended, and the SHPB method with viscoelastic input and output bars is widely used as a technique of evaluation of the dynamic properties of their low impedance materials. When polymeric materials are used for input and output bars, it becomes necessary to correct measured waveforms to take into account the attenuation and dispersion generated by the wave propagation. Wang *et al*. [2] first researched a

T. Proulx (ed.), *Time Dependent Constitutive Behavior and Fracture/Failure Processes, Volume 3*, Conference Proceedings of the Society for Experimental Mechanics Series 15, DOI 10.1007/978-1-4419-9794-4_14, © The Society for Experimental Mechanics, Inc. 2011

viscoelastic SHPB technique. Much research has been reported [3]-[5] about viscoelastic SHPB technique with low impedance materials at high strain rate. However, it is not clear that the accuracy of the viscoelastic SHPB method depends on the materials used. Therefore, the applicable condition of the specimens which can be evaluated by the viscoelastic SHPB method is clarified by both the experiments and the numerical results in this work.

2. WAVE PROPAGATION IN VISCOELASTIC BARS

Based on the Elementary theory, a longitudinal strain pulse $\bar{\varepsilon}(x,\omega)$ propagating in a thin viscoelastic bar can be written as following expression in the frequency domain: [6]

$$\bar{\varepsilon}(x,\omega)=\bar{\varepsilon}(0,\omega)\cdot\exp\{-(\alpha+ik)\}x \quad , \tag{1}$$

where x, ω and i are the coordinate along the rod axis, angular frequency and imaginary unit, respectively. The strain waves of arbitrary points can be calculated by Eq.(1). The attenuation coefficient α and the wave number k are the functions of ω, and are related to the complex compliance as

$$\left.\begin{aligned} k^2-\alpha^2&=\rho\omega^2 J_1^*(\omega)\\ 2\alpha k&=\rho\omega^2 J_2^*(\omega)\end{aligned}\right\}, \tag{2}$$

where ρ is the material density. The complex compliance $J^*(\omega)$ is defined by the ratio of strain to stress as

$$J^*(\omega)=J_1^*(\omega)-iJ_2^*(\omega)=\frac{\bar{\varepsilon}(x,\omega)}{\bar{\sigma}(x,\omega)}. \tag{3}$$

When a 3-element solid model shown in Fig.1 is used especially, the real part $J_1^*(\omega)$ and the imaginary part $J_2^*(\omega)$ of the complex compliance are expressed as follows:

$$\left.\begin{aligned} J_1^*(\omega)&=\frac{1}{E_1}+\frac{E_2}{E_2^{\,2}+(\omega\eta_2)^2}\\ J_2^*(\omega)&=\frac{\omega\eta_2}{E_2^{\,2}+(\omega\eta_2)^2}\end{aligned}\right\}. \tag{4}$$

3. VISCOELASTIC SPLIT HOPKINSON PRESSURE BAR METHOD

3-1 Correction of Waveform

Figure 2 shows a viscoelastic SHPB setup. A specimen is sandwiched between viscoelastic input and output bars. Strain gages ① and ② are situated on the input and output bars, respectively. A compressive wave generated by an impact of a striker bar propagates along the input bar toward the specimen, and is measured as an incident pulse $\varepsilon_i^{①}(t)$ by the strain gage ①. Some part of the incident pulse is reflected at the bar / specimen interfaces, and is measured as a reflected pulse $\varepsilon_r^{①}(t)$. also by the strain gage ①. The remaining wave penetrates the specimen and is measured as a transmitted pulse $\varepsilon_t^{②}(t)$ by the strain gage ②. Let $\varepsilon_i^{①}(\omega)$, $\varepsilon_r^{①}(\omega)$ and $\varepsilon_t^{②}(\omega)$ be the Fourier transforms of the measured on the strain gages $\varepsilon_i^{①}(t)$, $\varepsilon_r^{①}(t)$ and $\varepsilon_t^{②}(t)$, respectively.

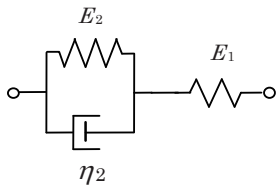

Fig.1 3-element viscoelastic model

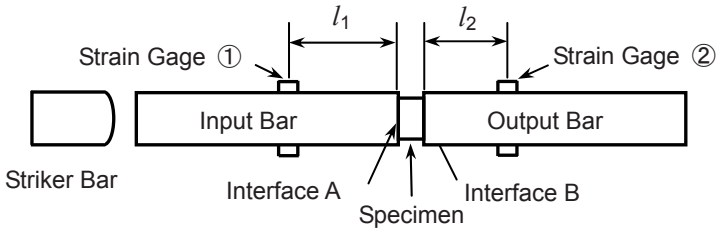

Fig.2 Schematic drawing of SHPB set-up

Based on Eq.(1), the following equations can be derived for correcting the individual strain pulses to be the waveforms at the interface A or B (bar / specimen interfaces):

$$\bar{\varepsilon}_i^{\,\mathrm{A}}(\omega) = \bar{\varepsilon}_i^{\,①}(\omega)\exp\{-(\alpha+ik)l_1\}\,, \tag{5}$$

$$\bar{\varepsilon}_r^{\,\mathrm{A}}(\omega) = \bar{\varepsilon}_r^{\,①}(\omega)\exp\{(\alpha+ik)l_1\}\,, \tag{6}$$

$$\bar{\varepsilon}_t^{\,\mathrm{B}}(\omega) = \bar{\varepsilon}_t^{\,②}(\omega)\exp\{(\alpha+ik)l_2\}\,, \tag{7}$$

where l_1 indicates the distance between the interface A and the strain gage ①, while l_2 denotes the distance between the interface B and the strain gage ②. The signs in exponential terms of Eqs.(6) and (7) must be pluses because reflected and transmitted pulses should be corrected in the opposite directions of their wave propagation. Making use of Eq.(5) to (7), the incident and reflected pulses can be corrected to be those at the interface A, while the transmitted wave can be corrected to be the value at the interface B. By applying the Fourier inverse transformation to Eqs.(5) to (7), corrected waveforms of incident, reflected and transmitted pulses in the time domain can be obtained as $\bar{\varepsilon}_i^{\,\mathrm{A}}(t)$, $\bar{\varepsilon}_r^{\,\mathrm{A}}(t)$ and $\bar{\varepsilon}_t^{\,\mathrm{B}}(t)$, respectively.

3-2 Stress and Strain of Specimen

In a conventional SHPB method using elastic bars, stress σ_S and strain rate $\dot{\varepsilon}_S$ of a specimen are given by

$$\sigma_S(t) = \frac{E\{\varepsilon_i^A(t)+\varepsilon_r^A(t)+\varepsilon_t^B(t)\}A}{2A_S}\,, \tag{8}$$

$$\dot{\varepsilon}_S(t) = \sqrt{\frac{E}{\rho}}\cdot\frac{\varepsilon_i^A(t)-\varepsilon_r^A(t)-\varepsilon_t^B(t)}{l}\,, \tag{9}$$

where E, ρ and A denote Young's modulus, density and cross-sectional area of the input and output bars, respectively. l and A_s show length and cross-sectional area of the specimen. Applying the Fourier transformation, and replacing the Young's modulus E by reciprocal of the complex compliance $J(\omega)$ of the input and output bars [7], we find the following equations for obtaining stress and strain of the specimen in the frequency domain:

$$\bar{\sigma}_s(\omega) = \frac{\{\bar{\varepsilon}_i^A(\omega)+\bar{\varepsilon}_r^A(\omega)+\bar{\varepsilon}_t^B(\omega)\}A}{2J(\omega)A_s} \tag{10}$$

$$\bar{\varepsilon}_s(\omega) = \frac{\bar{\varepsilon}_i^A(\omega)-\bar{\varepsilon}_r^A(\omega)-\bar{\varepsilon}_t^B(\omega)}{(\alpha+ik)\,l} \tag{11}$$

When the stress in the specimen is uniform, the loads at the interface A and B are equal.

$$\bar{\varepsilon}_i^{\,\mathrm{A}}(\omega)+\bar{\varepsilon}_r^{\,\mathrm{A}}(\omega) = \bar{\varepsilon}_t^{\,\mathrm{B}}(\omega)\,. \tag{12}$$

Then, the stress and strain of the specimen are given from substituting Eq.(12) into Eq.(10) and (11).

$$\bar{\sigma}_s(\omega) = \frac{A\bar{\varepsilon}_t^{\,\mathrm{B}}(\omega)}{A_s J^*(\omega)} \tag{13}$$

$$\bar{\varepsilon}_s(\omega) = -\frac{2\bar{\varepsilon}_r^{\,\mathrm{A}}(\omega)}{(\alpha+ik)l_s} \tag{14}$$

It is found that the stress and strain of the specimen can be calculated by the transmitted and reflected waves, respectively. When the Fourier inverse transformation is applied to Eq.(13) and (14), the stress and strain of the specimen in the time domain $\sigma_s(t)$ and $\varepsilon_s(t)$ can be obtained.

3-3 Evaluation of Viscoelastic Properties

The complex compliance of a test material can be calculated as the ratio of strain to stress of the specimen:

$$J_s^*(\omega) = J_{s1}^*(\omega) - iJ_{s2}^*(\omega) = \frac{\bar{\varepsilon}_s(\omega)}{\bar{\sigma}_s(\omega)} \tag{15}$$

4. ANALYSIS OF WAVEFORMS USING ELEMENTARY THEORY

4-1 Reflection and Transmission at Interface

Consider uniform elastic bars Ⅰ and Ⅱ which contact at the interface as shown in Fig.3 [8]. When the incident wave $\varepsilon_i(t)$ reaches the interface, some part of wave is reflected to the medium Ⅰ as $\varepsilon_r(t)$ and the rest is transmitted to the medium Ⅱ as $\varepsilon_t(t)$. Assuming the force equilibrium and continuity of particle velocity at the interface, $\varepsilon_r(t)$ and $\varepsilon_t(t)$ are obtained in terms of $\varepsilon_i(t)$. Then, by applying the Fourier transform to their equations, the following equations for a viscoelastic medium in the frequency domain are obtained.

$$\bar{\varepsilon}_r = \frac{A_{\mathrm{II}}\rho_{\mathrm{II}}c_{\mathrm{II}} - A_{\mathrm{I}}\rho_{\mathrm{I}}c_{\mathrm{I}}}{A_{\mathrm{I}}\rho_{\mathrm{I}}c_{\mathrm{I}} + A_{\mathrm{II}}\rho_{\mathrm{II}}c_{\mathrm{II}}}\bar{\varepsilon}_i, \tag{16}$$

$$\bar{\varepsilon}_t = \frac{2A_{\mathrm{I}}\rho_{\mathrm{I}}c_{\mathrm{I}}}{A_{\mathrm{I}}\rho_{\mathrm{I}}c_{\mathrm{I}} + A_{\mathrm{II}}\rho_{\mathrm{II}}c_{\mathrm{II}}} \cdot \frac{c_{\mathrm{I}}}{c_{\mathrm{II}}}\bar{\varepsilon}_i, \tag{17}$$

where A_{I} and ρ_{I} represent the cross section of the bar and the material density correspondent to the medium Ⅰ, respectively. c_{I} is the functions of ω, and denotes the propagation velocity of medium Ⅰ. Similarly, A_{II}, ρ_{II} and c_{II} correspond to the medium Ⅱ. Fractions in right sides of Eq.(16) and (17) are defined as the coefficients of reflection $R = \bar{\varepsilon}_r / \bar{\varepsilon}_i$ and the coefficients of transmission $T = \bar{\varepsilon}_t / \bar{\varepsilon}_i$, respectively.

4-2 Calculation of Wave Propagation in Viscoelastic SHPB Method

Figure 4 shows the calculated values of the strain wave propagation in input / output bars and a specimen in the frequency domain. Let the reflectivity and transmittance when a strain wave propagates from the input / output bars to the specimen be R and T, and let them when a strain wave propagates from the specimen to the input / output bars be R' and T', respectively. When the same material is used for input / output bars, R' is equal to R by Eq.(19). Based on Eq.(1), the terms of waveform change after propagating in the distance l_1, l_2 and l_s are expressed by follows, respectively:

$$\left.\begin{aligned} B_1 &= \exp\{-(\alpha + ik)l_1\} \\ B_2 &= \exp\{-(\alpha + ik)l_2\} \\ B_s &= \exp\{-(\alpha_s + ik_s)l_s\} \end{aligned}\right\}, \tag{18}$$

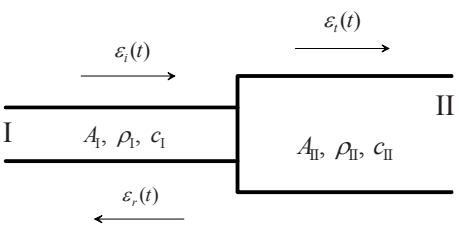

Fig.3 Propagation of strain waves at interface

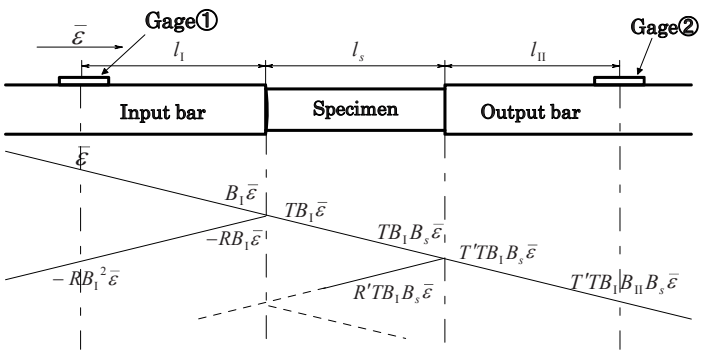

Fig.4 Propagation of predicted wave on viscoelastic SHPB method using Elementary theory

where α and α_s indicate the attenuation coefficient of input / output bars and a specimen, k and k_s denote the wave number of input / output bars and a specimen, respectively.

A compressive wave at the strain gage ① in the frequency domain assumed to be $\bar{\varepsilon}_i^{①}(\omega)$ as shown in Fig.4. The wave reaches the interface A as $B_1\bar{\varepsilon}_i^{①}(\omega)$, and part of it is reflected as $-RB_1\bar{\varepsilon}_i^{①}(\omega)$ and the rest is transmitted as $-TB_1\bar{\varepsilon}_i^{①}(\omega)$. Thus, the wave propagates repeating the reflection and transmission. Consequently, after propagating enough, the superposed wave signal $\bar{\varepsilon}_r^{①}(\omega)$ and $\bar{\varepsilon}_t^{②}(\omega)$ measured by the strain gage ① and ② can be calculated as follows:

$$\bar{\varepsilon}_r^{①}(\omega) = -RB_1^{2}\bar{\varepsilon}_i^{①}(\omega)\sum_{m=1}^{\infty}(1+TT'R^{2(m-1)}B_s^{2m}). \tag{19}$$

$$\bar{\varepsilon}_t^{②}(\omega) = TT'B_1B_2B_s\bar{\varepsilon}_i^{①}(\omega)\sum_{m=1}^{\infty}\{1+(RB_s)^{2m}\}. \tag{20}$$

Moreover, the stress $\bar{\sigma}^{\mathrm{A}}(\omega)$ and $\bar{\sigma}^{\mathrm{B}}(\omega)$ at the interface A and B can be calculated as following forms:

$$\bar{\sigma}^{\mathrm{A}}(\omega) = \frac{B_1\bar{\varepsilon}_i^{①}(\omega)}{J^*}\left\{1-R\sum_{m=1}^{\infty}(1+TT'R^{2(m-1)}B_s^{2m})\right\}, \tag{21}$$

$$\bar{\sigma}^{\mathrm{B}}(\omega) = \frac{TT'B_1B_s\bar{\varepsilon}_i^{①}(\omega)}{J^*}\sum_{m=1}^{\infty}\{1+(RB_s)^{2m}\}, \tag{22}$$

where J^* is the complex compliance of the stress bars. Applying the Fourier inverse transformation to Eq.(19), (20) and Eq.(21), (22), the strain and the stress in the time domain can be obtained, respectively.

4-3 Reflected Wave and Stress at Both Ends of Specimen

The input and output bars in the present SHPB method assumed to be made of PMMA. The viscoelastic behavior of PMMA was examined by preliminary experiments, and was identified by 3-element solid model $E_1 = 4.17$ GPa, $E_2 = 4.40\times10^{1}$ GPa and $\eta_2 = 2.25$ MPa・s shown in Fig.1. The mass density of PMMA is 1180 kg/m^3. The length and the diameter of the input / output bars are 1800mm and 20mm. The length and the diameter of the specimen are 7.5mm and 15mm, respectively. That is, the slenderness ratio of specimen $l_s/d_s = 0.5$ which is widely used in SHB method. The distance l_1 and l_2 are 700mm and 50mm. Figure 5 indicates the strain wave at the gage position ① as the initial condition. This is the waveform measured in the actual experiment by using the striker with the diameter of 15mm and the length of 100mm. The velocity of the striker bar is about 10m/s. Based on the

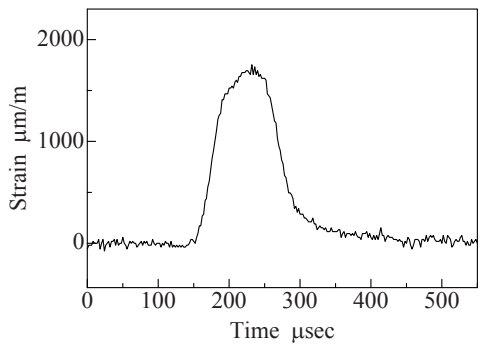

Fig.5 Incident strain wave on strain gage ①

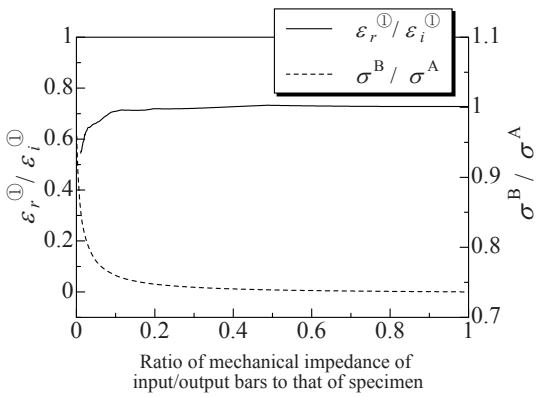

Fig.6 Proportion of reflected waves at interface A and stress at both interfaces

previously mentioned calculation method, reflected wave and stress at both ends of specimen are examined by changing the length and the characteristic value of the specimen. The specimen is also approximated to a 3-element solid model, and the parameter of E_1 is only changed.

Figure 6 shows the reflectivity at the interface A (solid line) and the stress distribution in the specimen (dotted line). The horizontal axis denotes the ratio of the characteristic values of the input / output bars to that of the specimen, the left vertical axis indicates the ratio of the peak value of $\varepsilon_r^{①}$ to that of $\varepsilon_i^{①}$ and the right vertical axis is the ratio of the peak value of σ^{B} to that of σ^{A}. The smaller the characteristic value of the specimen, the bigger the reflected wave is measured. The specimen of which the characteristic value is small has to be used in order to measure the bigger reflected wave. On the other hand, the smaller the characteristic value of the specimen, the bigger the difference of the load at both interfaces of the specimen is. The specimen of which the characteristic value is big has to be used in order to displace the specimen uniformly.

It is necessary for the Viscoelastic SHPB Method to use the experimental condition in which the specimen is deformed uniformity and the reflected wave of suitable size are measured. When the ratio of the characteristic values of the stress bar to that of the specimen is about 10%, $\sigma^{B}/\sigma^{A} \cong 0.99$ and the error is about 1%. If the ratio of the characteristic values is lower than 10%, the error suddenly grows and the difference of the load at both interfaces of the specimen generates. In addition, when the ratio of the characteristic values is about 20%, $\varepsilon_r^{①}/\varepsilon_i^{①} \cong 0.03$. If the ratio becomes lower than 20%, the value of $\varepsilon_r^{①}/\varepsilon_i^{①}$ gradually grows and bigger reflected wave comes to be obtained. Consequently, the appropriate experimental conditions of the Viscoelastic SHPB Method is 10～20% in the ratio of the characteristic values of the stress bar to that of the specimen.

5. VISCOELASTIC SPLIT HOPKINSON PRESSURE BAR TEST

The same sizes as the input / output bars and specimen in the analysis are used in the viscoelastic test. A polypropylene is tested as the specimen of one example. Figure 7 shows the experimental strain histories. Using Eqs.(5) to (7), the measured incident, reflected and transmitted strain pulses are corrected to be those at the interface A or B in the frequency domain. The stress and strain of the specimen is calculated by Eqs.(10) and (11). Then, the complex compliance of the specimen is obtained by Eq.(15) as shown in Fig.8. The white and black plots in the figure show J_{s1}^{*} and J_{s2}^{*}. The vertical bar indicates the standard deviation. Frequency dependence of the complex compliance can be approximated as the solid lines depicted in the figure by use of the 3-element viscoelastic model. Viscoelastic parameters of the model determined by a graphical method are also given in the

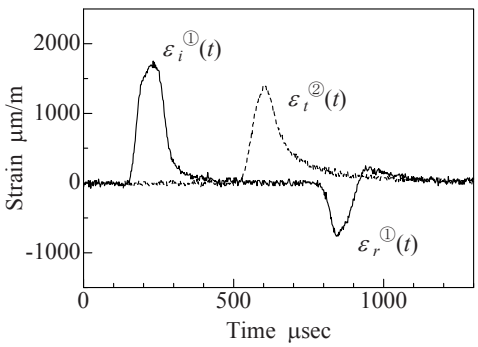

Fig.7 Typical strain records on polypropylene

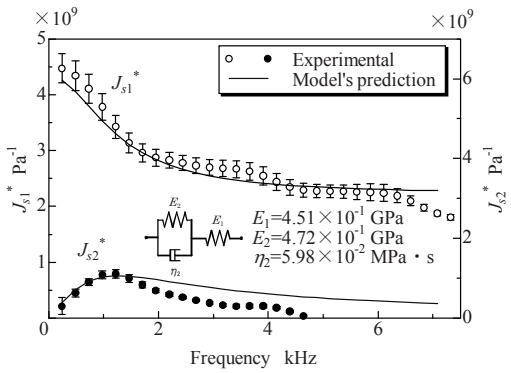

Fig.8 Complex compliance of experiment and model's prediction

figure. It is found that the 3-element viscoelastic model provides reasonable estimation of the dynamic behavior of the material. E_1 of the input / output bars and the specimen are 4.17 GPa and 4.51×10^{-1}GPa, respectively. The ratio of each E_1 is about 11%, and its value meets the requirement obtained by the analysis. Consequently, the dynamic properties of the specimen in the condition determined by the analysis can be evaluated at high accuracy in the viscoelastic SHPB method.

6. CONCLUSIONS

The conclusions obtained from the present study are summarized as follows:

・ The technique for calculating the waveforms in the viscoelastic SHPB method was proposed using the wave propagation analysis based on the Elementary theory.

・ It was clarified that we have to use the experimental condition in which the ratio of the characteristic values of the input / output bars to that of the specimen is about 10～20% in the viscoelastic SHPB method.

・ It was found that the viscoelastic properties of the specimen in the condition determined by the analysis can be evaluated at high accuracy in the actual viscoelastic SHPB tests.

7. REFERENCE

[1] Kolsky, H., An Investigation of Mechanical Properties of Materials at Very High Rate of Loading, *Proceedings of the Physical Society of London*, B62, (1949), pp.676-700.

[2] Wang, L., Labibes, K., Azari, Z. and Pluvinage, G., Generalization of Split Hopkinson Bar Technique to Use viscoelastic Bars, *International Journal of Impact Engineering*, Vol.15, No.5, (1994), pp.669-686.

[3] Sogabe, Y., Yokoyama, T., Yokoyama, T., Nakano, M. and Kishida, K., A Split Hopkinson Bar Method for Testing Materials with Low Characteristic Impedance, *Dynamic Fracture, Failure and Deformation*, PVP-Vol.300, The 1995 Joint ASME/JSME Pressure Vessels and Piping Conference, Honolulu, (1995), pp.137-143.

[4] Bacon, C., An Experimental Method for Considering Dispersion and Attenuation in a Viscoelasitc Hopkinson Bar, *Experimental Mechanics*, Vol.38, No.4, (1998), pp.242-249.

[5] Salisbury, C.P. and Cronin, D.S., Mechanical Properties of Ballistic Gelatin at High Deformation Rates, *Experimental Mechanics*, Vol.49, No.6, (2009), pp.829-840.

[6] Sogabe Y. and Tsuzuki M., Identifidation of the Dynamic Properties of Linear Viscoelastic Materials by the Wave Propagation Testing, *Bulletin of JSME*, Vol.29, No.254, (1986), pp.2410-2417.

[7] Flügge, W., *Viscoelasticity*, (1975), p.159, Springer-Verlag.

[8] Hayashi, T. and Tanaka, K., *Impact Engineering* (in Japanese), (1988), pp.11-12, Nikkan Kougyo Shinbunsya.

Proceedings of the SEM Annual Conference
June 7-10, 2010 Indianapolis, Indiana USA

WELDABILITY AND TOUGHNESS EVALUATION OF THE CERAMIC REINFORCED STEEL MATRIX COMPOSITES (TIB_2-RSMC)

E. Bayraktar[1, 2*], F. AYARI[1], D. Katundi[1], J-P. Chevalier[2], F. Bonnet[3]
[1]Supmeca -Paris, School of Mechanical and Manufacturing Engineering, France
[2]Chair of Industrial Materials, CNAM, Arts et Métiers, 75141 Paris 03 –France
[3]ARCELOR – Research, Paris, France
*Corresponding author: bayraktar@supmeca.fr; emin.bayraktar@cnam.fr

ABSTRACT
The general idea of this paper is to produce TiB_2 (ceramic particles) reinforced steel matrix composites. These ceramic particles are the best reinforcements for steel matrix composites because of their high thermal stability at higher temperature, high modulus of elasticity, good wetability, low density and their relative stability with steel matrix. This type of new composite family has received much attention as potential structural materials for their high specific strength and stiffness. Therefore, there is a significant interest in developing iron and steel matrix composites and evaluating dynamic behaviours due to their potential usage in automotive industry in future. Final purpose of this paper is to use of the steel sheet for the manufacturing of the lighted structure and manufacturing processes of this sheet.
Titanium carbide and titanium diboride TiB_2 reinforced steel matrix composites was therefore characterised by optical and scanning electron microscopy. Dynamic behaviours of the base metal and welded specimens have been tested to simulate under the impact-crash test conditions.

Keywords: *Steel matrix composites; Ceramic particles-TiB_2; Dynamic crash test; Welding*

1. Introduction

Recently, Metal Matrix Composites (MMCs) have received much attention in manufacturing engineering as potential structural materials for their high specific strength and stiffness [1-2, 3-6, 7-12]. Even if most of the work on MMCs is directed towards novel and light-weight engineering materials, there is also considerable interest in developing iron and steel matrix composites. Essentially, iron and steel matrix composites reinforced with TiB_2/TiC ceramic particulates have been the focus of intensive investigation, due to their ease of fabrication, low costs and isotropic properties. Potentially, they have good wear resistance with an excellent combination of low density and high toughness values [1, 4, 5]. For this reason, by making of fresh, ultrafine and stable ceramic reinforcements, the MMCs can demonstrate outstanding mechanical properties [6]. Among various ceramic particulates, titanium carbide (TiC) and titanium diboride (TiB_2) are possible materials because of their excellent properties, such as high hardness, low density, high melting temperature, high modulus, good wear and corrosion resistance [5, 7, 10-12]. Effectively, this material is a very attractive application in automotive industry (for environmental car due to light and high toughness properties). However, several limitations associated with the use of pure TiC and TiB_2 were found in literature [5-7, 9-12]. The high thermal expansion coefficient of TiC could lead to significant stresses across the preforms in the local reinforcing region, while the very high reaction heat released during the formation of pure TiB_2 could cause different types of pores in the matrix. In a first mode of realization, the weight contents expressed in percentage, titanium and boron of steel are such as:

$$2.5\% \leq Ti \leq 7.2\% \quad (1)$$

and also

$$(0.45 \times Ti)-0.35\% \leq B \leq (0.45 \times Ti) + 0.70\% \quad (2)$$

The second relation is written in an equivalent way

$$-0.35 \leq B \leq (0.45 \times Ti) \leq 0.70 \quad (3)$$

When

$$B - (0.45 \times Ti) \leq 0.35 \quad (4)$$

The precipitation of Fe_2B is much reduced, which increases ductility

T. Proulx (ed.), *Time Dependent Constitutive Behavior and Fracture/Failure Processes, Volume 3*, Conference Proceedings of the Society for Experimental Mechanics Series 15, DOI 10.1007/978-1-4419-9794-4_15, © The Society for Experimental Mechanics, Inc. 2011

This type of new composite steel is different from ultra high strength steels since here the specific stiffness is increased by at least %20. This is an important factor where stiffness is the design criterion mainly in car industry. These steels are prepared by continuous casting using actual industrial practices.
This study entails two major themes. The first theme concerns microstructural evolution of the composites sheets as base and welded structures due to their potential usage in automotive industry in future. The second theme aims well understanding of the relation between microstructure and mechanical properties, notably weldability and ductile brittle transition temperature of these steel matrix composite (TiB_2-RSMCs) sheets that recently invented and developed by ARCELOR Research Group – France [1].
Introducing these new composite steels in cars will reduce of the total weight. This is a major interest in general context of reduced fuel consumption and CO_2 emissions for the new design of future car. In fact, for minimum mass design, it should be changed either Young's modulus, E and or Density, ρ for specific stiffness (according to the Ashby's Diagram, performance index, $I_p = E/\rho$). As shown in Figure 1, it seems that the best solution for design of stiffness of parts (Buckling for example); Young's modulus, E, can be improved by using the ceramic reinforced composites, MMC [2]. In this Figure, among other ceramic particulates, TiB_2 appears to be the best reinforcement for weight reduction. This conclusion is based on mechanical and thermodynamic considerations as found both of the values for TiB_2 (E = 565 GPa, ρ= 4,52 g/cm^3). Typical microstructure (base metal) and stress-strain curve were indicated in the former report as given in the Figure 2 with work hardening evolution depending on the true strain [3].

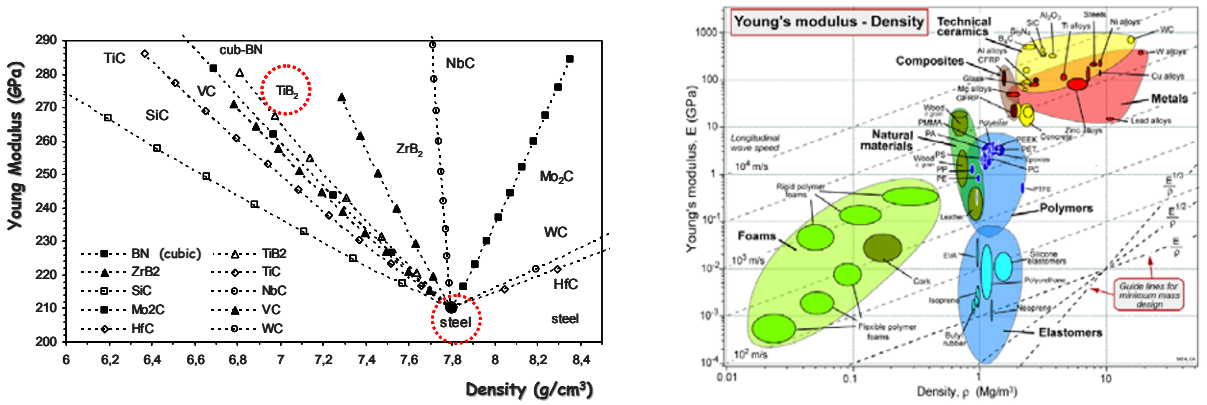

a) b)

Figure 1a) Comparison of the potential weight reduction of different systems: steel/ceramics and b) Evolution of Performance index, Ip depending on Young's modulus, E and or Density [2]

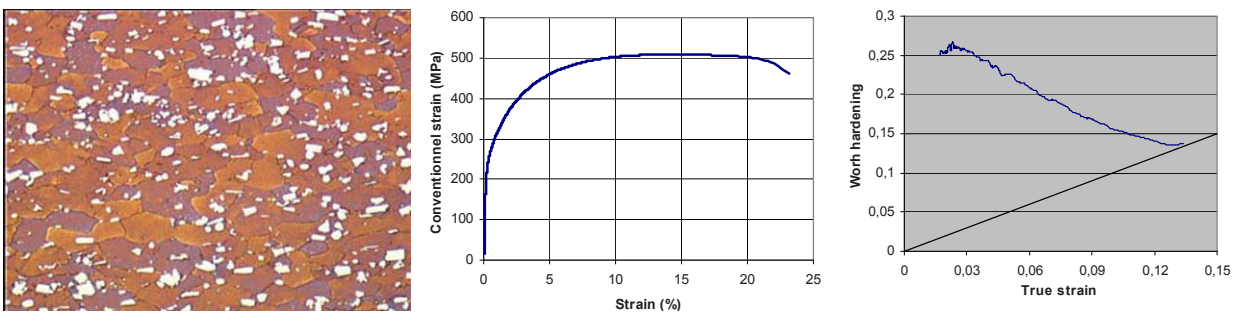

Figure 2 Typical microstructure (base metal) and stress-strain curve with work hardening evolution depending on the true strain [2]

2 Experimental conditions

Initially, the plate materials with a thickness of 2 and 3mm were made of special continuous casting by ARCELOR Research Group-France. After that only one fusion line welded by Gas Tungsten Arc (GTAW) process has been applied on the sheets. Two different compositions given with a code of 95A and 105 A, were examined. The values of carbon and manganese are 0.04% and 0.40% respectively.

Basically TiB_2 ceramic particulates were used as reinforced materials in the iron matrix. All other details can be found easily in the documents [1, 3].
First of all a detail metallographic analysis has been carried out. Evolution of TiB_2 ceramic particulates were observed in the weld bead-metal (WM) and Heat Affected Zone (HAZ) and Base Metal BM with surface percentage porosity, etc. Secondly, micro hardness and micro indentation tests have been done on the polished metallographic specimens. Micro hardness test were measured on the Schimadzu machine across the welds under 200g of load (HV) for both of the compositions. Micro indention study has been carried out on the standard instrument: MHTX S/N: 50-0121 with system and measurement parameters given here;
Contact F_n: 10 mN, Approach speed of indenter: 25 %/min, Acquisition rate: 10 Hz, Linear Loading for maximal load: 1000 mN and also Loading & Unloading speed: 2000 mN/min finally dwell time: 5s. **Micro indentation results were compared with that of the numerical analysis carried by using ABAQUS Code.**
Finally, for toughness evaluation of the TiB_2-RSMCs, impact –crash- tensile tests (ITT) have been carried out at different temperatures on the test specimens with a special geometry containing a smooth part (BM) and notched part (WM) with a special device mounted on an impact pendulum [7, 8]. Fracture surfaces of the broken specimen with ITT were analysed by means of Scanning Electron Microscope (SEM) to understand the damage behaviour of the TiB_2-RSMCs specimens under crash.

3 Results and Discussion

3.1 Microstructural evaluation

The microstructural evaluation of the results showed that different mechanisms of evolution of reinforcements in steel matrix were effective. First of all, this evaluation gave us information on the size effect and distribution of the ceramic particulates in the matrix. The morphology of the ceramic particulates and the matrix has been evaluated in metallurgical point of view. This information has allowed understanding the cohesion and wetability of the ceramic particulates with matrix.
Generally, TiB_2 ceramic particulates grew in hexagonal prismatic or rectangular shape. The micrographs given in Figures 3 and 4 show the morphology and distribution of TiB_2 reinforcements produced in steel matrix given in three different zones (Weld Metal, WM, Heat Affected Zone, HAZ and also Base Metal, BM) for the codes 95A and 105A respectively.

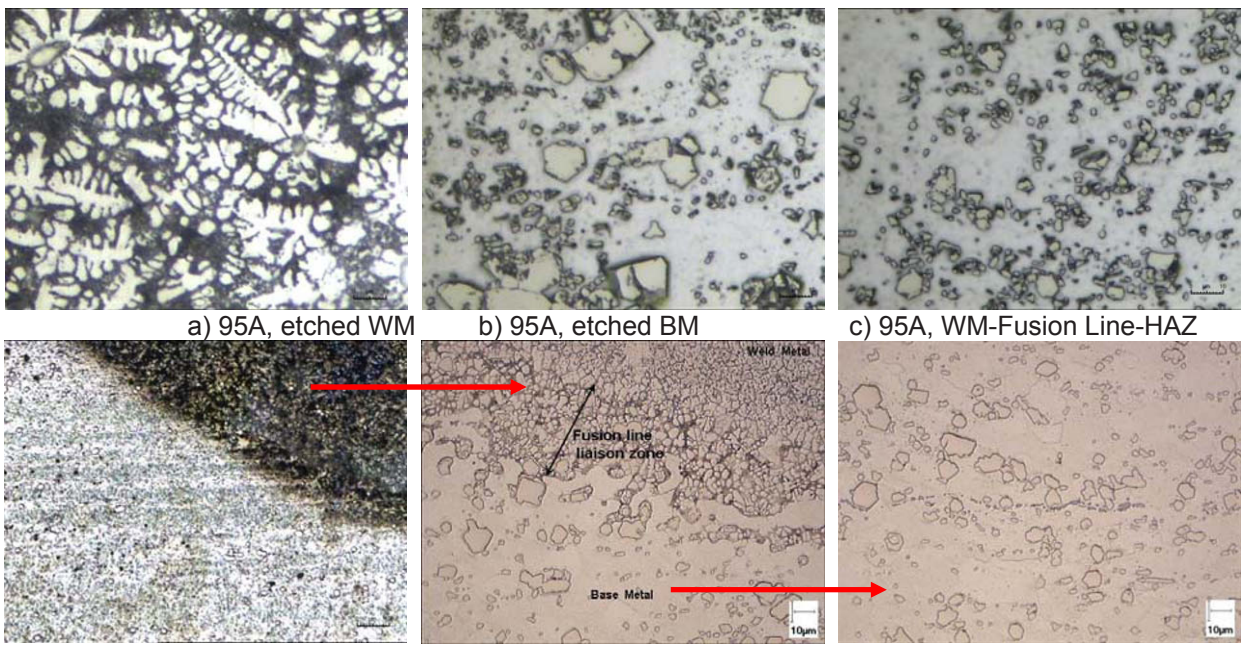

a) 95A, etched WM b) 95A, etched BM c) 95A, WM-Fusion Line-HAZ

d) 95A, Weld bead and detail of the liaison zone e) detail of Base Metal

Figure 3 Evolution of the microstructure of TiB_2-RSMCs specimens for the composition of Code: 95A In three different zones: WM, BM and also HAZ with liaison zone

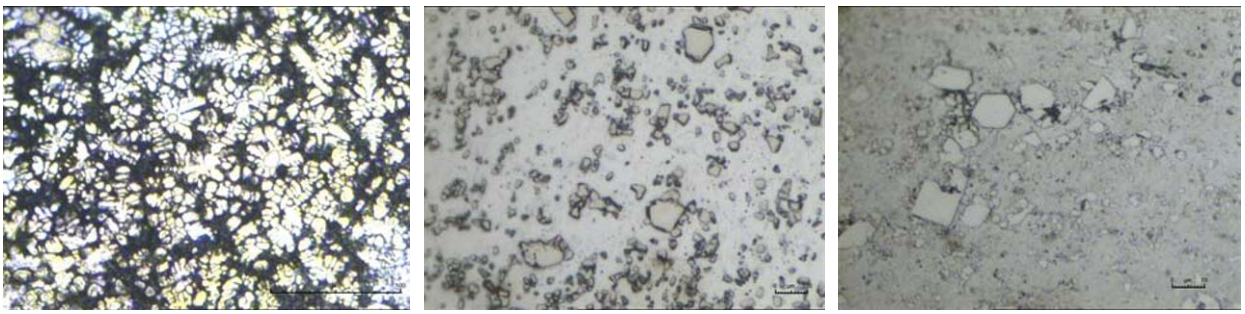

a) 105A, etched, WM b) 105A, etched, BM c) 105A, WM-Fusion Line-HAZ

Figure 4 Evolution of the microstructure of TiB_2-RSMCs specimens for the composition of Code: 105A In three different zones: WM, BM and also HAZ

In fact, solubility of iron in the TiB_2 remains less than 4 % it means that system Fe/TiB_2 keeps intact the mechanical properties of TiB_2.

In the system Fe-B-Ti, TiB_2 precipitates in steel by eutectic solidification (this avoids the primary precipitation of borides in the liquid metal). (Volume fraction is variable between 13 % and 15 %, eutectic composition). These values were found with the surface percentages of the TiB_2 ceramic particulates calculated by image analysis found for two compositions of the codes 95A and 105A. Weld Bead, after solidification, gives regularly a dendritic structure for both of the compositions. This type of structure is always developed around the ferrite nuclei. This solidification type gives a eutectic nature that is adapted to high volume continuous casting process.

3.2 Evaluation of micro hardness and micro indentation and impact tensile behaviour

Micro hardness measurements are shown in the Figures 5a and 5b. as the mean values for three different zones (BM, HAZ, and WM). Each zone contains the mean values of 5 measurements taken from the each zone for two compositions. It seems that the steel composition – code 105A gives the higher values than that of the steel composition – code 95A. Probably, this case is related to the population of TiB_2 particles distributed in the matrix that is a little bit higher than that of the composition – code 95A.

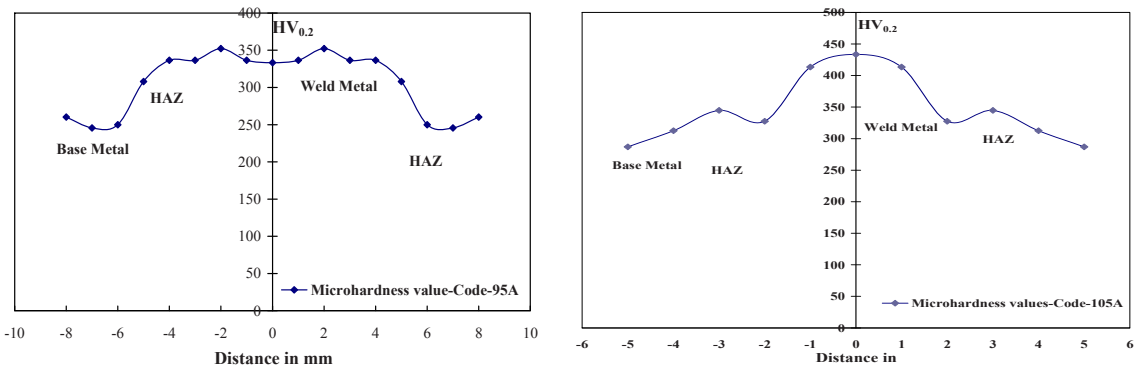

a) Code-95A b) Code-105A

Figure 5 Micro hardness values measured on the three different zones, BM, HAZ and also WM, a) for the code-95A and b) for the code-105A

Additionally, the measurements values of micro indentation have been summarised in the Table 1 for each zone (BM, HAZ and WM) of two compositions and micro indentation values were taken only on the ceramic plates. This test gave useful information about the Young modulus and critical hardness values in each local zone. Evolution of micro indentation test during the penetration has been also established depending on the applied load. In this case, useful information can be obtained by means of the evolution of applied force with time that can be obtained more detail information about the mechanical properties of

the each zone of the steel matrix composite. Typical micro indentation prints taken on the matrix and also on the TiB_2 ceramic particulates have been shown in the Figures 6a and 6b.
Evolutions of micro indentation during the penetration have been indicated depending on the applied load. Naturally, indentation curves (loading/unloading curve) for both of these compositions can be drawn from these evaluations. These curves give an easily analysis for the elasto-plastic zones separately during the micro indentation.
The next idea after the micro indentation test is to see the levels of the stress distribution just under the indenter as a function of the applied load. By this way, the plastic zone in the local zone where the contact with indenter occurred. A numerical study has been carried out by using ABAQUS code. Numerical application was given here only for the steel code 105A.
Figure 7 indicates the stress field distributions for "S11" and "S22" just under the micro indenter in the contact zone during the last increment loading step respectively. Here, the site of the plastic zone on the contact axis but well under the contact area (typical observation of "Hertz" point). Thus it is easy to obtain the curve for the evolution of the plastic energy depending on the time during the loading and unloading step as indicated in the Figure 6.

Table 2 Micro indentation results given for three different zones (BM, HAZ and WM)

Base Metal	**Code 95A**	**Code 105A**	**Heat Affected Zone**	**Code 95A**	**Code 105A**
Depth (μm)	4.75	4	Depth (μm)	3.8	3.7
Indentation HV	222	307	Indentation HV	298	315
Young Modulus (GPa)	160	278	Young Modulus (GPa	180	218

Weld Metal	**Code 95A**	**Code 105A**	**Only ceramic TiB_2**	**Code 95A**	**Code 105A**
Depth (μm)	3.4	3.4	Depth (μm)	1.5	1.2
Indentation HV	345	334	Indentation HV	3188	2998
Young Modulus (GPa)	202	232	Young Modulus (GPa	360	369

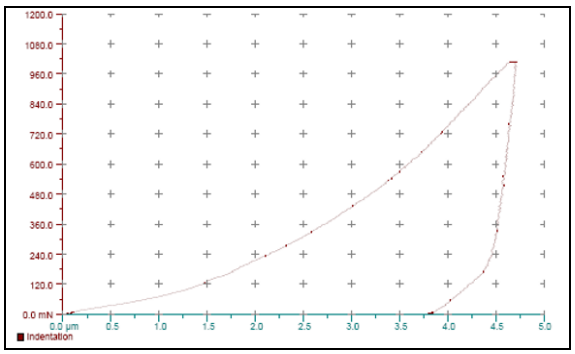

a) 95A, loading-unloading

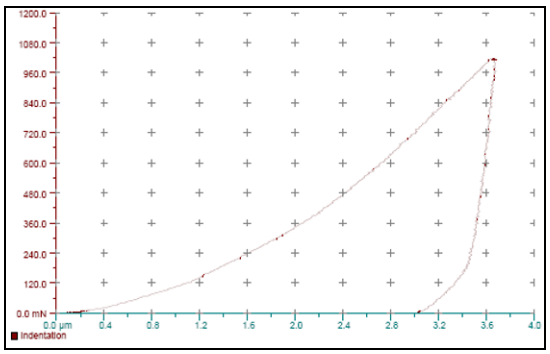

d) 105A, loading-unloading

Figure 6 Evolution of micro indentation during the penetration depending on the applied load showing by indentation (loading-unloading) curves for the steel codes 95A, and 105A

Finally, true displacement levels have been indicated as a function of true distance just at the contact zone in the Figures 8a and 8b for different increments during the loading - unloading steps respectively. It is very useful tool for evaluation of the critical value for the passage to the plastic zone for each local area of the tested materials.
Finally, in order to study the mechanical damage and evaluate the toughness evaluation of the TiB_2 reinforced steel matrix composites (TiB_2-RSMCs), impact – crash - tensile tests (ITT) have been carried out at different temperatures on the test specimens with a special geometry. As indicated in the experimental section, the specimens including a smooth part (BM) and notched part (WM) with a special device mounted on an impact pendulum [8]. All other details for this type of test technique can be found in the references 8 and 9. According to the testing conditions and material toughness, fracture occurs in one of these two zones with a very sharp transition [8, 9].

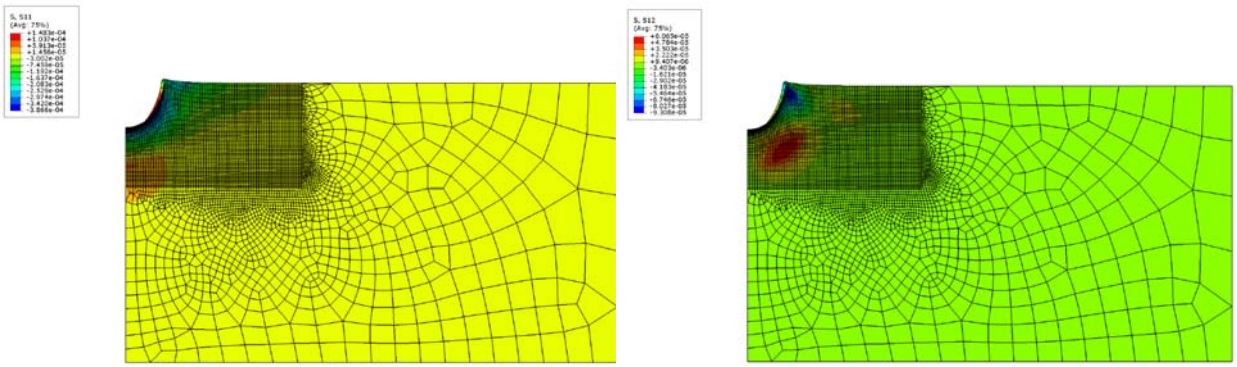

Figure 8 Stress fields “S11” (left) and “S22” distribution under the indenter for the steel code 105A in the contact zone at the last increment loading step

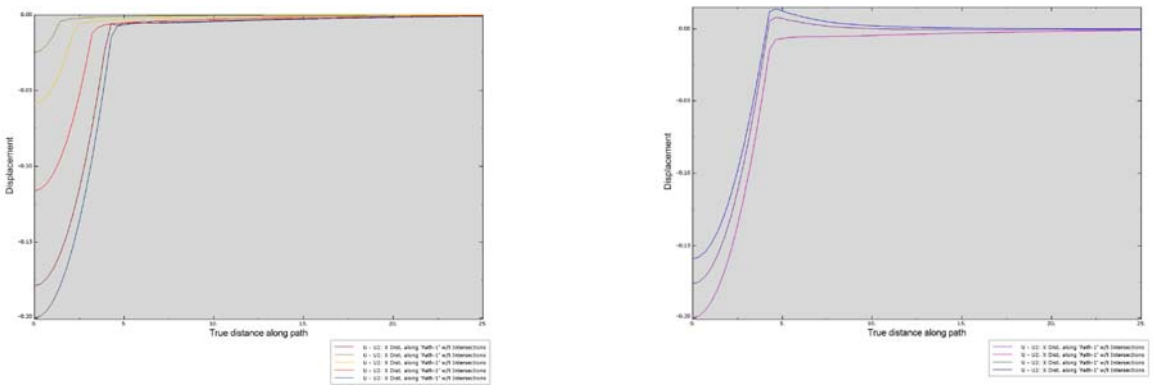

Figure 7 True displacement versus true distance curves in loading step (left) and in unloading step (right) for different increments at the contact zone

The Figures 9a and 9b show the evolution of the Ductile – Brittle Transition Temperature (DBTT) of the different grades of TiB_2 reinforced steel matrix composites. Thus, for the steel code 105A, the DBTT are found to be around -13°C and -30°C for the thicknesses of 3 mm and 2 mm respectively. Energy levels at the fracture cases vary between 20J and 60 Joules respectively for this series. These results are related basically the surface percentage of the TiB_2 reinforced plates in the steel matrix. It means that the higher surface percentage and heterogeneous distribution of the TiB_2 reinforced plates in the steel matrix gives the lower resistance to the impact conditions and naturally gives a weak ductile-brittle transition temperature. Meanwhile, these values are determined to be -5°C and -39°C for the steel code 95A, for the thicknesses of 3 mm and 2 mm respectively. The higher resistance to impact conditions with the steel code 95A is observed for the reasons discussed just above in this text. Energy levels at the fracture cases vary between 20J and 60 Joules respectively for this series.

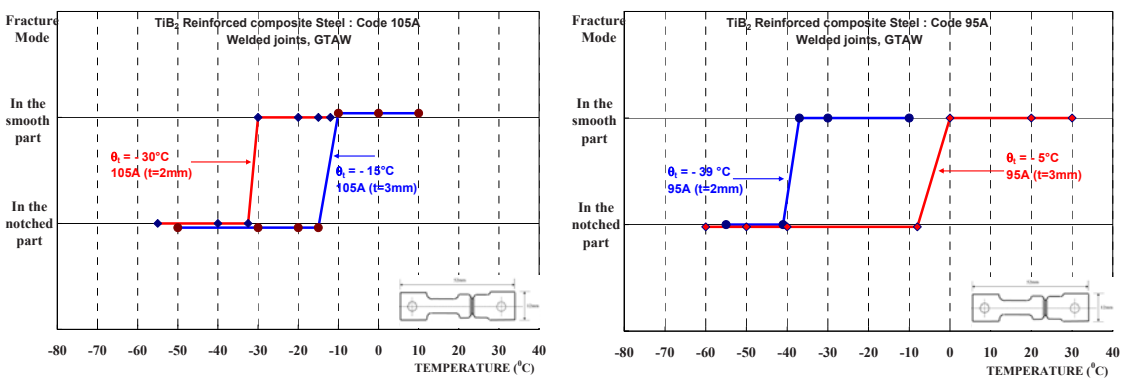

a) Steel code 105A b) Steel code 95A

Figure 9 Ductile Brittle Transition diagram, DBTT of TiB_2 reinforced steel matrix composites for the specimens taken from the steel code of 95A and 105A in case of two thicknesses (welded joints, GTAW)

Only for information about the dynamic damage behaviour after the impact tensile test, the fracture surfaces of the broken specimens for the codes 95A and 105A were analysed by Scanning Electron Microscopy, SEM (Figures 10a and 10b). SEM pictures show typical cleavage surface in case of brittle fracture of the specimens. There is quasi no porosity and there is any debonding of the TiB_2 particles from steel matrix on the studied specimens (Figures 11a and 11b). However, very small secondary cracks just under the fracture surfaces in some of the specimens (only for the code of 105A).

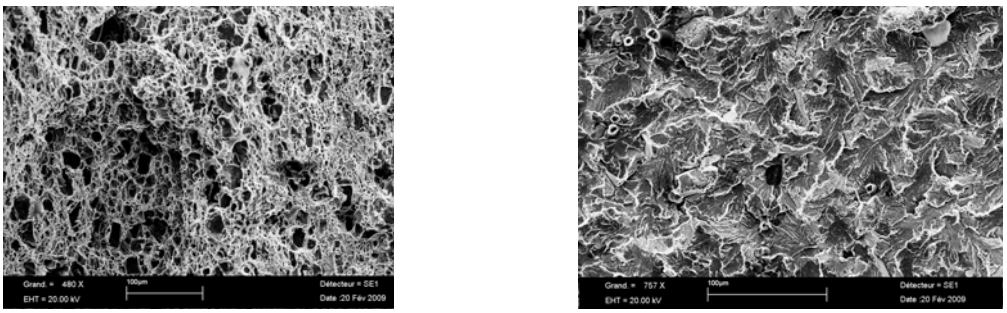

Figure 10a Fracture surfaces of the steel code 95A obtained after impact-tensile-crash test: Ductile fracture (left) and Brittle fracture showing a cleavage surface (right)

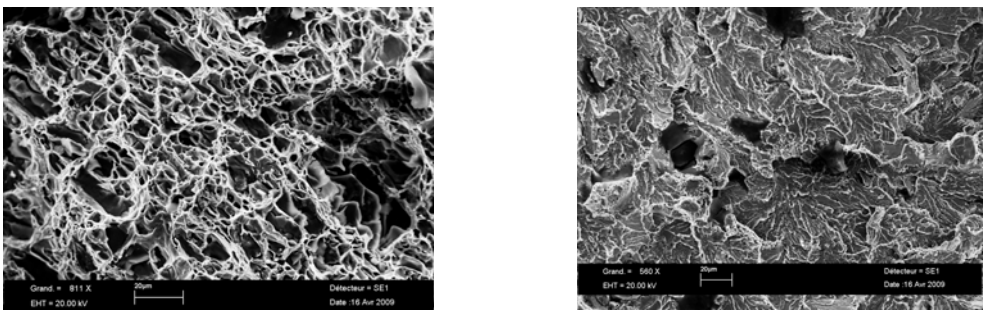

Figure 10b Fracture surfaces of the steel code 105A obtained after impact-tensile-crash test: Ductile fracture (left) and Brittle fracture showing a cleavage surface (right)

4 Conclusions

-TiB_2 particulate reinforced MMC_S sheets were successfully manufactured as proposed in the in the reference 1 Patent (ARCELOR MITTAL-RESEARCH).
-In the system Fe-B-Ti, TiB_2 precipitates in steel by eutectic solidification, this avoids the primary precipitation of borides in the liquid metal.
-Weldability of this new steel family has a big potential success in manufacturing engineering
-Weld bead shows finer eutectic structure.
-There is no abnormal evolution in HAZ (e.g. grain growth)
-Preliminary works suggest that this product (originally developed for the car industry) should find other applications for all of the structures designed by stiffness (ex: energy domain, road transport and railway...).

Acknowledgement
This project “ANR-ADRERA” is going on. The financial support by the ARCELOR-MITTAL Research Group, France is gratefully acknowledged.

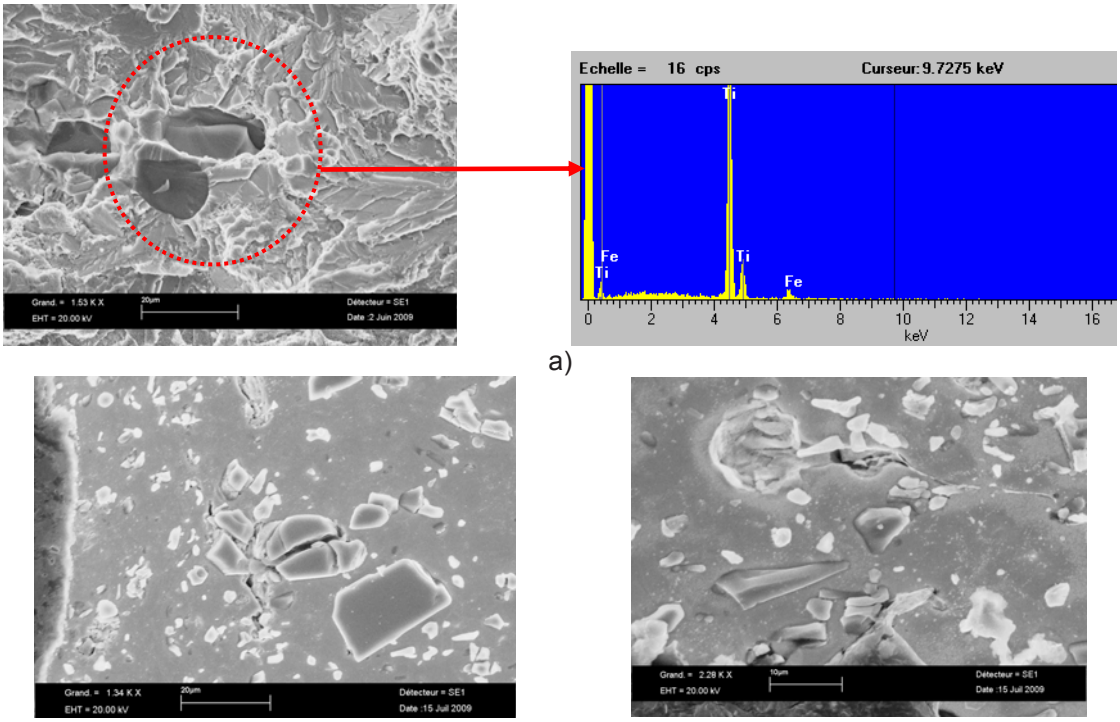

Figure 11a) Composite steel sheet Code 105A EDS Analysis on the fracture surface (Brittle cleavage) and b) secondary crack observed under the notch (left) and in the weld part (right)

References

[1] ARCELOR Research group; Patent EP 1 897 963 A1, Bulletin 2008/11, 20p, 2008

[2] Materials Selection in Mechanical Design", 3rd edition by M.F. Ashby, Butterworth Heinemann, Oxford, 2006, Chapters 1 – 3 and CES EduPack software-Grant design, 2008

[3] F. Bonnet et al, Arcelor Mittal-Research, internal report, 2009, 63p,

[4] Jiang Q.C., Ma B.X., Wang H.Y., Wang Y., Dong Y.P., Fabrication of steel matrix composites locally reinforced with in situ TiB_2–TiC particulates, Composites Part A: Applied Science and Manufacturing, 37, 1, 133-138, 2006

[5] Akhtar F., Askari S. J., Shah K. A, Xueli Du, Guo S., Microstructure, mechanical properties, electrical conductivity and wear behavior of high volume TiC reinforced Cu-matrix composites, Materials Characterization, 60, 4, 327-336, 2009,

[6] Mukhopadhyay A., Raju G.B., Basu B., Suri A.K., Correlation between phase evolution, mechanical properties and instrumented indentation response of TiB_2-based ceramicsJournal of the European Ceramic Society, 29, 3, 505-516, 2009

[7] Yang Y., Wang H., Liang Y., Zhao R., Jiang Q., Fabrication of steel matrix composites locally reinforced with different ratios of TiC/TiB_2 particulates using SHS reactions of Ni–Ti–B_4C and Ni–Ti–B_4C–C systems during casting, Materials Science and Engineering: A, 445-446, 398-404, 2007

[8] Bayraktar E., Kaplan D., Buirette C. and Grumbach M., Application of Impact tensile testing to the welded thin sheets, Journal of Materials Processing Technology - JMPT, 145, I, 27-39, 2004

[9] Bayraktar, E., Grumbach, M., Kaplan, D., Effect of forming rate on the impact tensile properties of the steels under crash test. JAMME, J. Achievement in Mater. Manufacturing Eng. 20 (1), 55–60, 2007

[10] Wang H.Y., Huang L., Jiang Q.C., In situ synthesis of TiB2–TiC particulates locally reinforced medium carbon steel–matrix composites via the SHS reaction of Ni–Ti–B4C system during casting, Materials Science and Engineering A 407, 98–104, 2005

[11] Wang Y., Zhang Z.Q., Wang H.Y., Ma B.X. and Jiang Q.C., Effect of Fe content in Fe–Ti–B system on fabricating TiB2 particulate locally reinforced steel matrix composites, Materials Science and Engineering A 422, 339–345, 2006

[12] P. Villars, A. Prince, H. Okamoto (Eds.), Handbook of Ternary Alloy Phase Diagrams, vol. 5, ASM International, 1997

Proceedings of the SEM Annual Conference
June 7-10, 2010 Indianapolis, Indiana USA

Nonlinear Viscoelastic Nanoindentation of PVAc

Fang Wang, Yong Wang,* Boshen Fu, Hongbing Lu
Department of Mechanical Engineering
University of Texas at Dallas, Richardson, TX 75080
hongbing.lu@utdallas.edu
*School of Mechanical and Aerospace Engineering
Oklahoma State University, Stillwater, OK 74078

ABSTRACT

A nonlinear viscoelastic nanoindentation analysis was conducted for polyvinyl acetate (PVAc) with a glass transition temperature of 29 °C. Nanoindentation using an MTS Berkovich nanoindenter was made on PVAc at different depths. The load-displacement curves were determined using nanoindentation. A nonlinear viscoelastic model was implemented in ABAQUS/Standard Code to analyze the nonlinear visceoasltic behavior of PVAc under nanoindentation. The effects of nonlinearity on the load-displacement curves, as well as on the indent impression were investigated.

1. Introduction

Nanoindentation is an effective technique to measure mechanical properties of small amounts of materials which would be a challenge for conventional tests. It is also an effective measurement technique to characterize material behavior at micron/submicron scale and can be applied to heterogeneous materials with mechanical properties varying spatially. Nanoindentation measurement involves 3D stress state and nonlinearity. Despite the fact that nanoindentation technique for measurements of some properties of elastic-plastic materials has been well established [1], nanoindentation on viscoelastic materials is not fully understood especially in nonlinear viscoelastic region. Polymers with low glass transition temperature, i.e. Polyvinyl acetate (PVAc) which has Tg=29°C, often shows negative unloading slope, giving nagative contact stiffness under nanoindentation. In this case, elastic solution is not applicable.

In this investigation, nonlinear viscoelastic properties of PVAc were determined by nanoindentation tests. Load-displacement curves were recorded using nanoindentation at different indentation depths. ABAQUS/Standard code with user defined subroutine was used to analyze the nonlinear viscoelastic behavior of PVAc under nanoindentation.

2. Nonlinear Viscoelastic Model

Three dimensional, nonlinear viscoelastic Burger's model for variable stress is expressed as:

$$\varepsilon_{ij}^{e} = \frac{1+\upsilon}{E}\sigma_{ij} - \frac{\upsilon}{E}\sigma_{kk}\delta_{ij} \tag{1}$$

$$\dot{\varepsilon}_{ij}^{s} = C_s J_2^{m_s}(t) s_{ij}(t) \tag{2}$$

$$\dot{\varepsilon}_{ij}^{t} + \frac{1}{t_\varepsilon}\varepsilon_{ij}^{t} = \frac{C_t}{t_\varepsilon} J_2^{m_t}(t) s_{ij}(t) \tag{3}$$

The components of the total strain tensor are the summation of elastic, steady creep, and transient creep components,

$$\varepsilon_{ij} = \varepsilon_{ij}^{e} + \varepsilon_{ij}^{s} + \varepsilon_{ij}^{t} = \varepsilon_{ij}^{e} + \varepsilon_{ij}^{s} + \sum_{i=1}^{n} \varepsilon_{ij}^{t_i} \tag{4}$$

T. Proulx (ed.), *Time Dependent Constitutive Behavior and Fracture/Failure Processes, Volume 3*, Conference Proceedings of the Society for Experimental Mechanics Series 15, DOI 10.1007/978-1-4419-9794-4_16, © The Society for Experimental Mechanics, Inc. 2011

where n is the number of Voigt units as shown in Figure. 1.

Eqs. (2) and (3) can also be written in integral form:

$$\varepsilon_{ij}^{s} = C_s \int_0^t J_2^{m_s}(t') s_{ij}(t') dt'$$

$$\varepsilon_{ij}^{t} = \frac{C_t}{t_\varepsilon} \exp(-t/t_\varepsilon) \int_0^t J_2^{m_t}(t') s_{ij}(t') \exp(t'/t_\varepsilon) dt'$$

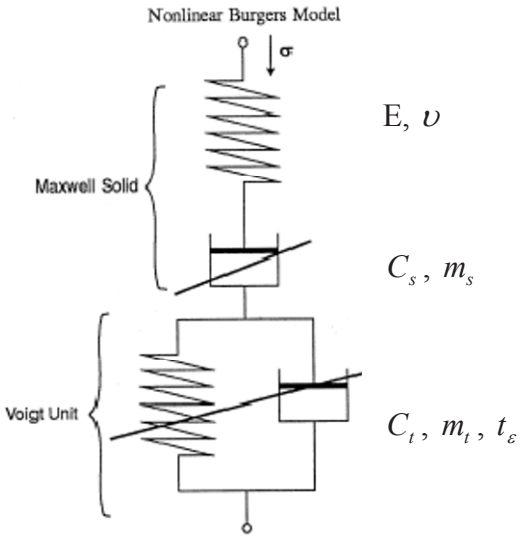

Figure. 1 Nonlinear Burger's model

A simple, stable integration operator for these equations is the central difference operator:

$$\dot{f}_{t+\frac{1}{2}\Delta t} = \frac{\Delta f}{\Delta t} \quad , \quad f_{t+\frac{1}{2}\Delta t} = f_t + \frac{\Delta f}{2}$$

where f is some function, f_t is its value at the beginning of the increment, Δf is the change in the function over the increment, and Δt is the time increment.

Jacobian matrix $\frac{\partial \Delta\sigma}{\partial \Delta\varepsilon}$ of the constitutive model, with $\Delta\sigma$ being the stress increments and $\Delta\varepsilon$ being the strain increments, can be derived by applying this to the above rate-dependent constitutive Eqs. (1)-(3).

Applying the central difference method to the elastic strain component as depicted in Eq. (1), yields

$$\varepsilon_{ij}^{e} + \frac{1}{2}\Delta\varepsilon_{ij}^{e} = \frac{1+\upsilon}{E}(\sigma_{ij} + \frac{1}{2}\Delta\sigma_{ij}) - \frac{\upsilon}{E}(\sigma_{kk} + \frac{1}{2}\Delta\sigma_{kk})\delta_{ij}$$

The stress and strain vectors for 3-D problem as defined in ABAQUS are

$$\sigma = (\sigma_{xx,} \quad \sigma_{yy,} \quad \sigma_{zz,} \quad \sigma_{yz,} \quad \sigma_{zx,} \quad \sigma_{xy})$$

$$\varepsilon = (\varepsilon_{xx,} \quad \varepsilon_{yy,} \quad \varepsilon_{zz,} \quad \varepsilon_{yz,} \quad \varepsilon_{zx,} \quad \varepsilon_{xy})$$

Therefore the elastic compliance matrix ($\frac{\partial \Delta \varepsilon_{ij}^{e}}{\partial \Delta \sigma_{kl}}$) can be written as

$$\begin{bmatrix} \frac{1}{E} & -\frac{\upsilon}{E} & -\frac{\upsilon}{E} & 0 & 0 & 0 \\ & \frac{1}{E} & -\frac{\upsilon}{E} & 0 & 0 & 0 \\ & & \frac{1}{E} & 0 & 0 & 0 \\ & & & \frac{1+\upsilon}{E} & 0 & 0 \\ & & & & \frac{1+\upsilon}{E} & 0 \\ & & & & & \frac{1+\upsilon}{E} \end{bmatrix} \text{symmetric} \tag{5}$$

Similar procedure is applied to Eq. (2) for steady creep component, gives

$$\frac{\Delta \varepsilon_{ij}^{s}}{\Delta t} = C_s J_2^{m_s}(t + \frac{\Delta t}{2}) \left(s_{ij}(t) + \frac{1}{2} \Delta s_{ij} \right)$$

Assuming $J_2(t) \approx J_2(t + \frac{1}{2}\Delta t)$, gives

$$\Delta \varepsilon^{s} = \Delta t C_s J_2^{m_s}(t) s_{ij}(t) + \frac{1}{2} \Delta t C_s J_2^{m_s}(t) \Delta s_{ij} \tag{6}$$

$$\frac{\partial \Delta \varepsilon_{ij}^{s}}{\partial \Delta s_{ij}} = \frac{1}{2} \Delta t C_s J_2^{m_s}(t)$$

For $s_{ij} = \sigma_{ij} - \frac{1}{3}\sigma_{kk}\delta_{ij}$, then

$$\frac{\partial \Delta \varepsilon_{ij}^{s}}{\partial \Delta \sigma_{ij}} = \frac{\partial \Delta \varepsilon_{ij}^{s}}{\partial \Delta s_{ij}} \frac{\partial \Delta s_{ij}^{s}}{\partial \Delta \sigma_{ij}} = \begin{cases} \frac{2}{3} \frac{\partial \Delta \varepsilon_{ij}^{s}}{\partial \Delta s_{ij}} = \frac{1}{3} \Delta t C_s J_2^{m_s}(t), & (i = j) \\ \frac{\partial \Delta \varepsilon_{ij}^{s}}{\partial \Delta s_{ij}} = \frac{1}{2} \Delta t C_s J_2^{m_s}(t), & (i \neq j) \end{cases} \tag{7}$$

The compliance matrix of steady creep ($\frac{\partial \Delta \varepsilon_{ij}^{s}}{\partial \Delta \sigma_{kl}}$) can be written as

$$\Delta t C_s J_2^{m_s}(t)\begin{bmatrix} \frac{1}{3} & 0 & 0 & 0 & 0 & 0 \\ & \frac{1}{3} & 0 & 0 & 0 & 0 \\ & & \frac{1}{3} & 0 & 0 & 0 \\ & & & \frac{1}{2} & 0 & 0 \\ & & & & \frac{1}{2} & 0 \\ & & & & & \frac{1}{2} \end{bmatrix}_{\text{symmetric}} \tag{8}$$

Finally for the transient creep component as defined in Eq. (3),

$$\frac{\Delta\varepsilon_{ij}^t}{\Delta t} + \frac{1}{t_\varepsilon}\left(\varepsilon_{ij} + \frac{1}{2}\Delta\varepsilon_{ij}\right) = \frac{C_t}{t_\varepsilon} J_2^{m_t}(t + \frac{\Delta t}{2})\left(s_{ij}(t) + \frac{1}{2}\Delta s_{ij}\right)$$

$$\Delta\varepsilon^t = \frac{1}{2t_\varepsilon + \Delta t}\left(2\Delta t C_t J_2^{m_t}(t) s_{ij}(t) - 2\Delta t\varepsilon^t + \Delta t C_t J_2^{m_t}(t)\Delta s_{ij}\right) \tag{9}$$

$$\frac{\partial\Delta\varepsilon_{ij}^t}{\partial\Delta s_{ij}} = \frac{\Delta t}{2t_\varepsilon + \Delta t} C_t J_2^{m_t}(t)$$

The compliance matrix of transient creep ($\frac{\partial\Delta\varepsilon_{ij}^t}{\partial\Delta\sigma_{kl}}$) can be written as

$$\frac{\Delta t}{2t_\varepsilon + \Delta t} C_t J_2^{m_t}(t)\begin{bmatrix} \frac{2}{3} & 0 & 0 & 0 & 0 & 0 \\ & \frac{2}{3} & 0 & 0 & 0 & 0 \\ & & \frac{2}{3} & 0 & 0 & 0 \\ & & & 1 & 0 & 0 \\ & & & & 1 & 0 \\ & & & & & 1 \end{bmatrix}_{\text{symmetric}} \tag{10}$$

From Eq. (4), total compliance is

$$\frac{\partial\Delta\varepsilon_{ij}}{\partial\Delta\sigma_{kl}} = \frac{\partial\Delta\varepsilon_{ij}^e}{\partial\Delta\sigma_{kl}} + \frac{\partial\Delta\varepsilon_{ij}^s}{\partial\Delta\sigma_{kl}} + \frac{\partial\Delta\varepsilon_{ij}^t}{\partial\Delta\sigma_{kl}} \tag{11}$$

By inversing the total compliance matrix, system stiffness matrix (Jacobian matrix) $\frac{\partial\Delta\sigma_{ij}}{\partial\Delta\varepsilon_{kl}}$ can be obtained from Eq. (11).

It should be noted that above Jacobian matrix takes into account of only the elastic deformation and creep deformation induced by stress increment. It can be seen from Eqs. (6) and (9), aforementioned creep strain is just a small part of the total steady and transient creep strain. The rest of the creep strain is developed over the

time period of the time increment and controlled by stress status. An artificial stress increment is introduced to include this creep strain into the system equation. This part of creep strain can be extracted from Eqs. (6) and (9) as

$$\Delta\varepsilon' = \Delta t C_s J_2^{m_s}(t) s_{ij}(t) + \frac{1}{2t_\varepsilon + \Delta t}\left(2\Delta t C_t J_2^{m_t}(t) s_{ij}(t) - 2\Delta t \varepsilon^t\right) \qquad (12)$$

A stress increment $\Delta\sigma' = C\Delta\varepsilon'$ is then added into the system equation to account for the creep strain in Eq. (12), with C being the Jacobian stiffness matrix calculated from Eq. (11).

3. Nanoindentaion Measurements on PVAc

An MTS Nano Indenter XP system was used for the nanoindentation measurements. This indenter can reach a maximum indentation depth of 500 μm and a maximum load of 500 mN. The displacement and load resolutions are 0.2 nm and 50 nN, respectively. Berkovich indenter tip, made of single crystal diamond, was used in this investigation. The nanoindentation tests were conducted in the air at room temperature (23°C) under a relative humidity about 50%. Figure 2 shows the load-displacement curves from nanoindentaion with 0.05 mN/s loading/unloading rate of different loading time.

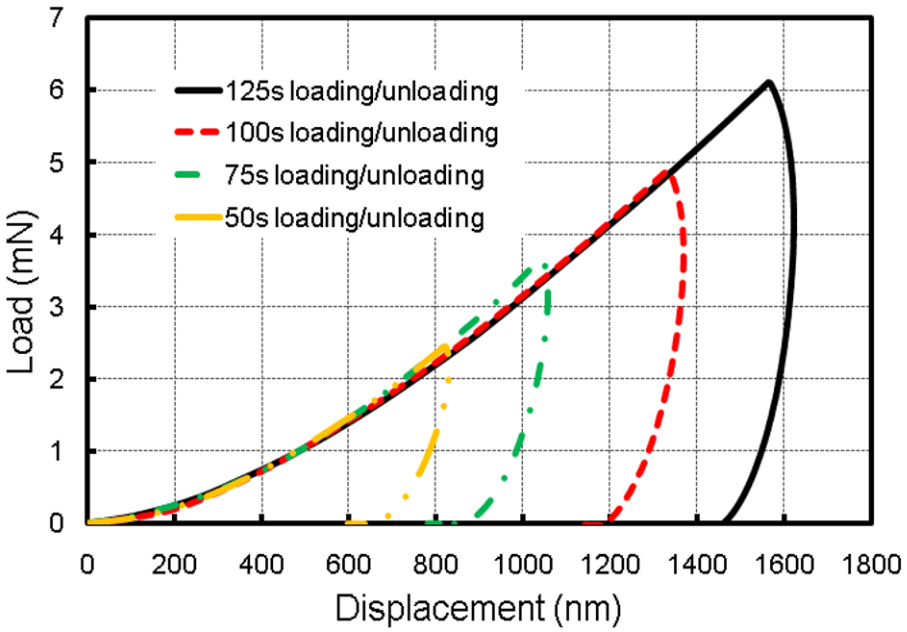

Figure 2. Load-displacement curves from nanoindentation (0.05mN/s)

4. Simulation of Nanoindentation on PVAc:

In this simulation work, a 3D rigid Berkovich indenter tip model using shell elements was created. Because of symmetric geometry structure of indenter tip, only 1/6 of entire PVAc sample is needed the simulation which takes shorter time to run than the entire model case. The symmetric boundary conditions were applied on the PVAc sample to obtain the identical boundary condition as entire model was used. The Berkovich indenter tip and PVAc part are shown in the Figure 3. A user defined subroutine code for ABAQUS/Standard [2] was developed based on the algorithm introduced in the section 2. To explore the nonlinear viscoelastic material properties of PVAc, an inverse problem has been solved to obtain the parameters for the nonlinear viscoelastic model as mentioned previously. Different parameters were used as input for the material model to run the simulation, and output load-displacement curves were compared with the experimental results. By adjusting the input parameters of material model, the simulation output curves are able to agree with the experimental results for some certain parameter values.[3] These values were determined as the parameters for the nonlinear viscoelastic model. After a reasonable agreement was reached, the same parameters were used in different loading /unloading time cases were simulated as well to indicate the viscoelastic response of the material model.

Figure 4 illustrates the load-displacement curve comparison between simulation results and experiment data at 50s, 75s, 100s and 125s loading/unloading times. All the simulation curves agree well with the experimental results which show the capability of this nonlinear viscoelastic model to describe the properties of PVAc. The input parameters obtained from simulation which output the agreeable curves with experimental results were listed in Table 1. while steady creep parameters ms=0.75. The stress and displacement distribution along the loading direction from simulation are shown in Figure 5. It is worthy to note that the residual stress and displacement still exist after unloading of the indenter tip. This is associated with the viscoelastic response of material.

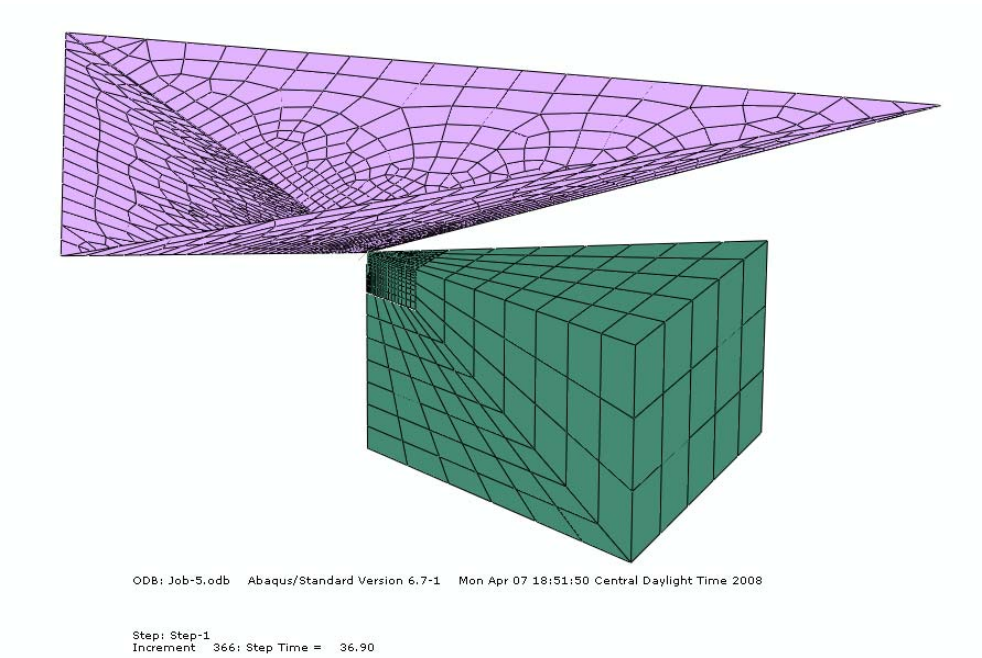

Figure. 3 FEA simulation model: Berkovich indenter using rigid shell element and 1/6 symmetric PVAc sample

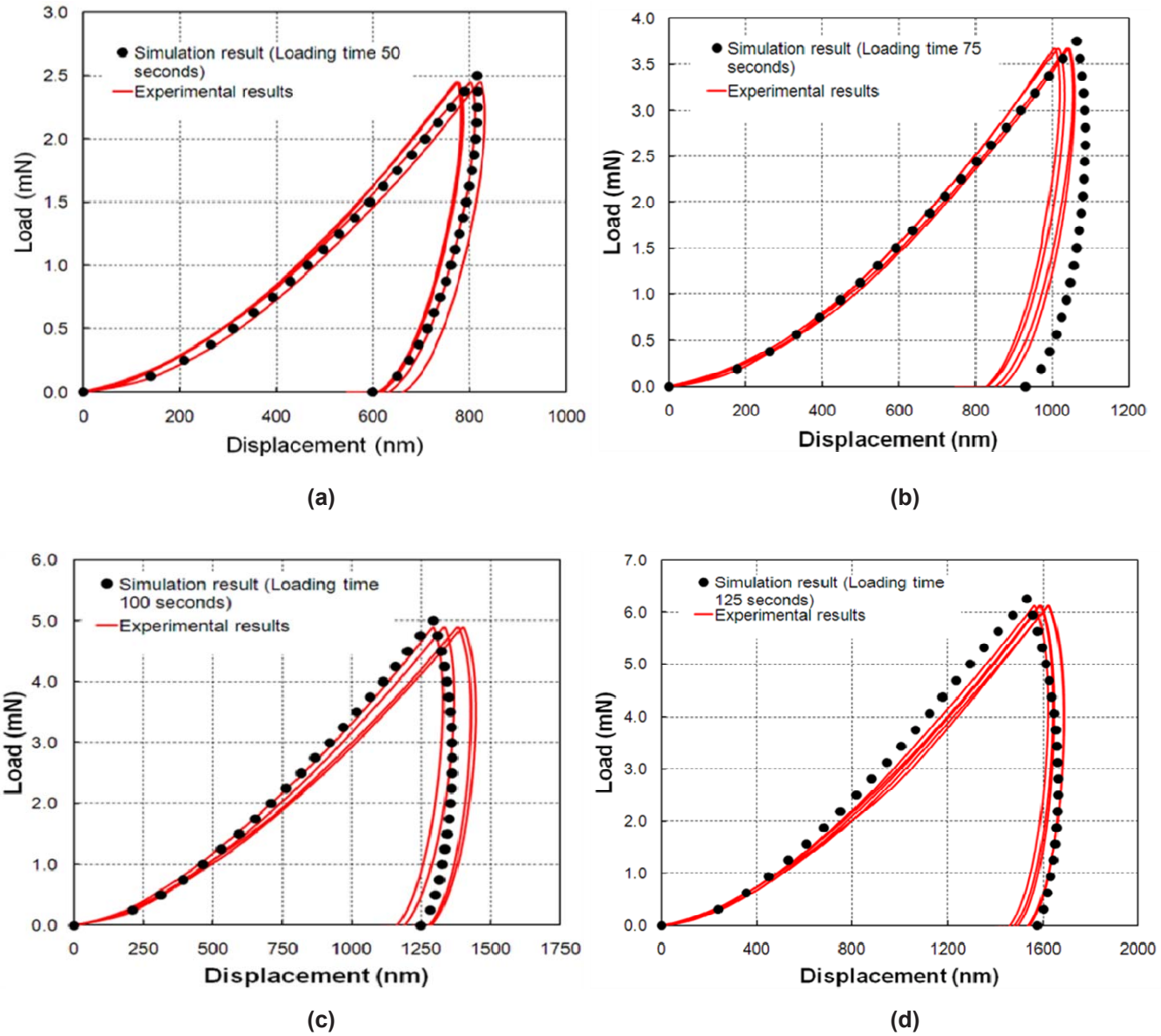

Figure 4. Simulation result (a) 50s loading/unloading time.(b) 75s loading/unloading time.(c) 100s loading/unloading time. (d) 125s loading/unloading time.

Table 1. Transient creep parameters

	N=1	N=2	N=3	N=4	N=5	N=6	N=7	N=8
Ct	0.23	0.1	0.1	0.05	0.05	0.05	0.05	0.05
mt	0.1	0.15	0.15	0.25	0.3	0.3	0.3	0.3
Tε (s)	0.25	3	50	100	125	150	250	300

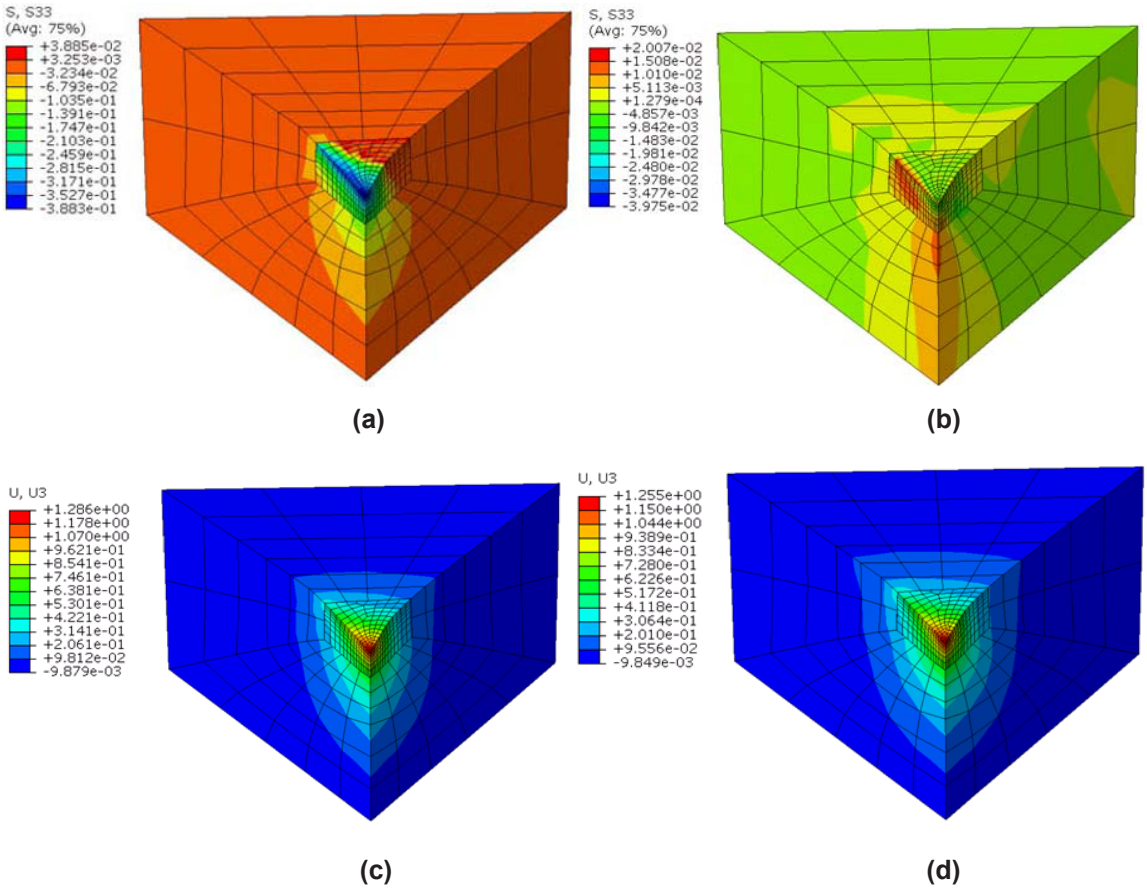

Figure 5. Simulation results. (a). Stress σ_z (GPa) distribution after loading. (b). Stress σz (GPa) distribution after unloading. (c). Displacement (μm) along z axis after unloading. (d). Displacement (μm) along z axis after unloading.

5. Conclusion

Nonlinear viscoelastic Burgers model can be implemented in ABAQUS/Standard simulation with a user define subroutine to analyze nanoindentation experimental results. Simulation results were compared to nanoindentation experiments with reasonable agreement at different indentation depth. Results show that the model could possibly simulate the indentation depths from 800 nm to 1500 nm.

Reference

[1] Oliver, W.C. and Pharr, G.M., 1992, “An Improved Technique for Determining Hardness and Elastic Modulus Using Load and Displacement Sensing Indentation Experiments,” J. Mater. Res., 7, pp. 1564-1583.

[2] ABAQUS Documentation V 6.8.,2009

[3] Liu, Y., Wang, B., Yoshino, M., Roy, S., Lu, H. and Komanduri, R., 2005, “Combined numerical simulation and nanoindentation for determining mechanical properties of single crystal copper at mesoscale,” J. Mech. Phys. Solids, 53, pp. 2718-2741.

Proceedings of the SEM Annual Conference
June 7-10, 2010 Indianapolis, Indiana USA

Theoretical and computational modelling of instrumented indentation of viscoelastic composites

Yan-Ping Cao[a)], Ke-Lin Chen

Applied Mechanics Lab, Department of Engineering Mechanics, Tsinghua University, Beijing 100084, China

Abstract: In this study, we investigate the indentation of viscoelastic composites by using a combination of theoretical and computational analysis. The composite is assumed to consist of two phases, i.e., the filler and the matrix, and they are linear elastic and linear viscoelastic material, respectively. Two cases are investigated: 1). hard fillers are embedded in a very soft matrix; 2). the matrix is much harder than the fillers. Particular attention is paid to the correlation between the indentation responses and the relaxation properties of the composites and the constituent. To this end, we first perform a theoretical analysis which is followed by a series of finite element computations. A number of conclusions have been drawn based on the theoretical and computational results, which may improve the current understanding of the indentation of viscoelastic composite materials, including some man-made biocomposites as well as biological soft tissues.

Keywords: Indentation; viscoelastic composites; finite element simulation

[a)] Corresponding author. Tel.: +86 10 62772520; fax: +86 10 62781824.

E-mail address: caoyanping@tsinghua.edu.cn (Y. P. Cao).

T. Proulx (ed.), *Time Dependent Constitutive Behavior and Fracture/Failure Processes, Volume 3*, Conference Proceedings of the Society for Experimental Mechanics Series 15, DOI 10.1007/978-1-4419-9794-4_17, © The Society for Experimental Mechanics, Inc. 2011

1. Introduction

Many natural biological materials, ranging from articular cartilage, vasculars to cells, are viscoelastic composites from the viewpoint of material science. Determining the mechanical properties of these viscoelastic biological materials is of great importance for the tissue engineering as well as for understanding the responses of cells or tissues to the mechanical stimuli (Levental et al., 2007; Lee et al., 2010). In addition, man-made biocomposites have received much attention during the past decades, which may be formed by a matrix and fillers (e.g. particles or fibers). Biocomposites find wide applications such as in drug delivery, tissue engineering and cosmetic industry (Thomas et al., 2007; Ramakrishna et al., 2004). In many cases, mechanical characterization of the composites as well as each constituent is crucial not only for their practical use, but also for understanding the connection between the microstructures and properties of the materials, and further optimizing the processing procedures.

In recent years, instrumented indentation has been proved to be a powerful tool for mechanical characterization of time-dependent materials (e.g. Shimizu et al.,1999; Fischer-Cripps, 2004; Lu et al., 2003; Cheng and Cheng, 2004; Cheng et al., 2006; Ngan et al., 2005; Ebenstein et al., 2006; Huang and Lu, 2006; Cheng and Yang, 2009; Oyen et al., 2003, 2007; Herbert et al., 2009; Cao et al., 2007, 2009), appears to be an efficient tool for evaluating the mechanical properties of viscoelastic composite materials, especially at a local area and/or at small scales.

In this study, we consider the indentation of a typical composite system consists of two constituents, i.e., the matrix and the filler, which are linear viscoelastic and linear elastic material, respectively. The objective is to investigate the connection between the indentation responses and the relaxation behaviour of both composites and the matrix. For such a purpose, a combination of theoretical and computational analysis has been carried out. The results together with a number of conclusions made in this study may improve the current understanding of the indentation of viscoelastic composite materials.

2. Theoretical analysis

Fig. 1 illustrates the indentation of a tw o-phase composite system by using a rigid indenter. In this study, it is assum ed that the m atrix and the fillers are perfectly bonded. Effects of the interface phase are omitted although they m ay play important roles in many cases.

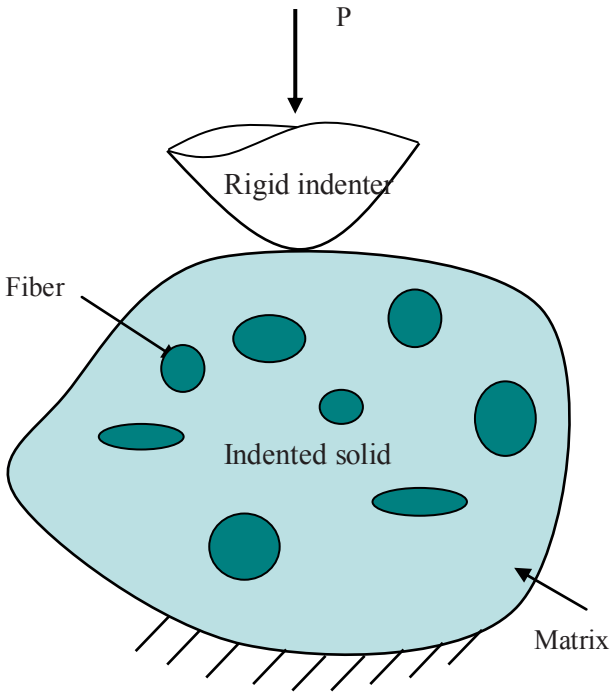

Fig. 1 Schematic drawing of a rigid indenter indenting into a composite solid.

We first consider the indentation of a rigid indenter with arbitrary profile indenting in to a com posite with a rbitrary shape (Fig. 1), for which both phases are homogeneous, isotropic and linear elastic materials and the constitutive relations read

$$\sigma_{ij,m} = 2G_m\varepsilon_{ij,m} + \lambda_m\delta_{ij}\varepsilon_{kk,m} = \frac{E_m}{1+\nu_m}\varepsilon_{ij,m} + \frac{E_m\nu_m}{(1+\nu_m)(1-2\nu_m)}\delta_{ij}\varepsilon_{kk,m}, \tag{1a}$$

$$\sigma_{ij,f} = 2G_f\varepsilon_{ij,f} + \lambda_f\delta_{ij}\varepsilon_{kk,f} = \frac{E_f}{1+\nu_f}\varepsilon_{ij,f} + \frac{E_f\nu_f}{(1+\nu_f)(1-2\nu_f)}\delta_{ij}\varepsilon_{kk,f}, \tag{1b}$$

where σ_{ij} and ε_{ij} are the components of the stress and strain tensors, respectively, ε_{kk} is the d ilatational str ain, G and λ are Lam é constants, E is Young's

modulus, and v is Poisson's ratio. δ_{ij} represents Kronecker delta. The subscripts 'm' and 'f' represent the matrix and the filler, respectively. Under given boundary conditions, the indentation load P may be a function of the following independent parameters:

$$P = g\left(h, E_m, E_f, v_m, v_f, c_0, c_1, c_2, \ldots, c_{\mathrm{M}}, d_0, d_1, d_2, \ldots, d_N, e_0, e_1, e_2, \ldots, e_{\mathrm{K}}\right), \quad (2)$$

where h is indenter displacement. $c_0, c_1, c_2, \ldots, c_M$ (M is a finite integer) are the geometric parameters used to describe the profile of the indenter in the contact region, and $d_0, d_1, d_2, \ldots, d_L$ (L is a finite integer) are the parameters describing the shape of the indented solid that affect the indentation responses. $e_0, e_1, e_2, \ldots, e_K$ (K is a finite integer) are the parameters representing the positions and geometric shapes of the fillers. The geometric parameters c_ξ ($0 \le \xi \le M$), d_η ($0 \le \eta \le N$) and e_ς ($0 \le \varsigma \le K$) should have the following dimensions

$$\left[c_\xi\right] = \left[h\right]^{R_\xi}, \quad (3a)$$

$$\left[d_\eta\right] = \left[h\right]^{r_\eta}, \quad (3b)$$

$$\left[e_\varsigma\right] = \left[h\right]^{b_\varsigma}, \quad (3c)$$

where R_ξ, r_η and b_ς are real numbers. Among the governing parameters in Eq. (2), h and E_m have the independent dimensions. Applying Pi-theorem in dimensional analysis (Barenblatt, 1996) to Eq. (2) leads to

$$P = E_m h^2 \Pi\left(\begin{array}{l} v_f, v_m, \frac{c_0}{h^{R_0}}, \frac{c_1}{h^{R_1}}, \frac{c_2}{h^{R_2}}, \ldots, \frac{c_M}{h^{R_M}}, \frac{d_0}{h^{r_0}}, \frac{d_1}{h^{r_1}}, \frac{d_2}{h^{r_2}}, \ldots, \frac{d_L}{h^{r_L}}, \\ \frac{e_0}{h^{b_0}}, \frac{e_1}{h^{b_1}}, \frac{e_2}{h^{b_2}}, \ldots, \frac{e_K}{h^{b_K}}, \frac{E_f}{E_m} \end{array}\right), \quad (4)$$

where Π is a dimensionless function.

In this study, we are interested in two cases: 1). hard fillers are embedded in a very soft matrix; and 2). the matrix is much harder than the fillers. For both cases, the

dimensionless parameter E_m / E_f may drop out of equation (4), and the indentation load-depth relation may be given by

$$P = E_m h^2 \Pi \left(\begin{array}{l} v_f, v_m, \dfrac{c_0}{h^{R_0}}, \dfrac{c_1}{h^{R_1}}, \dfrac{c_2}{h^{R_2}}, \ldots, \dfrac{c_M}{h^{R_M}}, \dfrac{d_0}{h^{r_0}}, \dfrac{d_1}{h^{r_1}}, \dfrac{d_2}{h^{r_2}}, \ldots, \dfrac{d_L}{h^{r_L}}, \\ \dfrac{e_0}{h^{b_0}}, \dfrac{e_1}{h^{b_1}}, \dfrac{e_2}{h^{b_2}}, \ldots, \dfrac{e_K}{h^{b_K}} \end{array} \right), \tag{5}$$

We further consider the indentation problem as addressed above, but we assume that the matrix material is linear viscoelastic instead of linear elastic, and the stress-strain relation given by

$$\sigma_{ij,m}(t) = \int_0^t \left[2G_m(t-\tau) \frac{\partial \varepsilon_{ij,m}(\tau)}{\partial \tau} + \lambda_m(t-\tau) \delta_{ij} \frac{\partial \varepsilon_{kk,m}(\tau)}{\partial \tau} \right] \mathrm{d}\tau , \tag{6}$$

G_m and λ_m in the time domain which are related to the relaxation modulus $E_m(t)$ and Poisson's ratio $v_m(t)$ by

$$G_m(t) = \frac{E_m(t)}{2\left(1+v_m(t)\right)}, \tag{7a}$$

$$\lambda_m(t) = \frac{E_m(t) v_m(t)}{\left(1+v_m(t)\right)\left(1-2v_m(t)\right)}. \tag{7b}$$

Assuming a time-independent Poisson's ratio, invoking the elastic-viscoelastic correspondence principle (Lee and Radok, 1960; Graram , 1965; Ting, 1966; Giannakopoulos, 2006), the indentation load-depth relation obtained from Equation (5) can be given by

$$\Psi\left(h(t)\right) = \int_0^t D_m(t-\tau)\,\mathrm{d}P , \tag{8}$$

where $D_m(t)$ is the creep compliance function of the matrix material and

$$\Psi\left(h(t)\right) = h^2 \Pi \left(\begin{array}{l} v_f, v_m, \dfrac{c_0}{h^{R_0}}, \dfrac{c_1}{h^{R_1}}, \dfrac{c_2}{h^{R_2}}, \ldots, \dfrac{c_M}{h^{R_M}}, \dfrac{d_0}{h^{r_0}}, \dfrac{d_1}{h^{r_1}}, \dfrac{d_2}{h^{r_2}}, \ldots, \dfrac{d_L}{h^{r_L}}, \\ \dfrac{e_0}{h^{b_0}}, \dfrac{e_1}{h^{b_1}}, \dfrac{e_2}{h^{b_2}}, \ldots, \dfrac{e_K}{h^{b_K}} \end{array} \right). \tag{9}$$

Equation (8) may be further written as

$$\Psi\left(h(t)\right) = \int_0^t D_m(t-\tau) \frac{\mathrm{d}P}{\mathrm{d}\tau} \mathrm{d}\tau . \tag{10}$$

We consider a relaxation test, where the displacement is described via a Heaviside step function,

$$h=\begin{cases} h_0 & (t\geq 0), \\ 0 & (t<0). \end{cases} \tag{11}$$

Inserting Eq. (11) into (10) gives

$$P(t)=\int_0^t E_m(t-\tau)\frac{\mathrm{d}\Psi}{\mathrm{d}h}h_0\delta(\tau)\,\mathrm{d}\tau\,, \tag{12}$$

where δ is the Dirac delta function. According to the integral property of the Dirac delta function, Eq. (12) becomes

$$P(t)=E_m(t)h_0\left.\frac{\mathrm{d}\Psi}{\mathrm{d}h}\right|_{h=h_0}. \tag{13}$$

It is noted that the parameter $h_0\left(\mathrm{d}\Psi/\mathrm{d}h\right)\big|_{h=h_0}$ in Eq. (13) is independent of time for a time-independent Poisson's ratio. The relaxation modulus of the matrix may be written in the following form (Fung, 1993)

$$E_m(t)=E_{m,0}\bar{E}_m(t) \tag{14}$$

where $E_{m,0}$ is the instantaneous modulus, representing the stiffness of a viscoelastic material at the instantaneous time when the external load acts, and $\bar{E}_m(t)$ is the reduced relaxation modulus (normalized relaxation modulus) which indicates the relaxation property of a viscoelastic material.

Inserting equation (14) into (13) leads to

$$\bar{E}_m(t)=\frac{P(t)}{P(0)}. \tag{15}$$

where $P(0)$ is the indentation load at the starting point of relaxation. Equation (15) contains interesting and insightful information. Firstly, it indicates that when a direct problem is considered, the indentation loads depend on the material properties of both the matrix and the fillers the geometric parameters of the system as well as the indentation depth. However, the relaxation feature of the indentation loads only depends on the reduced relaxation modulus of the matrix material and is independent of other parameters. Secondly, from the viewpoint of inverse analysis, the reduced

relaxation modulus of the matrix material can be measured simply from the indentation relaxation loads. It is not necessary to invoke the knowledge of the geometric parameters of the system (including the profiles of the indenter and the indented solids as well as the positions and shapes of the fillers) and the material properties of the fillers. For the indentation of porous substrates (E_f=0), which represents a limit of the case of $E_{m,l} >> E_f$ as investigated in this paper, we have demonstrated the applicability of equation (15) (Cao et al., 2010). Here, $E_{m,l}$ is the long-term modulus of the matrix material. However, it remains unclear to what extent the above theoretical result works when E_f is not zero. Bearing this point in mind, in next section, we will examine the conclusion drawn from the above theoretical analysis by using finite element computations.

3. Finite element computations

Finite element computations are performed by using the commercial software ABAQUS (2008). Detail information involved in the simulations is given as follows.

3.1 Details of the computational modelling.

In the simulations, the matrix material of the composite is assumed to be linear viscoelastic for which the relaxation modulus and Poisson's ratio are taken as $E_m(t)=900\left[1-0.4(1-e^{-t/100s})\right]$MPa and ν_m=0.4, respectively (the material properties taken here are used for illustration, but the conclusions may apply to realistic systems). In this case, the matrix material has an instantaneous modulus $E_{m,0}=900$MPa, long-term modulus $E_{m,l}=540$MPa and the characteristic relaxation time of $t_c=100s$. The modulus of the fillers varies from 540Pa to 100GPa and ν_f is taken as 0.3. The loading protocol adopted in the simulations is shown in Fig. 2, which is an approximation of the step function as given by equation (11). A good approximation

requires that t_1 at which the indentation displacement reaches its maximum value should be much smaller than t_c. Here we take $t_1=0.05\,t_c=5$s. The relaxation time t_r is taken as 1000s, which is much larger than the characteristic relaxation time of the material.

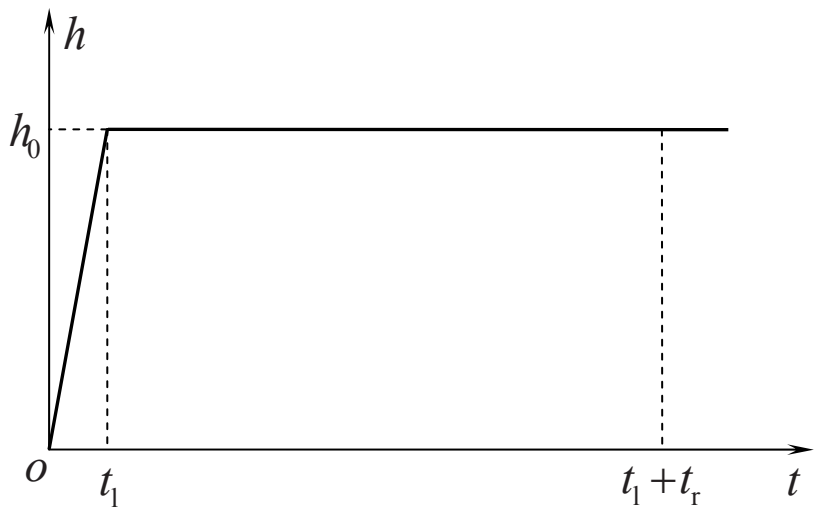

Fig. 2 Protocol used in the simulation of the indentation relaxation tests.

The following representative examples of practical interest are investigated.

Example A. Indentation of a cylindrical indenter with irregular shape into a composite substrate.

In this example, a cylindrical indenter with irregular profile is assumed to indent into a linear viscoelastic substrate containing elastic fibres. Fig 3(a) gives our two-dimensional computational model containing 27165 four-node bilinear plane strain quadrilateral elements with reduced integration and hourglass control, CPE4R. The bottom of the indented solid is fixed with other boundaries traction free. The deformed indented solid is shown as Fig. 3(b). The relaxation loads are recorded and used to verify theoretical result as given by equation (15).

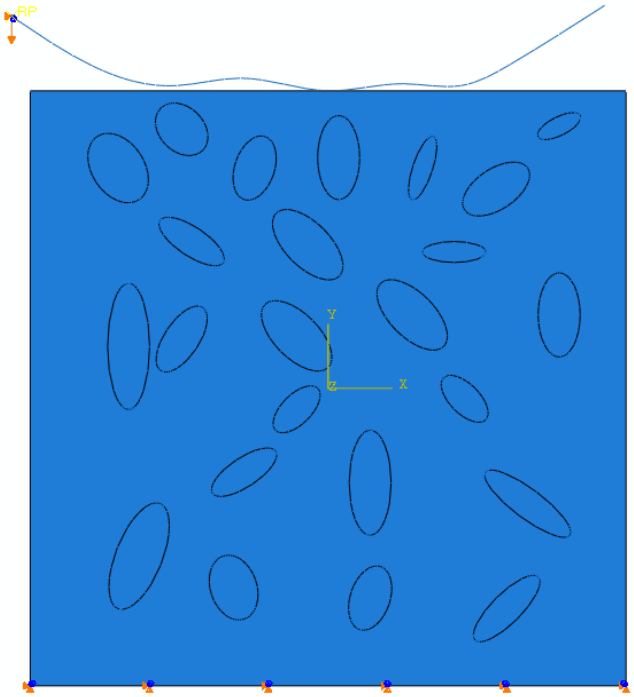

(a)

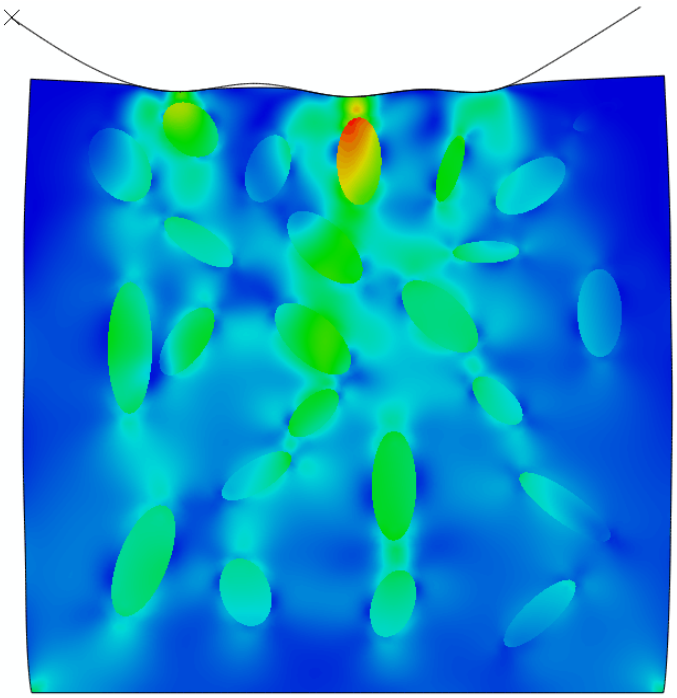

(b)

Fig. 3 A cylindrical i ndenter with irregular profile inde nting into a linea r viscoelastic substrate containing elastic fib res, (a). Co mputational model; (b). Deform ation of the indented solid at the maximum indentation depth.

Example B. Indentation of a cylindrical indenter into a substrate containing one particle.

Indentation tests can be performed at various length scales. This example examines the validity of the theoretical result by investigating a critical case, i.e., the contact area is smaller or comparable to the fiber size. Fig 4(a) gives the two-dimensional FEM mesh which consisting of 12961 four-node bilinear plane strain quadrilateral elements with reduced integration and hourglass control. The deformed mesh for the case of $E_{m,0} << E_f$ is depicted in Fig. 4(b).

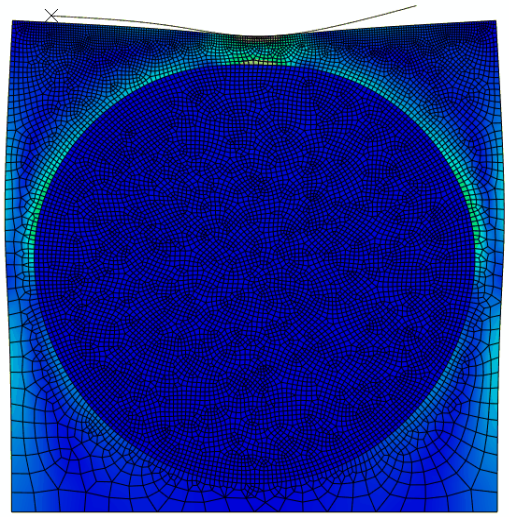

(a)

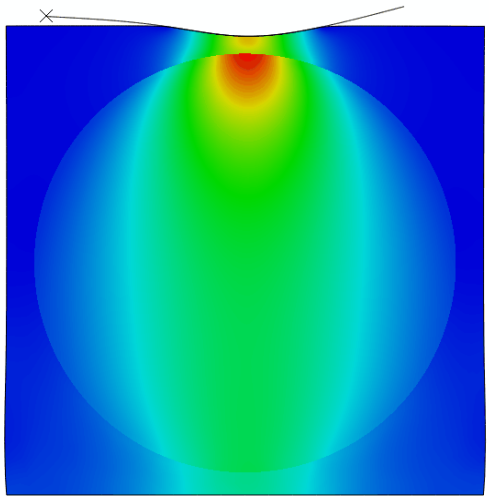

(b)

Fig. 4 A cylindrical indenter indenting a linear viscoelastic substrate containing one elastic fibre, (a). $E_f = 5.4\text{MPa}$; (b). $E_f = 100\text{GPa}$.

Fig. 4 shows that the deformation or stresses developed in the fiber are significant. In this example, the relaxation loads-time relation is also recorded, which will be used to examine the applicability of equation (15).

3.2 Results and discussions

For the examples (**A** and **B**) above, we focus on the displacement-controlled indentation. Through simulation, the mesh qualities are all checked to avoid extreme distortions and the convergences are ensured. The reduced relaxation moduli of the matrix materials are determined from the computed relaxation load-time relation and Equation (15). Fig. 5 shows a comparison of the identified results with the real solution for example **A**. The results show that when $E_{m,l}/E_f$ or $E_f/E_{m,0}$ is larger than 10, Equation (15) as given by the theoretical analysis works well.

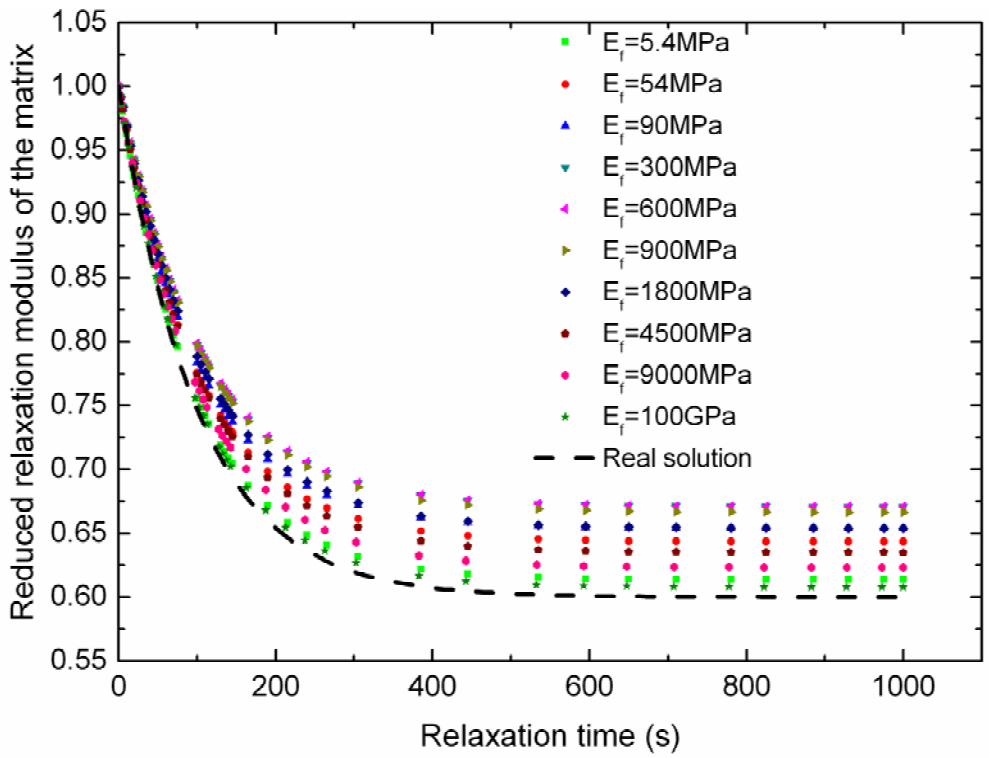

Fig. 5 A comparison of the identified matrix reduced relaxation modulus with real solutions (example **A**).

Fig. 6 demonstrates the comparison of the identified matrix reduced relaxation modulus by using Equation (15) to the real solution for example **B**. In this case, the applicability of Equation (15) requires that the ratio of $E_f / E_{m,0}$ is larger than 100 and $E_{m,l} / E_f$ greater than 1000. This example together with example **A** may indicate that the critical values of $E_f / E_{m,0}$ and $E_{m,l} / E_f$ beyond which Equation (15) works depend on the interplay between the indenter and the fillers. For instance, when the contact region is confined to one particleand the deformation or stresses developed in the particle are significant (example **B**), the critical values of $E_f / E_{m,0}$ and $E_{m,l} / E_f$ are very large. A more critical example is that indentation is performed on a single particle as shown in detail in the sequel; in this case, the theoretical analysis performed in section 2 is likely to be invalid.

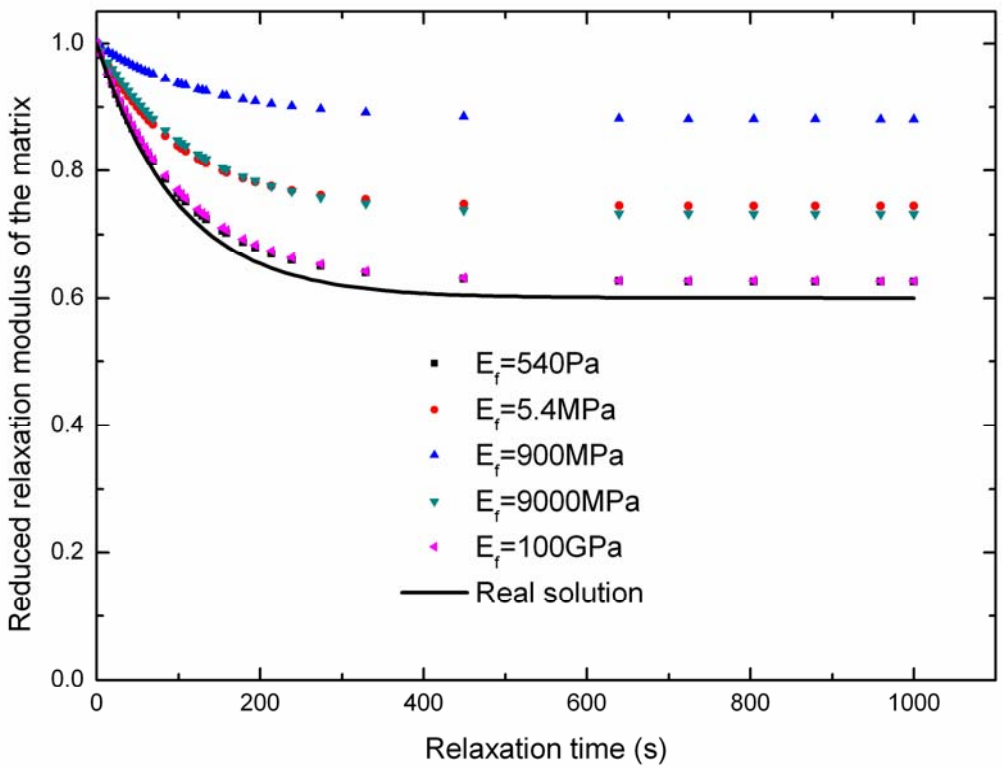

Fig. 6 A comparison of the identified matrix reduced relaxation modulus with the real solution (example **B**).

The representative examples presented above demonstrate the validity of our theoretical analysis to the indentation problems of practical interest, even when the indented solids undergo finite deformations. Nevertheless, the limitations in the theoretical analysis should be emphasized.

First, the constitutive law of the matrix involved in this study is limited to the linear viscoelastic model.

Second, the present study is limited to the case where the Poisson's ratio is time-independent and the instantaneous modulus and characteristic relaxation time do not change with loading. It is noted that these assumptions have been adopted in quite a few previous publications (e.g. Shimizu et al., 1999; Cheng et al., 2006; Oyen, 2005) and are indeed reasonable for various viscoelastic materials in engineering.

Third, it is pointed out that the examples examined in this study focus on the circumstances where the fillers are embedded into the matrix. It is important to mention a very critical situation, i.e., indentation is performed on a single particle. In this case, the modulus of the fillers may play a dominant role, and the theoretical analysis appears to be invalid. Thus it is unlikely to determine the relaxation property of the matrix from the indentation responses under such circumstances. In order to illustrate this point, we investigate an axisymmetric rigid cone indenting into a particle surrounded by the matrix, Fig. 7(a). Fig. 7(b) gives the deformation of the indented solid at the maximum indentation depth. The relaxation loads together with equation (15) are adopted to determine the reduced relaxation modulus of the matrix and the results given in Fig. 8. It is seen that the identified results are far from the real solution.

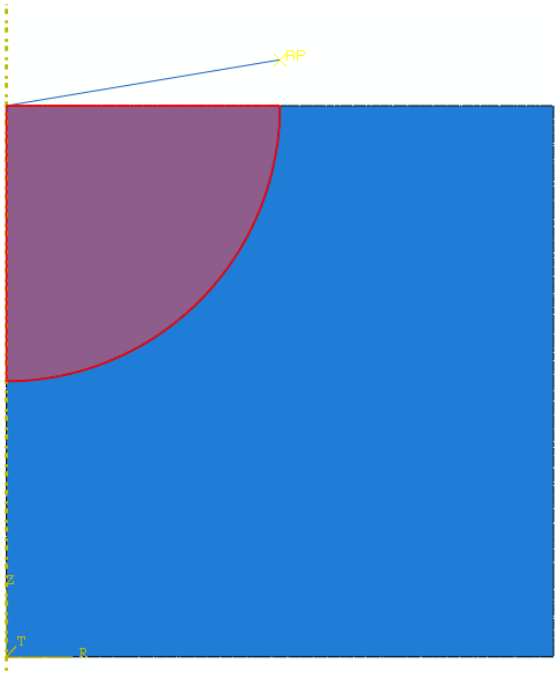

(a)

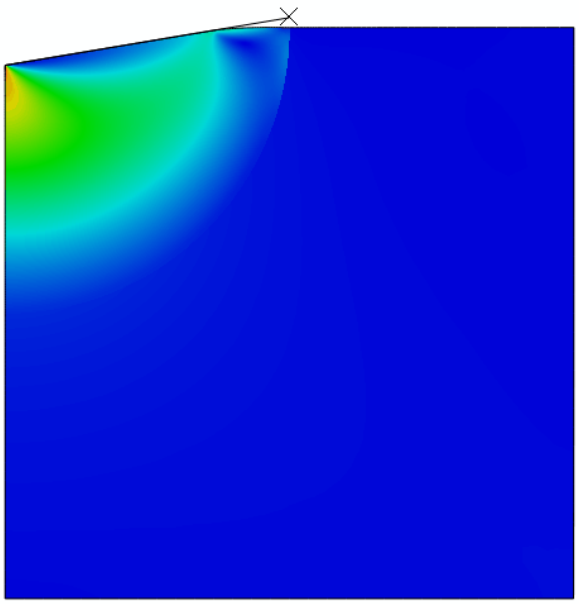

(b)

Fig. 7 A conical indenter indenting into a single particle em bedded in a linear viscoelastic matrix. (a). Computational model; (b). Deformation of the indented solid for the case of $E_f = 54\text{MPa}$.

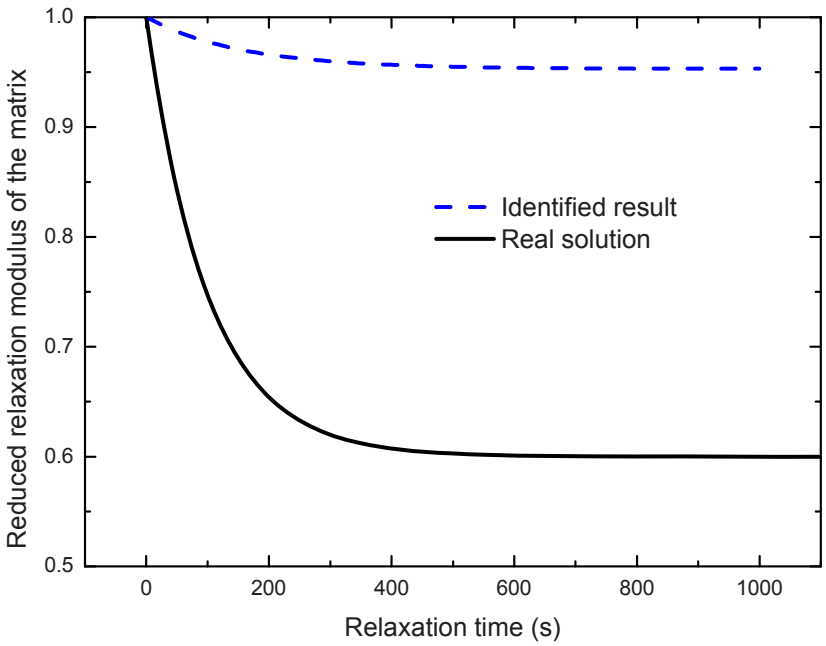

Fig. 8 A comparison of the identified reduced relaxation modulus of the matrix to the real solution (the indent is on the filler, $E_f = 54\text{MPa}$)

At last, it is emphasized that the theoretical analysis performed here is restricted to the two phase composite system. When the interface phase plays a key role in a system, caution should be taken when using the results and also the conclusions achieved in this study.

4. Conclusions

Instrumented indentation is an efficient approach for evaluating the mechanical properties of viscoelastic materials at small scales. In this study, we address the indentation of a two-phase composite system where the matrix material is linear viscoelastic and the fillers are linear elastic materials. In summary, the following contributions have been made.

Our theoretical analysis performed on a rigid indenter with arbitrary profile indenting into a composite with arbitrary shape reveals a simple correlation between the indentation relaxation loads and the reduced relaxation modulus of the matrix.

Such a simple relation holds true provided the conditions of $E_{m,l} >> E_f$ (or $E_{m,0} << E_f$) and the elastic-viscoelastic correspondence principle works.

Numerical experiments based on finite element analysis have been carried out to identify the extent to which the theoretical result is effective.

The results reported in this study together with the discussions provide insightful information and may facilitate the use of instrumented indentation to characterize the mechanical properties of viscoelastic composites which may include some biological soft tissues and man-made biocomposites.

Acknowledgements

Supports from the National Natural Science Foundation of China (Grant Nos. 10972112) and 973 Program (Nos. 2010CB631005) are acknowledged.

References

ABAQUS User's Manual , ve rsion 6.8. Providence: Hi bbit, Karlsson & Sorenson, 2008.

Barenblatt, G . I., Scaling, self -similarity and interm ediate asym ptotics, Cam bridge University Press, Cambridge, UK., 1996.

Cao,Y. P., Ma, D. C., Raabe, D. The use of flat punch indentation to determ ine the viscoelastic properties in th e time and frequency dom ains of a soft layer bonded to a rigid substrate, Acta Biomaterialia 5 (2009) 240-248.

Cao, Y. P., Ji, X. Y., Feng, X. Q., (2010) . Geometry independence of the norm alized relaxation functions of viscoe lastic materials in indenta tion, Philosophical Magazine, in press.

Cao, Y. P. Determ ination of the creep exponent of a power-law creep solid using indentation tests, Mechanics of Time-Dependent Materials 11 (2007) 159-172.

Cheng, Y. T., Cheng, C. M. Scaling, dim ensional analysis, and indentation measurements, Materials Science & Engineering R-Reports 44 (2004) 91-149.

Cheng, Y. T., Yang, F. Q. Obtaining sh ear relaxation m odulus and creep com pliance of linear v iscoelastic m aterials f rom instrum ented ind entation using axisym metric indenters of power-law profiles, Journal of Materials Research 24 (2009) 3013-3017.

Cheng, Y. T., Ni, W . Y., Cheng, C. M. N onlinear analysis of os cillatory indentation in elastic and viscoelastic solids, Physical Review Letters 97 (2006) 075506.

Ebenstein, D. M., Pruitt, L. A. Nanoindentation of biological materials. Nano Today 1 (2006) 26.

Fischer-Cripps, A. C. Multip le-frequency dynamic nanoinde ntation tes ting. J. Mater. Res. 19 (2004) 2981-2989.

Fung, Y. C. , Biom echanics: Mechanical pr operties of living tissues. S pringer, New York, Inc., 1993.

Giannakopoulos, A. E. Elastic and viscoelastic indentation of flat surfaces by pyramid indentors, Journal of the Mechanics and Physics of Solids 54 (2006) 1305-1332.

Graham, G. A. C. The contact p roblem in the lin ear theory of viscoelas ticity, International Journal Of Engineering Science 3 (1965) 27-45.

Herbert, E. G., Oliver, W. C. Lumsdaine, A,, Pharr, G. M. Measuring the constitutive behavior of viscoelastic so lids in the tim e and frequenc y dom ain using flat punch nanoindentation, Journal of Materials Research 24 (2009) 626-637.

Huang, G., Lu, H. B. Measurem ent of Young's re laxation modulus using nanoindentation, Mechanics of Time-Dependent Materials 10 (2006) 229-243.

Levental, I., Georges, P . C. and Janm ey, P. A., Soft biolo gical m aterials an d th eir impact on cell function, Soft Matter 3 (2007) 299-206.

Lee, E. H., Radok, J. R. M. The contact problem for viscoelas tic bodies, Journal of Applied Mechanics 27 (1960) 438-444.

Lee, B., Han, L., Frank, E. H., Chubins kaya, S., Ortiz, C., Grodzinsky, A. J., Dynamic mechanical p roperties of the tissu e-engineered m atrix asso ciated with individual chondrocytes. J. Biomech. 43 (2010) 469–476.

Lu, H., W ang, B., Ma, J., Huang, G., Vi swanathan, H. Measurem ent of creep compliance of solid polym ers by nanoindent ation, Mechanics of Tim e-Dependent Materials 7 (2003) 189-207.

Ngan, A. H. W., Wang, H. T., Tang, B., Sze, K. Y. Correcting power-law viscoelastic effects in elastic modulus measurement using depth-sensing indentation, International Journal of Solids and Structures 42 (2005) 1831-1846.

Oyen, M. L., Cook, R. F. J. Load–displacem ent behavior du ring sharp indentation of viscous–elastic–plastic materials. J. Mater Res 18 (2003) 139.

Oyen, M. L . Spherical indentation creep fo llowing ram p loading, Journal of Mater. Res. 20 (2005) 2094-2100.

Oyen, M. L., Sensitivity of polym er nanoindentation c reep m easurements to experimental variables. Acta Mater. 55 (2007) 3633.

Ramakrishna, S., Huang Z. M., Kum ar G. V., Batchelor,A. W ., Mayer J., An introduction to biocomposites. Imperial college press, London, 2004.

Shimizu, S., Yanagim oto, T., Sakai, M. Pyra midal indentation load-depth curve of viscoelastic materials, Journal of Materials Research 14 (1999) 4075-4086.

Thomas,V., Dean,D. R., Jose,M. V., Mathew,B., Chowdhury, S., and Vohra Y. K., Nanostructured biocom posite scaffolds based on collagen coelectrospun with nanohydroxyapatite, Biomacromolecules 8, (2007) 631-637.

Ting, T. C. T. Contact s tresses between a ri gid indenter and a viscoelastic half-space, Journal of Applied Mechanics 33 (1966) 845-854.

Proceedings of the SEM Annual Conference
June 7-10, 2010 Indianapolis, Indiana USA

Obtaining Viscoelastic Properties from Instrumented Indentation

Yang-Tse Cheng

Department of Chemical and Materials Engineering
University of Kentucky
Lexington, KY 40506, USA
ycheng@engr.uky.edu

ABSTRACT
Instrumented indentation is a powerful tool for probing small-scale mechanical behaviors of “soft” materials, such as polymers, composites, and biomaterials [1-3]. Since many soft materials deform viscoelastically, it is important to develop robust analysis methods for obtaining viscoelastic properties from indentation measurements. Extending the early work by such pioneers as Lee [4], Radok [5], Lee and Radok [6], Hunter [7], Gramham [8], and Ting [9], a number of authors have recently proposed methods for determining viscoelastic properties from indentation measurements [10-33]. In this presentation, we will discuss our recent results on modeling instrumented indentation in linear viscoelastic solids [34-40]. We will first examine the relationships between initial unloading slope, contact depth, and viscoelastic properties for various loading conditions, including load- or displacement-control [35-37]. We will then discuss several commonly used methods, such as the "hold-at-peak-load" and "hold-at-the-maximum-depth" techniques [38]. We will also evaluate methods for obtaining storage and loss modulus using dynamic indentation using either spherical or pyramidal indenters [39]. Furthermore, we will discuss a set of newly proposed methods for measuring shear relaxation modulus and creep compliance using axisymmetric indenters of power-law profiles [40]. Results on indentation in viscoplastic solids will also be presented. These investigations may help improve instrumented indentation techniques for measuring mechanical properties of soft materials.

REFERENCES
1. A.C. Fischer-Cripps: Nanoindentation, 2nd edition (Springer 2004).
2. M.R. VanLandingham: Review of instrumented indentation. J. Res. Nat. Inst. Stand. Tech. 108, 249 (2003).
3. G.M. Pharr, Y.-T. Cheng, I.M. Hutchings, M. Sakai, N.R. Moody, G. Sundararajan, and M.V. Swain: Introduction. J. Mater. Res. 24, 579 (2009).
4. E.H. Lee: Stress analysis in visco-elastic bodies. Quarterly Appl. Math. 13, 183 (1955).
5. J.R.M. Radok: Visco-elastic stress analysis. Quarterly Appl. Math. 15, 198 (1957).
6. E.H. Lee and J.R.M. Radok: The contact problem for viscoelastic bodies. J. Appl. Mech. 27, 438 (1960).
7. S.C. Hunter: The Hertz problem for a rigid spherical indenter and a viscoelastic half-space. J. Mech. Phys. Solids 8, 219 (1960).
8. G.A.C. Graham: The contact problem in the linear theory of viscoelasticity. Int. J. Engng. Sci. 3, 27 (1965); Contact problem in linear theory of viscoelsticity when time dependent contact area has any number of maxima and minima. Int. J. Engng. Sci. 5, 495 (1967).
9. T.C.T. Ting: Contact stresses between a rigid indenter and a viscoelastic half-space. J. Appl. Mech. 33, 845 (1966); Contact problems in linear theory of viscoelasticity. J. Appl. Mech. 35, 248 (1968).
10. B.J. Briscoe, L. Fiori, and E. Pelillo: Nano-indentation of polymeric surfaces. J. Phys. D: Appl. Phys. 31, 2395 (1998).
11. L. Cheng, X. Xia, W. Yu, L.E. Scriven, and W.W. Gerberich: Flat-punch indentation of viscoelastic material. J. Polymer Science: Part B: Polymer Physics 38, 10 (2000).
12. P.-L. Larrson and S. Carlsson: On microindentation of viscoelastic polymers. Polymer Testing 17, 49 (1998).
13. S. Shimizu, T. Yanagimoto, and M. Sakai: Pyramidal indentation load-depth curve of viscoelastic materials. J. Mater. Res. 14, 4075 (1999).
14. M. Sakai and S. Shimizu: Indentation rheometry for glass-forming materials. J. Non-Cryst. Solids 282, 236 (2001).

T. Proulx (ed.), *Time Dependent Constitutive Behavior and Fracture/Failure Processes, Volume 3*, Conference Proceedings of the Society for Experimental Mechanics Series 15, DOI 10.1007/978-1-4419-9794-4_18, © The Society for Experimental Mechanics, Inc. 2011

15. A.H.W. Ngan and B. Tang: Viscoelastic effects during unloading in depth-sensing indentation. J. Mater. Res. 17, 2604 (2002).
16. M.L. Oyen and R.F. Cook: Load-displacement behavior during sharp indentation of viscous-elastic-plastic materials. J. Mater. Res. 18, 139 (2003).
17. H. Lu, B. Wang, J. Ma, G. Huang, and H. Viswanathan: Measurement of creep compliance of solid polymers by nanoindentation. Mechanics of Time-dependent Materials 7, 189 (2003).
18. B. Tang and A.H.W. Ngan: Investigation of viscoelastic properties of amorphous selenium near class transition using depth-sensing indentation, Soft Materials 2, 125 (2004).
19. B. Geng, F.Q. Yang, T. Druffel, and E.A. Grulke: Nanoindentation behavior of ultrathin polymeric films. Polymer 46, 11768 (2005).
20. C.Y. Zhang, Y.W. Zhang, K.Y. Zeng, and L. Shen: Nanoindentation of polymers with a sharp indenter. J. Mater. Res. 20, 1597 (2005); Characterization of mechanical properties of polymers by nanoindentation tests. Phil. Mag. 86, 4487 (2006).
21. G. Huang and H.B. Lu: Measurement of Young's relaxation modulus using nanoindentation. Mechanics of Time-Dependent Materials 10, 229 (2006).
22. D. Tranchida, S. Piccarolo, J. Loos, and A. Alexeev: Accurately evaluating Young's modulus of polymers through nanoindentations: A phenomenological correction factor to the Oliver and Pharr procedure. Applied Physics Letters 89, 171905 (2006).
23. C.A. Tweedie and K.J. Van Vliet: Contact creep compliance of viscoelastic materials via nanoindentation. J. Mater. Res. 21, 1576 (2006).
24. M. Vandamme and F.J. Ulm: Viscoelastic solutions for conical indentation. International Journal of Solids and Structures 43, 3142 (2006).
25. C.K. Liu, S. Lee, L.P. Sung, and T. Nguyen: Load-displacement relations for nanoindentation of viscoelastic materials. J. Appl. Phys. 100, 033503 (2006).
26. A.E. Giannakopoulos: Elastic and viscoelastic indentation of flat surfaces by pyramid indentors. J. Mech. Phys. Solids 54, 1305 (2006).
27. M.L. Oyen: Analytical techniques for indentation of viscoelastic materials. Philosophical Magazine 86, 5625 (2006).
28. J. Deuschle, S. Enders, and E. Arzt: Surface detection in nanoindentation of soft polymers. J. Mater. Res. 22, 3107 (2007).
29. W.J. Wright, A.R. Maloney, and W.D. Nix: An improved analysis for viscoelastic damping in dynamic nanoindentation, Int. J. Surf. Sci. Eng. 1, 274 (2007).
30. N. Fujisawa and M.V. Swain: Nanoindentation-derived elastic modulus of an amorphous polymer and its sensitivity to load-hold period and unloading strain rate. J. Mater. Res. 23, 637 (2008).
31. E.G. Herbert, W.C. Oliver, and G.M. Pharr: Nanoindentation and the dynamic characterization of viscoelastic solids. J. Phys. D - Appl. Phys. 41, 074021 (2008).
32. C. Pichler, R. Lackner, and F.J. Ulm: Scaling relations for viscoelastic-cohesive conical indentation. Int. J. Mat. Res. 99, 836 (2008).
33. Y.P. Cao, D.C. Ma, and D. Raabe: The use of flat punch indentation to determine the viscoelastic properties in the time and frequency domains of a soft layer bonded to a rigid substrate. Acta Biomaterialia 5, 240 (2009).
34. Y.T. Cheng and C.M. Cheng: Scaling, dimensional analysis, and indentation measurements. Materials Science & Engineering R-Reports 44, 91 (2004).
35. Y.T. Cheng and C.M. Cheng: General relationship between contact stiffness, contact depth, and mechanical properties for indentation in linear viscoelastic solids using axisymmetric indenters of arbitrary profiles. Applied Physics Letters 87, 111914 (2005).
36. Y.T. Cheng and C.M. Cheng: Relationships between initial unloading slope, contact depth, and mechanical properties for conical indentation in linear viscoelastic solids. J. Mater. Res. 20, 1046 (2005).
37. Y.T. Cheng and C.M. Cheng: Relationships between initial unloading slope, contact depth, and mechanical properties for spherical indentation in linear viscoelastic solids. Mat. Sci. Eng. A 409, 93 (2005).
38. Y.T. Cheng, W.Y. Ni, and C.M. Cheng: Determining the instantaneous modulus of viscoelastic solids using instrumented indentation measurements. J. Mater. Res. 20, 3061 (2005).
39. Y.T. Cheng, W.Y. Ni, and C.M. Cheng: Nonlinear analysis of oscillatory indentation in elastic and viscoelastic solids. Physical Review Letters 97, 075506 (2006).
40. Y.-T. Cheng and F. Q. Yang: Obtaining shear relaxation modulus and creep compliance of linear viscoelastic materials from instrumented indentation using axisymmetric indenters of power-law profiles, J. Materials Research 24, 3013 (2009).

Proceedings of the SEM Annual Conference
June 7-10, 2010 Indianapolis, Indiana USA

Mechanical Properties Measurement of Sand Grains by Nanoindentation

Fang Wang, Boshen Fu, Reza A. Mirshams[1], William Cooper[2], Ranga Komanduri[3],
Hongbing Lu
Department of Mechanical Engineering
University of Texas at Dallas, Richardson, TX 75080
[1]University of North Texas, Denton, TX 76203
[2]Air Force Research Laboratory, Eglin Air Force Base, FL 32542
[3] Mechanical and Aerospace Engineering, Oklahoma State University, Stillwater, OK 74078
hongbing.lu@utdallas.edu

ABSTRACT

Nanoindentation was conducted on sand grains to measure the Young's modulus, hardness, and fracture toughness of individual sand grains. An inverse problem solving approach was used to determine the stress-strain relationship of sand by allowing finite element simulated load-displacement relationship to agree with measurement data. A cube-corner indenter tip was used to induce cracks emanating from the corners of the indenter tip to measure the fracture toughness. X-Ray Diffraction (XRD) technique was used to determine the crystal structure of sand grains.

1. Introduction

As a granular material, sand is conglomerate of discrete particles held together (but not bonded) with significant void space (50-64%) in between. Mechanical properties of sand grains, such as the Young's modulus, hardness, fracture toughness, and stress-strain relationships are of particular importance since their individual behavior dictates the overall behavior of the sand at macro scale. Moreover, the mechanical properties of the grains can vary with the mineral composition of sand, size, defect structure, and crystal orientation. The effect of grain size is due to the fact that larger grains would contain higher number of defects in the form of voids and ridges as well as cracks which may yield mechanical properties different than the smaller grain sizes. Furthermore, since the smaller sand grains usually stay at top layers and may affect more by wind while larger sand grains usually settles at bottom that may affect more by pressure which may cause different crystal structures and mechanical properties of sand grains with different sizes.

Nanoindentation technique is widely used to extract mechanical properties of small volume of materials. In this investigation, we have carried out nanoindentation tests using a Berkovich indenter on six different size groups of sand grains and recorded the load-displacement data. Young's modulus and hardness were obtained directly from the MTS Testworks software output based on the analysis of unloading segment using the method developed by Oliver and Pharr [1]. The representative stress-strain curves for different size samples were obtained, corresponding to the representative modulus and hardness obtained, for solving an inverse problem to determine the stress-strain relationship using FEM. Cubecorner nanoindenter tip was also used to generate cracks for measurement of fracture toughness. In all the cases the indent impressions were obtained using (MTS) NanoVision module. The lengths of the cracks developed were used to determine the range of fracture toughness values for the sand grains. Statistical analysis was conducted to determine the variability in the mechanical properties of sand grains.

2. Sand sample characterization

A sample of Eglin sand was washed and subsequently dried in an oven. The sample sand used for nanoindentation has widely distributed sizes. Multidirectional shaker was used to determine the size of the sand grains. The sieves use metal wire cloth with A.S.T.M. E-11 standard sieve series. To separate different sizes of the sand, the sand agglomerate is vibrated through a series of progressively smaller sieves that are stacked on

T. Proulx (ed.), *Time Dependent Constitutive Behavior and Fracture/Failure Processes, Volume 3*, Conference Proceedings of the Society for Experimental Mechanics Series 15, DOI 10.1007/978-1-4419-9794-4_19, © The Society for Experimental Mechanics, Inc. 2011

top of one another. After 10 minutes shaking time, the sand that falls through a mesh is given the designation of passed weight and the sand that remains on top of that mesh is designated as remaining weight. The passed weight versus grain size curve was plotted to obtain the sand size distribution curve as shown in Figure 1.

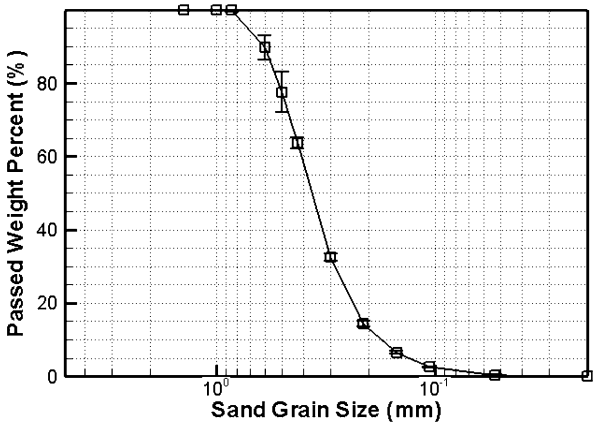

Figure 1. Size distribution curve of sand grains

In order to detect the crystal structure of sand grains, x-ray diffraction (XRD) tests were conducted on sand grains with different sizes. The XRD results were shown in Figure 1. The diffraction patterns of six sizes of sand grain samples are demonstrated in Figure 2 (a). Since the sand grains samples are randomly selected, the intensity values may vary for different batches thus are not given in the figure. Although most of the diffraction peak angles are same, there are some differences between these six patters which indicate sand grains with different sizes may have different crystal structures caused by different material constituents, defect structure etc. Comparing sand diffraction data against the database maintained by the International Centre for Diffraction Data, it is found the 0.212 mm size sand grain pattern can almost fully match the quartz diffraction pattern (Figure 2 (b)).

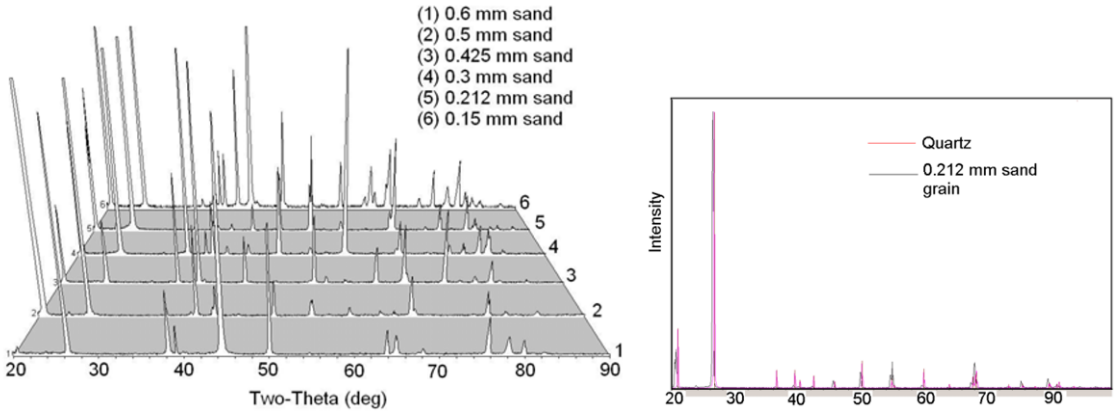

(a) (b)

Figure 2 (a) X-ray Diffraction pattern of Eglin sand grains.(b) X-ray Diffraction pattern comparison of quartz and 0.212 mm Eglin sand grains

The sand grains were embedded in an epoxy matrix and mounted in a sample holder. The samples were wet polished using an alumina abrasive powder (from Buehler Inc.) in water slurry. To obtain a smooth surface suitable for nanoindentation, the maximum abrasive size used in the final polishing was 50 nm. Figure 3 shows a polished sand surface with different grains oriented in different directions.

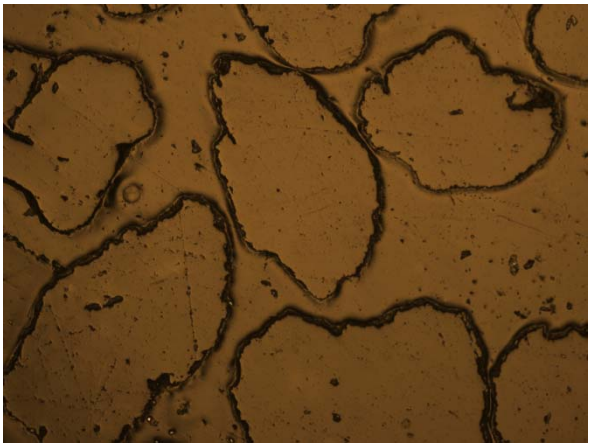

Figure 3. Magnified image of polished sand grains in an epoxy matrix

3. Nanoindentation tests in sand grains

An MTS Nano Indenter XP system was used for the nanoindentation measurements. This indenter can reach a maximum indentation depth of 500 μm and a maximum load of 500 mN. The displacement and load resolutions are 0.2 nm and 50 nN, respectively. Both Berkovich and cube-corner indenter tips, made of single crystal diamond, were used in this investigation. Nanoindentations were made on flat, polished sand grain surfaces under constant rate of loading.

Nanoindentations were carried out on 6 different sizes of sand grains with one test per grain. Young's modulus and hardness were obtained using the slope of the unloading curve and the values of load and contact area at maximum indentation depth. These were a direct output from the nanoindentation software. The distributions of modulus and hardness values are plotted in Figures 4 and 5, respectively. Six sizes of sand grains were embedded into the epoxy and polished separately. Nanoindentation measurements were conducted on these six samples. Table1 listed the Young's Modulus and Hardness of sand grains with different sizes from nanoindentation.

Using Weibull distribution function, we determined the median value (corresponding to P_{50} value) for Young's modulus of the six sizes of sand grains to be 97.44 GPa, 102.08 GPa, 108.9 GPa, 80.82 GPa, 77.48 GPa and 71.48 GPa respectively and hardness to be 13.21 GPa, 14.62 GPa, 15.55 GPa, 11.83 GPa, 10.92 GPa and 10.91 GPa respectively. Scattering in the data is attributed to different types of sand grains due primarily to variations in the material constituents, defect structure, and crystal orientations.

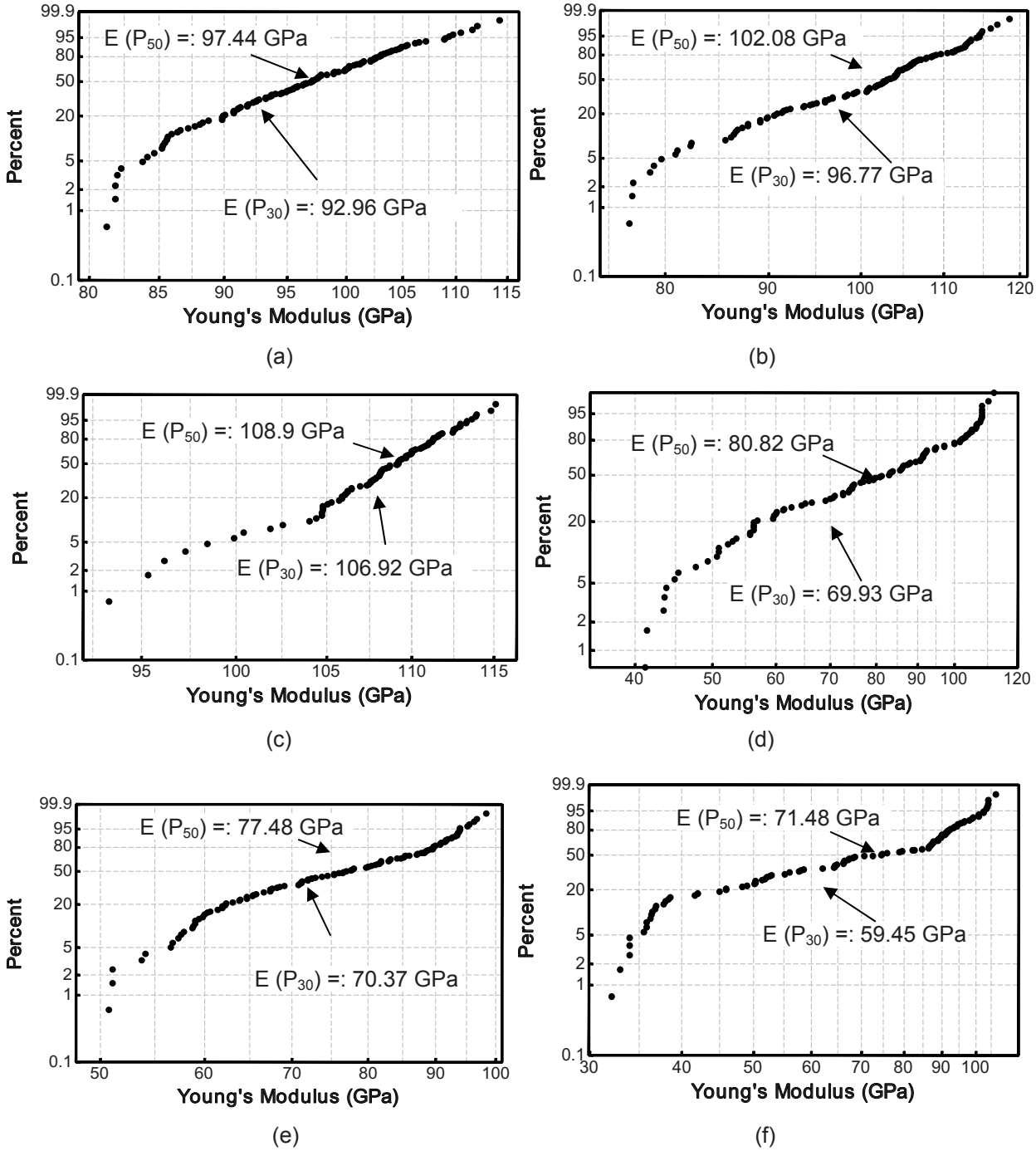

Figure 4(a): Weibull plot of Young's modulus from nanoindentations on 0.6 mm sand grains. (b): Weibull plot of Young's modulus of 0.5mm sand grains. (c): Weibull plot of Young's modulus of 0.425 mm sand grains. (d): Weibull plot of Young's modulus of 0.3mm sand grains. (e): Weibull plot of Young's modulus of 0.212 mm sand grains. (f): Weibull plot of Young's modulus of 0.15 mm sand grains.

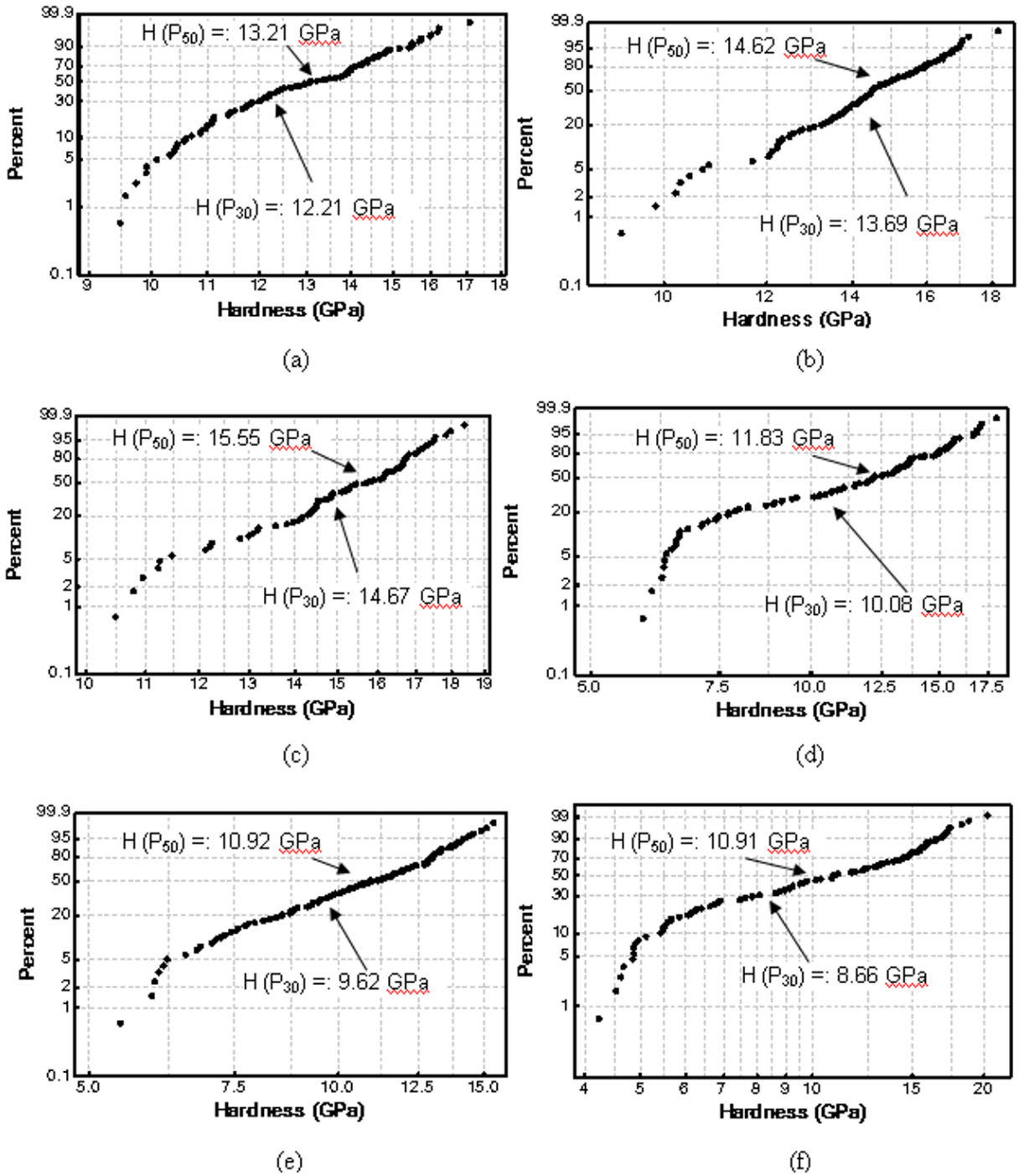

Figure 5(a): Weibull plot of hardness from nanoindentations on 0.6 mm sand grains. (b): Weibull plot of hardness of 0.5 mm sand grains. (c): Weibull plot of hardness of 0.425 mm sand grains. (d): Weibull plot of hardness of 0.3 mm sand grains. (e): Weibull plot of hardness of 0.212 mm sand grains. (f): Weibull plot of hardness of 0.15 mm sand grains.

It is well known that sand grains would generally behave in a brittle material under load. In order to estimate the fracture toughness, a formula derived by Pharr *et al.* [2] was used,

$$K_C = \alpha\left(\frac{E}{H}\right)^{0.5}\left(\frac{P}{c^{3/2}}\right) \qquad (1)$$

where α is an empirical constant which takes into account, the geometry of the indenter tip (for a cube-corner tip α = 0.032). Before proceeding with the nanoindentation on sand grains, a sample test was run on a standard fused silica sample (results not included here). The average value for fracture toughness obtained was 0.6 MPa-$m^{0.5}$ which is in reasonable agreement with the value reported for fused silica by Harding (1995) [3].

For sand, the values of the elastic modulus (E) and hardness (H) were obtained using the Berkovich nanoindenter tip prior to indenting with a cube-corner tip. Since we are interested in the ratio of E/H from the nanoindentation tests, we obtained an average value for the ratio as 8.5. In Eqn. (7), c is the crack length and can be determined from the surface scans obtained (two of the scans along with inverse images) are shown in Figure 6. Both 3D inverse images and 2D nanoindentation residual images are shown for details on the crack formation and fracture. It may be noted that due to slight errors in the alignment and inhomogeniety of the sand grain, it is rather difficult to induce three cracks with equal length. When there are differences between the crack lengths from the same indent, we have taken the average crack length for a particular indent. The histogram of the fracture toughness values obtained is shown in Figure 7(a) and the Weibull distribution in Figure 7(b). From the Weibull distribution, median value for the fracture toughness observed was 2.32 MPa-$m^{0.5}$ (range 1.3 to 4.0 MPa-$m^{0.5}$).

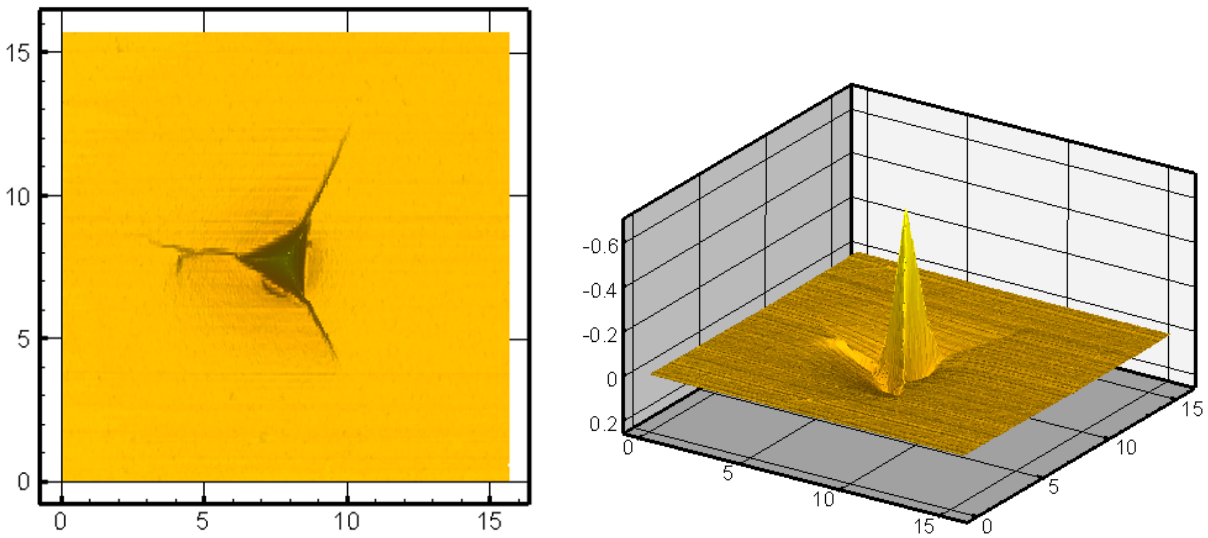

Figure 6: 2D residual surface profile and 3D inverse image showing cracks generated after nanoindentation using a cube corner tip at maximum load of 60 mN

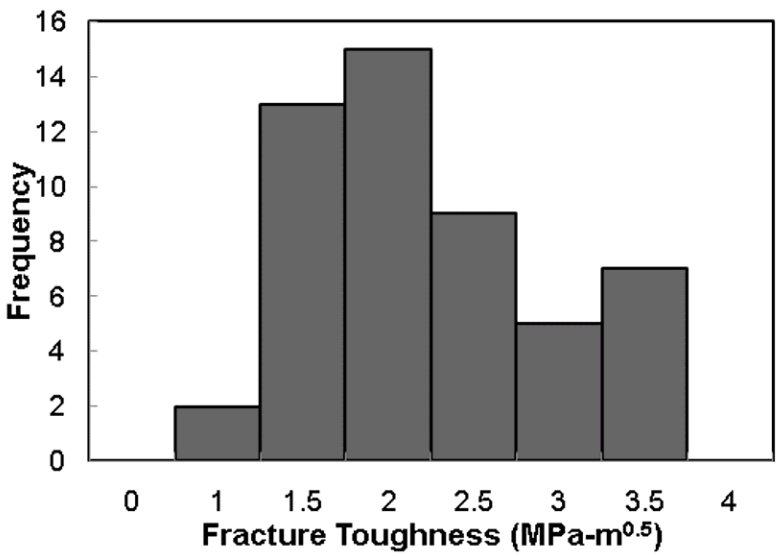

Figure 7(a): Distribution of fracture toughness for nanoindentations on different sand grains

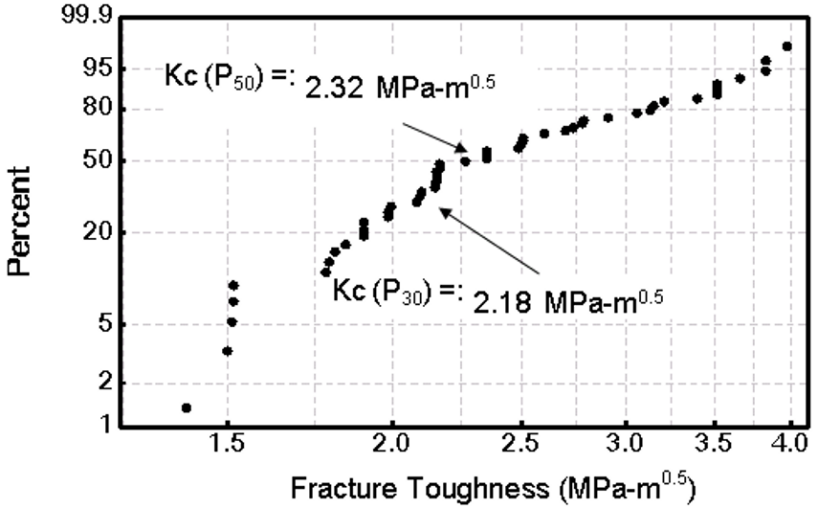

Figure 7(b): Weibull plot for fracture toughness from nanoindentations on different sand grains

4. Stress-strain response of Eglin sand grains

To determine the material properties parameters for granular sand material, nanoindentation experiment was modeled using FEM. To predict the elastic-plastic properties, von Mises yield criteria was used along with isotropic hardening to simulate the deformation characteristics of a sand grain. The plastic behavior under compression was assumed to satisfy the power law (Ramberg-Osgood) relationship between true stress and strain as

$\sigma_f = K \cdot \varepsilon^n$ for $\sigma_f \geq \sigma_y$ (2)

where n is the work hardening exponent, K is the reference stress value, and ε is the equivalent strain, $\varepsilon = \sqrt{\varepsilon_{ij}\varepsilon_{ij}} = \left(\varepsilon_y + \varepsilon_p\right)$, where ε_y is the yield strain and ε_p is the plastic strain. The von Mises equivalent stress is given as, $\sigma = \sqrt{\frac{3}{2}\sigma_{ij}\sigma_{ij}}$.

Within the linear elastic limit,

$\sigma = E\varepsilon$, for $\sigma \leq \sigma_y$ (3)

where E is the Young's modulus. In this work, ABAQUS V6.8-4 standard [4] was used to perform the calculations, assuming finite deformation characteristics. However, it is time consuming if the calculation only depends on fitting the simulation output with the experimental results since there are only a few parameters can be measured using nanoindentation, e.g. Young's modulus and parameter coupling effect might also increase the difficulty to obtain the reasonable values of material parameters, e.g. exponent of power law equation and yield stress. Therefore, a more efficient method should be concerned to overcome these problems. [5] reported a method to extract the stress-strain curve of single crystal materials by FEM simulation based the nanoindentation data. Their work is based on a relationship between hardness and flow stress first provided by Tabor [6] which is shown as the equation (4)

$H = C_\theta \cdot \sigma_f$ (4)

where C_θ is the "constraint factor" depending on the angle, θ, of indenter and flow stress is a characteristic value of plastic strain. The characteristic strain (ε_{char}) is able to be obtained for a given indenter angle. There have been several efforts to obtain the stress-strain curve by relating the hardness to stress and the indenter angle to characteristic strain. The power law equation of stress-strain relationship can be written as $K = \sigma_y(\sigma_y/E)^{-n}$ with the assumption linear elastic up to the yield strength. By combing equations (2), (4) and taking the logarithm, the hardness can be expressed as a function of E, σ_y, C_θ and ε_{char}, which is shown as equation (5),

$logH = n \cdot \log\left(\frac{E}{\sigma_y} \cdot \varepsilon_{char}\right) + \log\left(C_\theta \cdot \sigma_y\right)$ (5)

where the unknown values are only exponent n and yield stress σ_y for a given indenter angle. In this work, finite element simulation is used to solve the inverse problem to obtain the values of n and σ_y for the different size Eglin sand grains. Young's modulus, E, and hardness, H can be measured from nanoindenation experiments. We used

C_θ and ε_{char} values reported in [5] to calculate the input parameters n and σ_y for the FEM simulation. As mentioned previously, nanoindentation simulation results may be affected by parameters coupling, but based on equation (5) the two unknown parameters are dependable to each other, therefore, we just need to estimate one parameter and another value can be obtained using the equation automatically. In this case, only one parameter is estimated for the model's input and parameter coupling effect between yield stress and exponent has been considered.

The configuration for the FEM simulation of nanoindentation is shown in Figure 8. The Berkovich indenter was simulated based on its three sided pyramidal geometry. Because of the Berkovich indenter's axisymmetric geometry, only one sixth of the entire model was used in this simulation to concern the computational time. The displacement history from the experiment was given as input for the FE analysis. Poisson's ratio which was taken as 0.18 was used in this simulation and the values of Young's Modulus which is close to P50 value has been selected for different sizes. Also, the corresponding hardness values are substituted into equation (5) to calculate the unknown parameters. The different yield stress values were used to calculate the exponent value for the power law equation which is the input for the plastic behavior of sand. The output of the FE analysis was the resulting reaction force or load. This numerical load was plotted versus the displacement into the surface, to give load-displacement curve from the simulation. The mesh size selected was tested for convergence of the load-displacement curve. By changing the yield stress values for different size samples and compare the simulation output with experimental results until the reasonable agreement was reached, we can adjust the two unknown material parameters. The best-fit parameters were then used to determine the effective stress-strain relationship for the Eglin sand grain sample.

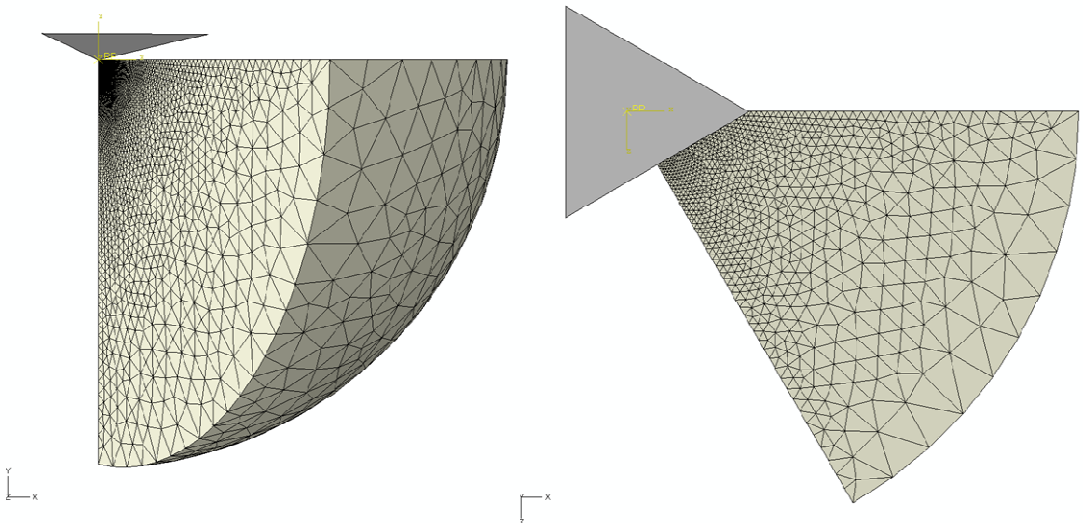

Figure 8 Side view and top view of axisymmetric Finite Element Analysis model for nanoindentation on 1/6 spherical sand grain using berkovich tip

It should be noted that the maximum strain up to which the stress-strain curve is valid, using this approach, is limited by the strain produced by the nanoindentation test [7]. No cracks were observed by examining the indent impressions (for the Berkovich indenter tip) obtained from Nanovision. Thus, the continuum plasticity material model was justified. As stated earlier, we used an inverse problem solving approach to determine the stress-strain relationship of sand at granular level by correlating the FEM simulated nanoindentation load-displacement data with the measured results. From the Figure 9, we can see the simulation results agree with the experimental results reasonably well. For all these six different sizes samples, and based on the representative experimental data P50, the values for yield stress and exponent of power law equation are about 2 ~ 3GPa and 0.99 ~ 1.15 respectively. These values with the measured Young's Modulus values can be used as the material parameters for the elastic-plastic constitutive model for Elgin sand grains.

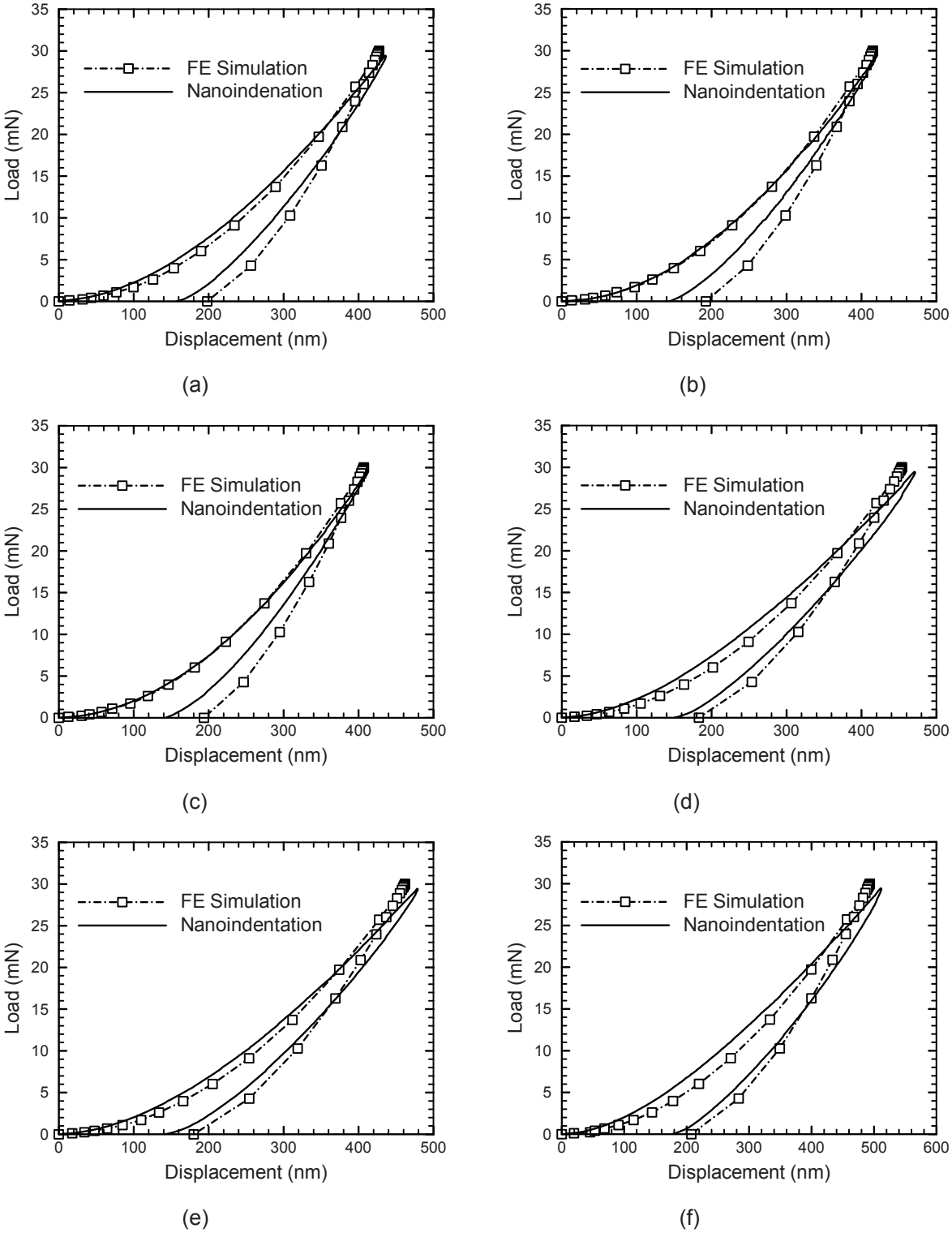

Figure 9 Comparison of experimental and simulation results for different size samples. (a): 0.6 mm sand grains. (b): 0.5mm sand grains. (c): 0.425 mm sand grains. (d): 0.3mm sand grains. (e): 0.212 mm sand grains. (f): 0.15 mm sand grains.

5. Conclusion

In order to assess the granular level mechanical behavior of sand, nanoindentation tests were conducted on individual sand grains to characterize their mechanical properties, namely, Young's elastic modulus, hardness, fracture toughness, and stress-strain relationship. Properties of six sizes of sand grains were concluded to obtain the size effect. As can be expected, a wide variation in the granular properties of sand was observed. Larger sand grains were found to have larger Young's modulus and hardness. The overall Young's modulus for the Eglin sand grains was found to be 90.38 GPa (range 33.4 to 119.8 GPa), hardness to be 12.84 GPa (range 4.2 to 20.3 GPa and fracture toughness to be 2.32 MPa-$m^{0.5}$ (range 1.3 to 4.0 MPa-$m^{0.5}$). Power-law was used to represent the homogenized and isotropic stress-strain behavior for sand at the granular level. However, the variation in the property value indicates that sand at granular level is very inhomogeneous and not isotropic due to different material constituents, defect structure, and crystal orientations. Need exists to establish the linkage between nanoindentation measured properties of sand grains with the observed macro properties for correct prediction of bulk behavior of sand. The data reported here can be used for mesoscale (granular) simulations of sand in which the individual sand grains would have different properties with the distributions obtained in this study.

Reference

[1] Oliver, W.C. and Pharr, G.M., 1992, "An Improved Technique for Determining Hardness and Elastic Modulus Using Load and Displacement Sensing Indentation Experiments," J. Mater. Res., 7, pp. 1564-1583.
[2] Pharr, G.M., Harding, D.S., and Oliver, W.C., 1993, "Measurement of fracture toughness in thin films and small volumes using nanoindentation method," Mechanical properties and deformation behavior of materials having ultra-fine microstructures, edited by M. Nastasi, D. M. Parkin, and H. Gleiter, Kluwer Academic Publishers, pp. 449-461.
[3] Harding, D.S., 1995, "Cracking during nanoindentation and its use in the measurement of fracture toughness," Materials Research Society symposia proceedings, 356 v.5, pp. 663-668.
[4] ABAQUS Documentation V 6.8, 2009.
[5] Shim, S., Jang, J., and Pharr, G. M., 2008, "Extraction of flow properties of single-crystal silicon carbide by nanoindentation and finite –element simulation," Acta Materialia, 56, pp. 3824-3832.
[6] Tabor, D., The hardness of metals, Oxford: Oxford University Press; 1951.
[7] Dao, M., Chollacoop, N., Van Vliet, K.J., Venkatesh, T.A., and Suresh, S., 2001, "Computational modeling of the forward and reverse problems in instrumented sharp indentation," Acta Mater., 49, pp. 3899-3918.

Proceedings of the SEM Annual Conference
June 7-10, 2010 Indianapolis, Indiana USA

Design and Implementation of Coupled Thermomechanical Failure Experiments

Bonnie R. Antoun[1], J. Franklin Dempsey[2], Gerald W. Wellman[2], William M. Scherzinger[2], Kevin Connelly[1]
[1]Sandia National Laboratories, Livermore, CA 94551-0969, USA
[2]Sandia National Laboratories, Albuquerque, NM 87185, USA

The importance of developing the capability to accurately and predictively model failure under combined thermal and mechanical loadings can not be overstated. Development of the necessary constitutive and failure models relies heavily on laboratory experiments that provide detailed information at several levels, from material characterization to laboratory scale validation experiments of increasing complexity, eventually leading up to full scale validation. This work is part of an interdisciplinary program that seeks to develop solutions to a large class of coupled thermomechanical failure problems. Coupled thermal-mechanical experiments with well-defined, controlled boundary conditions were designed and implemented through an iterative process involving a team of experimentalists, material modelers, computational developers and analysts.

First the basic experimental premise was selected: an axisymmetric tubular specimen mechanically loaded by internal pressurization and thermally loaded asymmetrically by side radiant heating, shown schematically in Figure 1. Then several integrated experimental-analytical steps were taken to determine the experimental details, with the caveat that the resultant thermal and mechanical loading profiles realistically represent actual component type of loadings. The boundary conditions were mostly thermally driven and were chosen so they could be modeled accurately; the experimental fixtures were designed to ensure that the boundary conditions were met. Every experimental design choice required input from and collaboration with the modeling and computation team members.

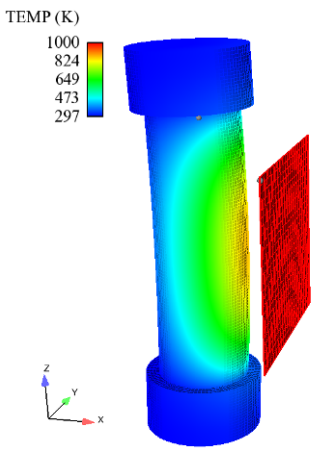

Fig. 1. Axisymmetric tubular specimen with side radiant heating

Designing the experimental thermal application system occurred as an evolutionary process, starting with simple heating methods and incrementally advancing to the final system that utilized fully programmable, integrated radiant heating system developed in our laboratory that can impart any type of desired heating profile. The system enables constant heat flux as the thermal input by radiantly heating an Inconel shroud that secondarily applies heat to the specimen. Figure 2 shows the thermal application system in use.

The mechanical system is incorporated into a large four-post 220 Kip MTS servohydraulic test frame (see Figure 2) that allows axial displacement and load control of the tubular specimen during heating and mechanical pressurization. Electronic pressurization control was programmed through an external channel of the MTS system and applied using a series of regulators via a Nitrogen gas bottle. Preliminary, uncoupled analyses were used to size the specimen diameter, height and thickness with experimental consideration of maximum pressure loads and fixture design. Iterations of analyses and experiments were used to efficiently determine heating parameters including lamp and heating shroud design, set off distance between the lamps and shroud and between the shroud and specimen, obtainable ramp rates, and the number and spatial placement of thermocouples. Coupled thermal-mechanical analyses were then completed to finalize the specimen design. Cooled, pressurizing specimen fixtures were developed that allowed mechanical and thermal function while maintaining the desired boundary conditions. A schematic of the fixtures is shown in Figure 3. Specimens were made of from 89 mm (3.5 in.) diameter 304L stainless steel tube, with an overall length of 355 mm (14 in.) and a long reduced section to achieve desired wall thickness. Specimens were painted with Pyromark™ paint to maintain a known surface emissivity and were instrumented with at least sixteen 24 gage Type K intrinsic thermocouples, locations were provided by the thermal modeling team. Specimen deformation and dimensional changes were measured in-situ with optical photography methods. Figure 4 shows

T. Proulx (ed.), *Time Dependent Constitutive Behavior and Fracture/Failure Processes, Volume 3*, Conference Proceedings of the Society for Experimental Mechanics Series 15, DOI 10.1007/978-1-4419-9794-4_20, © The Society for Experimental Mechanics, Inc. 2011

a side view of an instrumented specimen during testing. Note the shroud on the left, the cooling and pressurization tubes top and bottom and the thermocouples attached to the front, back and sides of the specimen.

A fully automated, coupled thermomechanical failure test bed has been developed and successfully tested and used for complex experimental investigations of failure. Examples of results obtained with this capability are described in [1].

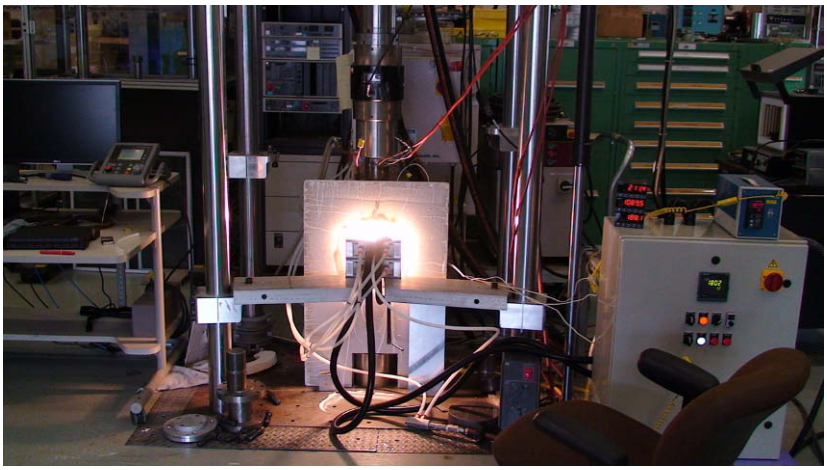

Fig. 2. Thermal application with radiant heating from quartz lamps

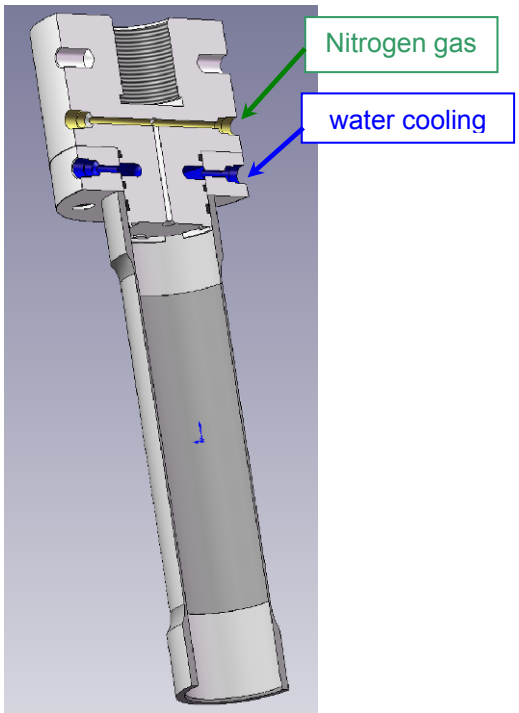

Fig. 3. Schematic of cooled, pressurizing fixtures

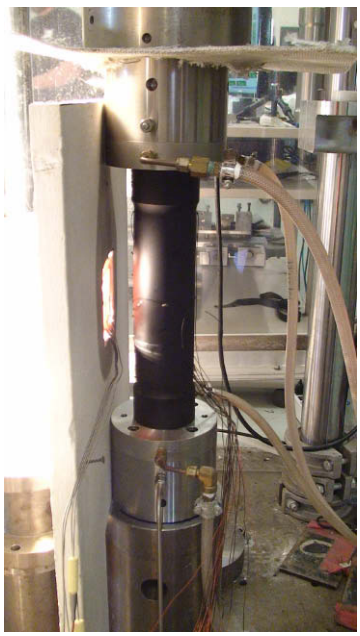

Fig. 4. Photograph of instrumented 304L stainless steel specimen during testing

ACKNOWLEDGEMENTS

Sandia is a multiprogram laboratory operated by Sandia Corporation, a Lockheed Martin Company, for the United States Department of Energy under Contract DE-ACO4-94AL85000.

REFERENCES

1. Antoun, B. R., Dempsey, J. F., Wellman, G. W., Scherzinger, W. M., Connelly, K., and Romero, V. J., "Coupled Thermal-Mechanical Experiments for Validation of Pressurized, High Temperature Systems," *Proceedings of the 2010 SEM Annual Conference and Exposition on Experimental and Applied Mechanics*, Indianapolis, Indiana, June 7-10, 2010.

Proceedings of the SEM Annual Conference
June 7-10, 2010 Indianapolis, Indiana USA

The Role of Interface and Reinforcement in the Finite Deformation Response of Polyurethane-Montmorillonite Nanocomposites

Amit K. Kaushik[1], Dr. Ming Yang[2], Dr. Paul Podsiadlo[3], Prof. Anthony M. Waas[4], Prof. Nicholas A. Kotov[2] and Prof. Ellen M. Arruda[1*]

Department of Mechanical[1], Chemical[2], Aerospace[4] Engineering, University of Michigan, Ann Arbor, MI 48109. [4]Argonne National Laboratory, Center for Nanoscale Materials, Argonne, IL 60439. *Corresponding Author: arruda@umich.edu

ABSTRACT

Nanoscale control over the structures is critical in designing nanocomposites with advanced properties. Structural parameters such as interface and volume fraction of reinforcement have tremendous effects on the mechanical properties of the nanocomposites, yet have proven difficult to control uniformly and consistently. Here we investigate the effect of reinforcement and interface on the finite deformation response of polyurethane (PU-) montmorillonite (MTM) nanocomposites at low and high strain rates. The multilayered PU-MTM nanocomposites, with alternate layers of PU and MTM, were manufactured using an exponential layer-by-layer (e-LBL) manufacturing technique. The systematic variation in MTM nanoparticle was obtained by either replacing several layers of MTM by polyacrylic acid (PAA) or by varying the thickness of PU layer. The interface was altered by replacing MTM layers by PAA. The deposition of PAA resulted in the formation of a complex polymer layer due to its diffusion through PU layer. The nanocomposites demonstrated an increasing yield strength and stiffness with increased strain rate and MTM volume fraction. The weaker interface interaction between the polymer and MTM nanoparticles resulted in a decreased yield strength and stiffness. The design parameters that will result in structures with optimum mechanical properties will be demonstrated.

INTRODUCTION

To make an optimum use of the stiffening effect of reinforcement in the composite system, the most efficient load transfer from the polymer matrix to the reinforcement is required. It is very well known that effective load transfer between the matrix and the reinforcement is vital in increasing the strength of the composite system. The effective load transfer takes place through the interface between the two constituents and depends crucially on the interfacial strength between the matrix and the filler. In this work, we investigate the role of the interfacial strength in controlling the finite deformation response of PU-MTM nanocomposites. Here, we change the interface by incorporating another polymer polyacrylic acid (PAA) that is negatively charged and diffuses into PU matrix to alter the interface between the positively charged PU and negatively charged MTM nanoparticles[1]. The deposition of PAA along with PU results in a so-called "exponential" growth in the film thickness which is detailed in the following section[2]. This process not only allowed us to alter the volume fraction of nanoparticles and the

T. Proulx (ed.), *Time Dependent Constitutive Behavior and Fracture/Failure Processes, Volume 3*, Conference Proceedings of the Society for Experimental Mechanics Series 15, DOI 10.1007/978-1-4419-9794-4_21, © The Society for Experimental Mechanics, Inc. 2011

interface but also allowed us to alter the structure of the multilayered nanocomposites without changing the volume fraction of MTM nanoparticles.

EXPERIMENTAL TECHNIQUES

Scanning Electron Microscope (SEM) was used to characterize the thickness of the nanocomposites. Thermogravimetric analyzer (TGA) was used to determine the loading of MTM nanoparticles in the nanocomposites. An in-house built tensile tester was used to perform low-rate mechanical tests in tension[3]. The material strain in the nanocomposites was measured using digital image correlation.

SYNTHESIS OF NANOCOMPOSITES

A series of PU-MTM nanocomposites with wide range of volume fractions of MTM nanoparticles was prepared using the e-LBL manufacturing process. While PU used was a positively charged polyelectrolyte, the PAA and MTM nanoparticles were negatively charged. The manufactured multi-layered PU/PAA/MTM nanocomposites were characterized as uniform-layered and hierarchical-layered nanocomposites. The uniform-layered nanocomposites had the $(PU/PAA/PU/MTM)_n$ deposition sequence and the hierarchical-layered nanocomposites had the $(PU/PAA/(PU/MTM)_m)_p$ deposition sequence[1]. The design variable in the uniform-layered nanocomposites was the thickness of PU layer. The design variables in the hierarchical-layered nanocomposites were the thickness of PU layer and the parameter p.

RESULTS AND DISCUSSION

The film thickness in the e-lbl manufactured nanocomposites grew linearly with the number of bilayers as shown in Figure 1. This growth in thickness is much larger as compared to the l-LBL nanocomposites[2]. The incorporation of MTM nanoparticles, however, reduced the rate of thickness growth. Figure 1 shows the thickness growth of PU/PAA and uniform and hierarchical PU/PAA/PU/MTM nanocomposites with 6 v.% MTM nanoparticles. The presence of MTM nanoparticles reduced the diffusion of polyelectrolytes through the thickness owing to their highly dense layer.

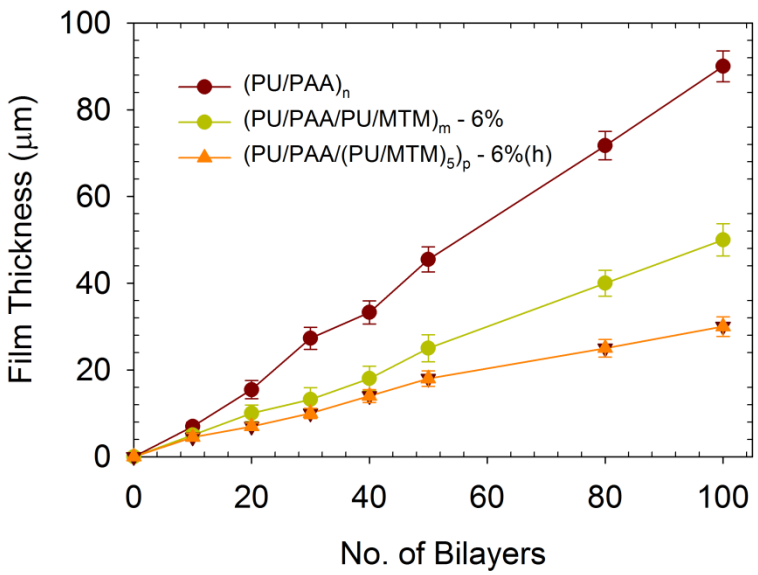

Figure 1: Film thickness as a function of bilayers

The layered PU/PAA/MTM nanocomposites demonstrated an increase in the stiffness, yield strength and ultimate tensile strength when compared with pure PU (Figure 2 and Table 1)[1]. With only PAA incorporated at the nanoscale, the yield strength increased ~7 times and stiffness increased more than an order of magnitude when compared with PU. With 3 v.% MTM nanoparticles, the yield strength increased to ~20 MPa and the stiffness also increased to 0.75 GPa. The stiffness and yield strength continued to increase with an increase in the volume fraction of MTM nanoparticles. This enhancement in mechanical properties, viz., stiffness, yield strength and ultimate strength is attributed to the strong MTM nanoparticles alignment parallel to the direction of applied load that allowed a substantial fraction of the load to be transferred to the stiffer, stronger MTM nanoparticles. The ultimate strain-to failure, however, decreased with increased volume fraction of MTM nanoparticles. This is attributed to the reduced thickness of PU with an increase in the MTM volume fraction. Hence, the thickness of PU controlled the ultimate strain-to-failure of the nanocomposites.

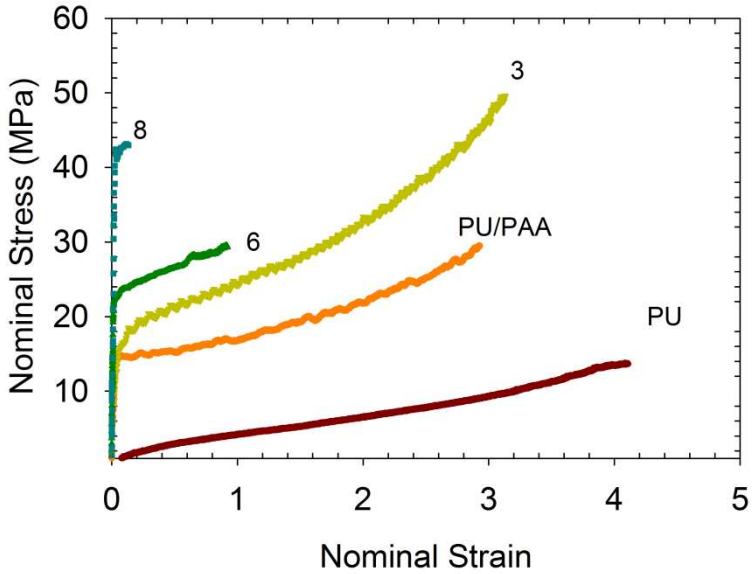

Figure 2: Representative nominal stress-strain curves for the layered PU/PAA/MTM nanocomposites. Numbers represent the volume fraction of MTM nanoparticles.

In order to investigate the role of interface in these nanocomposites, a nanocomposite with 6 v.% MTM nanoparticles was prepared with uniform and hierarchical layering. The schematic of these nanocomposites, compared along with a uniform-layered nanocomposite with 3 v.% MTM nanoparticle is shown in Figure 3. The hierarchical nanocomposite consisted of the same PU thickness as the uniform nanocomposite with 3 v.% MTM nanoparticles. The thickness of PU layer in 6 v.% MTM uniform nanocomposite was smaller than that in 3 v.% MTM nanocomposite or hierarchical nanocomposite with 6 v.% MTM nanoparticle.

The presence of several layers of MTM in the hierarchical layered nanocomposites resulted in a reduced diffusion of PAA through the film thickness. This suggested that in these nanocomposites lesser amount of negatively charged PAA interacted with the negatively charged MTM nanoparticles. This implied that the hierarchical nanocomposites inherited increased interfacial strength between the matrix and reinforcement.

Figure 4 shows the constitutive stress-strain responses of the above uniform and hierarchical nanocomposites. The hierarchical nanocomposite demonstrated higher stiffness, yield strength and ultimate strain-to-failure in comparison with the uniform nanocomposite with the same volume fraction of MTM nanoparticles. This increased stiffness and strength is attributed to the larger interfacial strength in the hierarchical PU/PAA/MTM nanocomposites which resulted in the effective load transfer between the matrix and the nanoparticles. The larger failure strain is because of the presence of larger PU thickness.

Hence, in this work we have investigated the role of volume fraction of MTM nanoparticles and the interfacial strength in controlling the finite deformation response of nanocomposites of PU, PAA and MTM. The nanocomposites were manufactured using the e-LBL manufacturing technique. Here we demonstrate that it is possible to prepare nanocomposites that can inherit increased stiffness strength and ductility simultaneously.

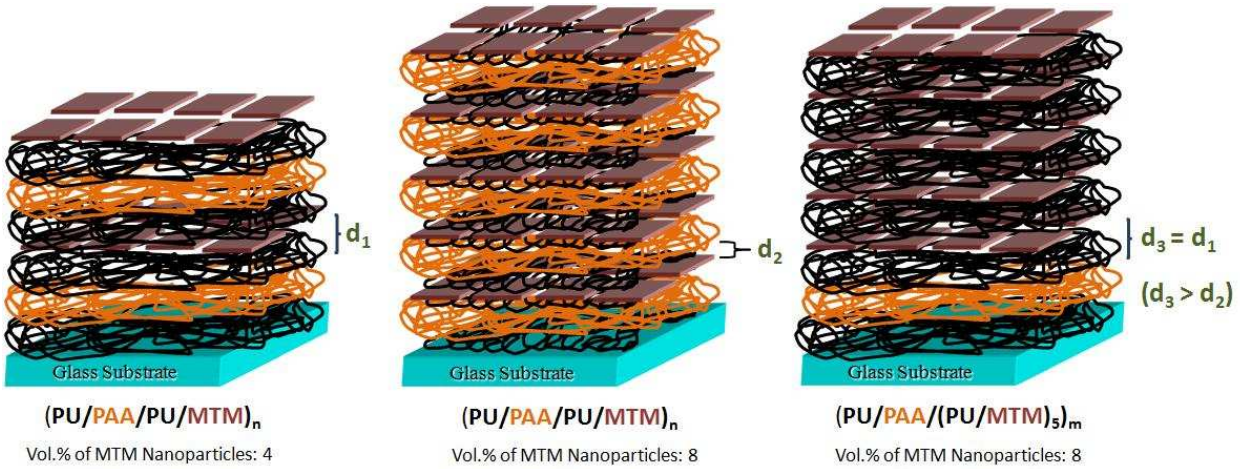

Figure 3: A schematic showing the structure of uniform layered PU/PAA/MTM nanocomposite with 3 v.% (left) and 6 v.% MTM (middle) nanoparticles and a hierarchical nanocomposite with 6 v.% (right) MTM nanoparticles.

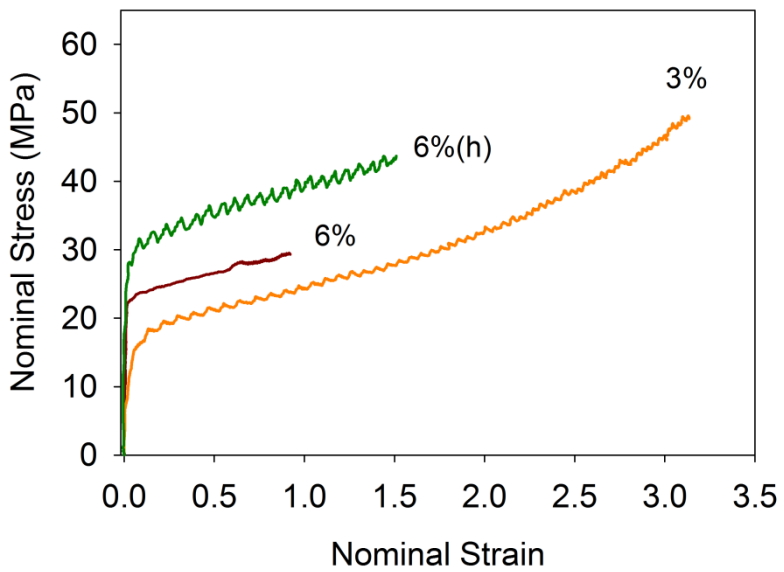

Figure 4: Representative stress-strain constitutive responses of uniform and hierarchical PU/PAA/MTM nanocomposites. Here numbers represent the MTM volume fraction and h represents the hierarchical nanocomposite.

REFERENCES

[1]. Kaushik Amit, Podsiadlo Paul, Yang Ming, Waas Anthony, Kotov Nicholas, Arruda Ellen. Design parameters in controlling the finite deformation response of polymer nanocomposites. In preparation

[2]. Podsiadlo Paul, Michel Marc, Lee Jungwoo, Verploegen Eric, Kam Nadine, Ball Vincent, Lee Jaebeom, Qi Ying, Hart John, Hammond Paula Kotov Nicholas. Exponential growth of LBL films with incorporated inorganic sheets. Nano Letters, 8(6): 1762-1770, 2008.

[3]. Kaushik Amit, Podsiadlo Paul, Qin Ming, Shaw Charles, Waas Anthony, Kotov Nicholas, Arruda Ellen. The role of nanoparticle layer separation in the finite deformation response of layered polyurethane-clay nanocomposites. Macromolecules, 42: 6588-6595, 2009.

Proceedings of the SEM Annual Conference
June 7-10, 2010 Indianapolis, Indiana USA

Time-temperature Superposition and High Rate Response of Thermoplastic Composites and Constituents

Pierce D. Umberger, Virginia Tech, Department of Engineering Science and Mechanics, 106 Norris Hall, Blacksburg, VA 24061, pierceu@vt.edu
Scott W. Case, Virginia Tech, Department of Engineering Science and Mechanics
Frederick P. Cook, Virginia Tech, Department of Engineering Science and Mechanics

1 Abstract

The high strain rate response of ultra high molecular weight polyethylene (UHMWPE) laminae and laminates is of interest to support computational modeling of applications where impact damage may occur. In this study, the efficacy of utilizing time-temperature superposition principles (tTSP) to determine the high strain rate response of UHMWPE composites is investigated. Constituent and composite tensile properties are measured at various temperatures and strain rates. Testing was completed at thermo-rheologically equivalent temperature-strain rate combinations to evaluate the effectiveness and limitations of the shifting approach. Analysis of modulus and failure data indicated that at the composite level, tTSP may not be applicable, while at the lamina level tTSP may be applicable, therefore high strain rate properties are estimated.

2 Introduction

UHMWPE composites are used in applications requiring lightweight materials that are very strong and have favorable properties at high strain rates. However, measuring strain rate dependent properties at the strain rates is not possible using standard servo-hydraulic test equipment.

One of the original developers of the Spectra fiber, Prevorsek, first determined the properties of Spectra 1000 fibers to be strain rate dependent by conducting testing at rates from 10^{-2} and 10^{2} s^{-1} and demonstrating that elastic modulus increases with strain rate [7]. Tan, et al. (2006) used a Split Hopkinson bar to develop constitutive properties of Aramid fibers (also used in high-strain rate applications) at high strain rates and traditional tensile test methods at quasi-static strain rates. They found that Twaron aramid fibers are strain-rate sensitive, both in constitutive properties and failure mechanism [9].

More recently, Koh et al. (2007) performed high strain rate testing of SpectraShield laminates using a tensile split Hopkinson bar. Samples consisted of 7mm wide, 25mm gage length [0,90] SpectraShield product. They found that up to strain rates of 400 s^{-1}, there is an increase in stress and stiffness at failure and a decrease in strain with an increase in strain rate. At strain rates greater than 400 s^{-1}, this trend reverses, reducing failure stresses and stiffness, and seeing an increase in failure strain. The study cites SEM images of broken filaments that undergo ductile and shear failure, as opposed to the brittle failures seen below 400 s^{-1} (and above quasi-static strain rates)[4].

Time-temperature superposition (tTSP) is based on the principle that the properties of certain materials at various strain rates may be estimated by performing tests at corresponding (but differing) rates and temperatures. It is used on time-dependent materials to estimate their properties on time scales much longer or shorter than is convenient or possible to test at. Stiffness or compliance data taken at different temperatures may be shifted left or right along a time scale to create a master curve. This master curve can then be used to predict the behavior of the material at time scales or strain rates that are not physically achievable on test equipment [3]. While it is only directly applicable to amorphous polymers, tTSP has also been applied to failure mechanisms by Miyano et al., who successfully shifted composite strength data over time to predict long-term durability in graphite fiber/vinyl ester (GFRP) laminates [5].

In 2007, Alcock et.al. investigated the effects of temperature and strain rate on the mechanical properties of highly oriented polypropylene (PP) tapes and all-PP composites. The authors analyzed strain rate and temperature effects on tensile modulus and strength and developed master curves for each. In this case, it was found that different shift factors were used to shift modulus and strength, indicating that different mechanisms contribute to these failures. These master curves were used to predict the constitutive behavior of the tapes and composites at various strain rates, including those that are difficult to achieve with physical testing. The author notes that the PP composite is a complex system, and is difficult to model as a thermo-rheologically simple material [1].

T. Proulx (ed.), *Time Dependent Constitutive Behavior and Fracture/Failure Processes, Volume 3*, Conference Proceedings of the Society for Experimental Mechanics Series 15, DOI 10.1007/978-1-4419-9794-4_22, © The Society for Experimental Mechanics, Inc. 2011

Alcock used the Arrhenius equation to determine a_T, the factor relating time and temperature. The Arrhenius equation is generally accepted as applicable to amorphous polymers [2], though Alcock has applied it to a more complex polypropylene composite. To apply the Arrhenius equation, a constant thermal activation energy, E_a, is defined. The shift factor between two temperatures is therefore defined as

$$ln(a_T) = \frac{E_a}{R}\left(\frac{1}{T} - \frac{1}{T_{ref}}\right) \tag{1}$$

where R is the universal gas constant, T_{ref} is the absolute reference temperature, and T is the absolute temperature at which the shift factor is to be computed [1].

In this paper, temperature and rate dependence is investigated for UHMWPE fiber, lamina, and laminates, and time-temperature superposition is applied to estimate high strain rate properties.

3 Sample Preparation

For this paper, Spectra S3000 fibers, S3000 unidirectional material (not commercially available), and SpectraShield 3124 laminates were used. The unidirectional samples are referred to as lamina, and the SpectraShield 3124 samples are referred to as laminates.

3.1 Fiber Processing

Single S3000 UHMWPE fibers were laterally separated from tows using forceps, taking care to minimize twisting, bending, or kinking of the fibers. Attempts at bonding fibers to cardboard tabs were unsuccessful due to the low surface friction and high strength of the fibers. Instead, fibers were wrapped and bonded to 2 mm cylindrical cardboard mandrels, leaving a 10 mm gauge length.

3.2 Lamina Processing

Sheets of Honeywell pre-preg, the precursor to the commercial SpectraShield product, were created in a unit processing testing lab, with all Spectra fibers oriented in one direction and evenly distributed on a sheet of silicone paper, then sprayed with the proprietary Kraton matrix. To create lamina panels, multiples of these sheets were placed with the fibers facing each other, then pressed at approximately 116 °C and 18 MPa, and held for 10 minutes.

3.3 Laminate Processing

Sheets of the Honeywell commercial SpectraShield 3124 product (which has a lay-up of [0,90]) were cut to the desired dimensions and stacked in the desired configuration. Panels were pressed at 4.79 MPa (with the sides unconstrained) and heated from room temperature to 125 °C. Once the temperature stabilized, the pressure was increased to 19.15 MPa and the temperature brought to 128.9 °C. The panels were held at this temperature for approximately 15 minutes, and then were allowed to cool under pressure.

4 Testing Procedure

4.1 Creep Compliance Testing

A TA Q800 DMA was used to conduct creep compliance tests of fiber, lamina, and laminates. Fiber specimens were wrapped around adhesive-coated cardboard mandrels and gripped in the thin-film fixture on the DMA with a gauge length of approximately 10mm. Laminate specimens were cut from larger panels using a razor blade to dimensions of approximately 20 mm by 6 mm and gripped with a gauge length of approximately 8mm. A creep compliance temperature sweep program was set up for which the temperature of the sample was varied from -80 °C to 40 °C at

10 °C increments. A tensile load of 0.14 N for fiber samples and 15 N for lamina/laminate samples was applied and the elongation of the sample was measured for 10 minutes.

4.2 Fiber Testing

Fiber tensile testing was conducted in the same TA Q800 DMA with attached furnace and liquid nitrogen cooling chamber. The mandrel-wrapped fiber specimens were gripped in the thin-film fixture and the fibers were loaded at constant strain rate to failure. Tensile tests were carried out at temperatures between -100 °C and 25 °C at strain rates of $5x10^{-4}$ s^{-1} to $5x10^{-2}$ s^{-1}.

4.3 Lamina/Laminate Testing

Lamina and laminate tensile tests were conducted using an MTS hydraulic load frame equipped with a liquid-nitrogen cooled temperature chamber , shown in Figure 1. For room temperature testing, the temperature chamber was not activated, and the temperature for all tests was between 24.5 °C and 25.5 °C.

Figure 1: MTS load frame with temperature chamber and lamina sample with extensometer attached.

5 Results

The initial test plan was to develop a master curve and shift factors from tensile testing alone. To complete this, a matrix of fiber and lamina tests at a wide range of sub-ambient temperatures and various strain rates was developed. As Figure 2 shows, though overall trends may be evident, there was too much scatter in each data set to accurately construct a master curve. Similar scatter exists in the tensile modulus and strain at failure data for all sample types.

The next iteration of the tTSP plan was to perform a creep compliance temperature sweep to construct a master curve and shift factors, and then apply those shift factors to tensile data. The assumption here is that the same mechanisms governing the behavior of the material in creep are governing the tensile properties, specifically elastic modulus, tensile strength, and strain at failure.

A shifted plot of laminate creep compliance data is shown in Figure 3 below. The accompanying shift factors are shown in Figure 4. This same method was used for all other fiber, lamina, and laminate samples. Some resulting shift factors are shown in Figure 5.

To verify that these creep compliance shift factors can be applied to tensile data, such as tensile strength, tensile stress at failure, and tensile modulus, samples were tested at room temperature and at a lower temperatures corresponding to a one- and two-decade shift, and at strain rates 10 and 100 times slower. The two resulting data sets should be comparable if the assumption of creep compliance equivalence is valid. From Figure 6, we can see that the fiber

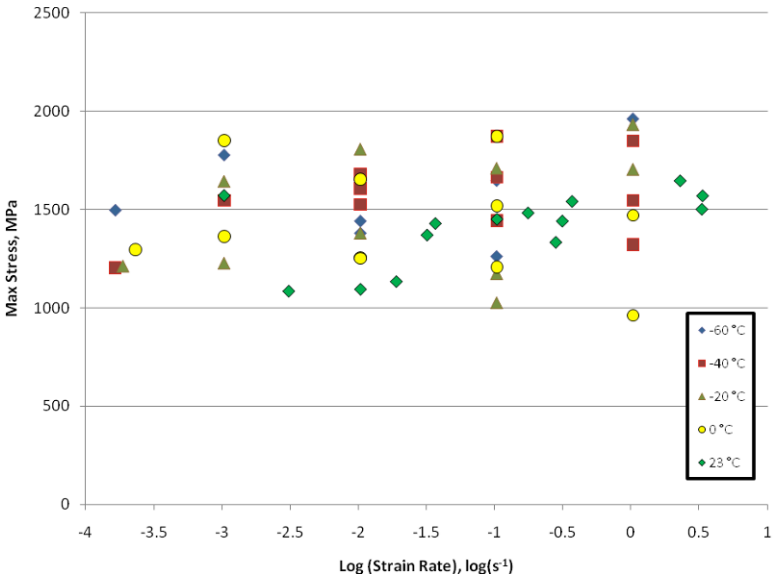

Figure 2: Lamina stress at failure vs. strain rate at various temperatures.

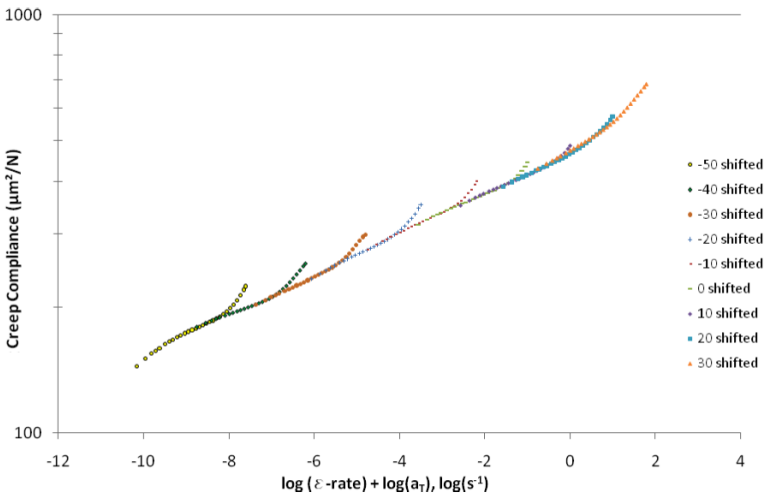

Figure 3: Shifted creep compliance of a laminate sample.

tensile strength at equivalent rate/temperature combinations is comparable. Additionally, the Weibull distribution of the strength for these "equivalent" sets are comparable, as shown in Figure 7.

Figures 8 and 9 contain strength and elongation at failure data from many different lamina and laminate tests. All data not from room temperature has been shifted using the creep compliance shift factors determined for that material. Laminate strength has been estimated from lamina strength based on the strength of the number of fibers in the direction of loading.

Note that the solid line is a linear regression of log(shifted strain rate) and strength of 53 specimens tested at a variety of strain rate-temperature combinations. The dashed lines represent a 68% prediction interval on future values of strength. The error bars on each data point represent one standard deviation of uncertainty [6].

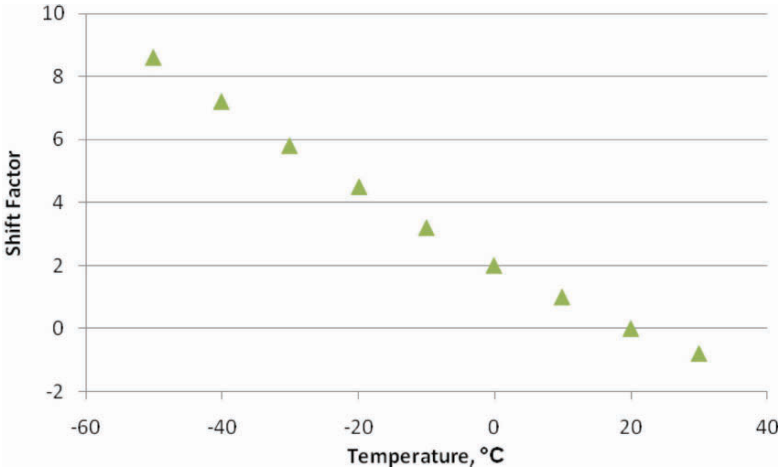

Figure 4: Shift factors associated with the master curve in Figure 3.

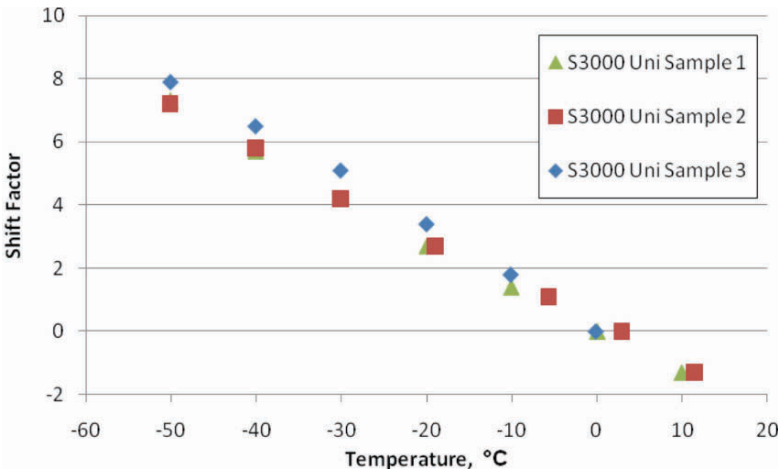

Figure 5: Shift factors for lamina taken from creep compliance data.

6 Discussion

It should be noted that we give data for strain at failure for lamina and laminate samples, but not single fibers. This is due to both our gripping and strain measurement methods. For fiber testing, we rely on crosshead measurement to determine strain. Despite the fact that our fibers are wrapped, bonded, and gripped, some fiber slipping does occur at high loads. As a result, we have little confidence in our measurements of strain at failure.

One of the largest sources of uncertainty for the lamina and the laminate tensile testing was in the use of the temperature chamber to bring the sample to the desired temperature. The material has been demonstrated to have anisotropic thermal conductivity [8]. While the chamber is cooled, the grips are heated by the hydraulic oil in the load frame. The result is uncertainty in the true temperature of the sample. This uncertainty is accounted for in the error bars on the shifted strain rate measurements. In contrast, the DMA chamber used for creep compliance and fiber tensile testing is very small and the grips reach the same temperature as the sample, with a degree of control better than 0.1 °C

Another source of uncertainty in the laminate tests was that some of the specimens appeared to have failed in shear rather than in the normal direction. It is well documented in composites that there is a critical off-angle at which a unidirectional specimen is dominated by shear failure instead of normal failure. Because of the extremely large

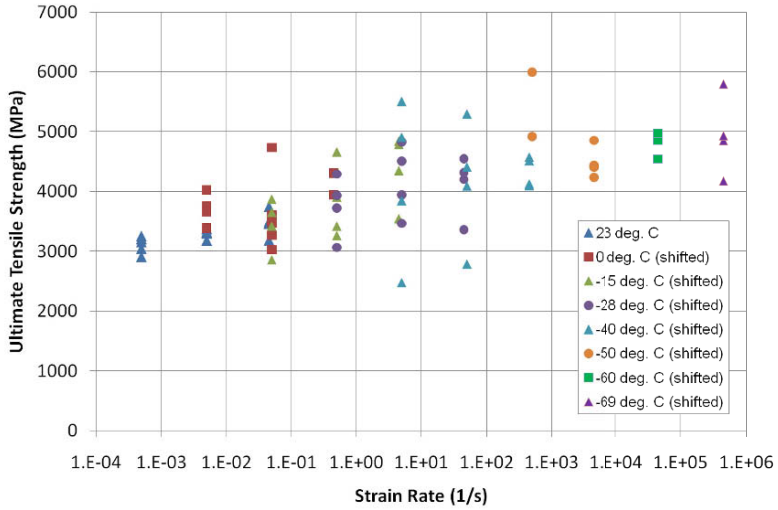

Figure 6: Fiber stress at failure vs. strain rate at various temperatures.

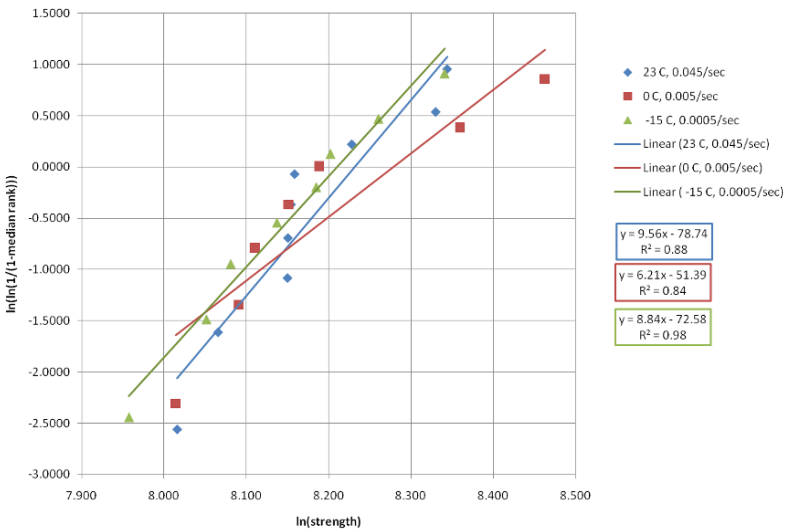

Figure 7: Weibull Distribution of fiber strength for three thermorheologically equivalent strain rate/temperature combinations.

ratio of fiber stiffness to matrix stiffness in our composite, the off-angle is very small, and it is impossible to align the specimen in the grips such that every test results in a normal failure.

A third source of uncertainty is the process of shifting the creep compliance data to create master curves. When Alcock et al. (2007) shifted their failure data, they cautioned that using an Arrhenius activation energy constant to describe the tTSP behavior of his poly-propylene composite was a simplification of a more complex material system. They further cautioned that only amorphous polymers can be directly shifted using an activation energy approach to tTSP, and that although their shifted data appears valid, it is possible that large deviations are present in strain-rate ranges far from those tested [1].

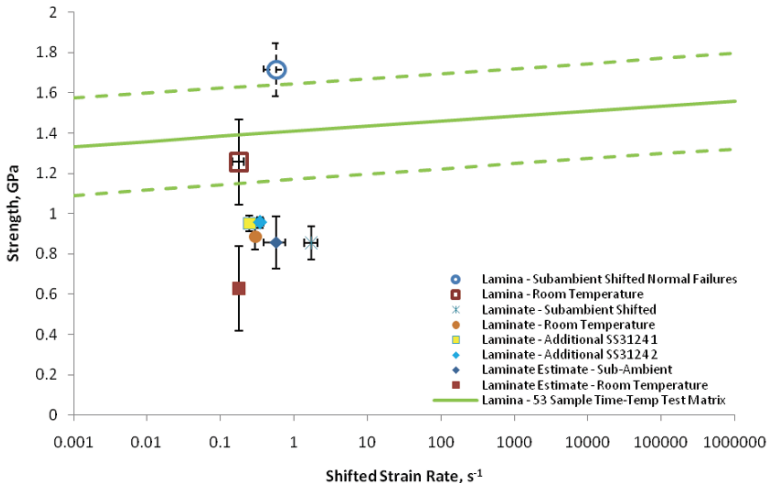

Figure 8: Strength master chart.

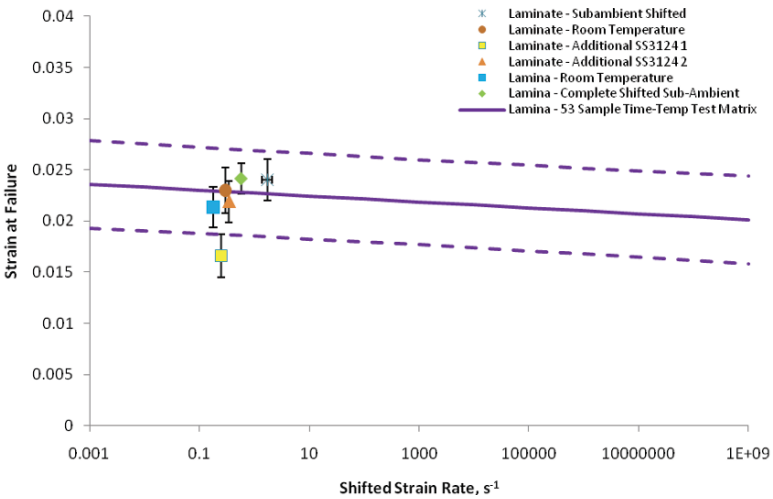

Figure 9: Strain at failure master chart.

7 Conclusions

There is potential in using time-temperature superposition values from creep compliance testing to shift tensile properties. Assumptions about how to measure the shift factors made prior to the tensile testing were later challenged, which resulted in changing the shifted strain rates. These shifted strain rates did not align as well with the room temperature rates, so a direct comparison of the data sets is not possible. In the future, it is recommended that a more exhaustive test of this method be undertaken, involving several different rate and temperature combinations. To be statistically significant, a large number of tests must be performed at each rate-temperature combination.

It was also observed that as levels of complexity are added to the material system, the rate-dependent behavior of the material becomes more complex. A lamina system containing only fibers in one direction is much simpler than a cross-ply system. The up-turn in creep compliance over time for each temperature is much less pronounced for lamina than for laminate, resulting in a smoother master curve that the researcher may have more confidence in. The data presented in this study should be further investigated and validated by using the various composite system models to utilize fiber data to predict lamina and laminate properties.

8 Acknowledgements

Research was sponsored by the Army Research Laboratory and was accomplished under Cooperative Agreement Number W911NF-06-2-0014. The views and conclusions contained in this document are those of the authors and should not be interpreted as representing official policies, either expressed or implied, of the Army Research Laboratory or the U.S. Government. The U.S. Government is authorized to reproduce and distribute reprints for Government purposes notwithstanding any copyright notation heron.

Bibliography

[1] Barkoula N.M. Reynolds C.T. Govaert L.E. Peijs T. Alcock B., Cabrera N.O. The effect of temperature and strain rate on the mechanical properties of highly oriented polypropylene tapes and all-polypropylene composites. *Composites Science and Technology*, 67:20612070, 2007.

[2] Kaneko K. Ariyama T., Mori Y. Tensile properties and stress relaxation of polypropylene at elevated temperatures. *Polymer Engineering and Science*, 37 Iss. 1:81–90, 2004.

[3] Brinson L. Brinson H. *Polymer engineering science and viscoelasticity*. Springer, 2008.

[4] Tan V.B.C. Koh C.P., Shim V.P.W. Response of a high-strength flexible laminate to dynamic tension. *International Journal of Impact Engineering*, 35:559–568, 2007.

[5] Naoyuki S. Miyano Y., Nakada M. Accelerated testing for long-term durability of gfrp laminates for marine use. *Composites: Part B*, 35:497–502, 2004.

[6] Peck E.A. Montgomery D.C. *Introduction to linear regression analysis*. Wiley, 1982.

[7] Harpell G.A. Prevorsek D.C., Kwon Y.D. Spectra composite armor: dynamics of absorbing the kinetic energy of ballistic projectiles. *Tomorrow's Materials: Today*, 34-II:1780–1791, 1989.

[8] E. Skow. Processing and thermal properties of molecularly oriented polymers. *Massachusetts Institute of Technology ETD*, Online, 2007.

[9] Zeng X.S. Tan V.B.C. Characterization and constitutive modeling of aramid fibers at high strain rates. *International Journal of Impact Engineering*, 32:1737–1751, 2006.

Proceedings of the SEM Annual Conference
June 7-10, 2010 Indianapolis, Indiana USA

MEASURING TIME DEPENDENT DIFFUSION IN POLYMER MATRIX COMPOSITES

SP Pilli[1], V Shutthanandan[1], LV Smith[2]
[1]Pacific Northwest National Laboratory, Richland, WA 99352, USA
[2]Washington State University, Pullman, WA 99164, USA

Corresponding author e-mail address: siva.pilli@pnl.gov

ABSTRACT: Moisture plays a significant role in influencing the mechanical behavior and long-term durability of polymer matrix composites (PMC's). The common methods used to determine the moisture diffusion coefficients of PMCs are based on the solution of Fickian diffusion in the one-dimensional domain. Fick's law assumes that equilibrium between the material surface and the external vapor is established instantaneously rather than over an extended period of time. A time dependent boundary condition has been shown to improve correlation with bulk diffusion measurements, but has not been verified experimentally. Surface moisture content in a toughened quasi-isotropic laminate system, $[0/\pm60]_s$, was analyzed using Nuclear Reaction Analysis (NRA). It was found that the moisture content increased nearly linearly with time.

MOISTURE ABSORPTION MODELS: Numerous diffusion models have been proposed over the years to model hygrothermal effects in polymers beginning with Fick [1] in 1855, who found that the flux of the solvent is proportional to the negative concentration gradient. The one dimensional form of Fick's law is

$$\frac{\partial C}{\partial t} = -D\frac{\partial^2 C}{\partial z^2} \tag{1}$$

$$C(z,0) = C_i(z), -L, \le z \le L, t \le 0 \tag{2}$$

$$C(\pm L,t) = C_L(t), t > 0 \tag{3}$$

where D is the mass diffusion coefficient, z is the through thickness direction, and C is the volumetric moisture concentration. The subscripts i and L refer to the initial saturation concentrations, respectively.

The value of the diffusion coefficient, D, is found from weight-gain data. The weight gain for the sorption and desorption of fluids in composites do not always concur with Fickian diffusion. Long and Richman [2], have used a time-dependent boundary condition to explain the non-Fickian behavior where the moisture content at the boundary ($\pm L$) was

$$C(\pm L,t) = \left[C_0 + C_1\left(1 - e^{-\beta t}\right)\right]H(t) \tag{4}$$

Weitsman expanded the time-dependent boundary condition with [3]

$$C(\pm L,t) = \left[C_0 + \sum_{n=1}^{N} C_n\left(1 - e^{-\beta_n t}\right)\right]H(t) \tag{5}$$

T. Proulx (ed.), *Time Dependent Constitutive Behavior and Fracture/Failure Processes, Volume 3*, Conference Proceedings of the Society for Experimental Mechanics Series 15, DOI 10.1007/978-1-4419-9794-4_23, © The Society for Experimental Mechanics, Inc. 2011

Models incorporating a time-dependent boundary condition have obtained improved correlation with experiment. Unfortunately, the authors of these approaches did not have experimental techniques to measure the surface moisture content directly.

RESULTS: Surface moisture content in a toughened quasi-isotropic laminate system, $[0/\pm60]_s$, was analyzed using Nuclear Reaction Analysis (NRA) [4]. The control environment consisted of D_2O vapor at 80% RH and 60°C. The exposure temperature (60°C) was below the glass transition temperature of the composite (T_g = 195°C). Samples were soaked for different intervals of time (1 day, 2days, 4 days, etc.) and traditional gravimetric analysis was performed in addition to the surface moisture concentration measurement using NRA. Figure 1 shows the NRA measured surface moisture content as a function of time. The moisture content is linearly increasing with time indicating a time dependent boundary condition. Some samples at longer times show a lower surface moisture concentration. A similar discrepancy was also observed in gravimetric analysis indicating a specimen preparation issue. Further studies are being conducted to correlate the measured moisture content with the proposed boundary conditions (4) and (5). This correlation will provide an enhanced description of the boundary, which in turn will improve the diffusion predictions involving complex geometries.

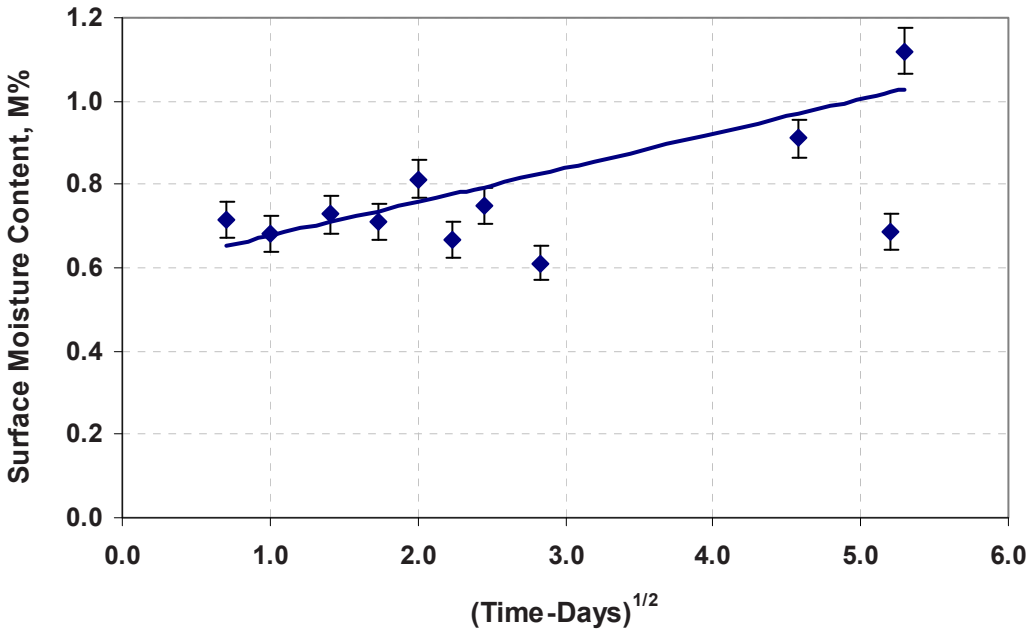

Figure 1. A plot of surface moisture concentration as a function of time

REFERENCES:

1. Fick, A., On Liquid Diffusion. Philosophical Magazine, 1855. **10**: p. 30-39.
2. Long, F.A. and D. Richman, Concentration gradients for diffusion of vapor in glassy polymers and their relation to time dependent diffusion phenomena. Journal of American Chemical Society, 1960. **82**: p. 513-519.
3. Weitsman. Y. J., A Continuum diffusion model for viscoelastic materials. Journal of Physical Chemistry, 1990. **94**: p. 961-968.
4. Pilli, S.P., et al., A novel accelerated moisture absorption test and characterization. Composites Part A: Applied Science and Manufacturing, 2009. **40**(9): p. 1501-1505.

Proceedings of the SEM Annual Conference
June 7-10, 2010 Indianapolis, Indiana USA

New Strain Rate Dependent Material Model for Fiber Reinforced Composites

Meyer, L. W.[1], Mayer, M.[1*]

[1]Nordmetall GmbH, Hauptstrasse 16, 09221 Adorf, Germany
www.nordmetall.net
lothar.meyer@nordmetall.net
*michael.mayer@nordmetall.net

ABSTRACT

A new strain rate dependent material and failure model referred to as the M^2C Model was generated suitable for modeling the static and dynamic material behavior of fiber reinforced composites. The M^2C consists of an orthotropic viscoelastic constitutive model in combination with an enhancement of the Failure Mode Concept (FMC) of Cuntze for dynamic loading conditions and was implemented into the finite element Code LS-DYNA3D as user defined material model. A [0°|90°] glass fiber reinforced composite was investigated under different types of loading and loading directions within seven orders of magnitude of strain rate. The finite element results are compared with experimental results. In the principal loading directions and under arbitrary loading conditions an impressing agreement was achieved.

1 INTRODUCTION

Due to their excellent mechanical properties Fiber Reinforced Composites (FRC) are applied in a wide and growing field of applications, e.g. avionic industry, sports industry, ballistic protection etc. In the last decades the dimensioning and design processes of composite structures are increasingly based on numerical methods. It is generally known that the material behavior of FRC is dependent on the loading direction and on the rate of strain [1-3]. For isotropic materials the strain rate dependent material behavior is often investigated and known and high quality databases can be found in the literature. Compared to isotropic metallic materials constitutive modeling of FRC is more complex. For anisotropic materials complete and high quality investigations of the strain rate dependent material behavior are rare. Due to the different components of fibers and matrices and the different laminate layups a direct comparison to the material behavior of fiber reinforced composites is difficult. For isotropic materials many constitutive models are implemented in finite element analysis codes whereas only simple constitutive material and failure models are available for anisotropic materials.

For close to reality structural numerical simulations profound and high sophisticated strain rate dependent material and failure models are required. In this report a new strain rate dependent material and failure model for fiber reinforced composites the, so called M^2C model, will be presented.

2 MATERIAL BEHAVIOR AND CONSTITUTIVE MODELING

For fiber reinforced composites different principal strategies for constitutive modeling are used which can be separated into micro and macro mechanical based models, Fig. 1.

On the micro mechanical level the different components (fibers, resin, interface) are treated separately. The anisotropic structural behavior is achieved by combination of several isotropic material models with its appropriate geometric constraints. Well known strategies for modeling the anisotropic material behavior on the micro level are known in the literature for example the Method of Cells (MoC) from Aboudi [4, 5], or the Representative Volume Model [6]. Micro mechanical material models are less suited for modeling the global structural answer of a composite part due to the immense numerical effort. Furthermore, the strain rate dependent behavior of the components must be known. The experimental investigation of the constitutive parameters are difficult and often not unique.

T. Proulx (ed.), *Time Dependent Constitutive Behavior and Fracture/Failure Processes, Volume 3*, Conference Proceedings of the Society for Experimental Mechanics Series 15, DOI 10.1007/978-1-4419-9794-4_24, © The Society for Experimental Mechanics, Inc. 2011

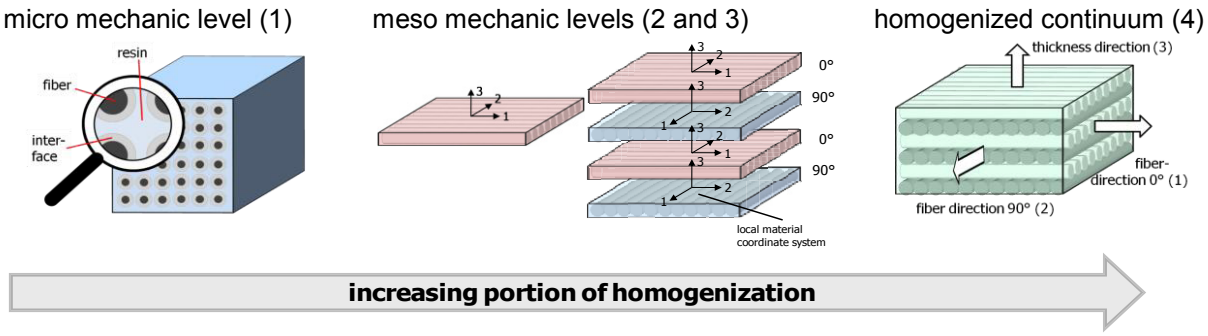

Fig. 1: Different scales of modeling for fiber reinforced composites (FRC).

The meso mechanic level is obtained by homogenizing the material properties in one composite layer or multiple separated layers, in which the anisotropic material properties have to be directly included in the constitutive formulations. A furthermore smearing over two or more composite layers leads to the homogenized continuum. For the meso mechanic level or the homogenized continuum different theoretical continuum based approaches can be found in the literature. The variety of available material models in the literature is immense so only the basic theoretical approaches can be summarized. Viscoelastic material models are generally used to describe the long time material behavior or the material behavior under cyclic loading. Viscoplastic material models are often used to model the strain rate dependent material behavior of composites under off-axis loading. From experimental tests the calculation of the constitutive parameters is considerable easier and unique. Material models in the meso scale or based on the homogenized continuum are suited for modeling and calculating the structural material answer of composite parts.

In Fig. 2 the principal strain rate dependent material behavior of a [0°|90°] glass fiber reinforced composite in different loading directions is summarized.

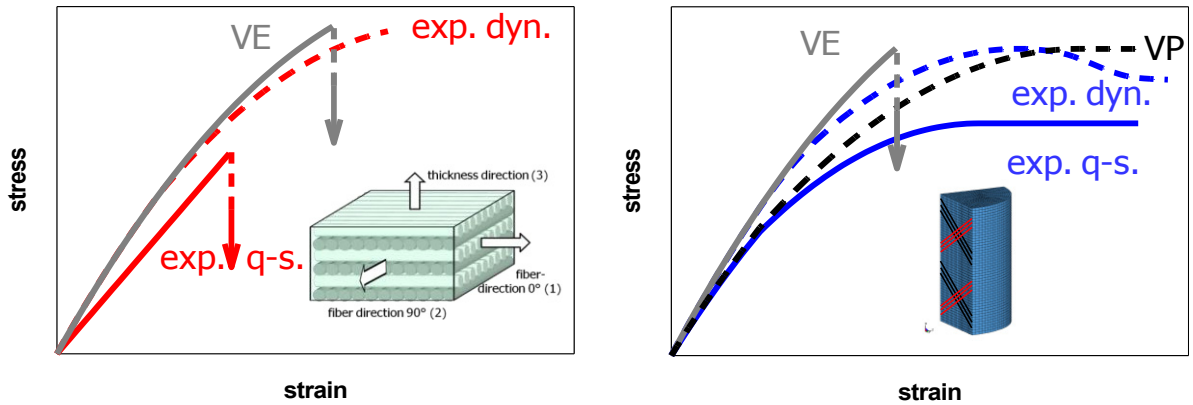

Fig. 2: Principal strain rate dependent material behavior of a [0°|90°] glass fiber reinforced composite in different loading directions.
(a) principal stress-strain curves in fiber-, thickness direction and under interlaminar shear loading.
(b) principal stress-strain curves under intralaminar shear loading.

Under quasi-static compression loading, the material behavior is linear-elastic until failure (exp. q-s.), Fig. 2a. the Young's modulus increases with increasing strain rate. Under dynamic loading higher stresses are measured compared to quasi-static loading. Also the compression strength increases under high strain rate loading. The depicted principal stress-strain behavior in Fig. 2a is measured in fiber direction, thickness direction and under interlaminar shear loading and can very accurately be modeled with viscoelastic (VE) material models. Viscoplastic (VP) material models are used to describe time dependent flow processes of materials. When the material behavior under quasi-static loading conditions is purely elastic, e.g. in fiber direction, plastic flow is excluded in the constitutive equation. In these loading directions the stress-strain behavior is independent on strain the rate of strain.

The material behavior in Fig. 2b is typical for a intralaminar shear loading of a [0°|90°] reinforced composite (±45° to the fibers). The material obeys a distinct non-linear stress-strain behavior under quasi-static and dynamic loading conditions due beginning and successive growing internal damage mechanisms at small strains. Large shear deformations up to 0.2 with remarkable shear stresses are reached. The intralaminar Shear modulus is less strain rate dependent compared to loading in fiber direction. For modeling the global material behavior under intralaminar shear loading viscoplastic (VP) constitutive models are suited. Viscoelastic models are less suited because the plastic material behavior can not be described.

Considering all different main loading directions it can be ascertained that viscoelastic material models are in general best suited to describe the strain rate dependent material behavior of fiber reinforced composites.

3 DEVELOPMENT OF THE M²C MODEL

3.1 Constitutive orthotropic viscoelastic material model

The M²C model is a combined strain rate dependent constitutive material and failure model. The constitutive model is based on an orthotropic viscoelastic formulation. With the assumption of the Boltzmann Superposition principle a continuous stress history can be formulated with a hereditary-integral

$$\sigma_{ij}(t) = \int_{\tau=0}^{\tau=t} \frac{d\varepsilon_{kl}(\tau)}{d\tau} \cdot G_{ijkl}(t-\tau) \cdot d\tau \tag{1}$$

where σ_{ij} is the stress tensor and ε_{kl} is the strain tensor. G_{ijkl} includes the material properties and is referred to as the relaxation function. The relaxation function consistent with the “fading memory hypothesis” can be written in form of a Prony series where the $\lambda^n = \frac{\eta_n}{G^n}$ are the relaxation times.

$$G_{ijkl}(t) = G_{ijkl}^{\infty} + \sum_{n=1}^{N} G_{ijkl}^{n} \exp\left(-\frac{t}{\lambda^n}\right) \tag{2}$$

This formulation is equivalent to a generalized Maxwell model. Insertion of equation (2) in (1) and an arbitrary strain history leads to the stresses

$$\sigma_{ij}(t) = G_{ijkl}^{\infty}\,\varepsilon_{kl}(t) + \sum_{n=1}^{N}\left[G_{ijkl}^{n}\,\varepsilon_{kl}(t) + \frac{-G_{ijkl}^{n}}{\lambda^n}\int_0^t \varepsilon_{kl}(\tau)\exp\left(-\frac{(t-\tau)}{\lambda^n}\right)d\tau\right] \tag{3}$$

Equation (3) contains the complete strain history and is therefore not suited to be implemented into a finite element analysis code. A transition to calculate the stress increment $\Delta\sigma_{ij}(t_m)$ due to a strain increment $\Delta\epsilon_{ij}(t_m)$ with the time step size $h = t_m - t_{m-1}$ leads finally to

$$\Delta\sigma_{ij}(t_m) =$$

$$G_{ijkl}^{\infty}\,\Delta\varepsilon_{kl}(t_m) + \sum_{n=1}^{N}\left\{G_{ijkl}^{n}\,\Delta\varepsilon_{kl}(t_m) + \frac{\lambda^n}{h}\left[1-\exp\left(\frac{-h}{\lambda^n}\right)\right] - \left[1-\exp\left(\frac{-h}{\lambda^n}\right)\right]\sigma_{ij}^{n}(t_{m-1})\right\} \tag{4}$$

The total stress increment due to an arbitrary strain history is now dependent on the

- elastic stress increments
- viscoelastic stress increments in the time step including their partial relaxation
- viscoelastic stresses of the previous time step $\sigma_{ij}^{n}(t_{m-1})$ with corresponding relaxation

Equation (4) is implemented as user defined material model into the finite element code LS-DYNA3D. The Number of Maxwell branches was chosen with $N = 6$. From experimental tests the values for the relaxation times were fixed with $\lambda_1 = 0{,}7 \cdot 10^{-1}$ s … $\lambda_6 = 0{,}7 \cdot 10^{-6}$ s.

3.2 Development of a strain rate dependent Failure Model suited for FRC

In literature for anisotropic materials approximately 1000 different failure models are known. They can be divided into mathematical and physically based formulations and are formulated for the unidirectional layer of a FRC. The ancestor of all anisotropic failure models was Hill (1948), [7]. In the following decades many mathematical based failure criterions have been developed, amongst others Tsai-Hill, Hoffmann and the well known Tsai-Wu failure criterion. The advantage of all these failure models is their simplicity. Only one single equation has to the solved. All fracture events are treated similar and no information about the occurring failure mode can be concluded leading to imprecise calculations of the material strength.

With physically based failure models a better strength evidence of FRC has been achieved because the different failure conditions are considered separately. Hashin [8] is regarded as the ancestor of all physically based failure criterions. The World Wide Failure Exercise (WWFE) in 1998 showed that the new "action plane failure model" of Puck [9] and the Failure Mode Concept (FMC) of Cuntze [10-12] are the best suited failure models for unidirectional layers of FRC under quasi-static loading [13]. The FMC of Cuntze is a global failure criterion based on irreducible tensor invariants and separates five different failure modes, Fig. 3 (a) and 3(b). Each failure mode is related to one failure mechanism and one material strength value. The formulation of the FMC is equivalent to a "series failure system model" accumulating the adjacent so called Stress Efforts of each interacting failure mode to the total Stress Effort. The failure envelope of a unidirectional glass fiber reinforced layer in the $\sigma_2 - \tau_{21}$ stress space is presented in Fig. 3 (c) with the appropriate constitutive formulation where the parameter m represents a material dependent interaction coefficient. Failure occurs when the total Stress Effort is greater than 1.0.

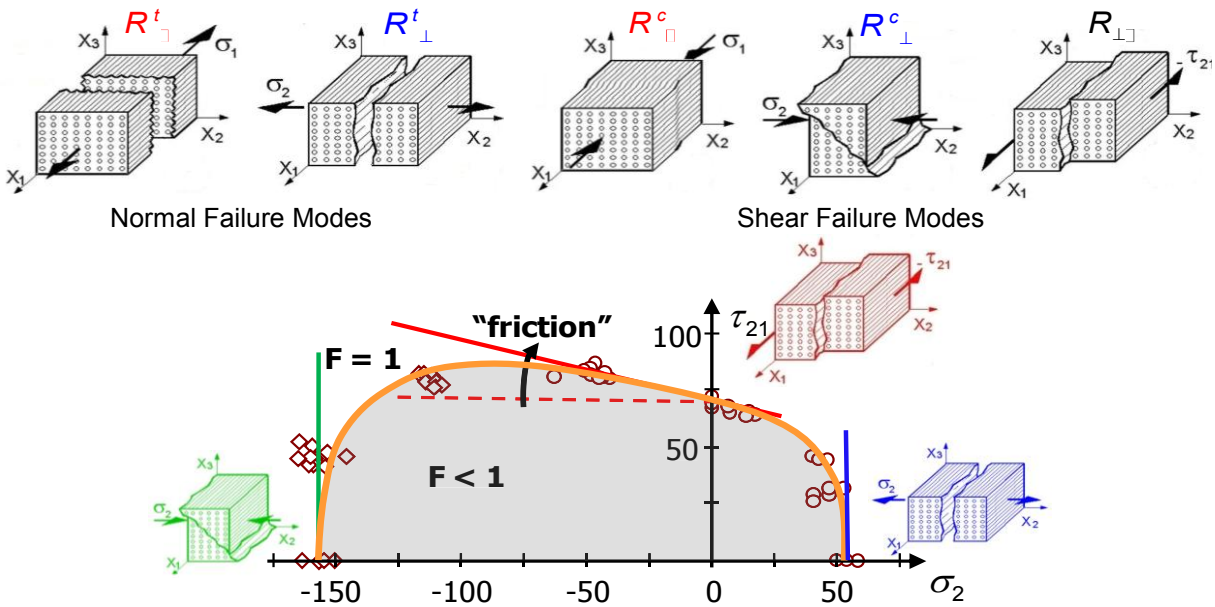

Failure envelope in the $(\sigma_2 - \tau_{21})$ stress space

Fig. 3: Normal and Shear Failure Modes in a unidirectional FRC layer and resulting FMC failure envelope in the $(\sigma_2 - \tau_{21})$ stress space under quasi-static loading after Cuntze.

The FMC, formulated for a single unidirectional layer, was generalized by Cuntze for orthotropic fabric materials and separates nine different failure modes. The FMC for orthotropic fabrics was extended by Mayer and Meyer [14-16] for multidirectional layers to model the strain rate dependent material strength behavior. The strain rate dependent FMC is implemented as user defined subroutine into the finite element code LS-DYNA3D.

In figure 4 the principal strain rate dependent material strength of the [0°|90°] glass fiber reinforced composite in the $(\sigma_3 - \tau_{31})$ stress space is presented. It is obvious that the principal strength in thickness direction $\bar{R}_3$ and the interlaminar shear strength $\bar{R}_{31}$ increase under high strain rate loading and the material fails when the strain rate dependent total Stress Effort reaches the value of 1.0. Three different failure modes occur, interlaminar tension failure (delamination), interlaminar shear failure and compression failure in thickness direction. From experimental

investigations the material strength in all principal loading directions is known in a functional dependency of strain rate.

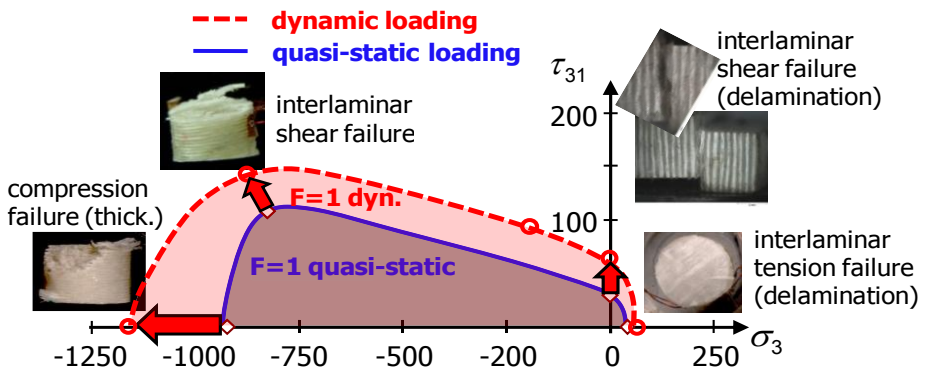

$$Eff^m = \sum \left(Eff^{(mode)}\right)^m$$

$$= \left(\frac{\sigma_1 + |\sigma_1|}{2\bar{R}_1^t}\right)^m + \left(\frac{-\sigma_1 + |\sigma_1|}{2\bar{R}_1^c}\right)^m + \left(\frac{\sigma_2 + |\sigma_2|}{2\bar{R}_2^t}\right)^m + \left(\frac{-\sigma_2 + |\sigma_2|}{2\bar{R}_2^c}\right)^m + \left(\frac{\sigma_3 + |\sigma_3|}{2\bar{R}_3^t}\right)^m$$

$$+ \left(\frac{-\sigma_3 + |\sigma_3|}{2\bar{R}_3^c}\right)^m + \left(\frac{\tau_{12}^2}{\bar{R}_{12}^2}\right)^m + \left(\frac{|\tau_{23}|}{\bar{R}_{23} - \mu_{23} \cdot \sigma_3}\right)^m + \left(\frac{|\tau_{31}|}{\bar{R}_{31} - \mu_{31} \cdot \sigma_3}\right)^m = 1$$

Fig. 4: Extension of the FMC by Mayer and Meyer. Principal strain rate dependent material strength in the $(\sigma_3 - \tau_{31})$ stress space and FMC formulation implemented into LS-DYNA3D.

The M^{2}C-Model is the combination of the orthotropic viscoelastic constitutive model and the strain rate dependent FMC. In addition a dynamic enhancement of the Hill model referred to as the M^{2}H model was also implemented into the finite element code LS-DYNA3D.

4 Material Testing

The strain rate dependent mechanical behavior of a [0°|90°] glass fiber reinforced material was investigated within seven orders of magnitude of strain rate from quasi-static loading ($\dot{\varepsilon} = 10^{-4}\, s^{-1}$) to impact rates of strain ($\dot{\varepsilon} = 10^{3}\, s^{-1}$) in the principal loading directions which are denoted as fiber direction(s), thickness direction, under intra- and interlaminar shear loading. For quasi-static and quasi-dynamic material testing a universal and a servo-hydraulic testing device were used. The dynamic material behavior at $\dot{\varepsilon} \approx 100\, s^{-1}$ and $\dot{\varepsilon} \approx 10^{3}\, s^{-1}$ were performed using a drop weight tower, Fig. 5 and a Split-Hopkinson-Pressure Bar. Cylindrical specimen with an aspect ratio of L/D =1.0 were tested. For interlaminar shear loading a special shear hat specimen was applied. The specimens were instrumented with strain gages. The interlaminar shear deformation was measured with a high-speed electro-optical extensometer, Fig. 6.

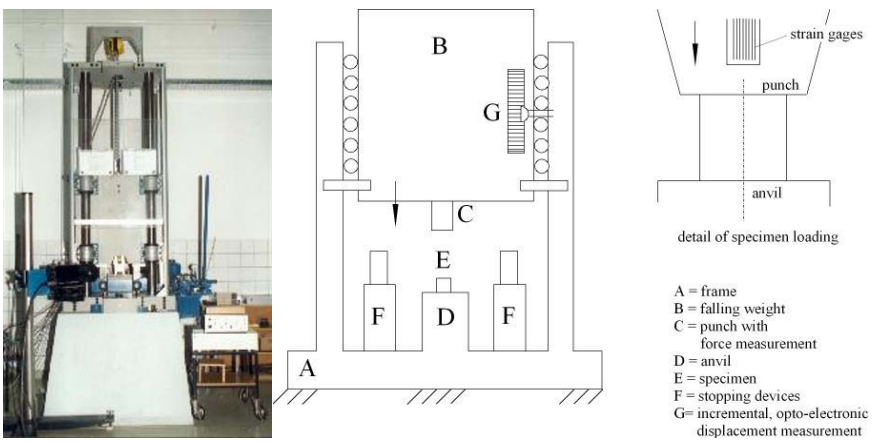

Fig. 5: Drop weight tower and schematic diagram, Nordmetall GmbH.

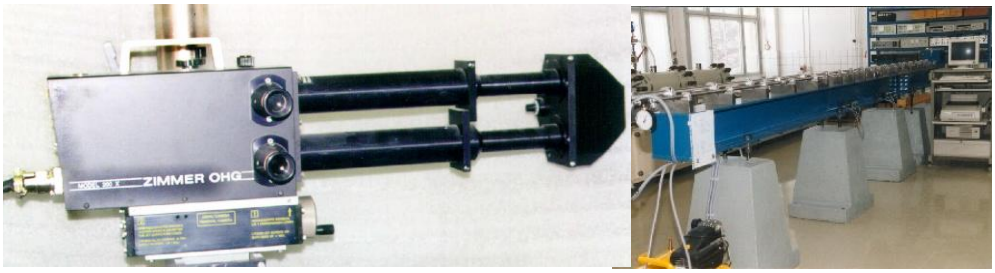

Fig. 6: Electro-optical extensometer and Split Hopkinson Pressure Bars, Nordmetall GmbH.

5 RESUTLS AND DISCUSSION

5.1 Experimental results: Material behavior in fiber direction

The strain rate dependent material behavior in fiber direction under compressive loading is presented in Fig. 7. The material behavior under quasi-static loading is linear-elastic until failure. Three strain rate effects can be observed. The Young's modulus increases with increasing strain rate from 34.3 GPa under quasi-static loading of approximately +55% up to 53 GPa at stain rates of $(\dot{\varepsilon} \approx 1000\ s^{-1})$. With increasing strain rate the slope of the stress strain curves in the nonlinear region decreases stronger with increasing strain and strain rate. The compressive strength in fiber direction increases in the order of approximately +90% compared to quasi-static loading.

The failure of the material begins when damage between the fibers and the resin occurs. This leads to a local kinking of fibers and fiber bundles resulting in a local micro delamination. The so called micro-shear buckling mechanism recurs in adjacent layers so that on the global scale an interlaminar shear band occurs inclined at 45° to the loading direction. The wedge effect induces global delamination.

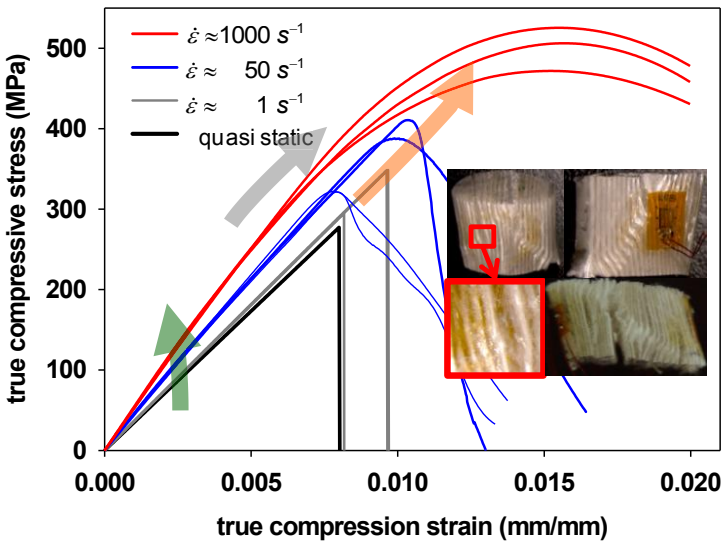

Fig. 7: Strain rate dependent material behavior in fiber direction under compressive loading and specimen after testing

5.2 FEA results in comparison with experimental test data

The constitutive material parameters in all the principal loading directions are calculated from the viscoelastic overstresses compared to the quasi-static stress-strain curves with a least squares fitting procedure. The experimental tests in the principal loading directions are simulated using the strain rate dependent M^2C model within LS-DYNA3D and compared to the experimental test data.

In order to check the accuracy of the M^{2}C model the experimental tests have been simulated with the finite element code LS-DYNA3D. Therefore, exact numerical models of the testing devices are generated. The numerical results are compared with the experimental test data. Fig. 8 depicts the static and dynamic material behavior in fiber direction. The constitutive parameters are summarized in table 1.

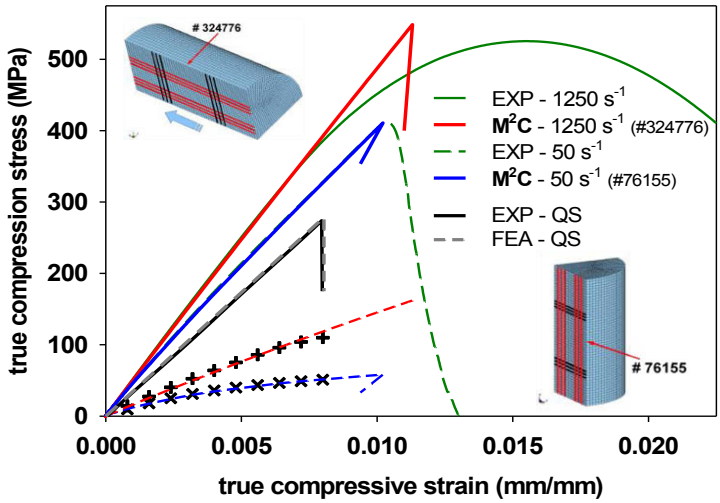

Fig. 8: FEA results with the M^{2}C model in fiber direction at different rates of strain compared to experimental test data.

The numerically calculated stress-strain curve in fiber direction of the experimental test in the drop weight tower at strain rates of $\dot{\varepsilon} = 50\ s^{-1}$ can excellently be represented with the M^{2}C model. At strain rates of $\dot{\varepsilon} = 1250\ s^{-1}$ the calculated stress strain curve at strains $\varepsilon > 0.006$ is nearly linear until failure compared to the experimentally measured material behavior. In the experiment, onsetting internal damage mechanism and beginning failure are leading to a slightly declining stress-strain-curve. Fig. 9 shows the viscoelastic overstresses compared to the quasi-static loading case.

The M^{2}C model is perfectly suitable to describe the strain rate dependent compressive strength, within a deviation of less than 3% compared to the real test, table 1.

Table 1: Constitutive parameters in fiber direction. Comparison experiment with the M^{2}C Model.

Fiber direction	**Compression test, $\dot{\varepsilon}$=50 s^{-1}**		**Compression test, $\dot{\varepsilon}$=1000 s^{-1}**	
	E_1 [GPa]	**Strength [MPa]**	**E_1 [GPa]**	**Strength [MPa]**
Experiment	46.2	415	55	527
M^{2}C (FEA)	46.8	403	50.5	534
Delta [%]	+1.3	-2.9	-8.2	+1.3

In thickness direction and under interlaminar shear loading the M^{2}C model is suitable to represent the strain rate dependent material and strength behavior in similar accordance compared to the results of the experimental tests. Due to the distinct nonlinear material behavior under intralaminar shear loading the M^{2}C model is only capable to represent the dynamic shear stress-shear strain at small shear strains because plastic deformation cannot be depicted within a viscoelastic constitutive equation. But the M^{2}C model is suited to predict the strain rate dependent intralaminar shear strength in good accordance to the experimentally measured material behavior.

5.3 Validation of the M²C Model with 10° and 80° out of plane off axis tests

With previously unknown dynamic loading conditions the accuracy of the M²C model is validated. Two cylindrical out of plane off-axis specimen with fibers inclined 10° and 80° to the loading direction are tested in the drop weight tower. A combination of stresses in fiber and thickness direction with superimposed interlaminar shear stresses occurs in the specimen. The numerical calculated and experimentally measured material behavior with a fiber orientation of 80° to the loading direction is presented in Fig. 9. In order to point out the differences of the new developed strain rate dependent physically based M²C model to a second new mathematically based strain rate dependent Hill criterion referred to as M²H model was generated. Both material strengths are depicted in Fig. 9.

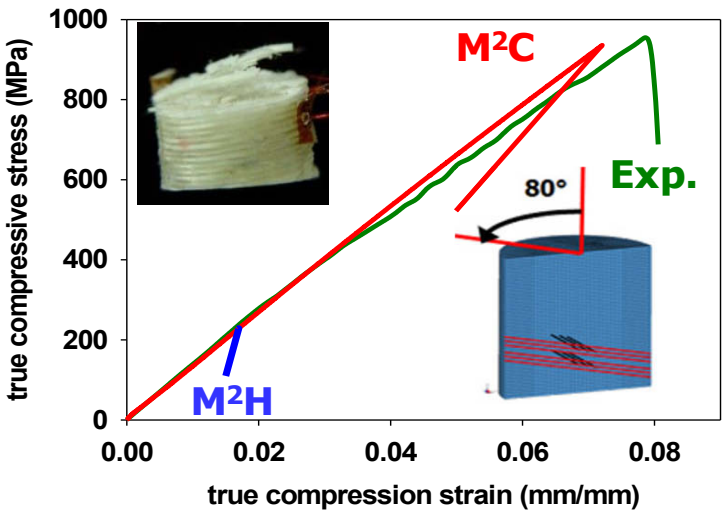

Fig. 9: Material behavior under dynamic out of plane off-axis loading with fibers inclined 80° to the loading direction. Comparison of M²C model with experiment.

Even under previously unknown dynamic loading conditions an excellent agreement between the M²C model and the experiment is obvious. The developed M²C model is capable to predict precisely the onset of failure under combined compression in thickness direction with superimposed interlaminar shear loading. The specimen show an interlaminar shear failure. The dynamic Hill failure criterion in the M²H model predicts a material strength which is 76% lower than the real test because internal frictional effects that increase the material strength are only included in the physically based M²C model, see also Fig. 3 and Fig.4.

This comparison shows that the M²C model is suitable to describe the material behavior and the onset of failure under arbitrary loading conditions.

5.4 Specific features of the new developed physical based M²C Model

Physically based failure models exhibit the advantage that they provide detailed information about the failure position and the occurring failure mode. The strain rate dependent material behavior under interlaminar was investigated with a rectangular interlaminar shear hat specimen. The M²C model is capable to separate all nine possible occurring failure modes in multidirectional laminates. Figure 10 depicts the Total Stress Effort and dominant failure modes in the specimen at maximum load tested at a shear strain rate of $\dot{\gamma} \approx 120\, s^{-1}$ and the corresponding orientation of the fibers. For the failure of the specimen two failure modes tension failure in thickness direction (delamination) and interlaminar shear failure are dominant.

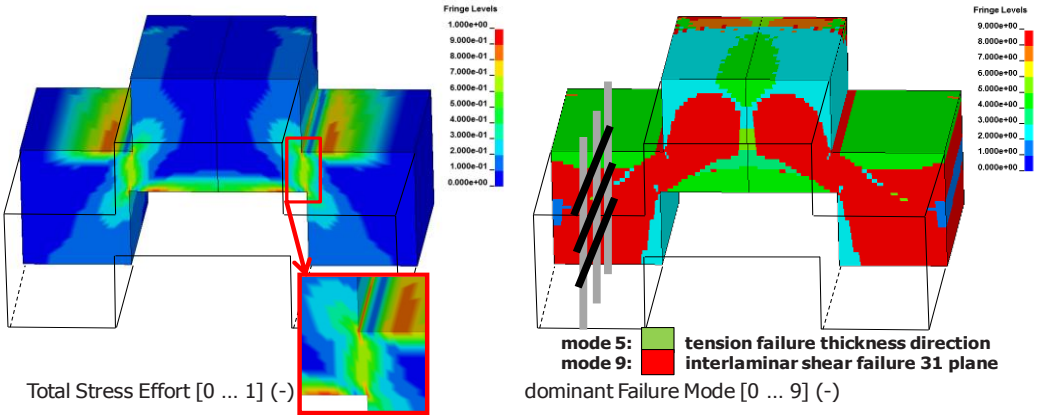

Fig. 10: Total Stress Effort and dominant failure mode in a rectangular shear hat specimen.

The corresponding dominant failure mode (equivalent to the maximum value of the particular stress efforts) indicates a shear failure mode. The new M^2C model assures the precise prediction of the failure position and the occurring failure mode. This feature is essential for designing and dimensioning processes.

6 SUMMARY

A new orthotropic viscoelastic constitutive material model in combination with a new physical based strain rate dependent failure model referred to as the M^2C model, was developed and implemented into the finite element code LS-DYNA3D. The static and dynamic material behavior of a [0°|90°] glass fiber reinforced composite was investigated under different types of loading and within seven orders of magnitude of strain rate from $\dot{\varepsilon} = 10^{-4}$ s^{-1} to $\dot{\varepsilon} = 10^{3}$ s^{-1}. The numerical results of the M^2C model in the principal loading directions show an excellent accuracy compared to the experimental test data.

A validation of the M^2C model under previously unknown dynamic loading conditions was successful. It can be concluded that the presented model allows for close to reality calculations of the strain rate dependent material behavior and a precise prediction of the strain rate dependent onset of failure. Simultaneously, the M^2C model ensures the precise prediction of the failure position and the occurring failure modes in structural parts made of fiber reinforced composites.

REFERENCES

[1] Song, B.; Chen, W.; Weerasooriya, T.: Quasi-static and dynamic Compressive Behavior of a S-2 Glass/SC15 Composite, Journal of Composite Materials 37 (2003), p. 1723-1743, 2003.

[2] Harding, J.: Effect of strain rate and specimen geometry on the compressive strength of woven glass-reinforced epoxy lamainates, Composites 24 (1993), Vol. 4, p. 323-332, 1993.

[3] Tasdemirci, A.; Hall, I. W.: Numerical and experimental studies of damage generation in a polymer composite material at high strain rates. In: Polymer Testing 25 (2006), p. 797-806.

[4] Aboudi, J.: A continuum theory for fiber reinforced elastic-viscoplastic composites. Int. J. Eng. Sci. 20 (1982), Vol. 5, p. 605-621, 1982.

[5] Aboudi, J.: Effective constitutive equations for fiber reinforced viscoplastic composites exhibiting anisotropic hardening. Int. J. Eng. Sci. 21 (1983), Vol. 9, p. 1081-1096, 1983.

[6] Bennett, J. G., Habermann, K. S.: An Alternate Unified Approach to the mechanical Analysis of Composite Materials, J. Compos. Mater. 30 (1996), Vol. 16, p. 1732-1747, 1996.

[7] Hill, R.: A theory of the yielding and plastic flow of anisotropic materials, Proc. Roy. Soc. London 193 (1948), Vol. 1033, p. 281-297, 1948.

[8] Hashin, Z.: Failure criteria for unidirectional fiber composites, Journal of Applied Mechanics 47 (1980), p. 329-334, 1980.

[9] Puck, A.: Festigkeitsanalsyse von Faser-Matrix-Laminaten: Modelle für die Praxis. Carl Hanser Verlag München Wien, 1996.

[10] Cuntze, R. G.: The Failure Mode Concept - A New Comprehensive 3D-Strength Analysis Concept for any Brittle and Ductile behaving Material. Proceedings European Conference on Spacecraft Structures, Materials and Mechanical Testing, Braunschweig, 4. - 6. Nov. 1998 (ESA SP 428, Feb. 1999), European Space Agency, 1998.

[11] Cuntze, R. G.; Freund, A.: The predictive capability of failure mode concept-based strength criteria for multidirectional laminates. Comp. Sci. Tech. 64 (2004), p. 343-377, 2004.

[12] Cuntze, R. G.: The predictive capability of failure mode concept-based strength criteria for multidirectional laminates. Part B., Compos. Sci. Tech. 64 (2004), p. 487-516, 2004.

[13] Soden, P. D.; Kaddour, A. S.; Hinton, M. J.: Recommendations for designers and researchers resulting from the world-wide failure exercise. Comp. Sci. Tech. 64 (2004), p. 589-604, 2004.

[14] Mayer, M.: Modellierung des statischen und dynamischen Materialverhaltens faserverstärkter Kunststoffe, PhD. Thesis, TU Chemnitz 2010, to be published.

[15] Meyer, L. W.; Mayer, M.: Static and dynamic material behavior of fiber reinforced composites – Modeling and Testing, Presentation at the International Symposium on Plasticity 2009, St. Thomas, U.S. Virgin Islands, January 3-8, 2009.

[16] Mayer, M.: Modellierung des statischen und dynamischen Werkstoffverhaltens faserverstärkter Kunststoffe, Presentation at the 5th Nordmetall Kolloquium, 2.-3.12.2009, Adorf, 2009.

Proceedings of the SEM Annual Conference
June 7-10, 2010 Indianapolis, Indiana USA

Effect of Crystallinity and fiber volume fraction on Creep Behavior of Glass Fiber Reinforced Polyamide

Takenobu SAKAI [a], Yuto HIRAI[b] and Satoshi SOMIYA [b]
a Tokyo Metropolitan University, 1-1, Minami-Osawa, Hachioji, Tokyo, 192-0397, Japan
b Keio University, 3-14-1Hiyoshi kohoku-ku Yokohama Kanagawa, 223-8522, Japan

ABSTRACT Thermoplastic Polyamide (PA) is known as Nylon®, and its FRP are one of the engineering plastics. It is very important for them to reveal accurately the visco-elastic behavior. Furthermore, PA is a crystalline polymer, and it is necessary to consider the effect of crystallization on mechanical properties. The purpose of this study was to make clear the effect of crystallization and fiber volume fraction on creep behavior of PA and its composites. The creep test was performed using the materials which adjusted crystallinity on each fiber volume fraction. As a result, these materials conformed to Arrhenius type of time-temperature superposition principle, and these effects on creep behavior had the time retardation effect. To compare the creep behavior on these effects, we made the grand master curves for crystallinity and fiber volume fraction. Obtained two grand master curves were compared each other, the shapes of these curves are similarly, and we can superposed them. It is therefore, the creep behavior including each conditions have the same behavior. Using these curves and shift factors, we can calculate the creep behavior, and be able to estimate the creep behavior with the effect of arbitrary time, temperature, crystallinity and fiber contents.
Key words: *Polyamide, Creep analysis, Time-temperature superposition principle, Polymeric Composites, Crystallization, Crystallinity*

Introduction

Polyamide (PA) is known as Nylon® and used in many fields of human being. Some PA is used as a string for the operation and some PA is used in the field of mechanical engineering. In our living life, it is important that we keep the reliability of materials, and we have to consider about the creep behavior of materials. Creep behavior can be described in terms of visco-elastic behavior. Since this behavior greatly influences the reliability of structures, it is very important to understand and control in materials design. Plastics and their FRP's are used in various environments; it must be comprehended about the influence factors on creep behavior. The influence factors on creep behavior are, for example, time, temperature, fiber contents on composites, crystal of polymers occurred by the molecular chains rearranged and so on. These factors were researched by many researchers. Previous studies have investigated the effects of fiber contents on the creep behavior of polycarbonate (PC), glass fiber reinforced-polycarbonate (GFRPC), poly (propylene-co-ethylene) (PPE) composites, and Carbon fiber reinforced thermoplastics as polyamide [1-5]. The effect was shown to be equivalent to the strengthening of the resin matrix. The effect of crystallinity on creep behavior was researched, too [6-8].

In our previous research [9-14], it became clear that the effects of influence factors, which are physical aging, fiber volume fraction, crystallinity and crystal grain size, on creep behavior. These effects have been enabled to describe as the value of shift factors which was calculated from making master curves of these factors. These shift factors shows the retardation effect on creep time by the influence factors. It was revealed that the effect of the crystallinity and the fiber contents has a similar influence on the creep behavior. Therefore, the purpose of this study is to expand the possibility of a new material design by understanding the relation between the crystallinity and the fiber contents, and to analyze the creep behavior of PA that considers fiber contents and crystallinity.

Linear visco-elastic theory

Creep deformation was evaluated according to visco-elastic theory using the creep compliance function $D_C(t)$. This value is based on the linear visco-elastic equation for creep strain as follows:

$$\varepsilon(t) = \int_0^t D_C(t-\tau, T)\frac{d\sigma}{d\tau}d\tau \quad (1)$$

where, $\varepsilon(t)$ shows the temporal response of the amount of creep strain, and $D_C(t,T)$ shows the temporal response of the creep compliance at temperature T with external force acting.

T. Proulx (ed.), *Time Dependent Constitutive Behavior and Fracture/Failure Processes, Volume 3*, Conference Proceedings of the Society for Experimental Mechanics Series 15, DOI 10.1007/978-1-4419-9794-4_25, © The Society for Experimental Mechanics, Inc. 2011

By the way, in order to calculate creep deformation based on a visco-elastic theory, it is necessary to determine $D_C(t)$ of the time region ranging from several seconds to several years on all temperature conditions, but it is actually difficult. Therefore, time-temperature superposition principle is used for accelerated test. To make the master curve of creep compliance can describe the creep behavior of long region. To produce a master curve of creep compliance, the creep compliance curves were shifted horizontally until they completely overlapped the curve of the reference temperature. Then the shift factors were gotten by making a master curve and it shows the amount of shifting and the retardation effect on time. In this study, because it is assumed that this superposition principle can be also applied to other influence factors than temperature, the creep analysis based on the time-temperature superposition principle was carried out.

Materials and Experimental Procedure

PA (LEONA1300S) and GFRPA (15G15, 1300G) were used and they were made by Ashahikasei Co. Ltd., (Japan). The weight fractions (volume fractions) for the glass fiber used as test specimens were 0% (0%), 15% (7%) and 33% (15%), which are denoted hereafter as G0, G7 and G15, respectively. The dimension of specimens is 60×10×2.5mm. It was reported that the crystallinity can be adjusted by heat treatment with changing the holding temperature and time [15], [16]. In this study, the crystallinity of the PA and GFRPA was adjusted by changing the heat treatment time from 0 to 10 hours.

A densimetry test performed to calculate the crystallinity of materials. Densimetry test was carried out using the water substitution method by AX-120 analytical balance (SHIMADZU, Co., Ltd.,). The crystallinity was calculated by using the following equation (2) from the obtained density.

$$x = \frac{d_c\left(d_m - d_a\right)}{d_m\left(d_c - d_a\right)} \tag{2}$$

X : crystallinity (%)
d_c : crystalline density(1.24kg/m^3)
d_a : amorphous density(1.09kg/m^3)
d_m : material density

In case of GFRPA, the density only of the resin was calculated from the density of the composite by using the following equation (3).

$$d = d_f V_f + d_m V_m \tag{3}$$

d : composite density
d_f : fiber density(2.57kg/m^3)
d_m : material density (matrix density)
V_f : fiber volume fraction

Three points bending test was performed to examine mechanical properties of the material. Used three points bending test machine was TCM-5000C made by MINEBEA Co., Ltd., which is universal materials testing machine of Instron type. The cross head speed was 0.5mm/min. The span length was 40mm.

Three-point bending creep test was carried out in silicon oil surroundings using Temperature Deflection under Loading Machine, HDT VSPT Tester S-3M (TOYOSEIKI Co., Ltd.,). The span length is 40mm. The applied loads were 10% load of their static bending strengths measured by three points bending test. The test temperatures were 40, 50, 60, 70 and 80ºC, and test time is 1000min. Struik recommended producing master curves from momentary creep data only, i.e., from creep test data such that $t_t \le t_a/10$, where t_t is the test time and t_a is the length of the aging treatment. Based on this recommendation, the creep test performed after heat treatment for t_a ($10 \times t_t$) is called the short term method. Using this method, the results of the creep test differ slightly according to the effect of physical aging. However, we don't need to consider the effect of physical aging during creep test.

The effect of crystallinity on the creep behavior of PA and GFRPA

Previous reports [17], [18] have the results of the creep behavior on them including the effect of time, temperature,

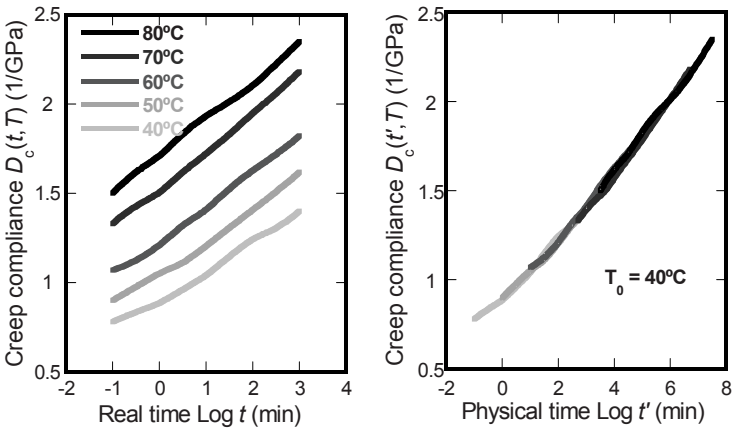

Fig. 1 (a) Creep compliance curves and (b) their master curve of PA (crystallinity χ = 33%)

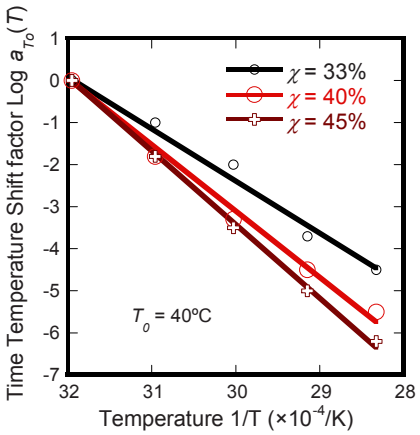

Fig. 2 Time-temperature shift factors of PA with various crystallinity (Reference curve: 40ºC)

fiber contents. These reports were discussed the application of the time-temperature superposition principle on PC and GFRPC. In those reports, the grand master curve of creep compliance was discussed, and the effect of fiber contents on creep behavior showed the retardation effect on time. In this study, to understand the effect of crystallinity on creep behavior of PA and GFRPA, creep test was carried out with the elevated temperature.

We performed the three-point bending creep test using the short term method on PA and GFRPA at various elevated temperatures. To clarify the creep phenomena, creep compliance curves were drawn for each test temperature. The creep compliance curves of PA (Crystallinity: χ = 33%) are presented in Fig. 1(a), which shows that a greater test temperature and increased creep test time resulted in higher creep compliance. To discuss the application of the time–temperature superposition principle, the master curve of creep compliance is given in Fig. 1(b), for a reference temperature of 40ºC. To produce the master creep compliance curve, the creep compliance curves were shifted horizontally until they overlapped the curve for the reference temperature completely. The master curve was obtained by replacing the real time t for each shifted curve by the physical time t' at the reference temperature T_0. The amount of the shift required to create the master curves is called the time–temperature shift factor. The shift factor curve for PA is plotted as an Arrhenius-type plot in Fig. 2. This curve is a straight line at temperatures above 40ºC, demonstrating that the creep phenomenon complies with the time–temperature superposition principle in Arrhenius mode. And other PAs have different crystallinity and GFRPA have the same tendency as PA, the time-temperature superposition principle in Arrhenius mode was applied on every specimen.

Next, to confirm the effect of crystallinity on creep behavior, every master curve of PA were shown on the same graph in Fig. 3(a). It shows that a less crystallinity and increased creep test time resulted in higher creep

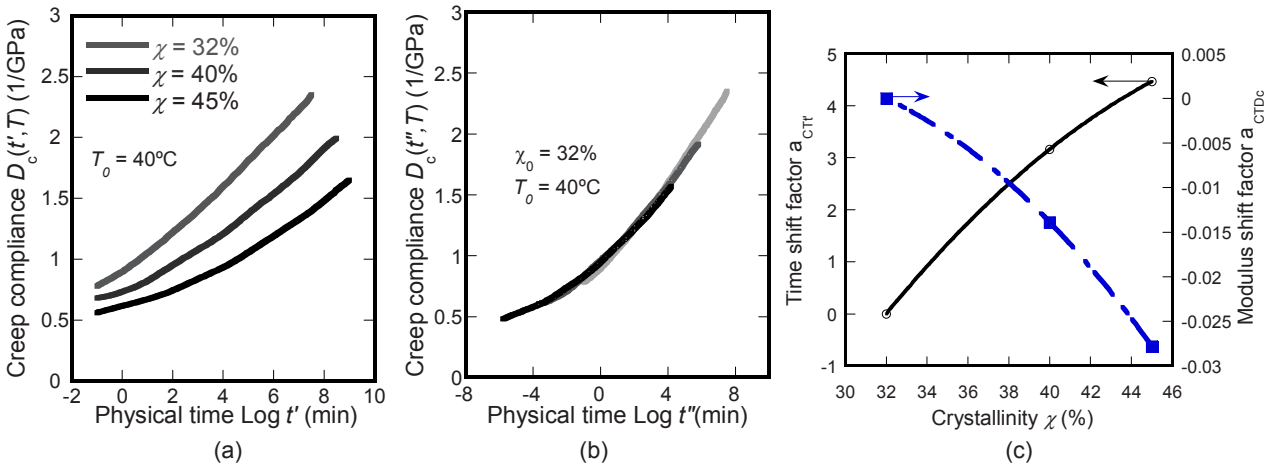

Fig. 3 (a) Master curves for creep compliance, (b) grand master curve for crystallinity and (c) time and modulus shift factors for crystallinity of PA (Reference curve: χ = 32%, T_0 = 40ºC)

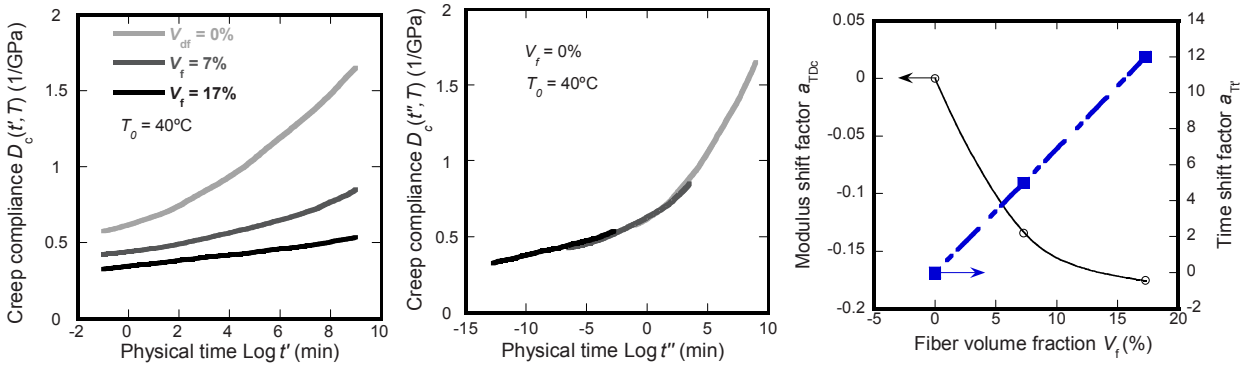

(a) (b) (c)

Fig. 4 (a) Master curves (b) grand master curve for fiber contents and (c) time and modulus shift factors for fiber contents (Referenced curve: V_f = 0%, T_0 = 40ºC)

compliance. To confirm the effect of crystallinity on creep behavior, the grand master curve for crystallinity was drawn by shifting horizontally and vertically until they overlapped with the reference master curve. Figure 3(b) shows the grand master curve for crystallinity. It showed that the creep compliance curves of PA have different crystallinity are parts of the grand master curve, and the shape of the grand master curve is as same as the creep compliance curves have different crystallinity. This shows the same creep behavior as the arbitrary crystallinity. The movements of the horizontal and vertical direction are shown in Fig. 3(c). The movement of the vertical direction is based on the modulus of the specimens, and that of the horizontal direction is applied to the effect of the retardation on time. Crystal part makes the creep behavior delay, and it is thought that it is a cause that the mobility of the molecule decreases when the crystallinity improves, and the viscosity decreases. On GFRPA the same tendency was obtained, and creep deformation under arbitrary crystallinity can be estimated using only the master curve and shift factors on each fiber contents.

The effect of fiber contents on the creep behavior of PA and GFRPA

Next, the effect of fiber contents on creep behavior was discussed with PA and GFRPA which have the fixed crystallinity (χ = 45%). The time-temperature superposition principle in Arrhenius mode was applied on these PA and GFRPA, too. The master curves of PA and GFRPA tested at the elevated temperature were shown in Fig. 4 (a). These curves were made by shifting the creep compliance curves to horizontal direction until they overlap each other. Figure 4 (a) shows that a less fiber contents and increased creep test time resulted in higher creep compliance. To confirm the effect of fiber contents on creep behavior, the grand master curve for fiber contents was drawn by shifting horizontally and vertically until they overlapped with the reference master curve (Referenced curve: V_f = 0%). Figure 4(b) shows the grand master curve for fiber contents. It showed that the creep behaviors of GFRPA are same as PA's behavior and the creep behavior of PA and GFRPA depends on the PA resin's behavior. The movements of the horizontal and vertical direction are shown in Fig. 4(c). The movement of the vertical direction is based on the modulus of the specimens by mixing fiber, and that of the horizontal direction is applied to the effect of the retardation on time.

Possibility of long-term estimation of creep deformation with the effect of crystallinity and fiber contents

We discussed the influence factors of crystallinity and fiber contents on creep behavior, and then these factors show two effects. One is the modulus change on materials, and the other is the retardation effect on time. That is the same effects on both factors. Then we tried to reveal the relationship of the both factors. In Fig. 3 (b) and Fig. 4 (b), the shapes of these curves are looked similarly, so we tried to superpose each other to make the great-grand master curve. To make the great-grand master curve, we have to choice the reference curve. The reference curve was decided in consideration of the relation between two grand master curves as the curve of χ = 32% and V_f = 0%. The crystallinity of the grand master curve for fiber contents is χ = 45%, then the curve was shifted to the horizontal and vertical direction using the modulus and time shift factors for crystallinity by making the grand master curve for crystallinity. And we got the great-grand master curve as shown in Fig. 5. The great-grand master curve is smooth so the effects of crystallinity and fiber contents on creep behavior were the same and we could control the creep behavior using changing the crystallinity and fiber contents by using the great-grand master curve and the shift factors.

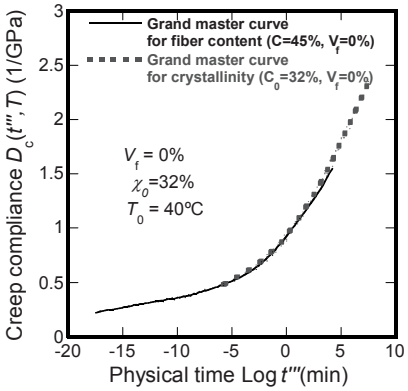

Fig. 5 Great grand master curve with grand master curves for crystallinity and fiber contents on PA and GFRPA

Estimation of the creep deformation

Creep deformation under various influence factors can be estimated using only the great-grand master curve and shift factors. In previous report [14], the estimation method was explained. At first, it is necessary to obtain an approximate expression of the master curve. The approximate expression by the prony series that Schapery [17]-[19] had proposed was used and the expression is shown in expression (4).

$$D_C(t) = C_e + \sum_{i=1}^{N} C_i (1 - e^{\frac{-t}{\tau_i}}) \tag{4}$$

C_e : Initial creep compliance, C_i : Relaxation modulus, τ_i : Relaxation time

The creep deformation was estimated based on expression (4). To estimate the creep behavior, the effects of influence factors shown in shift factors were built into expression (1). These shift factors were multiplied on the test time t, because these effects were shown as the retardation effects on time. Expression (5) shows the creep compliance with the effect of time, temperature and fiber volume fraction.

.

$$D_C\left(t, T, V_f\right) = D_C(t \times a_{TR} \times a_{Tt'}) + a_{TD_C} \tag{5}$$

V_f : Fiber volume fraction

Expression (6) shows the creep compliance with the effect of time, temperature and crystallinity.

$$D_C\left(t, T, C\right) = D_C(t \times a_{CTR} \times a_{cTt'}) + a_{cTD_C} \tag{6}$$

a_{CTR} : Time shift factor for crystallinity, a_{cTDc} : Modulus shift factor for crystallinity

By using expressions (4), (5) and (6), the creep deformation was estimated with the effect of time, temperature, crystallinity and fiber volume fraction.

These expressions show that this creep analysis technique using the expression of great-grand master curves and shift factors of the influence factors are usefulness as the result of creep analysis that considered the influence factor on the creep behavior. In addition, the application of time- temperature superposition principle was certified with the effect of fiber volume fraction and crystallinity.

Conclusion

The estimation method of creep deformation considering the effect of influence factors was produced, and the application of time- temperature superposition principle was discussed on the effect of fiber volume fraction and crystallinity. The grand master curves for crystallinity and fiber contents were obtained with the shifting the master cures. Time and modulus shift factors for crystallinity and fiber contents show the effect of modulus on specimens and the retardation effect of creep behavior. Therefore, it will be able to estimate the creep behavior including the effect of reinforced fiber using these shift factors and great-grand master curve. It might be able to estimate the creep behavior including the effect of time, temperature, fiber volume fraction, and crystallinity. These results show

the applicability of the time-temperature superposition principle. Finally, we proposed how to estimate the creep behavior using viscoelastisity theory, including the effect of time, temperature, fiber volume fraction and crystallinity. Therefore, it should be possible to control the creep deformation by controlling temperature, the amount of fiber volume fraction, the effect of crystallinity.

Reference

1) K. K. Biswas, M. Ikueda, S. Somiya, “Study on creep beha-vior of glass fiber reinforced polycarbonate”, Advanced Composite Materials, Vol.10, No. 2-3, pp.265–273 (2001)
2) N. Iwamoto and S. Somiya, “Effect of the Fiber Volume Fraction on Creep Compliance of Fiber Reinforced Ther-moplastic Polyimide: #AURUM”, Journal of The Japan So-ciety of Mechanical Engineers, Vol.61, No.589, pp.1951-56 (1995)
3) S. Somiya, “Creep Behavior of a Carbon-Fiber Reinforced Thermoplastic Resin”, Journal of Thermoplastic Composite Materials, Vol.7, No.2, pp.91-99 (1994)
4) K. Igarashi and S. Somiya, “Effect of Fiber Volume Fraction on Creep Compliance of Composites of Metamorphic Poly-Phenylene Ether with Stainless Steel Fiber”, Journal of The Japan Society of Mechanical Engineers, Vol.62, No.600, p.1761-1766 (1996)
5) K. K Biswas, S. Somiya and J. Endo, “Creep Behavior of Metal Fiber-PPE Composites and Effect of Test Surround-ings”, Mechanics of Time-Dependent Materials, Vol.3, No.1, pp. 85-101 (1999)
6) CHEN M., Crystallinity of Isothermally and Nonisothermally Crystallized Poly(Ether Ether Ketone) Composites, Polymer Composites, 19, 6, 689-697 (1998)
7) WEN-YEN CHANG, MING-SONG, Cooling and annealing properties of copolymer-type polyacetals and its crystallization behavior, Journal of applied polymer science, 34, 5, 1997-2023 (1987)
8) SUKHANOVA T, MATVEEVA G, VYLEGZHANINA M ‘Morphology and Properties of Poly(oxymethylene) Engineering Plastics’ Macromolecular symposia, 214, 135-145 (2004)
9) Takenobu SAKAI*, Koji KUSUMOTO, Satoshi SOMIYA, Material Design Method on Creep Behavior of Glass Fiber Reinforced-Polycarbonate, 4th International Conference on Mechanics of Time Dependent Materials, New York, U.S.A. (2003-10)
10) Takenobu SAKAI, Koji KUSUMOTO, Satoshi SOMIYA, Estimation Method of Creep Deformation of Glass Fiber Reinforced-Polycarbonate, 5th International Conference on Mechanics of Time Dependent Materials, Karuizawa, Japan (2005-10)
11) Takenobu SAKAI, Satoshi SOMIYA, Time-temperature dependence behavior of physical aging on creep behavior of PC, 2007 SEM Annual Conference, Paper No. 139, Springfield,U.S.A. (2007-6)
12) Takenobu SAKAI, Satoshi SOMIIYA, Estimation Corresponding to Temperature Change of Creep Behavior on Glass Fiber Reinforced-Polycarbonate, International Conference on Advanced Technology in Experimental Mechanics 2007, Fukuoka, Japan (2007-9)
13) Takenobu SAKAI, Koichi YAMADA, Satoshi SOMIYA , Effect of Crystallization on Creep Behavior of Glass Fiber Reinforced Polyacetal, SEM XI International Congress, Paper No. 151, Florida, USA (2008-6)
14) Takenobu SAKAI, Satoshi SOMIYA, Estimating Creep Deformation of Glass-Fiber-Reinforced Polycarbonate, Mechanics of Time Dependent Materials, Vol. 10, No. 3, pp185-199 (2006)
15) CHEN M., Crystallinity of Isothermally and Nonisothermally Crystallized Poly(Ether Ether Ketone) Composites, Polymer Composites, 19, 6, 689-697 (1998)
16) WEN-YEN CHANG, MING-SONG, Cooling and annealing properties of copolymer-type polyacetals and its crystallization behavior, Journal of applied polymer science, 34, 5, 1997-2023 (1987)
17) Schapery, R. A., On the characterization of nonlinear visco-elastic materials, Polymer. Engineering and Science, 9, 4, 295-310 (1969)
18) Schapery, R. A., Mech., Nonlinear Visco-elastic and Viscoplastic Constitutive Equations Based on Thermodynamics, Mechanics of Time-Dependent Materials, 1, 209-240 (1997)
19) Lou, Y. C. and Schapery, R. A., Visco-elastic characterization of a non-linear fiber-reinforced plastic, Journal of Composite Materials, 5, 208-234 (1971)

Proceedings of the SEM Annual Conference
June 7-10, 2010 Indianapolis, Indiana USA

Hybrid Metal-Ceramic Thermo-oxidation Protection Layers for Polymer Matrix Composites

Kishore V. Pochiraju
Stevens Institute of Technology, Hoboken, NJ
kishore.pochiraju@stevens.edu

Gyaneshwar P. Tandon
University of Dayton Research Institute, Dayton, Ohio
G. Tandon@wpafb.af.mil

Abstract

The use life of a high temperature polymeric composite is often reduced by the surface oxidation and ensuing degradation mechanisms. Oxidation and damage are closely coupled and oxidation accelerates after the onset of damage. Protective surface plies and coatings that decelerate or delay the oxidation-induced damage extend the useful life of high temperature composite structures. However, several earlier attempts were stymied by coating adhesion and durability problems. In this paper, we present a thermo-chemo-mechanical performance evaluation of lightweight metal thin film protective layers deposited on polymer matrix composites. The conceptual design of the barrier coating and the key step of fabricating metal top coats is described in this paper. The coating is applied on neat resins, lamina and laminates enabling the investigation of its effectiveness for oxidation and damage progression.

1. Thermo-Oxidative Degradation in High Temperature Polymeric Composites

Age-related degradation of High Temperature Polymeric Matrix Composites (HTPMCs) is a result of complex interactions between time-dependent *physical creep* and relaxation processes, temperature-dependent *chemical degradation* of polymer and interfaces and *oxidation induced degradation* [1]. Long term durability and performance of polymer matrix composites in high temperature environments is typically simulated using physical aging models [2-5] and with linear viscoelastic and time-temperature superposition models [6]. Inherent in the use of physical aging models is the assumption that the aging process is thermo-reversible, but non-reversible chemical aging, for example, chemical decomposition, hydrolytic degradation, oxidation, etc., can be equally significant. Literature from several research groups [7-20] focused on modeling various aspects of physical and chemical degradation.

Experimental characterization efforts [21-30] lead to understanding of microstructure evolution and mechanical behavior changes in composites. Majority of the reported work on the prediction of the long-term performance of HTPMCs has long been limited to physical aging [3,4,31] using visco-elastic and time-temperature superposition model frameworks. The thermal stability of the polymers is studied and enhanced by polymer chemists [32] by tailoring polymer backbones and end-caps which resulted in enhancing the chemical stability of the polymers. Understanding of mechanisms of age related degradation is now adequate and can lead to a comprehensive life and long-term durability prediction methodology for composite structures.

Thermo-oxidative stability of the HTPMC is typically determined in practice by weight loss behavior of the composites specimens. Use of a multi-scale approach to determine oxidative stability of composites with arbitrary fiber reinforcement structures from resin behavior has been of interest [16]. Figure 1 shows the schematic of one such multi-scale approach. As the fundamental mechanism based building block, the oxygen diffusivity, rate of oxidation reaction and damage evolution kinetics of the constitutent materials were determined in this framework. Although the computational framework can account for the degradation of all constituents, fibers are assumed to be diffusive but stable against oxidative degradation (Block A). This framework was applied to understand three

T. Proulx (ed.), *Time Dependent Constitutive Behavior and Fracture/Failure Processes, Volume 3*, Conference Proceedings of the Society for Experimental Mechanics Series 15, DOI 10.1007/978-1-4419-9794-4_26, © The Society for Experimental Mechanics, Inc. 2011

resin systems (PMR-15, BMI and AFR/PE-4) and the oxidation growth in these resins can be quantitatively predicted with time, temperature and pressure dependence. The oxidation behavior of composites at the lamina and laminate scales has been studied using representative volume elements. (Block-B) This work focused on PMR-15 composites and analyzed the mechanisms leading to highly orthotropic oxidation growth. Oxidation and damage growth along the fiber axis of the composite is comparably higher than the transverse to the fibers due to complicated interaction of the fiber interphase behavior, oxidation induced stress states and low fracture toughness of the fiber-matrix interface and the unreinforced matrix regions [33]. The damage evolution (Block-C) in the resin and at the interface plays a key role in determining the oxidation growth and composite degradation.

Figure 2 shows the oxidation and damage growth in a neat resin specimen. Noteworthy is the fact that the oxidation layer is deeper around the areas where discrete cracks are observed. Oxidation and damage growth are coupled processes with each accelerating the growth rate of the other. For unidirectional composites, the resin cure shrinkage, mismatches in the coefficient of thermal expansion of the fibers and matrix during the composite cure process give rise to localized micromechanical residual stresses and damage. At the lamina scale, the oxidation and damage growth in the transverse direction are low compared to that in the axial direction. The highly stressed fiber-matrix interphase regions and the interstitial (inter-fiber) matrix regions tend to oxidize and develop micro-mechanical damage at an accelerated rate. Micro-mechanical damage can cause additional permeation paths for oxygen and moisture deep into the composite. The presence of fiber sizing can have a strong influence on fiber-matrix interphase or interfacial properties [23,34-35] and can significantly affect the local diffusivity and/or thermal oxidative stability.

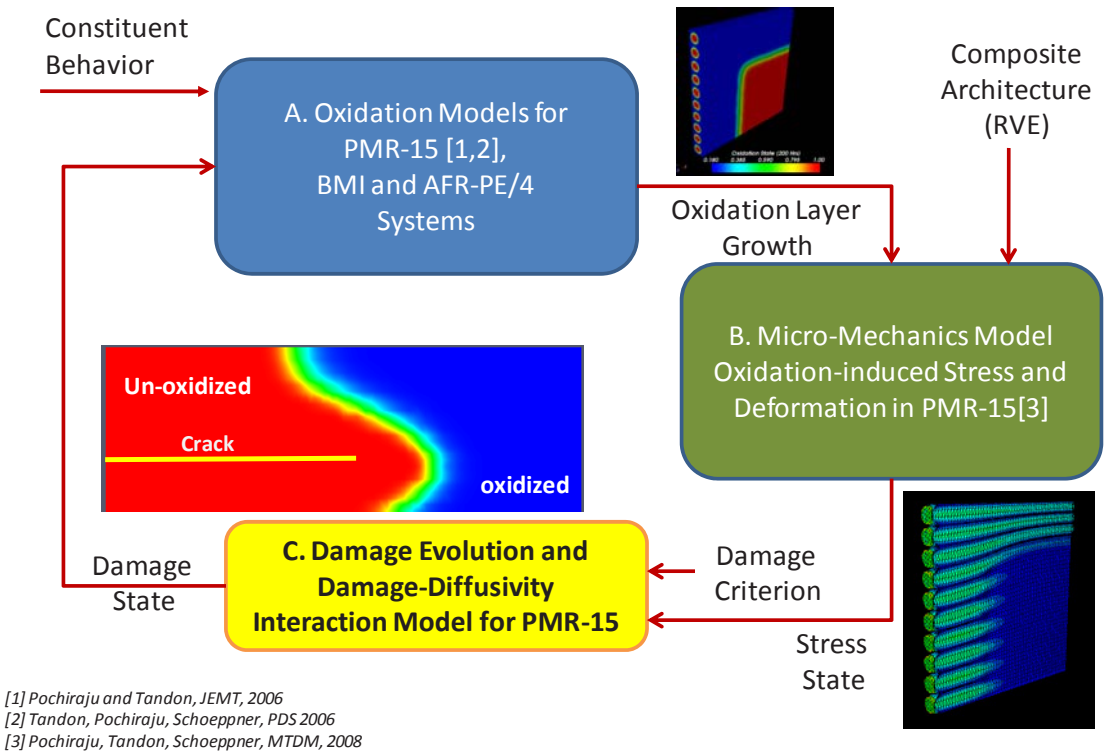

Figure 1: A multi-scale framework for thermo-oxidation modeling in HTPMCS.

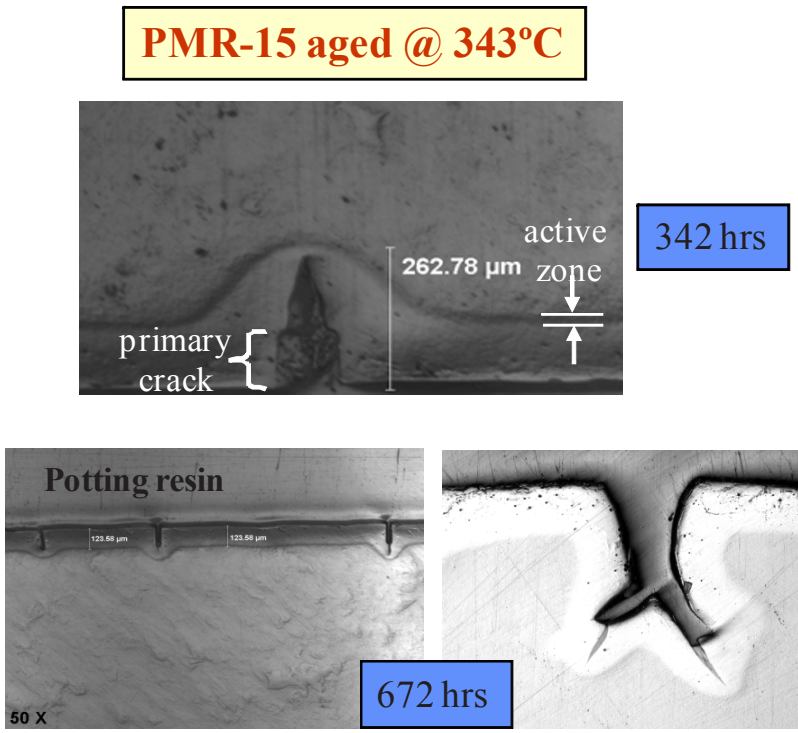

Figure 2: Oxidation layer growth (lighter regions) and damage evolution in a neat PMR-15 resin at 343 C.

The key findings from recent work on oxidative behavior of composites [1,16,33] can be summarized as follows:

- Oxidation layer growth in a neat resin depends upon the relative dominance of the oxygen diffusion rate in oxidized region and the reaction rate in the un-oxidized region. Diffusivity, porosity and damage growth in the oxidized resin plays a critical role.
- Chemo-mechanical models can be formulated for prediction of oxidation layer growth and can be quantitatively correlated with experimentation for both neat resins and unidirectional (UD) composites. Damage evolves in the oxidized zone in neat composites after several hours of exposure and oxidation layer is seen ahead of crack tips for all observations. There is material erosion from the edges typically after thousand hours of exposure causing inaccuracies in experimental measurements of oxidation growth and correlations with predictions.
- Oxidation in fiber-reinforced composites is orthotropic with axial direction of fiber being the preferred oxidation growth direction. Transverse oxidation growth correlates with growth rates observed in neat resins after accounting for the microstructure. Close coupling is observed between discrete crack growth rates and oxidation layer growth rates in axial direction. Damage evolution characterization is critical to oxidation prediction in composite materials.

In this effort, we are considering metal and metal-ceramic hybrid coating layers that decelerate oxidation and damage growth in high temperature aging environments.

2. Hybrid Oxidation Barrier Coating Strategy

Though complicated, tailoring of fiber reinforcement morphologies that meet the design requirements and development of practical manufacturing processes may be achievable. In this effort, we hypothesize hybrid composite architectures with polymer matrix composite substrate that address high temperature stiffness, strength, creep performance and weight requirements with a environmental barrier coating. The fundamental hypothesis is that enhancing fracture toughness of the coating layer that comprises of a impermeable metal layer

and a multi-functional bond layer will retard the microcrack growth and consequently oxidative degradation of the composite.

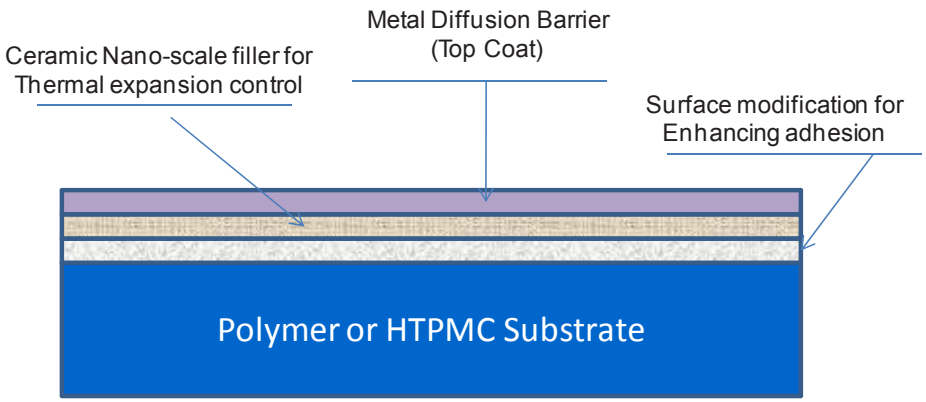

Figure 3: Use of ceramic nanofibers in the HTPMC to enhance oxidation resistance is as shown. The exposed surfaces will incorporate a thin nanofiber surfaces and the edges will use nanofiber reinforced polymer coatings.

We designed a three layer coating system that serves as a diffusion barrier and has the necessary mechanical strength and durability comparable to the use-life of the composite.

Figure 3 shows the general deployment of the coating layers on the composite structure. The structural geometry and fiber structure of the substrate composite can be designed based on the structural stiffness and strength requirements without concern for the oxidation performance. The oxidation performance is independently improved by reducing the soluble oxygen content available to the substrate. The objective for using the top metal coat is to realize a ductile oxygen diffusion barrier with low boundary sorption. The material with low boundary sorption curtails the soluble oxygen concentration available to the polymer and hence reduces the oxidation reaction and degradation rate. However, the metal top coats inevitably lead to strong thermal expansion coefficient mismatch and in the absence of a chemical bonding mechanism between the metal coats and polymer substrate, the adhesion and durability of coating is minimal. Therefore, a second nano-fiber reinforcement layer is used as the transition layer to mitigate the thermal expansion mismatch and increase the interlaminar strength. In order to provide a scaffold for the nano-fiber reinforcement and enhance the mechanical bonding between the polymer and nano-reinforcement, the composite surface is modified with nano-scale abrasion.

Since oxidation is a surface phenomenon and the fiber orientation at the surface determines the rate of growth, we consider two nanostructures for incorporation into the composite. The transverse surfaces require nanostructures that are incorporated over large surface areas. Surface veils with nano-fibers incorporated into the exposed ply or between the exposed and the second plies of the composite offer the potential to decelerate the oxidation growth as well as arrest the spread of micro-cracking into the thickness of the ply. Large aspect ratio nanofibers that are spun into random mats with one or two diameter thickness will be used on the exposed surfaces to enhance the fracture toughness by bridging cracks and reducing the oxygen sorption and diffusivity.

This paper focuses on the metal diffusion barrier layer and nano-composite bond layer effort is not described. The design, fabrication and characterization of the three-layer system is currently in progress.

3. Thermally Evaporated Metal Top Coats

In this secion, we describe the processing and performance of the thermally evaporated metallic coatings on the surface of neat resins. Both thermo-oxidative and mechanical stability of the coating are considered.

3.1 Specimen Preparation

The metal thin films are coated on the composite substrates using a thermal evaporator. Aluminum and Silver coatings are investigated. Thermal evaporation is a commonly used to coat substrates for moisture barrier and other applications. The process entails evaporating a metal source, called a “boat,” under high vaccum conditions. The specimens are placed in the evaporator and evacuated to high vacuum condition, typically in the range of 10^{-4}-10^{-6} mbar. Substrates can be heated to promote epitaxial crystal growth. Pure metals or combination of metals can thermally evaporated at the same time. The deposition rate is controlled to achieve uniformity and quick coverage. The distance between the source and the substrate controls amount and uniformity of deposition. The evaporation rate is normally determined by vapor density and its propagation velocity. Sensors are deployed inside the chamber to determine composition and for controlling composition with evaporation rate adjustments. Thermal evaporation has low material efficiency, particularly for large area and long duration evaporation.

Figure 4(a) shows the arrangement used in the thermal evaporator in this effort. The source is placed directly beneath the middle specimen. The source and the substrate holding the specimens were placed within a few inches. Figure 4(b) shows silver coated specimens. As 99.9% pure metals were used for coatings were shiny, oxidation free and demonstrated enough adhesion allowing handling and further aging experimentation.

Initial aging experimentation showed that the Al coatings peeled off during the initial hours (< 50) of aging time indicating poor adhesion to the surface. Further investigation showed that the coatings were possibly porous. Therefore, further experimentation and thermal evaporation process tuning was restricted to silver specimens.

(a) (b)

Figure 4: Surface of polyimide composite (a) before and (b) after coating.

3.2 Surface Characterization

The adhesion of the coating was observed to be strongly dependent on surface preparation and roughness. Neat resin specimens with smoother surfaces had less coating durability under isothermal aging and composites which had mold surface imprints exhibited higher coating adhesion. The surface roughness was studied under an Atomic Force Microscope. The surfaces roughness was determined before and after coatings for as manufactured composite surfaces. The as-manufactured neat resins had an average surface roughness of approximately 200 nm before coating and 50 nm after coating.

Several neat resin specimens were roughened using fine grit abrasives to increase the surface roughness before coating. Figure 4 (a) shows the AFM image of the sandblasted surface. The average surface roughness increased to 5000 nm after sandblasting. The coated surface is shows in Figure 5(b) which has an average surface roughness of 1500 nm.

Deposition of another layer of metal is an option further reduce the surface roughness and increase thickness of the metal layer. But, such the second layer increases the weight of the structure and alters the thermal deformation response of the layer. Use of a second interlayer material such as chromium which can enhance the adhesion of silver to the polymeric substrate is also a possibility. These variations are currently being investigated.

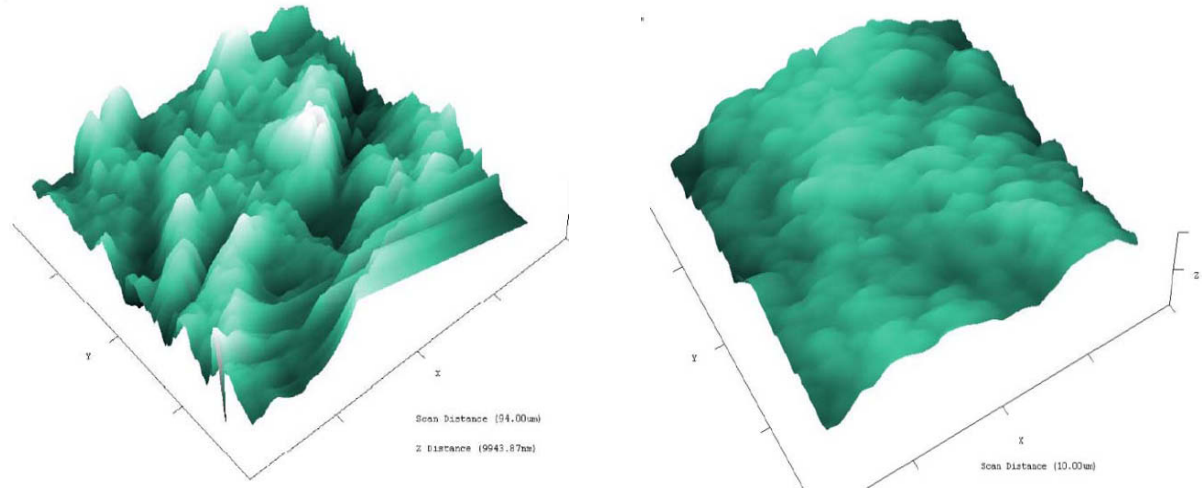

(a) (b)

Figure 5: AFM characterization of the surface. Both as-cast and roughened surfaces are studied to determine impact on coating adhesion. (a) Surface of roughened specimen (b) Same surface after coating with silver film

3.3 Thermo-Oxidative Performance

The coated surfaces were isothermally aged for upto 1700 hours. Aging temperature used was close to the typical working temperature for the material. The specimens were coated only on one side allowing the determination of the impact of coating on oxidation growth. The experimental procedure used for aging studies was reported in detail earlier [35]. Briefly, the specimens were baked in aging ovens in oxidative environment (air). The specimens were periodically removed, sectioned and placed back in the ovens. The sectioned pieces were mounted for optical microscopy. The oxidation layer sizes are determined by color changes in the specimen. Figure 6 shows the top and bottom surfaces of the aged specimen. The top is the coated side and the bottom is the uncoated side.

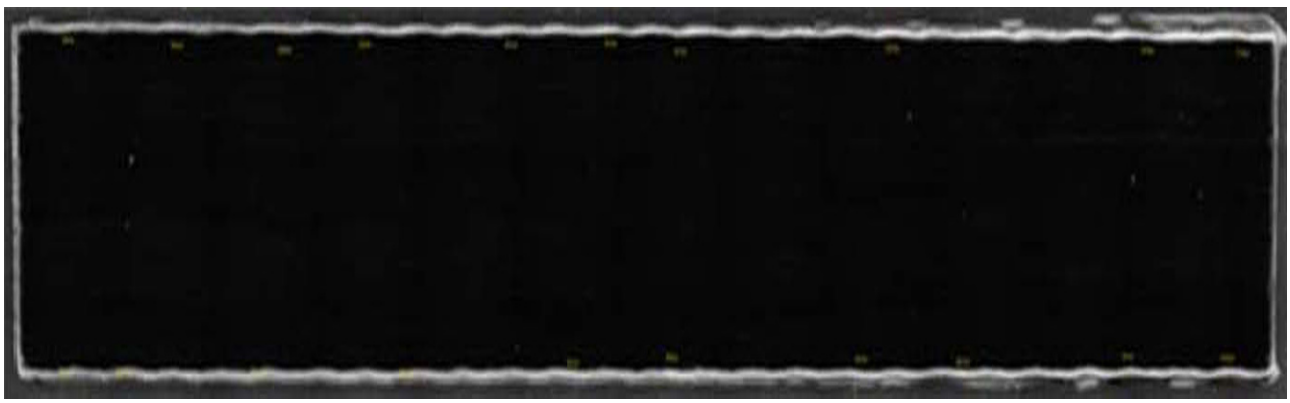

Figure 6: Dark-field image of oxidation in a cross section perpendicular to the fiber direction in a uni-directional composite

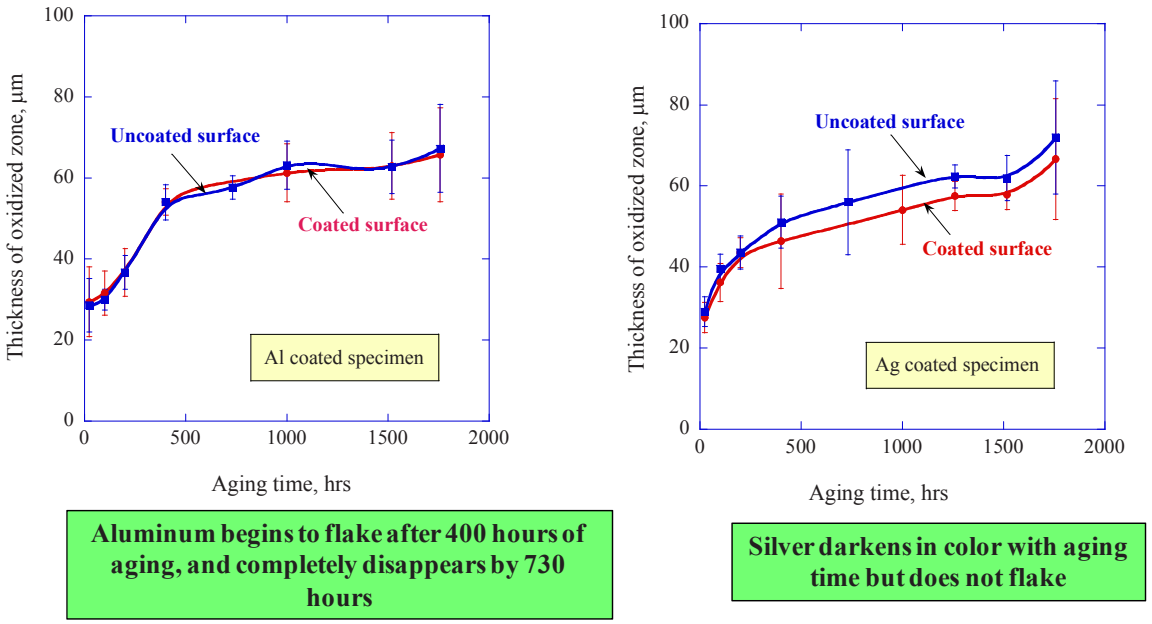

Figure 7: Oxidation growth profiles for Al and Ag coated specimens.

Figure 7 shows the oxidation growth on the top and bottom surfaces for the Al and Ag coated specimens. The oxidation layer size is similar on both sides for the Al coated specimens. Coating peel off was evident in these specimens during the initial hours of aging and the coating discolored and peel off entirely after 500 hours. The Ag coated specimen however shows some evidence of retardation of oxidation growth. The oxidation zone measurement in composite from optical microscopy is very coarse. Presence of damage also accelerates the oxidation growth. Therefore, the variability in oxidation zone size is high. As seen from the data for the uncoated side, the oxidation zone sizes have significant variation. The coated side however shows less variation indicating some arrest of damage due to oxidation. Although the results are strikingly conclusive, the effect of silver coating is definitely discernable in retardation of the oxidation growth. This motivates further optimization of the layer thickness and bond strength for metal coatings and the design of the nano-fiber inter-layers.

4. Concluding Remarks

This paper presents an experimental study on the effect of metal coating on the thermo-oxidation growth in high temperature composites. The oxidation behavior of the Silver coated surfaces is encouraging. They exhibited necessary ductility to withstand the thermally induced strains as well as the reduction in oxygen sorption and diffusion behavior.

Aluminum, a preferred material composition from the perspective of lower density, did not exhibit the necessary durability, which resulted in poor retardation of oxidation growth and was ineffective. However, this may be a lower weight alternative if the process is optimized.

5. Acknowledgments

Funding from AFOSR for the design of Hybrid Oxidation Tolerant Composites (Drs. J. Harrison and C. Lee, program managers) is gratefully acknowledged. Specimens fabrication and AFM roughness study are thanks to Mr. Nelson Pinilla, graduate research assistant at Stevens.

6. References

1. Schoeppner, G.A., Tandon, G. P, Pochiraju, K. V., (2007) " Chapter 9: Predicting Thermo-oxidative Degradation and Performance of High Temperature Polymer Matrix Composites", Multi-scale Modeling and Simulation of Composite Materials and Structures, Kwon, Young W.; Allen, David H.; Talreja, Ramesh R. (Eds.), ISBN: 978-0-387-36318-9, Springer, pp. 373-379.
2. Struik, L.C.E. (1978) Physical aging in amorphous polymers and other materials. Elsevier, Amsterdam
3. McKenna, G.B. (1992) Aging of polymeric resins: implications for composite performance. Proceedings of the Conference of the American Chemical Society, polymer preprints, vol 33., No 1., pp. 364-365.
4. Waldron, W.K. Jr. and McKenna, G.B. (1995) The nonlinear viscoelastic response and apparent rejuvenation of an epoxy glass. J Rheology 39:471-497
5. Brinson, L.C., Gates, T.S. (1995) Effects of physical aging on long term creep of polymers and polymer matrix composites. Int J Solids Struct, 32:827.
6. Colin, X., Marais, C., Cochon, J.L., Verdu, J. (1999) Damage/weight loss relationship for bismaleimide matrix under isothermal oxidation aging. Proc of the Int Conf on Recent Developments in Durability Analysis of Composite Systems, Brussels University, Belgium.
7. Colin, X., Marais, C., Favre, J.P. (1999) Damage/weight loss relationship of polymer matrix composites under thermal aging. Proc. ICCM-12, ICCM Europe Publications, T. Massard and A. Vautrin, eds.
8. Colin, X., Marais, C., Verdu, J. (2001) A new method for predicting the thermal oxidation of thermoset matrices: application to an amine crosslinked epoxy. Polymer Testing 20:795-803.
9. Colin, X., Marais, C., Verdu, J. (2001) Thermal oxidation kinetics for a poly(bismaleimide). J. Applied Polymer Science 82:3418-3430.
10. Colin, X., Marais, C., Verdu, J. (2005) Kinetic modeling of the stabilizing effects of carbon fibers on thermal aging of thermoset matrix composites. Comp Sci and Tech 65:117-127.
11. Tsotsis, T.K. (1998) Long-term thermo-oxidative aging in composite materials: experimental methods. Journal of Composite Materials 32:1115-1135.
12. Wang, S.S., Chen, X. (2006) Computational micromechanics for high-temperature constitutive equations of polymer-matrix composites with oxidation reaction, damage, and degradation. Journal of Engineering Materials and Technology 128: 81-89.
13. Wang, S.S., Chen, X., Skontorp, A. (2003) High temperature mechanics modeling and experiments of thermal oxidation, degradation and damage evolution in carbon fiber/polyimide composites. Proc. American Society for Composites 18th Technical Conference, Univ. of Florida, Gainesville, FL.
14. Wang, S.S., Chen, X., Skontorp, A. (2003) High-temperature mechanics modeling and experiments of thermal oxidation, degradation and damage evolution in carbon/fiber/polyimide composites. Technical Report CEAC-TR-03-0106, University of Houston.
15. Pochiraju, K.V., Tandon G.P. (2006) Modeling thermo-oxidation layer growth in high temperature resins. Journal of Engineering Materials and Technology 128:107-116.
16. Tandon, G.P., Pochiraju, K.V., Schoeppner, G.A. (2006) Modeling of oxidative development in PMR-15 resin. Polymer Degradation and Stability 91:1861-1869.
17. Wise, Gillen and Clough (1997) Quantitative model for the time development of diffusion-limited oxidation profiles. Polymer, 38:1929-1944.
18. Celina, M., Wise, J., Ottesen, D.K., Gillen, K.T., Clough, R.L. (2000) Correlation of chemical and mechanical property changes during oxidative degradation of neoprene. Polymer Degradation and Stability 68:171-184.
19. McManus, H.L., Foch, B.J., Cunningham, R.A. (2000) Mechanism-based modeling of long-term degradation. J Comp Tech and Research 22:146-152.
20. Bowles, K.J. (1991) Effect of fiber reinforcements on thermo-oxidative stability and mechanical properties of polymer matrix composites. NASA TM 103648.

21. Bowles, K.J. (1999) Durability of graphite-fiber reinforced PMR-15 composites aged at elevated temperatures. J Comp Tech and Research 21:127-132.

22. Bowles, K.J., Jayne, D., Leonhardt, T.A., Bors, D. (1993) Thermal stability relationships between PMR-15 resin and its composites. NASA TM 106285.

23. Bowles, K.J., Jayne, D., Leonhardt, T.A. (1993) Isothermal Aging Effects on PMR-15 Resin. SAMPE Quarterly, 24:2-9.

24. Bowles, K.J., Tsuji, L., Kamvouris, J., Roberts, G.D. (2003) Long-term isothermal aging effects on weight loss, compression properties, and dimensions of T650-35 fabric-reinforced PMR-15 composites – Data. NASA TM-2003-211870.

25. Bowles, K. J., Madhukar, M., Papadopolous, D. S., Inghram, L., McCorkle, L. (1995) The effects of fiber surface modification and thermal aging on composite toughness and its measurement. NASA TM-

26. Tsuji, L.C., McManus, H.L., Bowles, K.J. (1998) Mechanical properties of degraded PMR-15 resin. NASA Technical Report, 1998-208487, pp 1-18.

27. Abdeljaoued, K. (1999) Thermal oxidation of PMR-15 polymer used as a matrix in composite materials reinforced with carbon fibers. MS thesis, Ecole Nationale Superieure des Arts et Metiers, Paris.

28. Gates, T.S., Feldman, M. (1994) The effects of physical aging at elevated temperatures on the viscoelastic creep of IM7/K3B. NASA-TM-109114.

29. Gates, T.S. (2003) On the use of accelerated test methods for characterization of advanced composite materials. NASA/TP-2003-212407.

30. Schoeppner G.A., Tandon, G.P., Ripberger, E.R. (2006) Anisotropic oxidation and weight loss in PMR-15 composites. Composites Part A: Applied Science and Manufacturing (accepted July 2006).

31. Sullivan, J.L. (1990) Creep and physical aging of composites. Comp Sci and Tech 39:207.

32. Meador, M.A., Johnston, J.C., Frimer, A.A., Gilinsky-Sharon, P. (1999) On the oxidative degradation of nadic endcapped polyimides: 3. synthesis and characterization of model compounds for end-cap degradation products. Macromolecules, 32:5532-5538.

33. Pochiraju K.V., Tandon, G.P., Schoeppner, G.A. (2008) Evolution of stress and deformations in high-temperature polymer matrix composites during thermo-oxidative aging, Mechanics of Time-Dependent Materials, Vol. 12: pp . 45–6.

34. Paipetis, A., Galiotis, C., Effect of fiber sizing on stress transfer efficiency in carbon/epoxy model composites. Composites Part A 27A, 755-767 (1996).

34. Upadhyaya, D., Tsakiropoulos, P., Evaluation of the effect of sizing levels on transverse flexural and shear strengths of carbon/epoxy composites. Journal of Materials Processing Technology 54, 17-20 (1995).

35. Tandon, G. P., Ragland, W. R. and Schoeppner, G. A. (2009) “Using Optical Microscopy to Monitor Anisotropic Oxidation Growth in High-Temperature Polymer Matrix Composites,” to appear in Journal of Composite Materials, Vol 32, No. 5, pp. 583-603

Proceedings of the SEM Annual Conference
June 7-10, 2010 Indianapolis, Indiana USA

Degradation phenomena under water environment of cotton yarn reinforced Polylactic-acid

Satoshi SOMIYA and Takanobu OOIKE
Keio University, Faculty of science and Technology, Department of Mechanical engineering
3-14-1 Hiyoshi Kouhoku-ku Yokohama Japan, E-mail: somiya@mech.keio.ac.jp

Abstract : Recently, many green composites have been developed, and utilization of those materials have been is advanced. Because many biodegradable plastics usually show affinity to a human body, in this research, using cotton yarn and Polylactic acid (PLA), which is a typical biodegradable polymer, a green composite was developed as a medical substance. Although the mechanical properties of some biodegradable plastics were far lower than that of an engineering plastic. It is necessary to raise the mechanical properties of a biodegradable plastic to the level which is equal to metal medical material. Furthermore at the practical use, the influence from water absorption is strongly received. The material design of green composites using Cotton yarn/PLA has been done including the effect of water absorption.

Introduction

Recently, many green composites have been developed, and several sorts of utilization of them are advanced [1]. It was pointed out that elastic modulus of metal biomaterial was usually too higher than bone. Instead of metal medical materials, these materials were begun to use because escaping from the effect of Allergy to metal . The change from a metal biomedical material to green composites is tried. This main reason is for suppressing generating of the allergies by a metal ion. In this research, using Polylactic acid (PLA) which is a typical biodegradable polymer [2, 3] and cotton yarn, a green composite which had unidirectional fiber orientation was developed, and also the mechanical properties were evaluated. Although the mechanical properties of the present biodegradable plastic were far lower than that of the general engineering plastic, the mechanical properties of the developed composite checked having exceeded them. Now, at the practical use, the influence from water absorption is strongly received. The time dependency of the degradation of tensile strength by water absorption was evaluated quantitatively. Moreover, from the observation of the fracture mechanism, it was shown clearly that fracture process is classifiable into the domain for which strength reduction depends on absorption moisture, and the domain of time accompanying the chemical degradation of material.

T. Proulx (ed.), *Time Dependent Constitutive Behavior and Fracture/Failure Processes, Volume 3*, Conference Proceedings of the Society for Experimental Mechanics Series 15, DOI 10.1007/978-1-4419-9794-4_27, © The Society for Experimental Mechanics, Inc. 2011

Experimental method and used materials

Used biodegradable resin was Polylactic acid (PLA) and in this research, LACEA H-100J, which was made from Mitsui Chemicals Co., was used. Research on the affinity of PLA and a human body is done until now [4, 5]. Molding pressure was 1.2MPa molding temperature was 180C and pressure holding time was 40min. The thickness of the molded plate was 3mm. To research of the effect of liquid on the mechanical properties, pure water was chosen. The tensile strength and the elastic modulus of PLA are 28MPa and 1GPa, respectively. The reinforcement was a cotton yarn made from Kanebo Co. Since the strength of the yard was difficult to determine a cross-section area, it assumed that cross-section form was circular immersed in resin, and was calculated from the measurement value of the diameter. The fracture strength of the cotton yarn was 320MPa. When composites were designed, it can attain to calculate the required amount of reinforcement by a mixture's law in many cases. In "mixture's law", the fracture strain of fiber is lower than matrix is assumed. On the other hand, in the case of this composition of the materials, since the tensile fracture strain of cotton yarn is more than twice as large as the fracture strain of resin, it is difficult for the calculation which uses a mixture's law for material design. Then, it is necessary to presume the fiber content from an experimental result. In this research, the contents of cotton yarn was widely changed, and it adjusted and created so that a volume fraction might be V_f=30%, V_f=46% and V_f=56%. In the examination, resin (V_f =0%) were added to these, and four kinds of fiber volume fraction were used.

Development of green composites instead of metal-biomaterial for bone

After performing an operation on a bone fracture part, in order to protect the repaired portion, bone plates which use a substitute bone are used. Although the metal material is used as an alternative substance of this part, development of a nonmetallic substance is desired. Because the tools fixed in the shape of bridge construction on both sides of a fracture part were specifically used, it was assumed that tensile force acts on this component. For the purpose, the mechanical property about tensile deformation was measured. Moreover, it is secured sanitarily and it not only has the same mechanical properties as a bone in this material, but does not come to start the immunoreactions of a human body. Generating allergy is reported although metal material is most often used, and those many have sufficient mechanical properties. As a result of investigating the tensile strength of a general bone, it became clear that it was in the range of 80 to 114MPa. Moreover, it is reported that a period required for bony reproduction, the usable years of the bone for substitution, is less than 2000 hours. From the above conditions, as for the development goal, tensile strength made 90MPa and usable years 2000 hours. However, since conduction of load is attained as bony reproduction progresses, the role of a support component decreases. Therefore, it carried out that strength fell to 10% within the period of 2000 hours to approving.

It decided to use PLA to which utilization is advanced as an engineering plastic for industry in a biodegradable plastic. It is known that PLA not only shows biodegradability, but cannot do an immune antibody. As a fault, the strength of a biodegradable plastic is a low thing as compared with it of a general-purpose plastic. The tensile strength of used PLA is 28MPa. This is about 1/3 of the strength needed this time. In order to raise this

strength, it tried to reinforce using cotton yarn. The reason for having used cotton yarn is that it can obtain easily. This combination is a material called a green composite. After winding cotton yarn to the unidirectional direction, the specimen plate was made by the immersion treatment of PLA resin solution. The tensile test was carried out using the specimen cut out from plate in the direction of fiber orientation.

Fig. 1 (a) and (b) shows the change to the volume fraction of tensile strength and a tensile modulus which were obtained by the tensile test. The tensile modulus and strength of resin be expressed by a linear function to a volume fraction. From this, the mechanical properties of the unidirectional Cotton/PLA composite material were understood that it can calculate using a mixture's law. In other words, it was found that it is the material in which a materials design is possible. It was recognized that it can attain if tensile strength 90MPa of the fiducially point of a design is more than V_f=30% at least. And the modulus of composites of V_f =30% increases by 4 times as compared with it of used resin. In this material development, although tensile load is taken up as first theme, it is necessary to take into consideration deformation by compressive load, and the deformation to torsion load. However, under the present circumstances, information required to determine these mechanical properties values is not fully acquired.

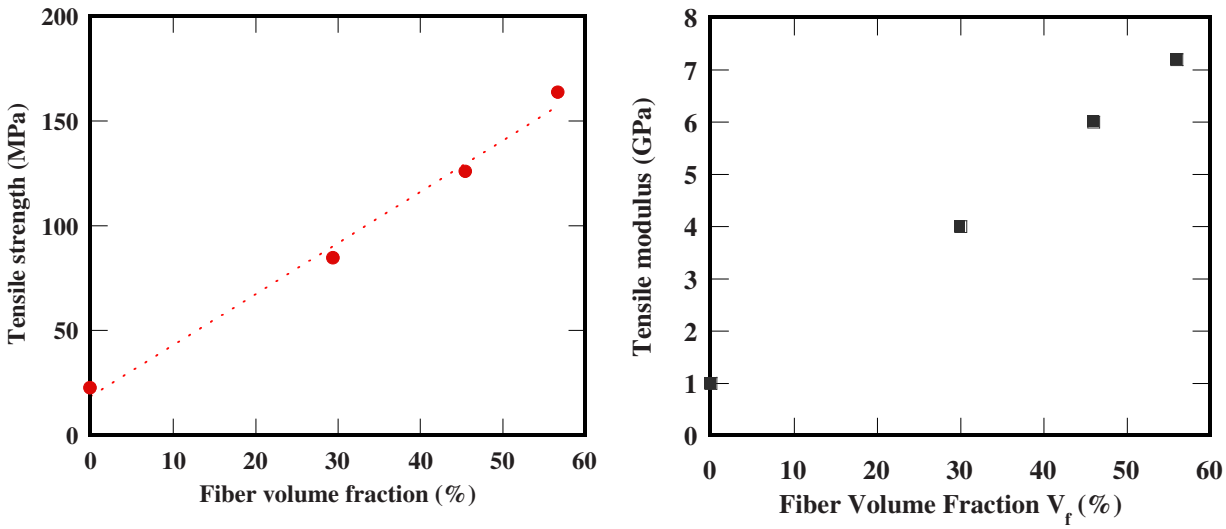

(a) Tensile strength of resin and FRPs (b) Tensile modulus resin and FRPs

Fig.1 Tensile strength and modulus of Cotton/PLA composites

The water absorption phenomena and degradation phenomena of pure resin

When all material used in the human body, the change of mechanical properties becomes very important caused by water absorption especially. Moreover, PLA is a biodegradable plastic, and since it is rich in water at affinity, it needs to investigate change of the mechanical properties accompanying water absorption, and chemical nature in detail. However, as shown in Fig. 3, when immersion time exceeded 2000 hours, both tensile strength of wet specimen and again dryness of the wet specimen fell quickly. It is assumed that not only absorbed water but chemical degradation advances from this after immersion of 2000 hours or more to

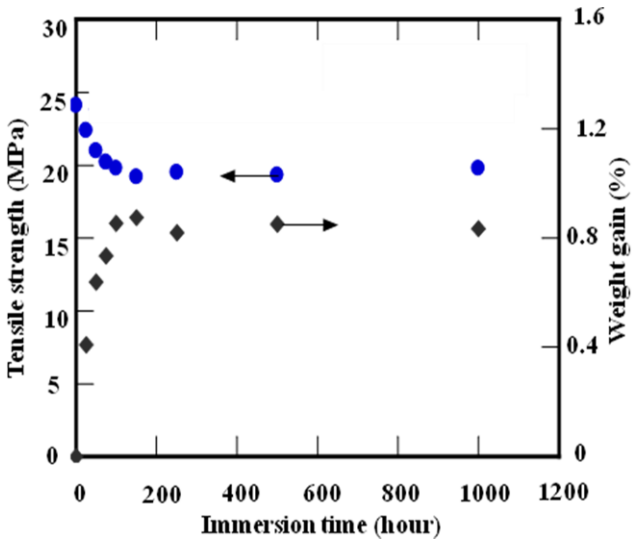

Fig. 2 Water absorption phenomena and tensile strength of immersed PLA resin until 2000 hours

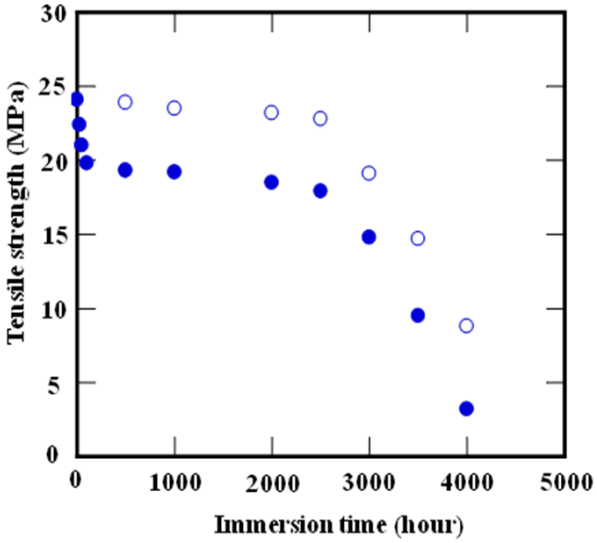

Fig3 Tensile strength of PLA immersed and dried after immersion treatment. Solid circle; wet specimen, Open circle; dried material after immersion treatment

degradation of mechanical properties according to the water in less than 2000 hours being assumed. Then, elution of the material accompanying water absorption was investigated. The specimens were dried completely after being immersed in pure water and the change of mass was measured. Fig. 4 showed the result of measuring the amount of reduction of mass and mass slightly decreased till 1500 hours, and later than it, rapidly decreased. It was assumed that the reason in which mass decreased is in elution. Although elution of polymer itself and elution of the decomposed material in the molecule of polymer were assumed by the cause of reduction in mass, in order to investigate the mechanism, analysis by FT-IR was carried out to it. Chemical degradation assumed generating in the portion of an ester bond C=O in main chain. Since the wave

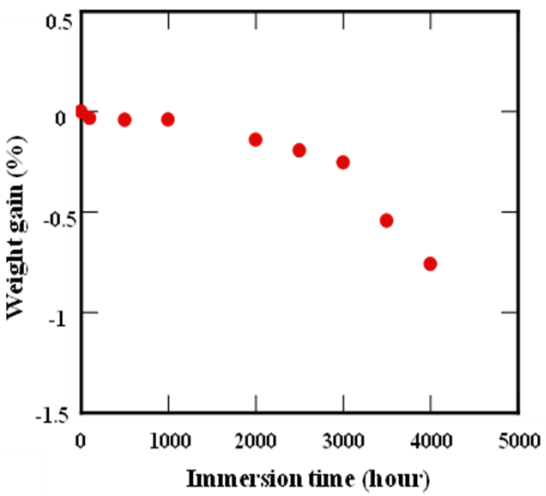

Fig.4 The change of mass loss according to immerse in pure water of resin at 40 C

number which shows C=O bond was about 1800cm^{-1}, distribution of the range of 1900cm^{-1} was investigated from the wave number 1700^{-1} as shown in Fig.5 (a). Reduction of the area of the wave at about 1800cm-1 accompanying water absorption shows decrease of number of an ester bond, and the amount of cutting of the ester bond which occurs in main chain in PLA resin increases.

It measured in the area which opted for change of wave quantity according to the standard. Fig. 5 (b) shows the change of the area accompanying progress to pure water at immersion time. From change of the color of the material accompanying immersion treatment, it was checked till about 2000 hours that elution of the material from the surface takes place too. Moreover, when this time was passed, it turned out that elution of the material from an inside increases.

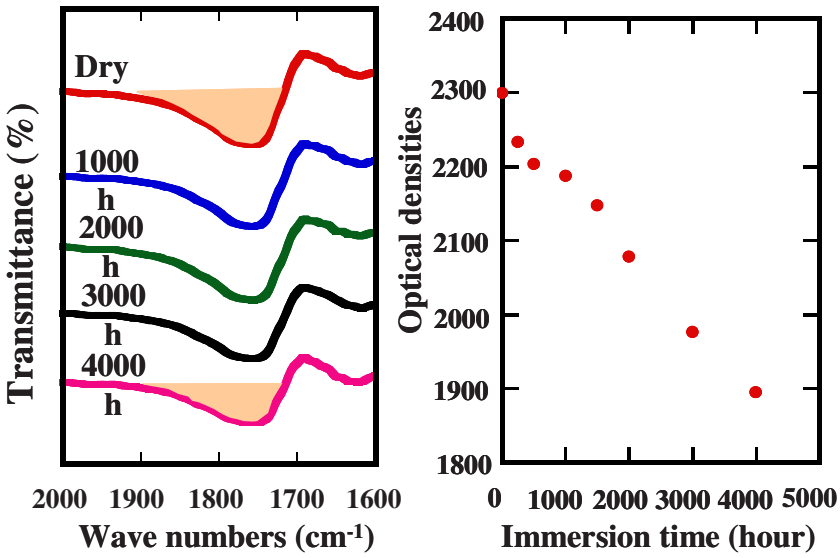

(a) Distribution of wave number after immersion treatment

(b) Decrease of the ester bonding increasing immersion treatment

Fig. 5(a), (b) Analysis of chemical degradation caused by water with FT-IR method

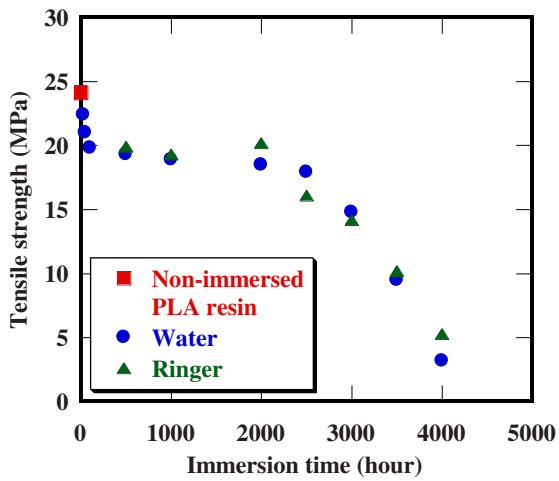

Fig.6 Comparison of tensile strength of specimen immersed in pure water and Ringer's solution

Although degradation of PLA has been studied using pure water, when an alternative substance was used for a human body, it is necessary to consider the influence which a difference of pure water and humors has on degradation phenomenon. Ringer's solution was used instead of humors, degradation of the strength of PLA was investigated, and it compared with the result in pure water. Fig. 6 shows the tensile strength by immersion time 4000 hours. Also when there was no difference in both results and the result of the examination by pure water was used for the inside of the body, it found that it was possible to use the result of this research.

Degradation of Cotton/ PLA composites caused by water absorption

Fig. 7 shows the process of degradation of the strength of Cotton/PLA composites of all the fiber volume fractions. The speed to which strength falls is accelerated while a fiber volume fraction increases. By the way, with resin material, the first domain to which strength falls gently by water absorption, and the second domain to which it falls rapidly by chemical splitting existed. Existence of these domains was investigated about the composite material. As a result, it became clear that in the volume fraction V_f = 46% or less of material, two domains existed. However, with the increase in a fiber volume fraction, the width of the first domain decreases, i.e., the time to the start of rapid strength reduction becomes short, and that of it is completely lost with V_f=56% of material. That is, it was found that strength reduction advances linearly with the increase in immersion time. The possibility of the materials design of the Cotton/PLA composites which can be used as an alternative material for 2000 hours on the assumption that such degradation occurs was examined.

By the way, in cotton yarn and PLA composites, it turned out that the rate that a chemical degradation domain not only increases, but strength falls is accelerated with the increase in fiber volume fraction. While strength improved with mixing of a fiber, it turned out that strength is remarkably influenced by water absorption. In order to perform an improvement in quality in the future, it is very important to investigate how water has influenced the process of destruction.

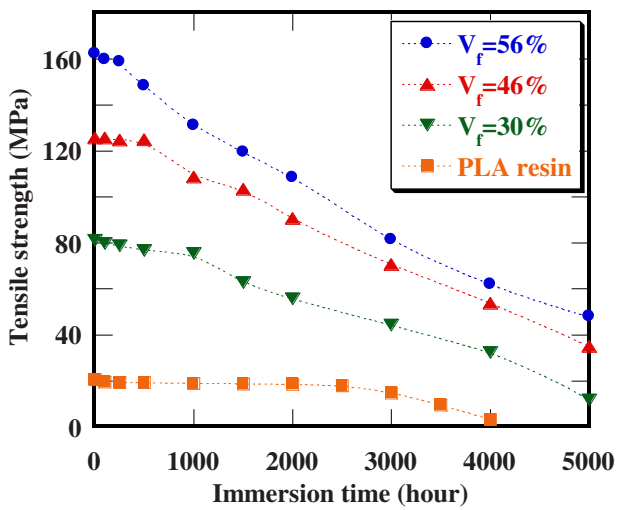

Fig. 7 Degradation of tensile strength after water immersion of Cotton yarn/ PLA

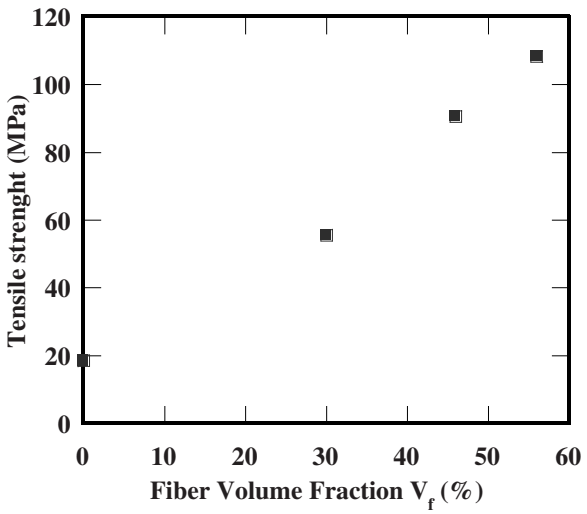

Fig. 8 Residual strength of water immersed Cotton yarn/PLA composites at 2000 hours

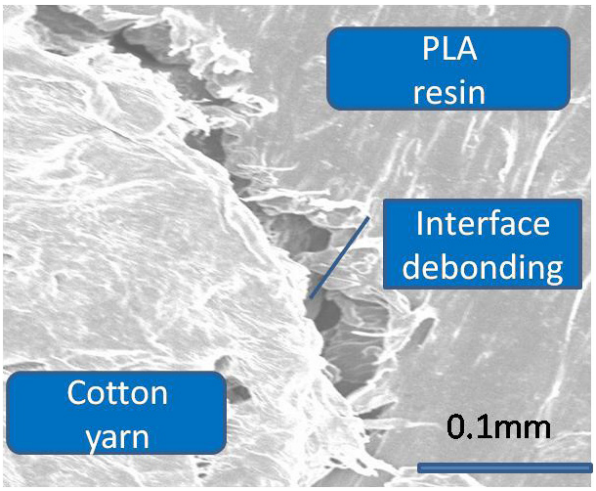

Fig. 9 Interface depending caused by water immersion
observed using the electron microscope(SEM).

In the case of cotton yarn / PLA composites used by this research, it was assumed that chemical degradation of resin and fiber are promoted by mixing of a fiber, or the interface around yarn was weakening by the water. It was assumed that chemical degradation of resin is promoted by mixing of a fiber, or a fiber and an interface become weak with water from this. In the case of thread, when water reduces the coefficient of friction between the single fibers which constitute thread, it is possible that tensile strength falls. However, in the case where immersion of the resin is carried out to thread, it does not become a factor which a single fiber is fixed and falls. It is assumed from degradation of resin by a fiber being difficult to think that the interface around a fiber deteriorated. Moreover, it was not observed that fibers broke at lower strain and a crack occurs from the part. On the other hand, the pullout length of the thread increased from the fracture surface with the increase in immersion time. So, the interface of thread and resin on the cross section which cut the specimen was observed by SEM. Fig. 9 shows in the state of the interface of resin and yarn. In this figure, the crevice exists in the interface and it is shown that the interface debonding occurred. Although this debonding is propagated along with thread, a debonding makes resin generate a crack, and that crack starts progress in the rectangular direction to tensile stress. It was found that the effect of thread as a reinforcement not only decreases by the debonding generated in the direction of an axis of thread, but the crack which intersects perpendicularly in the yarn direction occurs from a debonding, and it reduces strength. By improving the adhesion strength between thread and resin as a future improvement, the indicator in which improvement in strength was still more possible was acquired.

Finally, Fig. 8 shows the result of plotting the tensile strength in immersion time 2000 hours to a fiber volume fraction from Fig. 7. The figure shows that strength is increasing linearly to V_f. If this result is used, when the strength which is a design intention can create the material of 90MPa at more than fiber volume fraction V_f=50% and permits 10% of strength reduction during practical using, it turns out that it can attain about fiber volume fraction V_f=40%. From the result, this composite material showed clearly that it can be used as a

tailored material above.

Conclusions

The purpose of this research was to developed biodegradable bone plate of affinity for a living body instead of a metal bone plate. In this research, the green composite which used biodegradable resin as a matrix was created. PLA resin was selected as a matrix and general-purpose cotton yarn was used as reinforcement. The mechanical properties at the time of dryness of an alternative material which is needed for the design of composites, especially tensile strength were observed. Furthermore, in order to use material in a living body, it measured change of the tensile strength after being immersed in water till 4000 hours. In this research, the unidirectional orientation Cotton yarn strengthening PLA composites was created. The fiber volume fraction of the created composites was taken as from resin simple substance Vf=0% to 56%. As a result, if it was V_f=50% of a composites also on which conditions under dryness and moistness, it was shown that can change into metal material and it can be used. As these conclusions, it was shown clearly that a materials design is possible with the used material composition.

Reference

[1] K. Oksman and M. Skrifvars, “Natural fibers as reinforcement in Polylactic acid (PLA) composites” Composites Science and Technology. Vol.63 No.9 pp. 1317-1324 (2003)

[2] S.H. Hyon, K. Jamshidi, Y. Ikada, S. Higashi, Y. Kakutani and T. Yamamuro., “Bone Filler from Poly(lactic acid)-Hydroxyapatite” Japanese Journal of Polymer Science and Technology Vol42 No.11 (1985) PP 771-776 in Japanese.

[3] Y.Z. Wan, Y.L. Wang, X.H. Xu and Q.Y. Li “In Vitro Degradation Behavior of Carbon Fiber –Reinforced PLA Composites and Influence of Interfacial Adhesion strength” Journal of Applied Polymer Science Vol.82 No.1 pp. 150-158 (2001)

[4]N. A. Weir, F. j. Buchan and J.F. Orr., “Degradation of Poly-L-lactite. Part I in vitro and in vitro physiological temperature degradation” Proc. of the institute of Mechanical Engineering. Part H, Journal of engineering in medicine. Vol, 218 No.H5 pp 307-319 (2004)

[5] A. Piattelli “Early tissue reactions to polylactic acid responsible membranes: a histological and histochemical study in rabbit” Biomaterials Vol.19 No.10 pp.889-896 (1998)

Proceedings of the SEM Annual Conference
June 7-10, 2010 Indianapolis, Indiana USA

Advanced Accelerated Testing Methodology for Life Prediction of CFRP laminates

Yasushi MIYANO and Masayuki NAKADA
Materials System Research Laboratory, Kanazawa Institute of Technology
3-1 Yatsukaho Hakusan Ishikawa 924-0838, Japan
miyano@neptune.kanazawa-it.ac.jp

ABSTRACT The advanced accelerated testing methodology (ATM-II) for the long-term life prediction of CFRP laminates exposed to an actual loading having general stress and temperature history is proposed in this paper. Three conditions as the basis of ATM-II are introduced with the scientific bases. The long term fatigue strength of CFRP laminate under an actual loading is formulated based on the three conditions. The creep compliance and time-temperature shift factors of matrix resin, which perform an important role for time and temperature dependence of long-term life of CFRP laminates, are also formulated based on the modified time-temperature superposition principle. The applicability of ATM-II is confirmed by predicting the long-term fatigue strength of CFRP laminates for marine use.

Key words: CFRP, Life prediction, Viscoelasticity, Marine

1. Introduction

Carbon fiber reinforced plastics (CFRP) are now being used for the primary structures of airplanes, spacecrafts and others as well as ships, in which the high reliability should be kept during the long-term operation. Therefore, it would be expected that the accelerated testing methodology for the long-term life prediction of CFRP structures exposed under the actual environments of temperature, water, and others must be established.

A strategy of accelerated testing is shown as the following steps, 1) data collections of accelerated testing, 2) durability design, 3) development of highly reliable structures. First, the accelerated testing methodology should be established for polymer composites. Our developed methodology will be generic and can be applied to centrifuge, generator, flywheel, aircraft, wind turbine, marine and automobile.

T. Proulx (ed.), *Time Dependent Constitutive Behavior and Fracture/Failure Processes, Volume 3*, Conference Proceedings of the Society for Experimental Mechanics Series 15, DOI 10.1007/978-1-4419-9794-4_28, © The Society for Experimental Mechanics, Inc. 2011

In this paper, we propose an advanced accelerated testing methodology (ATM-II) which can be applied to the life prediction of CFRP laminates exposed to an actual load and environment history. First, three conditions as the basis of ATM-II are introduced with the scientific bases. One of these conditions is the fact that the time and temperature dependence on the strength of CFRP laminates is controlled by the viscoelastic compliance of matrix resin. Second, the formulations of creep compliance and time-temperature shift factors of matrix resin are carried out based on the modified time-temperature superposition principle. And the formulations of long-term life of CFRP laminates under an actual loading are carried out based on the three conditions. Third, the applicability of ATM-II for the long-term life prediction of CFRP laminates for marine use is confirmed under dry and wet conditions.

2. Advanced Accelerated Testing Methodology (ATM-II)

2.1 Concept of ATM-II

ATM-II is established with three following conditions,

(A) The time and temperature dependence of strength of CFRP is controlled by the viscoelasticity of matrix resin. Therefore, the time-temperature superposition principle for the viscoelasticity of matrix resin holds for the strength of CFRP.

(B) The strength degradation of CFRP holds the linear cumulative damage law as the cumulative damage under cyclic loading.

(C) The failure probability is independent of temperature and load histories.

A key component of ATM-II is also the empirical observation (A), which has been demonstrated its applicability for various CFRP laminates and their structures. Based on the condition (A), it is possible to calculate the strength variation of CFRP laminates by the viscoelastic compliance of matrix resin determined by the creep compliance of matrix resin and the history of load and temperature changed with time. With the condition (B), it is possible to calculate the strength degradation by load cycles undergoing to the linear cumulative damage law. With the condition (C), the reference strength and the failure probability can be obtained by measuring the static strength of CFRP laminates at an arbitrary strain rate under room temperature. The formulation for long-term fatigue strength of CFRP laminates exposed to an actual load and environment history are conducted under the three conditions of ATM-II.

The procedure for determining the materials parameters in the formulation of ATM-II is illustrated in Figure 1. First, the change in compliance of viscoelastic matrix resin is measured over time at a constant temperature. The tests are repeated for several elevated temperatures, which results in several compliance curves with the function of time. The time-temperature shift factor are then determined by shifting the creep compliance curves for

several temperatures into time scale to form a master curve of creep compliance at a reference temperature. The time-temperature shift factor is thus the measure of the acceleration of the life of matrix resin by means of the elevated temperatures. The next step is to obtain the creep strength master curves of CFRP laminates. This step consists of two parts. The first part is to determine static strength master curve of CFRP laminates from the static loading tests conducted at a single strain rate and several elevated temperatures using the time-temperature shift factor for matrix resin, and the second part is to convert the static strength master curve to the creep strength master curve of CFRP laminates. Third, the master curves of fatigue strength of CFRP laminates at zero stress ratio are determined by conducting the fatigue tests at several stress levels, a single frequency, stress ratio (zero stress ratio) and temperature using static strength master curve. Finally, the master curves of fatigue strength at an arbitrary stress ratio are determined by the creep strength master curve and the fatigue strength master curves at zero stress ratio. Through these procedures, all of materials parameters in the formulations can be determined for the long-term fatigue strength at an arbitrary load condition in which the stress and temperature arbitrarily changed with time.

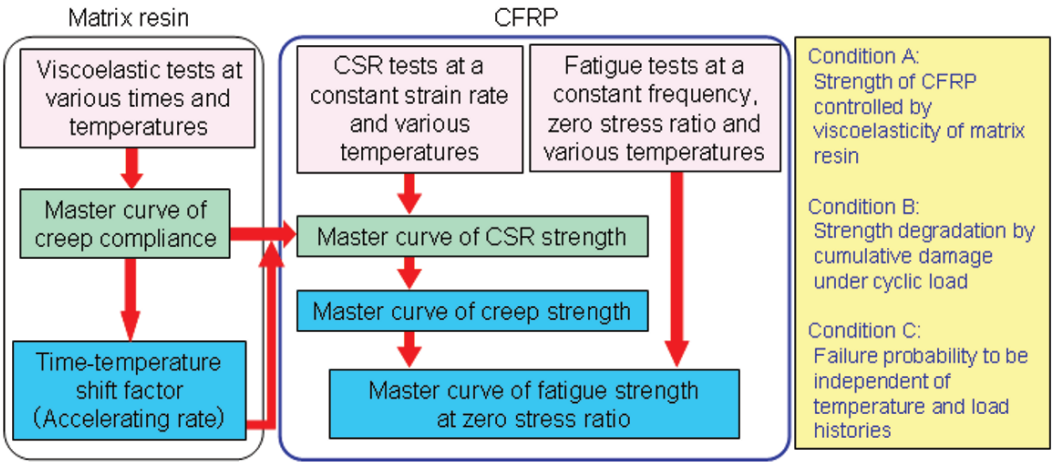

Figure 1 Procedure of ATM-II for CFRP laminates

2.2 Formulation of long-term fatigue strength of polymer CFRP laminates under actual loading

The long-term fatigue strength exposed to the actual loading where the temperature and load change with time can be shown by the following equation based on the conditions of A, B and C.

$$\log\sigma_f(t',T_0,N_f,R,P_f)=\log\sigma_{f0}(t_0',T_0)-n_r\log\left[\frac{D^*(t',T_0)}{D_c(t_0',T_0)}\right]-\frac{(1-R)}{2}n_f\log\left[\frac{2N_f}{1-k_D}\right]+\frac{1}{\alpha}\log[-\ln(1-P_f)] \quad (1)$$

The first term of left part shows the scale parameter for the strength at the reference temperature T_0, the reduced reference time t_0', the number of cycles to failure N_f = 1/2 and the stress ratio R = 1.

The second term shows the variation by the viscoelastic compliance of matrix resin which depend on temperature and load histories. The viscoelatic compliance can be shown by the following equation. (Condition A)

$$D^*(t', T_0) = \frac{\varepsilon(t', T_0)}{\sigma(t', T_0)} = \frac{\int_0^{t'} D_c(t'-\tau', T_0)\frac{d\sigma(\tau')}{d\tau'}d\tau'}{\sigma(t', T_0)}, \tag{2}$$

where, D_c shows the creep compliance of matrix resin and $\sigma(\tau')$ shows the stress history. t' in the above equation is the reduced time at the reference temperature T_0 and can be shown by the folowing equation.

$$t' = \int_0^t \frac{d\tau}{a_{T_0}(T(\tau))}, \tag{3}$$

where, a_{To} shows the time-temperature shift factor of matrix resin and $T(\tau)$ shows the temperature history.

The third term shows the degradation by the cumulative damage under cyclic load. The N_f and R in this term show the number of cycles to failure and the stress ratio at the final step, respectively. The k_D shows the Accumulation index of damage defined as the following equation based on the condition (B).

$$k_D = \sum_{i=1}^{n} \frac{n_i}{N_{fi}} < 1, \tag{4}$$

where n_i and N_{fi} are the number of cycles and the number of cycles to failure at the loading of step i, respectively.

The forth term shows Weibull distribution as the function of failure probability P_f based on condition C.

3. Modified time-temperature superposition principle

The formulation for the master curve of creep compliance of matrix resin D_c in Equation (1) and the time-temperature shift factor of matrix resin $a_{To}(T)$ in Equation (3) should be performed for the long-term fatigue strength of CFRP laminates under the actual loading. The master curve of D_c can be represented by two tangential lines, whose slopes are m_g and m_r, respectively. With these parameters, the master curve of D_c can be fit with the following equation,

$$\log D_c = \log D_c(t_0', T_0) + \log\left[\left(\frac{t'}{t_0'}\right)^{m_g} + \left(\frac{t'}{t_g'}\right)^{m_r}\right], \tag{5}$$

where t_0' is an initial reduced time at a reference temperature T_0. The t_g' is the reduced glassy time at a reference temperature T_0. The m_g and m_r are the parameters.

The modified time-temperature superposition principle was proposed for the determination of reliable master curve for the creep compliance of matrix resin. The vertical shifting as well as the horizontal shifting should be performed for getting the reliable master curve of creep compliance of matrix resin. The necessity of vertical shift was cleared theoretically and experimentally. The details of results are beyond the scope of this paper.

The horizontal time-temperature shift factor $a_{T_0}(T)$ that is the amount of the horizontal shift, can be fit with the following equation,

$$\log a_{T_0}(T) = \frac{\Delta H_1}{2.303G}\left(\frac{1}{T}-\frac{1}{T_0}\right)\mathrm{H}(T_g - T) + \left[\frac{\Delta H_1}{2.303G}\left(\frac{1}{T_g}-\frac{1}{T_0}\right) + \frac{\Delta H_2}{2.303G}\left(\frac{1}{T}-\frac{1}{T_g}\right)\right]\left[1-\mathrm{H}(T_g - T)\right], \tag{6}$$

where G is the gas constant, 8.314×10^{-3} [kJ/(Kmol)], ΔH_1 and ΔH_2 are the activation energies below and above the glass transition temperature T_g, respectively, and H is the Heaviside step function. The vertical temperature shift factor, $b_{T_0}(T)$, which is the amount of the vertical shift, can be fit with the following equation,

$$\log b_{T_0}(T) = b_1(T - T_0)\mathrm{H}(T_g - T) + \left[b_1(T_g - T_0) + b_2(T - T_g)\right]\left[1-\mathrm{H}(T_g - T)\right], \tag{7}$$

where b_1 and b_2 are the slopes of two line segments below and above T_g.

Alternatively, the viscoelastic behaviors of matrix resin can be represented by the storage modulus E' which can easily be measured with experimental devices such as the dynamic mechanical analyzer (DMA) conducted at various frequencies and temperatures. Note that D_c can approximately be obtained from E' by using

$$D_c(t) = 1/E'(f). \tag{8}$$

where it can be considered that the frequency f is equal to the inverse of time $1/(4t)$.

4. Long-term life prediction of CFRP laminates under dry and wet conditions

The long-term fatigue strength for three kinds of CFRP laminates under dry and wet conditions are formulated by substituting the measured data in Equation (1). Three kinds of CFRP laminates are plain woven T300 carbon fibers fabric/vinylester (T300/VE), plain woven T700 carbon fibers flat fabric/vinylester (T700/VE-F) and multi-axial knitted T700 carbon fibers fabric/vinylester (T700/VE-K) for marine use. These CFRP laminates were prepared under two conditions of Dry and Wet after molding. Dry specimens by holding the cured specimens at 150°C for 2 hours in air, Wet specimens by soaking Dry specimens in hot water of 95°C for 120 hours were respectively prepared.

4.1 Creep compliance and time-temperature shift factors

The creep compliances at various temperatures under Dry and Wet conditions shown in the left side of Figure 2 were shifted horizontally and vertically to construct the smooth master curve of creep compliance shown in the right side of this figure. The activation energy ΔH_1 in the horizontal time-temperature shift factor $a_{T_0}(T)$ shown by Equation (6) and the parameter b_1 in the vertical temperature shift factor $b_{T_0}(T)$ shown by Equation (7) were determined through the construction of creep compliance master curve. Additionally, the storage moduli under Dry condition measured at various temperatures in the relative high temperature range were also shifted horizontally and vertically to construct the smooth master curve of storage modulus. The activation energy ΔH_2, the parameter b_2 and T_g in Equations (6) and (7) which are the parameters in the high temperature range were determined through the construction of storage modulus master curve.

The material parameters of $D_c(t_0', T_0)$, t_g', m_g and m_r in the creep compliance master curve shown by Equation (5) are determined by fitting the creep compliance master curves under Dry and Wet conditions shown in Figure 2.

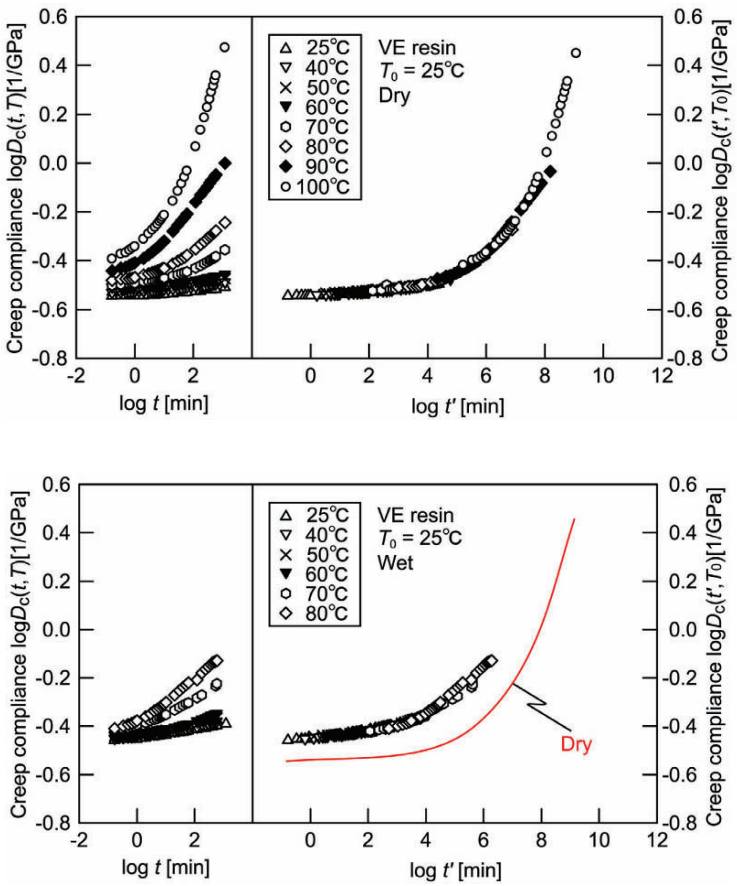

Figure 2 Master curves of creep compliance of matrix resin under Dry and Wet conditions

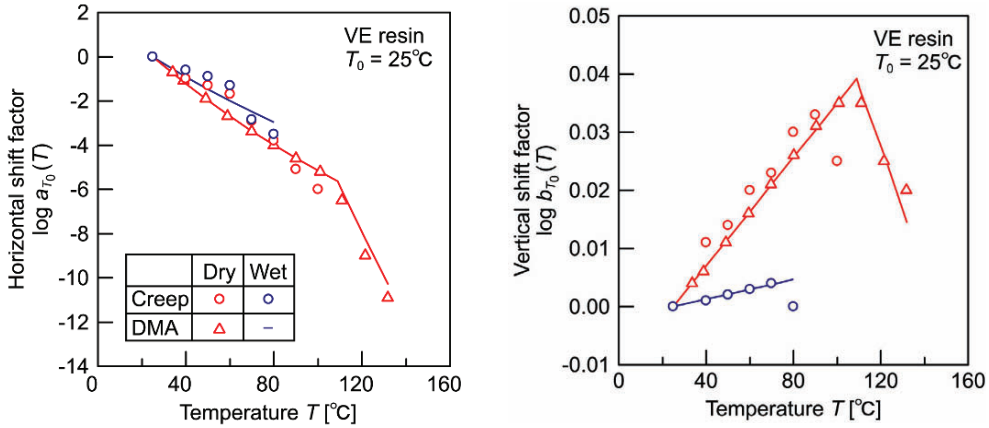

Figure 3 Horizontal and vertical shift factors under Dry and Wet conditions based on the modified time-temperature superposition principle

4.2 Flexural static strength of CFRP laminates under Dry and Wet conditions

The left side of each graph in Figure 4 shows the flexural static strength σ_s versus time to failure t_s at various temperatures T for three kinds of CFRP laminates under Dry and Wet conditions, where t_s is the time period from initial loading to maximum load during testing. The master curves of σ_s versus the reduced time to failure t_s' were constructed by shifting σ_s at various constant temperatures along the log scale of t_s using the same time-temperature shift factors for D_c and E' of matrix resin shown in Figure 3. The flexural static strength for three kinds of CFRP laminates under both of Dry and Wet conditions were formulated by using Equation (1). The formulated curves of flexural static strength of all three kinds of CFRP laminates under both conditions agree well with the experimental data. It is cleared from Figure 4 that the σ_s for all of three CFRP laminates under both of Dry and Wet conditions strongly decreases with increasing time, temperature and water absorption and that the time, temperature and water absorption dependent behavior for the flexural static strength is just the same for three kinds of CFRP laminates although the scale parameters σ_s of static strength for three kinds of CFRP laminates at an initial reduced time at a reference temperature are clearly different from each other, because the carbon fibers and weave structure are different. It is concluded that the time, temperature and water absorption dependent behavior for the flexural static strength of CFRP laminates is perfectly controlled by the viscoelastic behavior of matrix resin.

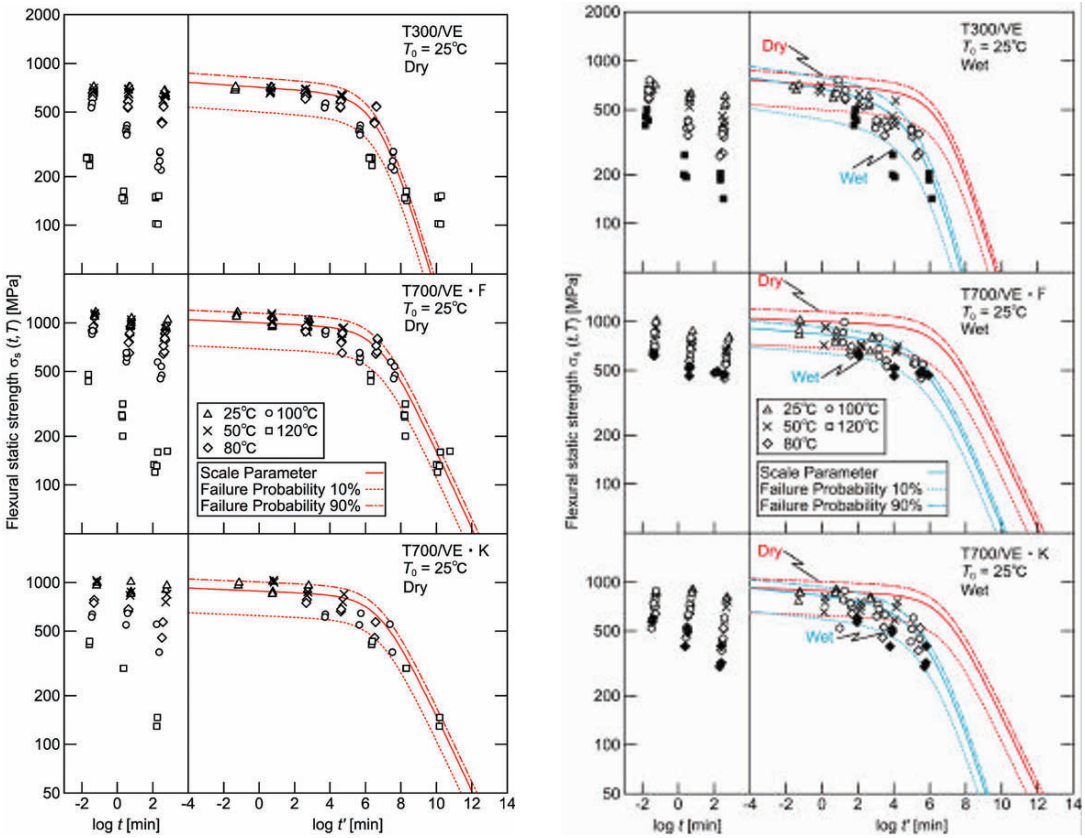

Figure 4 Master curves of flexural static strength of three kinds of CFRP laminates under Dry and Wet conditions

4.3 Flexural fatigue strength of CFRP laminates under Dry and Wet conditions

To construct the master curve of flexural fatigue strength σ_f, we need the reduced frequency f' in addition to the reduced time to failure t_f' defined by the following equations

$$f' = f \cdot a_{T_0}(T), \quad t_f' = \frac{t_f}{a_{T_0}(T)} = \frac{N_f}{f'} \tag{9}$$

where N_f is the number of cycles to failure. The master curves of fatigue strength versus the reduced time t' for distinct N_f can be constructed as depicted in solid curves in Figure 5. It is cleared from this figure that the σ_f of all three CFRP laminates strongly decreases with time to failure, temperature although the σ_f decreases scarcely with N_f. The effect of number of load cycles on the flexural strength of these CFRP laminates is negligible small.

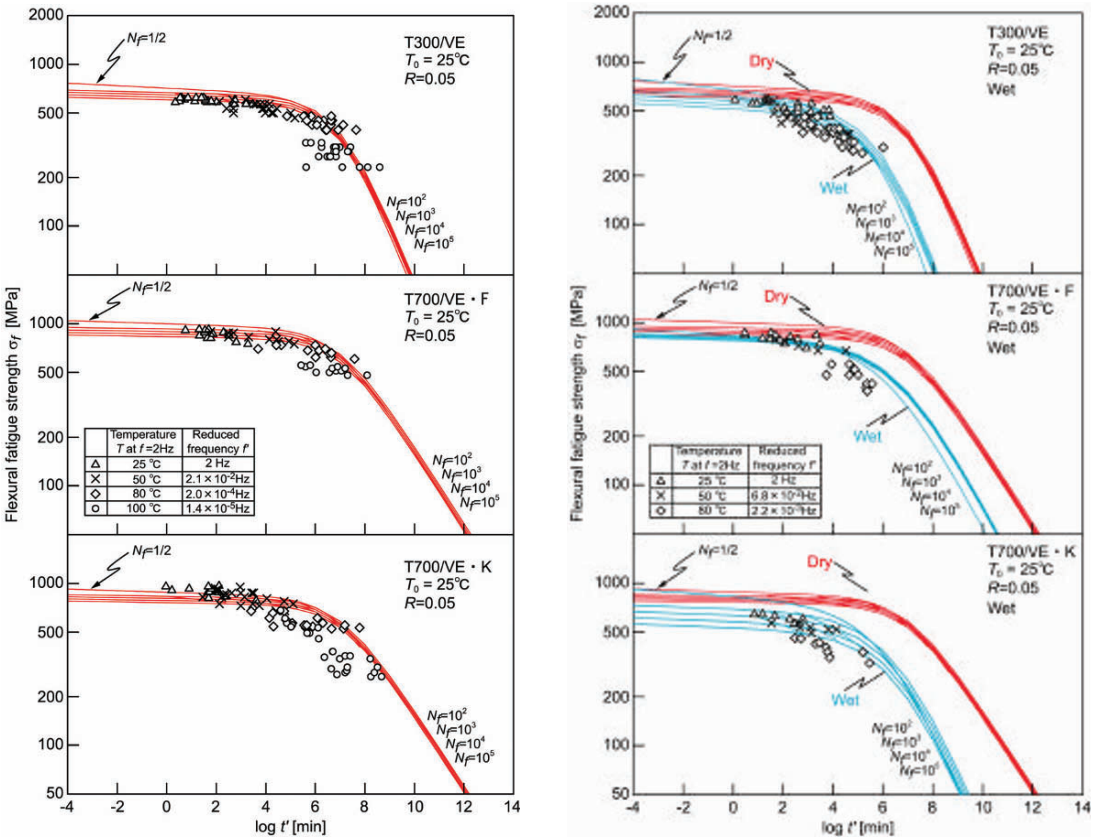

Figure 5 Master curves of flexural fatigue strength of three kinds of CFRP laminates under Dry and Wet conditions

5. Conclusions

The advanced accelerated testing methodology (ATM-II) for the long-term life prediction of CFRP laminates exposed to an actual loading having general stress and temperature history was proposed in this paper. Three conditions as the basis of ATM-II were introduced with the scientific bases. The long term fatigue strength of CFRP laminate under an actual loading was formulated based on the three conditions. The creep compliance and time-temperature shift factors of matrix resin, which perform an important role for time and temperature dependence of long-term life of CFRP laminates, were also formulated based on the modified time-temperature superposition principle. Finally, the applicability of ATM-II was confirmed by predicting the long-term fatigue strength of CFRP laminates for marine use.

Acknowledgements

The authors thank the Office of Naval Research for supporting this work through an ONR award with Dr. Yapa

Rajapakse as the ONR Program Officer. Our award is numbered to N000140611139 and titled “Verification of Accelerated Testing Methodology for Long-Term Durability of CFRP laminates for Marine Use”. The authors thank Professor Richard Christensen, Stanford University as the consultant of this project and Toray Industries, Inc. as the supplier of CFRP laminates.

References

1. Miyano, Y., and Nakada, M., Cai, H., “Formulation of long-term creep and fatigue strengths of polymer composites based on accelerated testing methodology”, Journal of Composite Materials, Vol.42, pp.1897-1919 (2008).
2. Christensen, R., and Miyano, Y. “Stress intensity controlled kinetic crack growth and stress history dependent life prediction with statistical variability”, Int. Jour. of Fracture, Vol.137, pp.77-87 (2006).

Proceedings of the SEM Annual Conference
June 7-10, 2010 Indianapolis, Indiana USA

Dynamic Properties of Foam with Negative Incremental Bulk Modulus

Yun-Che Wang*
Assistant Professor
Department of Civil Engineering; Center for Micro/Nano Science and Technology
National Cheng Kung University
No.1, University Road, Tainan, Taiwan 70101
Tel.: +886 6 2757575 ext. 63140. Fax: +886 6 2358542
E-mail: yunche@mail.ncku.edu.tw
*Corresponding author

Tim Jaglinski
Visiting Assistant Professor
Department of Engineering Science
National Cheng Kung University

Hsiu-Tsung Chen
Research Assistant
Department of Civil Engineering
National Cheng Kung University

ABSTRACT

Nonmonotonic load-displacement curves obtained from buckled tubes and single foam cells subjected to displacement controlled uniaxial compression are due to negative stiffness of the structural elements in the post-buckled regime. In the continuum limit, non-monotonic stress-strain curves obtained for elastomeric foams under volume controlled hydrostatic compression indicate negative incremental bulk moduli. Negative bulk moduli arise from cell rib buckling stabilized from collapse by the volumetric constraint. The objective of this work was to obtain an understanding of the material conditions necessary for non-monotonic constitutive behavior in open celled foam. For instance, amplitude degradation of the previously obtained incremental negative bulk modulus was observed after a small number of cycles. Commercial polyurethane foams with a pore size of 30 pores per inch (ppi) were subjected to quasi-static volume compression at strain rates of 5 $x10^{-3}$ and slower as well as constant volume bulk relaxation tests at ambient temperature. Negative incremental stiffness was observed in two of three specimens cut from the same parent material, however the detailed behavior was highly specimen and cycle dependent. Time dependent tests disclosed power law behavior for constant volume bulk relaxation. Dynamic tests were affected by parasitic damping in the test apparatus and control electronics. Foams showing negative incremental bulk moduli will be used in future work as inclusions in positive stiffness matrices for the development of exterlibral composites.

T. Proulx (ed.), *Time Dependent Constitutive Behavior and Fracture/Failure Processes, Volume 3*, Conference Proceedings of the Society for Experimental Mechanics Series 15, DOI 10.1007/978-1-4419-9794-4_29, © The Society for Experimental Mechanics, Inc. 2011

I. Introduction

The concept of negative stiffness has been shown to be a pathway to extremal material behavior. Negative stiffness is defined as a reversal in the usual directional relationship between casual forces and ensuing deformations [1]. The enhancing effects of negative stiffness were first demonstrated in a Reuss type composite composed of rubber tubes of positive stiffness in series with a tube in a post buckled state [2]. The composite structure possessed mechanical damping orders of magnitude above the base tube material. It is noted that unlike the negative structural stiffness associated with resonance of elements in metamaterials [3], in this case negative stiffness arises from stored elastic energy resulting from deformation of some of the composite tube elements into the post buckled regime.

Extension of the lumped Reuss composite to distributed material systems has resulted in a number of metal matrix composites displaying effective behavior outside the bounds obtained from the usual composite theory. For these composites, negative stiffness was provided by ceramic inclusions undergoing ferroelastic phase transitions triggered through temperature changes. A number of anomalous mechanical behaviors were obtained including enhanced mechanical damping during torsion [4], broad damping peaks [5] and macroscopic material instability [6]. Most notably, transient dynamic Young's Moduli greater than diamond were obtained for composites composed of barium titanate ($BaTiO_3$) inclusions in a cast tin (Sn) matrix [7].

For the metal matrix composites, negative stiffness of the composite inclusions has never been measured directly, rather, it is inferred from effective composite behavior. Negative stiffness is not normally observed as it is unstable unless constrained either by surface traction or displacement control. As an further example of inference, nonmonotonic stiffness and enhanced damping were observed during the martenisitic phase transition of polycrystalline indium-thallium alloys when subjected to cooling rates on the order of 40^{o}C/min [8]. Both of these effects were not observed in single crystals of the same material and can only be explained by considering the polycrystallite as a composite material. Portions of the polycrystallite constrain some of the grains giving rise to negative stiffness effects. For composites or polycrystalline materials, the effects of inclusion negative stiffness on the effective composite behavior are obtained from weighted averages between the constituent properties [1].

Negative incremental *structural* stiffness has been measured in post-buckled tubes [2] and models of single foam cells [9]. A incremental negative *material* stiffness, or bulk modulus in the continuum sense, was observed (Fig. 1) for bulk foam during volumetric compression [10]. In all of these studies, displacement control was necessary to observe the instability after a range of applied strain. For the bulk foam, volume constraint was achieved by a large mismatch between the bulk modulus of the sample, $K \approx 50$ kPa, and that of the water, $K \approx 2$ GPa. Negative bulk moduli arise from cell rib buckling stabilized from collapse by the volumetric constraint.

The present work is centered on understanding the dynamic properties of foam possessing negative incremental bulk modulus. The constitutive understanding will be used to guide the design of future foam composites having a negative stiffness phase. A secondary objective is to determine the cause of the loss of negative incremental stiffness with repeated cycling observed under quasi-static conditions (Fig 1b). Ultimately, we intend to (1) explore the range of allowable material structure which can give rise to negative incremental bulk modulus namely pore size, pore shape, and base foam material, (2) determine the dynamic range of observable negative stiffness (loading rate), (3) determine time dependent constitutive equations and (4) and measure the dynamic properties (complex moduli and mechanical damping) as a function of volumetric strain. In the present manuscript preliminary data is presented, current experimental difficulties are discussed and a path forward outlined.

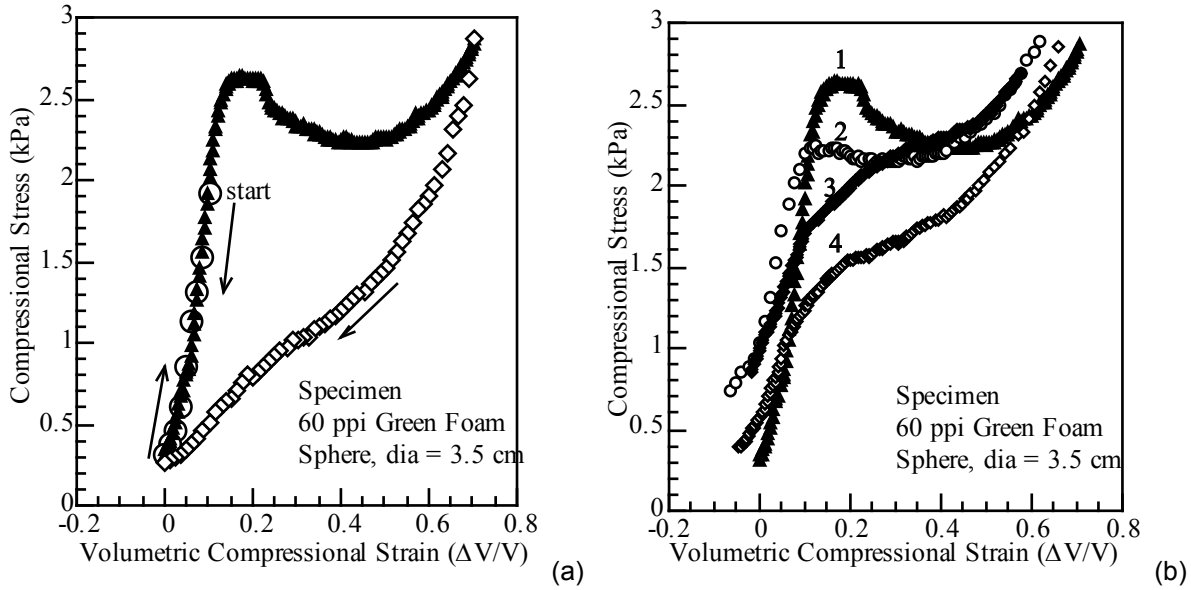

Fig. 1. (a) Nonmonotonic behavior in a load-unload cycle of a 60 ppi, 3.5 cm diameter sphere in displacement (volumetric) control. (b) Cycle dependence in repeated tests. Adapted from [10].

II. Materials and Methods

Foam specimens were sectioned from "Scotch Brite" (3M, Minnesota, USA) polyurethane foam. The foam was open celled, white in color and had an estimated pore size of 900 μm. This pore size corresponds to ~30 pores/inch (ppi). Visually, pores appeared to be iconic tetradecahedrons with little apparent anisotropy, however, pores in fact have an elliptical shape with an aspect ratio of 1.62. For compression tests, foam specimens had a volume of approximately 20 cm^3.

A volumetric compression chamber was built which could be held in a 25 kN servo-hydraulic MTS load frame. The test chamber was a 20 cm long acrylic tube with a 13 mm inner diameter and wall thickness of 5 mm. The tube was capped by 1 cm thick stainless steel covers. The top plate contains a piston to control volume with a cylinder diameter of 25 mm and total effective length of 7 cm (a total volume of 34.4 cm^2). When installed in the servo-hydraulic load frame, the bottom plate is rigidly held in the bottom grip, the top grip holds the piston. The working fluid was tap water at ambient temperature. Care was taken to eliminate as many air bubbles as possible from the system during filling, after installation into the load frame the system was cycled a number of times (without loading the sample) to bleed any air from the lines. To provide surface constraint, and hence volume compression, foam specimens were sealed inside thin rubber membranes (Durex Fetherlite Ultima, Norcross, Georgia) using electrical tape. An air escape tube, with access through the bottom plate, was also included.

Water pressure was measured using an Impress (Berkshire, UK) DMP 331 (model# 110-0400-3-5-100-N40-1-000) pressure sensor which uses a stainless steel membrane for pressure measurement. The sensor has a 0-100 mbar gauge pressure range corresponding to a 0-10 VDC output. Output voltages were recorded on an Agilent Technologies DSO7032A digital oscilloscope. Linear displacements of the piston were measured using the MTS's linear voltage displacement transducer (LVDT) and native control electronics, to correlate in time the displacement signal was also recorded on the second channel of the scope.

III. Results and Discussion

A. Incremental Negative Stiffness

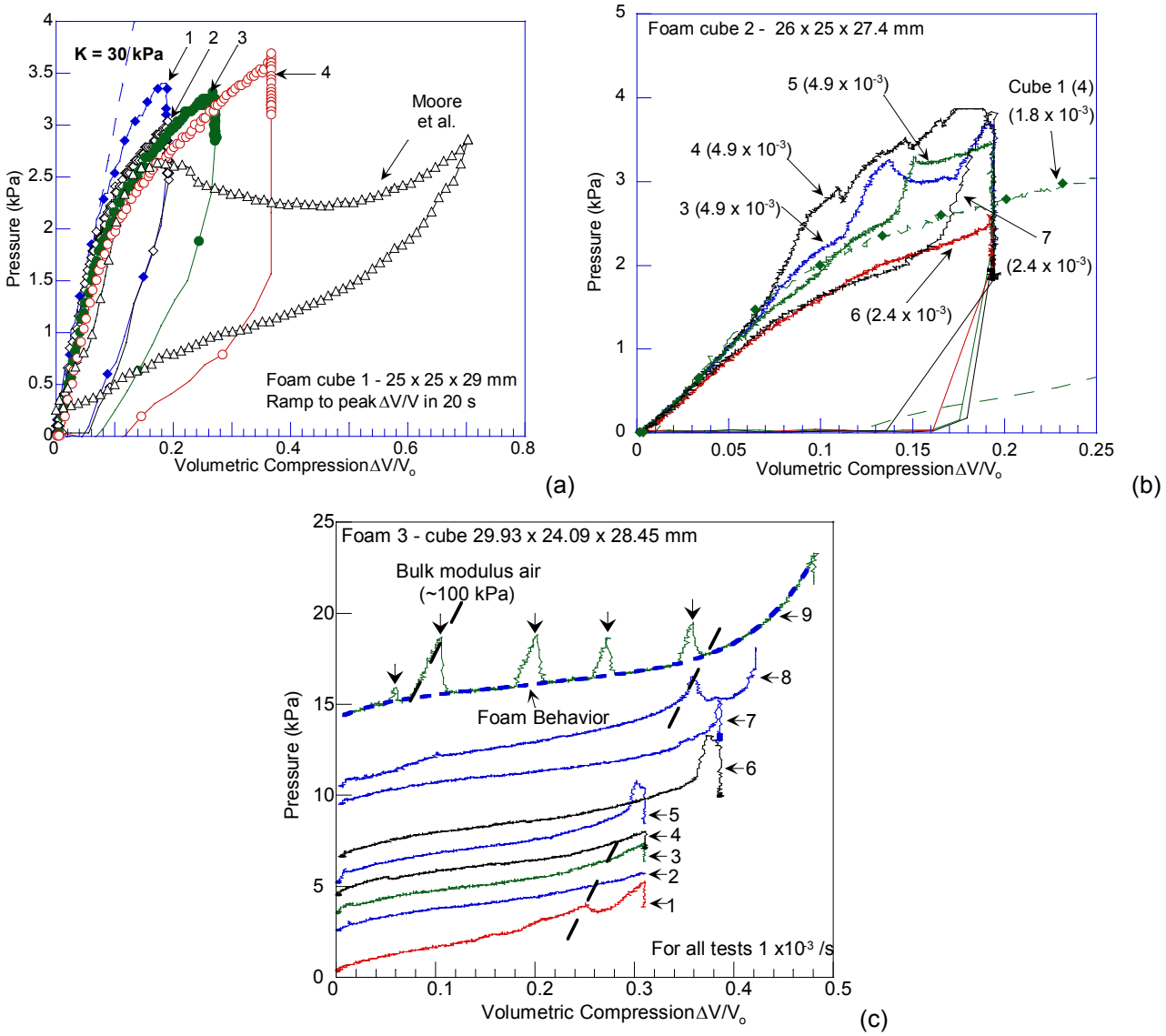

Fig. 2 – First three foam cubes tested in volumetric compression. (a) Cube 1 did not display negative incremental modulus as compared to data from Moore et al. [10]. (b) Cube 2 displayed reversals, however, behavior was not consistent for repeated cycles. Test #4 from cube 1 is shown as a comparison to cube 2. (c) Cube 3 also displayed inconsistent reversals which shifted in strain ranges with repeated tests. Also shown in (c) are intentional closures of the air relief tube, marked by the arrows in test #9, to determine if the membrane was sealing air inside the specimen.

Three cube foam samples were tested of roughly the same volume (18.1, 17.8 and 20.5 cm^3) and cut from the same original piece of material. Cubes 2 and 3 displayed reversals in their pressure-volume compression curves indicating negative incremental bulk modulus (Fig. 2b,c). Cube 1 did not display a reversal (Fig 2a). It is noted that the pore size of the present specimens is 30 ppi or roughly twice as large as the 60 ppi foam specimens previously studied [10]. For cubes 2 and 3, reversals were different in both the character and strain range for repeated tests. Cube 3 showed rapid increases in bulk modulus which were thought to be caused by the membrane temporarily sealing the air relief tube, hence causing compression of the trapped gas. This was tested by intentionally closing the air relief tube with its connection valve, as indicated in test #9 for cube 3 in Fig. 2c,

resulting in a transition from the bulk foam behavior to the bulk modulus of air (~100 kPa). However, the onset of the change is instantaneous and the release nearly so, relaxing back to the foam behavior. It is still unclear whether the rapid increases in test 5-8 are indicative of the true foam constitutive behavior or are experimental artifacts.

B. Dynamic Properties

As the main thrust of this work is the determination of the dynamic properties of the foam, constant volume bulk relaxation and cyclic tests were conducted. For relaxation, power law behavior was obtained for low values of volumetric strain (Fig. 3a). The rise time of the volume compression pulse was rather long, and will be shortened in future tests.

For cyclic loading, no results from the foam are presented. A number of experimental issues must be overcome before accurate results for the foam can be obtained. Most importantly, though sinusoids can be stipulated and obtained for the MTS cross head displacements, corresponding pressure measurements made in the water (no specimen) are not sinusoidal. This is apparent in Fig. 3b as bending of the sinusoids, which are present at every value of precompression and are likely due to sliding/rolling of the piston o-rings. Secondly, the displacement sinusoid lags the pressure signal due to phase errors incurred from the MTS signal conditioning. Considering the displacement is the control signal it must lead the pressure response for passive materials. The pressure signal is recorded directly from the pressure sensor, the displacement signal runs through the native MTS electronics before being recorded on the scope. The parasitic damping can be estimated from the phase lag ($\Delta t = 0.086$ s) by $\tan \delta = \tan(2\pi\Delta t/T) = 0.277$, where T is the period of the sinusoidal wave. Removing or correcting this lag will be important to get accurate measurements of the foam $\tan \delta$.

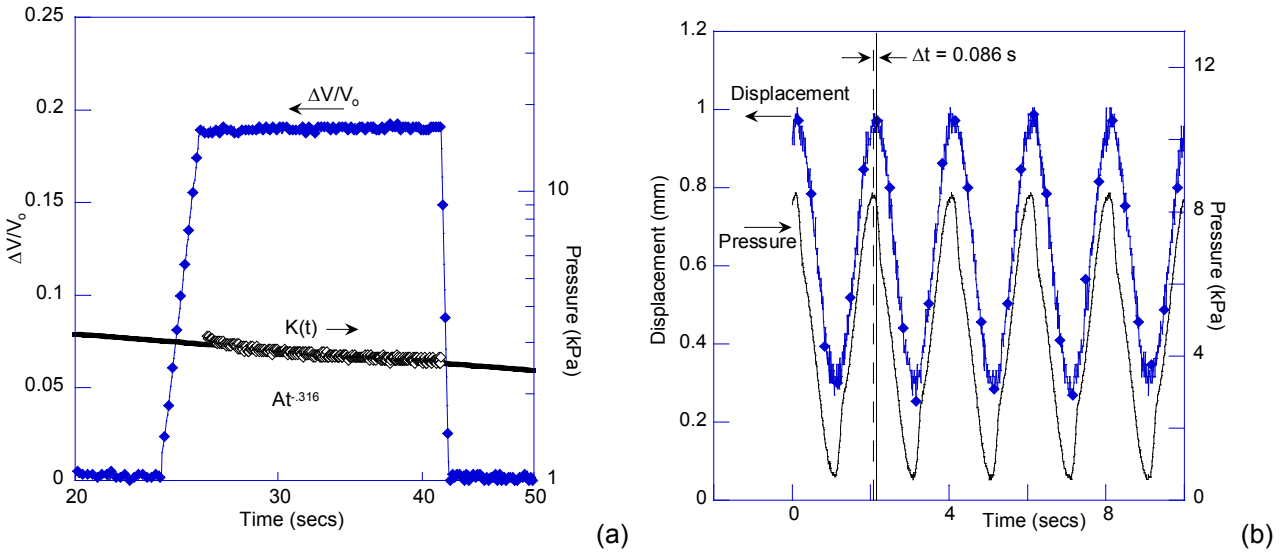

Fig. 3 – (a) Power law bulk relaxation behavior of the open celled foam. The volume compression pulse is not a not a step function, hence data are not reported until several seconds into the test. (b) Dynamic loading of the water only, hence the machine response. The pressure response is not sinusoidal and leads the displacement control signal. The time shift is due to phase errors incurred from the MTS electronics.

IV. Conclusions

Negative incremental bulk moduli were observed in a large pore size, open celled foam during preliminary quasi-static volumetric compression tests at strain rates on the order of 5 $x10^{-3}$ /s and slower. However, the obtained behavior is not consistent between samples cut from the same parent material or for repeated cycles of each

specimen. Some rapid reversals in the pressure-volumetric compression curves may be due to sealing of the membrane from the ambient atmosphere. Constant volume bulk relaxation tests disclosed power law behavior for low volume compressions; more testing is required using step function inputs to quantify the behavior. Frequency tests need further investigation due to mechanical coupling in the piston and electronic phase errors.

Acknowledgements

The authors are grateful for a grant from Taiwan National Science Council under the contract number NSC 98-2221-E-006-131-MY3. Experimental help from J. W. Lien is acknowledged.

References

[1] Lakes, R. S., "Extreme damping in composite materials with a negative stiffness phase," Phys. Rev. Ltrs. **86** (2001).

[2] Lakes, R. S., "Extreme damping in compliant composites with a negative stiffness phase," Phil. Mag. Ltrs **81** (2001).

[3] Ding Y., Liu Z. Qiu C., Shi J., “Metamaterial with simultaneously negative bulk modulus and mass density,” Phys. Rev. Ltrs. **99** (2007).

[4] Lakes, R. S., Lee, T., Bersie, A., Wang, Y. C., "Extreme damping in composite materials with negative stiffness inclusions", Nature **410** (2001).

[5] Jaglinski T, Stone DS, Lakes RS, “Internal friction study of a composite with a negative stiffness constituent,” J. Mats. Res. **20** (2005).

[6] Jaglinski T, Lakes RS, “Anelastic instability in composites with negative stiffness inclusions,” Phil. Mag. Ltrs. **84** (2004).

[7] Jaglinski, T., Kochmann, D., Stone, D., Lakes, R. S. "Materials with viscoelastic stiffness greater than diamond," Science **315** (2007).

[8] Jaglinski T., Frascone P., Moore B., Stone D.S., Lakes R.S., “Internal friction due to negative stiffness in the Indium-Thallium martensitic phase transformation,” Phil. Mag. **86** (2006).

[9] Rosakis, P., Ruina, A., and Lakes, R. S., "Microbuckling instability in elastomeric cellular solids," J. Mats. Sci. **28** (1993).

[10] Moore B, Jaglinski T, Stone DS, Lakes RS, “Negative incremental bulk modulus in foams,” Phil. Mag. Ltrs**. 86** (2006).

Proceedings of the SEM Annual Conference
June 7-10, 2010 Indianapolis, Indiana USA

A Note on Automated Time-Temperature and Time-Pressure Shifting

M. Gergesova, B. Zupančič, and I. Emri
Center for Experimental Mechanics, Faculty of Mechanical Engineering, University of Ljubljana, Aškerčeva 6, 1000 Ljubljana, Slovenia – marina.gergesova@fs.uni-lj.si

ABSTRACT

Time-dependent material functions of engineering plastics within the exploitation range of temperatures extend over several decades of time. For this reason material characterization is carried out at different temperatures and/or pressures within a certain experimental window, which for practical reasons extends typically over four decades of time. For example, when relaxation experiments in shear, are performed at different constant temperatures and/or pressures, a set of segments is obtained. Using the time-temperature and/or time-pressure superposition principle, these segments can be shifted along the logarithmic time-scale to obtain a master curve at a selected reference conditions.

This shifting is commonly performed manually ("by hand"), and requires some experience. Unfortunately, manual shifting is not based on a commonly agreed mathematical procedure which would, for a given set of experimental data, yield always exactly the same master curve, independently of a person who executes the shifting process. Thus, starting from the same set of experimental data two different researchers could, and very likely will, construct two different master curves.

In this paper we propose mathematical methodology which completely removes ambiguity related to the manual shifting procedures. Paper presents the derivation of the shifting algorithm and its validation using several simulated- and real- experimental data.

Keywords: time-temperature (-pressure) superposition principle, master curve, algorithm for automated time-temperature shifting, long-term behavior of polymers

1. Introduction

The shear relaxation modulus of polymeric materials typically exhibits three regions, which are determined by time (or temperature, or pressure), as schematically shown in Figure 1. The first region is called glassy, where the properties are constant and the material is hard and brittle. As one waits longer in time (or increases temperature, or decreases pressure), the test material enters the transition region, where the material properties drastically change. By waiting longer (or increasing temperature further, or decreasing pressure further) we come to the rubbery region, where the material behaves like a rubber. The modulus stays close to constant if the material is cross linked (e.g., rubbers), while in the case of non-cross linked materials (most thermoplastics), the material enters the flow region. In regard to this, the value of the modulus in the glassy state becomes, G_g, and in the rubbery (or equilibrium) state, G_r (or G_e). These regions can be related to the volume behavior explained in [1], where the transition region is narrowed to the dashed vertical line.

T. Proulx (ed.), *Time Dependent Constitutive Behavior and Fracture/Failure Processes, Volume 3*, Conference Proceedings of the Society for Experimental Mechanics Series 15, DOI 10.1007/978-1-4419-9794-4_30,

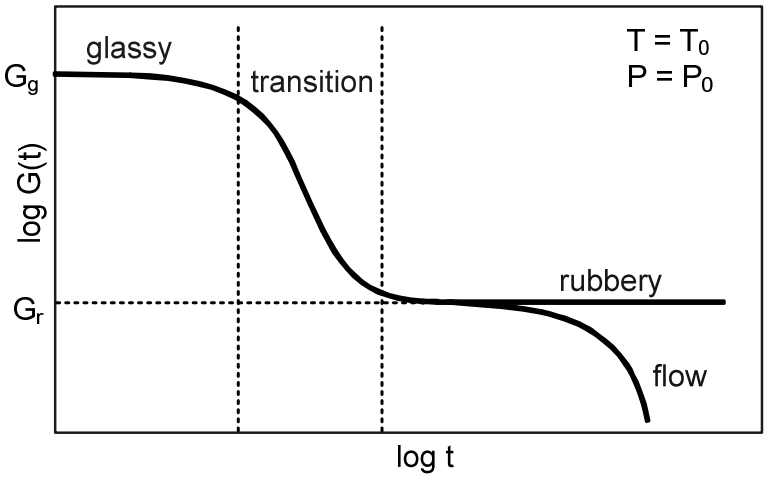

Figure 1: Schematic representation of the shear relaxation modulus, $G(t)$: Four regions of $G(t)$ for a polymer

The curve, shown in Figure 1, usually extends over several decades of time, which are physically impossible to measure. For this reason, data are collected from experiments within a certain time interval, commonly called the *experimental window*, which typically extends over four decades of time [3]. When experiments are performed at different constant temperatures, and/or different constant pressures, a set of $G(t)$ segments is obtained. Using the time-temperature $(t-T)$ and/or time-pressure $(t-P)$ superposition principle (if applicable), these segments can be shifted along the logarithmic time-scale to obtain the master curves schematically shown in Figure 2 [2]. If the superposition principle is valid, the master curves represent the long-term behavior of the material, at the chosen reference conditions, T_0 and P_0.

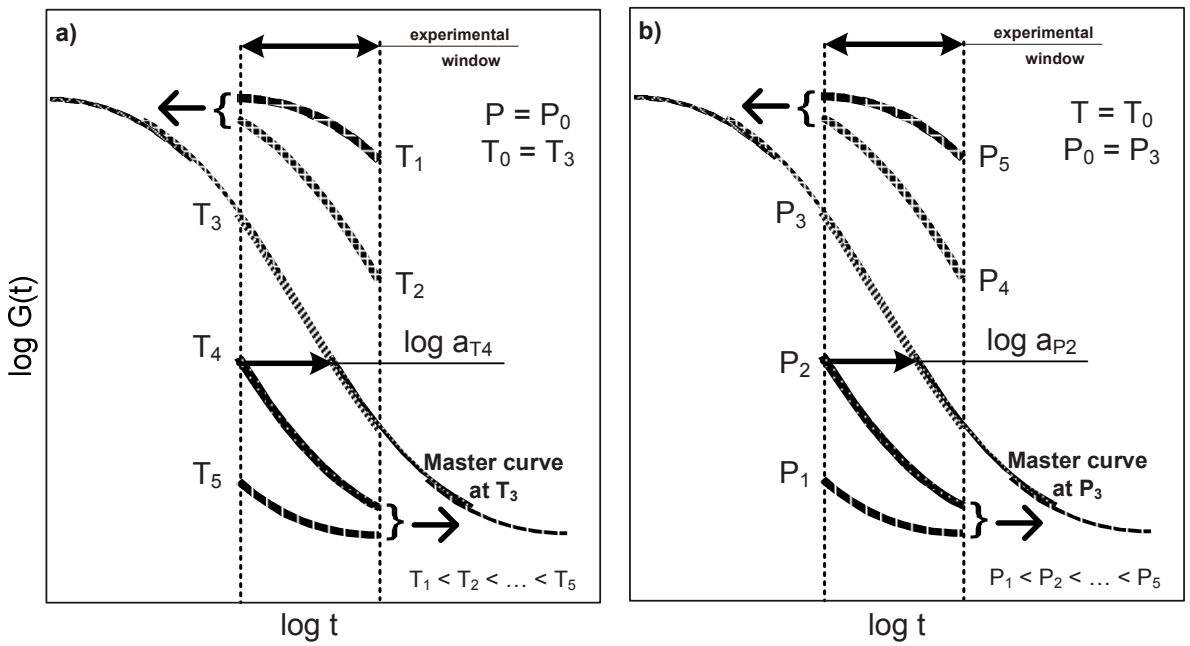

Figure 2: Schematics of (a) $t-T$ superposition of $G(t)$ for reference temperature $T_0 = T_3$, and (b) $t-P$ superposition of $G(t)$ for reference pressure $P_0 = P_3$

This shifting is commonly performed “by hand”, and requires some experience. Unfortunately, »hand-shifting« is not based on a commonly agreed mathematical procedure which would, for a given set of experimental data, yield always the same master curve. Thus, starting from the same set of experimental data two different researchers could, and very likely will construct two different master curves. Knauss W.G. [3] and Zhao J. et al. [4] presented the shift factors as function of temperature obtained by two different authors. They assumed that in spite of the scatter the data are precise enough. However, slight variations in the shift factors with temperature can influence on the accuracy of the master curve [5].

Along with “hand shifting” there are different numerical procedures for calculation of shift factors. Most of them are based on the least-square method where shift factors are determined by minimizing the sum of square errors in horizontal distances between adjacent segments in the overlapping area [5]-[8]. There are also algorithms which allow, for example, calculating shift factors iteratively [9], or by matching the first derivatives of neighboring curves [10], or by minimizing the total arc length of the master curve [11], etc.

Practically, all of these methods include, as a preliminary step, fitting of the experimentally obtained segments. However, the approximating procedure by itself is not universal. The authors suggest variety of the interpolation functions starting from a simple linear fitting and finishing with multi parameter complex expressions.

The shifting procedure is therefore one of the weakest points in the utilization of the time-temperature, or equivalently, time-pressure superposition principle.

In this paper we propose simple mathematical methodology, which completely removes the previously mentioned problems related to shifting of the experimental data in the process of constructing the master curve at selected reference temperature and pressure conditions. Proposed algorithm predicts unique master curve and completely removes ambiguity related to different shifting procedures.

For the simplicity reasons we will discuss the time-temperature shifting for the shear relaxation data. However, it is obvious that shifting procedure as such is independent of conditions at which the data were obtained, as long as the superposition principle is valid.

2. The Shifting Algorithm

Let us now assume that the experiments were performed at constant pressure $P = P_0$, and at M different temperatures, i.e., $\left\{T_j;\, j = 1,2,\cdots,M\right\}$. Furthermore, let each of the M measured segments be given with N_j discrete datum points,

$$G\left(T_j,t\right) = \left\{G_{j,i} = G_i\left(T_j\right), t_i;\ i = 1,2,\ldots,N_j\right\}. \tag{1}$$

Experimental data on relaxation modulus and creep compliance are commonly presented as a discrete datum pairs in a double logarithmic scale. Taking this in consideration the complete set of experimental data may then be expressed as

$$\mathcal{G}\left(T,t\right) = \left\{\log G_{j,i} = \log G_i\left(T_j\right), \log t_{j,i} = \log t_i\left(T_j\right);\ j = 1,2,\cdots,M;\ i = 1,2,\cdots,N_j\right\}. \tag{2}$$

Let us select the temperature T_κ as a reference temperature, and the corresponding data measured at these conditions as a reference segment of the master curve,

$$\mathcal{G}\left(T_\kappa,t\right) = \left\{\log G_{\kappa,i}, \log t_{\kappa,i};\ \ i = 1,2,\cdots,N_\kappa\right\}. \tag{3}$$

To construct the master curve at the selected temperature T_κ we need to shift all segments measured at $T_j > T_\kappa$ to the right, and the remaining segments, measured at $T_j < T_\kappa$ to the left along the logarithmic time-axis, so as to obtain a "smooth" master curve, as schematically shown in Fig. 2. The shifting must be executed sequentially, starting with segments measured at $T_{\kappa+1} > T_\kappa$, and $T_{\kappa-1} < T_\kappa$, until all of the segments are brought together. The individual horizontal shifts, $\log a\left(T_j; j \neq \kappa\right)$, obtained in this process represent a set of discrete values that describe the so-called time-temperature superposition principle, which is commonly modeled with the WLF model [1, 2].

The set of temperatures, $\left\{T_j, j = 1, 2, \cdots, M\right\}$, at which relaxation or creep experiments are performed should be selected such that segments measured at two consecutive temperatures, e.g., T_κ, and $T_{\kappa+1}$ will overlap sufficiently to allow effective construction of the master curve. The common "rule of thumb" is that this overlapping should be at least one logarithmic decade of time.

The first datum point of the segment $(\kappa+1)$, i.e., $\log G_{\kappa+1,1}$, and the last datum point of the segment κ, i.e., $\log G_{\kappa,N_\kappa}$ represent strengths of the first and the last datum point in the window where the two segments overlap, as shown in Fig. 3.

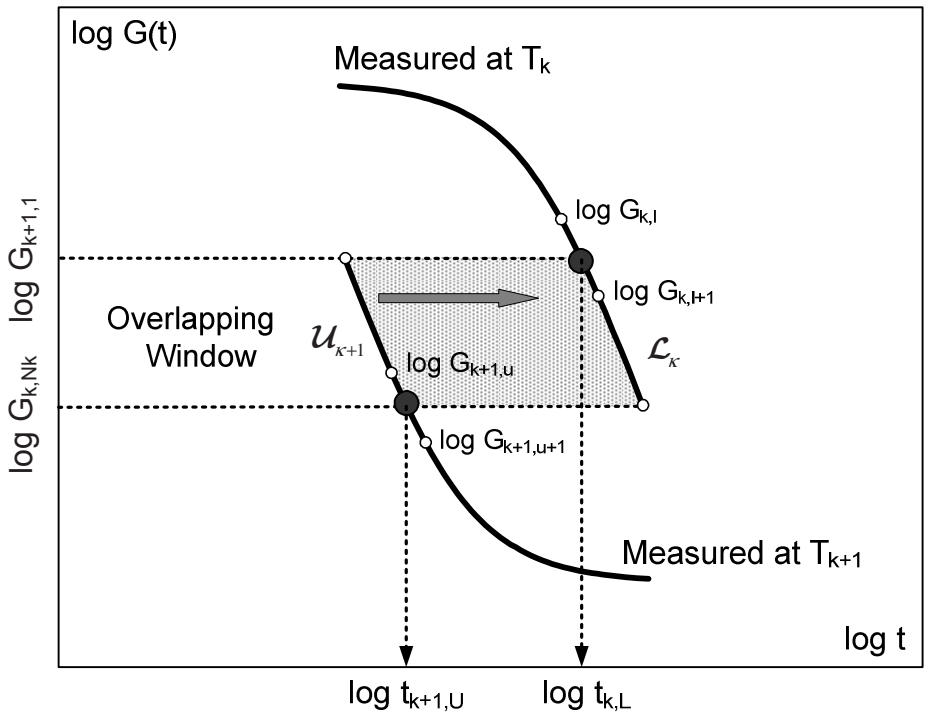

Figure 3: Schematics of the shifting procedure

The overlapping sets of two segments we denote as

$$\mathcal{U}_{\kappa+1} = \left\{\log G_{\kappa+1,n}, \log t_{\kappa+1,n}; n = 1, 2, \cdots, U_{\kappa+1}\right\}, \text{ and} \tag{4}$$

$$\mathcal{L}_\kappa = \left\{\log G_{\kappa,n}, \log t_{\kappa,n}; n = L_\kappa, L_\kappa + 1, \cdots, N_\kappa\right\}. \tag{5}$$

The location of the last datum point of the set $\mathcal{U}_{\kappa+1}$, i.e., $\log G_{\kappa+1,U_{\kappa+1}} = \log G_{\kappa,N_\kappa}$, may be expressed as

$$\log t_{\kappa+1,U_{\kappa+1}} = \log t_{\kappa+1,u} + \left(\log G_{\kappa+1,u} - \log G_{\kappa+1,U_{\kappa+1}}\right) \cdot \frac{\log t_{\kappa+1,u+1} - \log t_{\kappa+1,u}}{\log G_{\kappa+1,u} - \log G_{\kappa+1,u+1}}. \tag{6}$$

Whereas the location of the first datum point of the set $\mathcal{L}_\kappa$, i.e., $\log G_{\kappa,L_\kappa} = \log G_{\kappa+1,1}$, is given in the form,

$$\log t_{\kappa,L_\kappa} = \log t_{\kappa,l} + \left(\log G_{\kappa,l} - \log G_{\kappa,L_\kappa}\right) \cdot \frac{\log t_{\kappa,l+1} - \log t_{\kappa,l}}{\log G_{\kappa,l} - \log G_{\kappa,l+1}}. \tag{7}$$

To construct the master curve at the selected temperature T_κ we need to shift the segment measured at $T_{\kappa+1}$ to the right along the logarithmic time-axis, so as to obtain the “smooth” master curve. Thus, in the ideal case, for all data within the Overlapping Window the condition

$$G_\kappa(t) = G_{\kappa+1}(t \cdot a_{\kappa+1}) \tag{8}$$

must be fulfilled. We may intuitively see that in the case of real data, which contain experimental error, and even more so for the synthetic data without an experimental error, we would obtain an optimal overlapping of the two curves when the shaded area between the two curves is equal to zero, see Fig. 3. Hence,

$$A = A_\kappa - A_{\kappa+1} = 0, \tag{9}$$

where

$$A_{\kappa+1} = \sum_{n=1}^{U_{\kappa+1}-1} \left[\frac{\left(\log t_{\kappa+1,n+1} + \log a_{\kappa+1}\right) + \left(\log t_{\kappa+1,n} + \log a_{\kappa+1}\right)}{2} \cdot \left(\log G_{\kappa+1,n+1} - \log G_{\kappa+1,n}\right) \right], \text{ and} \tag{10}$$

$$A_\kappa = \sum_{n=L_\kappa}^{N_\kappa-1} \left[\frac{\log t_{\kappa,n+1} + \log t_{\kappa,n}}{2} \cdot \left(\log G_{\kappa,n+1} - \log G_{\kappa,n}\right) \right]. \tag{11}$$

Combining equations (9) – (11), we may calculate the shift factor belonging to the segment measured at $T_{\kappa+1}$,

$$\log a_{\kappa+1} = \frac{A_\kappa - \sum_{n=1}^{U_{\kappa+1}-1} \left[\frac{\log t_{\kappa+1,n+1} + \log t_{\kappa+1,n}}{2} \cdot \left(\log G_{\kappa+1,n+1} - \log G_{\kappa+1,n}\right) \right]}{\sum_{n=1}^{U_{\kappa+1}-1} \left(\log G_{\kappa+1,n+1} - \log G_{\kappa+1,n}\right)}, \tag{12}$$

which is equal to,

$$\log a_{\kappa+1} = \frac{A_\kappa - \sum_{n=1}^{U_{\kappa+1}-1} \left[\frac{\log t_{\kappa+1,n+1} + \log t_{\kappa+1,n}}{2} \cdot \left(\log G_{\kappa+1,n+1} - \log G_{\kappa+1,n}\right) \right]}{\log G_{\kappa,N_\kappa} - \log G_{\kappa+1,1}} \tag{13}$$

This algorithm is valid for shifting the segments measured at $T_j > T_\kappa$. For shifting those segments that were measured at $T_j < T_\kappa$ we need to modify the algorithm as follows,

$$\log a_{\kappa-1} = \frac{A_\kappa - \sum_{n=L_{\kappa-1}}^{N_{\kappa-1}-1}\left[\frac{(\log t_{\kappa-1,n+1} + \log t_{\kappa-1,n})}{2}\cdot\left(\log G_{\kappa-1,n+1} - \log G_{\kappa-1,n}\right)\right]}{\log G_{\kappa-1,N_{\kappa-1}} - \log G_{\kappa,1}}, \tag{14}$$

where

$$A_k = \sum_{n=1}^{U_k-1}\left[\frac{\log t_{k,n+1} + \log t_{k,n}}{2}\cdot\left(\log G_{k,n+1} - \log G_{k,n}\right)\right].$$

From the experience with the "hand-shifting" of response function segments we know that there are four main parameters that determine the goodness of the shifting procedure, i.e., (i) the size of the window on G-axis where the two segments overlap, i.e., size of the Overlapping Window (OW); (ii) the degree of segments inclination within OW, (iii) the magnitude of the experimental error present in the measured response function segments, and (iv) the number of (measured) discrete datum points per decade.

In this paper we limit our analysis to the effect of the OW size, and the number of (measured) discrete datum points per decade on the goodness of time-temperature shifting.

3. Examples and Discussion

We examined the proposed automated shifting procedure on simulated experimental data (synthetic data) generated from the known discrete spectrum $H(\tau)$ using Lorentzian type of distribution [12], i.e.,

$$H_i^L = H^L(\tau_i) = \frac{2}{\left(\frac{\tau_i}{\tau_0}\right)^r + \left(\frac{\tau_0}{\tau_i}\right)^r}. \tag{16}$$

By changing the two parameters of the Lorentzian distribution, τ_0 and r, one can generate response functions with different degree of inclination. Parameter $\log\tau_0$ defines the location of the spectrum maximum along the logarithmic response-time-axis, whereas the parameter r determines the width of the spectrum. For $r \to \infty$ the Lorentzian distribution becomes a single line spectrum, and for $r = 0$ the so called "box" distribution, i.e., all spectrum lines have the same strength. The two extremes furnish response functions with the largest and the smallest inclinations that are possible for the time-domain response functions. Thus, by changing τ_0 and r we may systematically analyze the effect of the response function inclination on the accuracy of time-temperature shifting.

For the analysis presented here we have selected $\log\tau_0 = -0.7$, and $r = 0.122$, along with $G_g = 1260\,MPa$, and $G_e = 92\,MPa$ for the glassy and the equilibrium modulus, respectively. We have generated 61 spectrum lines, ranging from $\log\tau = -15$ to $\log\tau = 15$ seconds, i.e., two lines per decade. Strengths of the generated spectrum lines were normalized according to

$$\sum_{i=1}^{i=61} H_i^L = G_g - G_e \,. \tag{17}$$

According to this we have,

$$H(\tau) = \left[\frac{H_i^L}{\sum_{j=1}^{j=61} H_j^L} \left(G_g - G_e\right),\ \tau_i;\ i = 1,\ 2,\ 3, \cdots,\ 61 \right]. \tag{18}$$

The spectrum is presented in Fig. 4.

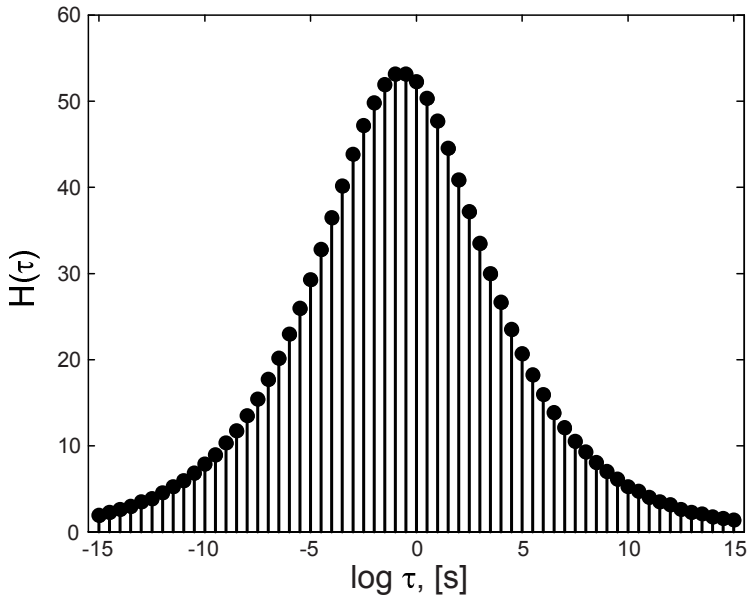

Figure 4: Relaxation spectrum modeled by Lorentzian distribution, with $\log \tau_0 = -0.7$, $r = 0.122$, $G_g = 1260\,MPa$, and $G_e = 92\,MPa$

The simulated "experimental data" were then generated from

$$G(t) = G_e + \sum_{i=1}^{i=61} H_i \exp\left(-t/\tau_i\right) = G_g - \sum_{i=1}^{i=61} H_i \left[1 - \exp\left(-t/\tau_i\right)\right]. \tag{19}$$

The spectrum and the glassy and equilibrium moduli which we have selected closely mimic the shear relaxation modulus of the standard PA6-BS400N produced by BASF. Comparison of the measured relaxation function [13] and the simulated data, at the reference temperature $T_0 = 50^\circ C$, are shown as dots and continuous curves, respectively, in Fig. 5.

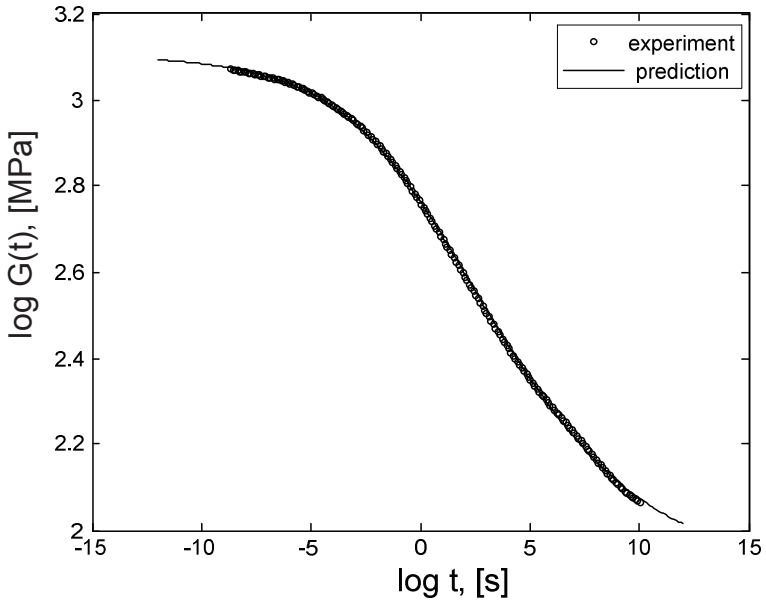

Figure 5: Comparison of measured and simulated data for PA6-400N at $T_0 = 50^\circ C$

The analysis to the effect of the OW size, and the number of (measured) discrete datum points per decade on the goodness of time-temperature shifting were performed within the OW that was positioned at the point of largest inclination of the response function, which at the reference temperature $T_0 = 50^\circ C$ positioned roughly at $G(T_0) = 2.57\,MPa$. We have used previously determined WLF constants, i.e., $C_1 = 225.35$, and $C_2 = 944.62^\circ C$ to obtain the two segments that define the OW. In addition to the segment at the reference temperature $T_0 = 50^\circ C$ we have selected the segment that corresponds to the temperature $T_1 = 62^\circ C$.

In order to mimic the real experimental data the two synthetic response function segments should contain experimental error. To implement this, we generated noisy data according to the following equation,

$$\tilde{G}_{\kappa,i} = G_{\kappa,i} \cdot (1 + \theta_i \cdot \delta),\ i = \overline{1, N_\kappa}, \tag{20}$$

where θ_i are uniformly distributed random values, $-1 \le \theta_i \le 1$. Thus, the relative error for $\tilde{G}_{\kappa,i}$ in comparison with $G_{\kappa,i}$ does not exceed $\delta\%$. In our case the noise level, δ, was fixed to 5%. Two such "experimental segments" with 10 datum points per decade and the OW size of 0.1 decade are shown in Fig. 6.

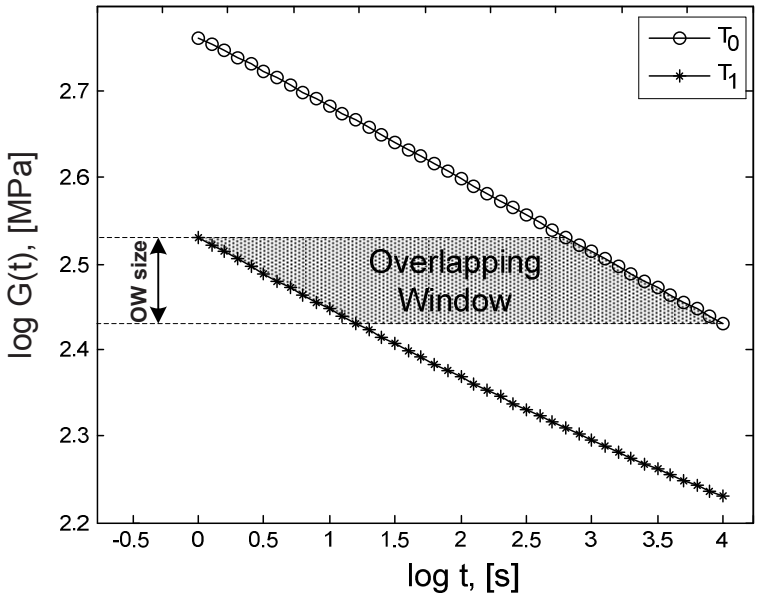

Figure 6: "Experimental segments" for $T_0 = 50^\circ C$ and $T_1 = 62^\circ C$, with 10 datum points per decade and the OW size of 0.1 decade

3.1. The effect of the number of experimental datum points per decade

We will first analyze the effect of the number of "experimental" datum pints per decade on the goodness of the automated shifting procedure. Since our OW (overlapping window) is defined along the ordinate, the density of "experimental" datum points per decade within the OW, N_G, is expressed in respect to the $\log G(t)$ axis. The interrelation between the N_G and density along the $\log t$ axis N_t may be obtained from

$$N_G = \frac{N_t}{\chi}, \tag{21}$$

where χ indicates the inclination of the response curve. In our case inclination was $\chi = 0.08$, which means that density along the $\log G(t)$ axis was larger than that in direction of $\log t$ axis. Since sampling of the data acquisition systems is performed along the time axis we will obtain larger density of data along the $\log G(t)$ axis for flat portions of the response function, i.e., where $\log G(t) \approx const$, which is beneficial for the proposed shifting algorithm. Figure 7 shows the ration between the relative total error, E, and the "experimental error", δ, as function of density of datum points for three different sizes of overlapping window, i.e., $OW = 0.01 \ \ decade$, $OW = 0.1 \ \ decade$, and $OW = 0.2 \ \ decade$. This ratio shows how much the time-temperature shifting process performed with the proposed algorithm contributes to the overall (total) error that is present in the master curve. The "experimental error" in both segments was $\delta = 5\%$. The maximum relative total error, E, of the reconstructed master curve was obtained by comparing the reconstructed master curve with the original theoretical response function calculated from the selected Lorentzian spectrum.

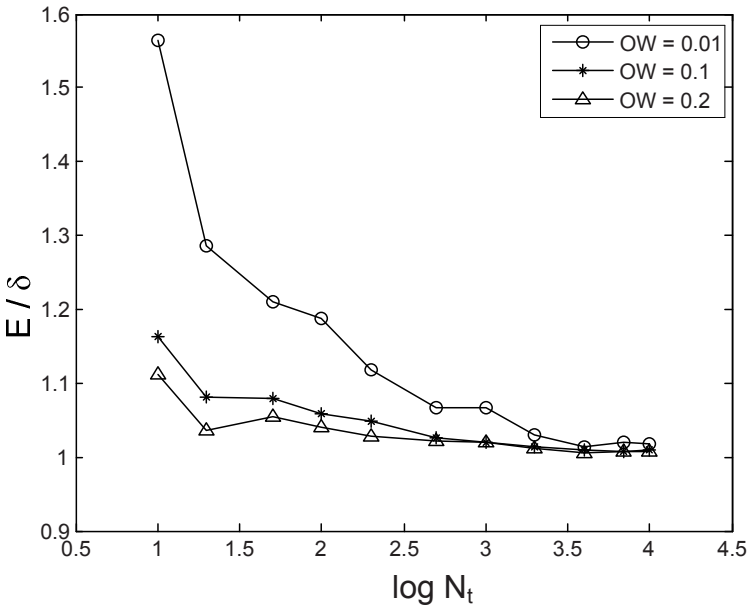

Figure 7: Effect of the datum points density on the error of the automated time-temperature shifting for $OW = 0.01 \ \ decade$, $OW = 0.1 \ \ decade$, *and* $OW = 0.2 \ \ decade$

The analysis presented in Fig. 7 shows that by increasing the density of "experimental data" one may substantially reduce the required size of the overlapping window, which is of paramount importance for decreasing the size of the experimental window and consequently the total required time for the time-dependent characterization of materials. From Fig. 7 one may conclude that an optimal density of datum points would be probably about 4000 datum points per decade. For this density of discrete data the contribution of the time-temperature shifting to the overall error of the master curve is about 1.01 times larger then the corresponding "experimental error", i.e., $E = 1.01 \cdot \delta$, which is practically negligible.

3.2. The effect of the Overlapping Window size

Here we have systematically analyzed the effect of the overlapping window size on the error that adds to the experimental error due to the time-temperature shifting when performed with the proposed algorithm. The results are shown in Fig. 8. From this analysis we may conclude that the size of the OW may be as small as 0.01 decade, or even less. Essentially the size of OW is limited with the magnitude of the "experimental error", δ. It is intuitively evident that the OW size may not be smaller then the experimental error within the OW, providing the density of the discrete datum points is very large, i.e., $N_t \to \infty$.

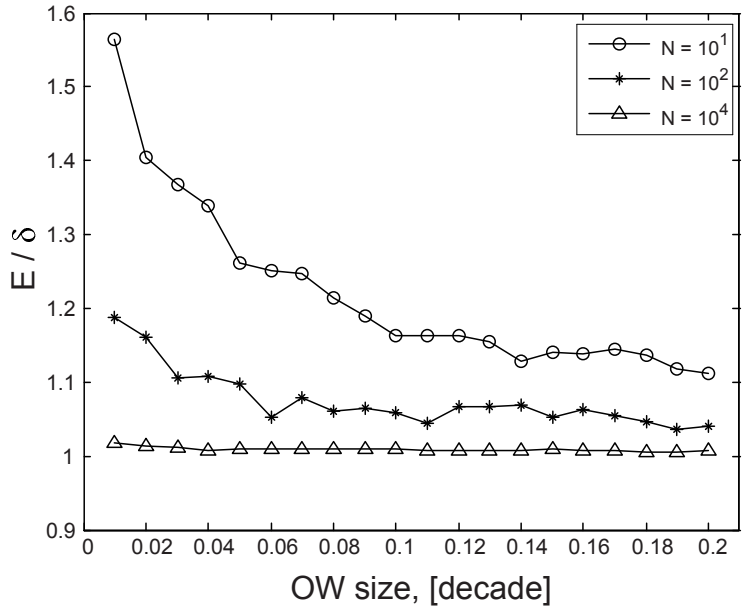

Figure 8: Effect of the OW size on the error of the automated time-temperature shifting for, $N_t = 10^1 / decade$, $N_t = 10^2 / decade$, and $N_t = 10^4 / decade$

4. Conclusions

In this study we proposed mathematical methodology which completely removes ambiguity related to the manual shifting procedures. Thus, using the proposed algorithm the shifting procedure becomes a unique solution. In addition, the proposed approach allows accurate error estimation caused by the shifting process. In this paper we analyzed the effect of the datum point density and the size of the overlapping window on the error magnitude caused by the shifting procedure. The results of the analysis may be nicely presented as a 3D diagram, shown in Fig.9.

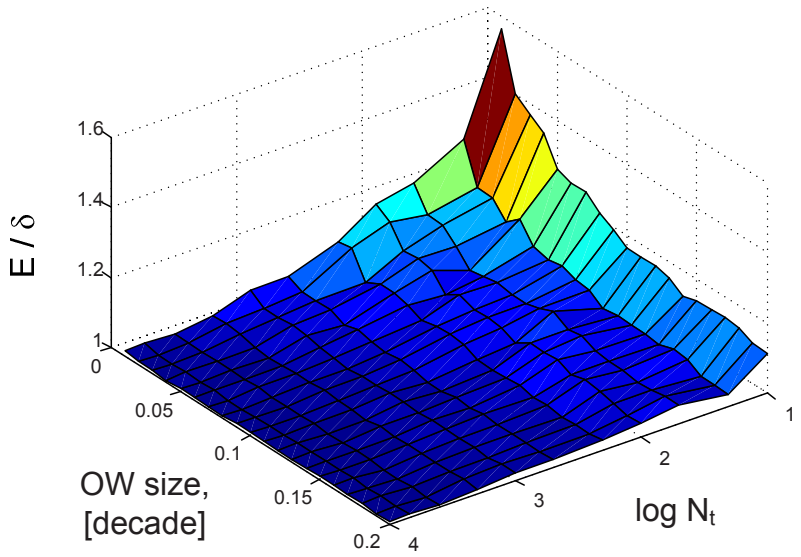

Figure 9: 3D diagram summarizing the effect of the datum points density and the size of the overlapping window.

Diagram presents the ratio of the relative total error, E, and "experimental error", δ, as function of the density of datum points per decade along the logarithmic time scale, $\log N_t$, and size of the overlapping window, OW. From the diagram we clearly see that the relative total error, E, becomes practically identical to the experimental error when $\log N_t \geq 3.5$, i.e., accuracy of the master curve is essentially given with the accuracy of measurements. Hence, shifting has negligible contribution to the error of the master curve.

These findings may be summarized as flows:

(i) The error arising from the shifting process strongly depends on density of experimental data within the overlapping window (OW), N_G.Density of data within the OW is related to the density of data along the logarithmic time scale through the relation $N_t = N_G \cdot \chi$, where χ denotes the inclination of the response curve in $\log t - LogG(t)$ coordinate system.

(ii) The ultimate density of datum points with the OW is $N_G > 1000$.

(iii) The size of the overlapping window is given with the relation, where $OW \geq 2 \cdot \log(1+\delta)$, where δ denotes the "experimental error".

(iv) The contribution of the shifting process to the total error of the master curve for $N_G > 5000$ is equal to $E = 1.01 \cdot \delta$

5. Literature

1. Tschoegl N.W., Knauss W.G., Emri I. *The effect of temperature and pressure on the mechanical properties of thermo- and/or piezorheologically simple materials in thermodynamic equilibrium – A critical review*, Mechanics of Time-Dependent Materials, **6(1)**, 53-99, 2002.

2. Ferry J.D. *Viscoelastic Properties of Polymers*, 3rd edition, John Wiley & Sons, New York, 1980.

3. Knauss W.G. *The sensitivity of the time-temperature shift process to the thermal variations – A note*, Mechanics of Time-Dependent Materials, **12(2)**, 179-188, 2008

4. Zhao J., Knauss W.G., Ravichandran G. *Applicability of the time-temperature superposition principle in modeling dynamic response of a polyurea*, Mechanics of Time-Dependent Materials, **11(3-4)**, 289-308, 2007.

5. Alwis K.G.N.C., Burgoyne C.J. *Time-temperature superposition to determine the stress-rupture of aramid fibers*, Applied Composite Materials, **13(4)**, 249-264, 2006.

6. Honerkamp J., Weese J. A note on estimating mastercurves, Rheologica Acta, **32(1)**, 57-64, 1993.

7. Buttlar W.G., Roque R., Reid B. *Automated procedure for generation of creep compliance master curve for asphalt mixtures*, Journal of the Transportation Research Board, **1630**, 28-36, 1998.

8. Barbero E.J., Ford K.J. *Equivalent time temperature model for physical aging and temperature effects on polymer creep and relaxation*, Journal of Engineering Materials and Technology-Transaction of the Asme, **126(4)**, 413-419, 2004.

9. Caracciolo R., Giovagnoni M. *Frequency dependence of Poisson's ratio using the method of reduced variables,* Mechanics of Materials, **24(1)**, 75-85, 1996.

10. Hermida E.B., Povolo F. *Analytical-numerical procedure to determine if a set of experimental curves can be superimposed to form a master curve*, Polymer Journal, **26(9)**, 981-992, 1994.

11. Cho K.S. *Geometric interpretation of time-temperature superposition*, Korea-Australia Rheology Journal, **21(1)**, 13-16, 2009.

12. Emri I., von Bernstoff B.S., Cvelbar R., Nikonov A. *Re-examination of the approximate methods for interconversion between frequency- and time-dependent material functions*, Journal of Non-Newtonian Fluid Mechanics, **129(2)**, 75-84, 2005.

13. Emri I., von Bernstoff B.S. *The Effect of Molecular Mass Distribution on Time-Dependent Behaviour of Polyamides*, Journal of Applied Mechanics, **73(5)**, 752-757, 2006.

Proceedings of the SEM Annual Conference
June 7-10, 2010 Indianapolis, Indiana USA

Application of Fractional Derivatives Models to Time-dependent Materials

M. Sasso[a], G. Palmieri[a], D. Amodio[a]

[a] *Università Politecnica delle Marche, Dipartimento di Meccanica*
via Brecce Bianche, 60131 Ancona - Italy
e-mail: m.sasso@univpm.it, g.palmieri@univpm.it, d.amodio@univpm.it

ABSTRACT

Visco-elastic properties of polymers and elastomers are of fundamental importance to understand their mechanical behavior, especially dealing with dynamic and vibration problems. In this paper experimental results of a series of compression and tension tests on specimens of styrene-butadiene rubber and polypropylene plastic are presented; tests consist in cyclic loading at different frequencies, relaxation tests and creep tests. Experimental data are used to calibrate some linear viscoelastic models; besides the classical approach based on a combination in series or parallel of standard mechanical elements (springs and dashpots), a new method based on differential equations of fractional order (Fractional Derivative Model) is investigated. The two approaches are compared analyzing their capability to reproduce the experimental data.

Keywords: viscoelasticity, fractional derivatives, elastomers, polymers.

1. INTRODUCTION

Polymeric materials are nowadays widely used in many and many applications, especially where light weight and low cost are expected. However, they are often called to carry out structural tasks; in such cases, their mechanical properties has to be accurately investigated as it happens for classical engineering materials. This class of materials are known to have time-dependent behavior, meaning that the constitutive relation between stress and strain is strongly influenced by time, even at room temperature; obviously, the correct modeling of this time-dependency is fundamental to obtain reliable results from analytical or FE computations involving elastomers or polymers.
Typical situations where the phenomenon is evident are creep, relaxation and sinusoidal dynamic loading; they are schematically summarized in fig. 1.

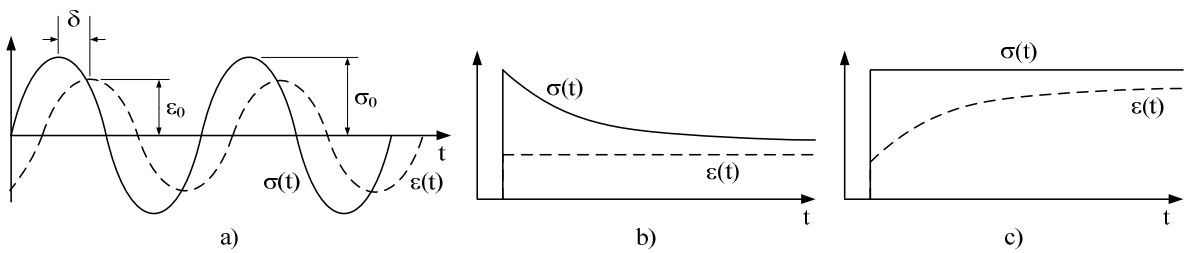

Fig. 1: types of test considered: a) cyclic, b) relaxation, c) creep.

T. Proulx (ed.), *Time Dependent Constitutive Behavior and Fracture/Failure Processes, Volume 3*, Conference Proceedings of the Society for Experimental Mechanics Series 15, DOI 10.1007/978-1-4419-9794-4_31, © The Society for Experimental Mechanics, Inc. 2011

The creep consists in a deformation that increases along time at constant stress, and can be described in integral form by the following equation,

$$\varepsilon(t) = \frac{\sigma}{E} + \int_0^t K(t-\tau)\dot{\sigma}(\tau)d\tau \tag{1}$$

while relaxation is when stress changes during time at a fixed deformation, and is expressed as

$$\sigma(t) = E\varepsilon(t) + \int_0^t F(t-\tau)\dot{\varepsilon}(\tau)d\tau \tag{2}$$

In equations 1 and 2, ε is the strain, σ is the stress, E is the elastic modulus, K and F are the creep and relaxation functions respectively.
On the other hand, the study of the response of viscoelastic materials to sinusoidal loading leads to the definition of the dynamic elastic moduli, which in general are complex function of frequency; in fact, if a sinusoidal deformation ε^* is applied to the material with frequency ω

$$\varepsilon^* = \varepsilon_0\left[\cos(\omega t) + i\sin(\omega t)\right] = \varepsilon_0 \exp(i\omega t) \tag{3}$$

a phase displacement δ is observed in the stress law σ^*

$$\sigma^* = \sigma_0\left[\cos(\omega t + \delta) + i\sin(\omega t + \delta)\right] = \sigma_0 \exp\left[i(\omega t + \delta)\right] \tag{4}$$

It follows that the elastic modulus E^*, expressed as the ratio between the complex stress and the complex deformation, is also complex:

$$E^* = \frac{\sigma^*}{\varepsilon^*} = E'(\omega) + iE''(\omega) \tag{5}$$

The real and the imaginary part are usually referred to as the storage and loss modulus respectively, and are function of the loading frequency. Their ratio is related to the phase difference between stress and strain according to:

$$\frac{E''(\omega)}{E'(\omega)} = \tan\left[\delta(\omega)\right] \tag{6}$$

In this work, the aforementioned kinds of experimental tests have been carried out on a Styrene-Butadiene (SBR) rubber and on a Polypropylene (PP) plastic by means of a servo-pneumatic testing machine.
Cyclic deformation tests have been conducted at different frequencies, obtaining storage and loss moduli as a function of excitation frequency. On the other hand, data from creep and relaxation tests have been post-processed in the frequency domain by Fourier transform, which permitted to use the constitutive equation in the complex domain in a manner similar to the case of cyclic loadings.
The data have been successively fitted with several constitutive models based on standard linear solid elements (spring and dashpot); then, special emphasis is given to an emerging approach which uses fractional derivatives mathematics to describe the linear viscoelastic problem.

2. LINEAR VISCOELASTIC MODELS

In this work, a number of generalized lumped parameter models [1-6] and some models with fractional derivatives have been explored. In this section the main characteristics of this models are described.

2.1. Standard Linear Models (SLM)

Consider a simple Maxwell element made of a spring and a dashpot, as shown in fig. 2a.

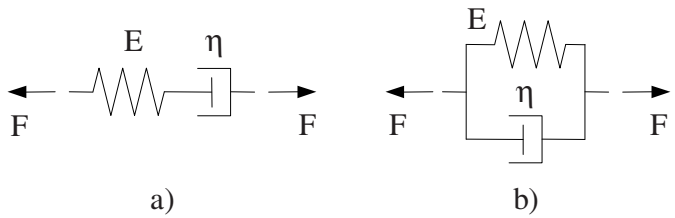

Fig. 2: a) Maxwell element, b) Voigt-Kelvin element,

Given the stiffness E and the viscosity η, the differential equation relating stress to strain is:

$$\dot{\varepsilon} = \frac{\dot{\sigma}}{E} + \frac{\sigma}{\eta} \tag{7}$$

Turning to the frequency domain, eq. (7) yields to the following expression for the complex modulus:

$$E^* = E' + iE'' = \frac{\omega^2\eta^2 E}{E^2 + \omega^2\eta^2} + i\frac{\omega\eta E^2}{E^2 + \omega^2\eta^2} \tag{8}$$

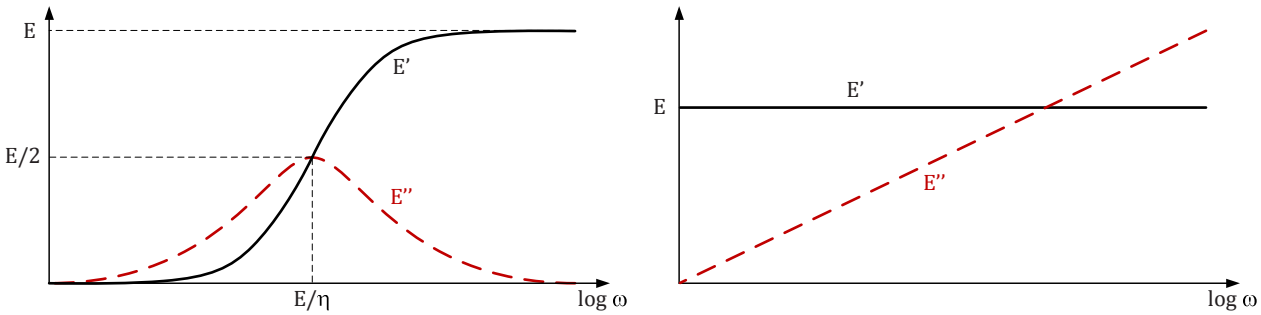

Fig. 3: Storage (E') and Loss (E") moduli for single Maxwell (a) and (b) Voigt models.

which is represented in fig.3a as function of frequency, with the typical bell-shaped loss modulus, which intersects the S-shaped storage function at its inflexion point (corresponding to pulsation $\omega = 1/\lambda = E/\eta$).
In order to obtain a good description of the viscoelastic behavior in a wide range of frequencies, a generalized Maxwell model (GM) has been adopted, consisting of a combination of a spring in parallel with 8 Maxwell elements and a damper, according to the sketch reported in Fig. 4.

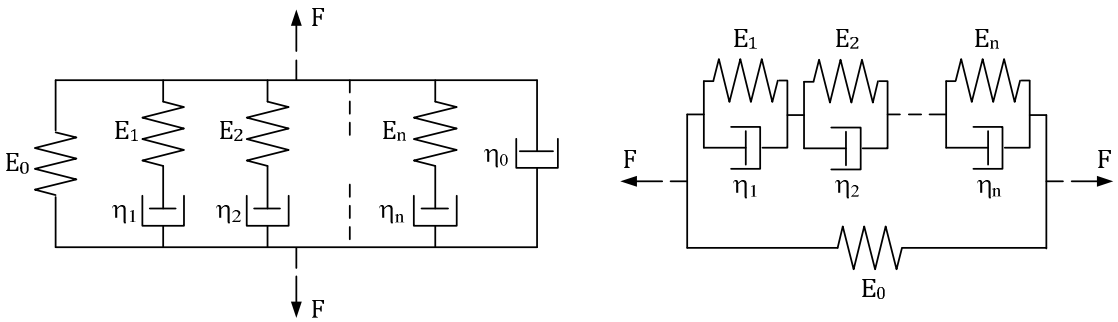

Fig. 4: Generalized models: a) Maxwell, b) Voigt.

The stiffness of the spring is purely real (storage) with modulus E_0, while in the branch with dashpot only the stiffness is purely imaginary (loss) and equal to $i\omega\eta_0$. For n parallel branches, the total stiffness is equal to the sum of the stiffness of individual branches so, recalling the complex stiffness of a Maxwell element given in (8), the global stiffness of the complex generalized model of fig. 4a can be written as:

$$E^* = E_0 + \sum_k \left(\frac{\omega^2 \eta_k^2 E_k}{E_k^2 + \omega^2 \eta_k^2} + i \frac{\omega \eta_k E_k^2}{E_k^2 + \omega^2 \eta_k^2} \right) + i\omega\eta_0 \tag{9}$$

Moreover, a generalized Voigt model (GV) has been used as well, consisting in a connection of 8 Kelvin-Voigt simple models (fig. 2b) in series plus a spring in parallel, conducting to the finale shape shown in fig. 4b. The global stiffness of the generalized model of fig. 4b is given by:

$$E^* = E_0 + \left[\sum_k \left(E_k + i\omega\eta_k \right)^{-1} \right]^{-1} \tag{10}$$

2.2. Fractional derivative model (FDM)

A model with fractional derivative is a sort of interpolation between the viscous and elastic behavior. It is known that a spring element connects the stress with the zero-order derivative of the deformation, while for a viscous element the stress depends on the first time derivative of the deformation. It is quite difficult to apply FDM in the time domain, but fortunately they are easy to deal with in the frequency domain. For this reason, the analysis of the mechanical response of these models have been performed in the frequency domain, provided that the transitions to the time domain and vice versa are possible through the forward and backward discrete Fourier transform.

Extending a general constitutive equation for viscoelastic materials (based on integer order derivatives) to fractional orders of derivation [3], a generic type of equation is obtained in the form:

$$\sum_{n=0}^{N} a_n \frac{d^{p_n} \sigma(t)}{dt^{p_n}} = \sum_{m=0}^{M} b_m \frac{d^{q_m} \varepsilon(t)}{dt^{q_m}} \qquad 0 \le p_n, q_m \le 1 \tag{10}$$

According to Riemann-Liouville definition [7], the *n* order derivative of a function *f*(*t*), with $n \in R$, $0 \le n \le 1$, is defined as:

$$\frac{d^\alpha f(t)}{dt^\alpha} = f^{(\alpha)}(t) = \frac{1}{\Gamma(1-\alpha)} \frac{d}{dt} \int_0^t \frac{f(\tau)}{(t-\tau)^\alpha} d\tau \qquad 0 \le \alpha \le 1 \tag{11}$$

where $\Gamma(1-\alpha)$ is

$$\Gamma(1-\alpha) = \int_0^\infty x^{-\alpha} e^{-x} dx \tag{12}$$

A fundamental property of the fractional derivative regards its Fourier transform (analogous property applies for the Laplace transform), in fact the following holds:

$$\Im\left[f^{(\alpha)}(t) \right] = (i\omega)^\alpha \Im\left[f(t) \right] \tag{13}$$

In practice, the equation (7) is defined by choosing a limited number of orders of derivation; in addition, some authors [8-10] introduce the constraint $p_n = q_m$, leading to the so called fractional Zener model, with $M=N=1$, $p_0=q_0=0$, $p_1=q_1=\alpha$:

$$\sigma(t)+\lambda^{\alpha}\sigma^{(\alpha)}(t)=E_{\infty}\varepsilon(t)+E_{0}\lambda^{\alpha}\varepsilon^{(\alpha)}(t) \tag{14}$$

Applying the Fourier transform to (14) and exploiting the property given in (13), it is found:

$$E^{*}=\frac{E_{\infty}+E_{0}\lambda^{\alpha}(i\omega)^{\alpha}}{1+\lambda^{\alpha}(i\omega)^{\alpha}} \tag{15}$$

The trend of the storage and loss moduli as a function of characteristics parameters E_0, E_∞, λ, α is shown in fig. 5.

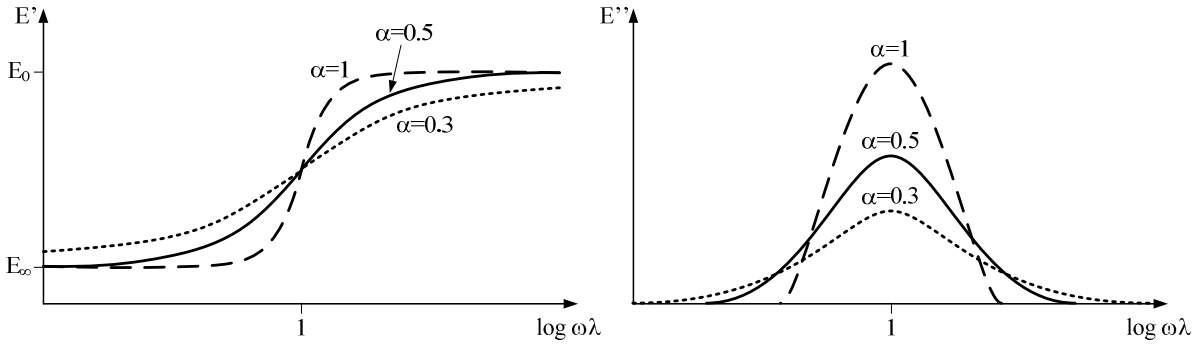

Fig. 5: Storage and Loss moduli for the fractional Zener model.

The same principle of putting more elements in parallel or series can be applied with FDM also. Among various configurations here investigated, the simple configuration shown in fig. 6 seems to be sufficiently accurate in describing the experimental data of the three types of mechanical tests carried out, introducing only one further parameter, η_0; it follows that in (15), the terms $i\omega\eta_0$ has to be added.

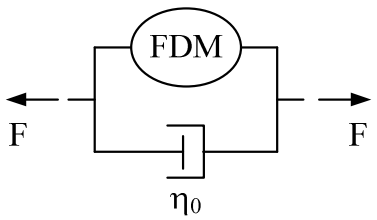

Fig. 6: FDM element in parallel with a linear viscous dashpot.

For the sake of synthesis, data are not reported for other configurations analyzed, either because these models have provided worse results, or because they have yielded an accuracy very similar to that obtained with the configuration of Figure 6, but using a larger number of parameters.

3. EXPERIMENTAL TESTS AND MATERIAL PARAMETERS IDENTIFICATION

In this section we will discuss the experimental procedure for the characterization of commercial SBR rubber and Polypropylene plastic. The following tests have been conducted:

- Compression tests on cylindrical SBR specimens (h:40mm, Ø: 20 mm);
- Tensile tests on flat rectangular SBR specimens (see fig. 7);
- Tensile tests on ISO 527-2 polypropylene specimens.

It must be noted that, although both rubbers are classified as SBR, they are mould in different shapes and their composition are not necessarily identical, so must be treated as different materials.
The SBR specimens have been subjected to creep, relaxation and cyclic tests; no cyclic tests have been carried out on PP specimens. Proper lubrication has been adopted between specimen and machine surfaces in the compression tests to reduce friction and barreling; in this way, the deformation has been considered uniform and the stress uniaxial.

The experimental apparatus for tests on rubber consists of a tensile uniaxial servo-pneumatic machine (Si-Plan®) with a LVDT and a 3 kN load cell for displacement and force evaluation; then, true stress and strain are easily computed. For PP specimens, the apparatus consists in a standard electro-mechanical machine (Zwick® Z050) equipped with a macro-extensometer for high precision measurement of the elongation within the gauge section. All tests were performed at room temperature (20 ℃).
Both in the dynamic and in creep/relaxation tests, deformation was chosen within relatively small values (up to 5% in rubber and 2.5% in plastic), remaining in a region where the material behavior can be considered as linear. The cyclic tests have been performed from zero load up to the imposed maximum (instead of reversed cycles) to avoid specimen separation from grips or inflection.

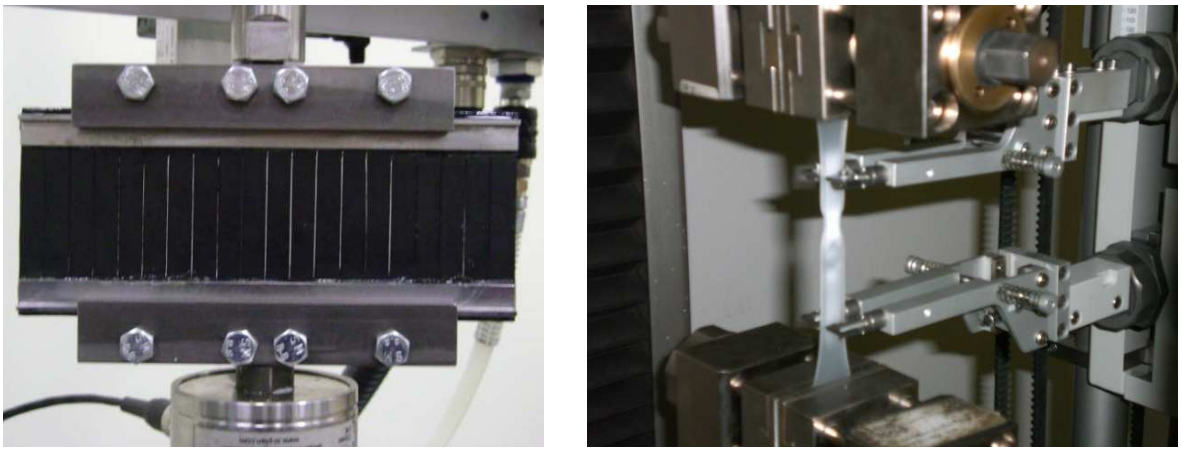

Fig. 7: tension on SBR (left) and PP (right) specimens.

The dynamic tests were carried out (only for rubbers) at 6 different values of frequency between 10^{-3} and 20 Hz. The measured displacement and force show a phase shift that depends on the excitation frequency; performing the FFT of the stress and of the strain signals, the complex values σ^* and ε^* for the assigned excitation frequency are computed, enabling to determine the storage and loss moduli for that frequency accordingly to (5). The creep tests consisted in the application of a constant stress (-0.47 MPa and +0.61 MPa for SBR, and +8.2 MPa for PP), and in the measurement of the deformation along time. Similarly, the relaxation tests consisted in the imposition of a constant strain (-4.8% and +7.8% for SBR and +2.3% for PP) and evaluation of subsequent stress decay.
The fitting procedure for extracting the characteristic parameters of the three models treated was conceived as a minimization problem of an error function based on deviations between the experimental and numerical values. In particular, this error function encompasses the differences of all three types of experimental tests. In the cyclic tests the error is defined directly on the values of the storage and loss moduli at different frequencies, in the creep and relaxation tests it is related to strain and stress respectively. In the latter two cases, the mechanical responses of the model have been computed in the frequency domain, then anti-transformed into the time domain obtaining temporal patterns of strain and stresses which are comparable with experimental data. The normalized error function to be minimized is in the following form:

$$f_e = \sum_{i=1}^{N_R}\left(\frac{\sigma_i^{(exp)}-\sigma_i^{(num)}}{\sigma_i^{(exp)}N_R}\right)^2 + \sum_{i=1}^{N_C}\left(\frac{\varepsilon_i^{(exp)}-\varepsilon_i^{(num)}}{\varepsilon_i^{(exp)}N_C}\right)^2 + \sum_{i=1}^{N_\omega}\left[\left(\frac{E'_i{}^{(exp)}-E'_i{}^{(num)}}{E'_i{}^{(exp)}N_\omega}\right)^2 + \left(\frac{E''_i{}^{(exp)}-E''_i{}^{(num)}}{E''_i{}^{(exp)}N_\omega}\right)^2\right] \quad (16)$$

where N_R, N_c, N_ω are the number of samples for the relaxation, creep and cyclic tests.
The results of the material parameters identification are shown in the following pictures by comparing the numerical and experimental curves. It must be noted that for each material, a unique set of parameters have been computed for every constitutive model.
Figures 8a, 8b and 8c refer to cyclic, creep and relaxation tests respectively on cylindrical rubber specimens (compression); figures 9a, 9b and 9c refer to tensile tests, again on rubber; figures 10a and 10b show the results obtained in creep and relaxation test (in tension) carried out with polypropylene specimens.

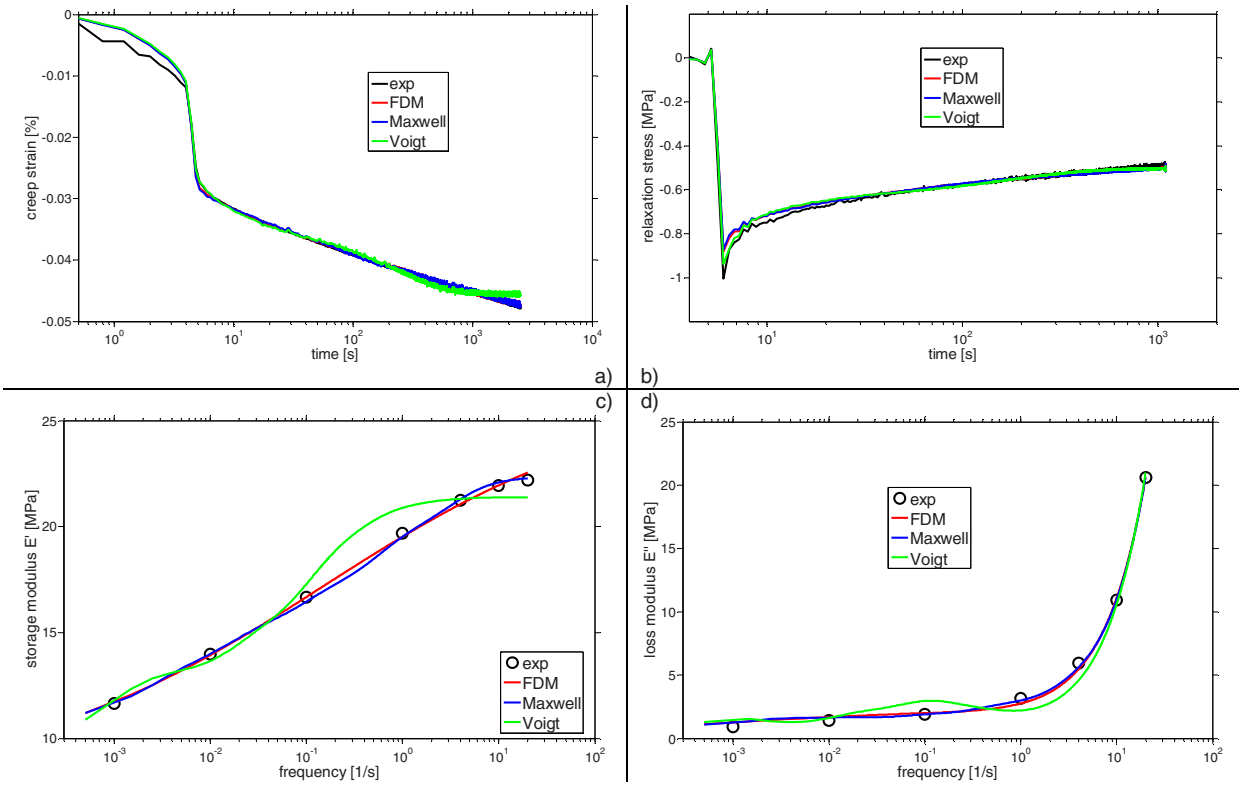

Figure 8: comparison of experimental and numerical results for SBR rubber in compression
a) creep, b) relaxation, c) storage modulus, d) loss modulus

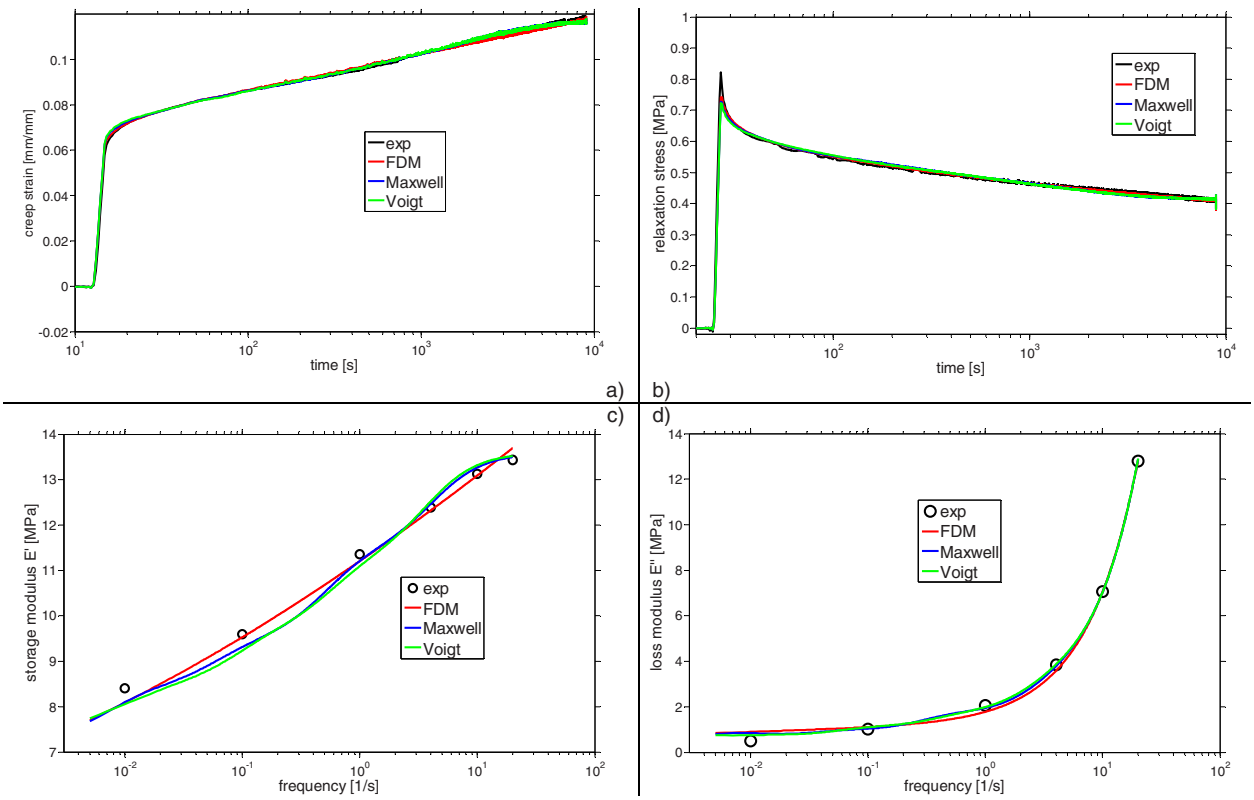

Figure 9: comparison of experimental and numerical results for SBR rubber in tension
a) creep, b) relaxation, c) storage modulus, d) loss modulus

Tables from 1 to 3 resume the best fitting parameters for the constitutive models explained above, together with their error with respect to experimental data.
By mere comparison of global normalized error, it is observed in general a good performance of the models adopted; in particular the GM gave the best global fitting for the rubber tests in compression, the GV was better for the tensile tests on rubber, and finally the FDM provided the best matching with experimental data on polypropylene. The worst cases are represented by the relatively poor matching of Maxwell curves with PP experiments, and Voigt curves with SBR compression data; the performances of FDM are more uniform within the three materials tested. However, another aspect, which probably represents the major advantage of FDM over other models, has to be considered, that is the number of parameters to be identified by the minimization procedure: FDM uses much less parameters than GM and GV, reducing the analytical effort especially with regard to the first attempt solutions, whose choice is often somewhat “exotic”.

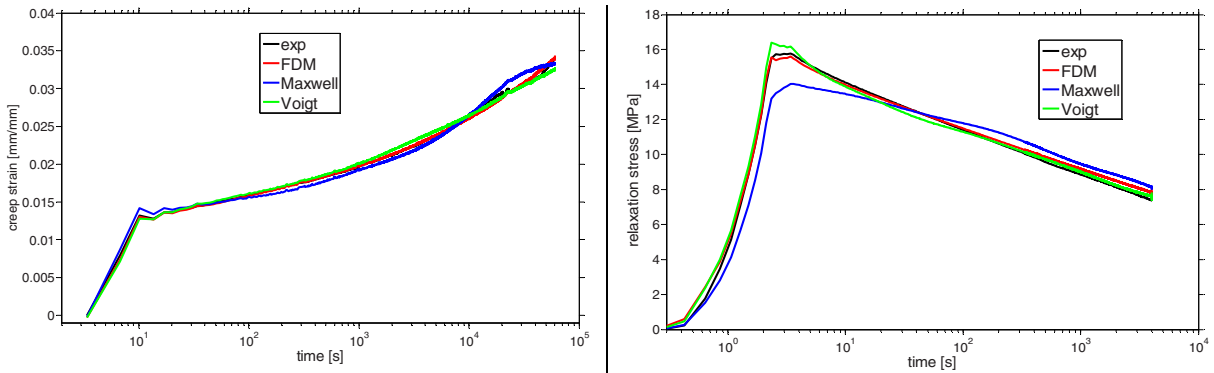

a) b)

Figure 10: comparison of experimental and numerical results for Polypropylene in tension
a) creep, b) relaxation

Table 1: best-fitting parameters of the Fractional Derivative model

	λ [s]	E_∞ [MPa]	E_0 [MPa]	α	η_0 [MPa·s]	Err%
SBR comp	1.069	7.926	26.42	0.2607	0.1539	4.3
SBR tens	$2.14 \cdot 10^{-4}$	2.486	31.43	0.1261	0.0915	6.3
PP tens	$4.54 \cdot 10^{-4}$	-10885	13061	0.0075	67.2036	2.1

Table 2: best-fitting parameters of the generalized Maxwell model

	λ_{min}	λ_{max}	E_0	η_0	E_1	E_2	E_3	E_4	E_5	E_6	E_7	E_8	Err%
SBR comp	-1.35	4.07	2.27	2.68	1.90	1.85	2.03	0.94	1.23	0.387	9.06	0.161	3.7
SBR tens	-1.43	5.0	2.07	1.97	1.05	1.14	0.856	1.23	0.010	0.101	5.14	0.099	5.2
PP tens	-5.0	3.87	2.03	2.769	5.16	14.64	34.19	72.67	119.7	185.7	245.1	14.6	11.0

Table 3: best-fitting parameters of the generalized Voigt model

	λ_{min}	λ_{max}	E_0	E_1	E_2	E_3	E_4	E_5	E_6	E_7	E_8	Err%
SBR comp	-1.92	3.33	7.83	13.87	599.9	127.9	25.13	16.74	568.0	4.38	46.9	9.5
SBR tens	-2.03	3.48	3.69	11.48	26.99	27.96	24.14	30.66	14.93	15.14	3.56	5.1
PP tens	-1.46	5.0	53.8	1092	2891	2949	2525	3000	1292	936.9	483.2	4.8

It was found in fact that FDM parameters are less affected by guess solution value adopted at the beginning of the minimization process (indeed, it is probably due to the limited number of coefficients), which could be performed as an unconstrained optimization; on the contrary, both GM and GV suffered of significant dependence on guess parameters (which are numerous and not easy to choose) and, furthermore, they required the adoption of a constrained optimization approach to prevent the algorithm from converging to unfeasible solutions (i.e. negative stiffnesses, that would mean negative relaxation/retardation times).

4. CONCLUSIONS

The work presented the experimental results of cyclic, relaxation and creep tests on time dependent materials like SBR rubber and Polypropylene plastic. All tests have been conducted in a range of relatively small deformations, so that material can be reasonably treated as linear viscoelastic. Besides standard linear methods such as Maxwell and Voigt models (in their generalized version), an emerging approach based on fractional derivative calculus has been investigated. Its results in terms of matching with experimental data are comparable, in some cases even better, than GM and GV responses, with the noticeable advantage of using much less parameters; this not only reduces the computational effort in coefficients identification, but also prospects a possible better transferability of such constitutive models to loading conditions significantly different from the testing ones.

REFERENCES

[1] Chunyu Li, Jim Lua, “A hyper-viscoelastic constitutive model for polyurea”, *Materials letters*, 63, 877-880, 2009.

[2] N. Huber, C. Tsakmakis, “Finite deformation viscoelasticity laws”, *Mechanics of materials*, 32, 1-18, 2000.

[3] S.W. Park, “Analytical modeling of viscoelastic dampers for structural and vibration control”, *International Journal of Solids and Structures*, 38, 8065-8092, 2001.

[4] A.F.M.S. Amin, M.S. Alam, Y. Okui, “An improved Hyperelasticity relation in modeling viscoelasticity response of natural and high damping rubbers in compression: experiments, parameter identification and numerical verification”, *Mechanics of materials*, 34, 75-95, 2002.

[5] V.L. Popov, T. Geike, “A new constitutive model of rubber”, *Tribology International*, 40, 1012-1016, 2007.

[6] A.R. Bhuiyan, Y. Okui, H. Mitamura, T. Imai, “A rheology model of high damping rubber bearings for seismic analysis: identification of nonlinear viscosity”, *International Journal of Solids and Structures*, 46, 1778-1792, 2009.

[7] K.B. Oldham, J. Spanier, “The fractional calculus”, *New York: academic press*, 1974.

[8] R.L. Bagley, P.J. Torvik, “On the fractional calculus model of viscoelastic behavior”, *Journal of Rheology*, 30, 133-155, 1986.

[9] T.M. Atanackovic, “A modified Zener model of a viscoelastic body”, *Continuum Mech. Thermodyn.*, 14, 137-148, 2002.

[10] T.M. Atanackovic, B. Stankovic, “Dynamics of viscoelastic rod of fractional derivative type”, *ZAMM – Journal of Applied Mathematics and Mechanics*, 82, 377-386, 2002.

Proceedings of the SEM Annual Conference
June 7-10, 2010 Indianapolis, Indiana USA

Tissue- and Microstructural-level Deformation of Aortic Tissue under Viscoelastic/Viscoplastic Loading

Danial Shahmirzadi, Adam H Hsieh

Fischell Department of Bioengineering

3237 Jeong H Kim Engineering Building, University of Maryland, College Park, MD 20814

dshahmir@umd.edu, hsieh@umd.edu

ABSTRACT

Mechanical function of tissues in health and disease is regulated through interactions of phenomena spanning across multiple length scales. The multiscale nature of tissue biomechanics should be incorporated into modeling approaches if a full description of soft tissue biomechanics is sought [1-4]. While gross changes in geometry are sufficient for quantifying tissue-level deformations, quantification of microstructural deformations is more challenging [5-6]. There have been some advances over the past decade [7], but there remains many issues regarding how best to characterize changes in microstructure. In this study, we examined the relation between deformation of bovine aortic tissue at the tissue- and microstructural scales, during uniaxial stretch and after loads are removed. Specifically, circumferential aortic samples were subjected to small and large stretches. Some specimens were chemically fixed during stretch, and others released to undergo free retraction before chemical fixation. Specimens were measured macroscopically before/after loading, sectioned and stained histologically, and analyzed to examine microstructure. Image-based analysis of histology images have been effective in quantifying microstructural changes in soft tissues [8-14] and served as guidance to assess tissue microstructure. At the tissue scale, it is observed that sample's elongation is accompanied with width/thickness shrinkage in an isochoric manner. Microstructural investigations reveal straightening of (undulated) fibrillar network when tissue is stretched circumferentially; with variations different at inner and outer layers of wall thickness. Once recovered, samples exhibited larger permanent deformation toward outer layer, which possesses sparse elastic lamina. This study provides a microstructural basis for observations of local permanent stretch in artery tissues, and paves the way for further development of multiscale models of cardiovascular biomechanics.

METHODS

Aortas of 291±23 mm length were obtained from Angus male cattle (average age of 20-24 months) at a local abattoir. Proximally, each aorta was cut near the heart and, distally, above the abdominal bifurcation, and then transferred to the laboratory immersed in cold phosphate buffered saline. The tissue was carefully cleaned of large remnants of fat and attached connective tissues. Areas of the aorta containing vascular branch points and abnormalities were discarded. Circumferential specimens of 30mm×10mm size were excised from the aorta, with

T. Proulx (ed.), *Time Dependent Constitutive Behavior and Fracture/Failure Processes, Volume 3*, Conference Proceedings of the Society for Experimental Mechanics Series 15, DOI 10.1007/978-1-4419-9794-4_32, © The Society for Experimental Mechanics, Inc. 2011

thicknesses naturally varying in 3-8mm range. The specimens were preserved in phosphate buffer (PBS) solution with protease-inhibitor additives (per 1 Liter of PBS: 1mM of EDTA-Disodium salt, 1mM of EDTA-Tetrasodium salt, 5mM of Benzamadine, 10mM of NEM, 1mM of PMSF) until being used.

A custom apparatus was constructed to maintain specimens under controlled deformation over time and in solution. The apparatus consists of a frame and two movable clamps which can be secured at different distances apart on the stand, Fig. 1. Clamps were tightened over the tissue while relaxed. While one clamp was fixed, the second clamp was moved along the frame and secured at a known stretch. Some specimens were chemically fixed while held at a fixed stretch by immersing the clamps and tissue in fixative for 24 hours. For specimens to be tested after recovery from stretch, the specimen was released from the jig so it could retract for 45 minutes and then fixed for 24 hours.

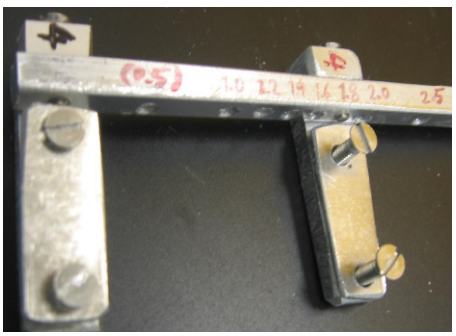

Fig. 1- Custom apparatus used to apply and hold the deformation of aortic specimens.

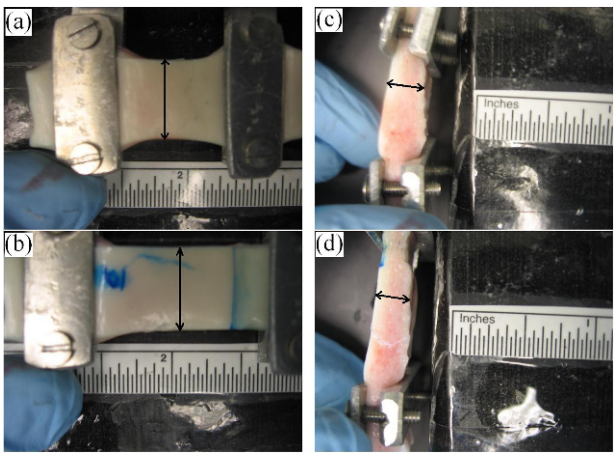

Fig. 2- Images acquired to analyze changes in specimen dimensions during tissue deformation. A ruler was included in the images to calibrate length measurements, carried out by the software ImageJ. Figure shows the width of the specimen before loading and after deformation recovery, (a) and (b), respectively; and the thickness of the specimen before loading and after deformation recovery, (c) and (d), respectively.

To quantify the tissue-scale changes in the specimens, images were acquired of specimens at each of the stages of unstretched, stretched, and after recovery (Fig 2). These images were analyzed using ImageJ software *(NIH, Bethesda, MD)* to obtain width and thickness measurements of each specimen.

For tissue fixation, we used a modified fixative solution consisting of 10% bleach and 15% formaldehyde in deionized water to better fix the elastin and collagen [15,16]. After fixing the microstructure, specimens went through paraffin-embedding tissue processing stages and sectioned and stained histologically. Histologic sections were made transverse to the layers to better describe the fibrillar orientation, and stained using a protocol which was a modification of Masson's trichrome with Verhoeff's hematoxylin [17,18]. In this protocol, the elastin is stained dark blue, the collagen is stained light blue, and proteoglycans are stained red. In a separate study, we sought to quantify the microstructural conformations seen in the histology images using different image-based techniques [11].

RESULTS

Different specimens at the unstretched state, under different levels of stretch, and after recovery from deformation were examined for microstructural measurements. Given the drastic change in the density of the elastin network

between inner and outer layers of the wall thickness, we separated our analyses into inner and outer layers of the aortic wall thickness. Figure 3 shows histology of an unstretched specimen (a), of specimens under 1.4 and 2.0 stretches (b) and (c), respectively, and of specimens after recovering from 1.4 and 2.0 stretches (d) and (e), respectively. Figure 4 shows images from outer regions of the wall, corresponding to the conditions shown in Figure 3.

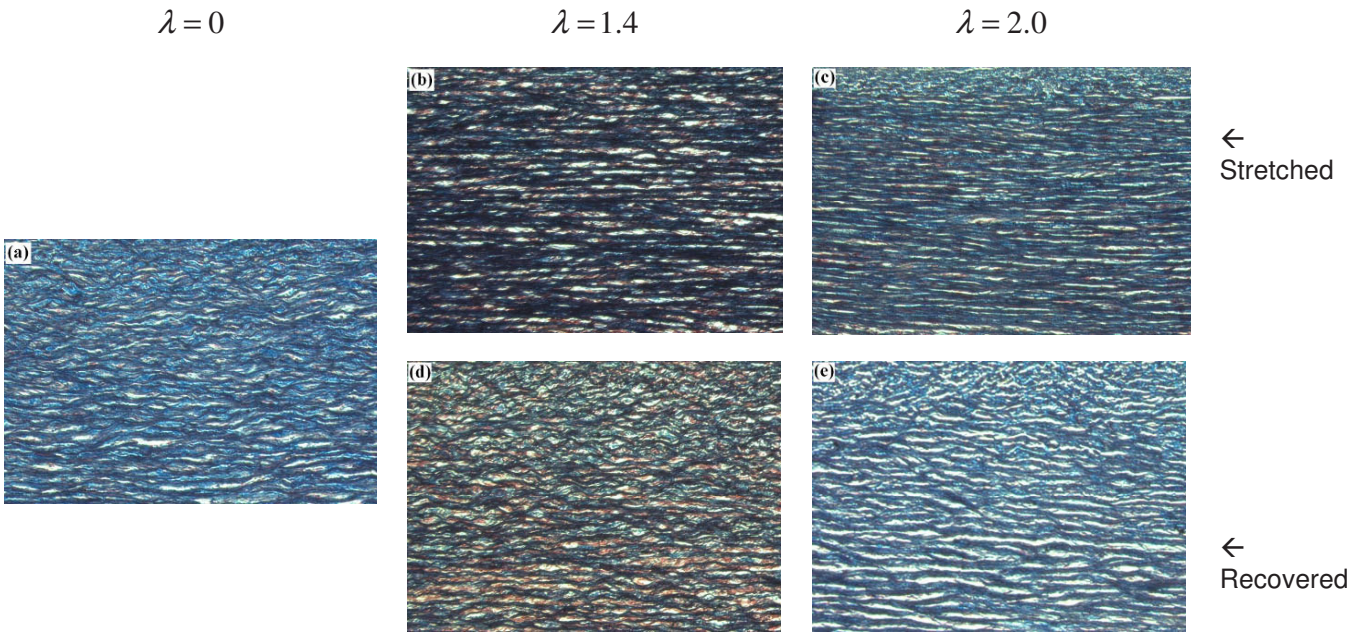

Figure 3- Histological sections of 'INNER' layer of aortic tissue. (a) Unstretched, (b) Stretched to 1.4 stretch, (c) Recovered from 1.4 stretch, (d) Stretched to 2.0 stretch, (e) Recovered from 2.0 stretch

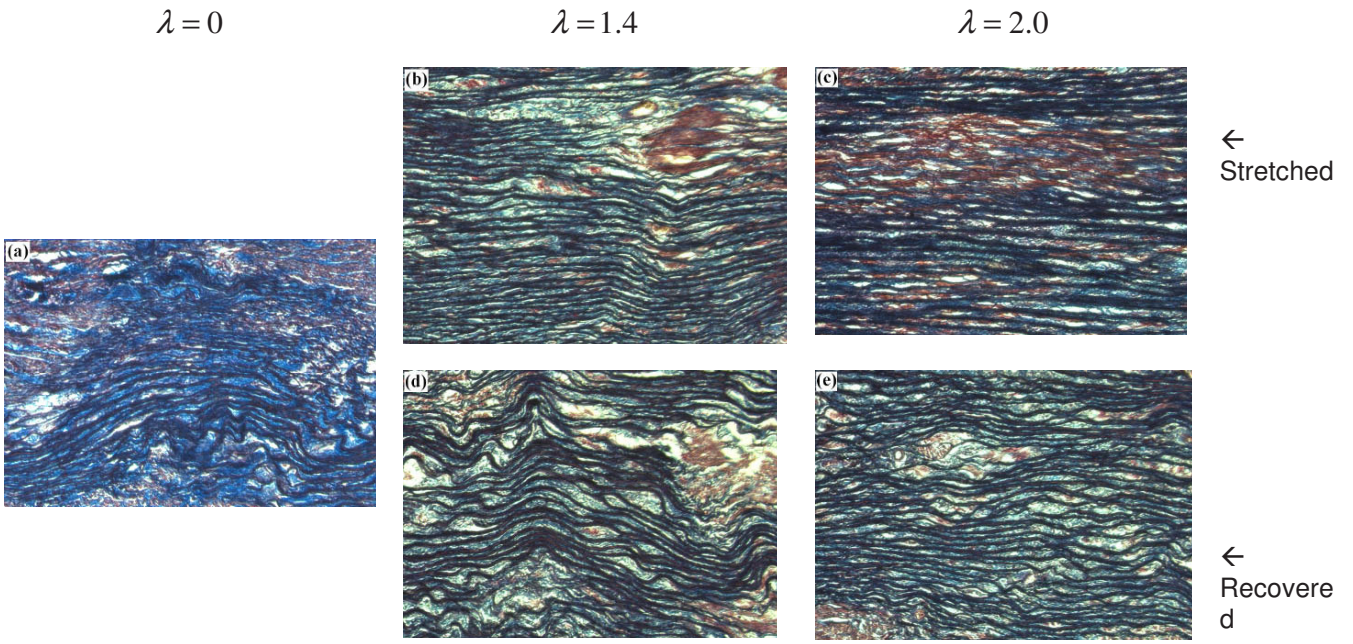

Figure 4- Histological sections of 'OUTER' layer of aortic tissue. (a) Unstretched, (b) Stretched to 1.4 stretch, (c) Recovered from 1.4 stretch, (d) Stretched to 2.0 stretch, (e) Recovered from 2.0 stretch

DISCUSSION

The main goal of this study was to probe the deformation of aortic specimens at the microstructural scale. The current understanding of governing mechanisms underlying microstructural alterations is limited, leaving many issues to be addressed before a comprehensive understanding of microstructural deformation can be obtained. We sought to examine the histological images obtained from different aortic specimens —in unstretched state, under stretch, and after recovering from stretch— to improve the knowledge base in this area of research.

Given our interest in the deformation of fibrillar elastin, we studied the inner and outer regions of the wall thickness separately. Distinctions between the histological observations of inner (intima, inner media) and outer (outer media, possible remnants of adventitia) regions of aortic wall thickness may be attributed to drastic increase in elastin's density and organization toward inner regions. Our observations suggest that the elastin network in the inner region is much more organized compared with that of the outer region, which undergoes deformations on the order of tissue-scale stretch.

Studying the microstructural alterations in specimens under increasing stretch shows that both in the inner and the outer media, stretching the tissue specimens has a direct effect on microstructure by straightening the fibrillar structure. Less intuitive observations were made for the microstructure of recovered tissue samples after being released from stretch. For samples recovered from 1.4 stretch, it was found that large portion of microstructural deformation is recovered, but does not fully recover to the initial conformation of unstretched tissue samples. Furthermore, when recovered from 2.0 stretch, even lower level of microstructural restoration occurs; hypothetically due to break down and dislocation of the extracellular matrix to which elatin network is anchored. These observations suggest that a certain amount of permanent deformation occurs during tissue loading. Such irrecoverable deformations have been observed in other tissues, but the mechanisms for restoration or remodeling of the tissue remain unknown.

We believe that the outcome of this study paves the way to achieve a better understanding of microstructural deformation. It should be noted that throughout the procedures we undertook in this study to prepare circumferential rectangular specimens from the originally cylindrical-shape aorta, the residual stress within the aortic wall is released [19,20], which, hypothetically, accompanies reconfiguration of a tissue's microstructure. As a result, we argue that the histological images obtained in this study might not accurately

represent those in intact aorta, but remain informative on how the fibrillar networks in the tissue can stretch and shrink as a tissue deforms.

REFERENCES

[1] He CM, Roach MR. The Composition and Mechanical Properties of Abdominal Aortic Aneurysms. J Vascular Surgeries, 20, 6-13, 1994.
[2] Weinberg EJ, Shahmirzadi D, Mofrad MRK. On the Multiscale Modeling of Heart Valve in health and Disease. J Biomechanics and Modeling in Mechanobiology, In press.
[3] Lillie MA, PhD Dissertation, University of Western Ontario, London, Canada, 1986.
[4] Shahmirzadi D, Hsieh AH, Microstructural Deformations of Arterial Tissue under Stress Relaxation and Deformation Recovery. BMES Annual Fall Scientific Meeting, Oct 7-10, Pittsburgh, PA, 2009.
[5] Avolio A, Jones D, Tafazzoli-Shadpour M. Quantification of alterations in structure and function of elastin in the arterial media. Hypertension, 32, 170-175, 1998.
[6] Shahmirzadi D, Hsieh AH. Quantifying Microscale Solid Area via Macroscale Measurements of Soft Tissues: Application to Elastin Fibers in Arterial Tissue. 5th Int Congress of Nano-Bio Clean Tech, Oct 27-30, San Francisco, CA, 2008.
[7] Bolender RP. Biological stereology: history, present state, future directions. Microsc Res Tech, 21, 255-261, 1992.
[8] Amenabar JM, Martins GB, Cherubini K, Figueiredo MA. Comparison between semi-automated segmentation and manual point-counting methods for quantitative analysis of histological sections. J Oral Sci, 48, 139-143, 2006.
[9] Castleman KR, Digital image processing, Prentice-Hall, New Jersey, 15-72, 1996.
[10] Shahmirzadi D, Hsieh AH. Characterizing deformation-induced changes in aortic microstructure using image processing techniques. SEM Fall Symposium and Workshop on Advanced Image-Based Measurement Methods, Oct 5-7, Columbia, SC, 2009.
[11] Shahmirzadi D, Hsieh HA, Bruck H. Quantification of Microstructural Alterations in Undeformed, Stretched and Recovered Specimens from Native and Elastin-Isolated Aortic Tissues. submitted
[12] Rubbens MP, et al. Quantification of the temporal evolution of collagen orientation in mechanically conditioned engineered cardiovascular tissues. Ann Biomed Eng, 37, 1263-1272, 2009.
[13] Daniels F, Ter Haar Romeny BM, Rubbens MP, Van Assen H. Quantification of collagen orientation in 3D engineered tissue. In: IFMBE Proceedings, 3rd Kuala Lumpur Int Conf Biomedical Eng, 15, 282–285, 2006.
[14] Tonar Z, et al. Microscopic image analysis of elastin network in samples of normal, atherosclerotic and aneurysmatic abdominal aorta and its biomechanical implications. J Applied Biomedicine, 1, 149-159, 2003.
[15] Lillie MA, Chalmers GWG, Gosline JM. Elastin Dehydration Through the Liquid and the Vapor Phase: A Comparison of Osmotic Stress Models. Biopolymers, 39, 627-639, 1996.
[16] Hopwood D, Some Aspects of Fixation with Glutaraldehyde, J Anat, 101, 83-92, 1967.
[17] Sheehan DC, Hrapchak BB, Theory and Practice of Histotechnology, St Louis, The Moxby Company, 190-191, 1980.
[18] Gravey W, et al. A Modified Verhoeff Elastic Van Geieson Stain. The Journal of Histotechnology, 14, 113-114, 1991.
[19] Fung YC. Biomechanics: Mechanical Properties of Living Tissues. Second Edition, Springer-Verlag, New York, 1993
[20] Shahmirzadi D, Hsieh AH, Haslach HW. Effects of Arterial Tissue Storage and Burst Failure on Residual Stress Relaxation. 34th Annual Northeast Bioengineering Conf, April 4-6, Providence, RI, 2008.

Proceedings of the SEM Annual Conference
June 7-10, 2010 Indianapolis, Indiana USA

Strain accumulation process in periodically loaded polymers

B. Zupancic, and I. Emri

Center for Experimental Mechanics, Faculty of Mechanical Engineering, University of Ljubljana, Askerčeva 6, 1000 Ljubljana, Slovenia – barbara.zupancic@fs.uni-lj.si

ABSTRACT

Within this paper we present the methodology for analyzing strain accumulation process in polymeric materials when exposed to periodical loading. Within each loading cycle material undergoes a combination of the creep and retardation process. At certain conditions the retardation process between two loading cycles cannot be fully completed. Consequently strain starts to accumulate, which leads to hardening of the material and ultimately to the failure of polymeric product. Critical frequency of the applied periodical loading depends on the material retardation time, while the magnitude of accumulated strain on the strength of corresponding discrete spectrum lines. Thus, the mechanical spectrum of polymeric material defines the intensity and the magnitude of accumulated strain.

We demonstrate developed methodology for predicting durability of periodically loaded polymeric materials for the case of polymeric nanocomposites with three different concentrations (0 wt.%, 1 wt.%, and 15 wt.%) of nanoparticles added into the polyamide matrix.

The results show that higher concentration of nanoparticles added into the polymeric matrix slows down the strain accumulation process and reduces the magnitude of accumulated strain.

INTRODUCTION

Theoretical model takes in consideration specific loading conditions in terms of the shear stress. Evolution of the shear stress within one loading cycle is modeled as a tooth-like function [1], shown schematically in Fig. 1.

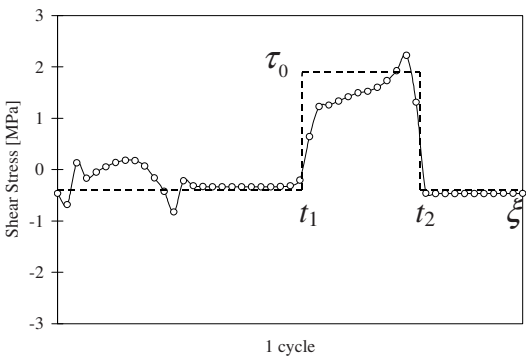

Figure 1 - *Schematics of the loading conditions in terms of the shear stress within one loading cycle.*

T. Proulx (ed.), *Time Dependent Constitutive Behavior and Fracture/Failure Processes, Volume 3*, Conference Proceedings of the Society for Experimental Mechanics Series 15, DOI 10.1007/978-1-4419-9794-4_33, © The Society for Experimental Mechanics, Inc. 2011

Loading conditions may be mathematically described as [1],

$$\tau(t) = \tau(0)h(t) + \tau_0 \sum_{n=1}^{n=N} \left\{ h\left[t - t_1 - (n-1)\xi \right] - h\left[t - t_2 - (n-1)\xi \right] \right\}. \quad (1)$$

The times t_1, t_2, and the duration of one load cycle ξ (shown in Fig. 1) are functions of the geometry, and the angular velocity. τ_0 presents the magnitude of the loading shear stress, Fig. 1.

THEORETICAL MODEL FOR STRAIN ACCUMULATION ANALYSIS

The strain response of the viscoelastic material exposed to the shear stress loading may be expressed as [2],

$$\gamma(t) = \tau(0)J(t) + \int_{0^+}^{t} J(t-s)\frac{\partial \tau(s)}{\partial s} ds \,. \quad (2)$$

Introducing Eq. (1) and Eq. (3), description of creep compliance function $J(t)$ in terms of discrete retardation spectrum,

$$J(t) = J_g + \sum_{i=1}^{K} L_i \left(1 - e^{-\frac{t}{\lambda_i}} \right), \quad (3)$$

into the Eq. (2), yields the following expression for the cumulative accumulated strain,

$$\gamma(t, t \le N\xi) = \tau(0)J(t) + \tau_0 \sum_{n=1}^{n=N} \sum_{i=1}^{K} L_i \left[1 - \exp\left(-\frac{\pi}{\omega\lambda_i} \right) \right] \exp\left(-\frac{(\kappa+\pi)(2(N-n)+1) - \pi}{\omega\lambda_i} \right). \quad (4)$$

Eq. (4) describes the time-dependent evolution of the strain accumulation in the material as a function of the angular velocity, ω, geometry parameter, $\kappa = \frac{l}{R}$, where l is the distance between the axes of the two pulleys, and R is the radius of the pulleys of the belt drive, and as a function of the number of cycles, N, to which the belt has been exposed to [1].

Analyzing strain accumulation in each consecutive cycle, we observe that at very small and very large operating angular velocities, there will be no strain accumulation. It is therefore evident that accumulated strain must have an extreme at some critical angular velocity, $0 < \omega_{CR} << \infty$, which determines critical operating conditions, at which the strain accumulation process is the most intensive [1].

APPLICATION OF THE STRAIN ACCUMULATION MODEL TO POLYAMIDE NANOCOMPOSITE MATERIALS

This part presents the analysis of the strain accumulation process in the periodically loaded polymeric nanocomposite materials by using developed numerical approach presented in [1, 3] that enables determination of critical loading conditions and consequently prediction of material's durability taking in consideration time-dependent material behavior.

Nanocomposites with three different concentrations of nanoparticles in the polyamide matrix were prepared by simple melt compounding procedure without the presence of any processing additive. Nanoparticles were made out of Sodium titanate nanoribbons (TiNRs); highly crystalline, synthesized at 175ºC, width of cca. 80-100 nm, and a length of 1000-3000 nm. Nanocomposite cylindrical specimens were made, with the length of cca. 40 mm and diameter of cca. 6 mm out of 3 different concentrations of nanoribbons compounded into the polyamide matrix: 0 wt.%, 1 wt.%, and 15 wt.%. Specimens were tested with the torsional creep experiment.

In Fig. 2 results of the torsional creep measurements are presented performed on three types of nanocomposite specimens.

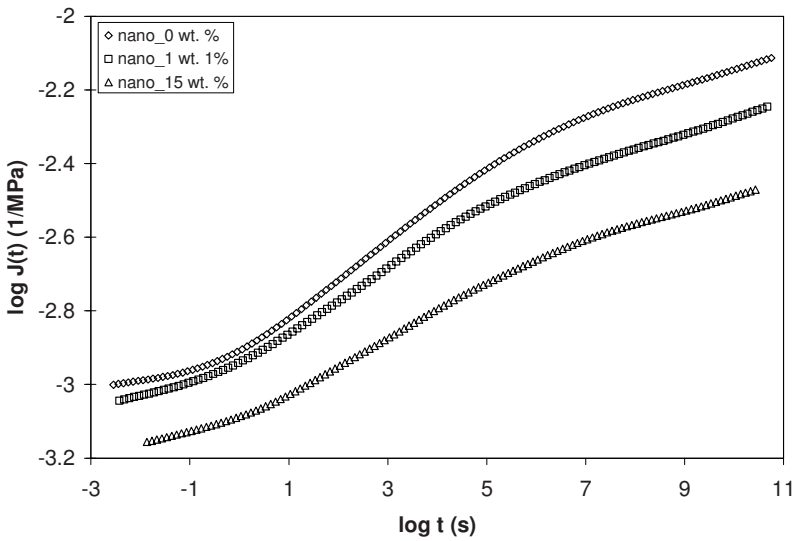

Figure 2 - *Creep compliance functions, $J(t)$, corresponding to nanocomposite specimens with three different concentration of nanoparticles.*

Time-dependent properties in terms of the retardation spectrum were then calculated from the measured shear creep compliance by using Emri-Tschoegl algorithm [4]. Retardation spectra shown in Fig. 3 served as input information for the strain accumulation analysis based on developed theoretical approach [1, 3] and determination of critical loading area of the most intensive strain accumulation process.

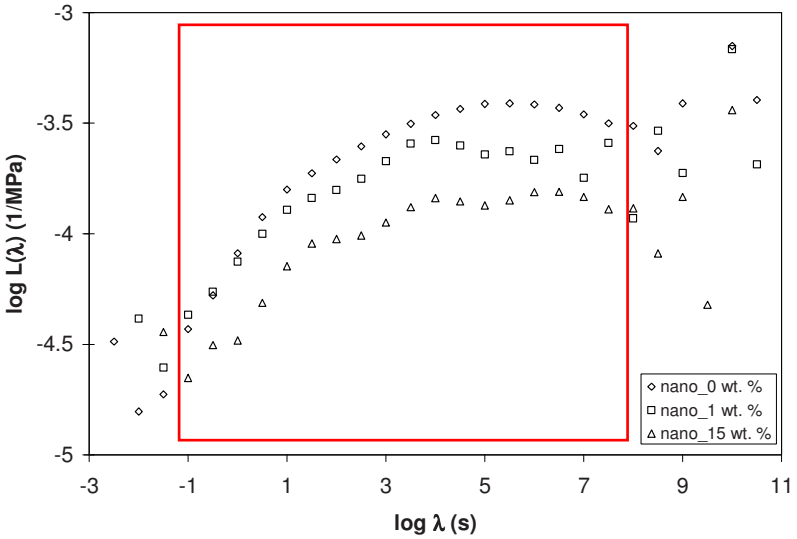

Figure 3 - *Retardation spectra, $L(\lambda)$, corresponding to nanocomposite specimens with three different concentration of nanoparticles.*

The analysis of the strain accumulation process should be performed within the time and consequently angular velocity domain where the measured time-dependent property of the material is known, except, if the contribution of spectrum lines outside the known time frame is negligible. In this case analysis of the strain accumulation can be extrapolated.

By using Eq. 4 we analyzed the effect of the number of loading cycles and angular velocity and to the strain accumulation process. Diagram in Fig. 4 shows the evolution of accumulated strain as a function of loading cycles.

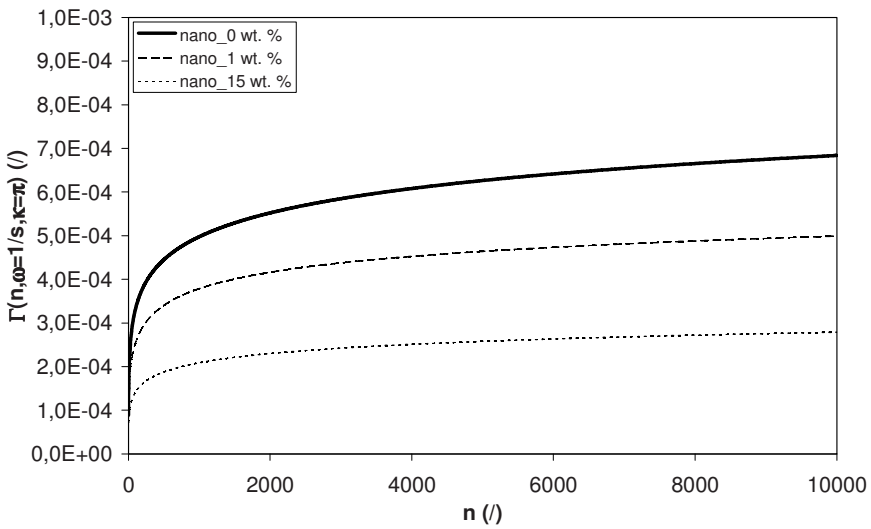

Figure 4 - *Diagram of cumulative accumulated strain, $\Gamma(n, \kappa = \pi, \omega = 1/s)$ as function of the number of loading cycles, n, for nanocomposites with three different concentration of nanoparticles.*

From diagrams above it can be observed that addition of the nanoparticles into the polymeric (PA) matrix decreases the magnitude of the accumulated strain.

Diagram in Fig. 5 shows the evolution of accumulated strain as a function of loading angular velocity.

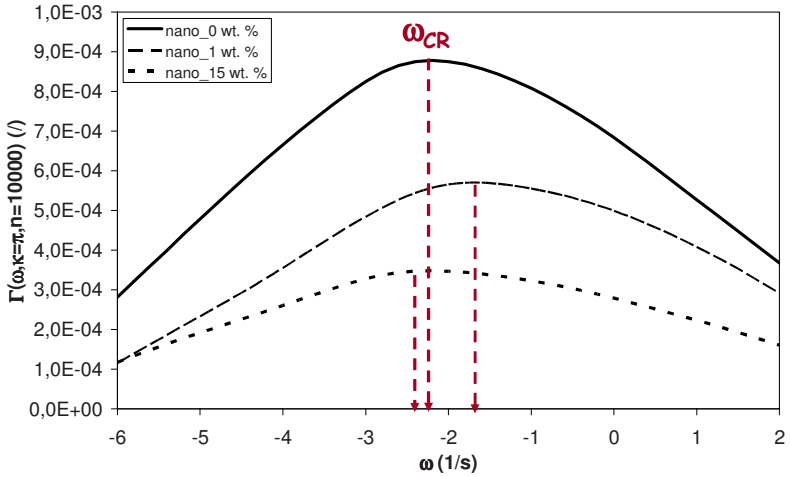

Figure 5 - *Diagram of cumulative accumulated strain, $\Gamma(\omega, \kappa = \pi, n = N = 10000)$, as function of operating angular velocity, ω , for nanocomposites with three different concentration of nanoparticles.*

From diagrams above again is observed the decrease in magnitude of accumulated strain and shift of critical operating angular velocity.

To demonstrate the use of criterion to determine critical angular velocity area, where the strain accumulation is the most intensive, we define certain upper limits of the accumulated strain, as shown with the cross-section plane (solid red contour) in Fig. 6 for all three types of analyzed nanocomposites, and project the cross-section curve (dashed red line) onto $n-\omega$ plane. We obtain different levels of critical angular velocity areas as shown in Fig. 6.

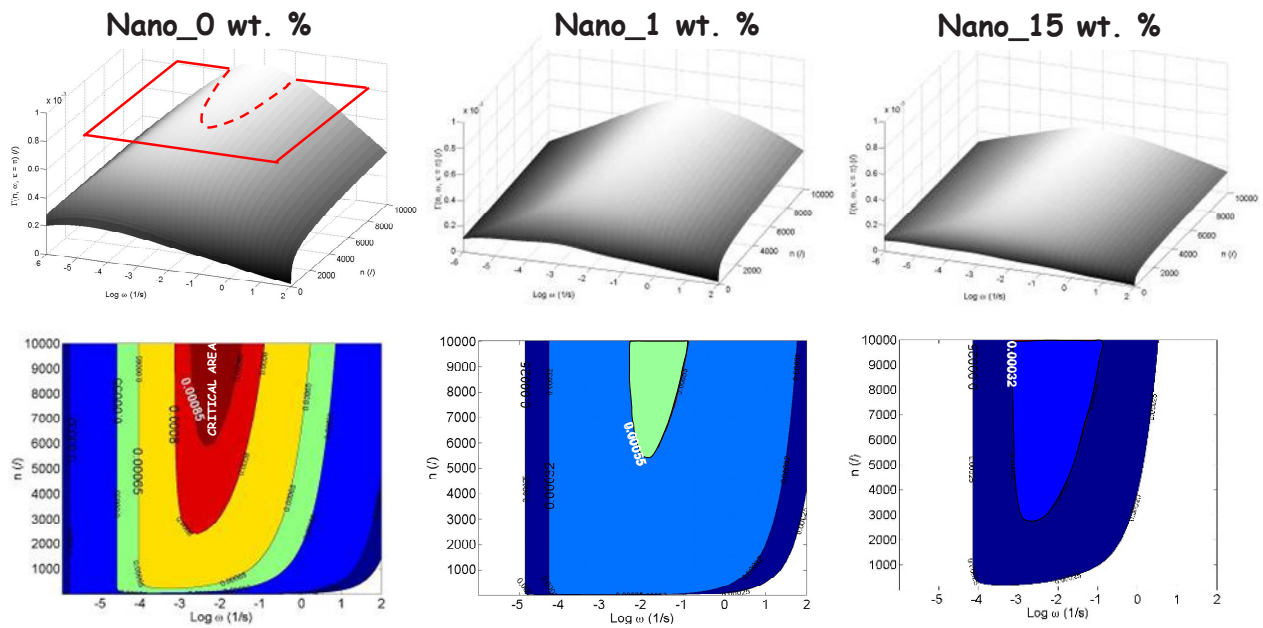

Figure 6 - *Angular velocity area corresponding to different values of the cumulative accumulated strain. Red area corresponds to the critical angular velocities of the most intensive strain accumulation.*

CONCLUSIONS

We demonstrated the application of developed theoretical approach for modeling the strain accumulation process in dynamically loaded polymeric products on the case of nanocomposite materials with different concentration of added nanoparticles into the polyamide matrix. The results showed that higher concentration of added nanoparticles slowed down the accumulation process and reduced the magnitude of accumulated strain. Consequently, this shows that addition of nanoparticles may contribute to the extension of the life span – durability of the polymeric material.

REFERENCES

1. Emri, I., Kramar, J., Hribar, A., Nikonov, A., Florjančič, U.*:* Time-dependent constitutive modeling of drive belts - I. The effect of geometry and number of loading cycles. *Mechanics of Time-Dependent Materials*, **10(3)**, 245-262, 2006.
2. Tschoegl, N.W.: The Phenomenological Theory of Linear Viscoelastic Behavior: An Introduction. Springer-Verlag, Berlin Heidelberg, 1989.
3. Zupancic, B., Emri, I.: Time-dependent constitutive modeling of drive belts – II. The effect of the shape of material retardation spectrum on the strain accumulation process. *Mechanics of Time-Dependent Materials*, **13(4)**, 375-400, 2009.
4. Emri, I., Tschoegl, N. W.: Generating line spectra from experimental responses. Part I: Relaxation modulus and creep compliance. Rheologica Acta 32:311-321 (1993).

Proceedings of the SEM Annual Conference
June 7-10, 2010 Indianapolis, Indiana USA

Viscoelastic and Viscoplastic Mechanical Behavior of Polymeric Nanofibers: An Experimental and Theoretical Approach

M. Naraghi, Postdoctorate Research Fellow, Northwestern University; Department of Mechanical Eng., 2145 Sheridan Rd, Evanston, IL 60208, m-naraghi@northwestern.edu
I. Chasiotis, Associate Professor, University of Illinois at Urbana Champaign

ABSTRACT

The viscous behavior of polymers in nanometer scale volumes can significantly differ from bulk, due to the large free surfaces and the dominating molecular heterogeneity at nanoscale. In this study, we present the first experimental investigation on the creep and strain rate behavior of electrospun polyacrylonitrile (PAN) nanofibers. The apparatus used in this study was a MEMS-based platform, developed by the authors with the addition of a feedback loop to (a) maintain constant force on a nanofiber during a creep experiment and (b) vary the applied strain rate to investigate the viscoplastic response of amorphous polymer nanofibers. The creep compliance was found to be highly dependent on the nanofiber diameter, increasing with its diameter. In agreement with previous literature studies, it was concluded that the higher stiffness of thinner nanofibers was due to higher molecular alignment. A semi-empirical model was proposed to describe the experimentally determined viscous response of the PAN nanofibers, was composed of a Langevin spring and an Eyring's dashpot to capture the strain rate sensitive yield stress and the orientation hardening observed in our experiments. The present experiments coupled with the semi-empirical model are among the first efforts to understand viscous phenomena at the nanoscale.

INTRODUCTION

The time and strain rate sensitivity of the mechanical behavior of polymeric materials have been extensively investigated at the bulk scale [1-5]. These studies primarily aimed at elucidating the viscous behavior of polymers [4] and at developing constitutive models for structural analysis and design, while capturing relaxation mechanisms of polymer macromolecules such as chain unfolding. However, the viscous behavior of polymeric nanomaterials has not yet received considerable attention partially due to inadequate experimental methods. The viscous behavior of polymeric nanofibers for instance can be substantially different from bulk due to the increased role of their free surfaces [6], the strong structural heterogeneity [7] and the reduced coherent chain entanglement network [8]. In this paper, our experimental studies on the time and strain rate sensitive mechanical behavior of polyacrylonitrile (PAN) nanofibers are presented. A MEMS based technique is harnessed to investigate the viscoelastic and viscoplastic mechanical behavior of amorphous polymeric nanofibers through creep and strain rate experiments. Finally, a semi-empirical model is applied to capture the viscous response of PAN nanofibers.

EXPERIMENTAL METHODS

The specimens were electrospun nanofibers from 9 wt.% solution of PAN in dimethylformamide (DMF). Following the past studies on the viscous mechanical behavior of bulk polymers [5,9,10], we employed our MEMS

T. Proulx (ed.), *Time Dependent Constitutive Behavior and Fracture/Failure Processes, Volume 3*, Conference Proceedings of the Society for Experimental Mechanics Series 15, DOI 10.1007/978-1-4419-9794-4_34, © The Society for Experimental Mechanics, Inc. 2011

based method [11] to study the viscoelastic response of PAN nanofibers by performing creep experiments. In addition, we carried out strain rate experiments to characterize their viscoplastic response at large deformations.

Creep Experiments on Polymeric Nanofibers

Creep experiments were performed via a previously developed MEMS-based tension test platform [11], by applying manual feedback to correct for material relaxation, i.e. reduction in the force applied to the sample. In such a creep experiment, the load is increased monotonically within ~5-10 s until the stress in the sample reaches the desired creep stress at time T. The specimen load and its extension are measured by using the digital image correlation (DIC) enhanced optical imaging method explained in [11]. In the course of an experiment, the nanofiber creep is accompanied by reduction in the loadcell deflection and thus the applied force. This reduction in force was compensated by further actuating the MEMS device to maintain constant force amplitude. It is to be noted that this procedure resulted in relatively smooth stress profiles. The time interval between successive feedback actions was ~2 seconds. Therefore, the experiments captured the viscoelastic response with time constants of a few seconds and more.

Strain Rate Experiments on Polymeric Nanofibers

In order to characterize the viscoplastic behavior of PAN nanofibers, uniaxial tension experiments were carried out at two strain rates, $2.5 \cdot 10^{-4}$ s^{-1} and 200 s^{-1}. The experimental procedures have been explained in [11,12]. The maximum and minimum strain rates were dictated by the available instrumentation for image recoding which is currently the state of the art in microscale experimentation [13]. For the slow strain rate tests a picomotor actuator actuated the MEMS testing platform, while the fast strain rate was conducted with a PZT actuator. Due to the material heterogeneities and the already established size effect of the mechanical behavior of polymeric nanofibers, we performed about 15 experiments at each strain rate to capture the effect of nanofiber diameter.

EXPERIMENTAL RESULTS

Effect of Nanofiber Diameter on Creep Response

Creep experiments were performed on six PAN nanofibers with diameters between 200-600 nm. Figure 1 shows three experiments where the data were normalized by the creep stress, which was 28-34 MPa. It is clear that the creep response of the PAN nanofibers is diameter dependent. The creep curves had an initial high rate

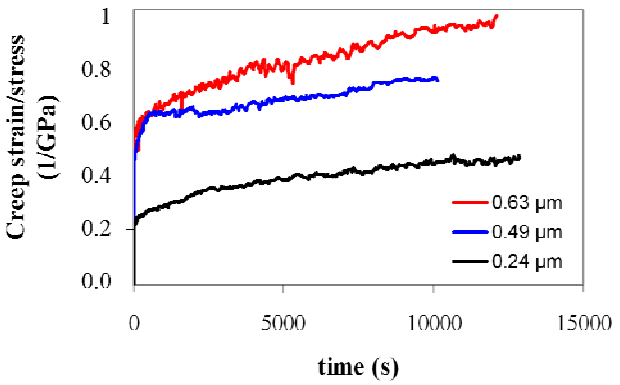

Figure 1. Creep compliance as a function of nanofiber diameter and time.

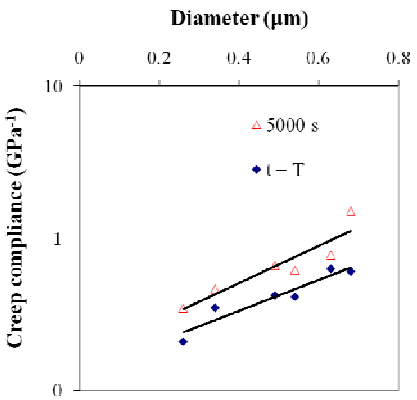

Figure 2. Creep strain per unit stress as a function of nanofiber diameter. Time t = T is the end of the initial ramp loading.

primary response followed by steady-state creep at long time scales. The creep compliance increased

monotonically with the nanofiber diameter, and at sufficiently long times the compliance of the 630 nm nanofiber was more than twice that of the 240 nm nanofiber.

Figure 2 shows the creep compliance of the samples as a function of nanofiber diameter at times t = T and t = 5,000 s (in the steady state regime of creep). In both cases, the creep compliance increased monotonically with the nanofiber diameter. A plausible explanation for this size effect lies with the higher molecular alignment in the thinner nanofibers, initiated by stretching and bending of the polymer jet during electrospinning and the reduced solvent content in the thin nanofibers compared to the thick ones. This trend is analogous and close in magnitude to the effect of molecular alignment on the creep response of glassy PS sheets reported by Shelby and Wilkes [14].

Viscoplastic Response of PAN Nanofibers

Strain rate experiments at 200 s^{-1} and 0.00025 s^{-1} were performed on nanofibers with diameters between 200-600 nm. Six samples were tested at each strain rate. Example plots of the true stress-logarithmic strain of nanofibers with initial diameters 300-400 nm are shown in Figure 3, consisting of an initial linearly elastic segment until softening at $\varepsilon \approx$ 3-5%. This softening can be considered as the onset of mutual sliding of PAN molecules, which requires sufficiently high stresses. Due to viscous effects, the initial slopes are less than the viscoelastic modulus, which could not be captured due to the limited strain resolution of ~0.1%. The measured elastic stiffness is then plotted in Figure 4(a) as a function of the nanofiber diameter and the applied strain rate pointing to strong strain rate sensitivity of the elastic stiffness of PAN nanofibers. From the strain rate experiments, it can also be realized that the load bearing capacity of the nanofibers increased with the strain rate for the three faster rates, as shown in Figure 4(b).

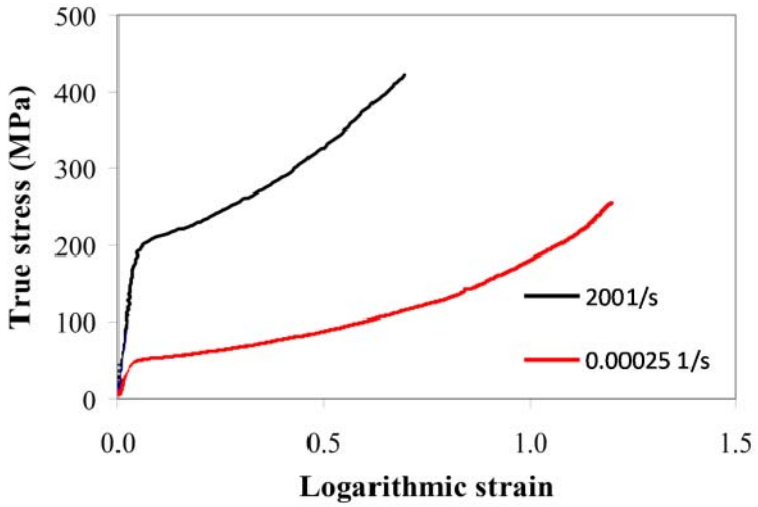

Figure 3. True strength vs. logarithmic strain for PAN nanofibers loaded at different strain rates.

Similarly to the creep experiments, the size effect in the mechanical properties of PAN nanofibers could be attributed to molecular alignment and reduced solvent content in the thinner nanofibers due to further stretching of thinner nanofibers during electrospinning. In addition to size effect, the trends in Figures 3 and 4 show that mechanical behavior of PAN nanofibers is highly rate sensitive, indicating the presence of multiple very short and long range relaxation/creep mechanisms. It is expected that at very high strain rates (potentially higher than the fastest rate in our experiments) all long range backbone relaxations are suppressed, resulting in glassy response and relatively constant elastic nanofiber stiffness. In the range of strain rates explored in this study, however, no convergence to a plateau behavior was observed.

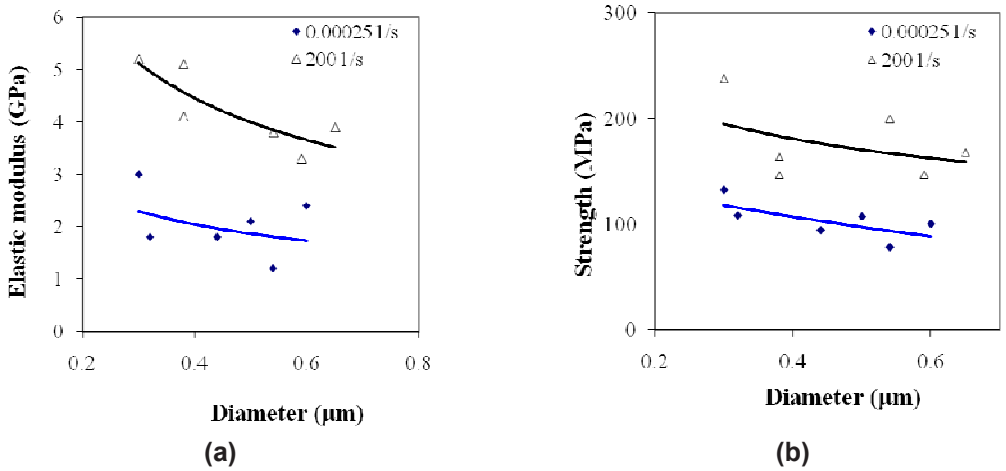

(a) (b)

Figure 4. Nanofiber **(a)** modulus and **(b)** strength as a function of diameter at two strain rates.

Modeling of the Mechanical Behavior of PAN Nanofibers

A semi-phenomenological model was applied to describe the post-yield hardening of amorphous PAN nanofibers. The model consisted of a linear spring in series with a combination of a Langevin nonlinear spring in parallel with a nonlinear dashpot. The linear spring controlled the mechanical response of the material at small deformations, the nonlinear spring accounted for hardening, and the dashpot controlled the yield process by using Eyring's time model [15]. This model is partly phenomenological and partly (Langevin spring) based on statistical mechanics of thermoplastics. This model has been successfully used before to capture the strain rate response of amorphous polymers [16] and thermoplastics [17,18]. The mathematical description of the model is:

$$\sigma = G_P\left(\lambda^2 - \frac{1}{\lambda}\right) + \sigma_y\left(\dot{\lambda}, \lambda, K\right) \qquad (1)$$

where λ, K, σ, σ_y and G_p are the stretch ratio, absolute temperature, true stress, yield stress and the strain hardening modulus of the nanofibers. This equation describes the post-yield behavior of polymeric materials under axial stretching and constant volume.

In order to examine the efficiency of this model in capturing the post yielding behavior of polymeric nanofibers subjected to the aforementioned strain rates, the values of the true stress for each sample were plotted as a function of λ^2-$1/\lambda$. A line was fitted to each dataset according to Equation (1), whose slope was the hardening modulus and the y-intercept was the yield stress. As seen in Figure 5(a) very good fitting of the experimental data by Equation (1) was obtained. By fitting Equation (1) to all the strain rate experiments, the values of Gp were calculated and plotted as a function of strain rate and diameter. The results are shown in Figure 5(b). It was found that the hardening modulus was strongly dependent on the nanofiber diameter, and that it was strain rate sensitive: it increased by a factor of 2-3 as the strain rate increased from $2.5 \cdot 10^{-4}$ s^{-1} to 200 s^{-1}. Theoretically speaking when the physical entanglement in thermoplastics is permanent [9], or similarly to cross-linked rubber, G_P is not strain rate sensitive. However, the present experimental results point to limited life time and relaxations of the initial entanglements in the network of PAN molecules, indicating that this entanglement network potentially deforms in a more coherent manner at higher strain rates, and therefore, G_P increases with strain rate.

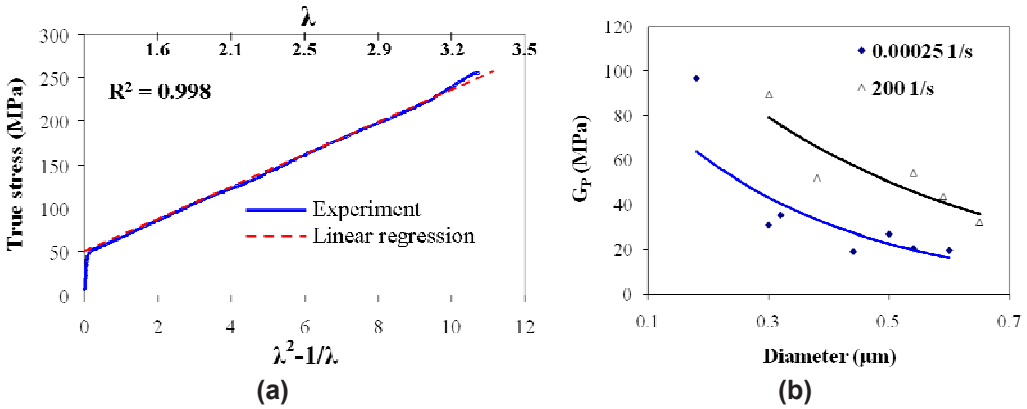

Figure 5. True stress vs. λ^2-$1/\lambda$ of a PAN nanofiber with initial diameter ~480 nm, loaded at 0.025 s^{-1}. The x-axis is linear w.r.t. λ^2-$1/\lambda$ and λ is the nanofiber stretch ratio.

CONCLUSIONS

The first experiments on the viscoelastic and viscoplastic behavior of polymeric nanofibers were reported. At small deformations, creep experiments were performed by manual feedback to the MEMS platform to maintain constant force on the sample. The viscoplastic behavior at large fiber extensions was investigated by strain rate experiments at two strain rates that differed by 6 orders of magnitude. The experimental results pointed to a strong size effect, in which the thinner nanofibers were stiffer and of lower creep compliance. This was attributed to molecular alignment and reduced solvent content in the thinner nanofibers. The experimental results were applied to a semi-empirical mechanical model which described their viscous behavior at large extensions. The model was based on a nonlinear dashpot in parallel with a nonlinear dashpot, which was previously used to capture the strain rate sensitivity of the mechanical behavior of amorphous polymers. The model fitting pointed to an increase in the hardening modulus with strain rate that could be owed to the limited life-time of entanglements in the PAN network and their enhanced relaxation at lower strain rates.

ACKNOWLEDGEMENTS

The authors acknowledge the support by the Solid Mechanics Program on Composites for Marine Structures under ONR-YIP grant #N00014-07-1-0888 with Dr. Y.D.S. Rajapakse as the program manager.

REFERENCES

[1] Imai Y and Brown N, 1976 The effect of strain rate on craze yielding, shear yielding and brittle fracture of polymers at 77K *Journal of Polymer Science, Polymer Physics Edition* 14 723-39

[2] Bauwens J C, Bauwens-Crowet C and Home`s G., 1969 Tensile yield-stress behavior of poly(vinyl chloride) and polycarbonate in the glass transition region. *Journal of Polymer Science : Part A-2* 7 1745–54

[3] Dioh N N, Ivankovic A, Leevers P S and Williams J G, 1994 High strain rate behaviour of polymers *Journal De Physique. IV : JP* 4 C8-(119-124)

[4] Bauwens J C, 1972 Relation between the compression yield stress and the mechanical loss peak of bisphenol-A-polycarbonate in the β transition range *Journal of Materials Science* 7 577-84

[5] Findley W N, Lai J S and Onaran K, 1989 Creep and Relaxation of Nonlinear Viscoelastic Materials *July Publisher: Dover Publications*

[6] Wu X F and Dzenis Y A, 2004 Size effect in polymer nanofibers under tension *Journal of Applied Physics* 102 044306

[7] Dayal P and Kyu T, 2006 Porous fiber formation in polymer-solvent system undergoing solvent Evaporation *Journal of Applied Physics* 100 043512

[8] Michler G H, Kausch H H and Adhikari R, 2006 Modeling of thin layer yielding in polymers *Journal of Macromolecular Science: Physics* 45 727-39

[9] Haward R N, 2007 Strain hardening of high density polyethylene *Journal of Polymer Science: Part B: Polymer Physics* 45 1090–9

[10] Haward R N, 1993 Strain hardening of thermoplastics *Macromolecules* 26 5860–9

[11] Naraghi M, Chasiotis I, Dzenis Y *et al.* 2007 A novel method for the mechanical characterization of polymeric nanofibers *Review of Scientific Instruments* 78 085108-1 - 8

[12] Naraghi M, Chasiotis I, Kahn H et al, 2007 Mechanical deformation and failure of electrospun polyacrylonitrile nanofibers as a function of strain rate. *Applied Physics Letters* 91 151901 1-3

[13] K. Jonnalagadda, I. Chasiotis, J. Lambros, R. Polcawich, J. Pulskamp, and M. Dubey, "Experimental Investigation of Strain Rate Dependence in Nanocrystalline Pt Films," Experimental Mechanics 50 (1)25-35, 2010

[14] Shelby M D and Wilkes G L, 1998 The effect of molecular orientation on the Physical ageing of amorphous polymers - dilatometric and mechanical creep behaviour *Polymer* 39 6767-79

[15] Haward R N and Thackray G, 1968 The use of a mathematical model to describe isothermal stress-strain curves in glassy thermoplastics Proceedings of the Royal Society of London Series A, Mathematical and Physical Sciences 302 453-72

[16] Arruda E M and Boyce M C, 1993 Evolution of plastic anisotropy in amorphous polymers during finite straining International Journal of Plasticity 9 697-720

[17] Haward R N, 2007 Strain hardening of high density polyethylene Journal of Polymer Science: Part B: Polymer Physics 45 1090–9

[18] Haward R N, 1993 Strain hardening of thermoplastics *Macromolecules* 26 5860–9

Proceedings of the SEM Annual Conference
June 7-10, 2010 Indianapolis, Indiana USA

Effect of Polyacrylate Interlayer Microstructure on the Impact Response of Multi-Layered Polymers

Joshua S. Stenzler and N. C. Goulbourne
Aerospace Engineering Department
University of Michigan
Soft Materials Research Laboratory
Ann Arbor, MI 48109
jstenz@gmail.com

Abstract

Soft polymers are widely used as interlayers and adhesives in multi-layered systems for defense applications. This research focuses on the large deformation response of several polyacrylate adhesives with varying microstructures. Understanding the mechanical response of these materials under numerous dynamic loading conditions is instrumental in deriving high fidelity constitutive models and optimizing performance when integrated into a multi-layered structure. In recent years, there has been an emphasis on rate dependence research of soft materials, such as thermoplastic polyurethanes/polyureas (moduli order of 3–5 MPa), at quasi-static and very high rates (SHPB), but not intermediate. The goal is to characterize ultra-soft polyacrylates (moduli on the order of 100–600 kPa) through a wide range of strain rates (0.001–1 /s) using different methods and modes of loading. Methods utilized are Instron (servohydraulic and ElectroPULS) tensile and compression testing, and intermediate instrumented impact on multi-laminates. Characteristics of the large, non-linear deformation testing response include: rate dependence, hysteresis, cyclic effects and strain softening. The microstructure and mechanical behavior of the polyacrylate adhesives is related to the capability to modulate impact loads for loading times of approximately 2 milliseconds.

1. Introduction

Transparent armor is utilized in military defense applications such as personnel protection (visors/shields/goggles) and air/ground vehicle windows. Typically, these optically clear, multi-layered polymer laminates are required to defeat incoming threats, withstand multiple impacts, and maintain optical clarity with minimal fragmentation and visual distortion for the user [1-3]. A typical configuration of transparent armor consists of multiple tough thermoplastic polymer outerlayers with rubbery interlayer adhesives. For many years, the component materials have consisted of the glassy polymers polycarbonate (PC) and poly(methyl methacrylate) (PMMA) with thermoplastic polyurethane (TPU) adhesives [4-5]. The transparency, toughness, and rate dependence of these three materials are the main reasons they are excellent choices for use in transparent armor to withstand projectile impact. Previous research by this group has compared the impact mechanics of multi-layered, impact resistant, polymer structures with two TPU interlayers and an optically clear polyacrylate [6]. It was shown that when utilized as an interlayer, the substantially more compliant polyacrylate had similar (if not less) fracture than the two TPU adhesives tested. The polyacrylate examined in the previous work is VHB 4905, which is an optically clear, solid acrylic adhesive with no discernible microstructure [6]. Therefore, the goal of this paper is to investigate the effect of three polyacrylates with varying microstructures and mechanical responses. VHB 4905 is included in this study for comparison purposes. Despite these new materials being opaque, a correlation is sought between microstructure and quasi-static material properties of the interlayers to impact performance and energy absorption mechanisms. Relationships of this sort would be useful in tailoring future polymers with superior impact performance that could be optically clear and utilized in transparent armor. Furthermore, the purpose of this research is to examine the role of soft, pressure-sensitive polyacrylate adhesives in the impact response of three-layered PMMA/PC multi-laminates.

T. Proulx (ed.), *Time Dependent Constitutive Behavior and Fracture/Failure Processes, Volume 3*, Conference Proceedings of the Society for Experimental Mechanics Series 15, DOI 10.1007/978-1-4419-9794-4_35, © The Society for Experimental Mechanics, Inc. 2011

Mechanical characterization of and the impact response of polyacrylates has not been extensively researched. Several researchers have utilized time-temperature superposition and dynamic mechanical analysis to model and characterize the viscoelastic response of 3M polyacrylates [7-8]. These results are focused on the design and optimization of adhesive joints as well as other civil engineering applications, not examining the impact response when utilized in an all-polymer multi-laminate. Townsend found that the mechanical response of a VHB adhesive is dependent on loading rate and duration [7], and Hennage reported that VHB polyacrylates are "far from a linear-elastic material" [8]. Much research has been published regarding the mechanical response and rate dependence of soft materials similar to polyacrylates such as: particle-reinforced rubber, polyurea, polyurethane, thermoplastic polyurethane, pig skin, silicone rubber, and low-density epoxy foam. Quasi-static and very high rate results were achieved by utilizing a universal testing machines and modified split Hopkinson pressure bars respectively [9-12]. Several of these groups focused on low strain rate dependence and large deformation behavior of the materials, including loading/unloading of the samples [13-15]. Qi and Boyce, and Yi et al. completed uniaxial cyclic compression testing on polyurethanes/polyureas over four decades of strain rate ($0.001–1\ s^{-1}$) and observed a highly non-linear response, strong rate dependence, hysteresis, cyclic softening, and residual strains following unloading. Residual strains, measured approximately one minute after test conclusions, were more substantial for samples loaded to larger strains [14]. It was also concluded that chemical composition significantly affects mechanical response as observed with residual strain magnitudes, hysteresis loop sizes, and on strain rate dependency [15]. Materials with slightly different compositions or microstructures have vastly different responses. This paper examines how polyacrylate microstructure affects mechanical response in tension for various strain rates and quasi-statically in compression. The mechanical characterization discussed in this paper may be considered a material level test at low strain rates. In order to test at higher strain rates, structural gas gun impact tests are conducted on three-layered multi-laminates with polyacrylate adhesives.

Gas guns are typically designed to obtain high impact speeds and are focused on impact velocity more than instrumentation. Typically, these experimental setups are unable to measure contact forces or sample deflection. They rely on analysis through measuring V_{50}, incident/residual impactor velocities to characterize energy dissipation, and post-impact visual inspection [16-26]. Due to signal transmission issues as well as the intensity of collisions, possible target perforation, and resulting fracture of high speed impact, instrumentation can be difficult and dangerous for both sensors and users. Therefore, only few research groups have attempted instrumentation of gas gun projectiles. Delfosse et al. used a 1.83 m long gas gun (44.5 mm inner diameter) capable of intermediate impact velocities of 7–50 m/s with a piezoelectric accelerometer instrumented impactor [27]. Their projectile had a trail wire leading to a digital oscilloscope as well as a relief valve to prevent double impact and to facilitate rebound of the impactor back into the launch tube. Optical sensors near the end of the barrel measured impact velocity. Levy and Goldsmith's gas gun was 1.37 m long with interchangeable barrels of inner diameters 6.35 and 12.7 mm capable of impact velocities from approximately 25–300 m/s. A silver-plated X-cut quartz disc instrumented the projectile and the signal is read by an oscilloscope [28]. For both instrumented gas guns, calibration is required for the fabricated load cells based on the masses ahead and behind the transducer. The pre-packaged Kistler load cell implemented in this research has a manufacturer provided calibration factor calculated for acceleration of the shock accelerometer's internal seismic mass.

This paper presents an experimental, systematic impact analysis for three-layered multi-laminates consisting of PMMA, polyacrylate, and PC for intermediate impact velocities (9–30 m/s). In total, four polyacrylate adhesives, provided by 3M, with varying material properties and microstructures are mechanically characterized using rate dependent tensile and quasi-static compression (Section 2 and 3). These materials are VHB 4905, VHB 5925, VHB 4936 and VHB 4930. Hsieh and Song have reported incident/residual impactor velocities and V_{50} data for high speed impact on layered PMMA/PC composites, but with no interlayer or instrumentation [22-23, 26]. Previous impact testing of monolithic polymer layers has typically been at low impact velocities (drop towers/pendulum), high impact speeds (large gas guns), and very high strain rate (split Hopkinson pressure bar) material testing. Therefore, a gap exists in the intermediate velocity range for polymer testing. Using a novel instrumented gas-gun setup, damage and energy absorption mechanisms are characterized both quantitatively and qualitatively through analysis of the impact response (Sections 4). In Section 5, quantitative force and displacement metrics, post-impact fracture observations, and quasi-static interlayer mechanical characterization are correlated to impact response. This research can help develop a better understanding of the impact mechanics of multi-layered structures. Specifically, how the individual material characteristics and microstructure of the interlayer affects the overall impact response and damage observed.

2. Polyacrylate Chemistry, Properties, and Microstructure

The VHB interlayers are soft, polyacrylates of varying colors and conformabilities with the chemical structure of the acrylate monomer shown in Figure 1a. They are all commercially available from 3M and are used in as-received condition being tacky at room temperature. Figure 1b shows the reported and measured material properties for the materials. Since they are polymers displaying strain rate dependence, the moduli are calculated from the linear portion of the quasi-static tensile testing results (Section 3.1). The Poisson ratio reported by 3M for the VHB polyacrylates (0.49) is typical for elastomeric, rubbery materials and reflects near incompressibility [29]. The glass transition temperatures and densities are reported by 3M. The properties for the four VHB polyacrylates vary substantially, although VHB 4936 and VHB 4930 have comparable values for tensile moduli (0.559/0.553 MPa) and densities (720/800 kg/m^3).

a)

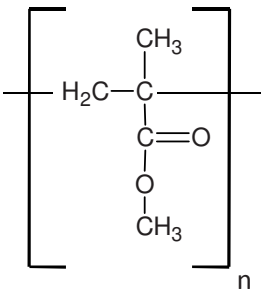

b)

Material	Color	As Received Thickness (mm)	Tensile Elastic Modulus (MPa)	Density (kg/m^3)	T_g (C)
VHB4905	None	0.5	0.127	960	-40
VHB5925	Black	0.635	0.351	590	-45.6
VHB4930	White	0.635	0.553	800	-34.4
VHB4936	Gray	0.635	0.559	720	-34.4

Figure 1. Polyacrylate a) chemical structure and b) material properties

Through communication with a 3M technical service scientist and visual inspection using an Omano OM3344 stereo microscope, the microstructure of each material is visualized and components are identified. Despite a common acrylic matrix material, the VHB polyacrylates have quite differing microstructures. Pictures shown of the top surface (45 times zoom) and representative schematics of the four polyacrylates' microstructures are shown in Figure 2. Note that VHB 4905 has no appreciable microstructure because it is a solid acrylic adhesive and can be considered incompressible (Figure 2a). VHB 5925 has collapsible air bubbles of varying sizes (~100 µm) with a distribution of approximately 44.4 per mm^2 and therefore is considered somewhat compressible (Figure 2b). VHB 4930 is similar to VHB 4905 in that it is solid acrylic and can be considered incompressible, but has rigid microspheres of equal diameter (~70 µm) dispersed at approximately 100 per mm^2 (Figure 2c). Like VHB 5925, VHB 4936 has compressible spaces but also has the microspheres in common with VHB 4930 (Figure 2d). In summary, VHB 4905 and VHB 4930 may be considered incompressible with a solid acrylic structure, VHB 5925 and VHB 4936 are compressible with collapsible air gaps/bubbles, and VHB 4936 and VHB 4930 have rigid microspheres incorporated into the acrylic matrix.

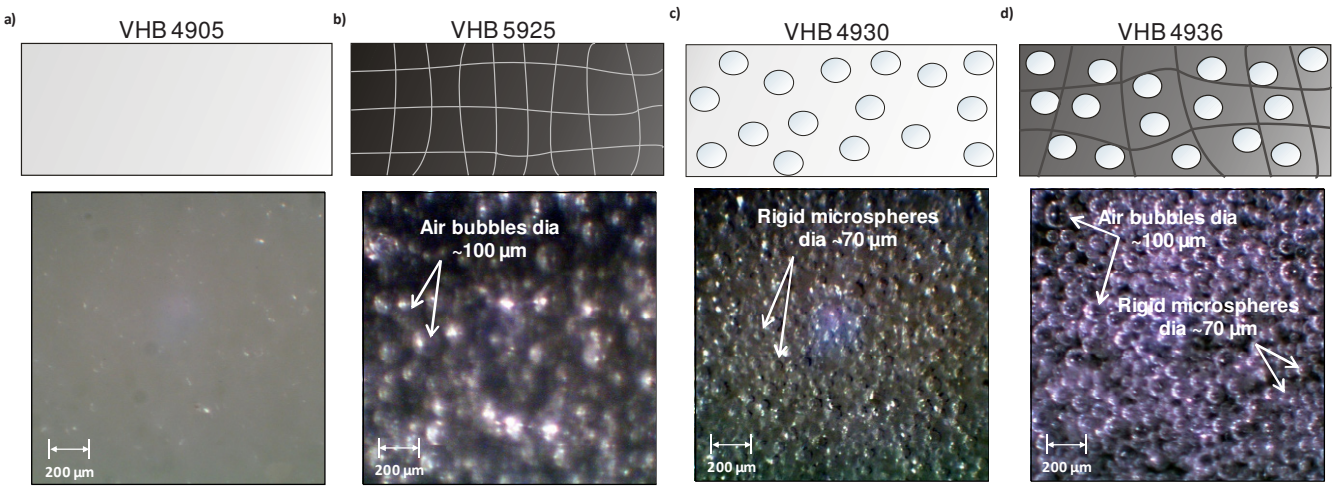

Figure 2. Representative schematic and stereomicroscope pictures (X45) of a) VHB 4905, b) VHB 5935, c) VHB 4930, and d) VHB 4936

3. Mechanical Characterization

3.1 Uniaxial Tensile Testing

As a baseline comparison for the four materials, tensile testing is completed at four different strain rates (0.001, 0.01, 0.1, and 1 s^{-1}). Dogbone samples cut using an ASTM standard die (D-638 Type IV) are loaded to a strain of 1.0 (15 mm) and then unloaded back to the starting position. An Instron ElectroPULS with a 250 N load cell is used for the highest rate testing (1 s^{-1}) and an Instron 5848 Micro-tester with a 50 N load cell is used for the lower rates. The ElectroPULS is required since the Micro-tester is incapable of reaching the desired crosshead speeds. In fact, once the load cell is isolated from the frame of the ElectroPULS, even higher rate testing could be carried out with capabilities up to ~1.7 m/s crosshead speeds. Note that the Instron's crosshead displacement, not an extensometer, is used to calculate strain. This is important because it is assumed that a dogbone sample facilitates a mostly uniform elongation of the gauge length of the polymer. For miniscule strains, a non-contact extensometer should be utilized (especially for soft polymers) to measure the true, non-linear small elongation of the material section. Contact extensometers are not an option due to the high compliance of test materials and large deformations investigated. Therefore, a method that could be utilized to accurately measure full-field, large strain using non-contact methods is two-dimensional DIC (digital image correlation). Figure 3 shows the tensile testing results (engineering stress as a function of strain) for the four polyacrylates at four strain rates, with each trace being the average of eight samples. It is clear from these results that the polyacrylates are non-linear and have strong rate dependence, hysteresis, strain softening, and residual strains. As the strain rate increases, the compliance decreases as the soft material is stretched at faster rates. It is also observed that for all of the materials, except VHB 5925, as strain rate increases the residual strain increases as well. This is not plastic strain as some is recovered with time, but is more indicative of the strain at which the sample is no longer in tension, or buckles over, during unloading. Figure 4 visualizes how the interlayers compare for each of the four strain rates. It is observed that VHB 4930 and VHB 4936 have similar responses for all strain rates and show little rate dependence when loaded at 0.001 and 0.01 s^{-1} (although residual strain still increases with rate). Note the order of polyacrylates in increasing tensile compliance is: VHB 4936/4930, VHB 5925, and VHB 4905.

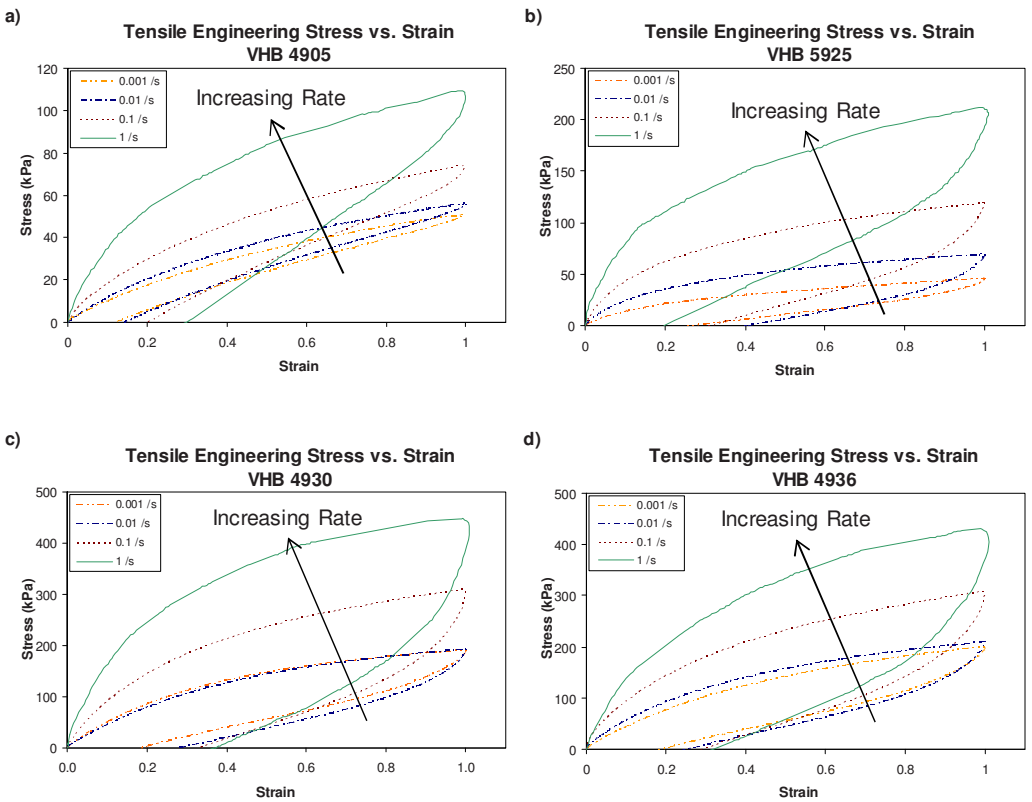

Figure 3. Tensile stress versus strain at four strain rates (0.001, 0.01, 0.1 and 1 s^{-1}) for a) VHB 4905, b) VHB 5925, c) VHB 4930, and d) VHB 4936

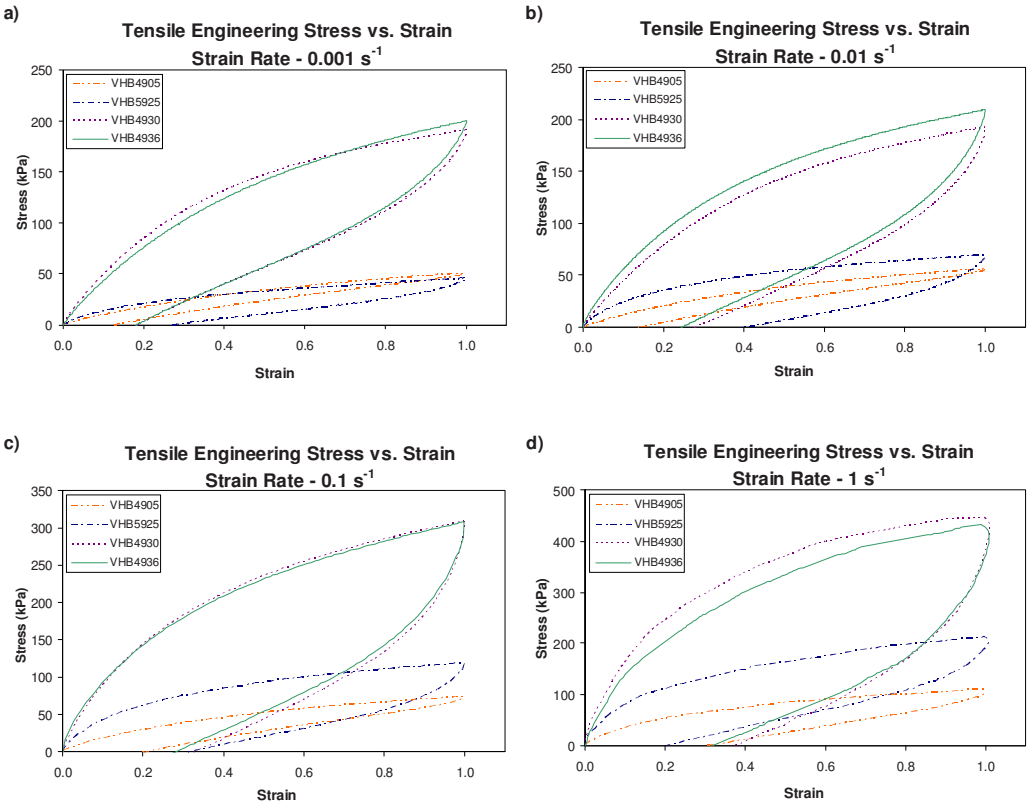

Figure 4. Tensile stress versus strain results for VHB polyacrylates at strain rates of a) 0.001, b) 0.01, c) 0.1, and d) 1 s^{-1}

Hysteresis is observed for all interlayers indicating that less force is required to unload than load the materials. Although the mechanisms for hysteresis are not well understood, it is known that it is indicative of how a changing microstructure affects energy absorption during a loading cycle. Loop areas under the stress/strain curves are considered the strain energy of the material or energy that the material dissipates during a loading cycle. A fully elastic material would have the same loading and unloading curve with no energy being dissipated or stored. The measured areas of these loops are normalized by the area of the quasi-static strain rate (0.001 s^{-1}) for each interlayer with results shown in Table 1. Since each material is normalized with respect to its own quasi-static area, all four polyacrylates may be compared in terms of relative increase of loop area. It is important to observe how the interlayers' energy dissipation capabilities translate with increasing strain rate. Increase in loop size with strain rate is representative of the material's ability to scale energy dissipation/absorption mechanisms with rate. With regard to loop area increase, it is observed that polyacrylates can be split into two groups: those with and without rigid microsphere inclusions. With the first decade increase in strain rate, all polyacrylates (except VHB 5925) have a relatively similar area increase. Over the next two decades of strain rate, VHB 4905 and VHB 5925 (no microspheres) have a substantially larger increase in loop area than VHB 4936 and VHB 4930 (microspheres). The relative area increase for the strain rate of 1 s^{-1} is on the order of 3.5 times for samples with microspheres and 5.5 times for those without. This implies that the samples with rigid inclusions do not dissipate as much energy during a loading cycle to a strain of 1. Results also show that energy dissipation in polyacrylates with collapsible gaps (VHB 5925 and VHB 4936) do not indicate any significant difference from samples without this microstructure (VHB 4905 and VHB 4930).

Table 1. Hysteresis loop area summary with normalized values with respect to the quasi-static strain rate

Interlayer		Strain Rate			
		0.001 s^{-1}	0.01 s^{-1}	0.1 s^{-1}	1 s^{-1}
VHB 4905	Area (kPa)	7.69	9.928	18.794	44.91
	$A/A_{quasi\text{-}static}$	1	1.29	2.44	5.84
VHB 5925	Area (kPa)	17.212	34.473	55.196	93.91
	$A/A_{quasi\text{-}static}$	1	2	3.21	5.46
VHB 4930	Area (kPa)	68.424	77.326	144.1	254.2
	$A/A_{quasi\text{-}static}$	1	1.13	2.11	3.72
VHB 4936	Area (kPa)	65.223	84.696	141.24	221.69
	$A/A_{quasi\text{-}static}$	1	1.3	2.17	3.4

3.2 Uniaxial Compression Testing

Compression of the polyacrylates is completed using an Instron 4204 frame with a 1 KN load cell. Since the interlayers are very thin (less than 1 mm), it is necessary to stack 19.05 mm (0.75 in) diameter samples to approximately 3 mm in height to ensure an adequate amount of strain could be achieved. A circular punch was used to consistently cut circular specimens. Since the polyacrylates are sticky, barreling of the stacks is inevitable and slippage between layers is impossible. The VHB stacks may be considered one solid material that compresses as a whole. The materials are compressed at a strain rate of 0.001 s^{-1} (0.003 mm/s) until the tests were stopped due to possible machine damage. Since the VHB stacks are so sticky and soft, they can compress to very high strains without compromising the stack structure. The plots shown in Figure 5 are averages of three samples. It is observed that VHB 4936 and VHB 4930 have somewhat similar responses, which was also seen in the tensile results. Note that VHB 4936 strain hardens more significantly than VHB 4930 and that VHB 4905 is less compliant in compression than 5925 (opposite of tensile results). This is due to the common compressible microstructure of VHB 4936 and VHB 5925. Initially, the collapsible air gaps are compressed (more compliant than incompressible samples), but eventually they can no longer be compressed and hardening occurs. This is more pronounced in VHB 4936 than VHB 5925 suggesting VHB 5925 has a larger amount of compressibility. Note the polyacrylates' order of increasing compressive compliance is: VHB 4930, VHB 4936, VHB 4905, and VHB 5925.

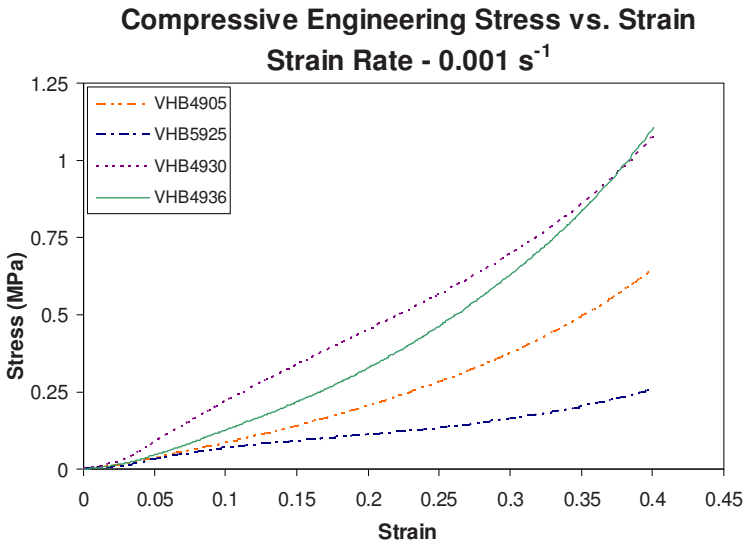

Figure 5. Quasi-static compressive stress versus strain for VHB polyacrylates

4. Normal Plate Impact Experiments

4.1 Instrumented Experimental Setup

An intermediate impact velocity gas gun (9–30 m/s) is utilized to conduct impact testing on multi-layered samples consisting of a PMMA front layer, PC back layer, and polyacrylate adhesive at strain rates on the order of 100 s^{-1}. The gas gun is instrumented, recording contact force and out-of-plane deflection throughout the impact event (Figure 6). Typically, high speed gas guns are unable to measure contact forces or sample deflection and rely on analysis through measuring V_{50}, incident/residual velocities, and post-impact visual inspection [16-26].

A custom instrumented test facility is built for impact testing at low to intermediate impact velocities using a lightweight, hemi-spherical, steel impactor (28.5 grams) with a diameter of 1 cm (0.4”). An HDPE sheath and cap protect the shock accelerometer embedded in the impactor and the cap minimizes tension on the cable connection and provides a flat surface for propulsion. Impact specimens are clamped in place by a steel bracket exposing 161.29 cm^2 (12.7 cm/5 in sides) of the original 232.25 cm^2 (15.24 cm/6 in sides) square panel. The mass ratio between the samples (~95 grams) and impactor is 3.3. The diameter of the impactor (1 cm) to the span of the sample (12.7 cm) is approximately 0.08. The impactor diameter (1 cm) to specimen thickness (3.675–3.81 mm) ratio ranges from 2.62–2.72. For a structural test such as described in this paper, these ratios describe the elastic deformation mechanisms available for the setup. A more complete description and pictures of operation and data acquisition procedure for the experimental setup can be found in [30].

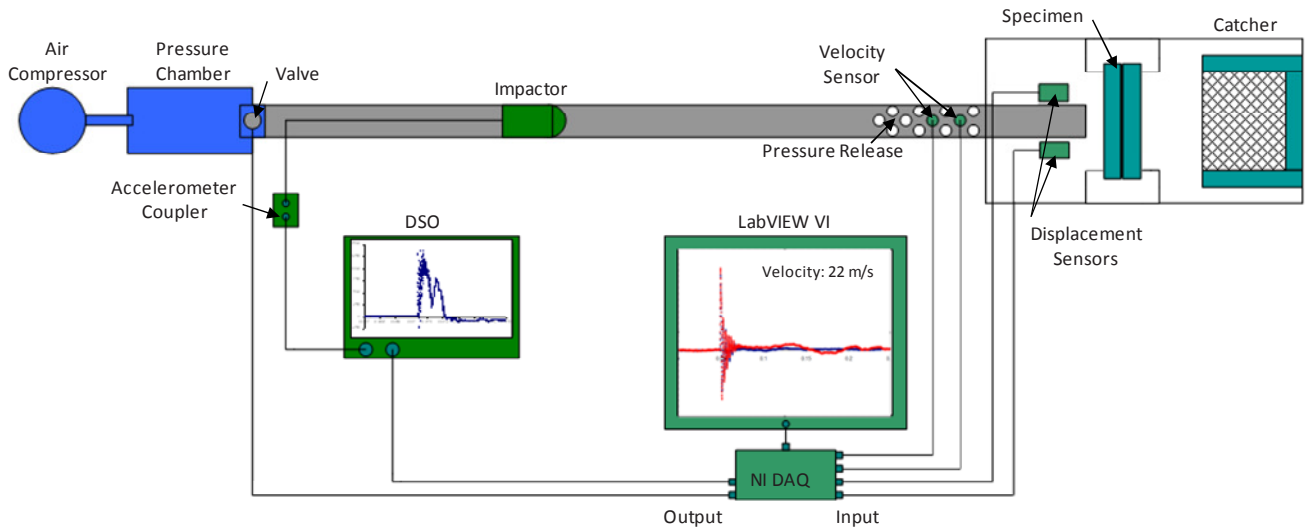

Figure 6. Schematic of intermediate velocity instrumented experimental setup

4.2 Impact Force and Displacement Results

By overlaying force and displacement traces on the same time axis, the sequence of impactor deceleration and panel displacement can be better understood. Results are shown for impact velocities of 12 m/s (Figure 7) and 22 m/s (Figure 8). Contact force is measured at the center of the target while displacement is measured off-center (28.575 mm/1.125 in) symmetrically by two sensors, so that there is a delay observed between initiation of contact force and initial deflection. If displacement was measured at the impact site, the displacement curve would be shifted to the left so that both traces were initiated at the same time (for the loading rates considered). This time delay is measured for several representative samples for each interlayer and this value was shown to be consistently between 0.2 and 0.25 milliseconds. This is representative of the time required for the impact disturbance to propagate radially outward from the impact site to the point of laser measurement. Although magnitudes reported would be fractionally less than actual impact site displacement, concurrent analysis of force and displacement for the order of events assume the displacement trace is shifted accordingly.

At initiation of impact, both contact force and deflection begin to increase. The first force peak occurs during deflection and is observed before maximum displacement is reached. As the panel reaches its maximum displacement, a decrease of contact force on the impactor occurs, until a local minimum is achieved coinciding

with maximum deflection. Note that this contact force never reaches zero, therefore only a single impact is occurring. The contact force decreases to a local minimum as the maximum displacement is approached. At the time of the local minimum, the multi-layered polymer has stored some elastic energy from the impact, and reloads the impactor as it deflects back towards its initial position. At this point, the energy stored is greater than the current instantaneous kinetic energy of the impactor and so the kinetic energy of the panel dominates the contact force signal. This impactor reloading (rebound) causes an increase in the net contact force resulting in a second force peak. The above sequence of events was verified using a high speed camera on representative samples by temporally aligning force traces with freeze frames of displacement/fracture milestones (contact initiation, maximum displacement, observation of reload cracks, etc.). Measures were taken to ensure the temporal alignment of all data acquired so that any delay observed is not electrical, and would be easily identified and explained mechanically.

a)

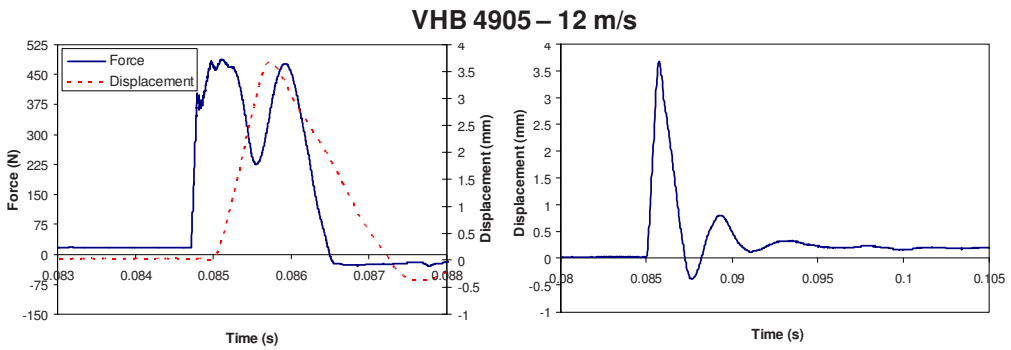

b)

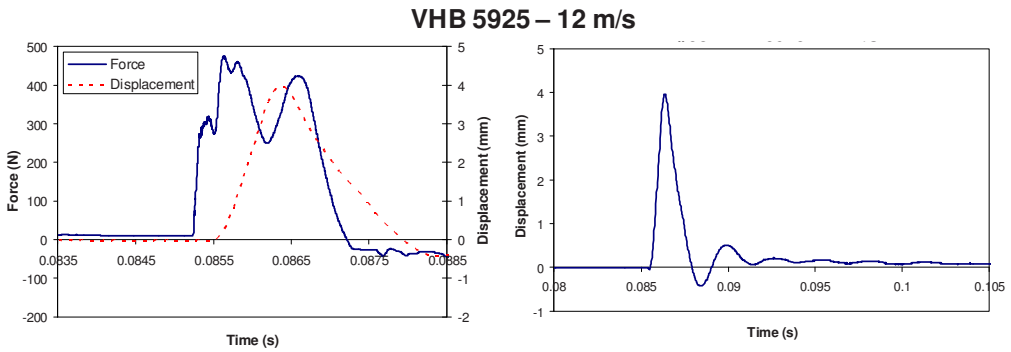

c)

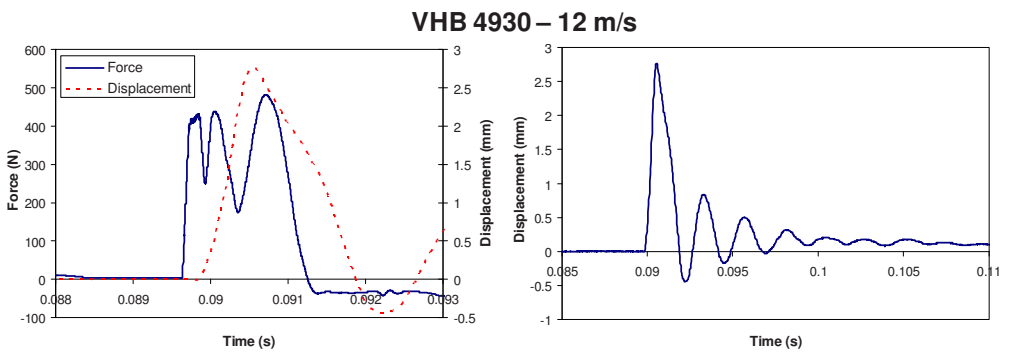

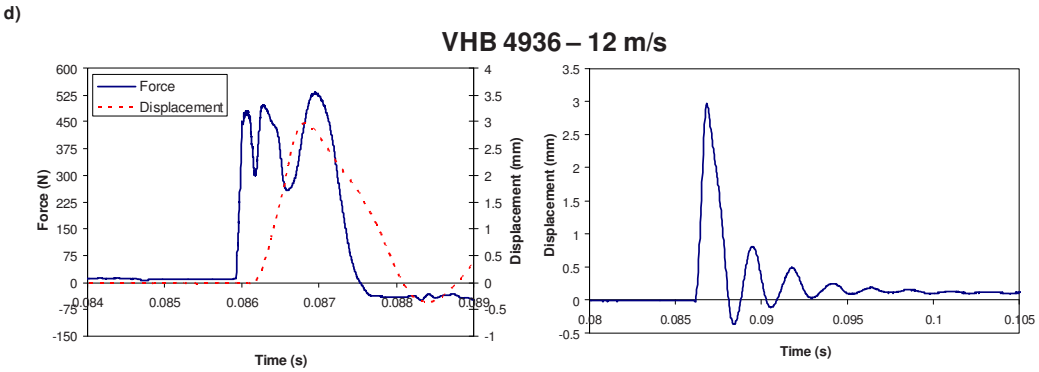

Figure 7. Representative force and displacement traces versus time for an impact velocity of 12 m/s on multi-laminates with a) VHB 4905, b) VHB 5925, c) VHB 4930, and d) VHB 4936 adhesives

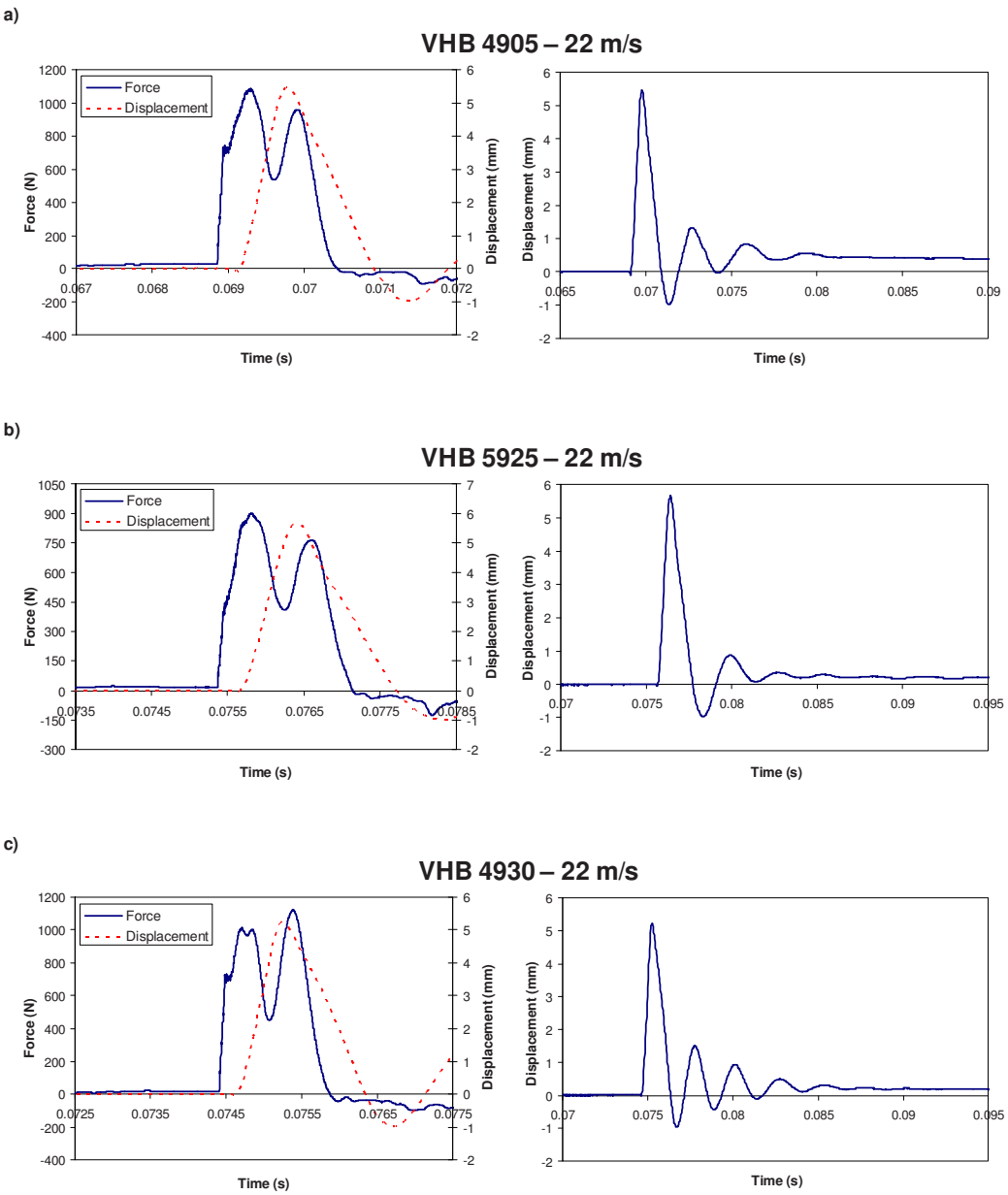

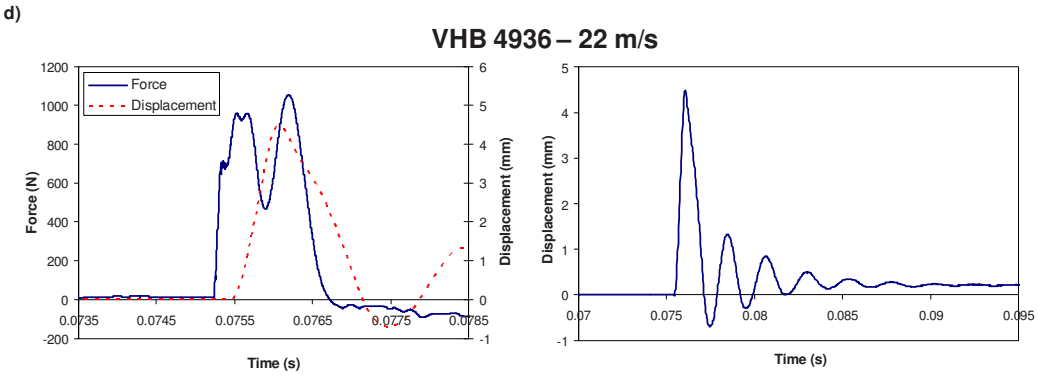

Figure 8. Representative force and displacement traces versus time for an impact velocity of 22 m/s on multi-laminates with a) VHB 4905, b) VHB 5925, c) VHB 4930, and d) VHB 4936 adhesives

As discussed previously, all force traces contain two main peaks representing loading and unloading of the multi-laminate samples, but VHB 4930 and VHB 4936 force traces have a slightly different shape. These multi-laminates display a second local minimum force during the loading peak for both impact speeds (Figures 7c, d and Figures 8c, d). It is discussed in Section 2 that a commonality in microstructure of these two materials is the inclusion of rigid microspheres. With the microspheres being so small (diameter of approximately 70 µm), it is believed that the decrease in contact force is not caused by their breaking or crushing. However, through communication with 3M, it is realized that translation of these microspheres in the acrylic matrix is possible. It is hypothesized that during impact loading, the localized force at the impact site temporarily displaces the microspheres resulting in a decrease in amplitude, although exact response rate and translation distance are unknown. To examine the feasibility of this theory, a frequency sweep using tensile dynamic mechanical analysis (DMA) is completed on the two solid polyacrylates with (VHB 4930) and without (VHB 4905) inclusions (Figure 9). The results of which have shown the modulus of both materials to substantially increase with rate. Given the rate dependence of the acrylic matrix, it is unclear if cooperative microsphere movement could occur in a matrix with an increased modulus. For example, the predicted strain rate of 100 s^{-1} for an impact velocity of 22 m/s corresponds to a modulus approximately 40–50 times the quasi-static value (Figure 1b). Nevertheless, it is shown above that the magnitude of force decrease reduces significantly with increasing impact velocity. This indicates that the responsible phenomenon is dependent on loading rate and local effective strain rate. It is theorized that at higher impact velocities, this secondary local minimum would completely disappear as the modulus of acrylic matrix increases becoming less compliant and severely restricts microsphere movement. But for lower impact velocities, it is unclear whether this phenomenon would become more accentuated. Therefore, further investigation is necessary on both ends of the impact velocity spectrum to truly determine what is causing the secondary force decrease for these two adhesives.

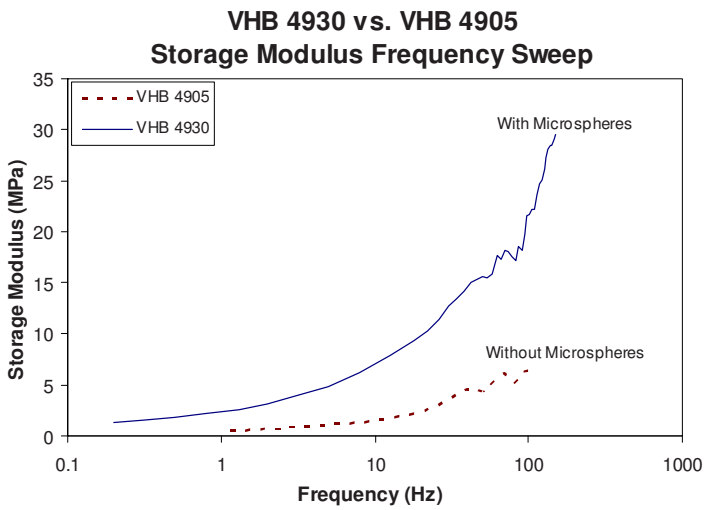

Figure 9. DMA frequency sweep on polyacrylates with (VHB 4930) and without (VHB 4905) microspheres

4.3 Energy Absorption/Dissipation Mechanisms

The impact energy incident on the multi-laminates is approximately 2 J for an impact velocity of 12 m/s and 7 J for an impact velocity of 22 m/s and impactor mass of 28.5 g. This energy can be dissipated/converted as a combination of: elastic energy (vibrational), plastic deformation, and fracture. For the transformation of the incident mechanical energy we neglect effects of heat and sound produced by the impact, whereby these effects account for only a small fraction of the total energy of the process. Mechanisms to absorb the impact energy are dependent on system material properties, adhesion characteristics and boundary conditions, as well as other parameters such as impactor head shape (hemi-spherical, conical, flat-headed, etc.) and impactor eccentricity, and angle during loading. These factors are inherent in the experimental setup geometry, specimen configuration, and impact velocity. In this research, the effect of normal impact of a hemi-spherical impactor on the multi-laminate is the primary focus.

This study may be summarized as impact testing utilizing a relatively small diameter, lightweight impactor incident on a large, thin, multi-layered sample. As shown in Figures 7 and 8, the combination of these parameters causes large elastic deflection to be a main component of the impact response, with maximum off-center displacements ranging from 3–6 mm for 12 m/s impacts and 4.5–8 mm for 22 m/s impacts. Changing any of the parameters/ratios discussed in Section 4.1 affects which energy absorption methods are realized and are dominant/secondary. For example, if the mass of the impactor and impact velocity was greatly increased, or the span and thickness significantly reduced, complete perforation with minimal deflection may occur. Based on the specific specimen geometry, bonding conditions, and experimental setup capabilities, combinations of elastic energy, plastic energy, and fracture mechanisms will occur corresponding to a measure of impact performance. Damage mechanisms that were characteristic of the configurations studied include: local fracture at the impact site, delamination, local plastic flow, and barely visible impact damage (BVID).

For impact velocities of 12 and 22 m/s, damage was considerably different for the four multi-laminate configurations studied. Figure 10 shows the damage and fracture observed after a 22 m/s impact with a representative summary of crack formation for both impact velocities in Table 2. Note that this fracture pattern is similar to that reported by Song and Hsieh for higher speed impacts (100 and 400 m/s) on monolithic PMMA with a central impact site and numerous, relatively equally spaced, radial cracks which is due to boundary condition effects [22]. For example, it is anticipated that a larger specimen should lessen boundary effects. Since sample size is consistent for all impact testing in this study, comparison within this set is valid. Note the cracks observed in this research are solely in the PMMA front layer (intralayer) with no damage visibly detected in the interlayers or the PC back layer. Therefore, the soft interlayers and PC in the bonded multi-laminates deform entirely elastically during impact, except for very slight BVID in the back side of the PC outerlayer. This may cause residual stresses and affect impact performance for repeated loading not explored in this study. For both impact speeds, the polyacrylate that shows the largest fracture area (crack lengths) is VHB 5925 with the remaining three having similar crack length ranges (Table 2). Note that for both impact velocities, the polyacrylates with rigid microspheres (VHB 4930 and VHB 4936) have more radial cracks than samples without these inclusions (VHB 4905 and VHB 5925). With the impactor having a hemi-spherical surface acting on a planar section, most of the bonded samples impacted at 22 m/s show a slight local indentation at the impact site (except VHB 5925), approximately 5 mm in diameter. At the lower impact velocity, only radial cracking is present and this indentation isn't observed. This circular impact site damage conically disperses through the PMMA forming a larger diameter circle at the PMMA/adhesive interface than on the front face. This conical shape of cracking at a PMMA impact site was also observed by Rai and Singh [31]. They conducted drop tower impact testing on multi-layered PMMA and soft adhesive samples with impact energies less than 120 J. It is also viewed that for the higher impact velocity both crack number and length are larger than the multi-laminates impacted at 12 m/s. Note that only two of the multi-laminates displayed delamination for impacts at 22 m/s, as shown in Figure 10a (VHB 4905) and Figure 10c (VHB 4930). As discussed previously, the microstructure of these two polyacrylates is observed to be acrylic without air gaps (Section 2), facilitating delamination. It is hypothesized that during loading, instead of impact energy being absorbed by collapsible areas present in the other two adhesives, delamination becomes a more pronounced energy dissipation mechanism. No pictures are shown for the samples impacted at 12 m/s due to very similar damage patterns (5 or 6 radial cracks of varying lengths) that are very thin and challenging to photograph. It is proposed that at the lower velocity, the soft interlayer modulates the impact whereas at the higher velocity, the interlayer behaves as a much stiffer material due to rate dependence.

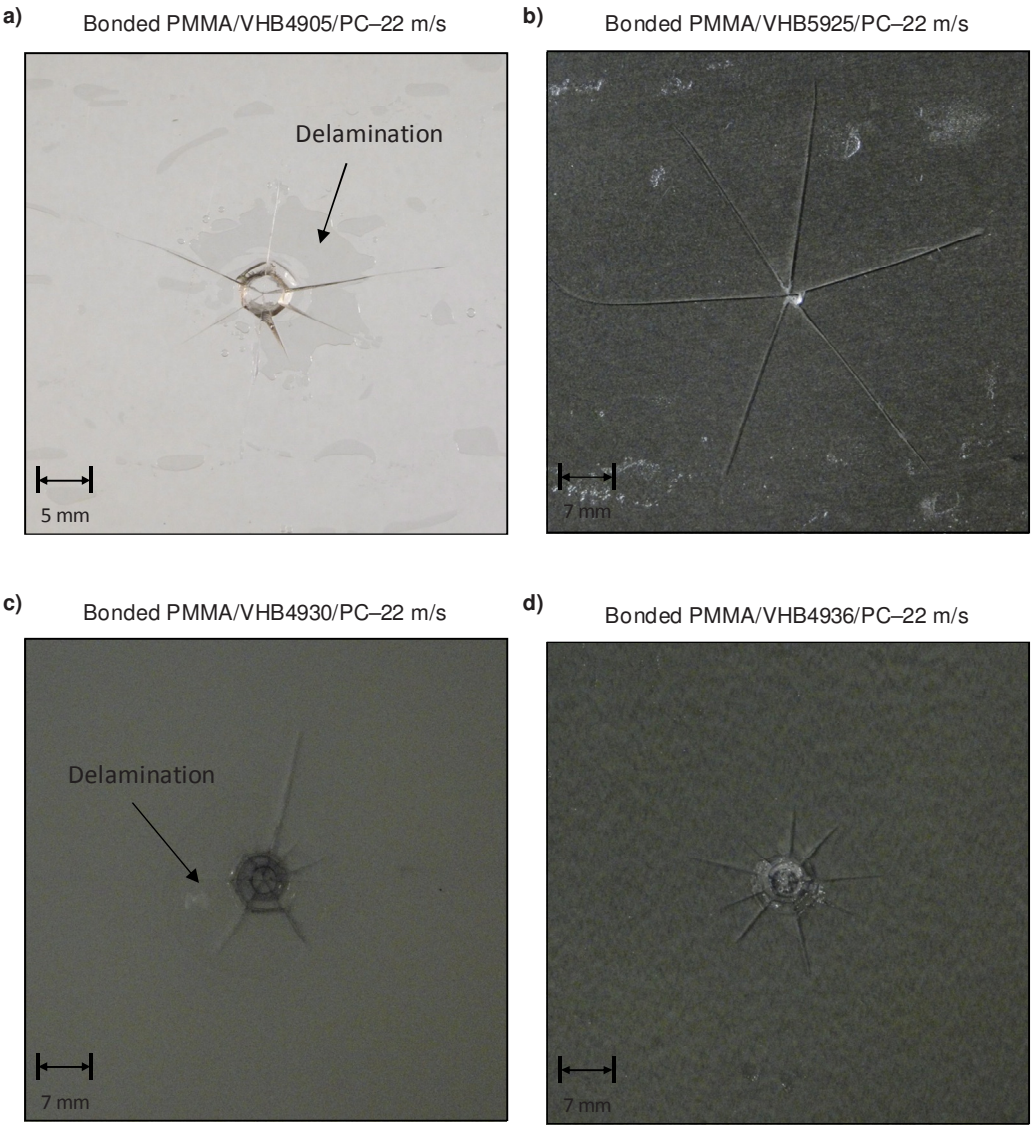

Figure 10. Representative pictures of fracture observed for 22 m/s impact on multi-laminates with a) VHB 4905, b) VHB 5925, c) VHB 4930, and d) VHB 4936 adhesives

Table 2. Fracture summary for samples with polyacrylate adhesives impacted at 12 and 22 m/s

Impact Velocity (m/s)	Interlayer	Impact Site Diameter (mm)	Crack Length Range (mm)	Number of Radial Cracks
12	**VHB4905**	N/A	9 – 11	5
	VHB5925	N/A	17 – 25	5
	VHB4930	N/A	10 – 13	6
	VHB4936	N/A	9 – 12	6
22	**VHB4905**	5	17 – 22	7
	VHB5925	2	31 – 36	6
	VHB4930	5–10	9 - 25	9
	VHB4936	5	11 – 17	9

5. Discussion

The mechanical characterization of the four polyacrylate elastomers in tension and compression is outlined in Section 3. Experimental results for the force and displacement traces recorded during impact for two impact speeds (12 and 22 m/s) on three-layer multi-laminates with PMMA and PC outerlayers, as well as the post-impact fracture analysis are presented in Section 4. In this section, the evolution of the mechanical response of the adhesives is discussed. Specifically, the rate-dependent properties and high damping behavior of the polyacrylate adhesives observed at lower rates is used as context to discuss the impact response at higher rates.

Six quantitative metrics are obtained from both force and displacement traces recorded during impact. Contact force metrics include: first and second force peaks (not double impact), and loading pulsewidth. Displacement metrics include: maximum displacement, transient response frequency, and settling time. Metric values reported are averages of three tests for each configuration and impact speed with error given as approximately ±1–10% (depending on the metric). The analysis below explains how the metrics correspond to multi-laminate impact mechanics, such as deformation behavior, energy absorption, and fracture mechanisms. In actuality, one quantitative metric cannot give insight into, or completely characterize, impact performance. A combination of multiple metric analyses and qualitative observation techniques are used to gain insight into why an interlayer may have superior or inferior impact performance over another. Figure 11 shows the methods for measuring the ten recorded force and displacement metrics on representative traces. Metric results are reported with individual error percentages calculated by the maximum deviation of the three data points from the metric average. Post-impact fracture observations are correlated to force and displacement metric trends.

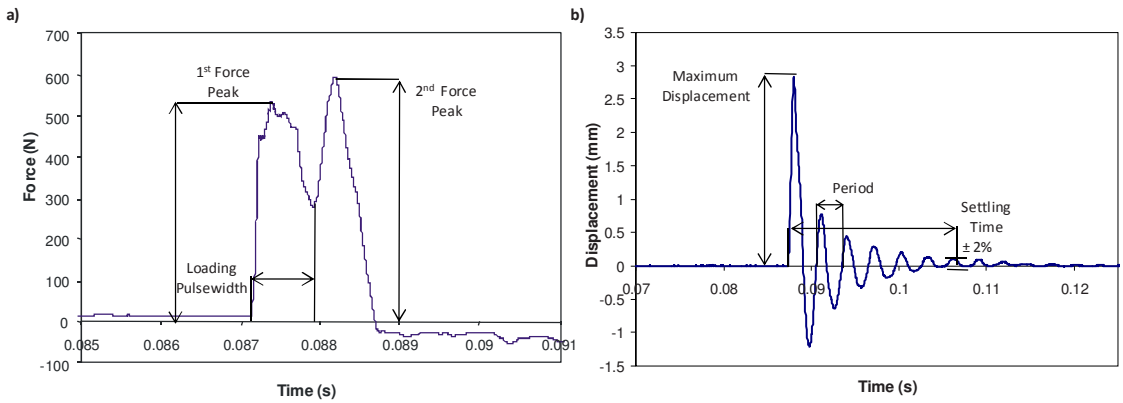

Figure 11. Quantitative metrics measured from a) force and b) displacement signals

5.1 First and Second Force Peaks

Contact force at the impact site is recorded using a shock accelerometer embedded in a steel impactor. The first force peak is measured as the maximum value during the loading of the multi-laminate. As expected, this metric is larger for the higher impact speed (Figure 12a). The initial response of the sample is heavily influenced by the glassy polymer outerlayers PMMA and PC as well as the effective stiffness of the multi-laminate. The order of first force peaks, in ascending order, is directly correlated to the interlayer quasi-static compressive compliance order (from most to least compliant) of: VHB 5925, VHB 4905, VHB 4936, VHB 4930 for both impact velocities (Figure 5). Note that VHB 5925, the polyacrylate with the most observed fracture, also has the lowest magnitude first force peaks. The second force peak characterizes the amount of elastic energy the multi-laminate is capable of storing during loading to maximum deflection, and the transfer to kinetic energy of the sample reloading the impactor. A substantial second peak is indicative of the absorbed energy reloading the impactor, while a smaller second peak reflects more energy converted to fracture. This is confirmed by observed increase in fracture in the front PMMA outerlayer for the VHB 5925 samples with the smallest force values (Figure 12b). Therefore, the first and second force peak metrics directly relate to the fracture observed (Figure 10 and Table 2). Note that for the two multi-laminates with rigid microsphere adhesives, the second is actually larger than the first force peak. This is observed for VHB 4930 (Figures 7c and 8c) and VHB 4936 (Figures 7d and 8d) for both impact velocities. Previous impact testing on the same multi-laminate configuration with TPU interlayers shows this same phenomena for Deerfield A4700 [6, 30].

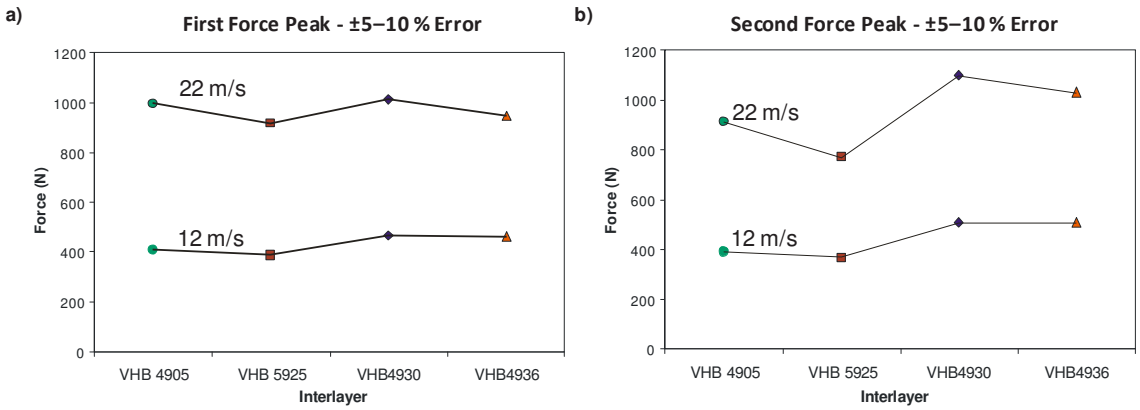

Figure 12. Polyacrylate metric comparison for a) first and b) second force peaks

5.2 Loading Pulsewidth and Maximum Displacement

The loading pulsewidth is measured from force initiation to local minimum and is indicative of the time required for the sample to decelerate impactor motion and absorb impact energy. A longer pulsewidth is consistent with longer contact time between the impactor and the multi-laminate, as well as increased time for damage/fracture to initialize and for cracks to propagate. For both impact velocities, it is clear that the multi-laminates with VHB 5925 adhesives had the longest times for loading followed by VHB 4905 (Figure 13a). For a given impact velocity, the multi-laminates able to decelerate the impactor the fastest appear to have the least fracture. Note that loading pulsewidths are shorter for the higher impact speed. This is consistent with Garland and Rogers who conducted low speed (less than 0.1 m/s) instrumented pendulum impact testing on elastic, nonconforming samples and showed that impact duration decreased with increasing initial velocity [32]. As the loading rate converges on the material wave speed, the material is incapable of deforming entirely elastically and the impact energy is discretely transferred in time to propagate out and away from the impact site.

Maximum displacement is recorded as the first positive peak of the sensor's data. As expected, it is observed that the multi-laminates deflect more at the higher impact velocity (Figure 13b). This is true for the intermediate impact speeds, boundary conditions, and mass/area ratios (Section 4.1) specific to this experimental setup. For example, if impact speed was greatly increased, there may not be any time for elastic deflection with complete sample perforation occurring. In this case, out-of-plane displacement would be minimal. In general for this impact testing, the greater the maximum out-of-plane displacement of the multi-layered structure, the more likely that local/global deformation or fracture will occur. At these velocities (12 and 22 m/s), it follows that the more a panel deflects the worse the observed fracture and impact performance. The trend observed for the multi-laminates is the same as the loading pulsewidth and second force peak in that the VHB 5925 samples are at extremes for both impact velocities. As shown in Figure 10 and Table 2, VHB 5925 multi-laminates have the longest cracks and fracture areas when compared to the other three polyacrylate samples.

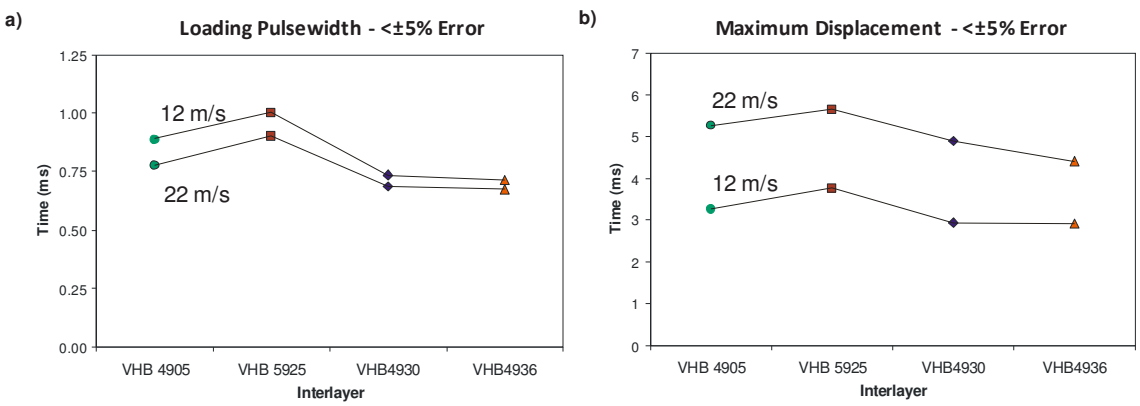

Figure 13. Polyacrylate metric comparison for a) loading pulsewidth and b) maximum displacement

5.3 Response Frequency and Settling Time

Two displacement metrics that are closely related to the sample's vibrational response following impact are the transient response frequency and settling time. It is desirable to measure the transient response frequency because it is reflective of the multi-layered structure's mechanical properties. Since the specimen masses are all relatively similar, the response frequency is mainly dependent on the effective stiffness of the multi-laminates. In general, the dissipation of impact energy as vibrational energy is considerable for systems with relatively low natural frequencies, as is the case here. The least compliant polyacrylates (VHB 4936 and VHB 4930) have the highest response frequencies due to the rigid microsphere inclusions increasing sample stiffness (Figure 14a). Since frequency is measured immediately after the impactor loses contact, response frequencies are also indicative of the properties of the damaged panels and reflect the residual mechanical properties of the multi-laminate.

A metric that is more indicative of the degree of damping in the polyacrylates is the 2% settling time of the multi-layered polymers. This is measured as the time required for the deflection of the multi-laminate (measured off-center) to settle within 2% of the maximum value around the final position. As shown in Figures 7 and 8, this final value is typically not zero as plastic deformation of the multi-layered polymer occurs during impact. The two polyacrylates with air gaps inherent in their microstructure (VHB 5925 and VHB 4936) have faster settling times than the "incompressible" adhesives (VHB 4905 and VHB 4930) for both impact velocities (Figure 14b). Note that settling times are faster for the higher impact velocity which coincides to faster response frequencies. A complete summary of all metric values is given in Table 3.

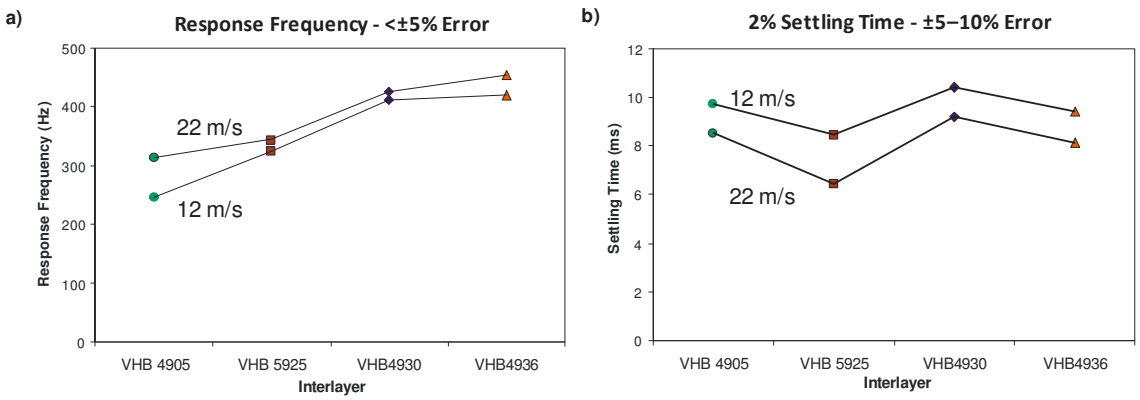

Figure 14. Polyacrylate metric comparison for a) response frequency and b) 2% settling time

Table 3. Complete summary of values measured for six force and displacement metrics

Component Materials	Impact Speed (m/s)	1st Force Peak (N)	2nd Force Peak (N)	Loading Pulsewidth (ms)	Maximum Displacement (mm)	Response Frequency (Hz)	2% Settling Time (ms)
PMMA/VHB4905/PC	11.8	410.6	390.7	0.887	3.25	244.5	9.71
PMMA/VHB4905/PC	21.4	994.3	913.3	0.777	5.24	312.5	8.5
PMMA/VHB5925/PC	11.9	386.8	369.1	1	3.75	324	8.43
PMMA/VHB5925/PC	22.1	917.3	769.1	0.9	5.63	343.3	6.43
PMMA/VHB4930/PC	12.7	466.6	510.7	0.736	2.94	412.4	10.4
PMMA/VHB4930/PC	21.9	1015.6	1098.8	0.689	4.88	426	9.19
PMMA/VHB4936/PC	12.3	463.7	510.5	0.715	2.92	419.1	9.39
PMMA/VHB4936/PC	21.9	945.3	1029.7	0.677	4.4	453.4	8.13

In summary, causality cannot be implied due to links observed between individual metrics and fracture. Future mechanical characterization and impact tests are required to further probe and verify true correlations. Overall, several energy absorption and fracture mechanisms of multi-laminate polymers are characterized in this paper. If stress thresholds are exceeded for these testing conditions and specimen geometry, fracture occurs. As discussed throughout Sections 4 and 5, by measuring and analyzing metrics, a better understanding of the impact

mechanics causing fracture is obtained. A combination of analyses of quantitative metrics and observed fracture mechanisms allows in-depth understanding of why some multi-laminates have more or less fracture than others. Intermediate impact velocity testing of PMMA and PC incorporated into multi-laminates with a soft, rate dependent polyacrylate adhesive has shown that impact performance is uniquely tied to the interlayer response and microstructure. Despite this layer being only a small fraction of the overall mass and several orders of magnitude softer than the PMMA and PC outerlayers, it has a large effect on the overall multi-laminate response and fracture.

6. Conclusion

The normal impact response of multi-layered, rate dependent polymer structures is complex and not well understood. This research focuses on gaining insight into impact mechanics of PMMA and PC multi-laminates with polyacrylate adhesives by relating interlayer mechanical characterization, measured quantitative force and displacement metrics, and qualitative energy absorption mechanisms and observed fracture. Extensive research has been conducted on the monolithic outerlayer components (PMMA and PC) at quasi-static strain rates (less than 1 s^{-1}), low velocities with drop towers/pendulums (impact velocities ranging 2–8 m/s), high velocities with gas guns (50–500 m/s), and very high strain rates using SHPBs (greater than 10^3 s^{-1}). Few have focused on intermediate rate (~100 s^{-1}) testing of polymers, and even less on multi-layered polymers. This study is unique in that it systematically characterizes the impact mechanics of an all-polymer multi-layered system, using an instrumented experimental setup in an intermediate impact velocity regime. Specifically, research focuses on the rate-dependent response of polyacrylate elastomers, which are filled polymers differing from the usually studied carbon-black filled rubbers.

Four polyacrylates with varying microstructures and properties (Section 2) are mechanically characterized by examining rate dependence in tension, and analyzing quasi-static response in compression (Section 3). The interlayers are four 3M polyacrylate elastomers (VHB 4905, VHB 5925, VHB 4930 and VHB 4936). As shown in Table 2, density, modulus, and glass transition temperatures all vary. An instrumented gas gun is used to impact fully clamped 161.29 cm^2 square samples (12.7 cm sides) with a 28.5 gram steel impactor travelling at 12 and 22 m/s (impact energies of approximately 2 and 7 J respectively). The experimental setup is developed from several researchers who have previously used an instrumented impactor in conjunction with gas guns for impact testing [27-28]. The novelty of the setup is that force and displacement during impact are recorded independently using a shock accelerometer embedded in the impactor and optical displacement sensors measuring multi-laminate out-of-plane deflection [6, 30]. Note that full field displacement measurements would be optimal over single point measurements, such as high speed digital image correlation (DIC) [33]. Six quantitative metrics are measured from the force and displacement traces for comparison between samples. Force metrics include: first force peak, second force peak, and loading pulsewidth. Displacement metrics include: maximum displacement, transient response frequency, and settling time. Energy conversion/dissipation mechanisms and fractography is completed post-impact and used for comparison between impact velocities, boundary conditions, and interlayers (Section 4).

Mechanical characterization of the interlayers is correlated to quantitative force/displacement metrics and damage/fracture to analyze the influence of the interlayer on impact performance. Although various correlations have been discussed regarding VHB 5925 multi-laminate's fracture and the presence (or lack) of rigid microspheres/air gaps with impact performance and metric trends, this does not imply causality. It is shown that samples with VHB 5925 have the longest cracks, lowest first and second force peaks, largest pulsewidth and maximum displacement, and fastest settling time. VHB 5925 is also the most compliant in compression and has the lowest density and glass transition temperature (Table 2). Despite impact results being too complex to directly relate to microstructure, several observations during the mechanical characterization of the polyacrylates may be linked. Samples with rigid microsphere inclusions show a decrease in compliance for both tensile and compressive loading (Figures 4 and 5), as well as less energy dissipation realized in smaller increases in hysteresis loop area with rate (Table 1). It is also concluded that the samples that contain collapsible air gaps are more compliant in compression than those without (Figure 5). In order to fully establish the relationships discussed in this paper, continued testing for a wider range of strain rates, impact velocities, and interlayer properties/microstructures is necessary.

References:

1. Patel, P.J., et al., *Transparent Ceramics for Armor and EM Window Applications.* Proceedings of SPIE, 2000. **4102**: p. 1-14.
2. Patel, P.J., et al., *Transparent Armor.* The AMPTIAC Newsletter, 2000. **4**(3): p. 1-13.
3. Sands, J.M., et al., *Protecting the Future Force: Transparent Materials Safeguard the Army's Vision*. Vol. 8 No. 4 ed. Vol. The AMPTIAC Quarterly. 2004.
4. Illinger, J.L., *Effect of Interlayer on Impact Resistance of Acrylic/Polycarbonate Laminates.* 1972: p. 1-15.
5. Illinger, J.L. and R.W. Lewis, *Effect of Adhesive Structure on Impact Resistance and Optical Properties of Acrylic/Polycarbonate Laminates.* Polymer Preprints, 1975. **16**(1): p. 545-550.
6. Stenzler, J.S. and N.C. Goulbourne, *Impact Mechanics of Transparent Multi-Layered Polymer Composites*, in *SEM Annual Conference & Exposition on Experimental and Applied Mechanics*. 2009: Albuquerque, NM.
7. Townsend, B.W., *Characteriztion and Lifetime Performance Modeling of Acrylic Foam Tape for Structural Glazing Applications*, in *Civil Engineering*. 2008, Virginia Polytechnic Institute and State University: Blacksburg.
8. Hennage, J., *Characterization of a Pressure Sensitive Adhesive (PSA) for Mechanical Design*, in *Mechanical Engineering*. 2004, Virginia Polytechnic Institute and State University: Blacksburg.
9. Sarva, S.S., et al., *Stress-strain behavior of a polyurea and a polyurethane from low to high strain rates.* Polymer, 2007. **48**(8): p. 2208-2213.
10. Shergold, O.A., N.A. Fleck, and D. Radford, *The uniaxial stress versus strain response of pig skin and silicone rubber at low and high strain rates.* International Journal of Impact Engineering, 2006. **32**(9): p. 1384-1402.
11. Shim, J. and D. Mohr, *Using split Hopkinson pressure bars to perform large strain compression tests on polyurea at low, intermediate and high strain rates.* International Journal of Impact Engineering, 2009. **36**(9): p. 1116-1127.
12. Song, B., W. Chen, and W.Y. Lu, *Compressive mechanical response of a low-density epoxy foam at various strain rates.* Journal of Materials Science, 2007. **42**(17): p. 7502-7507.
13. Dorfmann, A. and R.W. Ogden, *A constitutive model for the Mullins effect with permanent set in particle-reinforced rubber.* International Journal of Solids and Structures, 2004. **41**(7): p. 1855-1878.
14. Qi, H.J. and M.C. Boyce, *Stress-Strain Behavior of Thermoplastic Polyurethanes.* Mechanics of Materials, 2005. **37**(8): p. 817-839.
15. Yi, J., et al., *Large deformation rate-dependent stress-strain behavior of polyurea and polyurethanes.* Polymer, 2006. **47**(1): p. 319-29.
16. Roach, A.M., K.E. Evans, and N. Jones, *The Penetration Energy of Sandwich Panel Elements Under Static and Dynamic Loading. Part I.* Composite Structures, 1998. **42**(2): p. 119-134.
17. Roach, A.M., K.E. Evans, and N. Jones, *The Penetration Energy of Sandwich Panel Elements Under Static and Dynamic Loading. Part II.* Composite Structures, 1998. **42**: p. 135-152.
18. Vaidya, U.K., et al., *Ballistic Response of Graphite/Epoxy Composite Backed Polycarbonate Plates.* International SAMPE Techincal Conference, 1999. **31**: p. 77-84.
19. Yadav, S. and G. Ravichandran, *Penetration Resistance of Laminated Ceramic/Polymer Structures.* International Journal of Impact Engineering, 2003. **28**(5): p. 557-574.
20. Radin, J. and W. Goldsmith, *Normal projectile penetration and perforation of layered targets.* International Journal of Impact Engineering, 1988. **7**(2): p. 229-259.
21. Kohlman, W.G., *Ballistic performance of polycarbonate/polyester and polycarbonate/styrene-acrylonitrile microlayer sheets.* Polymer Engineering and Science, 1995. **35**(14): p. 1191-1195.

22. Song, J.W. and A.J. Hsieh, *Ballistic Impact Resistance of Monolithic, Hybrid and Nano Composites of PC and PMMA*. Proceedings of the American Society for Composites, 17th Technical Conference, 2002.
23. Hsieh, A.J. and J.W. Song, *Measurements of Ballistic Impact Response of Novel Coextruded PC/PMMA Multilayered-Composites.* Journal of Reinforced Plastics and Composites, 2001. **20**(3): p. 239-254.
24. Ball, A., *The Low Velocity Impact Behaviour of Glass-Polymer Laminated Plates.* Journal De Physique IV, 1997. **7**(C3): p. 921-926.
25. Ball, A. and H.W. McKenzie, *On the Low Velocity Impact Behaviour of Glass Plates.* Journal De Physique IV, 1994. **4**(C8): p. 783-788.
26. Hsieh, A.J., et al., *The Effects of PMMA on Ballistic Impact Performance of Hybrid Hard/Ductile All-Plastic-and Glass-Plastic-Based Composites.* 2004.
27. Delfosse, D., et al., *Instrumented Impact Testing at High Velocities.* Journal of Composites Technology & Research, 1993. **15**(1): p. 38-45.
28. Levy, N. and W. Goldsmith, *Normal impact and perforation of thin plates by hemispherically-tipped projectiles -- II. Experimental results.* International Journal of Impact Engineering, 1984. **2**(4): p. 299-324.
29. MacAloney, N. and N.C. Goulbourne, *Viscoelastic Characterization of Aliphatic Polyurethane Interlayers.* 2007: p. 1-36.
30. Stenzler, J.S., *Impact Mechanics of PMMA/PC Multi-Laminates with Soft Polymer Interlayers*, in *Mechanical Engineering*. 2009, Virginia Polytechnic Institute and State University: Blacksburg.
31. Rai, K.N. and D. Singh, *Impact resistance behavior of polymer nanocomposite transparent panels.* Journal of Composite Materials, 2009. **43**(2): p. 139-51.
32. Garland, P.P. and R.J. Rogers, *An experimental study of contact forces during oblique elastic impact.* Journal of Applied Mechanics, 2009. **76**(3): p. 031015 (8 pp.).
33. Gunnarsson, C.A., et al. *Deformation and Failure of Polycarbonate During Impact as a Function of Thickness*. in *SEM Annual Conference*. 2009. Albuquerque, NM.

Proceedings of the SEM Annual Conference
June 7-10, 2010 Indianapolis, Indiana USA

Visco-elastic Properties of Carbon Nanotubes and Their Relation to Damping

Dong Qian*[1] (Associate Professor, University of Cincinnati), Zhong Zhou[1] (Postdoctoral Fellow, University of Cincinnati)
[1]Mechanical Engineering, School of Dynamic Systems, University of Cincinnati, Cincinnati OH 45221-0072, *dong.qian@uc.edu

ABSTRACT In this presentation, we discuss semi-analytical approaches to the visco-elastic properties of the Carbon Nanotubes (CNTs) based on molecular dynamics (MD) simulation and continuum models. The visco-elastic properties of the CNTs defined in both the time and frequency domains have been obtained in terms of the creep compliance and the relaxation and complex modulus. The equilibrium visco-elastic properties were found to be strongly dependent on tube radius for both single-walled and multi-walled CNTs, while the chirality had no appreciable effect. For multi-walled CNTs, the interlayer interaction contributes significantly to the overall visco-elastic response. The time scale associated with the visco-elastic properties were found to be on the order of nanosecond. This time scale is reflected in the associated energy loss and damping mechanisms in CNT oscillators. From the computed visco-elastic properties, we further derived the quality factor *Q* for different tube geometries and load frequencies. We found that the *Q* factor is strongly influenced by the load frequency, in addition to the dependence on the tube radius. The predicted trends in terms of the dependence on the load frequency were further validated through comparison with experiments. The underlying mechanism for such trends was discussed in the context of thermoelastic theory.

1. Introduction

Carbon nanotubes (CNTs) have attracted significant attention because of their outstanding mechanical properties for possible nanotechnological applications such as ultrahigh frequency oscillators and sensors. Mechanical properties of CNTs have been extensively investigated (see review in [1]), however, time-independency of their mechanical properties has often been assumed in most of these studies. For applications under dynamic excitation, CNTs could be subjected to very high rate loading, and the mechanical response of CNTs could become time-dependent due to the strong coupling between the mechanical field and thermal field. Therefore, the time-dependent elasticity or the intrinsic visco-elastic property of CNTs associate with the energy dissipation becomes significant in terms of its influence on the performance of the device and materials.

Motivated by the significance of this important topic, we have investigated the visco-elastic properties and damping properties of CNTs based on molecular dynamics (MD) simulation and semi-analytical approaches developed in this study. We have derived visco-elastic constants of both single-walled (SW) and multi-walled (MW) CNTs and an estimate on the damping property (quantified by quality factor *Q*) was also developed. The influences of structure details and dynamic excitation frequency on these properties were studied.

2. Visco-elastic properties of CNTs in time-domain

For the purpose of extracting the time-dependent visco-elastic properties of CNTs, a theoretical nanoindentation model in the transverse direction was proposed. Considering CNT as a cylindrical shell subjected to two equal and opposite forces acting along a diameter (shown in Fig.1), and assuming there is no in-plane stretching so the deformation is inextensible, the elasticity theory gives the expression for radial deformation [2-3]

$$d \cong \frac{0.7(1-\nu)R^{3/2}F}{\pi h^{5/2}G} \tag{1}$$

where, *F* is indentation force, *R* and *h* are radius and thickness of CNT respectively. *G* is shear modulus, and *v* is Poisson's ratio. Based on this linear elastic solution, the following time-dependent relationship between displacement and applied force can be obtained by applying a hereditary integral operator [4],

T. Proulx (ed.), *Time Dependent Constitutive Behavior and Fracture/Failure Processes, Volume 3*, Conference Proceedings of the Society for Experimental Mechanics Series 15, DOI 10.1007/978-1-4419-9794-4_36, © The Society for Experimental Mechanics, Inc. 2011

$$d = \frac{0.7(1-\nu)R^{3/2}}{\pi h^{5/2}} \int_{-\infty}^{t} J(t-\tau)\frac{dF(\tau)}{d\tau} d\tau \tag{2}$$

where $J(t)$ is the shear creep compliance. In the current study, a constant-rate loading history $F(t)=v_0 t$ was used, and the creep compliance was represented by the generalized Kelvin model

$$J(t) = J_0 + \sum_{i=1}^{N} J_i (1 - e^{-t/\tau_i}) \tag{3}$$

where J_0 is the instantaneous creep compliance representing the "instantaneous" elastic properties when the CNT is subjected to a dynamic load, and $J_\infty = \sum_{i=0}^{N} J_i$ is the equilibrium creep compliance. Combing Eqs.(2)-(3), the final expression for time-dependent load-displacement relationship is derived as

$$d(t) = \frac{0.7(1-\nu)R^{3/2}}{\pi h^{5/2}} \cdot \left\{ \left(J_0 + \sum_{i=1}^{N} J_i \right) F(t) - \sum_{i=1}^{N} J_i v_0 \tau_i \left[1 - \exp\left(-F(t)/(v_0 \tau_i) \right) \right] \right\} \tag{4}$$

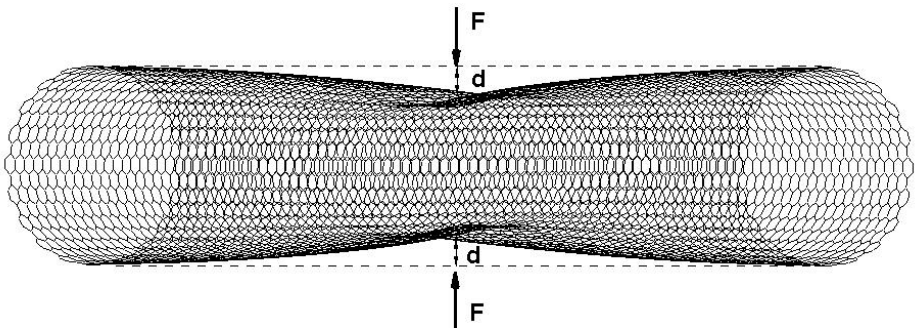

Figure 1. Schematic illustrating the indentation of CNT in the radial direction.

In the current computational study, MD simulation was carried out to simulate the dynamic response of CNT with the load-displacement curve as output. Visco-elastic properties of CNTs in time-domain (such as creep compliance) were then determined using Eq.(4). In the following context, we outline the result of creep compliance of SWCNTs.

Table 1 Creep parameters of selective single walled carbon nanotubes (τ=0.1*ns*).

(n_1, n_2)	R(*nm*)	J_0(1/*TPa*)	J_1(1/*TPa*)	$J_\infty=J_0+J_1$(1/*TPa*)
(8, 0)	0.313	0.403	0.578	0.981
(10, 0)	0.391	0.447	0.751	1.198
(16, 0)	0.626	0.507	1.194	1.700
(20, 0)	0.783	0.508	1.511	2.018
(26, 0)	1.018	0.504	2.016	2.520
(30, 0)	1.174	0.491	2.346	2.837
(36, 0)	1.409	0.446	2.823	3.269
(52, 0)	2.036	0.308	3.858	4.166

The calculated creep compliances of zigzag SWCNTs are listed in Table 1, in which the radii of the SWCNTs are in the range of 0.3 to 2.0 *nm*. In the MD implementation, the system was subjected to a constant energy NVE ensemble with a time step of 1 *fs*. The modeled lengths of SWCNTs were chosen to be larger than $2l_0$, where $l_0 \approx R(R/h)^{1/2}$ is the apparent length of the radial deformation under indentation along the axial direction from the loading point [5]. The loading rate v_0 was fixed at 16 *nN*/*ns*, and the deformation of nanotubes was restricted in the linear visco-elastic regime. The compliance coefficient J_1 was found to be sensitive to nanotube radius and increased with the radius. No obvious dependence of the instantaneous compliance J_0 on the nanotube radius was detected. The value of J_0 fell into the range of 0.3 to 0.5 (1/*TPa*), corresponding to an instantaneous shear

modulus, $G_0=1/J_0$, of 2-3.3 *TPa*. Consequently, the equilibrium compliance ($J_\infty=J_0+J_1$) increased with the increase of nanotube radius. This dependence was found to fit into a simple power law, $(J_\infty/J_\infty^*)=(R/R^*)^{0.785}$ as shown in Fig. 2, where J_∞^* and R^* are the corresponding values for a (8, 0) tube and are set as the reference values. In addition, a time scale on the order of nanosecond for SWCNTs to fully achieve to its equilibrium property was observed. For instance, the creep function of (26, 0) is given as $J(t) = 0.504+2.016\ (1-e^{-t/0.1})$, with J in *TPa* and t in *ns*. The creep function derives that it takes ~0.44 *ns* for the SWCNT to achieve 99% of its equilibrium compliance J_∞. This time scale is relevant for applications that involve CNTs operating at *GHz* frequency or serving as damping materials under high mechanical impact.

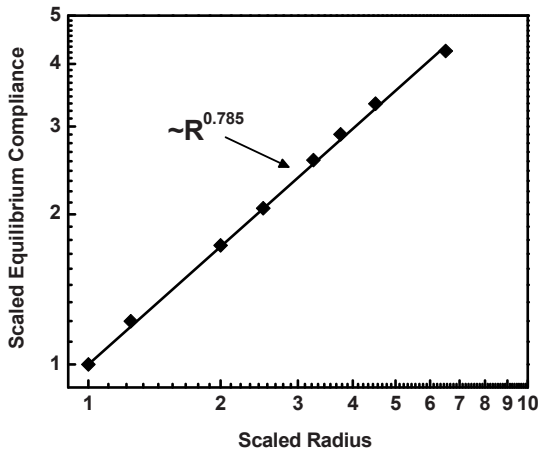

Figure 2. The equilibrium compliances versus radius dependence of SWCNTs.

3. Visco-elastic properties of CNTs in frequency-domain and implication for damping

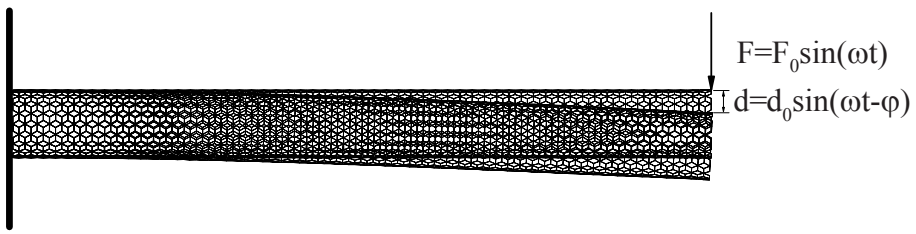

Figure 3. Schematic showing a CNT cantilever beam under dynamic bending.

In addition to the visco-elastic properties in the time-domain, we have also studied the visco-elastic properties in the frequency-domain. For this purpose, we have conducted numerical experiment on dynamic bending of CNTs cantilever beams by MD simulation. Fig.3 shows schematically a CNT beam under vertical bending force acting at the free end. The bending deflection of a cantilevered elastic beam is given by,

$$d = \frac{Fl^3}{3EI} \tag{5}$$

where F is the point force, l is length, and EI is the bending stiffness. The effective moment of inertia I of the CNT beam cross section is expressed as [6],

$$I = \frac{\pi}{4}\left[(R_e + \frac{h}{2})^4 - (R_i - \frac{h}{2})^4 \right] \tag{6}$$

where R_e is the mean radius of the outermost wall (external radius), R_i is the mean radius of the innermost wall (internal radius) and h is the thickness of the tube wall. For the CNTs oscillators under dynamic excitation $F(t) = F_0 \sin(\omega t)$, the time-dependent load-displacement relationship is given as,

$$d(t) = \frac{l^3}{6(1+\nu)I}\int_{-\infty}^{t} J(t-\tau)\frac{dF(\tau)}{d\tau}d\tau = \frac{l^3}{6(1+\nu)I}F_0\left|J^*(\omega)\right|\sin(\omega t - \varphi) = d_0 \sin(\omega t - \varphi) \tag{7}$$

where $J^*(\omega) = J'(\omega) - iJ''(\omega)$ is the complex shear compliance[7]. $\varphi = \tan^{-1}[J''(\omega)/J'(\omega)]$ is phase shift angle between imposed load and displacement response. It is a fundamental measure of damping and is also referred to as the loss angle. From Eq.(7), the storage and loss shear compliances can be calculated as

$$J'(\omega) = \left|J^*(\omega)\right|\cos\varphi = \frac{6(1+\nu)I_{eff}}{l^3}\frac{d_0}{F_0}\cos\varphi,\ J''(\omega) = \left|J^*(\omega)\right|\sin\varphi = \frac{6(1+\nu)I_{eff}}{l^3}\frac{d_0}{F_0}\sin\varphi \tag{8a,b}$$

Subsequently, the complex bending modulus is computed by $E^*(\omega) = 2(1+\nu)/J^*(\omega)$, with the storage and loss modulus are

$$E'(\omega) = \frac{l^3}{3I_{eff}}\frac{F_0}{d_0}\cos\varphi, \qquad E''(\omega) = \frac{l^3}{3I_{eff}}\frac{F_0}{d_0}\sin\varphi \tag{9a,b}$$

Table 2 Visco-elastic properties of selective cantilevered SWCNTs oscillators. (F_0=0.16 *nN*, *f*=7.96 *GHz*, *L*/*D*=10)

(n_1,n_2)	R_e (*nm*)	φ (*radian*)	d_0 (*nm*)	E' (*GPa*)	E'' (*GPa*)	*Q*
(5, 5)	0.339	0.0052	0.391	5737.5	29.8	192.3
(10, 0)	0.391	0.0064	0.416	5240.4	33.5	156.2
(14, 0)	0.548	0.0066	0.406	5104.6	33.7	151.5
(10, 10)*	0.678	0.0102	0.479	4716.4	48.1	98.0
(18, 0)*	0.705	0.0112	0.438	4596.3	51.5	89.3
(22, 0)	0.861	0.0134	0.481	4107.2	55.0	74.6
(15, 15)*	1.017	0.0149	0.505	3869.3	57.7	67.1
(26, 0)*	1.018	0.0151	0.505	3860.7	58.3	66.2
(34, 0)*	1.331	0.0195	0.684	2999.8	58.5	51.3
(20, 20)*	1.356	0.0235	0.617	3288.2	77.3	42.5
(25, 25)	1.695	0.0305	0.952	2178.9	66.5	32.8

Table 2 summarizes the complex modulus and *Q* factors of armchaired and zigzag SWCNTs. The loading frequency is $f=\omega/2\pi$=7.96*GHz* and the length to diameter ratio is *L*/*D*=10. The displacement amplitude d_0 and loss angle were computed from MD simulation. The *Q* factor was related to the loss angle through $Q = E'/E'' = (\tan\varphi)^{-1}$. The storage bending modulus decreased from 5737.5 *GPa* to 2178.9 *GPa*, while the loss modulus increased from 29.8 *GPa* to 66.5 *GPa*. From Table 2, we find that the *Q* factor decreases from 192.3 to 32.8 with the increase of nanotube radius, and such dependence can be fit with $Q \propto 1/R_e^{0.98}$ for SWCNTs, as shown in Fig. 4. It indicates that for CNT oscillators, more energy is dissipated when tube radius increases. Such a phenomenon was also observed in double walled (DW) CNT oscillators, as evident in Table 3 and also in Fig.4. Although the approximate inverse-proportion relationship for SWCNTs no longer holds in the case of DWCNTs, the same tendency of *Q* factor with respect to external radius is evident. Another interesting finding is that the chirality of SWCNTs has negligible influence on their visco-elastic properties, as is concluded by checking the visco-elastic parameters of the three groups of nanotubes marked with superscript '*' in Table 2, which have different chirality but approximately the same radius.

Table 3 Visco-elastic properties of cantilevered DWCNTs oscillators. (F_0=0.8 *nN*, *f*=31.85 *GHz*, *L*/*D*=5)

tube	R_e (*nm*)	φ (*radian*)	d_0 (*nm*)	E' (*GPa*)	E'' (*GPa*)	*Q*
(5,5)/(10,10)	0.678	0.0142	0.299	1434.1	20.4	70.4
(10,10)/(15,15)	1.017	0.0174	0.305	1123.2	19.5	57.5
(15,15)/(20,20)	1.356	0.0289	0.470	646.5	18.7	34.6
(20,20)/(25,25)	1.695	0.0548	0.699	403.6	22.1	18.2
(25,25)/(30,30)	2.034	0.1057	1.066	250.9	26.6	9.4

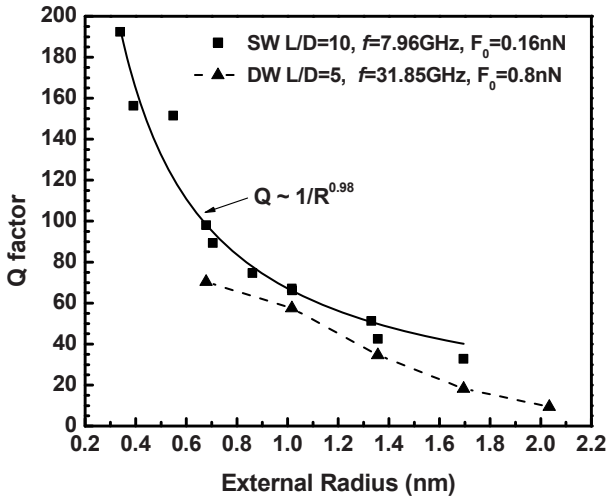

Figure 4. The quality factor *Q* versus external radius dependence for SW- and DWCNTs.

From Fig.4, we also notice the *Q* factors of MWCNTs are lower than that of SWCNTs, which is more evident from the comparison of CNTs with same innermost tube or outermost tube but different number of walls, plotted in Fig. 5. In both cases, *Q* factor decreased when number of walls (*N*) varied from 1 to 5. In MWCNTs, the tube walls interact through van der Waals' interaction, and such a weak interaction induces internal frictional energy dissipation when considerable inter-wall sliding occurs during oscillation, which is a plausible source of the increased damping [8].

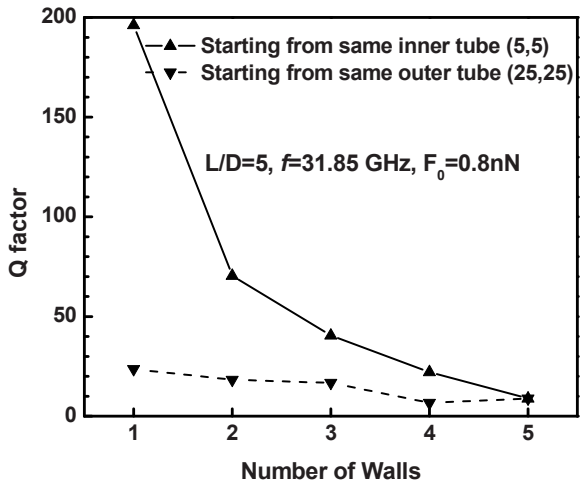

Figure 5. Comparison of *Q* factors of CNTs with different number of tube walls.

4. Comparison of *Q* factor with experiment

Currently there is no direct experimental data on the visco-elastic properties of the CNTs. However, quality factors *Q* in CNTs subjected to dynamic excitation have been reported [9-14]. Typically, the experimental measurements were based on the configuration of CNT beams subjected to flexural deformation through electro-static loads, and the excitation frequency ranged from several Megahertz to several hundred Megahertz. Based on the visco-elasticity model represented by generalized Kelvin model in Eq.(3) with a single retardation time τ, the *Q* factor can be derived as

$$Q = \frac{J'}{J''} = \frac{J_0(1+4\pi^2\tau^2 f^2)+J_1}{2\pi J_1 \tau f} \tag{10}$$

The predicted *Q* factors of CNTs with different diameters as a function of the load frequency are plotted in Fig.6 along with the corresponding experimental measurements. In the model predictions, the J_0 and J_1 values of CNTs with diameter beyond the range studied in Table 1 were computed using the scaling law obtained in section 2. It is seen that the current model yields predictions that are in the same order of magnitude as the experiment, and the observed frequency dependence of the *Q* factor is consistent with experiment. The low *Q* factor observed in high frequency is an indication that certain phonon modes have been activated that lead to enhanced energy dissipation through thermal consumption.

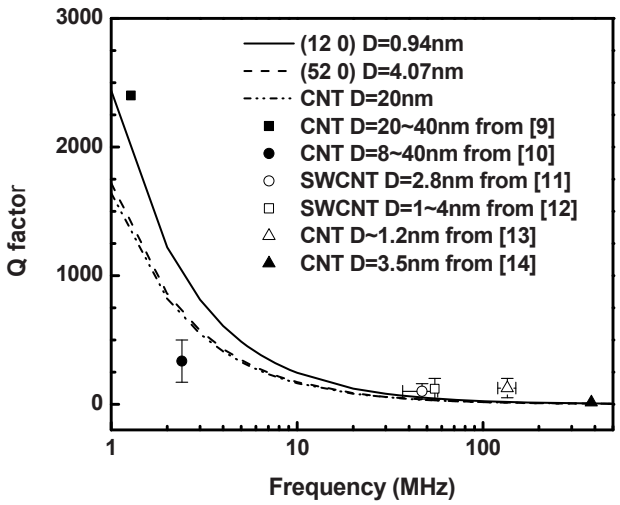

Figure 6. Comparison of the *Q* factors between model prediction and experimental measurement.

5. Conclusions

The time- and frequency-dependent visco-elastic properties of CNTs and their relation to mechanical damping have been investigated based on semi-analytical approaches and MD simulation. For both SWCNTs and MWCNTs, the visco-elastic properties defined both in time- and frequency-domain and the associated damping property were found to be strongly dependent on the tube radius. A time scale associated with the dynamic response of SWCNTs was observed on the order of nanoseconds. For MWCNTs, the inter-wall van der Waal's interaction plays a significant role in the overall mechanical response and damping. Furthermore, we derived the *Q* factors based on the theoretical visco-elastic model, and the predicted values for different tube geometries and load frequencies were validated through the comparison with experiments.

Acknowledgement
This work is supported by the National Science Foundation (Grants CMMI-0600583 and 0700107). Any opinions, findings, conclusions, or recommendations expressed in these documents are those of the author(s) and do not necessarily reflect the views of the National Science Foundation.

References

1. Qian, D., G.J. Wagner, W.K. Liu, M.F. Yu, and R.S. Ruoff, Mechanics of carbon nanotubes. *Applied Mechanics Reviews*, 2002. **55**(6): p. 495-533.
2. Zhou, Z., D. Qian, and M.F. Yu, A Computational Study on the Transversal Visco-elastic Properties of Single Walled Carbon Nanotubes and Their Relation to The Damping Mechanism (in press). *Journal Of Computational And Theoretical Nanoscience*, 2010.
3. Zhou, Z., D. Qian, and M.F. Yu, Energy dissipation and intrinsic loss in single walled carbon nanotubes due to anelastic relaxation (accepted). *Journal of Nanoscience and Nanotechnology*, 2010.
4. Lee, E.H. and J.R.M. Radok, The contact problem for viscoelastic bodies. *Transactions of the ASME, Journal of Applied Mechanics*, 1960. **27**: p. 438-444.
5. de Pablo, P.J., I.A.T. Schaap, F.C. MacKintosh, and C.F. Schmidt, Deformation and collapse of microtubules on the nanometer scale. *Physical Review Letters*, 2003. **91**(9).
6. Pantano, A., D.M. Parks, and M.C. Boyce, Mechanics of deformation of single- and multi-wall carbon nanotubes. *Journal Of The Mechanics And Physics Of Solids*, 2004. **52**(4): p. 789-821.
7. Zhou, Z. and H.B. Lu, On the measurements of viscoelastic functions of a sphere by nanoindentation. *Mechanics Of Time-Dependent Materials*, 2010. **14**(1): p. 1-24.
8. Yap, H.W., R.S. Lakes, and R.W. Carpick, Negative stiffness and enhanced damping of individual multiwalled carbon nanotubes. *Physical Review B*, 2008. **77**(4).
9. Purcell, S.T., P. Vincent, C. Journet, and V.T. Binh, Tuning of nanotube mechanical resonances by electric field pulling. *Physical Review Letters*, 2002. **89**(27).
10. Poncharal, P., Z.L. Wang, D. Ugarte, and W.A. de Heer, Electrostatic deflections and electromechanical resonances of carbon nanotubes. *Science*, 1999. **283**(5407): p. 1513-1516.
11. Witkamp, B., M. Poot, and H.S.J. van der Zant, Bending-mode vibration of a suspended nanotube resonator. *Nano Letters*, 2006. **6**(12): p. 2904-2908.
12. Sazonova, V., Y. Yaish, H. Ustunel, D. Roundy, T.A. Arias, and P.L. McEuen, A tunable carbon nanotube electromechanical oscillator. *Nature*, 2004. **431**(7006): p. 284-287.
13. Lassagne, B., D. Garcia-Sanchez, A. Aguasca, and A. Bachtold, Ultrasensitive Mass Sensing with a Nanotube Electromechanical Resonator. *Nano Letters*, 2008. **8**(11): p. 3735-3738.
14. Peng, H.B., C.W. Chang, S. Aloni, T.D. Yuzvinsky, and A. Zettl, Ultrahigh frequency nanotube resonators. *Physical Review Letters*, 2006. **97**(8).

Proceedings of the SEM Annual Conference
June 7-10, 2010 Indianapolis, Indiana USA

Ballistic Missile Defense System (BMDS) Solutions Using Remendable Polymers

Dr. Terrisa Duenas
tduenas@nextgenaero.com
NextGen Aeronautics, Inc.
2780 Skypark Drive Suite 400
Torrance, California 90505

Ms. Jennifer Schlitter, Dr. Naida Lacevic, Dr. Akhilesh Jha, and Ms. Karen Chai
NextGen Aeronautics, Inc.

Dr. Fred Wudl and Mr. Lucas Westcott-Baker
University of California, Santa Barbara

Dr. Ajit Mal
University of California, Los Angeles

Mr. Aaron Corder and Dr. Teng K. Ooi
Missile Defense Agency, Pentagon Defense

ABSTRACT

This work describes the cross-cutting technology for using remendable polymers for Ballistic Missile Defense System (BMDS) Interceptors to heal damaged missile structures. Matrix cracking and associated delamination of carbon-fiber ply skins on interceptor structures is addressed using a Mendomer-based polymer composite developed by the University of California, Santa Barbara (UCSB), the University of California, Los Angeles (UCLA), NextGen Aeronautics, US Army Aviation and Missile Research Development and Engineering Center (AMRDEC), and Missile Defense Agency (MDA) scientists and engineers. When used in place of conventional composite matrix materials, this material system enables in-situ healing of damaged carbon-fiber components. Both neat and composite samples were fabricated and examined for their remendable and shape memory properties. The neat polymer samples and polymer/Ni particle composites contained a significant number of voids. The carbon-fiber-polymer composite samples exhibit similar gas entrapment as well as inadequate carbon-fiber wet-out during fabrication. Despite the undesirable void content and inadequate carbon-fiber wet-out, the coupons exhibit appreciable remendable and shape memory properties. Further improvement and optimization of the composite layup process are needed to produce remendable carbon-fiber composites with adequate mechanical and structural properties. We also present preliminary molecular dynamics (MD) and finite element analysis (FEA) simulations to capture the behavior of these remendable material systems.

INTRODUCTION

The Ballistic Missile Defense System (BMDS) continues to seek technologies to produce components with enhanced durability and performance such as in long-range missile interceptors and sensor networks [1]. By applying remendable technologies, nanotechnology, and multiscale modeling, further improvements to these structures are expected. Carbon-fiber composites are desirable over metals in some aerospace applications due to their lightweight attributes and amenability to be conformed into complex anisotropic structures. Damage to composites such as matrix cracking and delamination will compromise the integrity of the composite. The

Approved for Public Release 10-MDA-5389 (5 APR 10)

T. Proulx (ed.), *Time Dependent Constitutive Behavior and Fracture/Failure Processes, Volume 3*, Conference Proceedings of the Society for Experimental Mechanics Series 15, DOI 10.1007/978-1-4419-9794-4_37, © The Society for Experimental Mechanics, Inc. 2011

presented work attempts to address this issue by developing remendable material systems. Remending occurs by the manual application of external stimuli while self-healing is autonomous. There has been some notable work performed in the area of self-healing structures. For example, the self-healing approach by White et al. (2001) incorporates healing agent-filled microcapsules and an associated catalyst integrated into the material system. When added at a small volume fraction, progressing cracks rupture the microcapsules, which allow the healing agent to combine with the catalyst and subsequently heal the crack [2]. In a study by Hayes et al. (2007), constituents are embedded in a conventional epoxy system to fill cracks. As cracks are identified, the system is subsequently heated which mobilizes the constituents and heals the system [3]. The advantage of these passive self-healing material systems over remendable material systems is in the autonomous response. However, while remendable systems inherently require manual intervention, their approach to healing is indefinitely repeatable and can be combined with damage detection methods to form active self-healing systems. In summary, conventional passive self-healing systems are limited in their repeatability and long-term resistance to damage, however they are passively autonomous. Active self-healing systems, while indefinitely resistant to long-term damage events require external damage detection packaging [4].

In our previous work, a repeatable remendable material was developed for use as a replacement matrix material for a composite. This material, developed at UCLA and termed “Mendomer,” is a highly crosslinked polymer that uses a “thermally reversible Diels-Alder cycloaddition” as its remendable mechanism [5, 6]. As the material is heated to its remending temperature, the fractured bonds reconnect to their original mates to restore a high percentage of strength to the material. Previous research has shown that this matrix material can be combined in a two-component system with 1) carbon-fiber or 2) magnetic particles to further enhance material properties. When the neat form of the Mendomer is combined with carbon-fiber, the material exhibits a shape memory effect when heated to the remending temperature. Because of this effect, the carbon-fiber-material system is returned to its original geometry and facilitates the return of cleaved surfaces to their original un-severed locations. This property is useful not only for actuator applications, but also in the healing process since this aids in the reconnection of broken bonds with their original counterparts [5]. Mendomers have also been combined with magnetic particles to form a composite that can be used to mitigate matrix cracking. This material system was developed by NextGen Aeronautics, UCLA, UCSB, AMRDEC and MDA [5]. The embedded magnetic particles impart internal and localized heating when used with an inductive heating apparatus. When subjected to an electromagnetic field, the heating from the magnetic particles induces healing of the Mendomer material. Several compositions, size distributions (dispersivity) and volume fractions of magnetic particles were characterized for their healing effectiveness. For nickel (Ni), healing time and rate could be adjusted with the choice of volume fraction and size of particles [7]. Embedding magnetic particles also allows for site-specific healing of the material depending on where the inductive heater coil is applied [5]. Portable inductive heating machines facilitate the healing of carbon-fiber composite skins in the field and in-situ, which eliminates the high-cost of part removal and replacement.

Based on this previous progress with the neat material and the two-component systems—i.e., the neat Mendomer with carbon-fiber and the neat Mendomer with magnetic particles—the two-component Mendomer/Ni microparticle matrix system was revisited to determine processing techniques and to predict material behavior of a new, three-component composite material. Consisting of neat Mendomer, Ni micropowder magnetic particles, and carbon-fiber, the three-component sample is fabricated and tested in the current research to create an advanced, remendable composite material.

SAMPLE FABRICATION

Two-component Mendomer/Ni matrix

Two-component Mendomer/Ni micropowder samples were fabricated to optimize manufacturing methods and Ni micropowder particle dispersion. These samples were formed from cylindrical compression and dog-bone tensile molds. The Mendomer/Ni micropowder mixture was prepared by first grinding Mendomer-400 with a mortar and pestle into a fine powder. Based on the mold volume, a 3% volume fraction percent of Ni micropowder (from Sigma-Aldrich) was then collected. Previous experiment with remendable materials found that a 3% volume fraction of Ni micropowder provided favorable properties for inductive heating with respect to heating rate and healing time [7]. The Ni micropowder was then thoroughly mixed with the Mendomer material, which was also in powder form. The combined mixture was then added to the sample molds. To minimize gas entrapment and

maximize packing, the molds were subjected to small shock vibration as well as manually packed to reduce void content. Samples were heated to the curing temperature of 150°C for 10-12 hours. The presence of voids preempted any meaningful mechanical property characterization. Instead, visual analysis focused on correlating images before and after damage and healing events.

Three-component Mendomer/Ni/carbon-fiber composite

Several three-component Mendomer/Ni micropowder/carbon-fiber samples were fabricated. The Mendomer/Ni micropowder was prepared as previously described. A 2x2 5K carbon-fiber weave cloth was trimmed into a small rectangular geometry and prepared for Mendomer/Ni powder application. The application of the powder mixture was subjective with only a visual attempt to apply an even amount of material. A high void content was expected due to the absence of agitation and packing as well as due to the high viscosity of the melted Mendomer material. The first sample was made with approximately 0.004 g/cm^2 of Mendomer/Ni powder and the second was increased to approximately 0.009 g/cm^2. Once the layup was complete, the samples were layered with high temperature rated peel ply, perforated Teflon, bleeder, and subsequently sealed in a vacuum bag. After attaching the vacuum pump, the samples were heated to 130°C. The temperature was then increased to 150°C for approximately 3 hours before the samples were removed for testing. (Full polymerization of the Mendomer does not occur until at least 10 hours.) Shape memory properties were verified using video analysis and simultaneous recording of inductive field exposure time. Mechanical tests were not performed due to the uncured state of the samples. Notwithstanding, shape memory, remending and mechanical properties will change as the these uncured samples reach full polymerization; in fact, as observed previously, mechanical properties may appear to improve as subsequent healing tests are performed.

ANALYSIS OF SAMPLES

Two-component Mendomer/Ni matrix optical inspection and healing investigation

The Mendomer/Ni micropowder samples were imaged to determine the Ni micropowder dispersion within the Mendomer matrix (Figure 1(a)). The Ni micropowder appears evenly distributed throughout the bulk of the material except near the top surface, where the absence of the darker Ni material is visible. This area (top surface) was also rough and uneven, but could be smoothened by sanding. After a baseline optical inspection, the samples were damaged and compared to assess remendability. The samples were damaged by compression using a vice to impart small cracks between 2 and 10 mm in length in the surface of the material. Completely cleaving the samples was avoided. Areas with an appreciable amount of surface cracks were imaged and noted for subsequent healing (Figure 1(b)). Samples were then healed by heating to the healing temperature of 130°C with an inductive heating apparatus (Superior Induction 7 kWHF induction heater) using a 3.0 kW "pencil"-type wound coil. The electromagnetic field was applied to the sample for approximately 60 seconds. The material began to heat in approximately 5 seconds. The material was then optically inspected again to determine the extent of healing.

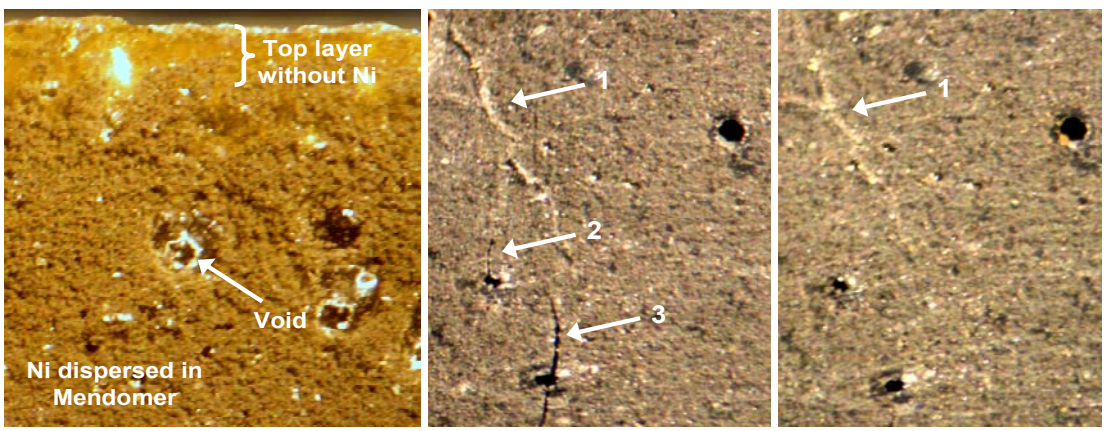

(a) (b) (c)

Figure 1. (a) Sample of Mendomer/Ni micropowder; (b) sample after damage with white arrows pointing to cracks; (c) sample after <60 seconds of inductive heating.

As shown in Figure 1(b-c), cracks 2 and 3 were completely healed. Crack 1 was less visible, but still present in the sample after heating was induced. Although the material was sufficiently heated to heal cracks 2 and 3, crack 1 was not completely healed. While difficult to see in the figure, the morphology of crack 1 is different than that of cracks 2 and 3, where crack 1 appears to be more of a hairline fracture than a surface fracture. Further investigation is necessary, but the large content of voids may have caused a misalignment of cleaved surfaces during vice compression. This may have affected the hairline fracture healing capability more than the surface fractures. Another possible reason crack 1 was not healed could be a lower density of Ni particles near the area resulting in less heat generation.

Three-component Mendomer/Ni micropowder/carbon-fiber shape memory investigation

The three-component Mendomer/Ni micropowder/carbon-fiber composite samples were similarly tested for their self-healing and shape memory capabilities using an inductive heater. Samples were first inspected for their matrix uniformity. Two types of composite samples were made---one with one ply and the other with three plies. After optically inspecting the 3-ply composite, it was determined that matrix distribution was too sparse (0.004 g/cm^2). This left voids and other dry areas of carbon-fiber where the Mendomer melt was insufficient to wet the material. In addition, the specimen appeared to be rigid and brittle. As a result, the sample experienced extensive fiber breakage with only minor deformation. These inferior mechanical properties were attributed to the abbreviated cure cycle. Despite fiber breakage and inadequate matrix integration, the sample exhibited remendability and shape memory behavior. After only 3 seconds in the presence of the electromagnetic field, the sample returned from its deformed shape to its undeformed, flat geometry.

The 1-ply composite sample was similarly inspected for even matrix distribution as previously discussed. Though more matrix material was used during sample fabrication per ply (0.009 g/cm^2), there was still an inadequate amount of matrix integration. The edges of the sample were frayed with loose carbon-fibers; these poorly wetted edges were cut away of the sample in order to provide a more uniform specimen. As expected, the 1-ply composite was considerably more flexible than the sample with three plies. The 1-ply sample was deformed conformally around a 0.5” rod. While the coiled shape could not be maintained, the coupon did retain a bent geometry. The sample was heated via an inductive heater to assess the remending and shape memory behavior. As shown in Figure 2, the sample returned to its flat, undeformed state after 3.5 to 4 seconds in the presence of an electromagnetic field. Evidence of significant heating is shown in Figure 2 where smoke was observed after approximately 3.5 seconds of inductive heating. Figure 2 shows tweezers suspending the side view of a flat rectangular specimen above an inductive coil.

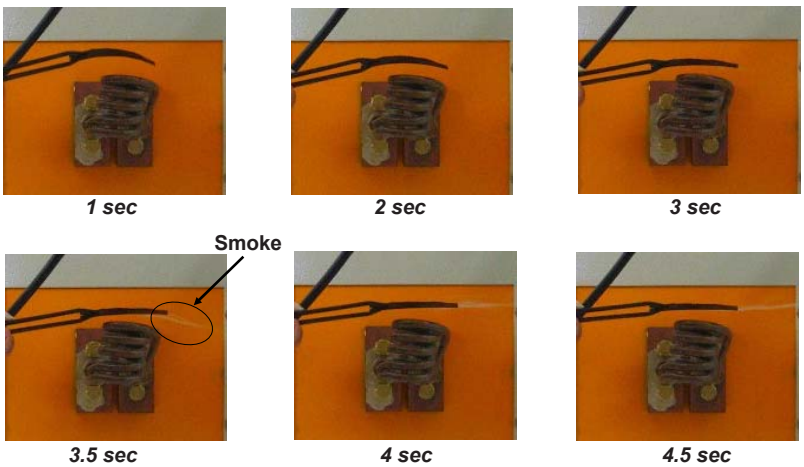

Figure 2. 1-ply Mendomer/Ni micropowder/carbon-fiber sample: 4.5 seconds of inductive heating causes shape change and sample burn/smoke.

Basic composite model

In order to improve understanding of the remendable mechanism, a modeling effort was initiated. Figure 3 schematically illustrates a carbon-fiber/magnetic particle enhanced Mendomer and length scales of interest for

addressing self-healing properties of the composite. The modeling approach includes finite element analysis (FEA) for continuum and mesoscale length scales and molecular dynamics (MD) for nanoscale effects. MD simulations are able to provide information about strength and range of interfacial interactions between magnetic particles. FEA simulations are able to provide information about mechanical properties of the composite as a function of magnetic particle volume fractions, size, and dispersivity. The information about the interfacial region gained in MD studies can be also used in FEA simulations. Similar approaches have been discussed in many reviews of multiscale modeling of polymer matrix composites [8].

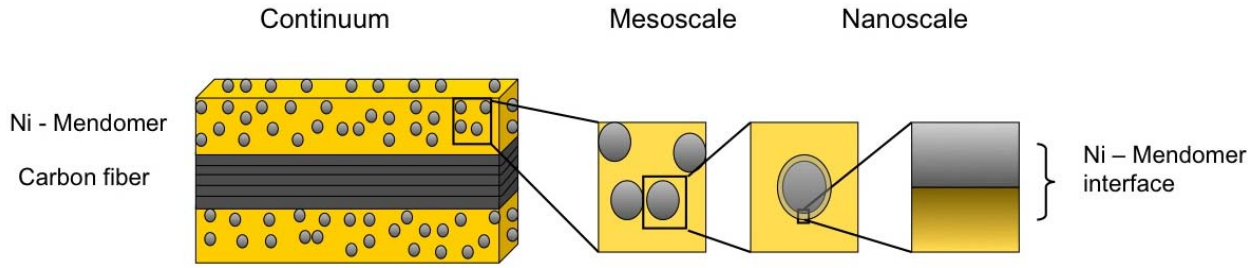

Figure 3. Schematic depiction of length scales of interest in understanding physical and mechanical properties of carbon-fiber composite with Mendomer polymer enhanced with magnetic particles.

MD simulations

LAMMPS (Large-scale Atomic/Molecular Massively Parallel Simulator) was chosen for this investigation [9] in order to validate the MD model and demonstrate the calculation of elastic constants via MD simulations. An initial configuration of 8 Mendomer chains was generated, which was energy minimized at a very low density. After energy minimization, the temperature of the system was increased to T = 300 K, and additional runs at constant volume and temperature and constant pressure and temperature were performed to randomize the configuration. However, calculations of Young's modulus for 8 Mendomer chain systems suffered from finite size effects. In order to avoid this problem, a larger system with 125 Mendomer chains was used. We used the same procedure as for the 8 Mendomers to randomize the sample. After equilibration of the larger neat (polymer only) system, Young's modulus was computed to be 1.1 GPa, which is 70% of experimental value [10]. In order to investigate the effect of size of Ni particle used in MD simulations, a Ni/Mendomer sample was generated using 4 nm diameter Ni particles. The nanocomposite interface region was characterized via the radial density function. The size of the interface region was found to be approximately 0.7-1 nm. The size of the interface region suggests that interfacial effects for this composite are negligible. Additionally, Ni/Mendomer model composite mechanical properties were characterized by computing the Young's modulus using a similar procedure as the neat Mendomer. Uniaxial extension was applied to a 3% volume fraction Ni/Mendomer system as shown in Figure 4(a). The value of Young's modulus was approximately 1.26 GPa, a 13% increase from the neat system.

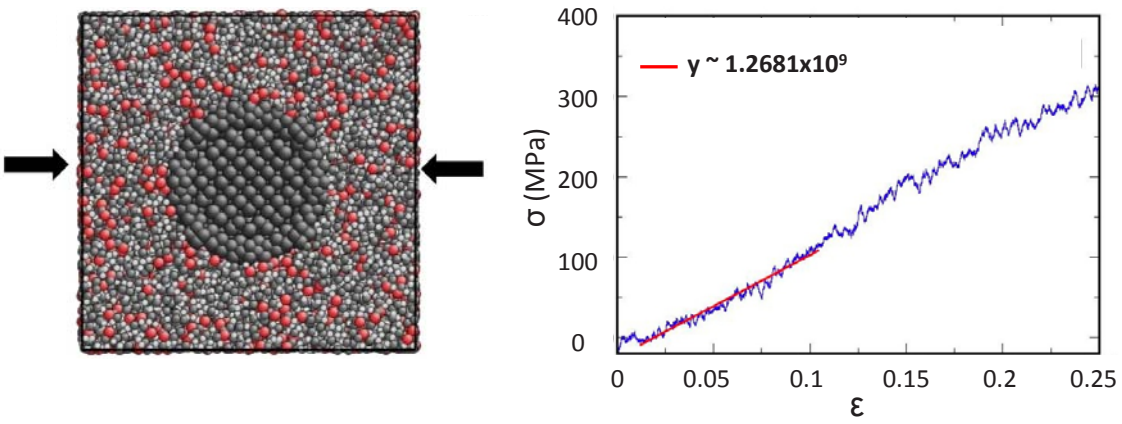

Figure 4. (a) Uniaxial compression is applied on Mendomer nano Ni composite in MD simulations. (b) Stress - strain behavior of the composite. From linear region (0.02 < ε < 0.1) Young's modulus is calculated to be ~1.26 GPa.

Finite Element Analysis

The objective of the FEA was to develop a model to understand how the Ni-particle size, dispersion, and volume fraction affect the elastic modulus of the two-component (Ni particles and polymer) composite. This model will be then developed to include the heat generation and heat flow due to the application of magnetic field on the composite. ANSYS was chosen as the FEA platform for structural analysis of the composite. The modeling effort resembles the previous effort in this area [11, 12, 13]. A graphical user interface using ANSYS UIDL and APDL was used to input the parameters of the model (Figure 5).

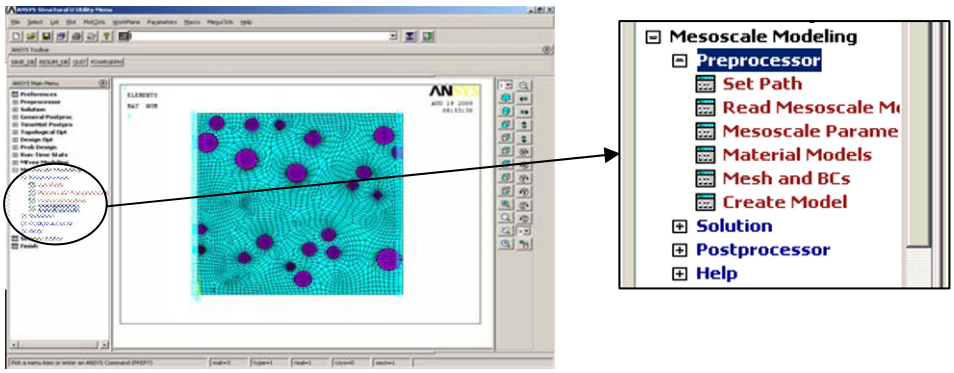

Figure 5. Graphical User Interface developed in ANSYS for modeling particulate composite.

For a given volume fraction in this cube, it is important to establish the cube edge length size that is neither too small to give solution that is dependent on a particular ensemble nor too large to unnecessarily require higher computational resources. The equivalent elastic modulus of the particle-matrix system as a function of cube edge length was calculated with particle radii uniformly distributed from 50 to 70 microns. The results converged at approximately 1500 microns. It is noted that at this length scale, MD simulations are computationally prohibitive. In order to verify the finite element simulation results, the effective elastic modulus obtained from this analysis was compared with that obtained from the experiments performed by Cho et al. (2006) [14]. It was found that the elastic modulus obtained from the experiment on vinyl ester resin and glass particles match well with the FEA results for different particle sizes (Figure 6(a)).

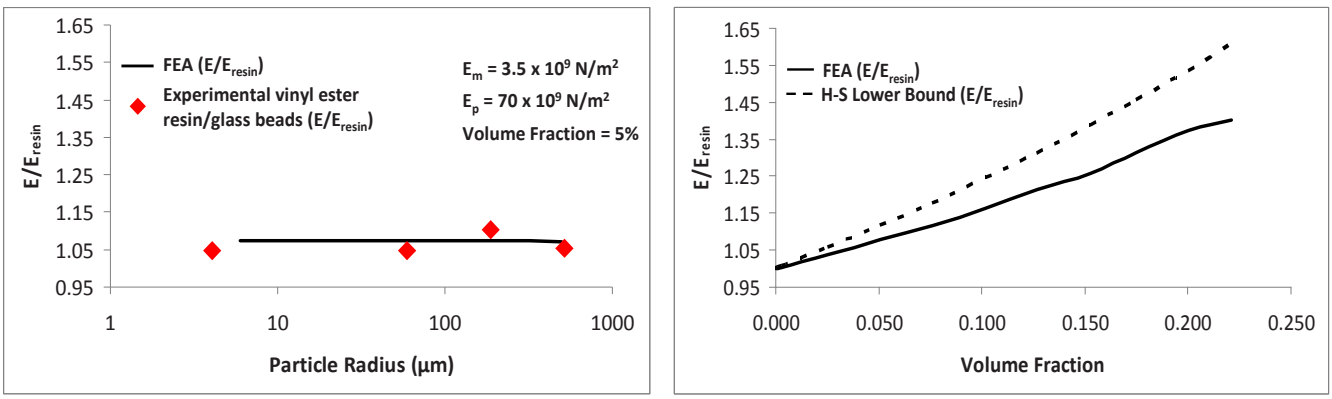

(a) **(b)**

Figure 6. (a) Validation of the finite element model: experimental data for vinyl ester resin and glass bead particles [14] and (b) effect of volume fraction on the effective elastic modulus as predicted by the FEA and Hashin-Shtrikman (HS) Lower Bound.

The effect of volume fraction on the elastic modulus of the Ni-Mendomer composite was also simulated. In this analysis, the result was compared with that obtained from the Hashin-Shtrikman Lower Bound. Figure 6(b) shows the comparison. It can be seen that the FEA predicts a slightly lower value than that predicted by the Hashin-Shtrikman Lower Bound. However, the two results are close. As expected, it was found that as the volume

fraction increases, so does the effective elastic modulus of the particle-matrix system. For example, at 3% Ni particle volume fraction, the effective modulus increases by about 6%. It should be noted that this increase in elastic modulus predicted by the FEA is half of that by the molecular dynamic simulations. Further studies are underway to determine the cause of this discrepancy.

CONCLUSIONS

In this paper we studied the remendable and shape memory effects of a composite made of Mendomer, Ni particles, and carbon fibers. The two-component (Mendomer and Ni particles) samples had an extensive network of large voids in the inner bulk of the sample. When the samples were damaged, remending was evident. Further quantitative analysis must be performed to determine the effect of misalignment and voids on healing. Fabrication processes must be improved to minimize the gas entrapment during the Mendomer/Ni micropowder melt and ensure composite strength. In the three-component samples with thinner layers of the matrix material, void evolution was less pronounced; this facilitated characterization of the shape memory properties of the material. Even with poor carbon-fiber wet-out, the material returned to its original shape within 3-5 seconds. Further investigation is necessary to determine the desirable composite layup process including the optimal amount of matrix combination necessary per ply. Initial modeling using molecular dynamic and finite element simulations successfully captured the effect of Ni particles on the elastic modulus of the composite.

REFERENCES

1 U.S. Department of Defense, “Ballistic Missile Defense Review,” DoD Release, 2010, (http://www.defense.gov/bmdr).

2 White, S.R., et al., “Autonomic healing of polymer composites,” Letters to Nature, Vol. 409, Pg. 794, 2001.

3 Hayes, S.A., et al., “Self-healing of damage in fiber-reinforced polymer-matrix composites,” Journal of the Royal Society Interface, Vol. 4, Pg. 381, 2007.

4 Duenas, T., et al., "Remendable Materials Using Structural Health Monitoring (SHM) To Solve Aerospace Problems, 7th International Workshop on Structural Health Monitoring, Sept. 9-11, Stanford, CA, Vol. 2, Pg. 2203, 2009.

5 Duenas, T., et al., “Multifunctional Self-Healing and Morphing Composites,” Conference Proceedings for the 25th Army Science Conference, Paper No. GP-03, 2006.

6 Chen, X., et al., “New Thermally Remendable Highly Cross-Linked Polymeric Materials,” Macromolecules, Vol. 36, Pg. 1802, 2003.

7 Duenas, T., et al., “Smart self-healing material systems using inductive and resistive heating,” Smart Coatings Symposium, Orlando, FL, 2009. - to be published

8 Muller-Plathe, F., “Scale-Hopping in Computer Simulations of Polymers,” Soft Materials, Vol. 1, Pg. 1, 2003.

9 Plimpton, S.J., “Fast Parallel Algorithms for Short-Range Molecular Dynamics,” J. Comp. Phys., Vol. 117, Pg. 1, 1995, (www.lammps.sandia.gov).

10 Murphy, E.B., et al., “Synthesis and Characterization of a Single-Component Thermally Remendable Polymer Network: Staudinger and Stille Revisited," Macromolecules, Vol. 41, Pg. 5203, 2008.

11 Sun, C.J., et al., “Effects of particle arrangement on stress concentrations in composites”, Materials Science and Engineering A, Vol. 405, Pg. 287, 2005.

12 Sun, C.J., et al., “Finite Element Analysis of Toughening for a Particle-Reinforced Composite,” Polymer Composites, Vol. 27, Pg. 360, 2006.

13 Sun, C.T., et al., “Finite element analysis of elastic property bounds of a composite with randomly distributed particles“, Composites Part A, Vol. 38, Pg. 80, 2007.

14 Cho, J., Joshi, M.S. and Sun, C.T,, “Effect of inclusion size on mechanical properties of polymeric composites with micro and nano particles,” Composites Science and Technology, Vol. 66, Pg. 1941, 2006.

Proceedings of the SEM Annual Conference
June 7-10, 2010 Indianapolis, Indiana USA

Experimental Characterization and Modeling of Shape Memory Material for Downhole Completion Applications

Chuanyu Feng, Goang-Ding Shyu, Sean Gaudette, Michael Johnson
Baker Hughes Inc, 14990 Yorktown Plaza Dr, Houston, TX 77040
Chuanyu.Feng@BakerHughes.com, Goang-Ding.Shyu@BakerHughes.com,
Sean.Gaudette@BakerHughes.com, Mike.Johnson@BakerHughes.com

ABSTRACT

Shape memory materials have promising applications in the oil and gas industry. A series of downhole completion applications based on this technology are under investigation at the Baker Hughes Center for Technology Innovation (CTI). The characterization of the shape memory materials, especially the time-dependent aspects of the material behavior, is critical for optimized product design, manufacturing and intended long-term applications. During manufacturing stage, rate-dependent hyperelastic behavior may be characterized by a series of potential functions, and shape memory behavior may be modeled through thermal effects or thermoviscoelastic effects. Thus, rate-dependent characterization tests were performed to determine the constants in the potential functions. For temperature- and rate-dependent shape recovery and stress recovery, experimental tests are critical for developing material models. In this paper, a brief review of different potential functions and shape memory models are presented and corresponding characterization results are discussed to facilitate further material modeling. In one of our targeted downhole completion applications, such information may be used for optimized product design and downhole performance prediction.

KEYWORDS

Shape memory material; Downhole completion; Potential function; Material characterization; Mechanical testing

INTRODUCTION

Shape memory material is a class of materials that are able to restore their permanent shapes from temporary shapes when conditions become favorable. Due to this attractive feature, shape memory materials are receiving more and more attention from the oil and gas industry. The shape memory material may be metal alloys or polymer-based materials. The shape memory effect of metal alloys relies on the temperature-dependent phase transformation while polymer-based shape memory is due to chemically or physically cross-linked networks. The shape transformation is usually activated by thermal stimulus even though other environmental stimuli exist [1]. In reality, the behavior of shape memory materials is time-, temperature-, and environment-dependent. The characterization of the time, temperature and environment dependence is critical for both the manufacture reshaping process and industrial applications. They are also the cornerstones for material constitutive model development.

Any single aspect of a non-linear time- and temperature-dependent material property is difficult to characterize and even more difficult to establish material constitutive models under different environments. In the case of shape memory materials, it is challenging to fully understand the material behavior. The state of the art of material modeling has been extended into complex three-dimensional deformation mode [1], but the characterization of the material in reality is not simple. Following the natural application steps of this type of material, the characterization may be classified into two categories, manufacturing process and shape recovery process. During the manufacturing process, the objective is to reshape the shape memory material and lock a temporary

T. Proulx (ed.), *Time Dependent Constitutive Behavior and Fracture/Failure Processes, Volume 3*, Conference Proceedings of the Society for Experimental Mechanics Series 15, DOI 10.1007/978-1-4419-9794-4_38, © The Society for Experimental Mechanics, Inc. 2011

shape while, for the shape recovery process, the objective is to recover the designed shape at a controlled recovery speed and controlled stress level.

For the manufacture reshaping process, the target is to lower the manufacturing cost while maintaining maximal shape recovery capacity and product performance. In our case, this means a selection of manufacturing temperature and appropriate reshaping parameters. Part of this problem has been discussed elsewhere [2]. In this paper, our focus is on the experimental characterization of material behavior during a simulated manufacturing process, and considerations to lower the capital expenditure as well as shape recovery capacity. Compared with the reshaping process, the shape recovery usually takes longer time to develop into a more stable configuration, especially for polymer-based shape memory materials. In most real applications, both shape and stress recovery is of concern, which makes it difficult to characterize the material. In this paper, our focus is to experimentally characterize the shape recovery and stress development at intermediate shapes, and discuss the contributing factors for the constitutive relation modeling.

MANUFACTURE RESHAPING PROCESS

To preserve the maximal shape recovery capacity and maintain optimized product performance, it is always desirable to reshape the material at reasonably elevated temperature. However, the selection of the manufacturing temperature is not straightforward. It involves numerous experimental characterizations of this material at different temperature and manufacturing conditions. The selection of temperature and manufacturing parameters also affects the final product performance. In this paper, the starting temperature is selected based on the glass transition temperature from loss modulus measurement. Since the material mechanical property is both temperature- and rate-dependent, both variables were investigated experimentally. In the targeted temperature ranges, the material was verified to be in rubbery state, and the mechanical property can be modeled as rate-dependent hyperelastic. As for the targeted application, the quicker the shape locking, the better the maximum recovery stress. More importantly, it may reduce the potential performance loss for the final product. Thus the manufacture reshaping process is desired to finish quickly, locking the shape in a short period of time.

Even though a comprehensive shape memory material model may be a logical choice, a hyperelastic material model is sufficient for the manufacturing process optimization. As discussed in the literature [3], for hyperelastic material, the constitutive model is either physical or phenomenological-based. Arruda-Boyce and Van der Waals models are physically motivated while others such as Ogden, Mooney-Rivlin, Neo-Hookean, Yeoh, and polynomial are all phenomenological-based. Currently, it is still not possible to directly obtain material constants from the material or deformation mechanism. Instead, they are usually derived from curve fitting of experimental data.

The temperature was selected based on the glass transition temperature and reshaping facility requirement, as noted by T1<T2<T3. The intention was to understand the temperature and time effect during the manufacturing process. The reshaping rate was selected based on targeted production rate requirement and reshaping facility capacity. It was noted as 0.5, 1.0, and 2.0 representing half, full, and doubled production rate respectively. Based on these parameters, a full matrix study of the reshaping process was conducted and results (including possible factors influencing the real product) were examined for selection of optimized production parameters. Although long-term performance needs further investigation during recovery and product lifetime, the selection of the operating parameters was merely based on short-term immediately measurable results.

RECOVERY PROCESS

The recovery process is to bring the shape memory material to its permanent or designed shape. The starting of this process depends on the environment and its temperature. It is also a highly time-dependent process. For polymer-based material, historically, the shape memory effect was modeled as a thermal process. It could be based on either rheological approaches or thermodynamic approaches. The explorations in the constitutive models were furthered from a simple one-dimensional case to more complex three-dimensional cases by different researchers [1, 4]. Such development of constitutive models is critical for complex applications and performance predictions.

From the point of experimental characterization, the recovery can be classified into two extreme cases, shape or strain recovery and stress recovery. Without constraints, the material may recover freely, and strain can be totally

restored. This is what was expected and referred to when one discussed shape memory materials. Another type of recovery is for stress under certain strain restraint. In this case, the material cannot recover freely. During the recovery, since the shape was constrained, the shape memory effects will force stress to develop. How the stress develops is of interest, as it governs the capacity of work to its environment or other objects. In the downhole application, the stress recovery is also related to the long-term performance of downhole products. Thus it is highly desirable to measure the long-term stress recovery performance directly.

Indeed, a combined strain and stress recovery is of interest for modeling development and verification. For this purpose, the strain recovery may be up to a certain point and then the stress recovery is switched on. After a certain period of time, the material may be re-strained to a larger strain level to repeat this process. It may be used to check the material resistance to external load. The combined experimental characterization requires an extended period of testing. Another important aspect is the environment. This process is very environment-sensitive. Depending on the environment the material emerged from, the recovery process is different. For downhole applications, it is necessary to evaluate hot wet conditions. For this reason, tests were performed both in air and water. High-temperature and high-pressure testing is out of the scope of this paper and will not be discussed here.

EXPERIMENTAL SETUP AND TESTING PROCEDURE

As shown in Figure 1, the simulation of manufacture reshaping process was performed using a MTS Insight 100KN machine from MTS. A customized environmental chamber is able to perform tests at the desired temperature range and fluid environment. Computerized control and programmable software package TestWorks 4 was used to reach targeted testing parameters, i.e. temperature and strain rate.

Due to the special structural characteristics of the shape memory material, samples were cored from a larger batch of material that has been through the same manufacturing process and has the same orientation as the final product. This will ensure the maximum fidelity of the testing results and repeatability. To make it even closer to the manufacturing process, the process was also under special consideration for sample preparation.

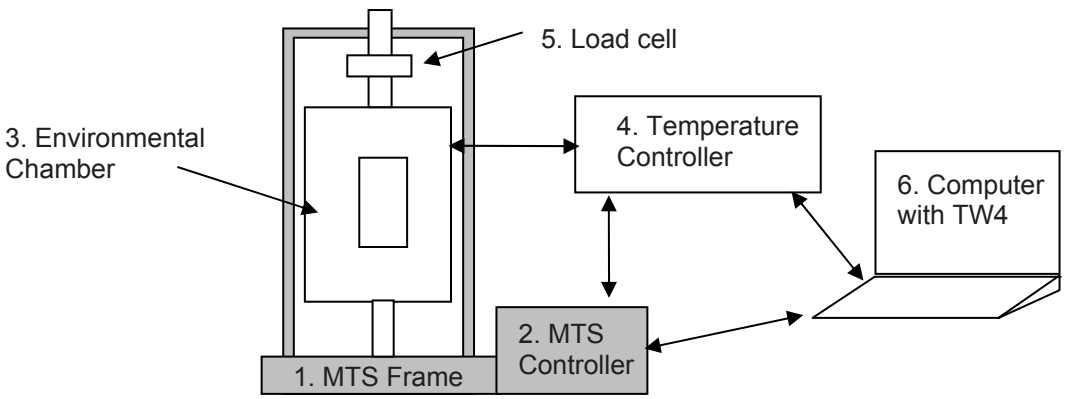

Figure 1. Schematics of experimental setup. 1. MTS loading frame, 2. MTS controller, 3. Environmental chamber, 4. Temperature controller, 5. Load cell, and 6. Computer with TW4 software.

The recovery characterization was performed using the same MTS loading frame. Different from the manufacture reshaping process, the characterization was very time-consuming. Most importantly, it is also temperature- and environment-sensitive. In this paper, recovery in air and water were investigated. In addition, a different in-situ test rig [5] was used to characterize the material under high temperature and high pressure at different fluid environments (In this paper, the results from the in-situ test rig will not be included). For the oil & gas industry, this is particularly important as downhole condition is usually at high temperature, high pressure, and harsh environment.

As shown in Figure 2, the characterization process includes a series of strain recovery and stress recovery. At the beginning, the material was put in the chamber and the test started with strain recovery. As the strain reached a certain level, the stress recovery was started and strain recovery was stopped. When stress recovery data was enough to predict relatively long-term performance under this strain level, the material was further strained to a

different level, and stress relaxation was monitored. These two sets of data provided different views of the recovery process. After the stress relaxation, strain recovery was continued until the test was stopped externally. During the recovery process, the dashed-line enclosed part may be repeated at a different strain level and more information may be obtained at a different strain level. Also, the whole process may be repeated at different fluid and different temperature levels.

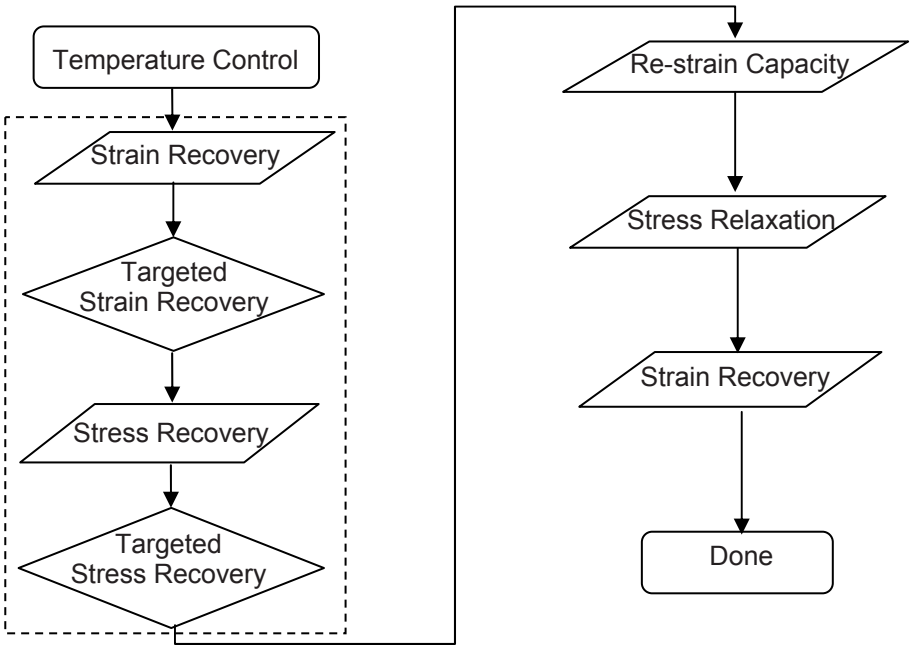

Figure 2. Flowchart of a typical recovery process.

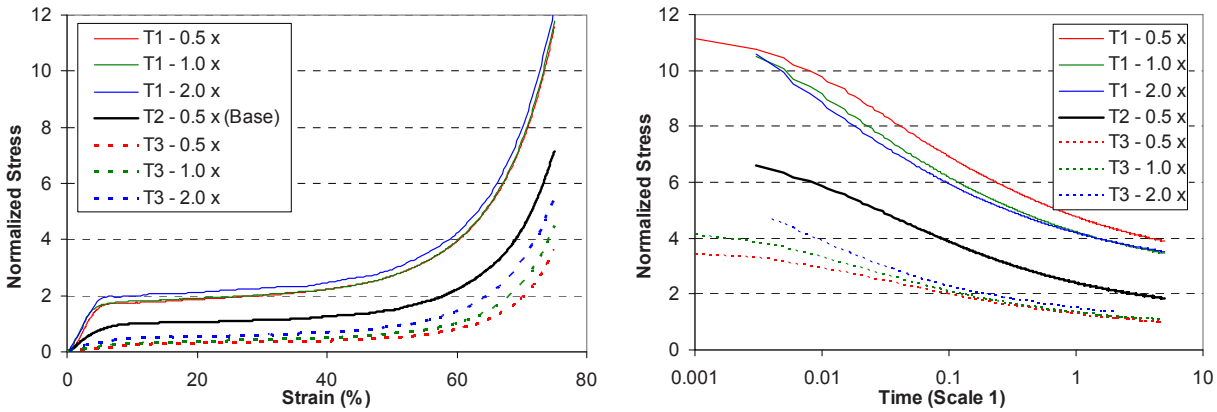

(a) Normalized stress strain curves (b) Normalized short term stress relaxation.

Figure 3. Characterization of manufacture reshaping process: short-term response at different temperature and production rates. The normalization was referenced at 10% strain level at T2, 0.5 x production rate.

PRELIMINARY RESULTS AND MODELING DISCUSSIONS

Due to the special material structures and manufacturing consideration, uniaxial compressive characterization tests were performed in a lateral constraint mode. Thus the testing data eliminate any lateral effects from the material. As shown in Figure 3, the manufacture reshaping process was characterized in term of normalized stress strain curves and short-term stress relaxation. To make the results more intuitive, the stress has been normalized at 10% strain level. Within the capacity of the manufacturing facility, as the temperature increased, the loading requirement decreased significantly. It implies that the temperature was the major controlling factor for the reshaping load requirement. The production rate only affected the reshape load slightly. As temperatures

increase, this effect becomes more significant. This implies that, for manufacturing equipment, a higher product rate at higher temperature is more economically feasible than a lower rate at lower temperature. The results provide useful guidelines for the design of manufacturing facilities as mass production becomes necessary.

Since the reshaping process is a relatively fast process, the stress relaxation only needs to be considered for a short period of time. Here the time scale in Figure 3(b) was obtained from previous full-scale article experiments (Time scale 1). As measured in Figure 3(b), the residual stresses were different at different reshaping temperature and production rates. The higher the temperature, the lower the frozen stress. This may not affect the long-term recovery stress level, but it could affect the short-term level of stress recovery and may be further investigated in the future. It should be noted that the results discussed here did not include other downhole performance factors investigated in-house. The final selection of manufacturing parameters must consider these factors in order to reach an optimized reshaping process.

After obtaining this information, the modeling of different manufacture reshaping processes was performed using hyperelastic material model with stress relaxation data. The results matched closely with full-scale articles both in deformation mode and loading requirements, and part of the results was published elsewhere [2].

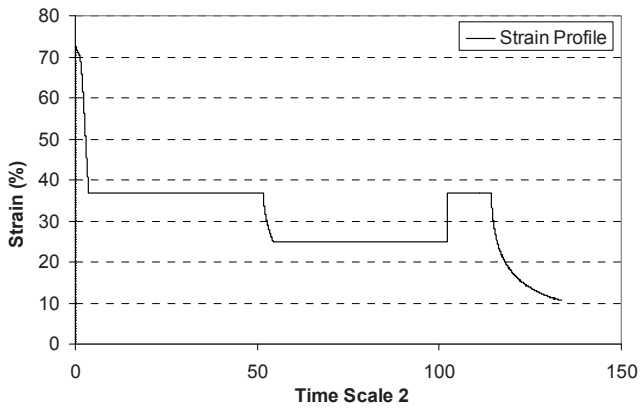

(a) Typical recovery strain profile.

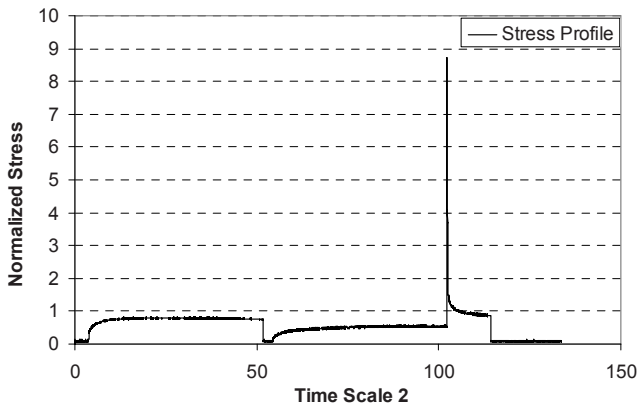

(b) Typical recovery stress profile.

Figure 4. A typical recovery process.

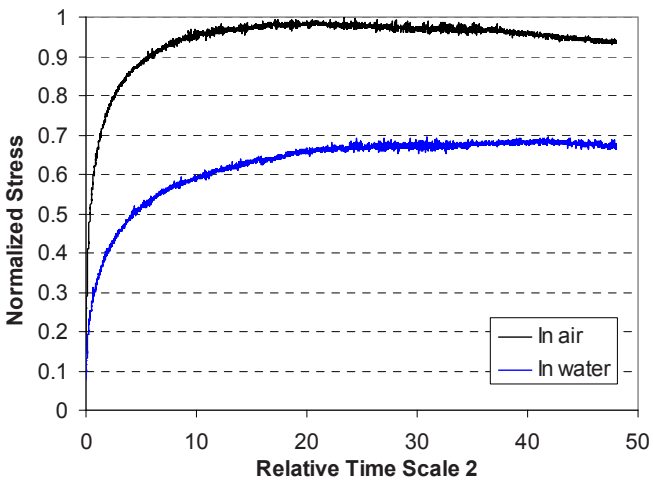

Figure 5. Comparison of stress under different environments. Maximum stress was normalized by the maximum stress in air, and the starting time was shifted to the same starting point.

Figure 4 shows a real recovery process as illustrated in Figure 2 under a specific temperature T_{air}. In this specific recovery process, the dashed line covered region in Figure 2 was repeated once to check the recovery and stress relaxation at certain strain levels. During the recovery process, shape recovery up to a certain strain level was measured and recovery rate was calculated. The stress recovery was then monitored for a certain period of time.

In this case, the unit of time scale 2 was significantly larger than that of the manufacture reshaping process time scale.

By calculating rate of strain recovery, it was found that the rate of strain recovery became slightly faster after the re-strain process. The difference was mainly demonstrated at a lower strain level. After the re-strain process, the stress relaxation was monitored for an extended period of time. It was concluded that, under a specific temperature, the final stress at certain strain state should be independent of loading history. As demonstrated in Figure 4(b), the stress recovery has two apparent stages. During the first stage, the stress starts to rise as the recovery proceeds. When it reached the maximum stress, the recovery entered the second stage. The characteristic of this stage is a near constant and slow declining stress. From Figure 4(b), it was also concluded that the final stress level depended on the strain level. The higher the strain level, the higher the final stress recovery. This is especially important for designing specific downhole applications.

Recovery as demonstrated in Figure 4 provided useful information for modeling the shape memory process in air. However, this behavior must be verified under different fluid environments. Following this consideration, recovery in water was tested. A comparative temperature T_{water} was selected to compare the recovery with T_{air}. Both deployment rate and stress recovery were found to be different at T_{water} as shown in Figure 5. The relative stress recovery is slower in water, and stress recovery level was smaller, which means in the governing equation for shape memory modeling, there should be a controlling factor to differentiate different testing fluids. Currently, more fluid tests were under investigation using an in-situ test rig [5], and ultimately, one can build a shape memory model to correlate different testing fluids as well as temperature effects. More results will be published as it becomes available. The difference in the environment may be considered a control variable in the constitutive equations,

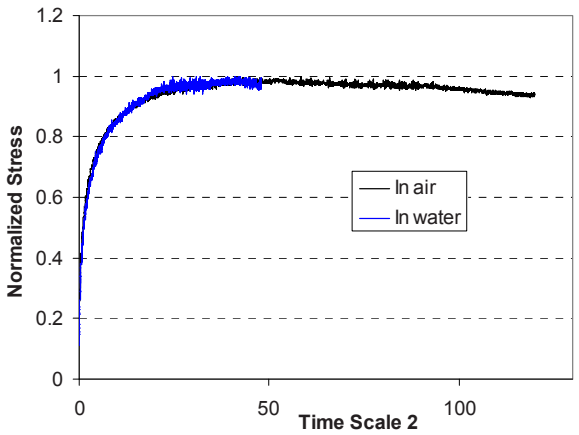

Figure 6. Similarity of stress recovery in different environments.

As demonstrated in Figure 6, by artificially extending the time scale of stress recovery in air, it was found that there exists similarity between stress recovery if the absolute stress level is omitted in this case for simplified modeling purpose. Using this as a guideline, more experimental tests should be performed to further the modeling of shape memory materials to explore the different fluid and temperature effects.

It is desirable to have a unified material constitutive model for the shape memory materials, but due to the nature of our application, it is the first step to characterize the material in different stage, and in the future, as material properties were obtained, a unified shape memory material model may be developed to cover the whole range of application. Ultimately, this may be used for design specific application shape recovery, and stress recovery. Also, it can be used to predict our product performance under different downhole conditions.

SUMMARY

In this paper, a thorough investigation of the manufacture reshaping process was presented, and key influencing factors including temperature and strain rate were investigated to facilitate the manufacturing parameter selection. It provided valuable information for optimized product design and production. By studying the rate and

temperature effects, it could also maximize the potential of manufacture facility, thus get the best return on investment.

The recovery process is very complex. An in-depth understanding of this process involves investigation of many inter-influencing parameters, such as temperature, time, and environment. It is very time-consuming. However, the study of the recovery characteristics helps us properly design the products for downhole application and downhole recovery schedule. As rig time is usually very expensive, such information may be used to properly design the downhole application and reduce the cost for customers. More importantly, the stress recovery information also provides the long-term resistance / stability information for the borehole. Through the recovery in both air and water, it was found generally true that the higher the strain level, the higher the ultimately recovered stress level. The ultimate modeling of shape memory effect for the innovative material still needs more characterization information. As the information becomes comprehensive, the model may be used for downhole recovery prediction and performance evaluation.

REFERENCE

[1]. Qi, H. J., Dunn, M. L., Long, K., Castro, F., and Shandas, R. Thermomechanical Indentation of Shape Memory Polymers, Behavior and Mechanics of Multifunctional and Composite Materials 2007, Proc. Of SPIE, Vol. 6526, 652615 (2007).

[2]. Feng, C., Shyu, G.D., Gaudette, S., and Johnson, M. H. “Shape Memory Material Manufacturing Design Optimization and Stress Analysis”, 2010 SIMULIA Customer Conference, May 25-27, 2010.

[3]. Abaqus analysis user's manual, Version 6.8/6.9, chapter 19, Hyperelasticity.

[4]. Liu, Y., Gall, K., Dunn, M. L., Greenberg, A.R., and Diani, J. Thermomechanics of Shape Memory Polymers: Uniaxial Experiments and Constitutive Modeling, International Journal of Plasticity 22 (2006), 279-313.

[5]. Yuan, Y., Goodson, J., HTHP In-situ Mechanical Test Rig and Test Method for High Temperature Polymers and Composites, SPE 113516, 2008 SPE Europec/EAGE Annual Conference and Exhibition, Rome, Italy, 9-12 June 2008.

Proceedings of the SEM Annual Conference
June 7-10, 2010 Indianapolis, Indiana USA

Mechanics of Persulfonated Polytetrafluorethylene Proton Exchange Membranes

Meredith N. Silberstein and Mary C. Boyce

Massachusetts Institute of Technology, Department of Mechanical Engineering, Cambridge, MA 02139, smeri@mit.edu

INTRODUCTION

Fuel cells enable direct chemical to electrical conversion of fuel to electricity, providing an efficient and clean process. Proton Exchange Membrane Fuel Cells (PEMFC), in which protons from hydrogen or methane cross a membrane to react with oxygen producing electricity, are the preferred transportable fuel cell. Nafion, a phase separated perfluorosulfonated ionomer, is the current benchmark membrane but still exhibits limited lifetime due to stress encountered during constrained cyclic hygro-thermal loading. In previous work [1] the viscoplastic nature of Nafion under uniaxial extension was experimentally characterized. The experimental results were used to develop a three-dimensional constitutive model which was then implemented within a finite element analysis software package. These results will be briefly reviewed. Here, the model is used to simulate the rate dependence of the stress and strain evolution in Nafion under the loading typically encountered during fuel cell operation. This loading consists of hygro-thermal cycling within partially constrained boundary conditions defined by other components of the fuel cell. This information could be used to either change the startup/shutdown procedure for a fuel cell or to guide the procedures used for accelerated membrane lifetime testing.

UNIAXIAL EXPERIMENTS AND MODEL

Nafion has been characterized under uniaxial tensile loading via monotonic, cyclic, and stress relaxation loading profiles. It was shown to exhibit elastic-viscoplastic behavior with a rate dependent yield, significant inelastic recovery during unloading, and stress relaxation that grows in magnitude throughout the yielding process. Additionally the mechanical properties, in particular the elastic stiffness and yield stress, are known to be strongly dependent on temperature and water content. A rheological depiction of the fully three-dimensional constitutive model which has been developed to capture the rate, temperature, and hydration dependence of the mechanical behavior of Nafion is shown in Figure 1 along with two characteristic fits of the model to experimental data.

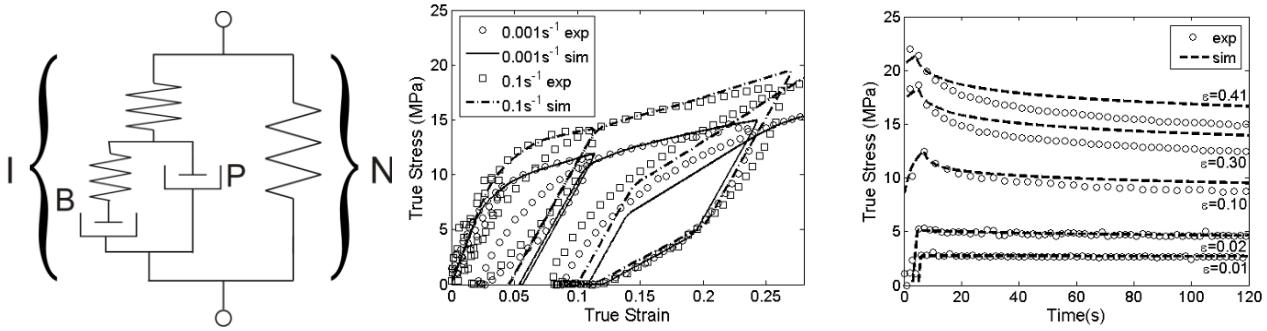

Figure 1. A constitutive model was developed to capture the mechanical behavior of Nafion: (a) rheological depiction of model (b) model fit to rate dependent cyclic data at 25ºC (c) model fit to stress relaxation data at 25ºC.

IN SITU FUEL CELL STUDY

The constitutive model is applied to model Nafion within a fuel cell. To simulate the in-situ loading we chose a geometry in the vein of the study of Kusoglu et. al. [2]. The specific geometry and boundary conditions are shown in a unit cell representation in Figure 2a; the membrane is bonded on both its top and bottom to a gas diffusion layer to form the membrane electrode assembly (MEA), the MEA is placed within aligned rigid bipolar plates which are half the length of the MEA (the land, the vertically open region is called the channel); to capture the

T. Proulx (ed.), *Time Dependent Constitutive Behavior and Fracture/Failure Processes, Volume 3*, Conference Proceedings of the Society for Experimental Mechanics Series 15, DOI 10.1007/978-1-4419-9794-4_39,

repeating nature of the unit cell, the MEA is not allowed to expand in the horizontal direction, the bipolar plates are subject to a constant force condition in the vertical direction. The membrane is then subjected to water content and temperature variation as shown in Figure 2b causing stresses due to the constraints which restrict free swelling of the membrane; the time period over which the water content and temperature change and the hold times are varied.

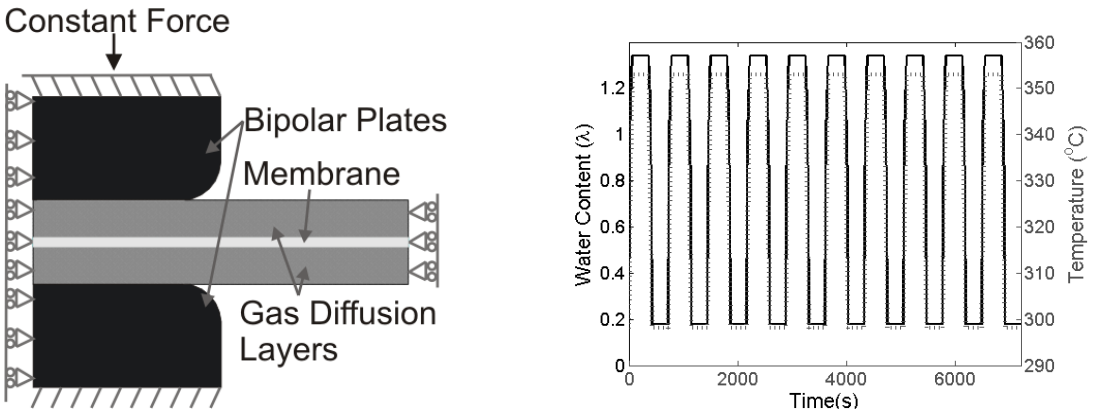

Figure 2. (a) Representative two dimensional fuel cell unit used to simulate cyclic hygro-thermal loading of the polymer electrolyte membrane. (b) Applied time history of water content and temperature (ramp rate and hold time varied).

Significant stresses are found to develop, particularly within the plane of the membrane, resulting in plastic straining of the membrane during both the swelling and deswelling processes. The specific stress and strain evolution arises from the interplay of the membrane expansion within a semi-constrained environment while the elastic and plastic material properties are evolving due to constitutive dependence on water content and temperature. There are many stress and strain histories of interest; here we choose to focus on the negative hydrostatic pressure that develops during drying and the cyclic plastic strains due to the connection of these two parameters with failure/potential pinhole formation and tearing. Figure 3 shows the pressure and effective plastic strain contours at the end of the first cycle. It can be seen that each has a maximum value just on the channel end of the land to channel transition. This supports the prevailing theory that hygro-thermal cycling contributes to pinhole formation in the channel region. Figure 4 shows how the pressure concentration and maximum effective plastic strain evolve with each cycle for four different loading histories. When there is a hold time between switching from swelling to deswelling the maximum negative pressure reached relaxes significantly from cycle to cycle. This relaxation occurs to a much lesser extent when there is no hold time. The maximum effective plastic strain per cycle depends primarily on hold time and increases only slightly with each cycle after the first three cycles. While it is not surprising that greater hold times lead to both greater plastic strains and relaxed pressures, it does suggest that a more direct link needs to be established between pinhole formation and a specific material condition. Some work has been done to this end (e.g. [3-5]) however there is no clear answer at this time.

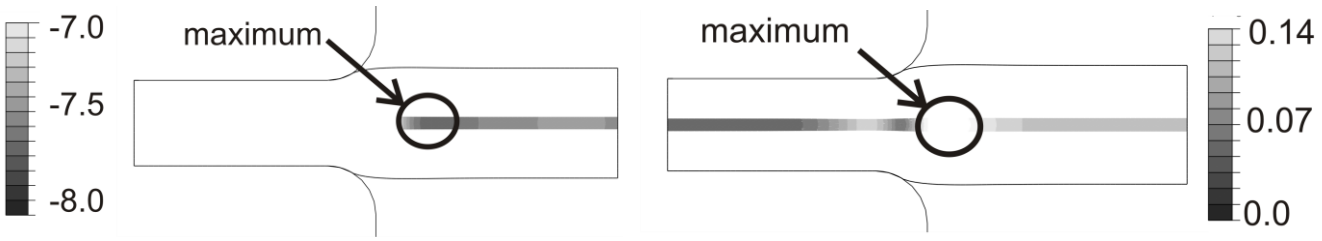

Figure 3. Contours of the state of membrane after a single hygro-thermal cycle: (a) Pressure (MPa) (b) Effective plastic strain.

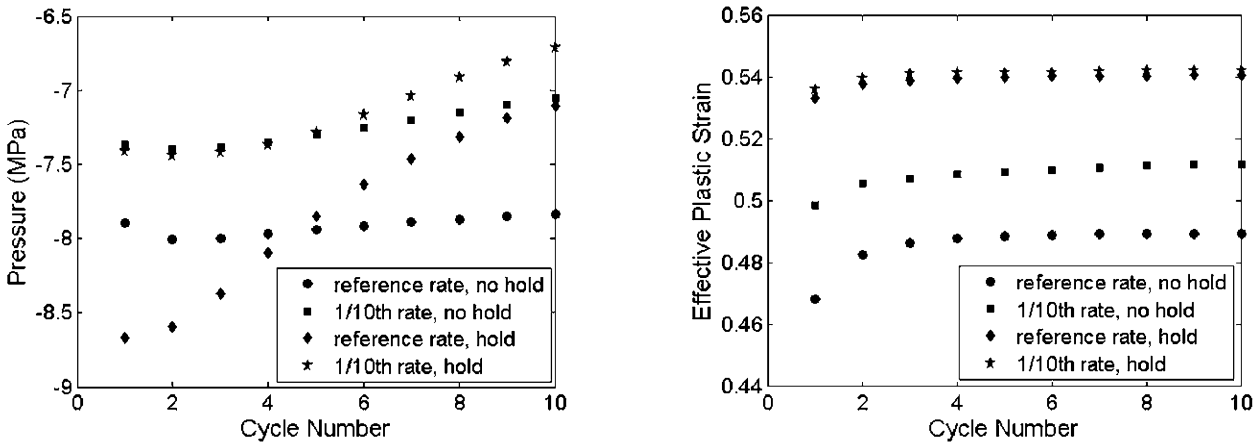

Figure 4. Rate effects on the cyclic deformation of Nafion in-situ (a) maximum negative hydrostatic pressure value that occurs during each cycle (occures when dry) (b) maximum effective plastic strain value that occurs during each cycle (occurs when hydrated).

CONCLUSIONS

A three dimensional constitutive model for Nafion has been used to simulate the stress and strain evolution of a membrane within an operating fuel cell. Specifically, the effect of the rate of hydrating/heating and dehydrating/cooling has been examined. The stresses that develop are large enough to cause plastic deformation on both hydrating and dehydrating. Negative hydrostatic pressure and effective plastic strain are looked at as predictors of mechanical failure. The evolution of negative hydrostatic pressure and effective plastic strain are both found to depend strongly on the hold time between cycles with the former decreasing and the latter increasing with increasing hold time. They are also found to have a non-negligible dependence of the same trends on the time period of hydrating/drying. Since the pressure and plastic strain have opposite trends it makes it difficult to draw any conclusions about what loading sequence would be the most harmful. If a more direct link could be established between membrane failure and one of these or an alternative parameter, then the simulation results could guide the loading profile used in accelerated lifetime testing.

ACKNOWLEDGEMENTS

This research was sponsored in by NSF grant CMMI-0700414 and the Masdar Institute.

REFERNCES

[1] Silberstein, MN. and Boyce, MC. “Constitutive modeling of the rate, temperature, and hydration dependent deformation response of Nafion to monotonic and cyclic loading.” *Journal of Power Sources,* accepted, 2010.

[2] Kusoglu, A. Karlsson, AM. Santare, MH. Cleghorn, S. and Johnson, WB. “Mechanical response of fuel cell membranes subjected to a hygro-thermal cycle.” *Journal of Power Sources,* 161:987-996, 2006.

[3] Huang, X. Solias, R. Zou, Y. Feshler, M. Reifsnider, K. Condit, D. Burlatsky, S. and Madden. T. “Mechanical endurance of polymer electrolyte membrane and PEM fuel cell durability.” *Journal of Polymer Science: Part B: Polymer Physics*, 44: 2346-2357, 2006

[4] Li, Y. Quincy, JK. Case, SW. Ellis, MW. Dillard, DA. Lai, YH. Budinski, MK. and Gittleman, CS.“Characterizing the fracture resistance of proton exchange membranes.” *Journal of Power Sources*, 185:374-380, 2008

[5] Li, Y. Dillard, DA. Case, SW. Ellis, MW. Lai, YH. Gittleman, CS. and Miller, DP. “Fatigue and creep to leak tests of proton exchange membranes using pressure-loaded blisters.” *Journal of Power Sources*, 194:873-879, 2009

Proceedings of the SEM Annual Conference
June 7-10, 2010 Indianapolis, Indiana USA

The influence of pressure on the large deformation shear response of a Polyurea

Maen Alkhader, W.G Knauss, G. Ravichandran
Graduate Aerospace Laboratories,
California Institute of Technology,
1200 E. California Blvd.,
Pasadena, CA 91125, USA
e-mail: wgk@caltech.edu

ABSTRACT
A new shear-compression experiment is developed to characterize the influence of hydrostatic pressure on the shear constitutive response of nearly incompressible viscoelastic materials undergoing large deformations. In this design, a uniform torsional shear stress is superposed on a uniform hydrostatic compressive state of stress generated by axially deforming samples confined by a stack of thin steel disks. The new design is effective in applying uniform multiaxial compressive strain while preventing buckling and barreling during inelastic deformation. In addition, it allows for the direct measurement of the stress and strain fields during the deformation history. The new shear-compression setup is developed to aid in characterizing the influence of pressure or negative dilatation on the shear constitutive response of viscoelastic materials in general and Polyurea in particular. Experimental results obtained with this technique illustrate the significant increase in the shear stiffness of polyurea under moderate to high hydrostatic pressures.

INTRODUCTION
Viscoelastic coatings which are usually used for abrasion protection and concrete surface enhancement, has recently been used to enhance blast and impact tolerance of steel plates and sandwiched structures. Recent studies show that backing steel plates with a layer of polyurea or embedding a layer of polyurea in a composite plate significantly enhances the resistance of the composite structure to high strain rate loading generated by impact or blast [1-3]. To utilize the full capability of polyurea, it is essential to characterize the mechanisms responsible for the enhancement of its impact resistance.
Although the theory of linear viscoelasticity is well understood it is likely incapable of characterizing the large strain response of viscoelastic materials under impact and blast loading. More importantly, linear viscoelasticity theory presumes the independence of the shear response from hydrostatic pressure, which is the main issue investigated in this study. Theoretical arguments [4, 5] as well as physical measurements [9] point to the ability of hydrostatic pressure to significantly alter the viscoelastic properties of polymers. Based on the free volume theory it can be argued that hydrostatic pressure reduces the free volume content and increases the energetic barriers for the chains' molecules to move [5]. Thus, hydrostatic pressure may shift the viscoelastic response of polymers towards the glassy phase.

This argument, highlighting pressure influence, is supported by the plate impact experiments performed on polyurea samples [6], were elevated hydrostatic pressure was seen to produce a spike in the shear strength. Although the experimental results in [6] do not provide a quantitative description to the shear strength sensitivity to hydrostatic pressure, the attempt to reproduce the same results using FE analysis [7] supported such a quantitative description; in this FE analysis a linear pressure term was needed to be added to the WLF time-temperature superposition equation to simulate the experimental data. Accordingly, the coupled efforts in [6] and [7] highlight the existence of a pressure driven mechanism specifically in Polyurea which contributes to its shear stiffening behavior high strain rate.
To investigate the interaction between the shear response of polyurea and the imposed hydrostatic pressure in more detail, and to aid in characterizing the constitutive response of polyurea under impact and blast loading, the present work proposes a new experimental procedure that adopts and modifies the confined compression setup proposed in [7, 8]. The outline of this paper is as follows: First, we describe under "Experimental Setup" the experimental apparatus and the finite element model used to ensure its functionality. After this description, the

T. Proulx (ed.), *Time Dependent Constitutive Behavior and Fracture/Failure Processes, Volume 3*, Conference Proceedings of the Society for Experimental Mechanics Series 15, DOI 10.1007/978-1-4419-9794-4_40, © The Society for Experimental Mechanics, Inc. 2011

material and specimen fabrication is discussed and issues related to data consistency are analyzed. The results are presented in the final section.

EXPERIMENTAL SETUP

The new design adopts and modifies the confined compression test [7, 8] to extend its functionality and provide it with the potential to serve as an effective tool in investigating the shear capability of polyurea as a function of pressure. Since the new design complements the original setup without altering its underlying principles: The original design is described first, along with its inherent small strain constraints that limit its ability to characterize the constitutive response of polyurea on a broader basis.

The confined compression test [7,8], presented in Fig 1-A, consists of a confining cylinder and a cylindrical loading rod. The specimen is placed inside the confining cylinder. The clearance between the sample and the confining cylinder should be as small as practically feasible. The outer diameter and material of the confining cylinder are chosen so as to provide adequate support to the specimen. Moreover, for convenience of data analysis it is preferred to design the confining cylinder such that it only deforms elastically. The confining cylinder enables the application of uniform multiaxial compressive strains and prevents buckling, barreling and localization during deformation of the specimen. The setup enables the simultaneous measurement of shear and bulk response of materials and is independent of the specimen's constitutive description.

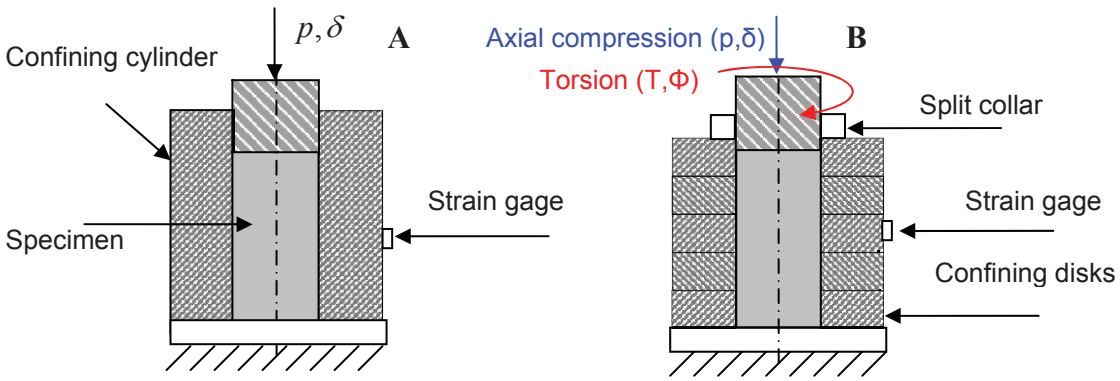

Fig 1: Schematics of the original (A) and modified confined compression setups (B).

Upon applying the axial compressive load to the sample by moving the loading rod into the confining cylinder, an axial strain ε_{zz} is developed and simultaneously a hoop strain $\varepsilon_{\theta\theta}$ at the outer surface of the confining cylinder. These two strains and the axial compressive force, *P*, are measured. From these values the stress and strain fields inside the specimen can be determined. Stress fields are computed using

$$\sigma_{rr} = \sigma_{\theta\theta} = -\frac{(b/a)^2 - 1}{2} E_c \, \varepsilon^c_{\theta\theta} \tag{1}$$

where E_c is the elastic modulus of the confining cylinder, *b* and *a* are its outer and inner diameters, respectively. The axial stress is computed from the compressive force *P*. Uniform strain fields in the specimen can be computed explicitly using

$$\varepsilon_{rr} = \varepsilon_{\theta\theta} = \frac{\varepsilon^c_{\theta\theta}}{2}\left[(1-\nu_c) + (1+\nu_c)\left(\frac{b}{a}\right)^2\right] \tag{2}$$

were ν_c is the Poisson's ratio of the confining cylinder. The computed principal stress and strain fields in the specimen can be decomposed into their hydrostatic and deviatoric components

$$\sigma_m = \frac{\sigma_{zz} + \sigma_{rr} + \sigma_{\theta\theta}}{3} \tag{3}$$

$$S_{ij} = \begin{bmatrix} 2/3(\sigma_{zz} - \sigma_{rr}) & 0 & 0 \\ 0 & 1/3(\sigma_{zz} - \sigma_{rr}) & \\ 0 & 0 & 1/3(\sigma_{zz} - \sigma_{rr}) \end{bmatrix} \tag{4}$$

$$\varepsilon_v = \frac{\varepsilon_{zz} + \varepsilon_{rr} + \varepsilon_{\theta\theta}}{3} \tag{5}$$

$$E_{ij}^{d} = \begin{bmatrix} 2/3(\varepsilon_{zz} - \varepsilon_{rr}) & 0 & 0 \\ 0 & -1/3(\varepsilon_{zz} - \varepsilon_{rr}) & 0 \\ 0 & 0 & -1/3(\varepsilon_{zz} - \varepsilon_{rr}) \end{bmatrix} \quad (6)$$

such that S_{ij} and E_{ij}^{d} are the deviatoric stress and strain tensors respectively, while σ_m and ε_v are the hydrostatic pressure and dilatation.

Theoretically, the aforementioned confined test configuration, Fig 1-A, can be used to characterize shear and time dependent viscoelastic properties of polymers as was demonstrated in [9]. However, the attempt to use the exact experimental configuration for polyurea highlights a drawback [10]. At room temperature and under low to moderate pressures polyurea is nearly incompressible; hence, the principal stresses describing its confined compressive response would have similar values, leading to small deviatoric stresses and strains. Accordingly, to characterize the shear constitutive behavior of polyurea as a function of pressure, the setup has to be modified to accommodate achieving higher shear stresses and strains independent of the pressure. To this end, the original setup [8] is augmented with a second step, in which, a torsional shear stress is superposed on the sample by means of a twist motion. Fig.1-B presents this modified two-step configuration. The torsional shear stress is decoupled from the hydrostatic pressure which is controlled by the amount of imposed axial compression. To accommodate for the twisting motion in the modified setup, the confining cylinder is replaced by a stack of steel disks separated by 0.002" thick Teflon sheets. In addition, a double split shaft collar (see Fig.1-B) is installed on the loading rod to impose a stabilizing force on the rings and to prevent polyurea from flowing in between the confining disks. The cylindrical steel disks would collectively provide the support and confinement to the sample and simultaneously minimize the frictional forces that would be generated at the specimen-cylinder interface during the angular twisting deformation of the sample. Teflon sheets provide for low friction between the rings and facilitate the uniformity of the relative rotation of the disks. The split collar is tightened just enough to achieve constant level of adequate support by allowing it to slide on the loading rod.

The modifications added to the confined compression setup are supported and justified by finite element analysis. The numerical simulations are used to provide substantial insight into the evolution of friction forces, their effect on the measured material shear response and the ability of the proposed modification to leverage and minimize friction forces to permit extracting the correct shear stiffness from the measurements.

The Finite Element method is implemented here by means of linear viscoelastic theory. Although linear viscoelasticity may not accurately represent the actual viscoelastic response of polyurea during the present measurements, we would argue that it aids significantly in providing substantial insight and assists in analyzing the planned experimental procedures to anticipate and debug experimental problems and ensure the accuracy of the extracted data.

For the FE models, the time dependent shear constitutive response of polyurea is obtained from [11] and represented by a 6 term Prony series. Poisson ratio is included in the model and assumed to have a constant value of 0.49. The bulk modulus was not specified and was computed by the FE software (ABAQUS). Contact wherever needed is modeled at the interfaces using a surface-to-surface contact algorithm with finite sliding, as well as, the geometric correction algorithm option provided by ABAQUS. The latter option minimizes discretization related errors associated with modeling the smooth cylindrical surfaces with finite elements.

The potential situation of performing the secondary twisting deformation in a solid confining cylinder is examined first. Two step FE simulations are performed with the model in Fig 2-A. The model includes confining steel cylinder whose outer to inner diameter ratio is 3 and a specimen with height and width of 8 mm. the axial strain is applied first at a strain rate of $1x10^{-3}$ s^{-1} followed by an angular twist, generating a shear strain rate of $1x10^{-3}$ s^{-1}. The coefficient of friction at the specimen-cylinder interface is varied between 0.001 and 0.1. For comparison, another analysis is performed without the confining cylinder, by considering torsional shear loading only. Results from these simulations are presented in Fig 2-B and confirm that increasing the coefficient of friction increases the required torque to twist the sample. Even a coefficient of friction of only 0.05 results in overestimating the shear stiffness of the sample by more that 4 folds at a pressure of 290 MPa.

To explain the trend seen in Fig 2-B the actual deformation pattern during the twisting of the sample is extracted from the simulations and is presented in Fig 3. This figure shows the initial shape, followed by the deformation pattern at two intermediate steps and ends up showing the final deformed shape for the case with a coefficient of friction of 0.1. The figure points to the existence of a localized boundary layer where most of the torsion is developing. The middle section is just going through rigid body rotation without developing shear strain. The existence of a strain gradient alters the local strain rate and in this particular case the strain rate increases at the specimen top and bottom boundaries. Since the material is viscoelastic and rate dependent, strain rate increase

causes the global response to overshoot the actual material's stress-strain response. The localized strain gradient grows with further twisting which complicates isolating friction effect during data reduction and analysis.

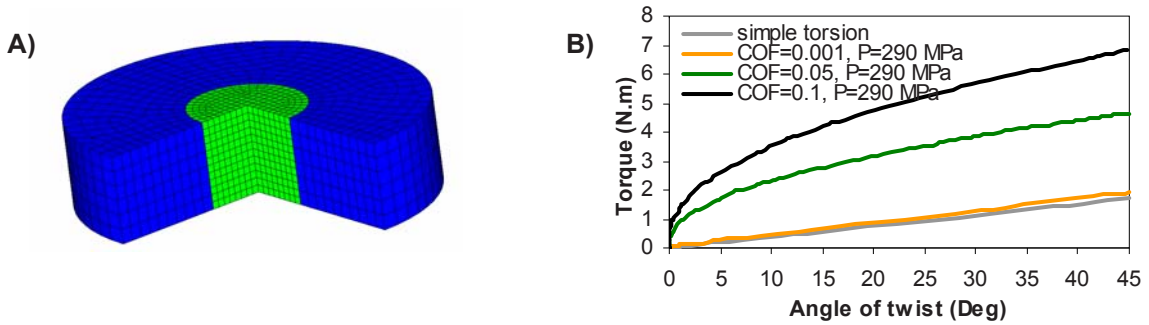

Fig. 2: FE analysis for assessing the role of friction at the interface between the specimen and a solid cylinder during twisting. A) The FE model, B) torque required to twist the linear viscoelastic sample at different friction values.

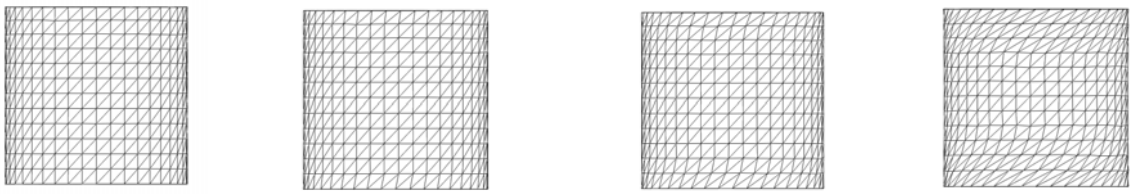

Fig 3. Torsional deformation pattern, showing the development of localized deformation with time. The FE model is based on a solid confining cylinder with a coefficient of friction of 0.1.

Since applying lubricants at the specimen-cylinder interface to reduce the coefficient of friction to significantly smaller than 0.05 is not practically feasible, the confining cylinder is replaced by the stack of cylindrical disks.
To asses the possibility of preventing friction from inducing substantial shear strain gradients we examine the use of a stack of cylindrical disks, and attempt to deduce reasonable dimensions of the disks to replace the solid cylinder, we revert again to a Finite Element model. Fig 4-A shows the FE model with 1 mm thick disks. In this FE model friction is assumed to exist only at the specimen-disks interface. The coefficient of friction is assumed to be 0.1. Results from these models are presented in Fig. 4-B and compared with the response obtained from the model with a solid confining cylinder and the same coefficient of friction. The figure shows that the thin disks can substantially reduce the role of friction. Although the disks may not eliminate friction completely, they prohibit friction forces from altering the predicted shear stiffness for most of the deformation history, excluding the first 3 degrees of rotation where the friction force is numerically ramped from zero to its plateau value computed from Coulomb friction model. More importantly, the shear stiffness predicted by the FE model with thin disks is almost identical to the known shear stiffness of the material. This result is consistent with the linear viscoelastic model used in the FE analysis in which the material shear stiffness is independent of hydrostatic pressure. Based on Fig 4-B, one can argue that both 1mm and 2mm disks can reasonably prevent the development of shear strain gradients and render the friction contribution to be time independent. Fig 5 qualitatively supports this latter argument as it shows the uniform shear strain distribution for the model with 2mm thick cylindrical disks. On the other hand, Fig 6 quantitatively illustrates how the angle of twist varies linearly along the height of the specimen for both setups, employing 1mm and 2mm thick discs. This linear variation represents the desired uniform shear strain. This FE analysis suggests thus that both 1mm and 2mm thick cylinders may provide sufficiently accurate results; it is clear that for reasons of practicality the 2mm configuration is more desirable.

The aforementioned simulations provide a guide for developing the experimental setup. The actual non-linear viscoelastic response, fitting tolerances, load cells capacity, and data acquisition resolution provide some experimental issues which physically constrain the experimental apparatus. In addition, modeling friction by coulomb friction model and modeling polurea using linear viscoelasticity may swerve the FE analysis predictions from the experimental results. For the final test setup, the confining thin cylindrical disks are made from steel and

have an outer diameter to inner diameter ratio of 1.56. With this ratio, two objectives were achieved. First, during the first step, the effective stress is minimal and both radial and axial stresses are almost equal. Second, high pressure levels can be achieved while the stresses in the disks are safely within the elastic limit. The elastically deforming cylinder not only facilitates data reduction and analysis, but increases the practicality of the process by re-using the cylinders for multiple tests.

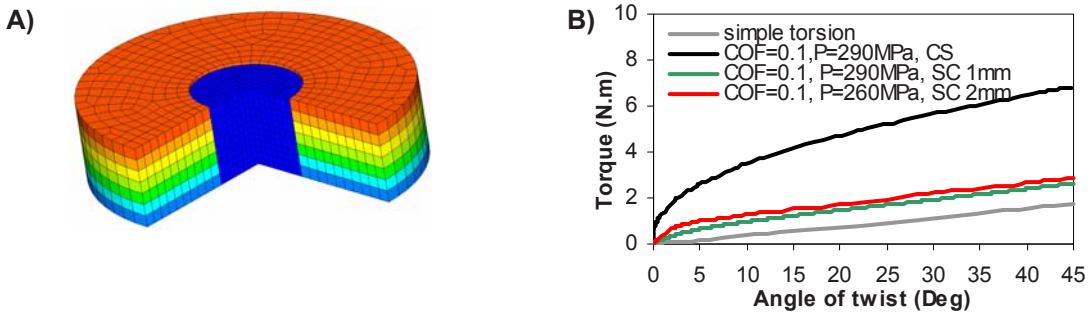

Fig. 4: FE analysis for assessing the effectiveness of the stacked disks to minimize the role of friction at the specimen-disks interfaces during twisting. A) The FE model, B) torque vs. twist

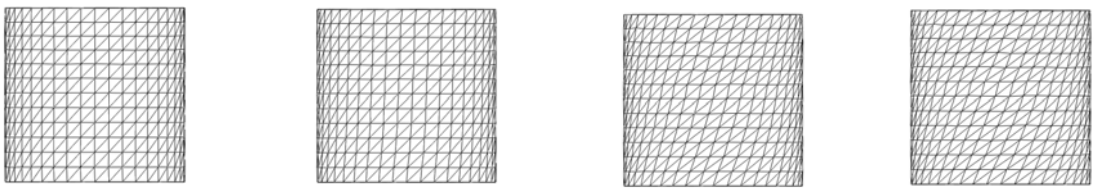

Fig 5. Torsional deformation pattern, showing the effectiveness of 2mm thin disks to establish uniform shear deformation. (maximum twist = 45 ^{o})

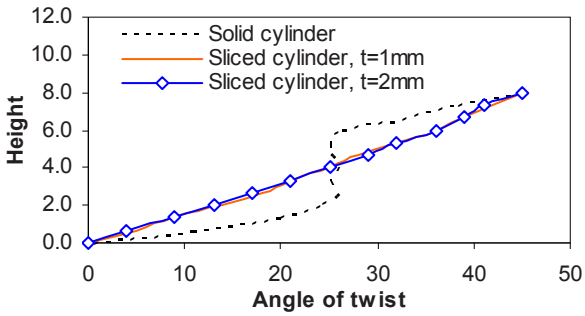

Fig 6: Angle of twist variation along the height of the specimen. A nearly linear variation is achieved by minimizing friction using thin cylindrical disks

To ensure effective torque transmition to the sample, without any slip at the top or bottom faces of the specimen, superglue compatible with polymers and rubbery materials is used for adhering samples securely to the steel interfaces at the loading zones. After each test, the glued interfaces are checked for defects or tear. For a benchmark, the constitutive shear response of polyurea at zero hydrostatic pressure is obtained by twisting some specimens without using the confining disks. This test is referred to in the following as “the simple shear test”.
The FE analysis illustrates that replacing the solid cylinder with a stack of 2mm thick cylindrical disks minimizes the effect of friction and provide results with acceptable accuracy. Although thinner disks would provide better performance, the 2mm thickness is limited by the availability of strain gages that are small enough to be fitted on the outside surface of a disc. The smallest strain gage made by Vishay Micromeasurements is used in this study; however strain gages are trimmed down to fit on the 2mm thick cylinders. Trimming of strain gages could lead to strain gage delamination which promotes erroneous strain readings. An engineering representative of Vishay was consulted on the issue. According to his recommendation, the area surrounded by the alignment signs imprinted on the gage is not compromised by cutting or trimming (see Fig. 7).

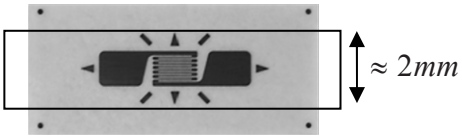

Fig. 7 Strain gage used in the experiment, showing the critical perimeter.

MATERIALS AND SPECIMENS

Functionality of the setup requires the specimens to closely fit the inner diameter of the confining cylinder. Any substantial gap at the specimen-cylinder interface would complicate data reduction and analysis. Rate and temperature sensitivity as well as the high compliance of polyurea makes machining of samples to within acceptable tolerances by turning on a lathe impractical. Accordingly, samples are cast to size. Casting is accomplished in Teflon molds since polyurea does not adhere well to Teflon. Short rods of 3" length are obtained from the molds. Rods are then cut into samples of proper length. Occasionally, some rods are sized on a lathe with the help of sand paper.

Isocynate under the commercial brand Isonate 134L from Dow Chemicals mixed with the curative Versalink P1000 from Airproducts provide the polyurea samples. A 4 to 1 ratio, curative to Isocyante by weight is used. Mixing and casting are accomplished in a custom built dry box In which the moisture content is controlled by silica gel. Upon introducing the silica gel, a waiting period of 30 minutes is required before the moisture content in the dry box drops to 8%.

The curative, Versalink P1000, is heated to 60 C and is allowed to cool to 45 C before mixing. At 45 C the curative looses much of its viscosity which reduces the air-bubble content in the cast Polyurea. After casting, Teflon molds are placed in a desiccator, which is then evacuated to force air-bubbles out of the cast products to the point that they are nearly not visible by the unaided eye.

EXPERIMENTAL RESULTS

Uniaxial compressive response of polyurea, as reported in [10], exhibits a nonlinear, inelastic stress-strain response. In reference [10] two types of ployurea were studied namely cast and sprayed Polyurea. Significant differences were reported for these two materials. Cast polyurea exhibits softer response and deforms under low stress levels to large strain levels; it does not exhibit any stiffening at large strains. The sensitivity of polyurea's constitutive response to the manufacturing process highlights the need to first characterize whether the polyurea prepared in this work would exhibit the same response as the cast polyurea tested in [10].

1) Simple shear response of Polyurea

Shear stress-strain response of polyurea, prepared for this work, exhibits a monotonically increasing response as shown in Fig 8. For the range of strains used in this figure, the initial part of the stress-strain response may be fitted with a linear function with a slope of 21 MPa. During the deformation history the stress maintains a monotonically increasing trend and does not exceed 2 MPa. This shear response is in good agreement with the shear response for cast polyurea reported in [10], which was determined using an Arcan apparatus and the compression confined test, Fig. 1-A. However, comparison is limited to 0.1 strain, the limit of the data reported in [10]

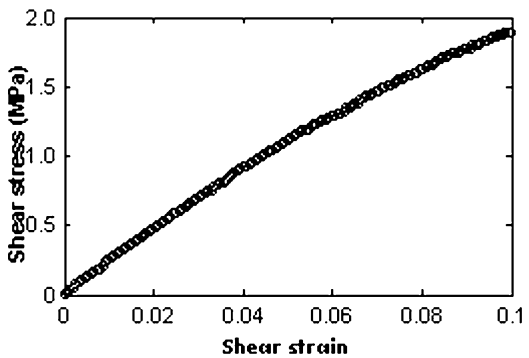

Fig. 8: Torsional shear response of Polyurea.

2) Confined response of Polyurea

Using the modified confined compression test configuration we obtain the multiaxial stress-strain response of polyurea. Fig 9-A shows the variation of the axial and radial stresses with axial strain. Both axial and radial stresses evolve in a similar manner. Compression stresses as high as 160MPa are achieved using the confined test. The initial nonlinear behavior is mostly related to minor imperfections in the specimen's geometry. The incompressibility of the fabricated cast polyurea is shown in Fig 9-A. The state of stress throughout the deformation history is close to hydrostatic compression. The three principal stress, axial, radial and hoop stresses are almost identical, which results in a very small value of effective stress. The bulk response is presented in Fig.9-B. Although the major portion of the bulk response, disallowing the initial adjustment of the specimen to the cylinder cavity, can be fitted with a linear response employing a bulk modulus of 2300 MPa, the response can also be fitted with the Tait equation (7) using B=212 and C=0.09 as fitting parameters.

$$\sigma_{kk} = B\left(\exp\left(\varepsilon_{kk}/C\right)-1\right) \tag{7}$$

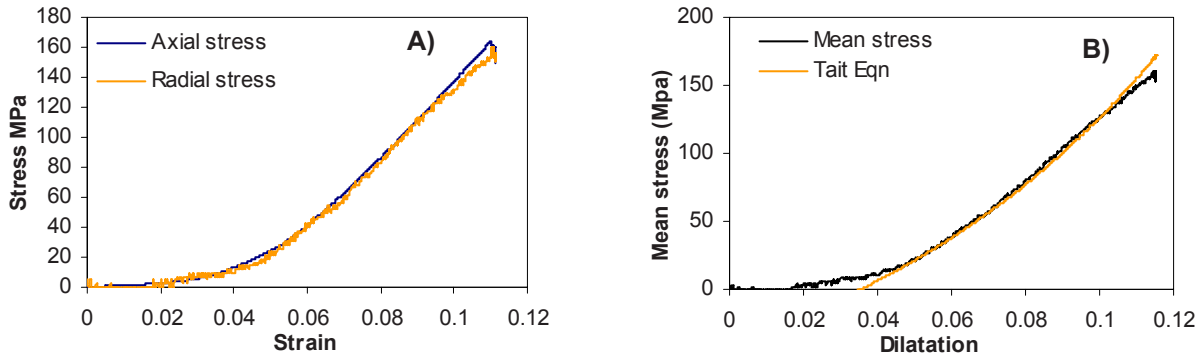

Fig. 9: Bulk confined response of polyurea, showing A) the evolution of the axial and radial stresses during compression, B) fitting the bulk response with the Tait equation.

The high incompressibility of polyurea and its deformability under small shear loads, combined with the ability of fitting the bulk response with the Tait equation are reminiscent of fluid-like behavior [10]. On the other hand, as illustrated in [10], porous Polyurea samples fabricated by the spraying technique do not exhibit a fluid-like behavior and have an effective shear response maximum value which approaches 6 times the shear stiffness of cast polyurea.

The confined multiaxial response of our samples exhibits virtual incompressibility, small and limited effective shear stiffness. In addition, the bulk response fits the Tait equation well. The aforementioned fits and trends are in good agreement with those established in [10]. We have established that our samples possess a porosity of about 1% and assume that the material examined in [10] possessed a similar porosity which we deem negligible and below the threshold for causing a significant effect on the polyurea's macroscopic response, a t least within the range of precision underlying our measurements.

It is essential to maintain a constant mean compression stress while applying the twisting deformation. The viscoelastic nature of polyurea would cause stress relaxation. The rate of stress relaxation driven by the bulk-intrinsic time dependent response of the polyurea is relatively small, but in tests lasting long the total drop in compression could be significant. Thus, maintaining a constant compression was accomplished by either introducing further axial compression during the imposed twisting deformation or by introducing a wait period before applying the twisting deformation. A waiting period of 3000 seconds was found to be sufficient for the compression and shear (twist) stresses to remain at a constant value to within 3.4%.

3) Shear response of polyurea, using the new confined test configuration.

Results from tests performed on polyurea samples at a strain rate of $1\text{x}10^{-5}$ s^{-1} are included in this section. A sampling rate of 100 points per second was used. The experimental data were first fitted with a Prony series of 20 terms. This large number of terms allows fits with an r^2 value above 0.99. Fig 10–A shows both the data and the fitted curve for the shear response at 40 MPa compression. All measurements are reduced in similar manner. Each test run is divided into three steps: The specimen is compressed axially first as in the regular confined

compression setup, and is then followed by a waiting period of 3000 seconds to allow all stresses to relax to a nearly constant value. Thereafter the torsional loading is applied at a constant rotation rate of 10^{-3} degree/sec. Fits representing measurements performed at pressures of 37, 71, 76, and 100 MPa are included in Fig 10-B. One observes that pressure is an influential parameter with the ability to amplify the shear stiffness of polyurea. For strains around of about 0.1, pressure is seen to increase the shear stiffness about 50% for a pressure of 100 MPa.

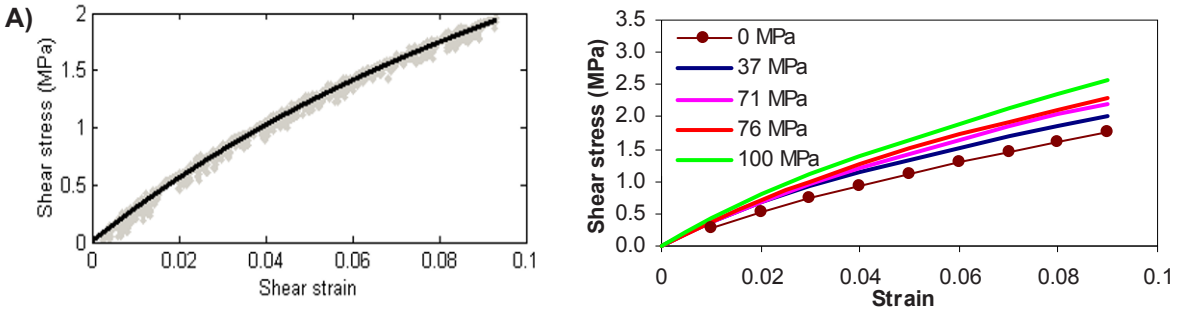

Fig. 10: Confined shear response of Polyurea, using 2mm thin cylindrical disks.

CONCLUSIONS

The development and evaluation of a new confined compression experimental design has been presented. The new design is intended for the determination of the shear constitutive behavior in the presence of significant pressure for this nearly incompressible viscoelastic material. The new design allows for applying uniform shear loading such that it is essentially independent of the applied pressure.

The multiaxial compressive behavior of cast polyurea has been investigated. Results illustrate soft shear response and limited shear stiffness of polyurea. The bulk response was observed to be nonlinear as represented by the Tait equation (which also represents the compressibility of sea water). To the extent that we simulate the measurements of the constitutive behavior for the cast polyurea we agree with the results published in [10].

Sufficiently high pressures superposed on shear deformations clearly have a significant influence on the shear response. The shear stiffness increases monotonically with increasing pressure for the pressure range investigated here. The enhancement in shear stiffness can be seen to be consistent with free volume arguments; negative dilatation associated with pressure reduces the free volume content and restricts the mobility of chain molecules, analogous to effect which temperature reduction has on the time-response of polymers. However, more light will be shed on this particular issue in our future work.

AKNOWLEGEMENT

The authors wish to thank Dr. Roshdy Barsoum of the Office of Naval Research through his guidance and cooperation and for the sustained support of this difficult effort under Grant ONR N000 14-09-1-0552.

REFERENCES

[1] Lee, g., Mock, W., Feddrly, J., Drotar, J., Balizer, E., Conner, M., “The effect of mechanical deformation on the glass transition temperature of polyurea.” Schok Compression of Condensed Matter, CP955,(2007).

[2] Amini, M., Issacs, J., Nemat-Nasser, S.,“ Effect of Polyurea on the dynamic response of steel plates.” Proceedings of the 2006 SEM annual conference and exposition on experimental and applied mechanics. St, Louis, MO, (2006).

[3]Bahei-El-Din, Y., Dvorak, G., Fredricksen, O.,“ A blast-tolerant sandwich plate design with a polyurea interlayer.” Int. J. of Solids and Structrues, 43, 7644-7658, (2006)

[4]Losi., G., Knauss, W., “Free Volume Theory and Nonlinear Thermoviscoelasticity.” Polymer engineering and science, Vol 32, 8. (1992)

[5]Tschoegel, N., Knauss, W., Emri, I., “The effect of temperature and pressure on the mechanical properties of themo- and/or Piezorheologically simple polymeric materials in thermodynamic equilibrium- A critical review.” Mechanics of Time-Dependent Materials, 6, 53-99, (2002).

[6] Jiao, T., Clifton, R., Grunschel, S., “ Pressure-sensitivity and tensile strength of an elastomer at high strain rates.” Shock compression of condensed matter. CP955, (2007).

[7] Amirkhize, A., Isaacs, Mcgee, J., Nemat-Nasser, S., “An experimentally-based viscoelastic constitutive model for Polyurea, including pressure and temperature effects. Philosophical magazine, Vol 86, 36, 5847-5866,(2006).
[8] Ma, Z., Ravi-Chandar, K.,” Confined compression: A stable homogeneous deformation for constitutive characterization.” SEM, Vol 40, 1,(2000).
[9] Qvale, D., Ravi-Chandar K., “Viscoelastic characterization of polymers under multiaxial compression.” Mechanics of time-dependent materials, 8, 193-214, (2004).
[10] Chakkarapani, V., Ravi-Chandar, K., Liechti, K., “Characterization of multiaxial constitutive properties of rubbery polymers.” Journal of engineering materials and technology, vol 128, 489-494, (2006).
[11] Zhao, J., Knauss, W., Ravichandran, G., “ Applicability of the time-temperature superposition principle in modeling dynamic response of Polyurea.” Mechanics of Time dependent materials, 11:289-308, (2007).

Proceedings of the SEM Annual Conference
June 7-10, 2010 Indianapolis, Indiana USA

Micromechanics models for predicting tensile properties of latex paint films

Eric W. S. Hagan[1,2], Maria N. Charalambides[2], Christina R. T. Young[3], Thomas J. S. Learner[4], Stephen Hackney[2]
[1] Tate, London, UK
[2] Mechanical Engineering Department, Imperial College London, London SW8 2AZ, m.charalambides@imperial.ac.uk.
[3] Courtauld Institute of Art, London, UK
[4] Getty Conservation Institute, Los Angeles, CA

ABSTRACT

The mechanical properties of latex paint films containing different volume fractions of TiO_2, $CaCO_3$ and kaolin were measured in uniaxial tension over a broad range of temperatures and crosshead speeds. Young's modulus results in the glassy region are first compared with several micromechanics theories for particle-filled composites containing elastic phases. It was found that the Mori-Tanaka theory [1, 2] slightly under-predicted the modulus enhancement, while the Lielens approach [3, 4] provided very accurate results. A nonlinear viscoelastic material model involving a Prony series and the neo-Hookean hyperelastic function was used to represent the tensile data up to relatively small strains (3-4%). Using the experimental data, the material model was calibrated and the parameters of the model were determined. The derived parameters were then used to re-construct time dependent shear modulus plots which were compared with the approximations given by Clements and Mas [5, 6] for the viscoelastic Mori-Tanaka theory in the time-domain. It was found that the experimentally observed modulus enhancement was much stronger than the predicted values in the rubbery region. This is attributed to the small particle size, the high level of constraint posed on the latex matrix at the particle interface or possibly the formation of a particle network.

INTRODUCTION

Latex coatings are extremely common in commercial, household and art-related fields; however, information pertaining to their mechanical properties is relatively sparse in literature. Mecklenburg and coworkers [7, 8] have studied the effects of temperature and moisture content on the properties of artists' acrylic (latex) paints using low strain rates in uniaxial tension. Hagan and Murray [9] performed similar work on artist paints, while considering additional factors such as age and aqueous cleaning treatments. For industrial coatings, Oosterhof [10] and Bondy and Coleman [11] investigated the effects of several formulation variables on the tensile properties of latex films after a short period of coalescence. One of the primary areas missing in this body of literature is a detailed analysis of the relaxation behaviour of latex films. This topic was addressed recently [12] for paint films containing TiO_2 particles, and nonlinear viscoelastic models were presented for the materials at different pigment volume fractions. In this paper, paints containing other types of inorganic particles are added to the investigation to allow an extensive review of the tensile results with respect to their agreement with micromechanics theories for composite materials.

Latex paints are mixtures of many different materials including binder resin, pigment and a variety of additives. The binder resin itself contains a high molecular-weight copolymer that is dispersed in water with surfactant to form micelles. As a dry film, a latex paint exhibits highly strain-rate dependent mechanical properties due to three main factors: (1) the glass-transition temperature is slightly below ambient temperature; (2) the molecular weight is very high; and (3) very little cross-linking is present. Inorganic particles are commonly used to alter the optical and mechanical properties of the dried films, with one of the

T. Proulx (ed.), *Time Dependent Constitutive Behavior and Fracture/Failure Processes, Volume 3*, Conference Proceedings of the Society for Experimental Mechanics Series 15, DOI 10.1007/978-1-4419-9794-4_41, © The Society for Experimental Mechanics, Inc. 2011

most common colourants being titanium dioxide (TiO_2). The importance of this white pigment is owed to its low toxicity and high refractive index. White particles with low refractive indices such as calcium carbonate ($CaCO_3$) and kaolin are frequently used as pigment extenders and fillers. These 'fillers' are commonly found with TiO_2 in artists' ground (basecoat) formulations.

MICROMECHANICS MODELS

Numerous analytical models are available in the literature to describe the Young's modulus enhancement, E^*/E^m, in particle-filled composites when each phase is elastic. Two well-known theories are the self-consistent model originally developed by Hill [13], and Mori-Tanaka [14] equations modified for composites by Tandon and Weng [1, 2]. These predictions rely on the concept of average strain in each phase and incorporate Eshelby's tensor, $\mathbf{E}$ [15, 16]. Lielens [4] proposed a modified theory for improved accuracy at high filler fractions after noting that the Mori-Tanaka theory under-predicts modulus enhancement in this region. A brief overview of the equations that define some micromechanics models is provided below. Superscripts *, *f*, and *m* are used to denote composite, filler and matrix respectively[1].

Considering the average strain in each phase, the general relationship for determining the stiffness tensor of a composite is given by Tucker and Liang [3] as

$$\mathbf{C}^* = \mathbf{C}^m + c^f\left(\mathbf{C}^f - \mathbf{C}^m\right)\mathbf{A} \tag{1}$$

where

$$\mathbf{A} = \hat{\mathbf{A}}\left[\left(1-c^f\right)\mathbf{I} + c^f\hat{\mathbf{A}}\right]^{-1} \tag{2}$$

The calculation in Equation (1) depends on the stiffness tensor of the matrix and filler ($\mathbf{C^f}$, $\mathbf{C^m}$), the filler volume fraction (c^f), and the strain enhancement tensors ($\mathbf{A}$, $\hat{\mathbf{A}}$). These strain enhancement tensors are defined by the ratios:

$$\begin{aligned}\hat{\mathbf{A}} &= \bar{\varepsilon}^f/\bar{\varepsilon}^m \\ \mathbf{A} &= \bar{\varepsilon}^f/\bar{\varepsilon}\end{aligned} \tag{3}$$

where $\bar{\varepsilon}^f$, $\bar{\varepsilon}^m$, $\bar{\varepsilon}$ are the average strains in the filler, matrix and composite respectively.

In the Mori-Tanaka method, Equations (1) and (2) are solved according to:

$$\hat{\mathbf{A}} = \left[\mathbf{I} + \mathbf{E}\mathbf{S}^m\left(\mathbf{C}^f - \mathbf{C}^m\right)\right]^{-1} \tag{4}$$

where $\mathbf{I}$, $\mathbf{E}$, and $\mathbf{S^m}$ are the unity matrix, Eshelby tensor, and compliance tensor ($\mathbf{S}=\mathbf{C}^{-1}$) respectively. The components of the Eshelby's tensor, $\mathbf{E}$, are functions of the matrix Poisson's ratio, ν^m, and the aspect ratio, β, of spheroidal inclusions. The aspect ratio is defined here as the length along the major axis of a spheroid divided by the diameter along the minor axis.

The Lielens [3, 4] approach involves first determining the upper and lower bounds for $\hat{\mathbf{A}}$ by using the filler and matrix as the reference material in Eshelby's tensor. This gives:

$$\begin{aligned}\hat{\mathbf{A}}^{upper} &= \left[\mathbf{I} + \mathbf{E}^f\mathbf{S}^f\left(\mathbf{C}^m - \mathbf{C}^f\right)\right] \\ \hat{\mathbf{A}}^{lower} &= \left[\mathbf{I} + \mathbf{E}^m\mathbf{S}^m\left(\mathbf{C}^f - \mathbf{C}^m\right)\right]^{-1}\end{aligned} \tag{5}$$

from which $\hat{\mathbf{A}}$ is interpolated between the bounds as

$$\hat{\mathbf{A}} = \left\{\left(1-f_L\right)\left[\hat{\mathbf{A}}^{lower}\right]^{-1} + f_L\left[\hat{\mathbf{A}}^{upper}\right]^{-1}\right\}^{-1} \tag{6}$$

with $f_L = \dfrac{c^f + (c^f)^2}{2}$. (7)

Van Es [17] gives composite moduli expressions resulting from a randomising method:

[1] Note that the term 'filler' here is used in the general context of micromechanics theory; it does not imply additives used in less costly coatings.

$$E^*_{2D} = 0.375E_{11} + 0.625E_{22} \quad \text{(fibre, random orientation in-plane only)}$$
$$E^*_{3D} = 0.184E_{11} + 0.816E_{22} \quad \text{(fibre, 3D random orientation)} \tag{8}$$
$$E^*_{3D} = 0.49E_{11} + 0.51E_{22} \quad \text{(disc, 3D random orientation)}$$

for fibre (β>1) and disc (β<1) shaped particles. E_{11} and E_{22} are the longitudinal and transverse Young's moduli respectively and they can be calculated from any of the micromechanics models outlined previously in this section.

Two semi-empirical methods commonly used for predicting the modulii of particle-filled composites are the Halpin-Tsai [18, 19] and Nielsen equations [20]. The Halpin-Tsai method is:

$$\frac{E^*}{E^m} = \frac{1+\left(\dfrac{E^f/E^m - 1}{E^f/E^m + \zeta}\right)\zeta c^f}{1-\left(\dfrac{E^f/E^m - 1}{E^f/E^m + \zeta}\right)c^f} \tag{9}$$

The shape factor parameter, ζ, accounts for the geometry of the filler and has a value of ζ=2 for spherical particles. The approach offered by Nielsen [20] is different in that the maximum packing fraction, ϕ_{max}, of the filler particles is taken into consideration. The Young's modulus enhancement is then given by:

$$\frac{E^*}{E^m} = \frac{1+(k_E - 1)\eta c^f}{1-\eta\psi c^f} \tag{10}$$

with η and ψ defined as:

$$\eta = \frac{E^f/E^m - 1}{E^f/E^m + k_E - 1}$$
$$\psi = 1 + \left(\frac{1-\phi_{\max}}{\phi_{\max}^{\,2}}\right)c^f$$

The Einstein coefficient, k_E, has a value of 2.5 for an incompressible matrix (ν^m=0.5), and its value drops to k_E=2.17 for ν^m=0.35 [21]. For hexagonal, close-packed, spheres the maximum packing fraction is ϕ_{max}=0.74 [21].

MATERIALS AND METHODS

Latex formulations based on a poly(butyl acrylate-co-methyl methacrylate) (BA/MMA) binder were provided by an artist paint manufacturer (Golden Artist Colors). Experiments with differential scanning calorimetry (DSC) showed the binder and all paint films to have a glass transition (T_g) at approximately 10˚C. The custom materials included a latex gel with no inorganic particles present, and the same latex with high concentrations of TiO_2 (rutile), $CaCO_3$ (aragonite), and kaolin (calcined) individually. The three formulations with inorganic particles were diluted with additional latex gel in order to provide several volume fractions in the dried films. The volume fractions of the inorganic particles resulting in the dried films were as follows:

a. 0.06, 0.13, 0.20, 0.25, 0.32, and 0.38 TiO_2
b. 0.07, 0.14, 0.22, and 0.28 kaolin
c. 0.08, 0.16, 0.24, 0.30, and 0.38 $CaCO_3$

The paints were prepared on thin polyester sheets using parallel tape layers to control thickness, and this was performed one year in advance of testing to provide well-coalesced films. The substrate was removed from the films one day prior to testing and specimens were cut to rectangular dimensions of 60mm x 6mm. The dry films had a thickness in the range of 0.12-0.2 mm. The fully prepared specimens were placed overnight in small enclosures with silica gel buffering at 50% relative humidity (RH) to control equilibrium moisture content.

Tensile tests were performed with an Instron (model 4301) universal testing machine fitted with a custom-built environmental enclosure [22] and a 100N load cell. Experiments were performed at five temperatures (-10, 0, 10, 20, and 30˚C), and relative humidity was controlled at 50% for T≥10˚C. The tests were performed along the casting direction at constant crosshead speeds of 0.05, 0.5, 5, and 50mm/min for each temperature.

Some tests were conducted along as well as across the casting direction in order to estimate the orientation of the particles within the paint films.

In order to compare modulus data with micromechanics theories it is necessary to determine the aspect ratio, β, of the inorganic particles being added to the polymer matrix and the elastic properties of each phase. Figure 1 shows scanning electron microscopy (SEM) images of each inorganic material used in this study. The TiO_2 particles are nearly spherical with a nominal diameter of ~300 nm. The image of kaolin shows a wide particle size distribution with an aspect ratio of the larger particles estimated as $\beta \approx 0.1$. Calcium carbonate (aragonite) fibres in Figure 1c have an aspect ratio of approximately four.

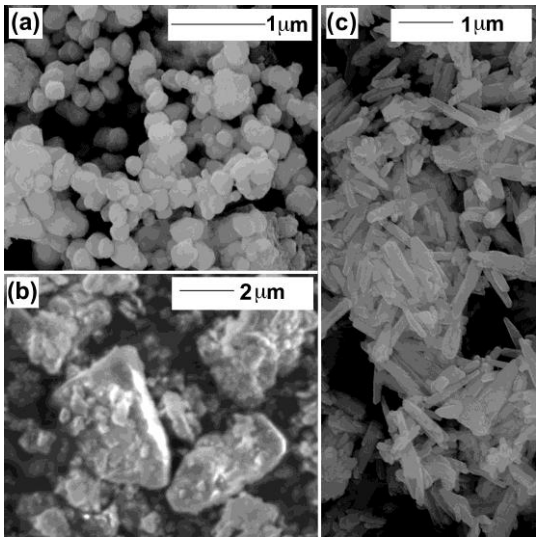

Figure 1. Scanning electron images of inorganic particles added to the latex paint binder: a. TiO_2 (rutile); b. kaolin (calcined); c. $CaCO_3$ (aragonite).

The mechanical properties of the three fillers were obtained from literature [23, 24] and are shown in Table 1 The Poisson's ratio of the matrix, ν_m, was assumed to be 0.35 in the glassy region [25] and 0.5 (incompressible) in the rubbery region.

Material	*K* (GPa)	μ (GPa)	*E* (GPa)	ν
TiO_2 [1]	216	112	287	0.278
$CaCO_3$ [1] (aragonite)	46.9	38.5	91	0.178
Kaolinite (poorly crystallised) [2]	45.2	22.1	57	0.290
BA/MMA Latex (5mm/min, 10˚C)	1.66	0.53	1.44	0.35

Table 1. Values of *K* and μ for white minerals from [1]Bass [24] and [2]Wang et al [23] with *E* and ν calculated assuming isotropy. Measured Young's modulus for the latex in the glassy region given at -10˚C, 5mm/min with other constants calculated assuming ν^m=0.35.

MODULUS ENHANCEMENT IN THE GLASSY REGION

Figure 2a shows all modulus data collected at 5mm/min, -10˚C. In fig 2b, the TiO_2 data are compared with several theories applicable to spherical particles embedded in an elastic matrix. The Mori-Tanaka curve is slightly lower than the experimental values at moderate to high volume fractions, while the Halpin-Tsai equation is slightly high overall. The best fits for these data are observed by the Lielens model and the Nielsen equation, using a maximum packing fraction of ϕ_{max}=0.74 for the latter.

The Lielens model is also compared to data from the films with kaolin and $CaCO_3$ since it can be used with non-spherical particles. Figure 2c shows data from the latex films containing $CaCO_3$ plotted with the theory for unidirectional aligned particles, 2D random alignment, and 3D random alignment (Equation 8). It is obvious

that the transverse data agree very well with the E_{22} values whereas the longitudinal data agree reasonably well with the 2D random orientation predictions. This suggests that the particles are 2D randomised within a plane through the film thickness and longitudinal axes. The short $CaCO_3$ fibers possibly became aligned when the wet paint was dragged in the longitudinal direction and then tilted in the thickness direction as the film dried.

The results for the latex with kaolin particles in Figure 2d are more difficult to interpret since a large particle size and shape distribution was observed in the SEM images, and it was only possible to estimate the aspect ratio of the larger particles. It does however seem that the particles are primarily 3D randomized and the aspect ratio estimate is widely applicable to the distribution of particles. This theory holds since the curve for the 3D random particles fits through the data points for the films tested in the *long* and *trans* directions.

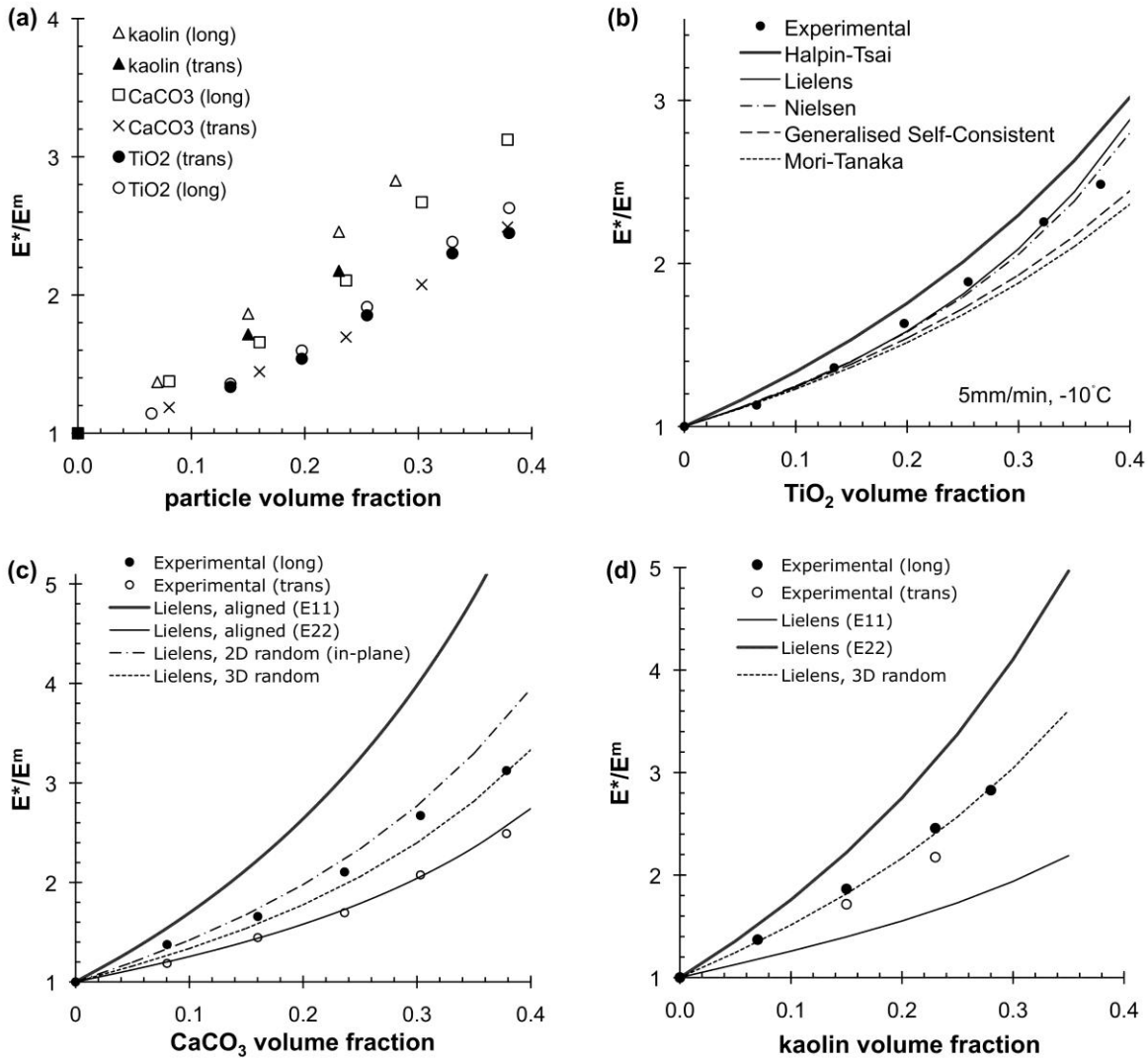

Figure 2. Comparison of experimental and theoretical Young's modulus enhancement in the glassy region using data at 5mm/min, -10˚C: a. Experimental data for three particle types; b. TiO_2 data and various micromechanics models; c. $CaCO_3$ data and Lielens theory; d. kaolin data and Lielens theory.

MODULUS ENHANCEMENT IN THE GLASS TRANSITION REGION

Tensile data are shown in Figure 3 for the films with 25% TiO_2 by volume to illustrate their time-dependent nature. The full set of data for the rest of the films can be found in [22]. A viscoelastic material model is presented for the stress-strain data using a neo-Hookean hyperelastic function in combination with a Prony series for the strain range of $0 \leq \varepsilon \leq 0.02$. The method employed is similar to that used in [12], where the Ogden

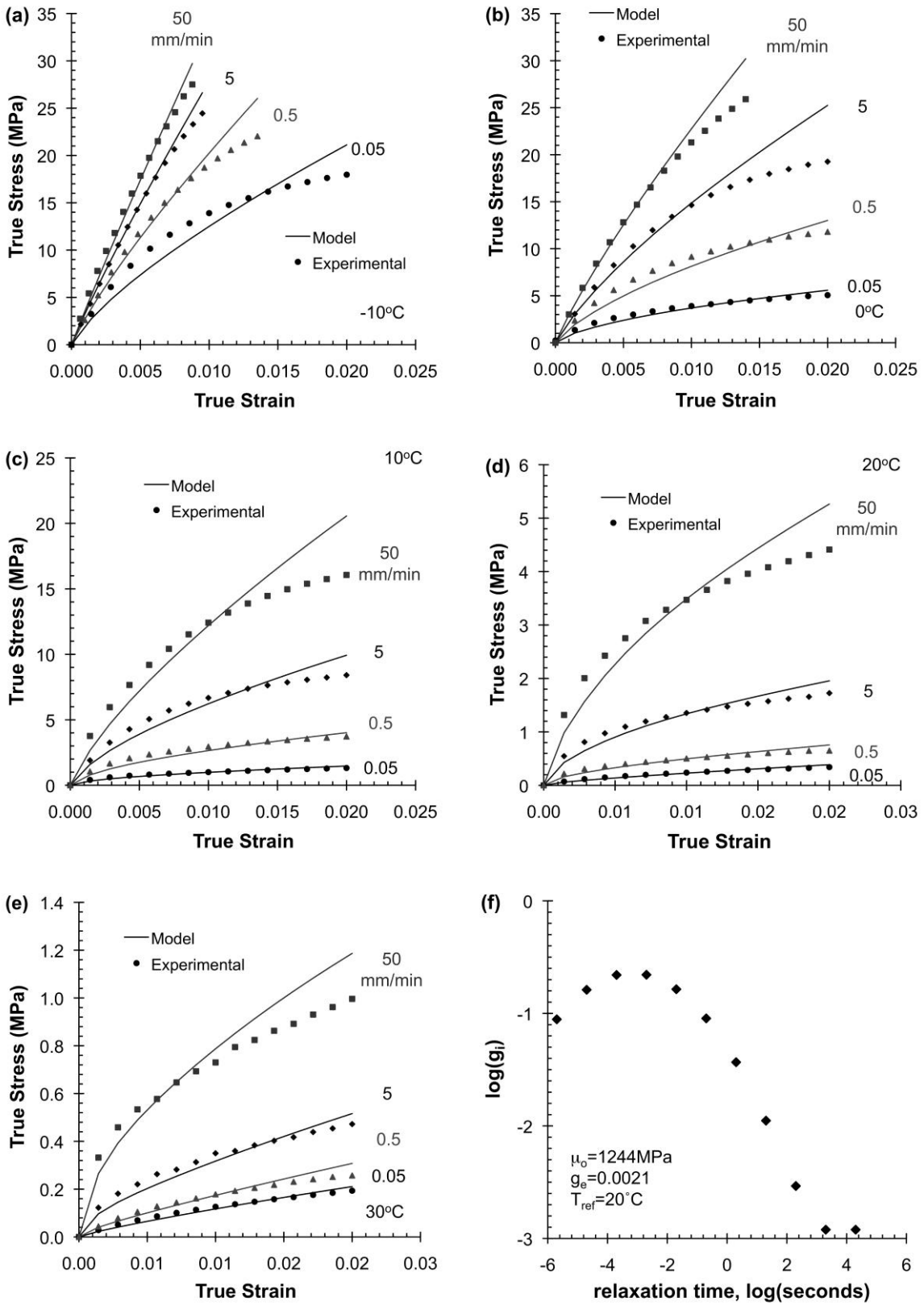

Figure 3. Stress-strain data and Neo-Hookean model for the BA/MMA latex with 25% TiO_2 at four crosshead speeds and five temperatures: a. -10˚C; b. 0˚C; c. 10˚C; d. 20˚C; e. 30˚C; f. Prony series.

model was combined with a Prony series to predict the tensile curves at large strains. The time-dependent true stress for an arbitrary loading history is given by the Leaderman form of the convolution integral [26, 27]:

$$\sigma_o(\lambda,t) = \int_0^t g(t-s)\frac{d\sigma_o(\lambda)}{ds}ds \tag{11}$$

where the instantaneous uni-axial stress-stretch relationship is given as:

$$\sigma_o(\lambda) = \mu_o\left(\lambda^2 - 1/\lambda\right) \tag{12}$$

for the neo-Hookean hyperelastic function. The stretch ratio, λ, is related to true strain by λ=exp(ε) and μ_0 is the initial shear modulus.

The time dependent function $g(t)$ is represented by the Prony series:

$$g(t) = g_e + \sum_{i=1}^{N} g_i \exp(-t/\tau_i) \tag{13}$$

where g_e and g_i are the relative weights of the equilibrium and i^{th} elements respectively (g_e=μ_e/μ_o, and g_i=μ_i/μ_o, with μ_o being the instantaneous shear modulus) and N is the number of elements in the series. Also note that:

$$g_e + \sum_{i=1}^{N} g_i = 1$$

In order to take into account the effect of the test temperature, the time-temperature superposition principle was used. The relaxation times at a given temperature are calculated from the shift factor, a_T, and the relaxation times, τ_i^{ref} , at a selected reference temperature, T_{ref}, according to:

$$\tau_i = a_T \tau_i^{ref} \tag{14}$$

The shift factor, a_T, values were determined experimentally by shifting plots of secant modulus versus initial strain rate obtained at different temperatures, until a smooth master curve was obtained [12].

A numerical approximation method based on the finite time increment formulation of the convolution integral in Equation 11 was employed [27] in order to derive an analytical expression for the stress at any time and corresponding strain. This allowed the model to be calibrated using the experimental data and the Excel Solver optimization tool. The best-fit material parameters are shown in Table 2 for all materials. The model fit can also be seen in Figure 6a-e for the 25% TiO_2 material. The agreement is reasonable considering that the model has to fit data obtained at very wide time scales and range of temperatures. Figure 6f shows the non-dimensional Prony series weights versus log(time) as a smooth bell-shaped curve. This was obtained by initially constraining the solver algorithm such that the g_i terms would fit to a Gaussian distribution function.

Element	Relax. Time	Latex Binder	13% TiO_2	25% TiO_2	38% TiO_2	16% $CaCO_3$	14% Kaolin	28% Kaolin
i	τ_i, s	g_i	g_i	g_i	g_i	g_i	g_i	g_i
1	2.E-06	1.09E-01	6.56E-02	8.86E-02	9.54E-02	6.07E-02	2.30E-01	1.23E-01
2	2.E-05	1.86E-01	1.42E-01	1.62E-01	1.66E-01	1.31E-01	2.22E-01	1.84E-01
3	2.E-04	2.35E-01	2.18E-01	2.20E-01	2.13E-01	2.05E-01	1.54E-01	2.14E-01
4	2.E-03	2.17E-01	2.38E-01	2.20E-01	2.02E-01	2.32E-01	1.54E-01	1.96E-01
5	2.E-02	1.47E-01	1.83E-01	1.64E-01	1.42E-01	1.90E-01	1.26E-01	1.41E-01
6	2.E-01	7.33E-02	9.99E-02	9.03E-02	7.32E-02	1.12E-01	6.76E-02	7.90E-02
7	2.E+00	2.68E-02	3.86E-02	3.68E-02	2.80E-02	4.79E-02	3.24E-02	3.48E-02
8	2.E+01	3.57E-03	1.06E-02	1.11E-02	2.05E-02	1.48E-02	8.84E-03	1.20E-02
9	2.E+02	1.49E-03	2.05E-03	2.93E-03	4.31E-03	3.30E-03	2.23E-03	3.25E-03
10	2.E+03	2.73E-04	5.41E-04	1.20E-03	4.07E-03	9.53E-04	5.55E-04	3.25E-03
11	2.E+04	2.73E-04	5.41E-04	1.20E-03	0.00E+00	9.53E-04	5.55E-04	3.25E-03
Equil.	-	7.11E-04	1.12E-03	2.09E-03	1.14E-02	1.17E-03	1.56E-03	6.27E-03
μ_o (MPa)		577	783	1244	1744	941	1254	1786

Table 2. Prony series and neo-Hookean parameters for the viscoelastic material models.

The micromechanics theory for a composite with elastic phases remains applicable for a viscoelastic matrix by means of the correspondence principle. Clements and Mas [5, 6] derived expressions for the bulk and

shear moduli of randomly oriented (and aligned) particle viscoelastic composites noting that $\mu^m(t) << K^m$ holds above the glass transition region. Their results for the bulk and shear time dependent moduli in the case of 3D random particle orientation are shown in Equations 15 and 16 respectively below:

$$K^*(t) = \frac{K^m K^f}{c^f K^m + c^m K^f} + \left[\frac{c^f c^m \left(K^f - K^m\right)^2 G^1}{9\left(c^f K^m + c^m K^f\right)^2} \right] \mu^m(t) \tag{15}$$

$$\mu(t) = \left(1 + \frac{4c^f}{5c^m} G_2\right) \mu^m(t) \tag{16}$$

where the parameters G_1 and G_2 are functions of the aspect ratio β. The function $\mu^m(t)$ is the time dependent shear modulus of the matrix, which can be defined by the Prony series (similar to the current work):

$$\mu^m(t) = \mu_o^m g^m(t) = \mu_o^m g_e + \sum_{i=1}^{N} \mu_o^m g_i^m \exp\left(-t/\tau_i\right) \tag{17}$$

Figure 4a shows several time-dependent shear modulus curves plotted from Equations 16 and 17. The curves were calculated by setting μ_o^m and g_i^m equal to the constants listed for the latex binder in Table 2. The time-dependent $\mu(t)$ curves are given versus log(time) for the various volume fractions of TiO_2. Figure 4b shows the shear time dependent modulus curves using the constants shown in Table 2 for each TiO_2 volume fraction; note that the latter constants were the values that resulted in the best fit of the viscoelastic model to the experimental data. There are obvious differences in Figures 4a and 4b, with the latter showing a much stronger enhancement at long times in the rubbery region. Therefore, the Clements and Mas theory can not be used to predict the composites behaviour in the region of high temperatures or long time scales.

A possible explanation for this discrepancy is that the small size of the TiO_2 particles results in a high specific surface area (surface area/volume) and the polymer becomes highly immobilised at the interface. In the glassy region, the entire matrix is constrained due to the decrease in free volume; therefore, less modulus gradient exists from the particle surface to the bulk polymer. Zosel [28] reported similar results from experiments on coatings with various polymer/pigment combinations. The modulus enhancement was within the expected range of values when tested below T_g; however, it became extremely strong in the rubbery region. Alternatively, the strong enhancement in the rubbery region could be due to the formation of a partcile network spanning through the sample geometry, leading to very strong particle interactions.

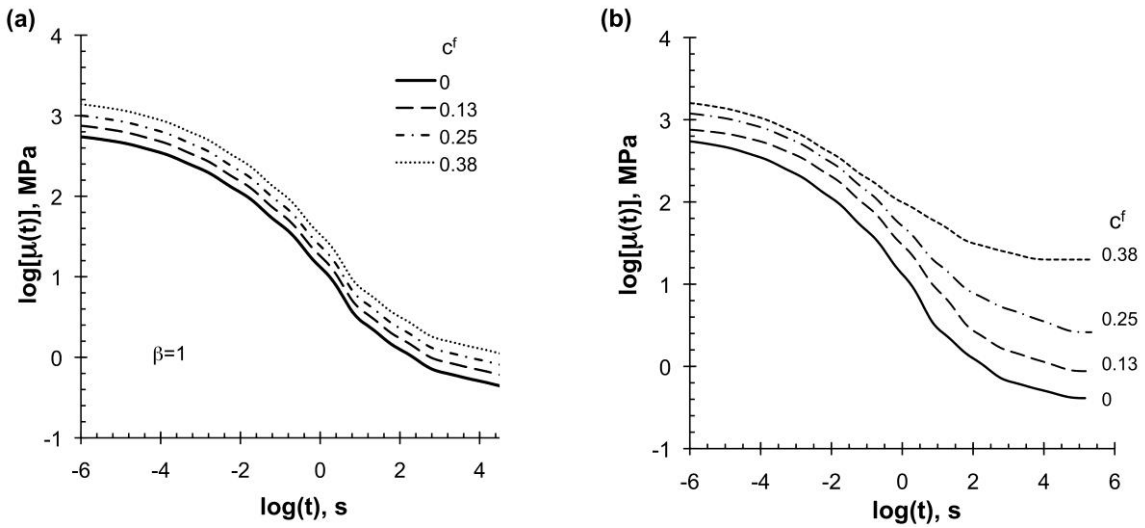

Figure 4. Shear time dependent modulus curves at T_{ref}=20˚C: a. Clements-Mas [5, 6] theory for a viscoelastic latex matrix (*q.v.* Table 2) filled with spherical TiO_2 particles (*q.v.* Table 1); b. Viscoelastic material model results using Table 2 values for films with TiO_2.

Shear time dependent modulus curves from the Clements-Mas theory (β=0.1) are shown with those calculated using the parameters in Table 2 for films with kaolin in Figure 5a and 5b respectively. A

comparison of the two graphs once again shows a stronger enhancement in the rubbery region than the micromechanics theory predicts. Curves for films containing TiO_2 and $CaCO_3$ are included in Figure 5b for comparison using the determined material parameters. It is interesting to note that the curves for 0.28 kaolin and 0.38 TiO_2 are very similar, and this is also true for 0.14 kaolin and 0.16 $CaCO_3$.

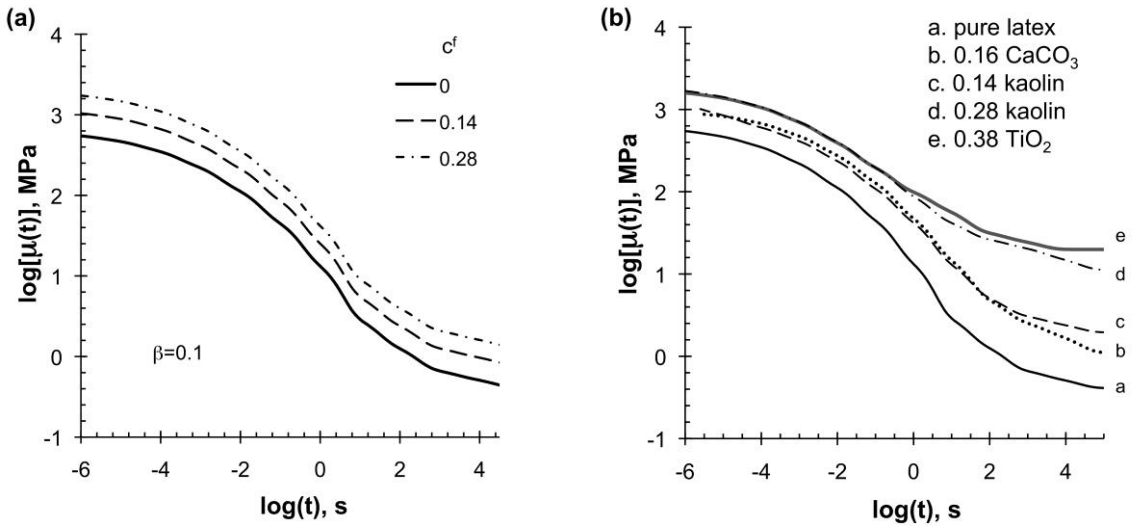

Figure 5. Shear time dependent modulus curves at T_{ref}=20˚C: a. Clements-Mas [5, 6] theory for a viscoelastic latex matrix (*q.v.* Table 2) filled with platelet kaolin particles having β=0.1 (*q.v.* Table 1); b. Viscoelastic material model results using Table 2 values for films with kaolin.

CONCLUSIONS

The effects of particle volume fraction and geometry were shown for the tensile behaviour of latex paint films. Young's modulus data in the glassy region showed good agreement with micromechanics theories, and the Lielens method was found especially accurate for films made with three different fillers. As expected, the lowest enhancement of Young's modulus was given by the TiO_2 particles since they were nearly spherical. Higher values were given by films with $CaCO_3$ when tested parallel to the casting direction; however, in the tranverse direction these films were similar to those containing TiO_2 as expected from micromechanics theories. The strongest enhancement was observed with films containing kaolin that were tested along the casting direction. Viscoelastic material models were fitted to tensile data in order to capture the response across the glass-transition region. The models fit well for low strains up to a relatively high volume fraction of 0.38 TiO_2. Time dependent shear modulus curves were plotted using the constants found from the viscoelastic model calibrations, and these were compared with the Clements-Mas equations for the Mori-Tanaka theory in the time-domain. The experimental results showed a much higher modulus in the rubbery region than predicted by the theoretical equations. This could be a result of the small particle size and the correspondingly high level of constraint posed on the polymer matrix, or possiblly a particle network formation.

ACKNOWLEDGEMENTS

The authors would like to thank the Deborah Loeb Brice Foundation and the Natural Sciences and Engineering Research Council of Canada (NSERC) for funding this project. We would also like to thank Golden Artist Colors for providing the custom paint formulations, and Brad Clements at Los Alamos National Laboratory for his advice at the onset of the project.

REFERENCES

1. Tandon, G.P. and G.J. Weng, *Average stress in the matrix and effective moduli of randomly oriented composites.* Composites science and technology, 1986. **27**: p. 111-132.
2. Tandon, G.P. and G.J. Weng, *The effect of aspect ratio of inclusions on the elastic properties of unidirectionally aligned composites.* Polymer Composites, 1984. **5**: p. 327-333.
3. Tucker, C.L.I. and E. Liang, *Stiffness predictions for unidirectional short-fiber composites: review and evaluation.* Composites science and technology, 1999. **59**: p. 655-671.

4. Lielens, G., P. Pirotte, A. Couniot, F. Dupret, and R. Keunings, *Prediction of thermo-mechanical properties for compression moulded composites.* Composites Part A, 1998. **29A**: p. 63-70.
5. Mas, E.M. and B.E. Clements, *Dynamic mechanical behaviour of filled polymers. II. Applications.* Journal of Applied Physics, 2001. **90**(11): p. 5535-5541.
6. Clements, B.E. and E.M. Mas, *Dynamic mechanical behaviour of filled polymers. I. Theoretical developments.* Journal of Applied Physics, 2001. **90**(11): p. 5522-5534.
7. Mecklenburg, M.F., C.S. Tumosa, and J.D. Erlebacher, *Mechanical behavior of artist's acrylic paints under equilibrium conditions.* Polymer Preprints, 1994. **35**(2): p. 297-298.
8. Erlebacher, J.D., M.F. Mecklenburg, and S.J. Tuman, *The mechanical properties of artists' acrylic paints with changing temperature and relative humidity.* Polymer Preprints, 1992. **33**(2): p. 646-647.
9. Hagan, E. and A. Murray, *Effects of water exposure on the mechanical properties of early artists' acrylic paints.* Materials Research Society Proceedings: Materials Issues in Art and Archaeology VII, 2005. **852**: p. 41-48.
10. Oosterhof, H.A., *Inherent properties of paint latex films in relation to their performance.* Journal of the Oil & Colour Chemists' Association, 1965. **48**: p. 256-279.
11. Bondy, C. and M.M. Coleman, *Film formation and film properties obtained with acrylic, styrene/acrylic, and vinyla acetate/VeoVa copolymer emulsions.* Journal of the Oil & Colour Chemists' Association, 1970. **53**: p. 555-577.
12. Hagan, E.W.S., M.N. Charalambides, C.R.T. Young, T.J.S. Learner, and S. Hackney, *Tensile properties of latex paint films with TiO2 pigment.* Mechanics of Time-Dependent Materials, 2009. **13**(2): p. 149-161.
13. Hill, R., *A self-consistent mechanics of composite materials.* Journal of the Mechanics and Physics of Solids, 1965. **13**(4): p. 213.
14. Mori, T. and K. Tanaka, *Average stress in matrix and average elastic energy of materials with misfitting inclusions.* Acta Metallurgica, 1973. **21**: p. 571-574.
15. Eshelby, J.D., *The elastic field outside an ellipsoidal inclusion.* Proceedings of the Royal Society of London. Series A, Mathematical and Physical Sciences, 1959. **252**(1271): p. 561-569.
16. Eshelby, J.D., *The determination of the elastic field of an ellipsoidal inclusion, and related problems.* Proceedings of the Royal Society of London. Series A, Mathematical and Physical Sciences, 1957. **241**(1226): p. 376-396.
17. van Es, M., *Polymer-clay nanocomposites: the importance of particle dimensions*, in *Polymer Materials and Engineering*. 2001, Delft University of Technology, PhD Thesis: Delft.
18. Halpin, J.C. and J.L. Kardos, *The Halpin-Tsai equations: a review.* Polymer Engineering and Science, 1976. **16**(5): p. 344-352.
19. Halpin, J.C., *Stiffness and expansion estimates for oriented short fiber composites.* Journal of Composite Materials, 1969. **3**: p. 732-735.
20. Nielsen, L.E., *Generalized equation for the elastic moduli of composite materials.* Journal of Applied Physics, 1970. **41**: p. 4626.
21. Nielsen, L.E. and R.F. Landel, *Mechanical Properties of Polymers and Composites*. 2nd ed. 1994, New York: Marcel Dekker.
22. Hagan, E.W.S., *The viscoelastic properties of latex artist paints*, in *Department of Mechanical Engineering*. 2009, Ph.D. thesis, Imperial College London: London, UK.
23. Wang, Z., H. Wang, and M.E. Cates, *Effective elastic properties of solid clays.* Geophysics, 2001. **66**(2): p. 428-440.
24. Bass, J.D., *Elasticity of Minerals, Glasses, and Melts*, in *Mineral Physics and Crystallography: A Handbook of Physical Constants*, T.J. Ahrens, Editor. 1995, American Geophysical Union: Washington, D.C. p. 45-63.
25. Tschoegl, N.W., W.G. Knauss, and I. Emri, *Poisson's ratio in linear viscoelasticity – a critical review.* Mechanics of Time-Dependent Materials, 2002. **6**(1): p. 41.
26. Leaderman, H., *Elastic and creep properties of filamentous materials and other high polymers*. 1943, Washington, D.C.: The Textile Foundation.
27. Goh, S.M., M.N. Charalambides, and J.G. Williams, *Determination of the constitutive constants of non-linear viscoelastic materials.* Mechanics of Time-Dependent Materials, 2004. **8**: p. 255-268.
28. Zosel, A., *Mechanical behaviour of coating films.* Progress in Organic Coatings, 1980. **8**: p. 47-79.

Proceedings of the SEM Annual Conference
June 7-10, 2010 Indianapolis, Indiana USA

Time Dependent Recovery of Shape Memory Polymers

F. Castro[1], K. K. Westbrook[1], J. Hermiller[2], D.U. Ahn[1], Y. Ding[1], H.J. Qi[1*]
[1]Department of Mechanical Engineering, University of Colorado, Boulder, CO 80309
(qih@colorado.edu)
[2]Cornerstone Research Group, Dayton, OH 45440

ABSTRACT Shape memory polymers (SMPs) are polymers that can recover the permanent shape from a temporary shape by external stimuli. In SMP applications, one of the major design considerations is the time necessary to recover the shape without external constraints, or free recovery rate. This paper investigates the free recovery behaviors of an epoxy-based SMP under shape memory (SM) cycles. We found that reshaping the sample at a low temperature and recovering from the deformation at a high temperature yields the fastest recovery rate whilst reshaping at a high temperature and recovering at a low temperature cannot recover the original shape within this work's experimental time frame. The possible mechanism for these observations is discussed.

1. INTRODUCTION

Shape memory polymers (SMPs) represent an important addition to the smart materials family. They can recover a permanent shape from a predetermined temporary shape after being exposed to an environmental stimulus, such as temperature, light or humidity [1-4]. The most commonly used SMPs are the ones responsive to temperature, called thermally activated SMPs (TASMPs, or thermally triggered SMPs). The SM behavior of TASMPs is due to the ability to store and release strain energy through material manipulation around a transition temperature. For an amorphous polymer-based SMP, this transition temperature is typically the glass transition temperature (T_g). The chain mobility of a TASMP changes drastically as the material changes between glassy and rubbery states. At the rubbery state (T>T_g), SMP molecules can relax toward equilibrium quickly; while at the glassy state (T<T_g) molecular relaxations toward equilibrium becomes extremely long. Detailed discussions on the SM mechanisms can be found in literatures [1, 3, 5, 6]. A typical SM cycle involves the following thermo-mechanical processes. First, the SMP sample is heated to a high temperature T_{H1} (typically close to or above its T_g) and then deformed. After the deformation is completed, the sample is cooled down to a temperature T_L (below T_g) while the external constraint is maintained. Subsequently, the constraint is removed and the sample retains the imposed deformation. The new shape is its temporary shape and the process of freezing this shape is called fixing. The SM effect is activated by increasing the temperature to a high temperature T_{H2} (typically close to or above the T_g). This procedure is called the recovery or deployment. There can be two types of recoveries: Constrained recovery is accomplished if the constraint is kept during the heating. If the constraint is removed before heating starts, a free recovery is achieved. In this paper, we are interested in the later. One of the most important considerations in designing SMPs' applications is their recovery characteristics. In the case of free recovery, a proposed parameter was to measure the material's ability to recover its original shape, i.e., the total strain recovery ratio[1]

$$R_{r,tot(N)} = \frac{\varepsilon_m - \varepsilon_{p(N)}}{\varepsilon_m}, \quad (1)$$

where ε_m is the applied strain and $\varepsilon_{p(N)}$ is the strain measured after the *N*-th SM cycles. $R_{r,tot(N)}$ quantifies the ability of a material to memorize its permanent shape after the *N*-th SM cycle. Studies performed on different SMPs [7, 8] used these parameters to evaluate and compare the effectiveness of recovery of new SMP materials. Another important design consideration of SMP is the time necessary to recover the shape, or free recovery rate. However, only limited work has been conducted on this aspect. Yakacki et al.[9] investigated the time dependent recovery of SMPs with the same rubbery modulus but different T_g. They also used the strain recovery rate to

T. Proulx (ed.), *Time Dependent Constitutive Behavior and Fracture/Failure Processes, Volume 3*, Conference Proceedings of the Society for Experimental Mechanics Series 15, DOI 10.1007/978-1-4419-9794-4_42, © The Society for Experimental Mechanics, Inc. 2011

quantify the response of SMPs that included magnetic particles [10]. Lendlein et al. [11] investigated the recovery as a function of temperature for different SMPs.

For any SMP, it is important to know how recovery rate can be influenced by thermal conditions. In this paper, we investigate recovery as a function of time and temperature. Experiments on the free recovery of an epoxy-based SMP under different thermal and mechanical conditions are performed in order to explore the time and temperature-dependent SM recovery behaviors. We also discusses future works for understanding free recovery rate of SMPs.

2. MATERIALS AND EXPERIMENTAL METHOD

An SMP material (Veriflex® E Epoxy-Based Shape Memory Polymer, VFE1-62) developed by Cornerstone Research Group Inc. (Dayton, OH) was used in this study. DMA and DSC experiments were performed to determine T_g. The T_g was determined to be 75°C and 52°C respectively. Recovery experiments were performed using a MTS Insight 10 universal testing machine together with a customized thermal chamber providing temperature control. The compression platens were modified to allow for fast temperature response [12] (Figure 1.). Teflon tapes were placed between the sample and the compression platens to reduce friction. Two reflective stripes were attached horizontally on the cylindrical samples to precisely determine the deformation or strain by a laser extensometer (model LE-05 by EIR). For all measurements, loading and unloading were performed at a strain rate of $0.01s^{-1}$.

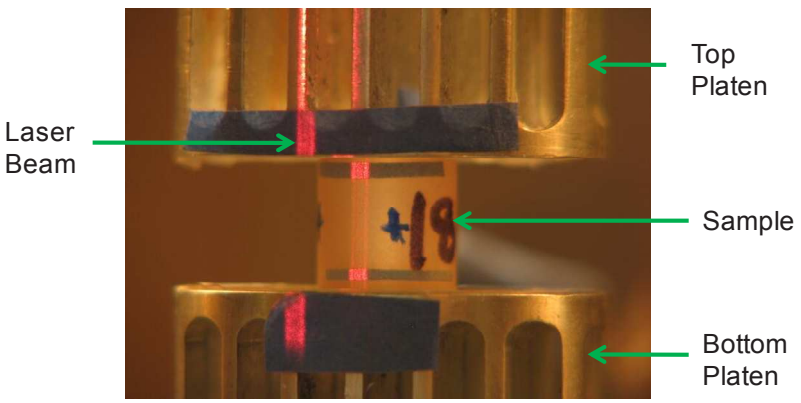

Figure 1. Experimental setups: Sample and compression platens.

For a SM cycle experiment and was conducted as the following: First, reshaping was achieved by compressing the sample to a strain of $\overline{e}$ at a high temperature T_{H1}, holding at that strain for a time period of t_1 =10 minutes (stress relaxation; in all the tested cases, stress reached a constant value in less than 10min (data not shown)), then cooling down to a low temperature T_L at a rate of 2.5°C/min. The sample stayed at the low temperature for a period of t_3 =60 minutes. Recovery was achieved by heating the sample to a high temperature T_{H2}. In most cases, heating rate was 2.5°C/min. A heating rate of 10°C/min was used for the case of heating rate comparison. The strain measurement continued for a period of t_5 after the end of heating. For the convenience of future discussions, we call T_{H1} "reshaping temperature" and T_{H2} "recovering temperature." T_{H1} and T_{H2} were varied around T_g. For all cases, the deformation level was 20% compressive strain and the temperature rate was 2.5°C/min for the cooling and heating steps. For these experiments, the reshaping steps were accomplished using a contact deformation extensometer (MTS, model 632.24F-50) to fix the displacement on the probe while the temperature was decreased.

During the experiments, the strain $\varepsilon(t)$ is calculated based on the instantaneous length. In order to quantify the ability of the material to recover its original shape, we define the recovery ratio as

$$R_{\text{Recovery}}(t) = \frac{\varepsilon_{\max} - \varepsilon(t)}{\varepsilon_{\max}}. \quad (2)$$

This parameter is based on the strain recovery proposed by Lendlein [1, 3]. The main difference is that the Lendlein's parameter was defined after the material underwent a complete SM cycle while this proposed calculation defines recovery ratio as a function of time.

3. RESULTS AND DISCUSSIONS

3.1 SM Cycle with Identical T_{H1} but Different T_{H2}

Figures 2 show the recovery ratio in an SM cycle during and after heating to T_{H2}=60, 80 and 100°C since heating started. All samples were deformed to 20% at T_{H1}=100°C and then cooled down to 40°C. In the figure, the recovery onset points are indicated. Also, the point where the temperature reaches T_{H2} is marked by a vertical dashed line. It is interesting to note that with T_{H1}=100°C, only at this temperature, the material can recover fully from the full deformation within the tested time period (T_{H2}=100°C, 99% recovery is reached in 29 minutes). For the recovery at 80°C, only 80% recovery ratio can be reached after 60 minutes; for 60°C, only 20% can be acheived. This is in drastic constrast to the recovery in isothermal experiments where 99% of strain recovery was seen within 46 minutes for 60°C and 9.5 minutes for 80°C. Clearly, the degree of recovery of the SMP is controlled by both T_{H1} and T_{H2}.

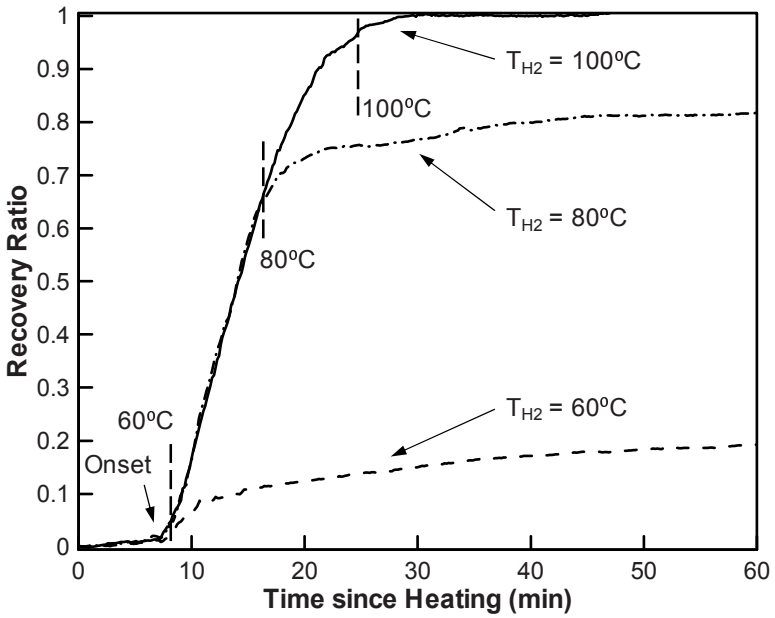

Figure 2. Recovery ratio as a function of time. Recovery onset points are indicated by an arrow.

3.2 SM Cycle with Different T_{H1} but Identical T_{H2}

To investigate the influence of reshaping temperatures to recovery rate and the recovery ratio, experiments were conducted with T_{H1}=60°C, 80°C and 100°C T_L=40°C, and T_{H2}=100°C. Figure 3 shows the recovery ratio as a function of time since heating. It clearly shows that for the same T_{H2}, a lower T_{H1} provides a faster recovery. In the case of reshaping at 60°C, 95% recovery is achieved at 68°C, corresponding to 11 minutes since heating; in the case of reshaping at 80°C, 95% recovery occurs at ~85°C or 17.8 minutes since heating. For the case of reshaping at 100°C, 95% recovery is reached at 100°C and 24 minutes after heating begins.

It is also clear that the onset temperature for the strain recovery decreases with the decreases of T_{H1}. For T_{H1}=60°C and 80°C, the onset temperature is ~50°C; T_{H1}=100°C, the onset temperature is ~56°C. This observation is qualitatively consistent with the "memory" effect: the SMP not only remembers the permanent state/shape, but is also influenced by the reshaping conditions, particularly T_{H1}. Furthermore, in all these cases, the onset temperatures are close to the T_g measured by CTE or DSC experiments.

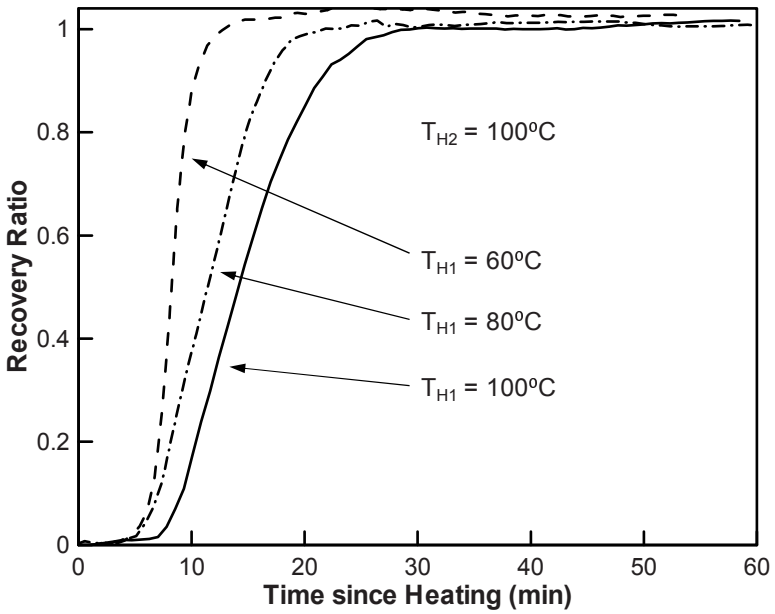

Figure 3. Recoveries in SM cycle experiments with same T_{H2} but different T_{H1}.

3.3 Discussion

The experimental results in this paper show that the free recovery in an SM cycle strongly depends on both T_{H1} and T_{H2}. Figure 4 shows the comparison for the cases of reshaping and recovery at 60°C or 100°C. Here, the fastest recovery occurs for the case of T_{H1}=60°C and T_{H2}=100°C. Interestingly, T_{H1}=60°C cannot recover the deformation at T_{H2}=60°C within our experimental time frame: only 70% of deformation is recovered 60 minutes after heating started. The slowest recovery occurs for the case of T_{H1}=100°C and T_{H2}=60°C. In this case, recovery ratio is only 22% in 60 minutes.

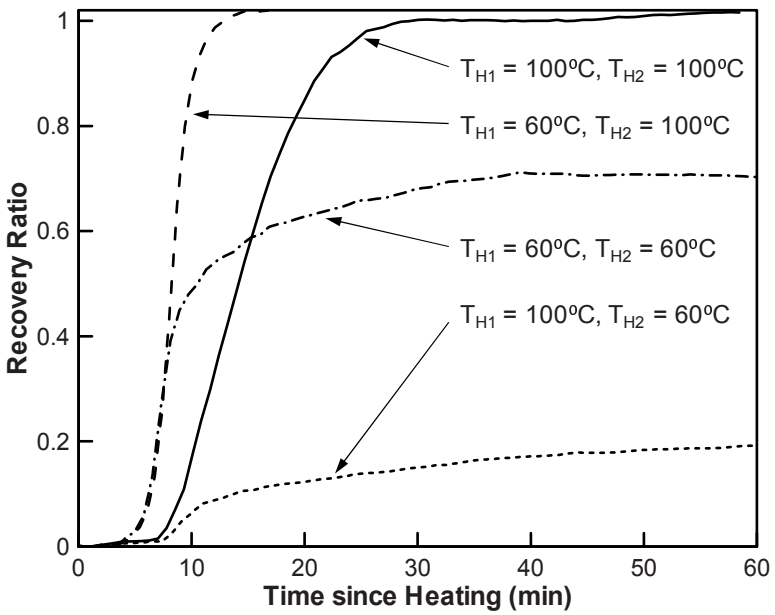

Figure 4. Comparison of recovery ratios of SM cycle experiments at different T_{H1} and T_{H2} with T_{H1} or T_{H2} being 60°C or 100°C.

Figure 4 indicates that both the kinetics and the degree of recovery strongly depend on the two temperatures. Glass transition in polymers is a process that occurs over a temperature range. Our experiments show that the onset of recovery is ~56°C, close to DSC T_g, although the recovery can be very slow at a temperature slightly above CTE T_g, such as 60°C, where recovery takes much longer than the time frame in our experiments (60 minutes). On the other hand, reshaping at a temprerature close to CTE T_g and recovery at a temperature above the DMA T_g yields the fastest recovery rate. The deformation at 60°C needs more energy than the deformation at 100°C. Therefore, it may appear that more energy is stored by reshaping at 60°C, which drives a faster recovery at a high temperature. However, it is known that the SM effect in amorphous polymers is due to the dramatic change of chain mobility and viscosity [13, 14]. It is unclear how energy storage mechanism can be achieved at a molecular level. In addition, thermomechancial behaviors of a polymer become very complicated as the material traverses the transition between glassy state and rubbery state, i.e. the so called "transition zone". Different relaxation modes, from structural relaxation that gives rise to glass transition to chain relaxations associated with conformational changes of the polymers, may be activated during reshaping and recovery. The relaxation times associated with these different modes strongly depend on the temperature. When reshaped at different temperatures to a given strain, the relative contributions to the total deformation from the inter- and intra-molecular interactions may vary. Therefore, future studies are needed to better understand and model the free recovery characteristics of SMPs at the molecular scale.

4. CONCLUSION

The rate of free recovery of shape memory polymers is a major consideration in designing SMP applications. This paper investigated the dependence of free recovery rate of an epoxy-based SMP on the thermal conditions through isothermal experiments and SM cycle experiments. Several observations were obtained. First, free recovery in the isothermal experiments in general demonstrates a much faster recovery rate than the free recovery in an SM cycle under the same recovery temperatures. Second, free recovery rate in the SM cycle experiments shows a strong dependency on the reshaping temperature and recovery temperature. In general, faster recovery can be obtained by reshaping at a lower temperature and recovery at a higher temperature. Third, recovery is only possible if the recovering temperature is equal or higher than the reshaping temperature. If the recovery temperature is lower than the reshaping temperature, even for the case where both temperatures are above T_g, recovery will be much slower. Although the observation of low temperature reshaping and high temperature recovery yielding the fastest recovery may suggest some energy storage mechanism in the SM cycle, it is unclear how this mechanism can be achieved at macromolecular level. In addition, different relaxation modes may be activated during reshaping and recovery, which may influence the recovery. Therefore, further studies are needed to understand and model these mechanisms on the molecular level and their relationship corresponding to deformation and contribution to the recovery observed.

ACKNOWLEDGEMENT

The authors gratefully acknowledge the support from a NSF career award (CMMI-0645219), Defense Advanced Research Projects Agency (DARPA) Phase II STTR (W31PQ-08-C-0011), and an AFOSR grant (FA9550-09-1-0195).

REFERENCE

1. Lendlein, A., et al., *Shape Memory Polymers, in Encyclopedia of Materials: Science and Technology.* 2005.
2. Mather, P.T., X.F. Luo, and I.A. Rousseau, *Shape Memory Polymer Research.* Annual Review of Materials Research, 2009. **39**: p. 445-471.
3. Lendlein, A. and S. Kelch, *Shape-memory polymers.* Angewandte Chemie-International Edition, 2002. **41**(12): p. 2034-2057.
4. Liu, C., H. Qin, and P.T. Mather, *Review of progress in shape-memory polymers.* Journal of Materials Chemistry, 2007. **17**(16): p. 1543-1558.
5. Liu, Y.P., et al., *Thermomechanics of shape memory polymers: Uniaxial experiments and constitutive modeling.* International Journal of Plasticity, 2006. **22**(2): p. 279-313.
6. Qi, H.J., et al., *Finite deformation thermo-mechanical behavior of thermally induced shape memory polymers.* Journal of the Mechanics and Physics of Solids, 2008. **56**(5): p. 1730-1751.
7. Behl, M. and A. Lendlein, *Shape-memory polymers.* Materials Today, 2007. **10**(4): p. 20-28.

8. Behl, M., et al., *Shape-memory capability of binary multiblock copolymer blends with hard and switching domains provided by different components.* Soft Matter, 2009. **5**(3): p. 676-684.
9. Yakacki, C.M., et al., *Unconstrained recovery characterization of shape-memory polymer networks for cardiovascular applications.* Biomaterials, 2007. **28**(14): p. 2255-2263.
10. Yakacki, C.M., et al., *Shape-Memory Polymer Networks with Fe3O4 Nanoparticles for Remote Activation.* Journal of Applied Polymer Science, 2009. **112**(5): p. 3166-3176.
11. Lendlein, A., et al., *Controlling the Switching Temperature of Biodegradable, Amorphous, Shape-Memory Poly(rac-lactide)urethane Networks by Incorporation of Different Comonomers.* Biomacromolecules, 2009. **10**(4): p. 975-982.
12. Westbrook, K.K., et al., *Improved Design for Thermo-Mechanical Experiments on Polymers Using Uniaxial Testing Equipment.* In Preparation., 2009.
13. Nguyen, T.D., et al., *A thermoviscoelastic model for amorphous shape memory polymers: Incorporating structural and stress relaxation.* Journal of the Mechanics and Physics of Solids, 2008. **56**(9): p. 2792-2814.
14. Castro, F., et al., *Effects of Thermal Rates on the Thermomechanical Behaviors of Amorphous Shape Memory Polymers.* Journal of Mechanics of Time Dependent Materials, 2009: p. Accepted.

Proceedings of the SEM Annual Conference
June 7-10, 2010 Indianapolis, Indiana USA

Structural Relaxation near the Glass Transition: Observing Kovacs Kinetic Phenomenology by Mechanical Measurements

Yunlong Guo, Roger D. Bradshaw*
Department of Mechanical Engineering
University of Louisville, Louisville, KY 40292

Abstract

This paper presents the structural relaxation behavior near the glass transition temperature (T_g) of poly (phenylene sulfide) (PPS). Since the test temperature is close to T_g, the specimen is able to reach equilibrium after isothermal or nonisothermal temperature jumps in the experimental time scale; as such, the classic phenomenology of structural relaxation into equilibrium can be pursued by mechanical testing (physical aging) in a temperature range near T_g. In our study, physical aging effects were observed by sequential creep test method using a dynamic mechanical analyzer (DMA). The physical aging of PPS near T_g from mechanical testing clearly showed the similar behavior from the classic volumetric responses found by Kovacs in 1960s. The mechanical aging shift factors manifested all of the three "essential ingredients" in the kinetics of structural relaxation which constitute the most physical phenomenology of glassy-forming materials: intrinsic isotherms; asymmetry of approaching equilibrium; and memory effects. The findings in this study offer a valuable approach to investigate the relationship between the mechanical response and thermodynamic properties (volume, enthalpy, etc.) during structural relaxation of glassy materials.

Background

It is well known that polymeric materials, when cooled rapidly below their glass transition temperature (T_g), fall into non-equilibrium state; thereafter, the materials evolve continuously towards their thermodynamic equilibrium. This evolution is called structural relaxation. During this relaxation process, many properties vary with time (specific volume, enthalpy); changes in mechanical properties (such as compliance and modulus) are specifically referred to as physical aging [1]. In 1960s', Kovacs [2] studied the structural relaxation phenomenon by measuring the volumetric response of polymers subject to various thermal histories. His findings can be summarized as three essential ingredients [3]: (1) temperature dependence of the intrinsic isotherm; (2) nonlinearity in the asymmetry of approaching equilibrium; and (3) complex relaxation behavior in memory effect. In isothermal testing, a polymeric material is quenched to a constant temperature T below T_g after rejuvenation (heat material to a temperature above T_g and anneal for some time to bring it back into thermodynamic equilibrium). In an isothermal test, the specific volume of the polymer deceases with time and levels off when approaching equilibrium. Figure 1 shows volume recovery data for a poly(vinyl acetate) (PVAc) in Kovacs's experiments under a series of isothermal conditions, each temperature jump is made from a mutual annealing temperature (T_0 = 40°C) to the final temperature (T_a), as indicated in the figure. It is clear that the sample requires much more time to reach the equilibrium state as the temperature becomes farther below T_g. This intrinsic isotherm behavior shows the temperature and time dependence of structural relaxation.

* Roger D. Bradshaw, 200 Sackett Hall, Department of Mechanical Engineering, University of Louisville, Louisville, KY, 40292, roger.bradshaw@louisville.edu

T. Proulx (ed.), *Time Dependent Constitutive Behavior and Fracture/Failure Processes, Volume 3*, Conference Proceedings of the Society for Experimental Mechanics Series 15, DOI 10.1007/978-1-4419-9794-4_43, © The Society for Experimental Mechanics, Inc. 2011

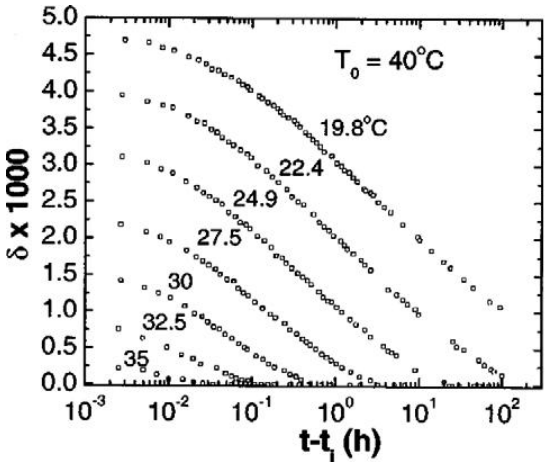

Figure 1. Volume recovery of PVAc in isotherms [2] where δ is thenormalized volumetric departure from equilibrium, defined as $\delta = (v(t)-v_{eq})/v_{eq}$. [3]

The asymmetry of approaching equilibrium test demonstrates the relaxation following more complex thermal histories. In this experiment, the material is allowed to reach thermodynamic equilibrium at temperatures $T_0 = T_1 \pm \Delta T$ after which the temperature is jumped to T_1 where the volume response is measured until the specimen reaches equilibrium. Figure 2 illustrates asymmetry of approaching equilibrium for a temperature "down-jump" ($T_1 < T_0$) and a temperature "up-jump" ($T_1 > T_0$). In this figure, the material (PVAc) was allowed to reach equilibrium at the two temperatures (30°C or 40°C). Subsequently, the material was subjected to a temperature change to 35°C. Although the magnitude of the temperature jump in both cases is 5°C, and both materials began in equilibrium at their respective starting temperatures, the volume recovers much more rapidly towards equilibrium in the down-jump experiment than it does in the up-jump experiment. This result shows the inherent nonlinearity of the structural recovery process and has been widely interpreted to imply that the material response (relaxation time) depends upon the instantaneous state or structure of the glass.

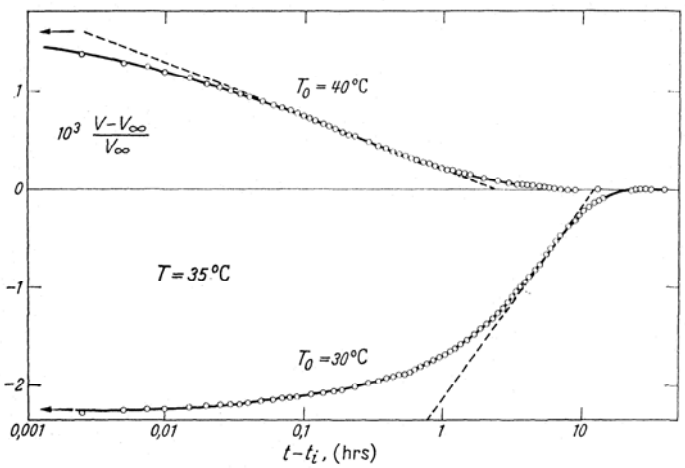

Figure 21. Normalized volumetric response of PVAc after single temperature jump. [2]

In Figure 3, the memory effect data is depicted. Memory effect is a more complicated relaxation behavior that is observed after two temperature jumps. Initially, the material is aged at a lower temperature for a time such that when the temperature is increased to a new temperature (T0), the specific volume is identical to the equilibrium volume for a material isothermally aged at T_0; this history is shown on the left in Figure 3. The right side of Figure 3 depicts the observed normalized volume response by Kovacs [2], who found that the material with two

temperature steps (curves 2-4 in Figure 3) had specific volumes that increased for a time and then decreased and merged into the isothermal response (curve 1) at T_0. The peak amplitude and time of the memory effect curves depend on the temperature departure from T_0 before up-jump and aging time (t_i) at that first temperature. The memory effect is an evidence for structural relaxationconsisting of many relaxation processes occurring on various time scales. As such, the relaxation behavior cannot be described by a single relaxation time; if this were the case, materials 2-3 would remain in equilibrium after the jump.

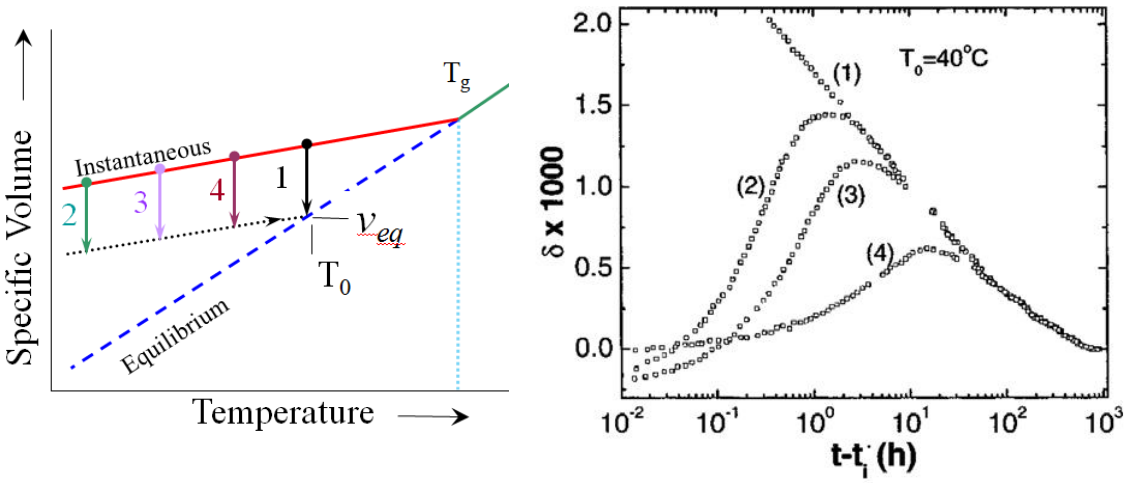

Figure 3. Memory effect data of PVAc in volume response: (left) schematic of volume-temperature history; (right) associated voume response after jump to T_{final} in 4 cases indicated (Kovacs). [2,3]

These three “essential ingredients” present material behavior during structural relaxation. The material evolves toward equilibrium, this process are nonlinear and involve processes acting at many time scales. Any theoretical framework aiming to model the relaxation behavior must be able to reproduce or predict all of these essential ingredients. Many techniques including dilatometry [4-5], differential scanning calorimetry (DSC) [6-7], dielectric spectroscopy [8], and fluorescence [9] have been utilized to monitor the structural relaxation, and findings consistent with Kovacs’s initial work are reported in the literature [4-9]. In this paper, we present the Kovacs kinetic phenomenon via mechanical measurements for polyphenylene sulfide (PPS), an engineering material used as the matrix for some fiber-reinforced composites.

This paper focuses upon investigation of physical aging behavior (mechanical relaxation) near T_g, in order to provide kinematic observation of mechanical properties of polymers when they approach to the structural equilibrium states at various temperatures.

Experimental

The material chosen for this study is 0.127 mm (5 mil) thick PPS film supplied by GE Advanced Materials as 280 mm by 216 mm sample sheets. Experimental specimens were cut manually to be 25.4 mm long (in the load direction) and 12.7 mm wide. The value of T_g, reported by the manufacturer for the PPS film is 92ºC; this value is consistent with our observations (92.2ºC) via the tanδ peak using the DMA. Details of measuring T_g and characterizing aging at least 15 ºC below T_g for PPS has been published elsewhere [10]. In the current study, the material is first headed to 5ºC above T_g and held for 5 minutes to erase internal stresses (rejuvenation). The material is then quenched to $T < T_g$ to place the material in the glassy state at is held at that temperature thereafter (isothermal relaxation), a series of creep and recovery tests are performed in order to characterize the aging state. This method is shown in Figure 4. In creep portions, the specimen is loaded by a constant stress, and the strain response is measured. Compliance $D(t)$ can be determined from creep tests by:

$$i^{th}\ Load\ Step \quad \rightarrow \quad t = t_e - t_{ei} \quad ; \quad D(t) = \frac{\varepsilon(t) - \varepsilon_{unload}(t)}{\sigma_0} \tag{1}$$

where t_{ei} is the aging time at the start of the i^{th} load step and t is the time elapsed since the load was applied in the i^{th} load step. For nonisothermal relaxation testing, the sample undergoes temperature up-jump(s) or down-jump(s) prior to mechanical measurements.

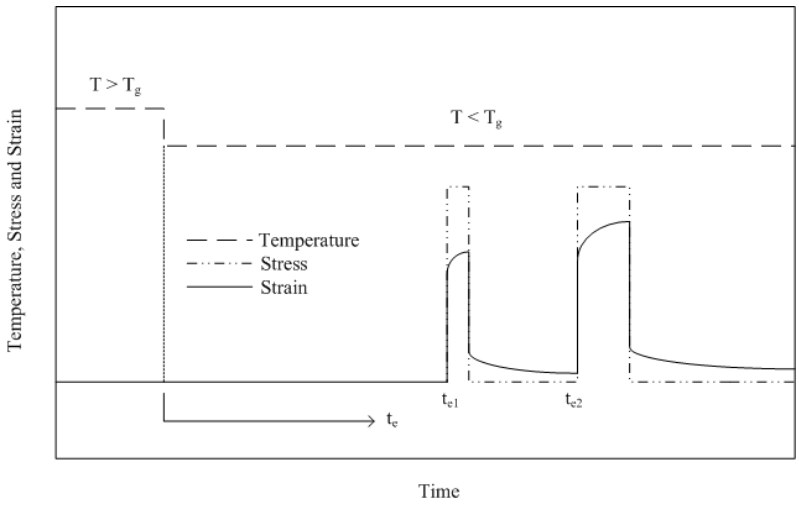

Figure 4. Schematic of isothermal creep tests for measuring mechanical relaxation.

Sequential creep tests lead to compliance curves at various aging times, as described by Equation 1. During aging/relaxation prcess, compliance response (D) is related to a reference curve (D_{ref}) by the equation: [11]

$$D(t)\,|_{t_e,T} = D_{ref}(a_{te}t)\,|_{t_{eref},T} \tag{2}$$

where t_{eref} is the reference aging time, t_e is the aging time of creep, T is temperature, and a_{te} is the aging shift factor. The shift factors are assumed to form a straight line in log-log scale versus aging time:

$$a_{te}(t_e)\big|_T = \left(\frac{t_{eref}}{t_e}\right)^{\mu(T)} \tag{3}$$

where μ is the shift rate at temperature T [1].

Results and Discussion

Isothermal aging is characterized at 81°C, 82°C, 83°C, 84°C, and 85°C. At each temperature, aging times of the sequential creep tests start with 0.039 hours and end at aging times between 1.25 hours and 20 hours depending on the time required to reach equilibrium. Stress levels applied in creep tests keep within linear viscoelastic regions at the test temperatures. For each temperature, at least three separate tests were performed using different specimens to validate that the experiments are reproducible.

Figure 5 summarizes the transition of aging shift factors (aging into equilibrium) at each temperature. For the left figure, data points from 3 specimens aged at 82°C are shown along with the line fits of the two regions (prior to equilibrium and after equilibrium). The right figure demonstrates similar curves for the other temperatures; fits of the data for all temperatures was quite similar to that at 82°C. It is clear that the aging shift rate (slope of non-equilibrium portion of line in log a_{te} – log t_e plot) and time needed to reach equilibrium (a_{te} = 1 as defined here) deceases with increasing temperatures. When test temperature is 85°C, 7°C below T_g, the material will reach non-aging state at the time after 5.1 min from quenching while at a test temperature 11°C below T_g, the material needs more than 2 hours to reach equilibrium. This time and temperature-dependent behavior is analogous to that in the volume recovery (Figure 1); therefore, the analysis on the relaxation time in mechanical and volumetric response can compare the relaxation timescale in polymers for these two aspects.

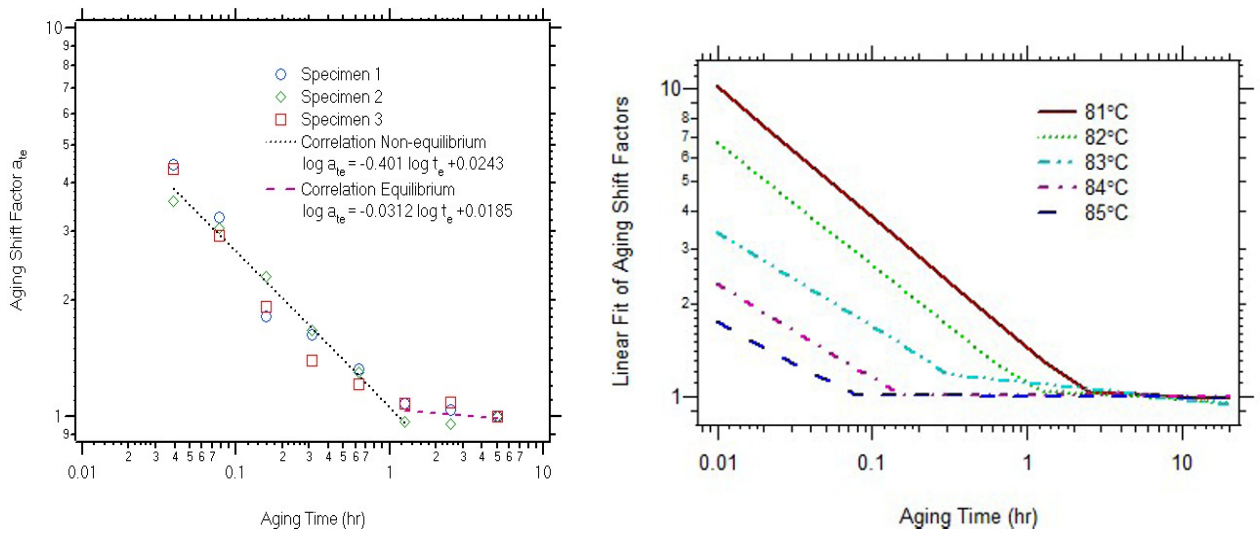

Figure 5. Linear fit of aging shift factors in aging and non-aging regions of PPS, at temperatures 81°C, 82°C, 83°C, 84°C and 85°C. [17]

After determining the times need to reach equilibrium at temperatures near T_g, nonisothermal aging tests in temperature down-jumps and up-jumps were performed. These mechanical tests indicate the well-known "asymmetry of approaching equilibrium" as shown in Figure 2. An example of asymmetry of approaching equilibrium is shown in Figure 6 from creep tests of PPS. The films were aged to equilibrium at 75, 80, 81, 85, 88 and 91°C, then jumped to 83°C; the aging shift factors were then determined. Figure 6 illustrates a_{te} data sets (2 specimens per condition) of these thermal histories and their Prony series fits over aging time from 200 seconds from temperature jump to reaching equilibrium at the final temperature (83°C). These plots show similarities of the thermodynamic and mechanical properties as the response of structural relaxation. This provides further evidence for the validity of predicting mechanical behavior of polymers using the existing models developed via volumetric or thermodynamic methods.

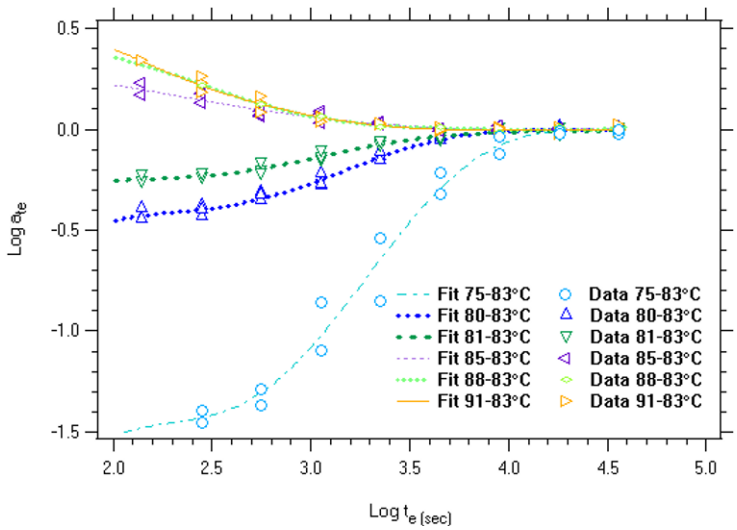

Figure 6. Asymmetry of approaching equilibrium of aging shift factors in PPS. [17]

The PPS material studied also manifests memory effects in creep tests after temperature up-jump. In this testing, the temperature up-jump thermal histories include 57°C-73°C, 63°C-73°C, and 67°C-73°C. The PPS

sample was quenched from 5°C above T_g to the first temperature, and held at that temperature for 14 hours, then temperature jumped to the final temperature, subsequently mechanical measurements were applied at various aging times.

Figure 7 summarizes the aging shift factors for temperature up-jump tests for PPS. For comparison, isothermal aging shift factors at these temperatures at similar aging times are also included. The nonisothermal aging shift factors in the single temperature up-jump cases manifest complex material behavior under such thermal conditions. The aging state of glassy polymers clearly depends on the thermal treatments. It is apparent that the mechanical shift factor after up-jump shows the memory effects in relaxation, the a_{te} increases with time and decreases after reaching maximum before merging into a_{te} response in isothermal aging, as found in volume recovery shown in Figure 3. These nonisothermal aging shift factors need to be modeled in order to describe mechanical behavior under time varying temperature conditions. The authors have developed the KAHR-ate model for this purpose; it is an extension of the KAHR (Kovacs-Aklonis-Hutchinson-Ramos) model for volume response to predict mechanical behavior. [14] It has been demonstrated in our work to provide excellent agreement with experimental data under a variety of thermal histories. [17]

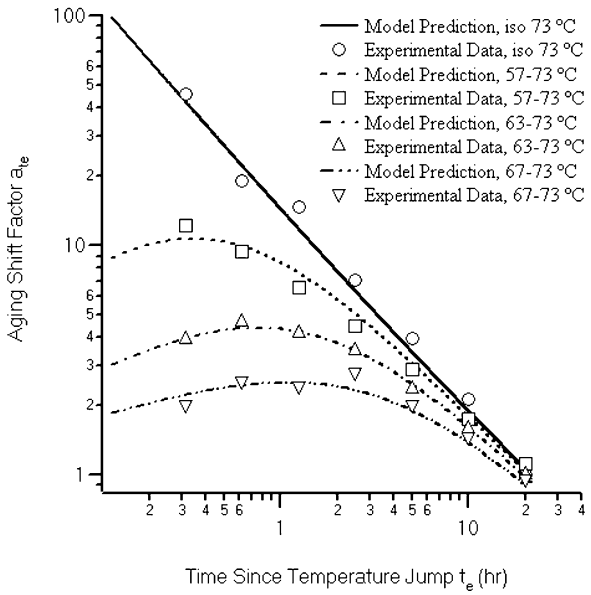

Figure 7. Aging shift factors of creep tests after temperature up-jump to 73°C for PPS; isothermal aging shift factors at the same temperature reported for comparison; lines are curve fit for a_{te}.

Conclusions

In our measurements in physical aging of PPS near the glass transition temperature, the three essential indigents in structural relaxation intrinsic isotherms, asymmetry of approaching equilibrium and memory effects are observed in aging shift factors. It provides direct evidence for relaxation timescale of mechanical properties in the whole structural relaxation. The physical aging of polymer-based systems is an issue requiring consideration in engineering part design. The results in this paper show that thermodynamic models for structural relaxation such as Tool-Narayanaswamy-Moynihan model [12-13], Kovacs-Aklonis-Hutchison-Ramos model [14] or Ngai's coupling model [15-16] could be used to describe mechanical behavior in the relaxation process. The relaxation timescale in various properties (volume, enthalpy, mechanical shift factor) needs to be investigated in future to find their intrinsic relationship in relaxation.

Acknowledgements

The authors would like to recognize Kentucky Science and Engineering Foundation (KSEF) for sponsorship of this work under the grant entitled KSEF-148-502-05-136, and Scott Cione, GE Advanced Materials, for supplying the film materials used in this study.

References

[1] Struik, L.C.E., Physical Aging in Amorphous Polymers and Other Materials, Elsevier Scientific Publishing Co., Amsterdam, 1978.
[2] Kovacs, A.J., Transition Vitreuse Dans Les Polymeres Amorphes. Etude Phenomenologique, *In Fortschritte der Hochpolymeren-Forschung*, **3**, p. 394-507, 1963.
[3] Mckenna, G.B., Glassy States: Concentration Glasses and Temperature Glasses Compared, *Journal of Non-crystalline Solids*, **353**, p. 3820-3828, 2007.
[4] Svoboda R., Pustkova, P. and Malek, J., Structural Relaxation of Polyvinyl acetate (PVAc), *Polymer*, **49**, p. 3176-3185, 2008.
[5] Svoboda R., Pustkova, P. and Malek, J., Relaxation Behavior of Glassy Selenium, *Journal of Physics and Chemistry of Solids*, **68**, p. 850-854, 2007.
[6] Simon, S.L., Sobieski, J.W., and Plazek, D.J., Volume and Enthalpy Recovery of Polystyrene, *Polymer*, **42**, p.2555-2567, 2001.
[7] Slobodian, P., *et al*., Enthalpy and Volume Relaxation of PMMA, PC and a-Se: evaluation of aging bulk moduli, *Journal of Non-Crystalline Solides*, **344**, p. 148-157, 2004.
[8] Matsuoka, S., *et al*., Phenomenological Relationship between Dielectric relaxation and Thermodynamic Recovery Processes near the Glass Transition, *Macromolecules*, **18**, p. 2652-2663, 1985.
[9] Royal, J.S., and Torkelson, J.M., Molecular-scale Asymmetry and Memory Behavior in Poly(vinyl acetate) Monitored with Mobility-Sensitive Fluorescent Molecules, *Macromolecules*, **25**, p. 1705-1710, 1992.
[10] Guo, Y. and Bradshaw, R.D., Isothermal Physical Aging Characterization of Polyether-ether-ketone (PEEK) and Polyphenylene Sulfide (PPS) Films by Creep and Stress Relaxation, *Mechanics of Time-Dependent Materials*, **11**, p. 61-89, 2007.
[11] Bradshaw, R.D., Characterization and Modeling of Viscoelastic Composite Laminates with Nonisothermal Physical Aging, Department of Mechanical Engineering, Ph.D. Dissertation, Northwestern University: Evanston, IL, 1997.
[12] Narayanaswamy, O.S., A Model of Structural Relaxation in Glass, *Journal of the American Ceramic Society*, **54**, p. 491-198, 1971.
[13] Moynihan, C.T., et al., Structural Relaxation in Vitreous Materials, *Annals New York Academy of Sciences*, **279**, p. 15-35, 1976.
[14] Kovacs, A.J., Aklonis, J.J., Hutchinson, J.M., and Ramos, A.R., Isobaric Volume and Enthalpy Recovery of Glasses. 2. A Transparent Multi-parameter Theory, *Journal of Polymer Science: Polymer Physics Edition,* **17**, p.1097-1162, 1979.
[15] Rendell, R.W., Lee, T.K., and Ngai, K.L., New Model of Physical Aging Effects in Enthalpy Recovery, *Polymer Engineering and Science*, **24**, p. 1104-1110, 1984.
[16] Ngai, K.L., Short-time and Long-time Relaxation Dynamics of Glass-forming Substances: A Coupling Model Perspective, *Journal of Physics: Condensed Matter*, **12**, p. 6437-6451, 2000.
[17] Guo, Y., Experimental Characterization and Modeling of Isothermal and Nonisothermal Physical Aging in Glassy Polymer Films, Department of Mechanical Engineering, Ph.D. Dissertation, University of Louisville: Louisville, KY, 2009.

Proceedings of the SEM Annual Conference
June 7-10, 2010 Indianapolis, Indiana USA

Creep Mechanisms in Bone and Dentin Via High-Energy X-ray Diffraction

Mrs. Alix C. Deymier-Black, Ph.D. Candidate, Department of Materials Science and Engineering, Northwestern University, 2220 Campus Dr, Evanston IL, 60208
E-mail: alixdeymier2010@u.northwestern.edu
Ms. Anajli Singhal, Ph.D. Candidate, Northwestern University
Mr. Fang Yuan, Ph.D. Candidate, Northwestern University
Dr. Jon Almer, Beamline Scientist, Argonne National Laboratory
Prof. David Dunand, Professor, Northwestern University

Extended Abstract

Bone and dentin are highly complex, hierarchical composite materials with exceptional properties due to their unique composition and structure. They are essentially the same material with varied structural organization. They are three phase composites made up of a ceramic component, hydroxyapatite (HAP), a polymeric or proteinaceous component, collagen, and fluid filled porosity. A number of macroscopic studies have shown that both dentin [1-6] and bone [7-9] undergo visco-elastic, creep deformation and stress-relaxation behaviors. The problem with these bulk experiments is that they do not give information about which phase is contributing to the macroscopic creep or how. Some of these inquiries have suggested that the collagen is not responsible [9] and that creep in hard biological materials is primarily due to dislocations in the HAP mineral. On the other hand, others have said that collagen is completely responsible for the creep [8, 10]. These uncertainties make it essential to use techniques that allow for the study of the behavior of these very different components simultaneously during loading, determining their participation in creep. One such technique is synchrotron diffraction.

Synchrotron diffraction has been used as a tool to determine the behavior of HAP and protein in bone and dentin under quasi-static loading conditions [11-15]. Viscoelastically it has been used to determine the behavior of collagen in unmineralized tendon [16, 17]. However, to date it has not been employed to determine the behavior of these phases in bone and dentin during visco-elastic loading. Such testing will help to determine exactly how HAP and collagen interact during creep.

Clean and disinfected fresh bovine femurs of a healthy 18-month old cow were cut into cuboids of dimensions 5.4 (± 0.02) x 3.9 (± 0.03) x 2.9 (± 0.05) mm^3, with the 5 mm dimension being along the long-axis of the femur. Also, lower incisors were extracted from the lower mandible of an other healthy 18-month old cow and cut into 1-2 quasi cylindrical root dentin samples with heights of 7.4 (± 0.03) mm and the natural tooth cross-section for each tooth. Both types of samples were then frozen in PBS at -20^{o}C until the time of the experiment. The samples then underwent *in situ* diffraction measurements in a MTS 858 load frame at the Advanced Photon Source, Argonne National Laboratory. The samples were maintained hydrated and at body temperature (37±1^{o}C) thanks to a temperature controlled hydration rig attached to the bottom platen.

Two types of compressive creep experiments were conducted on both bone and dentin samples. For both tests, the samples were placed on the lower platen of the load frame so that the X-ray beam passed through the vertical and horizontal center of the samples. For the first experiments, constant creep, the samples were rapidly loaded along the long-axis direction to a compressive load of -95 MPa and were maintained at this constant load for 3 hrs. Wide Angle X-ray Scattering (WAXS) and Small Angle X-ray Scattering (SAXS) diffraction patterns were recorded at intervals of 3 min. The diffraction patterns were collected on area detectors placed behind the sample, nominally perpendicular to the direction of the beam. A MAR345 detector recorded the WAXS patterns,

T. Proulx (ed.), *Time Dependent Constitutive Behavior and Fracture/Failure Processes, Volume 3*, Conference Proceedings of the Society for Experimental Mechanics Series 15, DOI 10.1007/978-1-4419-9794-4_44, © The Society for Experimental Mechanics, Inc. 2011

while a Bruker CCD recorded the SAXS patterns. In order to record both the WAXS and SAXS patterns at each point, the MAR345 was laterally translated out of the beam direction to expose the CCD detector. A pressed ceria powder (CeO_2, NIST SRM-674a) disc was used as a standard to calibrate the system. The second set of experiments, creep-load-unload, probed the changes in elastic properties with advancing creep time. Here, the samples were quickly loaded to -95MPa and the load was maintained for 1 hr. During the first hour, WAXS and SAXS measurements were taken every 3 min. The sample was then unloaded to zero stress and reloaded to -95 MPa in increments of -20 MPa. At each increment both a WAXS and SAXS pattern were obtained. The entire unloading and reloading process took approximately 1hr. Once reloaded, the cycle of creep, unloading and reloading was repeated twice.

The longitudinal and transverse strains in the mineral and collagen phase are calculated as previously discussed in the literature [13, 18], but a summary is given here. Changes in d-spacing, between the lattice planes in the HAP were used to determine elastic strains in the ceramic material described here as HAP strains. The basic diffraction parameters were first obtained by analyzing the ceria diffraction patterns using Fit2D. The parameters determined from this program – beam center, detector tilt and specimen-detector distance – were then fed into a series of MATLAB programs developed at APS. These programs fit the diffraction rings, giving the center of each peak of interest, HAP(00.2) in our case, as a radial distance from the beam center at various azimuthal angles, $R(\eta)$. The Cartesian plot for radial distance, $R(\eta)$, versus azimuth, η, for all stress levels intersect at a single radius R^* called the invariant radius. R^* represents the strain-free point and is used to calculate the orientation-dependent deviatoric strains using the equation: $\varepsilon(\eta) = \frac{(R(\eta) - R^*)}{R^*}$. Azimuthal angles of 90 and 270 ^{o} give the longitudinal strain, along the loading direction, and 0 and 180 ^{o} give the transverse strain.

In the case of the SAXS patterns, the well-defined peaks arise from the ~67 nm periodic gap spacing of the collagen matrix. In mineralized tissue like bone and dentin, the primary SAXS contrast associated with these peaks is between the relatively dense HAP particles, which are formed within the gaps, and the collagen matrix. Changes in the measured SAXS spacing with applied load therefore represent changes in the average HAP particle spacing, which in turn results from cooperative deformation between the collagen and HAP particles. Thus, the SAXS-derived strain will be described as the fibrillar strain. This fibrillar strain is measured in much the same way as the HAP strains using the third-order SAXS peak, except that a stress free point, R^*, is not measured. Instead, the stress free point is taken to be the radial distance, $R(\eta)$, of the rings when the sample is under zero load. Note that for the fibrils, transverse loads are difficult to determine due to low diffraction intensities at the 0^o and 180^o azimuths.

With these strain values much information can be gathered about the samples and their mechanical behaviors. In the case of the creep experiments the obtained strains are plotted versus creep time. If linear, the slope of the plots can be defined as creep strain rate and provide an idea of how quickly a sample accumulates or sheds strain during constant loading. For the non-creep segments of creep-load-unload measurements the HAP and fibrillar strains are plotted as a function of applied stress. The slopes of these applied stress versus phase strain plots are defined as the apparent modulus ($E_{app}=\sigma_{applied}/\varepsilon_{phase}$). This apparent modulus provides information about how load is transferred between the phases in the bulk material upon loading.

The diffraction rings provide a wealth of information which can be extracted by further examining peak-broadening and peak intensity. Radial peak broadening (ΔR_{meas}) can be caused by a number of effects including strain distribution within or between HAP crystals in the sampled population, the small size of the HAP platelets, as well as instrumental effects. The instrumental contribution for the (00.2) peak was calculated using the ceria standard. Assuming the peaks had a Gaussian shape, the mineral peak width (ΔR) was converted to $\Delta 2\Theta$ using $\Delta 2\Theta=\Delta R/z$, where z is the sample to detector distance. From this, the crystallite size (t) and root mean square strain (ε_{rms}), also known as microstrain, was calculated according to Noyan and Cohen [19]. Now, the variation in intensity along the azimuthal direction of diffraction peaks is due to preferential alignments of the diffractors, or texture. In order to determine how the orientation of the HAP platelets might change with continuing creep, the normalized intensity of the HAP (00.2) peak was plotted as a function of azimuth creating intensity peaks in the angles of preferred orientation. Changes in the distribution of intensity with time during creep were determined by measuring the full-width-half-max (fwhm) of the high intensity peaks as a function of time. An increase in the intensity peak fwhm represents a tilting of the platelets away from the preferential orientation and vice-versa.

Upon analyzing the diffraction patterns it was found that the bone and dentin samples showed very similar trends for the constant creep experiments. Immediately upon loading, strong compressive strains were measured in both WAXS and SAXS; however, with increasing time under constant load, the strain on the HAP phase decreased and the strain on the fibrils increased. In the case of dentin, the strain rate on either phase was linear with values of $2.0 \cdot 10^{-5}$ ε/min for the HAP and $-7 \cdot 10^{-6}$ ε/min for the fibrils. Bone on the other hand had a much greater changes in strain in the early stages of loading followed by plateaus. The maximum strain rate for the bones samples were $1.8 \cdot 10^{-5}$ ε/min for HAP and $-2.3 \cdot 10^{-5}$ ε/min for the fibrils. That the fibrillar strain, as a representation of the nano-scale composite strain, increased with creep time was expected. However, the strain trends for HAP are not. Reinforced composites, much like bone and teeth, usually exhibit the opposite behavior. It is expected that with increasing creep time, more and more load should be transferred from the weaker phase to the stiffer reinforcement phase, therefore causing an increase in elastic strain on the reinforcement. The exception to this rule occurs when there is delamination between the matrix and the reinforcement. As delamination of the interface occurs, the matrix can no longer transfer load to the reinforcement; as a result the matrix must carry more load and the reinforcement is allowed to elastically unload. Such a delamination scenario seems highly probable in both bone and dentin as the HAP-collagen interface is a weak one dominated by Van der Waals and electro-static forces [20, 21]. However, damage such as interfacial delamination will result in a change of composite stiffness as well as apparent stiffness due to a change in the ability to transfer load. Such a change would be seen in the creep-load-unload experiments.

The bone and dentin samples showed the same creep trends in the creep-load-unload experiments, as in the constant creep experiments. However, the apparent elastic moduli ($E_{app}=\sigma_{applied}/\varepsilon_{phase}$) of both the HAP ($E_{app}^{HAP}$) and the fibrils ($E_{app}^{fib}$) did not show significant changes after one, two or three hours of creep. The average E_{app}^{HAP} and E_{app}^{fib} for bone were 41±3.0 GPa and 13±0.94 GPa, respectively. For dentin, average E_{app} of 31±3.8 GPa and 9.6±0.5were measured for HAP and collagen. These values are higher than those usually measured in bone or dentin (Unpublished Data,[18]). This consistency in the apparent modulus values suggests that the extent of debonding at the time of modulus measurement was always the same. However, the increase in the apparent elastic modulus of HAP in bone and dentin may be due to delamination damage incurred in the first hour of creep. Although this supports the hypothesis that there is delamination damage, it does not explain why the apparent elastic moduli remain constant. There may be other mechanisms at play that might explain the unusual strain partitioning during creep.

The HAP platelets in dentin and bone are known to fall into two separate populations: intra-fibrillar and extra-fibrillar HAP. Although the exact distribution of HAP between these populations is debatable [22-24], it is possible that their different locations within the hierarchy of these mineralized biomaterials could cause vast differences in their strains. Therefore it is possible that the measured decrease in the overall HAP strain might actually be caused by a large decrease in strain on the extra-fibrillar HAP which overwhelms a small increase in strain on the intra-fibrillar HAP population. However, if this were true, it would cause a broadening of the peak due to the constant increase in HAP strain distribution or microstrain. Although there was an initial increase in broadening upon loading, such a continuous increase is not consistently seen from the broadening analysis thus ruling out a bi-modal strain distribution as a possible explanation. The unexpected strain partitioning between HAP and collagen may also be due to a HAP platelet tilting during loading. If more HAP platelets were to become longitudinally aligned upon loading, this would cause a better load distribution among the aligned platelets which would be recorded as a decrease in HAP strain. However, the broadening analysis results show that upon loading the HAP platelets tilt away from the longitudinal direction. This results in a decrease in the population of longitudinally aligned platelets and should cause an increase in the measured HAP strain. Tilting is therefore not a valid explanation for the decrease in HAP strain with increasing creep time.

Having eliminated other explanations for the unusual load portioning behavior between HAP and collagen in dentin and bone during creep, it seems that delamination damage is still the most reliable hypothesis. The only obstacle is the consistency of the apparent elastic moduli of HAP and collagen throughout creep. The obstacle however, may be overcome by considering the types of interactions at the HAP collagen interfaces. Although the interfacial behavior of mineralized biomaterials such and bone and teeth is not well understood, it is thought that the main bonding mechanisms are weak bonds such as Van der Waals and electrostatic forces [20, 21]. These interactions suggest not only that it would be easy for interfacial damage to occur, but also that the interfacial damage would be easily repaired upon unloading. This interfacial ‘healing’ process may be responsible for the constant apparent elastic moduli. Upon unloading the damaged interface would reform the broken bonds allowing

the material to return to its previous stiffness even after extensive delamination. It does seem however, that not all of the bonds are reformed upon unloading which explains that high apparent modulus of the HAP.

1. Korostoff, E., S.R. Pollack, and M.G. Duncanson, *Viscoelastic properties of human dentin.* Journal of Biomedical Materials Research, 1975. **9**: p. 661-674.
2. Trengrove, H.G., G.M. Carter, and J.A.A. Hood, *Stress relaxation properties of human dentin.* Dent. MAter., 1995. **11**: p. 305-310.
3. Wang, X., Y. Zhang, and Y. Cui, *Evaluation of dentinal viscoelastic properties based on its microstructural characters.* Advanced Materials Research, 2008. **32**: p. 229-232.
4. Jafarzadeh, T., M. Efran, and D.C. Watts, *Creep and viscoelastic behavior of human dentin.* Journal of Dentistry, Tehran University of Medical Sciences, 2004. **1**(1): p. 5-14.
5. Pashley, D.H., et al., *Viscoelastic properties of demineralized dentin matrix.* Dental materials, 2003. **19**: p. 700-706.
6. Jantarat, J., et al., *Time-dependent properties of human rooth dentin.* Dental materials, 2002. **18**: p. 486-493.
7. Yamashita, J., et al., *Collagen and bone viscoelasticity: a dynamic mechanical analysis.* Journal of Biomedical materials research, 2002. **63**: p. 31-36.
8. Bowman, S.M., et al., *Results from demineralized bone creep tests suggest that collagen is rsponsible for the creep behavior of bone.* Journal of biomechanical engineerig, 1999. **121**: p. 253-258.
9. Rimnac, C.M., et al., *The effect of temperature, stress and microstructure on the creep of compact bovine bone.* Journal of Biomechanics, 1993. **26**(3): p. 219-228.
10. Sasaki, N., et al., *Stress-relaxation function of bone and bone-collagen.* Journal of Biomechanics, 1993. **26**(12): p. 1369-1376.
11. Akhtar, R., et al., *Load transfer in bovine plexiform bone determined by synchrotron x-ray diffraction.* Journal of Materials Research, 2008. **23**(2): p. 543-550.
12. Almer, J.D. and S.R. Stock, *Internal strains and stresses measured in cortical bone via high-energy x-ray diffraction.* Journal of Structural Biology, 2005. **152**: p. 14-27.
13. Almer, J.D. and S.R. Stock, *Micromechanical response of mineral and collagen phases in bone.* Journal of Structural Biology, 2007. **157**: p. 365-370.
14. Gupta, H.S., et al., *Cooperative deformation of mineral and collagen in bone at the nanoscale.* PNAS, 2006. **103**(47): p. 17741-17746.
15. Borsato, K.S. and N. Sasaki, *Measurement of partition of stress between mineral and collagen phases in bone using X-ray diffraction techniques.* Journal of Biomechanics, 1997. **30**(9): p. 955-957.
16. Sasaki, N., et al., *Time-resolved x-ray diffraction from tendon collagen during creep using synchrotron radiation.* Journal of Biomechanics, 1999. **32**(3): p. 285-292.
17. Puxkandl, R., et al., *Viscoelastic properties of collagen: synchrotron radiation investigations and structural model.* Philosophical Transactions of the Royal Society of London Series B-Biological Sciences, 2002. **357**(1418): p. 191-197.
18. Deymier-Black, A.C., et al., *Synchrotron X-ray diffraction study of load partitioning during elastic deformation of bovine dentin.* Acta Biomaterialia, 2009. **In Press**.
19. Noyan, I.C. and J.B. Cohen, *Residual Stress: Measurement by Diffraction and Interpretation*, ed. B. Ilschner and N.J. Grant. 1956, New York: Springer-Verlag.
20. Walsh, W.R. and N. Guzelsu, *Compressive Properties of Cortical Bone - Mineral Organic Interfacial Bonding.* Biomaterials, 1994. **15**(2): p. 137-145.
21. Walsh, W.R., M. Ohno, and N. Guzelsu, *Bone Composite Behavior - Effects of Mineral Organic Bonding.* Journal of Materials Science-Materials in Medicine, 1994. **5**(2): p. 72-79.
22. Bonar, L.C., S. Lees, and H.A. Mook, *Neutron Diffraction Studies of Collagen in Fully Mineralized Bone.* Journal of Molecular Biology, 1985. **181**: p. 265-270.
23. Katz, E.P. and S.-T. Li, *Structure and Function of Bone Collagen Fibrils.* Journal of Molecular Biology, 1973. **80**: p. 1-15.

24. Kinney, J.H., et al., *The importance of intrafibrillar mineralization of collagen on the mechanical properties of dentin.* Journal of Dental Research, 2003. **82**(12): p. 957-961.

Proceedings of the SEM Annual Conference
June 7-10, 2010 Indianapolis, Indiana USA

High Local Deformation Correlates with Optical Property Change in Cortical Bone

Xuanhao Sun[a], Ji Hoon Jeon[a,b], Sarah Fuhs[a], John Blendell[c], and Ozan Akkus[a]*

[a]Weldon School of Biomedical Engineering, Purdue University, West Lafayette, IN, USA

[b]Currently at: LG Chemical/Research Park, Daejeon, Republic of Korea

[c]Department of Materials Science and Engineering, Purdue University, West Lafayette, IN, USA

* Author to whom correspondence should be addressed

Ozan Akkus, Ph.D.
Associate Professor
Weldon School of Biomedical Engineering
Purdue University
206 S. Martin Jischke Drive
West Lafayette, IN 47907-2032
ozan@purdue.edu

ABSTRACT

Bone is a biocomposite of collagen and apatite crystals which together constitute a striking hierarchical organization, though it can still become structurally compromised when external load exceeds its threshold. Mechanisms of bone damage have been proposed on different length scales corresponding to its hierarchical structure. However, the damage process was still not completely understood due to the complexity of bone's hierarchy. We previously reported an opaque process zone feature in bone under tensile loading, which could be stained only when samples were kept in loaded condition, in contrast to the classical damage, which could be stained after the removal of loading. In this study, Digital Image Correlation (DIC) methods have been used to quantify the local strain value at the micro-scale upon dark zone emergence. The process zones observed under transmission illumination was found to colocalize with the high-strain (up to 14%) regions calculated by DIC, and overlap best with the shape of principal strain (e1). The average strain value recorded at the edges of the process zones was about 1.1%, around the proposed threshold for collagen interfibrillar sliding. Thus, we speculate that collagen interfibrillar sliding might be among the causes for this dark zone phenomenon.

KEYWORDS: Bone damage, Digital image correlation, Strain

T. Proulx (ed.), *Time Dependent Constitutive Behavior and Fracture/Failure Processes, Volume 3*, Conference Proceedings of the Society for Experimental Mechanics Series 15, DOI 10.1007/978-1-4419-9794-4_45, © The Society for Experimental Mechanics, Inc. 2011

1. INTRODUCTION

The aging of the U.S. population will lead to a greater prevalence of bone fractures and result in an increasing healthcare burden for the society [1, 2]. Bone is a two-phase biocomposite of collagen and apatite crystals, and it embraces a striking hierachical organization on different length scale, representing an ideal example of the structure/function relationship in biological materials [3-6]. Bone fracture occurs when the external loads exceed its mechnical thresholds, either in the form of a single overload, which causes acute traumuas [7], or in the form of repetitive loading, causing fatigue-type failures [8]. On the other hand, aging [9] and certain bone diseases, such as osteoporosis [10], can change the intrinsic mechanical mechanical competence of bone and increase the fracture risk. Therefore, to reduce bone fracture incidence, understanding the damage mechanisms underlying bone fracture is essential.

Several bone damage mechanisms have been proposed according to its hierarchical structure on different length scales , such as microcracking, crack bridging on the microscale [11, 12], and sacrificial bonds, inter-collagen-fibrillar sliding at the nano scale [13, 14]. However, the bone damage processes, especially the prefailure damage and deformation mechanisms, are still not completely understood due to the complexity of bone's hierarchy. We previously reported an opaque process zone emerged in bone under tensile loading (**Fig. 2C**) [15], which was recently found to be stain by negatively charged stain only under the loading state, in contrast to the classical damage, such as microcracks, which could be stained after the removal of loading. In this study, Digital Image Correlation (DIC) methods have been used in this study to quantify the local strain value at the microscale upon the emergence of such process zones during tensile loading, so as to identify the possible deformation mechanism underlying such phenomenon.

2. MATERIALS AND METHODS

2.1. Sample preparation

Block beams from bovine femurs were prepared using a low-speed diamond blade saw (Buehler Ltd., Lake Bluff, IL). A V-notch, approximately half the depth of the remaining cortical thickness was introduced through the center of the beam using a mill (Series 5400, Sherline, Vista, CA). Block beams were sectioned into thin wafers, and polished with progressively finer grades of polishing papers and fine alumina powder (Buehler Ltd., Lake Bluff IL). Samples were sonicated between each polishing stage. The final dimensions of the notched wafer were approximately 50 × 4 × 0.2 mm.

2.2. Tensile test under light microscope

Samples were loaded using a miniaturized tensile test device (Ernest F. Fullam Inc., Latham, NY) which was fixed on the stage of a light microscope (BX51, Olympus America, Center Valley, PA) (**Fig. 1**). The device loads the sample symmetrically and maintains the point of interest in the middle of the field of view during loading. This setting allowed both transmission and reflection images to be taken during the loading process (**Fig. 2A**). During the entire tensile test, the samples were kept wet by Kimwipe strips wicking from the water reservoir below the specimen, and overall humidity around samples was maintained by a humidifier around 60%.

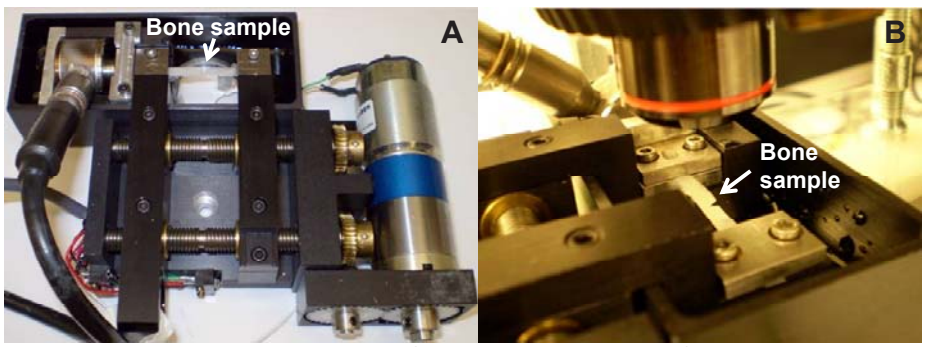

Fig. 1. Miniaturized tensile test device. (A) Overall view. B) Device fixed under light microscope.

2.3. Digital Image Correlation (DIC)

DIC was carried out using a public domain software (HighCorr, by Dr. K. Hemker at Johns Hopkins University), on Matlab platform. The software was modified to obtain 2D strain maps by numerical differentiation of the displacement fields. Local strain was measured by comparing reflection images of samples in the loaded condition after the process zone emerged to the corresponding baseline images before samples were loaded (n=15). By overlapping the principal strain field obtained from DIC with the transmission image, strain values at 5 different locations around the outer edge of process zone in each sample were recorded to find the strain at which the process zone emerges. Maximum peak strains within the process zone upon loading as well as the residual strain in the process zone region following unloading were also measured.

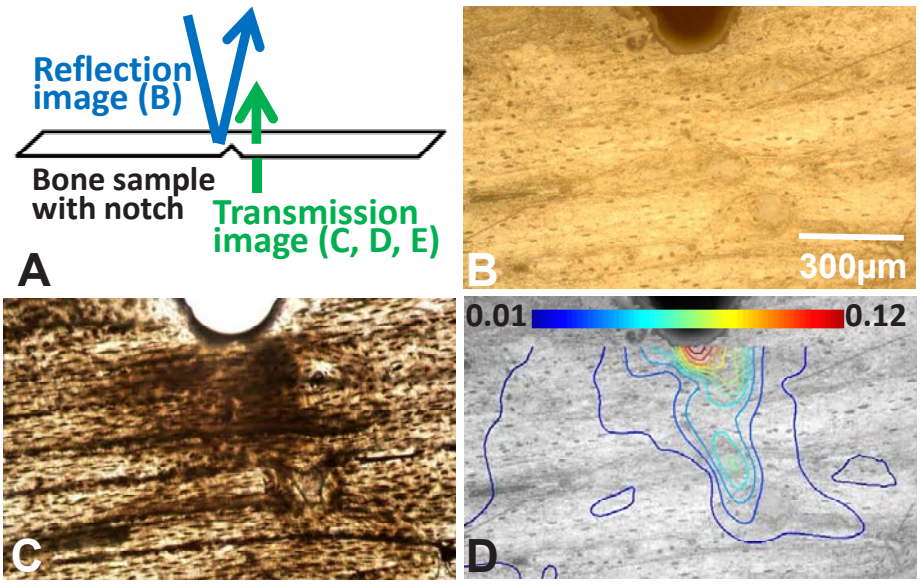

Fig. 2. Reflection, transmission, and DIC images of bone during tensile loading. A) The schema represents the reflection illumination light pathway (blue arrow) in "B" and the transmission illumination light pathway (green arrow) in "C"; B) reflection image with no noticeable change upon loading; C) transmission image showed a prominent "process zone" upon loading; D) Principal strain (e_1, amplitude depicted by the color-bar) field calculated by DIC from the reflection image "B", high strain region colocalized with "process zone" in "C".

3. RESULTS

The process zones observed under transmission illumination colocalized with high-strain regions, with peak principal strain at 9.4% ± 4.0% (mean ± SD, N=15) calculated by DIC. The shape of the process zone was best matched by the distribution of the principal tensile strain (e1) (**Fig. 2D**). Strain fields were highly heterogeneous and were irregularly shaped. The strain values recorded at the edges of the process zones were assumed to be related to the emergence of process zone. These values ranged from 0% to 3%, with an overall average of 1.1% ± 0.65% (**Fig. 3**). The maximum residual strain at the process zone upon unloading was found to be 2.7% ± 1.3% in 15 samples, as samples were unloaded from tension and process zone was mostly disappeared.

4. DISCUSSION

The overlapping of high strain fields calculated by DIC and the process zone confirmed that the underlying mechanism producing this opaque phenomenon was associated with deformation. Such deformation might create additional interfaces in bone which might alter the normal pathway of the light transmission through the bone. The mean strain value (1.1%) at which the process zone emerges in this study is similar to the strain values (0.91%) measured by small angle x-ray scattering (SAXS) at which the sliding between collagen fibrils was reported to occur under tensile loading [16]. However, at this point, we are not sure whether or not gaps could form axially during interfibrillar sliding, which might caused such opaque phenomenon in bone.

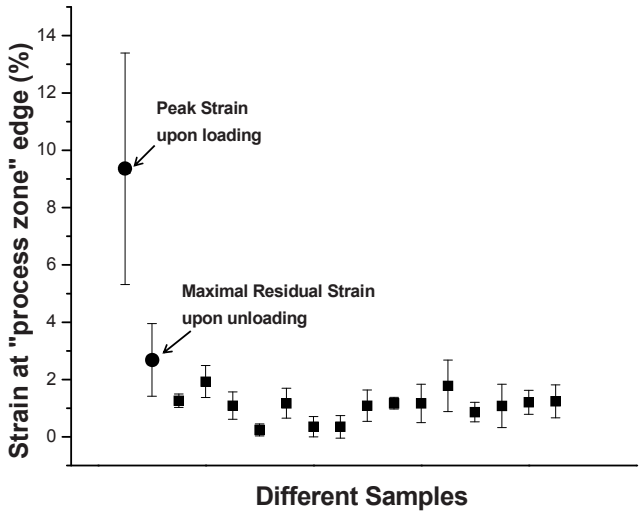

Fig. 3. Strain values associated with the process zone edges (N=15, square markers). Overall peak strain and maximal residual strain values are indicated by solid circles. Error bars represent the standard deviation.

The local strains at the microscale observed in this study were an order of magnitude greater (around 10%) than the macroscale strains at which bovine bone fails (for bovine femur, ε_{ult} is less than 1 % [17]), which indicates that substantially high local strains are implicit in the macroscopic strains as averaged over the continuum bone. In addition, up to 100% strain has been reported on isolated unmineralized collagen fibrils [18]; therefore, the peak strain values (up to 14%) observed in our study might result from deformations of collagen fibrils themselves, as opposed to fibrillar sliding. Highly heterogeneous and irregularly shaped strain fields demonstrate the intrinsic heterogeneous nature of bone. The relatively large variation in the strain values observed at the edge of the process zones is partially caused by the strain difference between bone surface (DIC of reflection images) and the entire thickness (transmission images). This might also explain why in some cases the process zone edges seemed to occur at locations of 0% strain: since at these locations, there might be no strain at bone surface, as calculated by DIC on reflection images, but internal deformation underneath the surface might still occur and cause the emergence of the observed process zone.

5. CONCLUSION

The opaque process zone observed in loading bone is a partially reversible and deformation-related phenomenon. Peak local strains observed at the microscale are one order higher than the macroscopic ultimate strain. Local strain values associated with the emergence of process zone on microscale suggested the interfibrillar sliding of collagen fibril might be one of causes for such opaque to occur.

ACKNOWLEDGEMENT

This study was funded by NSF CAREER-0449188 (OA). Support for Ji-Hoon Jeon was provided by the Korea Research Foundation Grant funded by the Korean Government (MOEHRD, Basic Research Promotion Fund) (KRF-2007-D00079).

REFERENCE

1. Iacovino, J.R., *Mortality outcomes after osteoporotic fractures in men and women.* Journal of Insurance Medicine. **33**(4): 316-320. 2001.
2. Melton, L.J., *Adverse outcomes of osteoporotic fractures in the general population.* Journal of Bone and Mineral Research. **18**(6): 1139-1141. 2003.
3. Weiner, S. and Wagner, H.D., *The material bone: Structure mechanical function relations.* Annual Review of Materials Science. **28**: 271-298. 1998.

4. Gupta, H.S. and Zioupos, P., *Fracture of bone tissue: The 'hows' and the 'whys'.* Medical Engineering & Physics. **30**(10): 1209-1226. 2008.
5. Donoghue, P.C.J. and Sansom, I.J., *Origin and early evolution of vertebrate skeletonization.* Microscopy Research and Technique. **59**(5): 352-372. 2002.
6. Fratzl, P., et al., *Structure and mechanical quality of the collagen-mineral nano-composite in bone.* Journal of Materials Chemistry. **14**(14): 2115-2123. 2004.
7. Tencer, A.F. and Johnson, K.D., *Biomechanics in orthopedic trauma : bone fracture and fixation*. 1994, London; Philadelphia: M. Dunitz ; Lippincott. 1994.
8. Jones, B.H., et al., *Exercise-Induced Stress-Fractures and Stress Reactions of Bone - Epidemiology, Etiology, and Classification.* Exercise and Sport Sciences Reviews. **17**: 379-422. 1989.
9. Burstein, A.H., Reilly, D.T., and Martens, M., *Aging of Bone Tissue - Mechanical-Properties.* Journal of Bone and Joint Surgery-American Volume. **58**(1): 82-86. 1976.
10. Cummings, S.R., et al., *Epidemiology of Osteoporosis and Osteoporotic Fractures.* Epidemiologic Reviews. **7**: 178-208. 1985.
11. Nalla, R.K., Kruzic, J.J., and Ritchie, R.O., *On the origin of the toughness of mineralized tissue: microcracking or crack bridging?* Bone. **34**(5): 790-8. 2004.
12. O'Brien, F.J., Taylor, D., and Lee, T.C., *The effect of bone microstructure on the initiation and growth of microcracks.* Journal of Orthopaedic Research. **23**(2): 475-480. 2005.
13. Fantner, G.E., et al., *Sacrificial bonds and hidden length dissipate energy as mineralized fibrils separate during bone fracture.* Nature Materials. **4**(8): 612-616. 2005.
14. Gupta, H.S., et al., *Nanoscale deformation mechanisms in bone.* Nano Letters. **5**(10): 2108-2111. 2005.
15. Jeon, J.H., Blendell, J., and Akkus, O. *On the Presence of Phantom Cracks in Bone*. in *ORS 55th Annual Meeting*. 2009.
16. Gupta, H.S., et al., *Cooperative deformation of mineral and collagen in bone at the nanoscale.* Proceedings of the National Academy of Sciences of the United States of America. **103**(47): 17741-17746. 2006.
17. Currey, J.D., *Bones : structure and mechanics*. 2002, Princeton, NJ: Princeton University Press. 2002.
18. Shen, Z.L., et al., *Stress-Strain Experiments on Individual Collagen Fibrils.* Biophysical Journal. **95**(8): 3956-3963. 2008.

Proceedings of the SEM Annual Conference
June 7-10, 2010 Indianapolis, Indiana USA

Probing Pre-failure Molecular Deformation in Cortical Bone with Fluorescent Dyes

Xuanhao Sun[a], Ji Hoon Jeon[a,b], John Blendell[c], and Ozan Akkus[a]*

[a]Weldon School of Biomedical Engineering, Purdue University, West Lafayette, IN, USA

[b]Currently at: LG Chemical/Research Park, Daejeon, Republic of Korea

[c]Department of Materials Science and Engineering, Purdue University, West Lafayette, IN, USA

* Author to whom correspondence should be addressed

Ozan Akkus, Ph.D.

Associate Professor

Weldon School of Biomedical Engineering

Purdue University

206 S. Martin Jischke Drive

West Lafayette, IN 47907-2032

ozan@purdue.edu

ABSTRACT

To reduce bone fracture incidence, gaining knowledge on the underlying bone damage mechanisms is essential. Although several mechanisms have been proposed on different length scales, the pre-failure deformation processes of bone are still not completely understood. We previously reported an opaque process zone feature in bone under tensile loading which colocalizes with high-strain regions. Unlike the classical damage which can be stained in the unloaded state, the process zone can be stained only when the sample is loaded. In this study, a wide range of fluorescent dyes with different molecular weights (MW) and charges were used to probe the size and charge properties of the structural features leading to process zone emergence. We found none of these fluorescent dyes tested were able to stain the process zone once the loading was removed. All of the negatively-charged dyes with MW less than 70 kDa stained the process zone, while the positively- or neutrally-charged dyes did not, except for the one with smallest MW tested (380 Da) in group of the positively charged dyes. Therefore, we proposed that certain molecular groups with positive charge in bone were exposed during process zone emergence under loading.

KEYWORDS: Bone damage, Fluorescent dye, Strain, Mineral crystal

T. Proulx (ed.), *Time Dependent Constitutive Behavior and Fracture/Failure Processes, Volume 3*, Conference Proceedings of the Society for Experimental Mechanics Series 15, DOI 10.1007/978-1-4419-9794-4_46, © The Society for Experimental Mechanics, Inc. 2011

1. INTRODUCTION

Bone fractures are painful events, and due to the aging of US population, the greater prevalence of bone fractures has been predicted, which will result in increasing healthcare burden for the society [1, 2]. Bone fracture occurs when the external loads exceed its mechnical thresholds, either in the form of a single overload, which causes acute traumuas [3], or in the form of repetitive loading, causing fatigue-type failures [4]. On the other hand, aging [5] and certain bone diseases, such as osteoporosis [6], can change the intrinsic mechanical mechanical competence of bone and increase the fracture risk. Therefore, to reduce bone fracture incidence, understanding the damage mechanisms underlying bone fracture is essential.

Bone is an ideal example of the structure/function relationship in biological materials with the hierarchical structures in the two-phase (organic collagen phase and inorganic apatite phase) composite encompassing different length scales [7-10]. Although several damage mechanisms have been proposed on these different length scales, such as microcracking, crack bridging on the microscale [11, 12], and sacrificial bonds, inter-collagen-fibrillar sliding at the nano scale [13, 14], the prefailure damage and deformation processes of bone are still not completely understood. We previously reported a partially reversible opaque process zone feature in bone under tensile loading which colocalizes with high-strain regions [15]. Unlike the classical damage forms (e.g. microcracks) which can be stained in the unloaded state, the process zone we observed can be stained only when the sample is loaded. Therefore, understanding the origin of this phenomenon may provide novel cues to deformation of bone in the pre-failure region. In this study, a wide range of fluorescent dyes with different molecular weights and charge properties were used to probe for the size and charge of the structual features which leading to emergence of such opaque process zone.

2. MATERIALS AND METHODS

2.1. Sample preparation

Block beams from bovine femurs were prepared using a low-speed diamond blade saw (Buehler Ltd., Lake Bluff, IL) (**Fig. 1**). A V-notch, approximately half the depth of the remaining cortical thickness was introduced through the center of the beam using a mill (Series 5400, Sherline, Vista, CA). Block beams were sectioned into thin wafers, and polished with progressively finer grades of polishing papers and fine alumina powder (Buehler Ltd., Lake Bluff IL). Samples were sonicated between each polishing stage. The final dimensions of the notched wafer were approximately 50 × 4 × 0.2 mm.

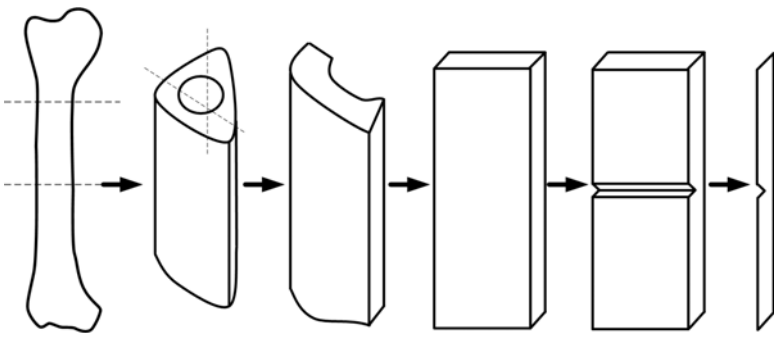

Fig. 1. Schema of wafer specimen preparation.

2.2. Tensile test under light microscope

Samples were loaded using a miniaturized tensile test device (Ernest F. Fullam Inc., Latham, NY) which was fixed on the stage of a light microscope (BX51, Olympus America, Center Valley, PA). The device loads the sample symmetrically and maintains the point of interest in the middle of the field of view during loading. This setting allowed both transmission and reflection images to be taken during the loading process. UV epifluorescent light source was used when imaging the fluorescent dyes. During the entire tensile test, the samples were kept wet by Kimwipe strips wicking from the water reservoir below the specimen, and overall humidity around samples was maintained by a humidifier.

2.3. Fluorescent staining

Fluorescent dyes of different molecular weights (MW) and charged groups (Table 1, Sigma, St. Louis, MO and Invitrogen, Frederick, MD) were locally applied at the notch tip for 15 mins under two conditions: 1) in the loaded condition when the process zone emerged (**Fig. 2A**); or, 2) after removel of the load and disappearance of the process zone. Samples were then thoroughly rinsed off by MilliQ water and staining results was examined by epifluorescent microscopy in reflective mode. Since it was found that samples were more readily stained while loading than after unloading, so if certain dye was found not to stain the samples in loaded condition, it was no more tested in unloaded condition. After tensile test, samples were kept in fluorescent dyes for an additional 2 days to ensure that sufficient time was given for the stain to penetrate in the unloaded state. At least 3 specimens were tested for each condition to confirm the repeatability of reported observations. Light microscopy (with X50 objective) was used in reflection mode to examine whether there were microcracks in the stained regions. Fluorescent images were taken using confocal microscopy (Fluoview1000, Olympus America, Center Valley, PA).

Table 1. Staining results of process zone by different fluorescent dyes.

Fluorescent dyes	MW [Da]	Charge	Staining While Loaded	Staining After Unloading
Calcein Blue	321	-	Yes	No
Oxytetracycline	497	-	Yes	No
Sulforhodamine 101	607	-	Yes	No
Calcein	623	-	Yes	No
Xylenol Orange	761	-	Yes	No
Dextran AlexaFluor488	3,000	-	Yes	No
Dextran OregonGreen	10,000	-	Yes	No
Dextran OregonGreen	70,000	-	No	Not tested*
Rhodamine 123	380	+	Yes	No
RhodamineB hexylester	627	+	No	Not tested*
FURA 2-AM	1,000	Neutral	No	Not tested*
Dextran TexasRed	3,000	Neutral	No	Not tested*

Not Tested: Stains which were unable to stain the process zone in the loaded state were not applied in the unloaded state since samples were more readily stained in the loaded state. MW: molecular weight.*

3. RESULTS

An opaque prcess zone emerged at the root of the notch under tensile loading while transmission microscopy mode was used (**Fig. 2A**), while there was no noticeable change in reflection images. Once samples were unloaded from tension, the process zone mostly disappeared. No microcrack-like features were found at the stained areas by high magnification reflection microscopy.

Staining results of process zone by different fluorescent dyes are summarized in Table 1. First, none of the fluorescent dyes tested in this study were able to stain the process once samples had been unloaded and process zone had disappeared. Second, all of the negatively charged dyes with MW less than 70 kDa were able to stain the process zone (**Fig. 2B**). The largest negative dye employed in this study was 70 kDa in MW and it was unable to acess the features associated with process zone. Third, positive or neutral charged dyes did not stain the process zone, except for Rhodamine 123, which had the smallest MW tested in positively charged group. Among these stained samples, areas with increased fluorescence under UV overlapped with the opaque process zone observed under transmission illumination. Lastly, staining unloaded samples in dye solution for additional 2 days did not bring out the observed process zone. Confocal images showed detailed features of stained area, and stain uptake was found to be at the interfaces of lamellar regions, woven regions, and also perimeters around vessels and holes, which acted as stress concentrators in bone during loading (**Fig. 2C**).

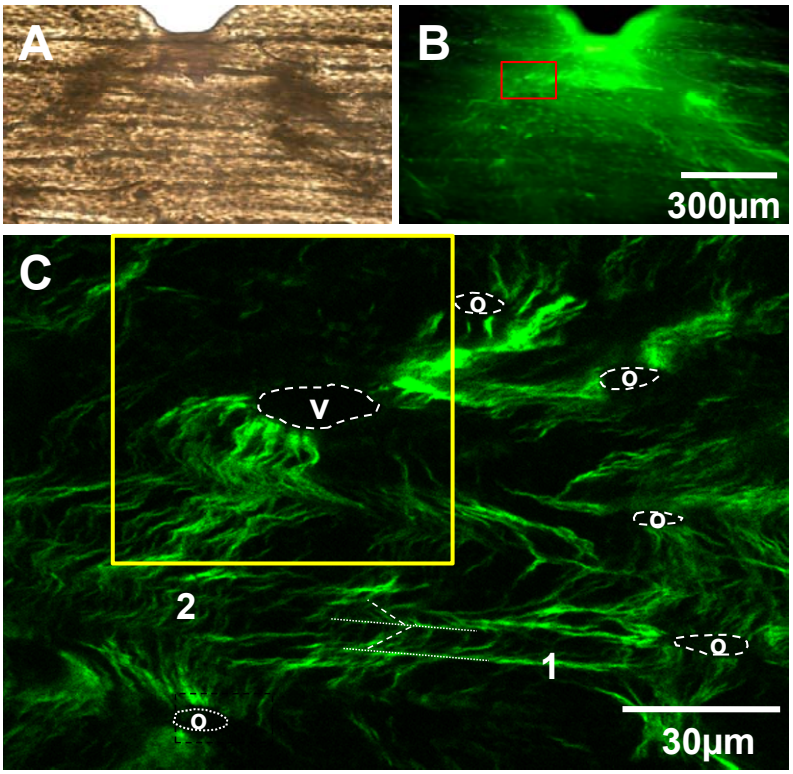

Fig. 2. Representative transmission (A) and matching fluorescence (B & C) images. A) display the “process zone” forming at the notch tip; B) staining of processzone in A by a negatively charged dye, Dextran AlexaFluor488, during loading; C) Higher magnification confocal image of the red inset in B, showing two kinds of stained features: straight lines along lamellar boundaries (labeled as ‘1’ and highlighted with a dotted line) and shorter tortuous lines crossing lamellae or in the woven matrix (labeled as ‘2’). Perimeters of vascular (v) and lacunar (o) pores are highlighted by dashed ellipses. Stain uptake in given lamellae were oriented in parallel and such orientations are highlighted using dashed lines in emulation.

4. DISCUSSION

The results indicates that there is a category of per-failure deformation process which exposes certain nano-scale structural features with positive charges. This deformation process is recoverable, since these structure features are no longer accessible to the fluorescent dyes upon unloading. This is in agreement with the observation by transimiison light microscopy that the process zone would disappear once loading was removed.

There is a size threshold somewhere between 10 kDa and 70 kDa in MW, which corresponds to the Stokes diameter of tens of nanometers [16]. Dye molecules above this size range cannot access the process zone, even under loading, indicating that exposed features were at a size scale comparable to the dimensions of mineral crystallites in bone [17]. Therefore, structural features leading to opacity are much smaller than conventional microcracks, which are at least at the order of several micrometers in size up to several hundred microns [18].

Another important finding was that these structural features exposed under load were charge-specific such that they interacted with negatively charged dyes much more easily than positively or neutrally charged dyes. Such loading-, dye-size and charge-dependent staining suggests that these features in the process zone may not be related to damage, but more likely to a deformation mechanism that is precursor to bone failure. While the identity of such exposed molecular features remains to be determined, the affinity to negatively charged dyes suggests the exposure of calcium moieties associated with the mineral crystals.

5. CONCLUSION

The opaque process zone observed in this study was different from the conventional microcracks. Certain nano-scale positively-charged structural features might be exposed in bone under loading prior to bone failure, like to be the calcium moieties on mineral crystals.

ACKNOWLEDGEMENT

This study was funded by NSF CAREER-0449188 (OA). Support for Ji-Hoon Jeon was provided by the Korea Research Foundation Grant funded by the Korean Government (MOEHRD, Basic Research Promotion Fund) (KRF-2007-D00079).

REFERENCE

1. Iacovino, J.R., *Mortality outcomes after osteoporotic fractures in men and women.* Journal of Insurance Medicine. **33**(4): 316-320. 2001.
2. Melton, L.J., *Adverse outcomes of osteoporotic fractures in the general population.* Journal of Bone and Mineral Research. **18**(6): 1139-1141. 2003.
3. Tencer, A.F. and Johnson, K.D., *Biomechanics in orthopedic trauma : bone fracture and fixation*. 1994, London; Philadelphia: M. Dunitz ; Lippincott. 1994.
4. Jones, B.H., et al., *Exercise-Induced Stress-Fractures and Stress Reactions of Bone - Epidemiology, Etiology, and Classification.* Exercise and Sport Sciences Reviews. **17**: 379-422. 1989.
5. Burstein, A.H., Reilly, D.T., and Martens, M., *Aging of Bone Tissue - Mechanical-Properties.* Journal of Bone and Joint Surgery-American Volume. **58**(1): 82-86. 1976.
6. Cummings, S.R., et al., *Epidemiology of Osteoporosis and Osteoporotic Fractures.* Epidemiologic Reviews. **7**: 178-208. 1985.
7. Weiner, S. and Wagner, H.D., *The material bone: Structure mechanical function relations.* Annual Review of Materials Science. **28**: 271-298. 1998.
8. Gupta, H.S. and Zioupos, P., *Fracture of bone tissue: The 'hows' and the 'whys'.* Medical Engineering & Physics. **30**(10): 1209-1226. 2008.
9. Donoghue, P.C.J. and Sansom, I.J., *Origin and early evolution of vertebrate skeletonization.* Microscopy Research and Technique. **59**(5): 352-372. 2002.
10. Fratzl, P., et al., *Structure and mechanical quality of the collagen-mineral nano-composite in bone.* Journal of Materials Chemistry. **14**(14): 2115-2123. 2004.
11. Nalla, R.K., Kruzic, J.J., and Ritchie, R.O., *On the origin of the toughness of mineralized tissue: microcracking or crack bridging?* Bone. **34**(5): 790-8. 2004.
12. O'Brien, F.J., Taylor, D., and Lee, T.C., *The effect of bone microstructure on the initiation and growth of microcracks.* Journal of Orthopaedic Research. **23**(2): 475-480. 2005.
13. Fantner, G.E., et al., *Sacrificial bonds and hidden length dissipate energy as mineralized fibrils separate during bone fracture.* Nature Materials. **4**(8): 612-616. 2005.
14. Gupta, H.S., et al., *Nanoscale deformation mechanisms in bone.* Nano Letters. **5**(10): 2108-2111. 2005.
15. Jeon, J.H., Blendell, J., and Akkus, O. *On the Presence of Phantom Cracks in Bone*. in *ORS 55th Annual Meeting*. 2009.
16. Tami, A.E., Schaffler, M.B., and Tate, M.L.K., *Probing the tissue to subcellular level structure underlying bone's molecular sieving function.* Biorheology. **40**(6): 577-590. 2003.
17. Kim, H.M., Rey, C., and Glimcher, M.J., *Isolation of Calcium-Phosphate Crystals of Bone by Nonaqueous Methods at Low-Temperature.* Journal of Bone and Mineral Research. **10**(10): 1589-1601. 1995.
18. O'Brien, F.J., et al., *Visualisation of three-dimensional microcracks in compact bone.* Journal of Anatomy. **197**: 413-420. 2000.

Proceedings of the SEM Annual Conference
June 7-10, 2010 Indianapolis, Indiana USA

The Influence of MgO Particle Size on Composite Bone Cements

M. Khandaker and S. Tarantini
Department of Engineering and Physics, University of Central Oklahoma, Edmond, OK 73034

ABSTRACT

Conventional poly Methyl MethAcrylate (PMMA) bone cement has a problem of stress-shielding due to big difference in strength between host bone and bone cement. Nanoparticles like MgO, Silver, $BaSO_4$ have been added to PMMA cement to improve bone healing and reduce infection. But the issue of stress-shielding due to the inclusion of the nanoparticle to PMMA is not understood yet. The objectives of this research were to determine whether inclusion of micro/nano sizes MgO particles on PMMA bone cement has any influence on the interface fracture strength. Cobalt™ HV bone cement (CBC), a commercial orthopedic bone cement, was used in this research as PMMA bone cement. Three-point bend test were conducted to find elastic and fracture properties of CBC, CBC with 36 μm MgO additives and CBC with 22 nm MgO additives. Fracture tests were also conducted on three groups of bone-cement specimen to find interface fracture toughness: (1) bone- CBC without MgO particles, (2) bone- CBC with 36 μm MgO particles, and (4) bone- CBC with 22 nm MgO particles. Experimental results show that MgO particle sizes has no significant effect on the adhesion strength.

BACKGROUND

Clinical follow-up studies in cemented total hip arthroplasties indicate that femoral prostheses loosening is a major problem [1]. Mechanical factors have been partly attributed to this loosening and consequent failure of the bone-cement interface. The other attribution to failure has been made to biological reaction to the cement. Recently, a number of experimental [2-4] and numerical studies [5-7] have been conducted to shed light on the failure of bone-cement interfaces. Lucksanasombool *et al.* [2] used a four-point delamination test to study the interfacial fracture toughness at a bovine tibia bone-cement interface, using three different cements. Wang and Agrawal [4] introduced an effective mixed-mode fracture toughness test, based on the sandwich concept, for bone-bimaterial interfaces. The mixed mode technique is invaluable when studying joints under complex loading conditions. Moreo *et al.* [1] proposed a theoretical mixed-mode failure model for bone-cement interfaces. Mann and Damron [5], Kopperdahl *et al*. [7] and Ichim *et al*. used [6] nonlinear fracture mechanics models in predicting the initiation and progression of interface failure of cemented bone-implant systems.

In every case where dissimilar materials are bonded together and undergo a subsequent change of dimension due to change of temperature, particle size and types, stresses develop at the interface due to mismatch of material properties. The magnitude of the stresses can be very large and may have a significant influence on the life of each material in the bonded construct. A current trend of biomaterial research is focused on the use of nanoparticles to solve the debonding problem between bone and cement by improving the fracture properties of composite cements [8-12]. The suitability of a nanocomposite cement to solve the debonding problem requires complete understanding of the fracture behavior of bone-composite cement interfaces. Though the incorporation of nanoparticles like MgO, Ag, hydroxyapatite to conventional cements showed improved biological and chemical properties [8-15], the influences of nanoparticles on the fracture toughness of the natural bone-composite cement made with these nanoparticles is not understand yet. Ricker *et al*. [11] research on PMMA cement showed increased surface roughness, and enhanced cell adhesion of mouse osteoblast cell on PMMA with the inclusion of MgO additives to PMMA. The suitability of inclusion of MgO additives to PMMA cement to solve the loosening problem requires examining the mechanical integrity of the MgO incorporated PMMA cement with bone. This research question for this study was: Do MgO particle size affect on interface fracture strength of bone-nanocomposite specimens? To answer the question the bone cements studied in this research were: (1) Cobalt™ HV bone cement (CBC), (2) CBC with 36 μm MgO additives, referred in this literature as μMgO-CBC and (3) CBC with 22 nm MgO additives, referred in this literature as nMgO-CBC. We have conducted three-point bend experiments on two groups of specimen homogenous (CBC, μMgO-CBC, nMgO-CBC) and bimaterial specimens (bone-CBC, bone-μMgO-CBC, bone-nMgO-CBC). Three-point bend (3PB) tests were conducted on the first group of specimens to measure elastic and fracture properties of the homogenous specimens. Three-point bend

T. Proulx (ed.), *Time Dependent Constitutive Behavior and Fracture/Failure Processes, Volume 3*, Conference Proceedings of the Society for Experimental Mechanics Series 15, DOI 10.1007/978-1-4419-9794-4_47, © The Society for Experimental Mechanics, Inc. 2011

(3PB) tests were conducted on the second group of specimens to measure the adhesion strength of the bi-material specimens.

MATERIALS AND METHODS

Design and manufacture of the setup and instrumentation

A custom made three point bend tester was designed and fabricated in this study. The complete setup is shown in Figure 1. A precision xyz stage was assembled with the base for microscopic viewing purposes via stage-base connector. A high precision microactuator (Newport™ LTA-HL® actuator) and motion controller (SMC 100) was used to push a slider. Two high quality surface finished aluminum rods were used to provide linear motion to the slider. A 50 lb load cell (Futek™ LCM300, model number FSH02630) with a sensor (Futek™ IPM500) was fastened to the slider at one end. The other end of the loadcell was connected with an indenter. To provide line load to a three point bend (3PB) specimen, the indenter edge was milled to round shape using $^{1}/_{32}$" radius concave endmills. The 3PB holder in the test setup was designed for convenient placing of the 3PB specimen on the top of two high strength steel rollers. Dimensions for the 3PB holder and load rod were obtained using ASTM E 399 [16]. A micrometer was placed parallel to the specimen. The purpose of the micrometer was to adjust the specimen position during fracture test so that the center of the notch of a 3PB specimen and the center of the indenter can be aligned collinearly. A needle was glued with the center rod of the micrometer for the precision positioning of the specimen. The calibration of the load cell sensor was done using Troemner™ precision weights sets. The actuator displacements were calibrated by a displacement variable reluctant transducer (Microstrain Microminiature DVRT).

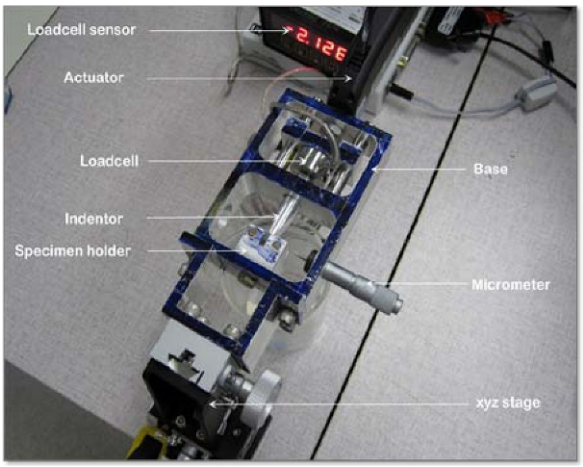

Figure 1 Experimental setup.

SAMPLE PREPARATION

Bone samples were extracted from the mid-diaphyses of fresh bovine femoral shaft obtained from a local abattoir. The femoral shafts were cut longitudinally into two blocks. Each block was milled down to a thickness of 2 mm. Bone coupons of (20×100~200×2) mm dimension were prepared from each block. The bone coupons was cut further to (20×10×2) dimension samples for bone-CBC specimens using (4×0.012×$^{1}/_{2}$) in. diamond wafering blade in a low-speed saw cutter (Buehler isomet 11-1180-100).

Both 36 μm and 22 nm sizes MgO powders were purchased from Sigma-Aldrich. According the manufacturer recommendation (Biomet, Inc), 10 grams of poly Methyl MethAcrylate (PMMA) beads was as added to 5 ml of benzoyl peroxide monomer to prepare the CBC specimen. In order to create samples of μMgO-CBC specimens, 10 percent (w/w) of the 36 μm and 22 nm size MgO additives powders (0.5 gm) were mixed with the PMMA (4.5 gm) and added to the monomer (5 ml). A glass mold as shown in figure Figure 2(a) was used to prepare different kinds of (20×60×4) mm cement and bone-cement blocks.

To prepare the different cement specimens, the cement was added to the top half of the glass molding chamber while the cement was in its doughy phase. To prepare the different bone-cement specimens, the (20×10×2) dimension bone blocks were placed in the mold first, and then cement was poured on top of it. A set of weights equivalent to 80 kPa pressure (clinically applied range [17]) were applied to the samples during the curing process. The pressure was initiated at exactly three minutes after the onset of mixing and was sustained throughout the curing period. After curing, the blocks were cut into (20×4×2) mm size using Buehler isomet low speed cutter. Double sided chuck was used to maintain the bond between the bone and cement specimens. The centre notches for SENB homogeneous and bimaterial specimens were prepared using a 3×0.006×$^1/_2$ in. wafering blade. During the specimen preparation procedures the bone was always kept moist with a saline solution. The dimension of the prepared homogenous and bimaterial specimens are represented in Figure 2(b) and Figure 2(c), respectively.

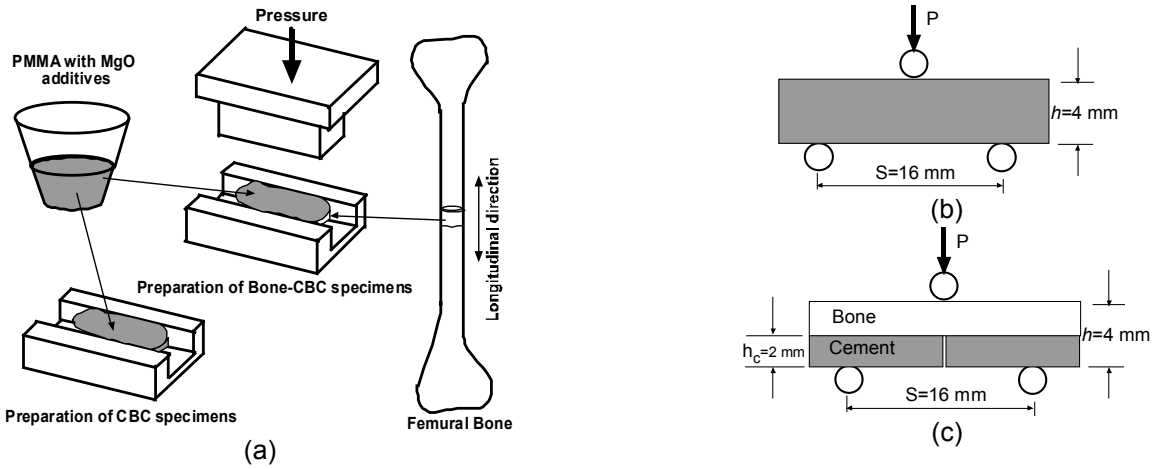

Figure 2 (a) Schematic view of specimen preparation, (b) dimension of the prepared cement specimen, and (c) dimension of the prepared bone-cement specimen.

EXPERIMENT

Three-point bend (3PB) tests were conducted on homogeneous and bimaterial specimens at room temperature using the 3PB stage. During the testing, the live bone samples were continuously kept moist using deionized water, as saline was too corrosive for the specimen holder. The specimens were mounted on the 3PB holder in the test stage. The optimal microscope (Nikon SMZ 1000 steromicroscope) was used to align the center of the specimen and the center of indenter. All specimens were loaded with a loading rate equal to 0.001 mm/s using nanoscale actuator. The load and displacement were continuously recorded until the fracture of the specimens.

DATA ANALYSIS

Several biomechanical parameters were derived from the 3PB test on various cement and bone-cement specimens. The value of Young's modulus, E for a three-point bend specimen was calculated using [18]: $E=kS^3/4BW^3$, where k is the stiffness of the specimen as measured by the slope of the load-deflection curve at the elastic region, S is the standard loading span for the 3PB specimen, B is the thickness, and W is the width of the specimen. For SENB test, the maximum load, P_{max}, at the onset of crack extension from the notch tip was used to calculate the fracture toughness, K_I using relationship [19]: $K_I=P_{max}Sf(\alpha)/BW^{3/2}$, where α is the normalized initial crack length ($\alpha=a/W$) and $f(\alpha)$ is a dimensionless geometric function . The following equation can be used to calculate $f(\alpha)$ [19]: $f(\alpha)=3(\alpha)^{1/2}[1.99-(\alpha)\ (1-\alpha)(2.15-3.93\alpha+2.7\alpha^2)]/[2(1+2\alpha)(1-\ \alpha)^{3/2}]$. Interfacial fracture toughness for a bi-material specimen was calculated using the equation by Zou et al. [20], $G_{IC}=P^2L^2(1/I_c-1/I_s)/8Eb$, where the subscript I_c is the moment of inertia of the specimen, and I_s is the moment of inertia of the bone. The previous equation assumes that the through-thickness crack occurring at the center of the beam and the interfacial pre-crack propagate symmetrically from the tip of the center crack. Therefore, the length of the pre-crack along the interface is zero.

RESULTS

Figure - 3(a) compares the 3PB load-displacement curves of a CBC, µMgO-CBC and nMgO-CBC specimens. The characteristics of the load-displacement curve of the CBC specimens were different from those of CBC with MgO additives specimens. There was no significant change of stiffness of specimen of CBC due to the inclusion of micro and nanosize particles to CBC. Ductility (ultimate displacement) of nMgO-CBC specimens was higher than bone and rest of the cement specimens. Figure - 3(b) shows a comparison of elastic strain energy of different kinds of CBC specimens. The results found no significant difference of elastic strain energy among the CBC, µMgO-CBC, and nMgO-CBC specimens.

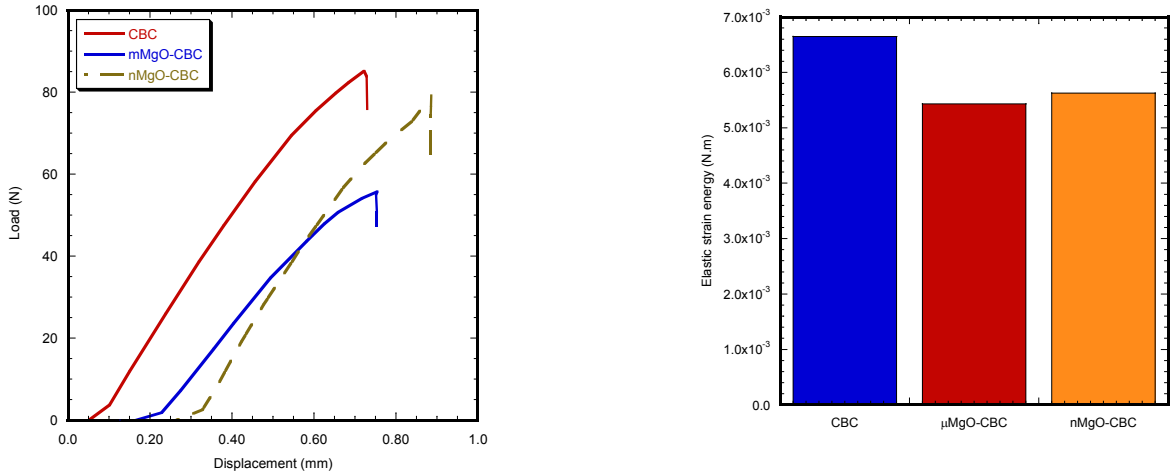

Figure 3 (a) Load vs. displacement plot of different kinds of 3PB CBC specimens, (b) variation of elastic strain energy for various kinds of CBC specimens.

Figure - 4(a) compares the SENB load-displacement curves of CBC, µMgO-CBC and nMgO-CBC specimens. The load-displacement characteristics of CBC specimens exhibited a long elastic and inelastic region before catastrophic failure. The total deformation before the commencement of failure for the nMgO-CBC specimens was higher than those of CBC and µMgO-CBC specimens. The initial slope of the loading curve for transverse bone specimen was higher than those of longitudinal and other cement specimens. The load-displacement behavior of all CBC specimens after achieving maximum load demonstrated that the CBC specimens failed in a more stable manner than those of bone specimen. The crack tip fracture toughness, K_{IC}, for each specimen was calculated from the maximum load value at which the load-displacement curve deviates from linearity. Figure - 4(b) shows fracture toughness of different CBC specimens in comparison with those of bone specimens. Figure shows that transverse notch bone specimen fracture toughness was significantly higher than the longitudinal notch bone specimen and CBC specimens.

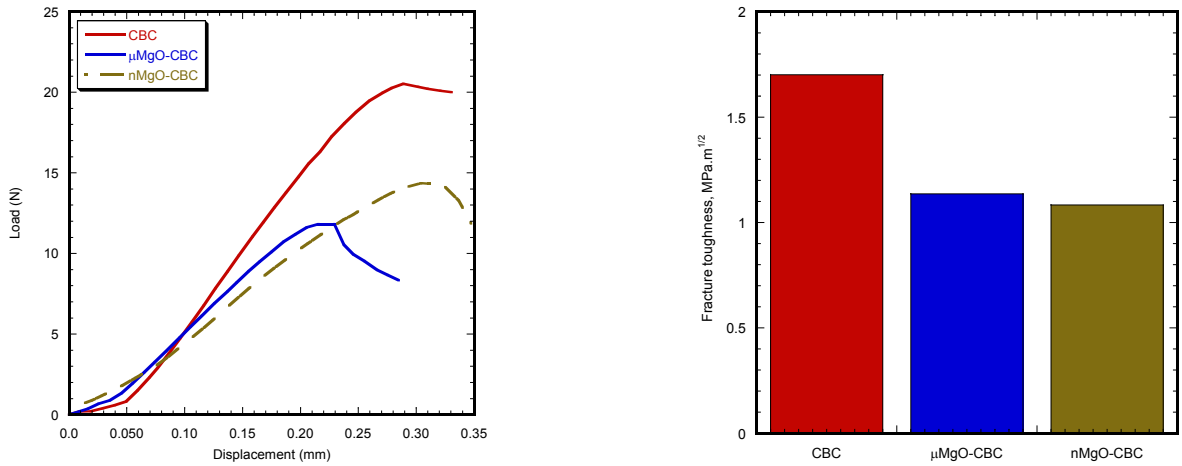

Figure 4 (a) Load vs. displacement plot of different kinds of SENB CBC specimens, (b) variation of fracture toughness for various kinds of CBC specimens.

Figure - 5(a) compares the SENB load-displacement curves between bone-CBC specimen and bone-μMgO-CBC specimen. Specimen broke at the Interface of the bone-nMgO-CBC specimens during the specimen preparation or immediately after loading during testing. Therefore, no interface fracture properties were extracted from the bi-material specimen made with 22 nm MgO additives. The load-displacement response of bone-CBC specimen specimens is characterized as initially elastic response, followed by a short inelastic region and then stable descending response. On the other hand, the load-displacement response of bone-μMgO-CBC specimens is characterized as having higher initially elastic response, broader inelastic region, and smoother descending response of load-displacement compared to those of longitudinal bimaterial specimens. Figure - 5(b) compares the interface fracture toughness values. Results shows MgO additives has insignificant affects on the interface fracture toughness of the CBC when compare with the CBC specimen without MgO additives.

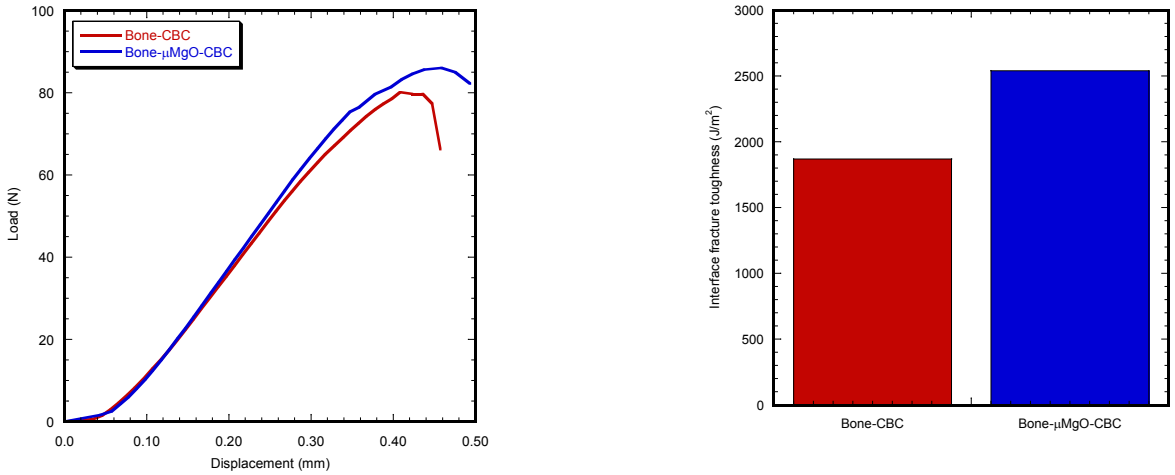

Figure 5 (a) Load vs. displacement plot of different kinds of SENB bone-CBC specimens, (b) variation of interface fracture toughness for various kinds of bone-CBC specimens.

CONCLUSIONS AND FUTURE WORKS

Comparing these properties for different kinds of CBC specimens, we found improved brittleness of CBC due to the inclusion of MgO micro/nano additives to CBC. But we found no noticeable improvement of integrity, mineralization, and amount of energy before breaking for CBC specimen due to the inclusion of MgO micro/nano additives to CBC. Benzyl peroxide monomer penetrates deep inside the PMMA beads in case CBC. The large molecular weight (M_W) of the PMMA beads (M_W = 100000) made it difficult for the PMMA beads to mix uniformly with the monomer. It creates voids, which are the weak points in the cement. This weak point in the CBC lead to stress concentration under external loading. Inclusion of MgO additives to CBC reduces its elastic properties compare to CBC due to the fact that particles with higher MW like PMMA dissolves in monomer slower than lower MW particles like MgO (M_W = 40.3, provided by the manufacturer). This decreases the amount of monomer available for wetting the PMMA powder during mixing, which leads to more weak points in the μMgO-CBC specimens. The detrimental effect on fracture properties produced by the MgO additives has been associated with the lack of adhesion between the MgO additives particles and the polymeric matrix. Cracks originate at the grain boundary between the MgO additives particles and the polymeric matrix. These cracks propagate along the boundary of the polymeric matrix. The non-catastrophic failure behavior of the μMgO-CBC and nMgO-CBC specimens indicates the presence of fracture toughening mechanism. Extrinsic toughening factors, like particle bridging, debonding at the poles of particle/matrix interface, crack trapping, and crack deflection around the MgO additives, may be the cause for this extrinsic toughening behavior. We found insignificant improvement of the mechanical integrity of bone-μMgO-CBC specimen due to the inclusion of 36 μm MgO particle additives into CBC. This improvement can be explained by the higher surface roughness CBC specimen at the interface between bone-CBC due to the inclusion of 36 μm MgO additives as found by Ricker *et al*.[8]. This higher surface roughness at the interface between bone and cement provides extra interlocking between cortical bone and CBC.

The researchers were unable to find significant improvement of mechanical properties of CBC due to the inclusion of MgO additives. In near future, research will be conducted to find appropriate biomaterials to enhance mechanical, biological and chemical properties of PMMA bone cement.

ACKNOWLEDGEMENTS

This publication was made possible by Grant Number P2PRR016478 from the National Center for Research Resources (NCRR), a component of the National Institutes of Health (NIH) and on-campus research grants support from University of Central Oklahoma (UCO). Its contents are solely the responsibility of the authors and do not necessarily represent the official views of NCRR or NIH or UCO.

REFERENCES

1. Moreo, P., Perez M.A., Garcia-Amar J.M., Doblare M., "Modelling the mixed-mode failure of cement-bone interfaces," Engineering Fracture Mechanics, **73**(10), 1379-1395 (2006).
2. Lucksanasombool, P., Higgs W.A.J., Higgs R., Swain M.V., "Interfacial fracture toughness between bovine cortical bone and cements," Biomaterials, **24**(7), 1159-1166 (2003).
3. An, Y.H., Draughn R.A., Mechanical testing of bone and the bone-implant interface. CRC (2000).
4. Wang, X.D., Agrawal C.M., "A mixed mode fracture toughness test of bone-biomaterial interfaces," Journal of Biomedical Materials Research, **53**(6), 664-672 (2000).
5. Mann, K.A., Damron L.A., "Predicting the failure response of cement-bone constructs using a non-linear fracture mechanics approach," Journal of Biomechanical Engineering-Transactions of the Asme, **124**(4), 462-470 (2002).
6. Ichim, I., Li Q., Li W., Swain M.V., Kieser J., "Modelling of fracture behaviour in biomaterials," Biomaterials, **28**(7), 1317-1326 (2007).
7. Kopperdahl, D.L., Roberts A.D., Keaveny T.M., "Localized damage in vertebral bone is most detrimental in regions of high strain energy density," Journal of Biomechanical Engineering-Transactions of the Asme, **121**(6), 622-628 (1999).
8. Shi, Z., Neoh K.G., Kang E.T., Wang W., "Antibacterial and mechanical properties of bone cement impregnated with chitosan nanoparticles," Biomaterials, **27**(11), 2440-2449 (2006).
9. Heo, S.J., Park S.A., Shin H.J., Lee Y.J., Yoon T.R., Seo H.Y., Ahn K.C., Kim S.E., Shin J.W., "Evaluation of bonding stress for the newly suggested bone cement: Comparison with currently used pmma through animal studies," Key Engineering Materials, **342-342**, 373-6 (2007).
10. Liu, H., Webster T.J., "Nanomedicine for implants: A review of studies and necessary experimental tools," Biomaterials, **28**(2), 354-369 (2007).
11. Ricker, A., Liu-Snyder P., Webster T.J., "The influence of nano mgo and baso4 particle size additives on properties of pmma bone cement," International Journal of Nanomedicine, **3**(1), 125-1 (2008).
12. Sirinrath, S., Thomas J.W., "Multiwalled carbon nanotubes enhance electrochemical properties of titanium to determine in situ bone formation," Nanotechnology, **19**(29), 95101-95101 (2008).
13. Lewis, G., "Alternative acrylic bone cement formulations for cemented arthroplasties: Present status, key issues, and future prospects," Journal of Biomedical Materials Research - Part B Applied Biomaterials, **84**(2), 301-319 (2008).
14. Khang, D., Kim S.Y., Liu-Snyder P., Palmore G.T.R., Durbin S.M., Webster T.J., "Enhanced fibronectin adsorption on carbon nanotube/poly(carbonate) urethane: Independent role of surface nano-roughness and associated surface energy," Biomaterials, **28**(32), 4756-4768 (2007).
15. Sirinrath, S., Chang Y., Xingcheng X., Brian W.S., Thomas J.W., "Greater osteoblast functions on multiwalled carbon nanotubes grown from anodized nanotubular titanium for orthopedic applications," Nanotechnology, **18**(36), 65102-65102 (2007).
16. ASTM, "Annual book of astm standards. Section 8," in D790-03 Standard Test Methods for Flexural Properties of Unreinforced and Reinforced Plastics and Electrical Insulating Materials. Philadelphia, PA, 2006.
17. Graham, J., Ries M., Pruitt L., "Effect of bone porosity on the mechanical integrity of the bone-cement interface," Journal of Bone and Joint Surgery-American Volume, **85A**(10), 1901-1908 (2003).
18. Cowin, S.C., Bone mechanics handbook, (2001).
19. Lucksanasombool, P., Higgs W.A.J., Higgs R., Swain M.V., "Fracture toughness of bovine bone: Influence of orientation and storage media," Biomaterials, **22**(23), 3127-3132 (2001).
20. Zou, L., Huang Y., Wang C.-a., "The characterization and measurement of interfacial toughness for si3n4/bn composites by the four-point bend test," Journal of the European Ceramic Society, **24**(9), 2861-2868 (2004).

Proceedings of the SEM Annual Conference
June 7-10, 2010 Indianapolis, Indiana USA

Small-scale mechanical testing: Applications to bone biomechanics and mechanobiology

Marnie M Saunders, Assistant Professor
Center for Biomedical Engineering, University of Kentucky, 205 Wenner-Gren Laboratory, Lexington, KY 40506-0070 marnie.saunders@uky.edu

ABSTRACT
Mechanical testing of biologic tissues requires flexible testing machines to accommodate a variety of testing needs. This paper will illustrate how a cost-effective testing platform was developed to accommodate a wide range of biomechanical testing applications including bone bending and torsion testing, soft tissue tensile testing and bone cell stimulation via fluid shear and substrate deformation. The goal is to demonstrate to the reader that unique issues arise when testing biologic tissues such as controlling for environment and maintaining specimen viability, but with proper care relatively reproducible and accurate testing results can be obtained with a simple, multi-purpose platform.

The bone research field is a multidisciplinary field in which researchers from the life sciences and engineering work to understand the development, structure, function and pathologies of bone. It is hoped that knowledge gained from this basic science understanding will result in improved implants, engineered replacement tissues and therapies/strategies to counteract metabolic bone diseases, to name a few applications. As the field continues to evolve the role of the traditional biomechanical engineer is evolving and few biomechanical engineers find themselves in a pure mechanical testing environment. Rather they are collaborating with biologists to quantify mechanical properties of bone in genetically altered animals, they are collaborating with material scientists to characterize novel biomaterials, and they are collaborating with bioengineers to develop devices and approaches to study bone at the cellular level. As such, biomechanical engineers need testing platforms and skill sets that can accommodate this range of interests. And, given the novelty of many of the research projects, off-the-shelf, commercial fixtures are not always available or appropriate. Our lab has approached this need by developing a multi-purpose, small-scale testing platform. In this paper we discuss the basics of our system, demonstrate its applications and acknowledge its limitations. The goal is to illustrate to the reader that mechanical testing of biologic tissues is a unique field and the testing results are only as good as the devices and techniques used to obtain them.

Mechanical testing machines have been a useful tool in the bone field for several decades. As such, there are several excellent papers and books available to the interested reader that detail appropriate mechanical testing procedures for bone [1-5]. The focus of this paper is on the development of a platform to cost-effectively deal with varied and sporadic biomechanical testing needs without sacrificing data accuracy. Furthermore, the goal is to show that this system can duplicate systems developed by other researchers to stimulate bone and bone cells, providing a powerful, multi-purpose testing frame. To begin the design and fabrication of our small-scale loading machine we looked to the types of commercial testing platforms available and considered the design against our current and likely future needs. Commercially, testing machines are uniaxial and biaxial with the latter comprising both torsional and rotational capabilities. Given that the vast majority of our testing needs are uniaxial we opted for the single axis design and determined that torsion capabilities using the single axis could be added at a later date. We set out initially to accommodate the most common types of testing needs in our lab: bend testing of bones, compression testing of hard tissues, tension testing of soft tissues, *in vivo* exercise loading, and fluid shear and substrate deformation of bone cells. While we have previously detailed the development of the loading platform [6], we will summarize briefly the major components and considerations of the machine. Generally single axis machines are on a fixed frame. While we will illustrate later in this article the advantages of using a movable frame, we found that an inexpensive way to create the two main components of the platform, the linear, vertical

T. Proulx (ed.), *Time Dependent Constitutive Behavior and Fracture/Failure Processes, Volume 3*, Conference Proceedings of the Society for Experimental Mechanics Series 15, DOI 10.1007/978-1-4419-9794-4_48, © The Society for Experimental Mechanics, Inc. 2011

motion and the base frame was to purchase a slide and milling machine table (Figure 1). The linear slide is driven by a servo motor selected for its programmability. The slide and table are connected via aluminum plates. All connections are slotted and keywayed to make assembly reproducible. To reinforce the machine for larger loads, side plates running the vertical length of the slide have been added (not shown in Figure 1). A range of transducers were purchased to accommodate a variety of testing needs. Load cells range from 50 gm to 445 N; torque cell capacity is 176.5 Nmm (25 oz-in); and, displacement sensors accommodate 5 and 25 mm of travel. As is typical of biomechanical testing, machine deformation is largely unaccounted for, but assumed to be negligible given that machine stiffness is much greater than specimen stiffness.

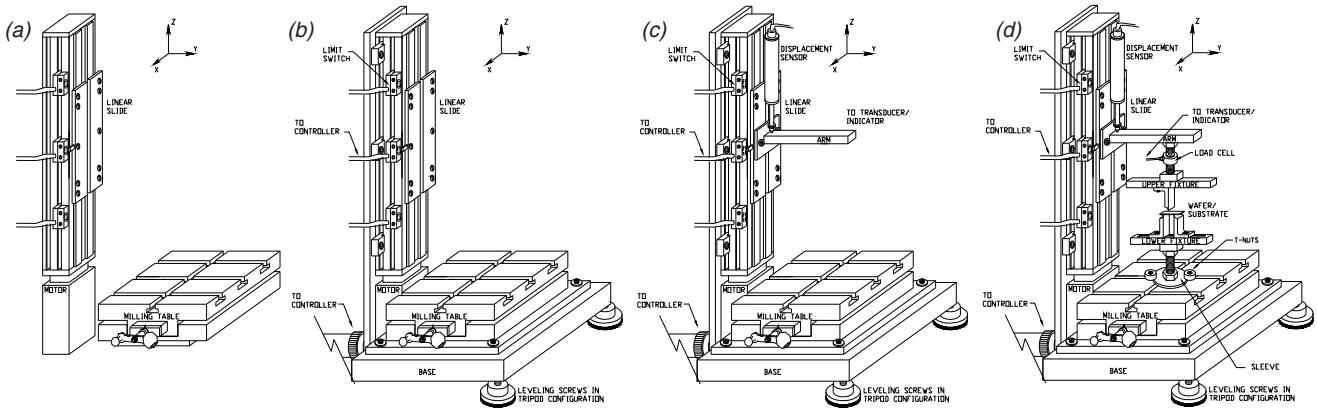

Figure 1. (a) Small-scale loading machine designed around a commercially-available linear slide and milling machine table. (b) Aluminum plates were fabricated to connect the slide and table and keywayed for easy and reproducible assembly. (c) An arm attached to the slide and t-slots in the milling machine table enable a variety of fixtures to be assembled in the platform, such as those shown for three-point bending (d).

Small-scale biomechanics work readily conducted with this machine includes bending, compression and tension. Since bending and compression do not require securing the bone ends during testing, the main concern with these tests is to ensure the load is applied correctly. For bending, the ideal test is with the bone under four-point loading. However, if care is not taken to ensure that loading is simultaneously on all four points of contact, such as using independent spring-loaded contacts, the data will be erroneous. We routinely conduct three-point bend testing which may yield less valuable information given that failure is at the point of contact. But it is much more reproducible at the small-scale to ensure that three points of contact are maintained. In addition, theoretically a point load is desired and the fixture where it comes in contact with the bone should be as thin as possible. We have found that in neonatal rat and adult mouse long bone models, aluminum fixtures (thickness = 0.5mm) are sufficient to fracture the bone without being pitted by it. Given the asymmetry of bone, bone will often roll and it may be necessary to apply a pre-load to the bone to ensure proper orientation in the frame. Extreme care must be taken to guarantee that the bone is not overloaded and damaged in this process.

For compression testing we utilize finely machined and polished platens that we assemble on axis and set the gap between them using gauge (Johansson) blocks (Figure 2a). The key to testing in compression is to ensure that the load is uniformly applied across the specimen surface and that the specimen loading surface and load cell are coaxial. We achieve this using a combination of swivel assemblies. Tension testing of tissue requires clamping the ends on axis (Figure 2b). Given that our loading machine does not have feedback control, it would be unadvisable to attempt to cyclically load (fatigue) soft tissue to failure given the high degree of hysteresis in these tissues. However, we do use this machine to conduct destructive tensile tests on soft tissues. We utilize aluminum (and polycarbonate) friction clamps and rigidly mount one clamp to the base and the other to the arm via a universal joint to allow for self-alignment. In addition to ensuring that the tissue can continue to self-align during testing, it is also important to verify that the load-displacement curves are indicative of a successful test. Typically with soft tissues a toe region initially will be evident as the tissues take on load. Following this, a distinct linear region is present and any fixture slip (displacement increase without subsequent load increase) or testing malfunction is readily identifiable in this region (Figure 2b). In failure, tissues that have been cut and allowed to heal or sutured will generally display a ‘step’ effect as the tissue fully separates. For homogenous tissues testing is fairly routine. However, when tissues are nonhomogenous additional concerns arise. For example, when conducting tensile testing on ligaments and tendons it is important to understand that they have a midsubstance

region that largely reflects the ligament/tendon properties and transition regions on both ends where the tissues insert into the bone/muscle. Given that these tissues minimally have three distinct regions, tensile testing reflecting only the overall tissue behavior is less than ideal. While extensometers can be added to the various regions of interest, the weight of these devices can interfere with accurate measurements. We use ink to place thin, contrast markings across the regions of interest and utilize video dimensional analysis (noncontact extensometry) to calculate the strain contribution in the individual regions as a function of the total strain. It is critical that living tissues be kept hydrated at all times in saline and we strive to test these tissues within 1-2 hr of harvest.

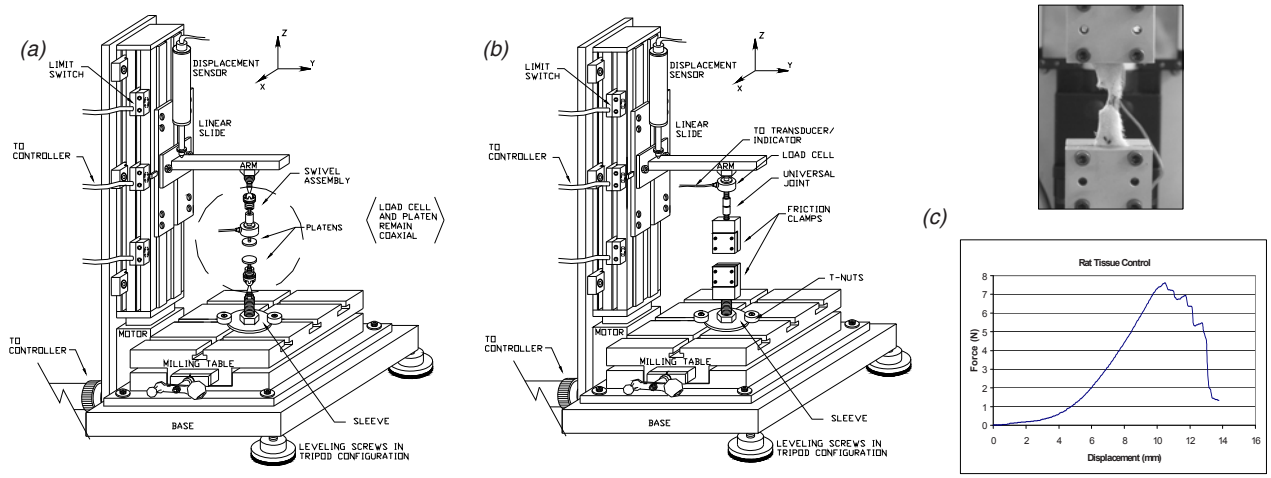

Figure 2. (a) Platen assembly for compression testing. Swivel platens adjust to ensure that the platen face is parallel to the surface of loading. (b) Friction grip assembly for tension testing. A universal joint enables the specimen to maintain axial alignment during testing. (c) A typical soft tissue tension test curve showing a step-wise failure and the corresponding photograph.

In addition to the specific loading mode fixtures demonstrated, a variety of generic fixtures found in many testing laboratories may also be interfaced with the platform. For example, the standard vise grip enables blocks and specimens with parallel faces to be conveniently constrained in the platform. In Figure 3, the vise fixture was used to clamp synthetic bone blocks while the pull-out performance of a mini-implant in the block was tested. A backing plate may be necessary to ensure that the block is not able to rotate during testing, particularly when a moment is created. When specimens are of an irregular geometry, hemispherical fixtures may be used. In these fixtures, concentric rows of drilled and tapped holes and pointed set screws are used to anchor irregularly shaped objects during tension/compression tests. In one of our more interesting and unusual tests, we used this type of device to hold a dolphin ear while the ossicles were mechanically deformed.

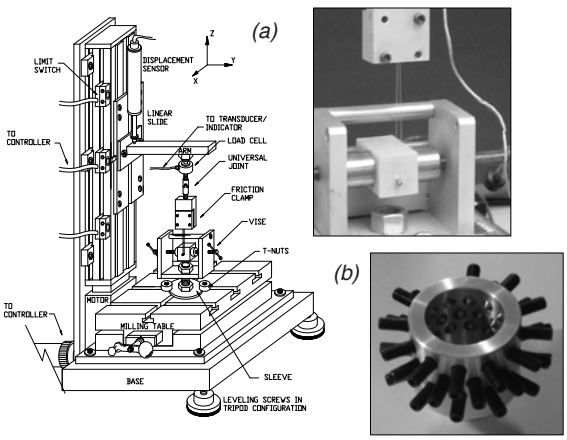

Figure 3. (a) Vise fixture mounted to the platform may be used to grip a variety of blocks. (b) Hemispherical fixture used to anchor irregularly shaped specimens.

As the system developed, it became necessary to expand our testing capabilities to include torsion. Rather than build a second platform utilized solely for torsion we opted to utilize the existing platform and linear motion. To generate torsion we fabricated a rack and pinion assembly, Figure 4. The rack attaches to the linear arm of the loading machine and the pinion center remains coaxial to the torque cell (176.5 Nmm) line of action and the mechanical/anatomical axis (approximately equal in our neonatal rodent limbs) of the specimen. Given the small-scale size, fixtures were developed enabling potting and placement of the specimens in the loading frame without loading the shaft to minimize unintentional shaft damage during setup. This work has been published and will not be discussed here at length [7]. However, it will be pointed out that rack compliance is critical given that the amount of rotation is not measured directly with an RVDT but is measured indirectly by calculating it from the linear displacement of the slide and the pinion size. Digital protractors on the arm are used to confirm that there is no out-of-plane motion of the rack. It is also important to note that while biomechanical tests on long bone

have typically been conducted with testing systems similar to this in which one end of the bone is fixed and the other is free to rotate [8-9], this is not a true 'torsion' test but more accurately a 'twist' test. Recently a pure torsion testing frame was developed and validated for bone using a force couple to generate the torque [10-11]. Where the latter system is clearly the appropriate one for determining material properties, structural properties are determined for a given loading mode (tension, compression, shear, …) and the 'twist' test is acceptable under these conditions. Additionally, the rack and pinion approach did not require the development of a single purpose testing system which for our sporadic torsion testing needs was not cost-effective.

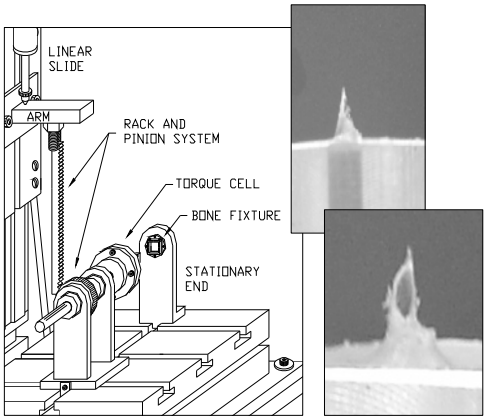

Figure 4. Rack and pinion assembly for torsion testing. Photograph of bone showing classic spiral fracture indicative of torsional failure.

On a final note, it would be remiss to not mention that biomechanical testing of rodent bones has the ultimate goal of affecting our understanding of the behavior of human bone. However, care must be taken to understand the age of the animal model in terms of human years. While it is tempting to look at overall lifespans and adjust accordingly, this may be too simplistic. Moreover, growth plate closure signifying skeletal maturity in humans, fails to occur in rats. In an interesting article by Quinn, the age of a rat in 'people' years is approximated for a variety of biological states [12]. In addition, this system may also be used to study small sections of human bone down to individual trabeculae. If this is the intended testing purpose, it should be appreciated that there are 'size effects' present [1]. For instance, a large bone will have more defects (weaker regions) and may therefore behave differently from a small bone/bone section with fewer defects. As a result of this phenomenon, small bones/sections may sustain higher stress prior to failure in comparison to large bones/sections [1]. Utilizing this system for human bone studies, researchers should be aware of the Weibull approach [13] and ways to handle the size effect issue in bone [14]. These issues are particularly important when dealing with fatigue of bone. It should also be noted that the testing platform we have developed is not ideal for extensive fatigue testing; the linear slide is not fatigue-rated.

In addition to the classic biomechanics studies conducted on tissues, research into mechanobiology and more specifically mechanotransduction is aimed at understanding how bone cells sense and respond to mechanical loading. Because bone cell response may be measured directly at the cellular level by quantifying cellular activity or indirectly at the tissue level by quantifying bone formation/resorption (the product of cell activity), both *in vitro* (cell) and *in vivo* (animal) mechanotransduction models exist. *In vitro* mechanotransduction platforms simulate the loading the cells experience in the physiologic environment and attempt to elucidate the pathways and mechanisms by which the cells respond. Brown has written an excellent review of these *in vitro* systems and their advantages and disadvantages [15]. Here we will justify the biological premise for fluid flow [16] and substrate deformation. In the native bone tissue osteocytes are housed in lacunae in the bone matrix and form a networked conduit, the lacuno-canalicular system, with other osteocytes via canalicular channels that connect the lacunae. This unique network enables osteocyte processes to physically connect in a shared pool of interstitial fluid that bathes this complex. The osteocytes in turn, are physically connected to osteoblasts, surface-residing, bone-forming cells that share a common lineage with the osteocyte. That is, osteocytes were formerly osteoblasts that in the process of forming bone walled themselves off and became encased in the bone matrix. This interconnectivity makes it possible for cells to sense biophysical signals and respond [17-19]. For example, during walking as the leg bones are cyclically loaded and unloaded, the interstitial fluid flows back and forth across the osteocytes. In this manner, osteocytes are able to sense the global (macroscopic/organ) loading at the local (microscopic/cellular) level and many believe this phenomenon is critical to mechanotransduction. To simulate this in the laboratory osteocytes and osteoblasts (acting as young osteocytes) are plated on glass slides and inverted on parallel plate flow chambers that are used to subject groups of cells in monolayer to physiologic levels of fluid shear [20].

Rather than use commercially-available syringe pumps or testing machines we opted to utilize our small-scale loading platform and mimic the setup of Jacobs, et al. [20]. Using tubing connected on one end to the plate inlet and on the other end to the syringe, an oscillatory waveform cycles the syringe plungers up and down which exposes the cells in the flow chamber to oscillatory fluid shear with a standard parabolic flow profile, Figure 5a. Initial fluid shear studies on osteoblasts utilized the osteoblast as a 'young' osteocyte given the difficulty of

isolating osteocytes from the mineralized bone matrix. Appreciating that osteoblasts are surface residing cells, substrate deformation may be a more appropriate model than fluid flow in these cells [21]. To accommodate this type of loading, a polycarbonate environmental chamber and reservoir with three-point bend fixtures were fabricated for the existing platform, Figure 5b. The reservoir enables the cells to be loaded in a hydrated environment to avoid cell death and also provides some secondary fluid shear forces. The environmental chamber is used in lieu of placing the machine in an incubator to avoid oxidation of the steel components of the slide and milling table. The environmental chamber controls for temperature via ceramic microheaters, pH via the addition of stabilizers in the medium, and humidity via the addition of a wetted sponge placed in the chamber. While *in vitro* studies are quite advantageous to study an isolated event, it is difficult (if not impossible) to translate the *in vitro* data to clinical relevance.

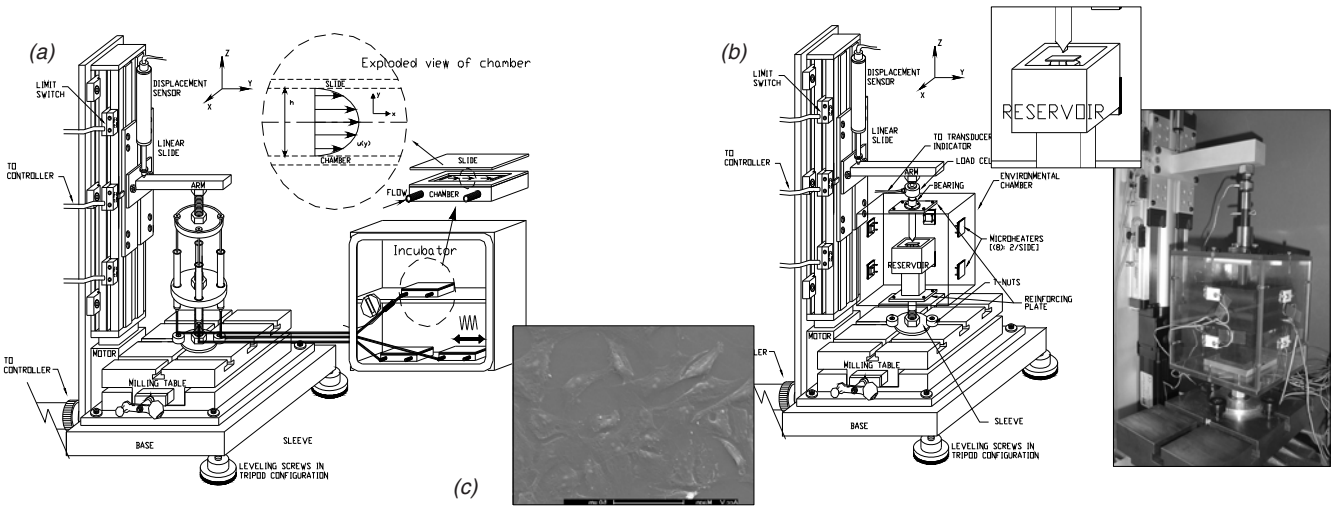

Figure 5. (a) Syringe assembly used to subject bone cells in a parallel plate flow chamber to physiologic levels of fluid shear (modified from the setup of Jacobs, et al.). (b) Substrate deformation assembly used to subject osteoblasts to physiologic levels of bending (and secondary fluid shear). The environmental chamber was developed to maintain temperature; pH and humidity were also regulated. (c) Cells in these systems are plated in monolayer on a synthetic substrate and subjected to stimulation.

More physiologically relevant than cellular or *in vitro* mechanotransduction models are living or *in vivo* models. These models include loading to simulate use and overuse and unloading to simulate weightlessness and bed rest/paralysis. For loading studies bones may be loaded by training the animals to stand on their hindlimbs while increasing the weight on their backs. A common way to accomplish this is to train rodents in cages with a live floor to send an electric shock as negative reinforcement and food as positive reinforcement [22]. Another method to apply load to *in vivo* models is to anesthetize the animals and put them in a device that loads the limbs in a desired manner [23-25]. Based on the work of Gross, we again utilized our platform and developed a fixture that enabled us to apply a concentrated, cantilevered load to rodent tibiae, Figure 6. In addition, the platform was designed to rotate such that the limb could be loaded in the anteroposterior or mediolateral orientation. For torsion and *in vivo* stimulation

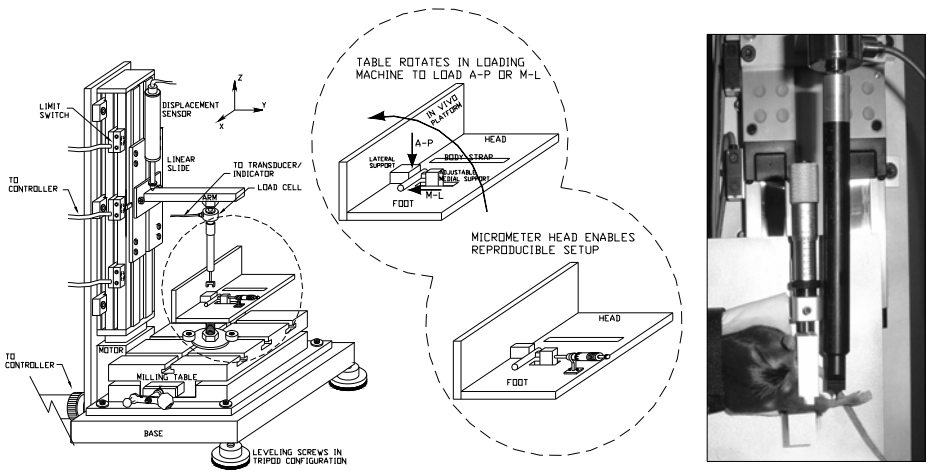

Figure 6. Bending assembly for in vivo stimulation studies. The platform rotates to load rodent tibiae in the anteroposterior (A-P; front-to-back) or mediolateral (M-L; side-to-side) orientations. A cantilevered loading is produced in which the proximal end of the tibia is held in place and the distal end is cyclically stimulated (modified from the setup of Gross, et al.).

studies the movable base of the milling machine table makes it trivial to align the specimens in the loading machine for testing. Unlike standard commercial testing systems, the planar motion provided by the table enables the attached fixtures to be dialed-in either front-to-back or side-to-side, then locked down for testing. When axial testing is required, a simple set of alignment fixtures may be used to reset the table for testing [6]. Although the use of a stationary base does not mean *in vivo* stimulation and torsion cannot be conducted, the movable table greatly simplifies fixture design and setup and improves testing resolution and accuracy by keeping the entire testing fixture on level with the platform table at all times. For example, if a fixed base had been used for torsion, the loading fixture would have to extend beyond the machine base. This would require additional design consideration to guarantee that the platform the animal rested on was level. If not, the rack and pinion would not properly align, testing would be inaccurate and fixture damage would ensue.

As any model does, *in vitro* and *in vivo* mechanotransduction systems have their own unique sets of advantages and disadvantages. For instance, while *in vitro* models enable the study of an isolated event or marker, disadvantages of these systems include the utilization of cells in monolayer, dissociation of the cells from the extracellular matrix and the inability to correctly preserve the three-dimensional (3D) architecture of the communication networks found in bone. While these drawbacks serve as arguments for the use of *in vivo* models these systems also have disadvantages. For example, normal loading of the bone may desensitize it to experimental stimulation and the physiologic complexity of the model makes it difficult to determine the effects of the isolated load.

To this end, our lab proposes that an *ex vivo* or organ culture model may be useful in mechanotransduction research. In this system the whole bone is isolated, loaded and the effect of the loading studied in culture, Figure 7. While these systems also have disadvantages, most notably that they are a 'dying' culture, they offer unique advantages that are attractive for bone mechanotransduction studies. For instance, they maintain the various bone cell types (osteocyte, osteoblast and osteoclast) in their appropriate ratios in a 3D environment with intact communication networks and in the native milieu. To validate the use of these models in mechanotransduction research we have previously shown that the bones in culture remain viable, grow and are capable of responding to mechanical stimulation with an increase in strength [4]. For stimulation, femurs from 2 day old neonatal rats were placed in the three-point bend fixtures (with padded, rubber bumpers) and subjected to 350 cycles of physiologic loading. Following loading, the bones were returned to culture for 1 wk then mechanically tested to determine structural effects of the loading. One bout of 350 cycles of stimulation increased bone stiffness 35% over nonloaded controls [26], suggesting that the models may be able to provide unique insights into bone and bone cell mechanoresponsiveness.

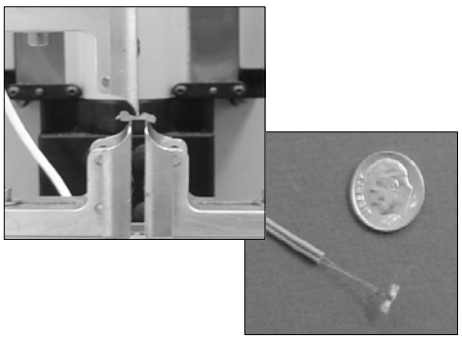

Figure 7. Organ culture (ex vivo) neonatal rodent models enable isolated, mechanically-induced mechanisms and pathways to be studied in environments that increase the physiologic relevance over in vitro models while simplifying the complexity over in vivo models.

The validation of the *ex vivo* mechanotransduction model makes it possible to study mechanisms and pathways of mechanically-induced bone formation using this approach. For example, in clinical treatment with distraction osteogenesis tensile force is applied to bone to elongate the tissue. While the condition is prevalent in both the orthopaedic and craniofacial fields, in the craniofacial field it may be used to correct airway obstruction and syndrome-associated facial deformities in which bone lengthening must be within fractions of a millimeter to achieve successful symmetry. Given that little is known of the mechanisms by which the phenomenon occurs, the procedure often reduces to a trial and error approach [27]. Understanding the pathways and mechanisms by which this occurs will help to make distraction outcomes more predictable and provide guidelines to assist in treatment. While the *ex vivo* approach may be used to model a variety of clinically-relevant scenarios involving mechanical load, it may also be used to study the effect of isolated factors on pathway response and outcome. For example, of particular interest to our lab is understanding the role of cellular communication in mechanically-induced bone formation. Using topical additives or transgenic models, cell-cell communication may be inhibited and the effect of the inhibition on mechanically-stimulated bone formation quantified. Thus, we believe these systems have tremendous potential for elucidating mechanotransduction pathways and mechanisms.

The field of bone biomechanics is rapidly changing. Engineers that want to take full advantage of this exciting field will find themselves having to accommodate a variety of testing needs. From our experience, we have found that a multi-purpose testing platform can be developed that can grow with a user's needs and accommodate research in the classic biomechanics and emergent mechanobiology fields. Furthermore, with an understanding of basic testing principles, loading platform limitations, and the unique issues associated with testing biologic organs, tissues and cells, these simple, cost-effective platforms can yield reliable data.

ACKNOWLEDGMENTS

Partial support for this work was provided by grants from The Whitaker Foundation, Life Sciences Greenhouse of Central Pennsylvania, National Institutes of Health (K25 AG022464) and National Science Foundation (0814194). The author gratefully acknowledges the significant contributions of machinists, Mr Larry Saunders and Mr Don Whitehaus. Thank you to past and present students for research contributions. This work is dedicated to the memory of Dr Glen O Njus, Associate Professor, The University of Akron (1953-2009).

REFERENCES

1. Currey JD. Measurement of the mechanical properties of bone. A recent history. Clin Orthop Relat Res 467:1948-1954, 2009.

2. Currey JD. Bones: Structure and mechanics. Princeton, NJ: Princeton University Press; 2002.

3. Cowin SC, ed. Bone Mechanics Handbook, 2nd ed. Boca Raton, FL: CRC Press; 2001.

4. An YH, Draughn RA eds. Mechanical testing of bone and the bone-implant interface. Boca Raton, FL: CRC Press; 2000.

5. Turner CH, Burr DB. Basic biomechanical measurements of bone: a tutorial. Bone 14:595-608, 1993.

6. Saunders MM, Donahue HJ. Development of a cost-effective loading machine for biomechanical evaluation of mouse transgenic models. Med Engr Phys 26:595-603, 2004.

7. Saunders MM, Burger RB, Kalantari B, Nichols AD, Witman C. Development of a cost-effective torsional unit for small-scale biomechanical testing. Med Engr Phys (in press), 2010.

8. Brodt MD, Ellis CB, Silva MJ. Growing C57B1/6 mice increase whole bone mechanical properties by increasing geometric and material properties. J Bone Miner Res 14(12):2159-2166, 1999.

9. Silva MJ, Ulrich SR. In vitro sodium exposure decreases torsional and bending strength and increases ductility of mouse femora. J Biomech 33:231-234, 2000.

10. Nazarian A, Bauernschmitt M, Eberle C, Meier D, Müller R, Snyder BD. Design and validation of a testing system to assess torsional cancellous bone failure in conjunction with time-lapsed micro-computed tomographic imaging. J Biomech, 41: 3496-3501, 2008.

11. Nazarian A, Entezari V, Vartanians V, Muller R, Snyder BD. An improved method to assess torsional properties of rodent long bones. J Biomech 42: 1720-1725, 2009.

12. Quinn R. Comparing rat's to human's age: How old is my rat in people years? Nutrition 21:775-777, 2005.

13. Weibull W. A statistical distribution function of wide applicability. J Appl Mech 18:293-297, 1951.

14. Bažant ZP, Pang SD. Mechanics-based statistics of failure risk of quasibrittle structures and size effect on safety factors. Proc Nat Acad Sci 103:9434-9439, 2006.

15. Brown TD. Techniques for mechanical stimulation of cells *in vitro*: A review. J Biomech 33(1):3-14, 2000.

16. Piekarski K, Munro M. Transport mechanism operating between blood supply and osteocytes in long bones. Nature 269:80–82, 1977.

17. Bonewald LF. Osteocytes as dynamic multifunctional cells. Ann NY Acad Sci 1116:281-290, 2007.

18. Bellido T. Summary – Osteocyte control of bone formation via Sost/sclerostin. J Musculoskelet Neuronal Interact 6(4):360-363, 2006.

19. Ott SM. Website link: http://depts.washington.edu/bonebio/ASBMRed/growth.html (Bone remodeling)

20. Jacobs CR, Yellowley CE, Davis BR, Zhou Z, Donahue HJ. Differential effect of steady versus oscillating flow on bone cells. J Biomech 31: 969-976, 1998.

21. Saunders MM, Taylor AF, Du C, Zhou Z, Pellegrini VD Jr, Donahue HJ. Mechanical stimulation effects on functional end effectors in osteoblastic MG-63 cells. J Biomech 39(8):1419-1427, 2006.

22. Buhl KM, Jacobs CR, Turner RT, Evans GL, Farrell PA, Donahue HJ. Aged bone displays an increased responsiveness to low-intensity resistance exercise. J Appl Physiol 90:1359-1364, 2001.

23. Turner CH, Akhter MP, Raab DM, Kimmel DB, Recker RR. A noninvasive *in vivo* model for studying strain adaptive bone remodeling. Bone 12, 73-79, 1991.

24. Hillam RA, Skerry TM. Inhibition of bone resorption and stimulation of formation by mechanical loading of the modeling rat ulna in vivo. J Bone Miner Res 10(5):683-689, 1995.

25. Gross TS, Srinivasan S, Liu CC, Clemens TL, Bain SD. Non-invasive loading of the murine tibia: an *in vivo* model for the study of mechanotransduction. J Bone Miner Res 17(3):493-501, 2002.

26. Saunders MM, Simmerman LA, Reed GL, Sharkey NA, Taylor AF. Biomimetic bone mechanotransduction modeling in neonatal rat femur organ cultures: Structural verification of proof of concept. Biomech Model Mechanobiol, 2010. (published online 2/19/10).

27. Van Sickels J. College of Dentistry, University of Kentucky. (personal correspondence), 2009.

Proceedings of the SEM Annual Conference
June 7-10, 2010 Indianapolis, Indiana USA

Determination of Fracturing Toughness of Bamboo Culms

Liou*, N.-S., Lu, M.-C.
Department of Mechanical Engineering, Southern Taiwan University
Yuang-Kang City, Tainan Hsien, Taiwan 710 R.O.C
email: nliou@mail.stut.edu.tw

ABSTRACT
Bamboo is an environmental friendly natural composite material reinforced by unidirectional fibers. Bamboo has been used as structural materials in Asia for centuries. In this study, the fracture toughness K_{IC}, of Moso bamboo was investigated by using ASTM E399 test method and the arc-shape bend specimens. The effect of moisture on the fracture toughness K_{IC} was investigated. It can be seen the fracture toughness decreases about 39% if the material under test was water-saturated.

INTRODUCTION
Bamboo is an environmental friendly natural composite material. Culm over 20 meter tall, 6 to18 cm diameter at breast height makes Moso bamboo one of the most important bamboo species for structure use. Vascular bundles act as reinforcements in bamboo and lignin in bamboo acts as a matrix. In Asia, bamboo has been used for centuries. Its strength and flexibility in the wind make it an ideal material for construction and household utilities. Compression, tension and bending properties of bamboo have been discussed for various bamboos. However, the studies of fracture properties such as stress intensity factor K and strain energy release rate G of bamboo are few. Bamboo specimen with crack under tensile test was use to investigate fracture properties of bamboo[1]. The critical value of energy release rate, G_{IC}, of Moso bamboo was measured by symmetric bending tests using double contilever beam specimen and calculated with the compliance of the specimen [2]. The fracture properties of Australian bamboo have been investigated [3]. In this study, the fracture properties of bamboo culms at the structural level were investigated. The fracture toughness K_{IC}s of dry and water-saturated bamboo culms were determined by using the arc-shape bend specimen specified in ASTM E399 based on linear elastic fracture mechanics theory under plane strain condition. The bamboo used for this study is Moso bamboo (Phyllostachys pubescens).

MATERIAL AND METHOD
The Mode I fracture toughness, i.e. the critical value of the stress-intensity factor K_{IC}, is measured by following the test method and arc-shaped bend specimen specified in ASTM E399 for determine fracture toughness under linear-elastic plane-strain condition. The culms between 0.75 and 5 m of a three year old Moso bamboo were used for making specimens. After air-drying, 10 mm wide ring was cut out of the bamboo culms and the arched shape bend specimen used for fracture test was cut from the ring (Fig. 1.).

T. Proulx (ed.), *Time Dependent Constitutive Behavior and Fracture/Failure Processes, Volume 3*, Conference Proceedings of the Society for Experimental Mechanics Series 15, DOI 10.1007/978-1-4419-9794-4_49, © The Society for Experimental Mechanics, Inc. 2011

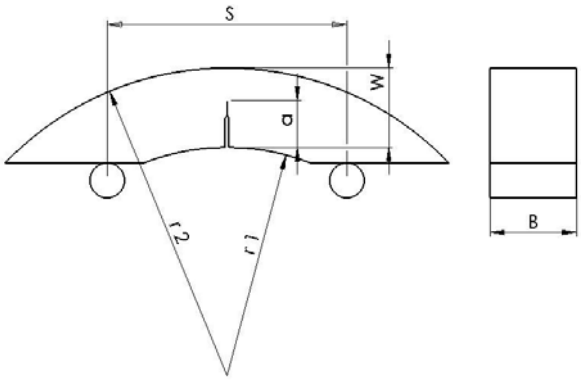

Figure 1: The arched shape bending specimen

For S=4W, The fracture toughness of arc-shape bend specimen can be calculated as follows :

$$K_Q = \frac{P_Q S}{BW^{3/2}}\left[1+\left(1-\frac{r1}{r2}\right)\cdot h_1\left(\frac{a}{W}\right)\right]\cdot f1\left(\frac{a}{W}\right). \quad \textbf{(1)}$$

Where

$$h_1\left(\frac{a}{W}\right) = 0.29 - 0.66\frac{a}{W} + 0.37\left(\frac{a}{W}\right)^2, \quad \textbf{(2)}$$

and

$$f_1\left(\frac{a}{W}\right) = \frac{\left[0.677 + 1.078\frac{a}{W} - 1.43\left(\frac{a}{W}\right)^2 + 0.669\left(\frac{a}{W}\right)^3\right]}{\left(1-\frac{a}{W}\right)^{3/2}}. \quad \textbf{(3)}$$

In above equations, P_Q is force(N), B is specimen thickness(m), S is span(m), W *is* specimen width(m), a is crack size(m), r_1 is inner radius(m) and r_2 is outer radius(m). The bend fracture tests were conducted by using Instron tensile test machine and custom made fixture as shown in Fig. 2.

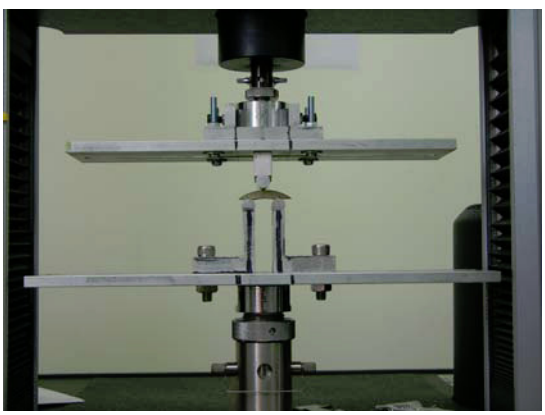

Figure 2: The arched shape bend test

In order to know the effects of moisture on the fracture toughness of Moso bamboo, the bend fracture tests were conducted on both air-drying and water-saturated specimens.

RESULT AND DISCUSSION

The force-deflection curves of specimens under arched shape bend test are shown in Fig. 3. It can be seen that the elastic modulus of water-saturated specimens is lower than that of air-drying specimens. The corresponding fracture toughness of air-drying and water-saturated specimens is listed in Table 1. It can be seen that the fractures toughness of water-saturated Moso bamboo decreases about 39%.

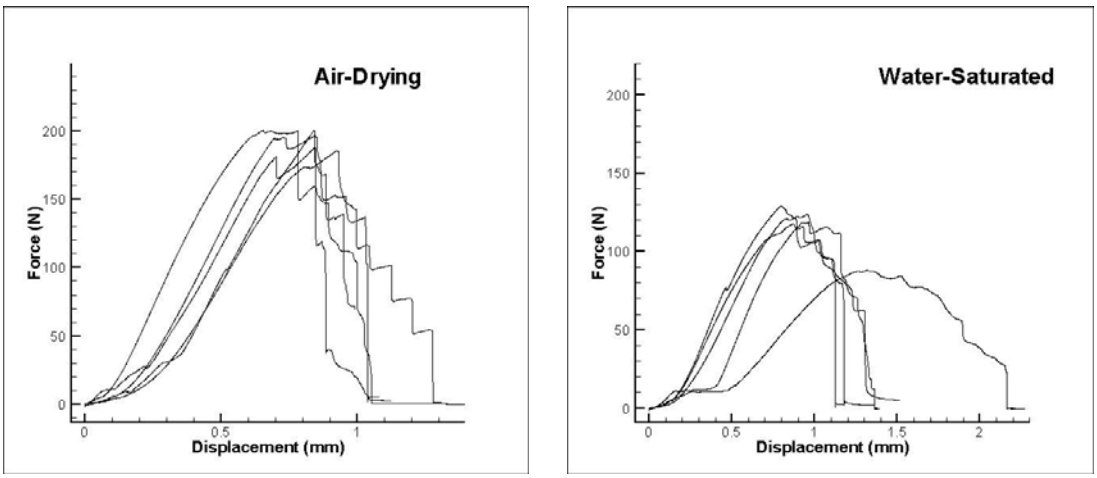

(a) (b)

Figure 3: The force-deflection curves of (a) air-drying and (b) specimens under arched shape bend test.

Air-Drying n=5	K_Q ($Pa\sqrt{m}$)
Average	31.2
STD	2.6

(a)

Water-Saturated n=5	K_Q ($Pa\sqrt{m}$)
Average	19.1
STD	2.6

(b)

Table 1: The fracture toughness of (a) air-drying and (b) water-saturated specimens under arched shape bend tests.

CONCLUSION

The arched shape bend tests show that the fracture toughness of bamboo culm can be affected by the moisture contents. The difference of fracture toughness between air-drying specimen and fully water-saturated specimens is about 39%. This moisture effect should be kept in mind when using Moso bamboo as structure materials.

ACKNOWLEDGEMENT

This research was supported by NSC 96-2221-E-218-048-MY3 from the R.O.C government.

REFERENCE

1. Amada, S. and S. Untao, *Fracture properties of bamboo.* Composites Part B-Engineering, 2001. **32**(5): p. 449-457.
2. Shao, Z.P., C.H. Fang, and G.L. Tian, *Mode I interlaminar fracture property of moso bamboo (Phyllostachys pubescens).* Wood Science and Technology, 2009. **43**(5-6): p. 527-536.
3. Low, I.M., et al., *Mechanical and fracture properties of bamboo.* Fracture of Materials: Moving Forwards, 2006. **312**: p. 15-20.

Proceedings of the SEM Annual Conference
June 7-10, 2010 Indianapolis, Indiana USA

Biomechanical Analysis of Ramming Behavior in Ovis Canadensis

Parimal Maity* and Srinivasan Arjun Tekalur,

Composite Vehicle Research Center,

Department of Mechanical Engineering,

Michigan State University,

2727 Alliance Drive, Lansing, MI-48910, USA.

*Email: maitypar@egr.msu.edu

ABSTRACT:

Horns have been hypothesized to help in absorbing shock and protecting the brain during ramming events. In general, horn is made of a α-keratin sheath covering a porous bone. The objective of the present study is to investigate the shock-absorptive role of the keratinous sheath and bony core of horns; particularly in Bighorn Sheep (Ovis Canadensis). A three dimensional complex structure of the bighorn sheep horn was successfully constructed and modeled using a computed tomography (CT) scan and Finite Element (FE) method, respectively. Computed tomography was also used to identify the porosity in the inner core of the horn. The horn was subjected to quasi-static loading of 3400 N (764.35 lbf) simulating the effect of both the composite nature of the horn and the porosity in the inner core. Three different 3-dimensional quasi-static analyses, a part of simplified homogenous horn, simplified composite horn and complex structure of horn were studied. The computed stresses, deflections and strain energy were compared for three different models. It was noticed that strain energy due to elastic deformation of the complex horn structure was more, as compared to simplified horn structure and composite horn structure models; whereas the ability of force transmission was found to be more in composite and complex structures of horn. This phenomenon was elucidated through the stress distribution in structure. This study will help designers in choosing appropriate material combination for successful design of protective structures against a similar impact.

INTRODUCTION:

In the past few decades, investigations of the mechanical properties of a large number of structures and systems in living organisms have seen considerable interest. Some of the biological composite structures are organized such that a hard phase provides stiffness and a porous or soft phase, enhances energy storage/dissipation capability. These biological structures can be potentially mimicked to design of light weight composite structures and tough armor structures. A wide variety of species of animals like Bighorn Sheep (Ovis Canadensis), Thomson's Gazelle (Gazella Thomsoni), Waterbuck (Kobus Ellipsiprymnus) and Gerenuk (Litocranius) take part in ramming with their horns absorbing the shock. Usually, their horns are curved structures which are made of unique hard hierarchical α-Keratin covering over a core of spongy bone. Nevertheless, the forces and energy generated during ramming should result in brain damage at least, yet these animals seem to suffer no ill effects.

T. Proulx (ed.), *Time Dependent Constitutive Behavior and Fracture/Failure Processes, Volume 3*, Conference Proceedings of the Society for Experimental Mechanics Series 15, DOI 10.1007/978-1-4419-9794-4_50, © The Society for Experimental Mechanics, Inc. 2011

These horns are designed such that the brain is protected from severe damage resulting from impact. In order to understand whether the horn absorbs a part of the energy or diffuses it to whole structures, an insight into the forces produced in ramming and their absorption or dissipation is necessary. Until the advent of advanced FE analysis, it was difficult to estimate the energy and forces produced in ramming and were based on Newton's Laws of Motion. Weber et al. [1] calculated the force generated in clashing of goats assuming that their body mass had fallen a known height under the acceleration due to gravity. Schaffer [2] estimated that sheep clash at a combined velocity of 22.1 m/s (Ovis Musimon) to 26.9 m/s (Ovis Canadensis, Ovis Ammon). Early attempts by Best &Raw [3], Geist [4], Walker [5] and Schaller [6] to measure the force and energy in the fighting of bighorn sheep (with average body mass is 100 kg and average shoulder height is 1.2 m) have been followed by film analyses (24 frames per second). Similar attempts to measure the velocity at which the horns clashed have been reported by Kitchener [7] among others. The value of maximum clashing velocity and maximum deceleration was 5.5 m/s and 30 m/s^2 respectively. In his study he assumed that the whole body mass was used to produce the force and energy. This study gave a force of about 3400 N and 2400 J of energy with a body mass of 100 kg. Conventional or modified beam theory has been used to calculate the stresses in the beam. Schaffer and Reed [8] calculated the ratio of compressive to tensile stresses in the horn of the sheep and found it to be1.7. Kitchener [7] estimated strain energy stored in the horn of the bighorn sheep and found that it is less than 1% of energy generated in the clash. Early attempts to estimate the shock absorption ability of the frontal sinuses in Bovids has been proposed by Geist [4], Schaffer and Reed [8] among others. Moreover, Farke [9] compared different models of goat skull including unvaulted (air filled space) frontal, vaulted (expanded) cortical bone-filled frontal, vaulted trabecular bone-filled frontal, vaulted frontal with unstrutted sinus and vaulted frontal with strutted sinus. He concluded that shock absorption capability of goat skull could be almost completely dominated by vaulted frontal with strutted sinuses. In his study, a 3D FE model was constructed based on CT scans of a goat skull and models were imported into the FE modeling package ALGOR FEMPro (v.20.0, Algor, Pittsburg, PA, USA). He concluded that future investigations will aim to model the energy absorption role of keratinous sheath and core of horn. Motivated by the simulations results of Farke [9] we created a FE model for horn of the bighorn sheep to determine the role of keratinous sheath and spongy bone core against shock absorption.

In literature, the simulation of Bighorn Sheep horn has not considered the effect of porosity in the structure, therefore, the objective of this study is to construct and model the Bighorn Sheep horn including porosity. The horn will be subjected to quasi-static loading of 3400 N which simulate effect of composite nature and porosity of the horn. At this point, we use a 3D FE model of the bighorn sheep horn to determine the elastic strain energy of horn as a penalty of the shock. Medical image data of horn are obtained from computed tomography (CT) scan. A 3D CAD model is made using a medical imaging and editing software MIMICS 9.1. Moreover, thickness of sheath material, diameter of the core and length were obtained from the CT scan to model a simplified horn. Stress distributions and strain energy are compared with the 3D FE analysis of simplified homogeneous structure (i.e. modulus of elasticity of the core is same as sheath), composite horn structure (i.e. modulus of elasticity of the core is same as compact bone) and complex horn structure.

CONSTRUCTION OF 3-DIMENSIONAL FINITE ELEMENT MODEL:

A 6 year old skull of bighorn sheep was procured. The skull had a length of 0.78 m with a base of 0.343 m. The base of the horn was assumed to be elliptical in shape and the length of the major and minor axis was approximately 110 mm and 90 mm, respectively. Two-dimensional theoretical models have been widely used to study the ramming behaviour during past decades under different loading and boundary conditions. These theoretical models typically consider the solid or compact bony structure of the horn and outer sheath covering. The structural architecture of simplified horn doesn't include any internal microstructure of the core and it can be assumed to be of curved prismatic shape. The proximal end or base of the core had a height and width of 90 mm and 70 mm, respectively. The height and width at the distal end was 45 mm and 25 mm, respectively. The proximal end of the sheath had a height and width of 110 mm and 90 mm, respectively. Similarly, height and width at the distal end was 80 mm and 90 mm, respectively. The overall length of the structure was considered as 0.2 m. The radius of curvature for the inner and outer surface of the structure was 98 mm, and 199 mm, respectively. A simplified horn structure was analyzed and results are compared with complex horn structure. Furthermore, taking the symmetry of the structure into account, half of the section was generated in this study. A CAD design software SolidWorks was used to geometrically define the simplified structure. The simplified structure is shown in Fig. 1a. Three dimensional simplified structure was imported into commercial FE package ABAQUS. The keratinous layer and inner core were meshed with four noded tetrahedral elements (C3D4R) and

eight noded 3D brick elements (C3D8R); the mesh in Fig. 1b contains around 99,000 and 15,000 elements respectively.

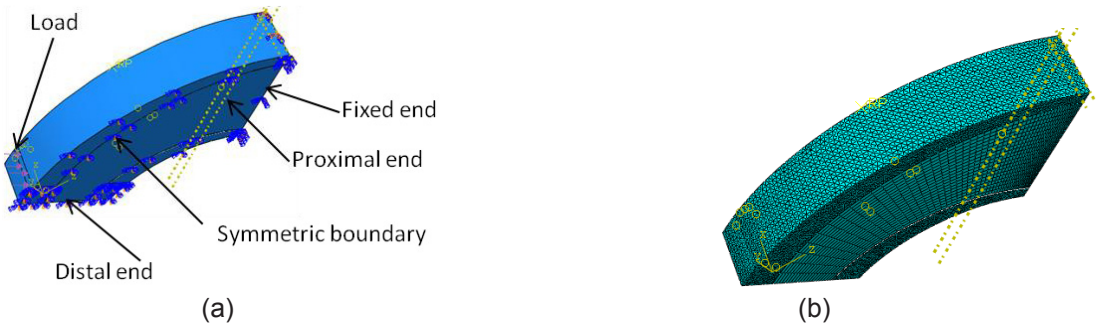

(a) (b)

Figure 1: (a) Geometry and (b) typical FE mesh is used to solve mainly for the stresses and strain energy of the simplified horn structures.

Recent advancement in image processing and mesh generation makes it possible to generate a realistic FE model of the bighorn sheep horn, which includes external sheath material as well as porous bone in the horn structure. First, CT medical images of a bighorn sheep horn were acquired. CT scans of sheep horn were done with inter-slice spacing of 0.625 mm. A CT scan of the bighorn sheep skull is shown in Fig. 2a. Compact bones do not have any empty spaces or air pockets that are visible to the naked eye. Porous bone also known as trabecular or cancellous bone mainly consists of delicate bars and sheets of bone. These delicate bars are called trabeculae, which branch and intersect to form a sponge-like network [10]. Figure 2b shows a typical CT scan slice of the spongy bone. The DICOM (Digital Imaging and Communications in Medicine) images generated in the CT scan are a series of 2D high resolution x-ray images that display density maps of the scanned horn structure. The brightest regions inside were the trabeculae that form the sponge-like network. The density variations in different live organs are usually identified with unique gray-scale value. In order to model the complex structure of horn, the DICOM images were processed with medical imaging and editing software MIMICS 9.1. In MIMICS, the region of each tissue was differentiated through contrast segmentation, and a gray-scale value. The received bighorn sheep skull did not have any live cells, therefore, automatic segmentation of the sheath and spongy bone from the horn structure is extremely difficult. Differentiation of the sheath and spongy bone in each DICOM image was accomplished manually. The complex 3D bighorn sheep horn structure was constructed by combing sheath and spongy bone materials of each CT scan slice. Figure 3 shows the 3D solid model of the bighorn sheep horn. Once the 3D structure was formed, tetrahedron elements were used to mesh the structure using MIMICS remesher. The resulting three-dimensional horn structure contains 530,372 elements and 87,555 nodes. A final meshed horn structure, comprising of sheath and spongy bone, was imported and assembled using FE package ABAQUS 6.7.1.

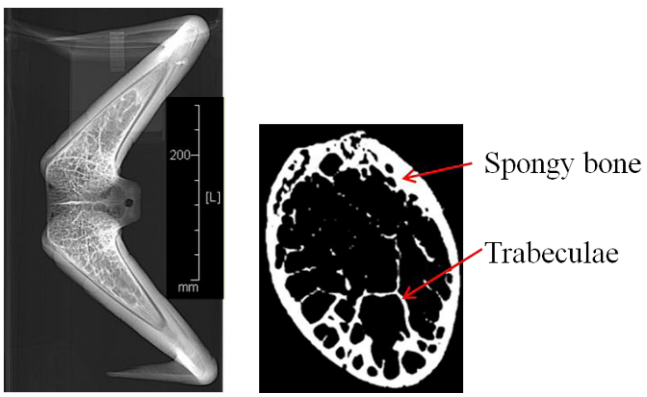

(a) (b)

Figure 2: (a) A CT scan of the Bighorn skull and (b) A CT scan slice of the spongy bone.

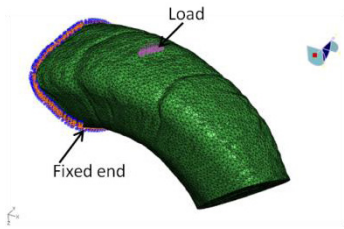

Figure 3: A FE mesh of the Bighorn sheep horn.

MATERIAL PROPERTIES:

All models used similar material properties. However, the current study is focused on the structural and geometrical shape of horn, and not on particular material properties of the horn. The mechanical properties of the horn sheath have been extensively studied. The average Young's Modulus, Poisson's ratio and density of horn sheath are defined as 3.9 GPa, 0.3 and 1.3 g/cm^3, respectively [11]. Since there is no data available for cortical bone of bighorn sheep horn, in the current analysis measured elastic modulus of human cortical bone was considered to be a reasonable value. The average Young's Modulus, Poisson's ratio and density of human bone are 12 GPa, 0.28 and 1.04 g/cm^3, respectively [12].

FINITE ELEMENT ANALYSIS AND BOUNDARY CONDITIONS:

The quasi-static loading was applied to all the structures and were modeled at the moment of peak force during impact, as estimated in previous studies by Kitchener [11]. The peak force was 3400 N corresponding to a body weight of 100 kg, velocity and deceleration of 5.5 m/s and 34 m/s^2 respectively. All the material properties have been characterized by considering isotropic, linear elastic behaviour at low strain rates. A static pressure load was applied over finite area corresponding to load of 3400 N. Rotations and displacements in 3-directions were set to zero at the proximal end or leading edge of the structures. Figure 3 shows the boundary condition of the FEA loading. Stresses in three normal directions were chosen to represent the stress distribution in the structures. To envisage the effect of geometry and porosity in the structure, deformational strain energy (U) was calculated over each structure.

RESULTS AND DISCUSSIONS:

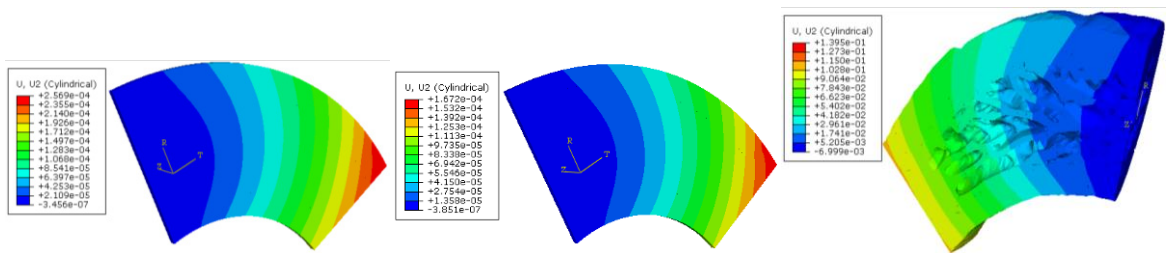

(a) (b) (c)

Figure 4: The deflection along axial direction for (a) simplified homogeneous horn with core and sheath modulus of 3.9 GPa, (b) simplified composite horn with core modulus of 12 GPa and (c) complex horn structure.

Figure 4a shows the deflection pattern in a simplified homogeneous horn along the axial direction. As expected, the cross-sectional area of the horn at the fixed end sustained the lowest deflection and the cross-sectional area of the horn under the load sustained maximum deflection. The maximum deflection was approximately 257 µm at the distal end. When the modulus of elasticity of the core was increased, the deflection reduced by 35% of that of the maximum deflection of simplified homogenous horn. However, maximum deflection for the complex horn at the distal end was only about 140 µm, which was about 45% less than the simplified homogeneous structure.

The parameter strain energy or elastic energy was used to describe the elastic deformation that a biological structure undergoes under an external force. Ideally, shock or energy absorbers of biological structures

experience large elastic deformation completely, as opposed to brittle fracture or plastic deformation. Strain energy was computed for the quasi-static loading. It was noticed that for the model with core modulus of elasticity 3.9 GPa, the stored energy was equal to 0.044 Nm. Strain energy decreased as core modulus increased; when the modulus of elasticity of the core was 12 GPa, the energy stored by the horn was 0.028 Nm. Therefore, it was clear that the energy absorbed by the stiffer core was lower than that of the homogeneous structure. The strain energy of the complex horn of the bighorn sheep was 0.187 Nm. Figure 5 shows strain energy variation with point of application of force acting on the horn of bighorn sheep from proximal end. Strain energy values did not increase monotonically with the increase in the point of application of force, towards the distal end. Possibly, this can be attributed to non-uniform thickness of sheath and variation in porosity of the core. Simulation result showed that the deflection of complex bighorn sheep horn was very small. Therefore, sources of strain energy could be due to the fact that larger elastic deformation was caused in spongy bone than in the compact bone of horn structure. From literature survey, the total energy in fighting event was 2400 Nm. This essentially means that very little percentage of total energy in a fighting was stored by the combination of spongy bone and keratinous sheath and the rest of the energy diffuses through other paths, which facilitate energy absorption and storage. Presence of sinuses, next to the horn and the neck muscle can be some of them. As mentioned earlier, Farke [9] also emphasized the contribution of frontal sinuses of the goat to store energy. A considerable amount of energy can be absorbed or stored by the muscle during contraction and stretch [13]. It is difficult at this point, to calculate the percentage of energy storage and absorption by the systems as a penalty of shock energy. It may be reasonable to assume that all three possibilities were perhaps undertaken in varying degrees.

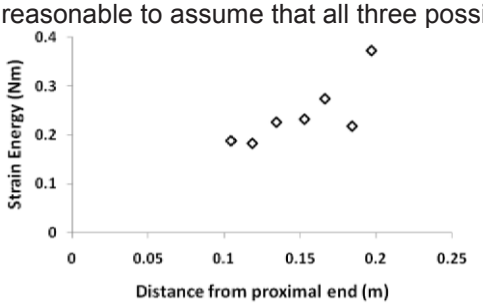

Figure 5: Strain energy with point of application of force acting on the horn from proximal end.

In order to make clear that energy storage and absorption have indeed taken place in sinuses and neck muscle, the following results were analyzed. The stresses in radial, circumferential direction and z - direction and principal stresses were computed.

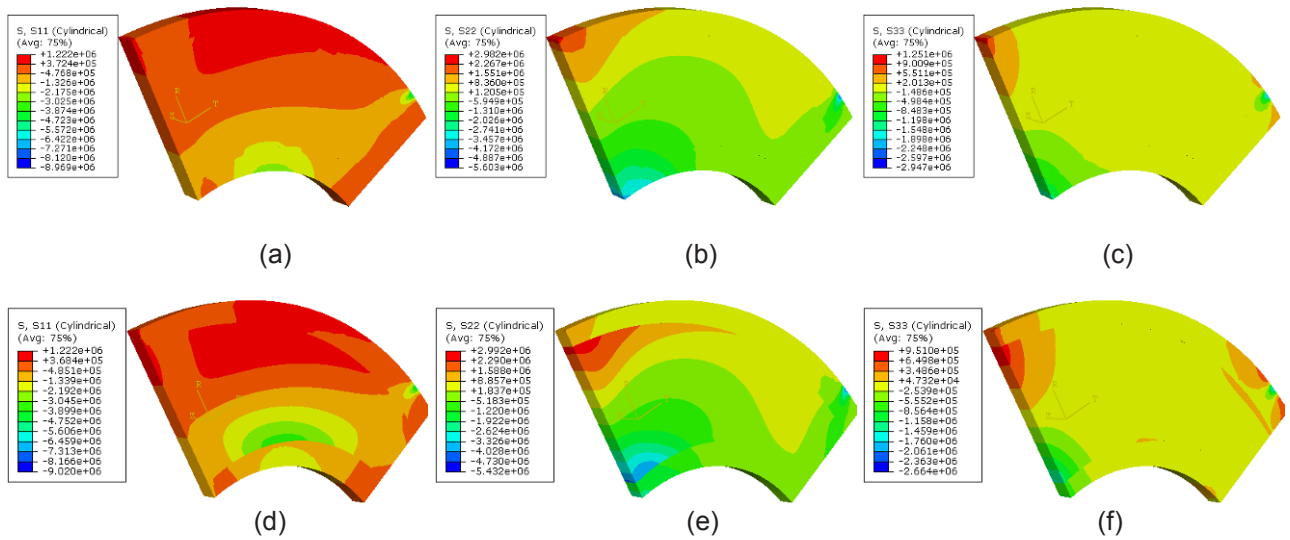

Figure 6: (a) Stresses in radial direction, (a) Stresses in circumferencial direction and (a) Stresses in z - direction for simplified and composite structure model.

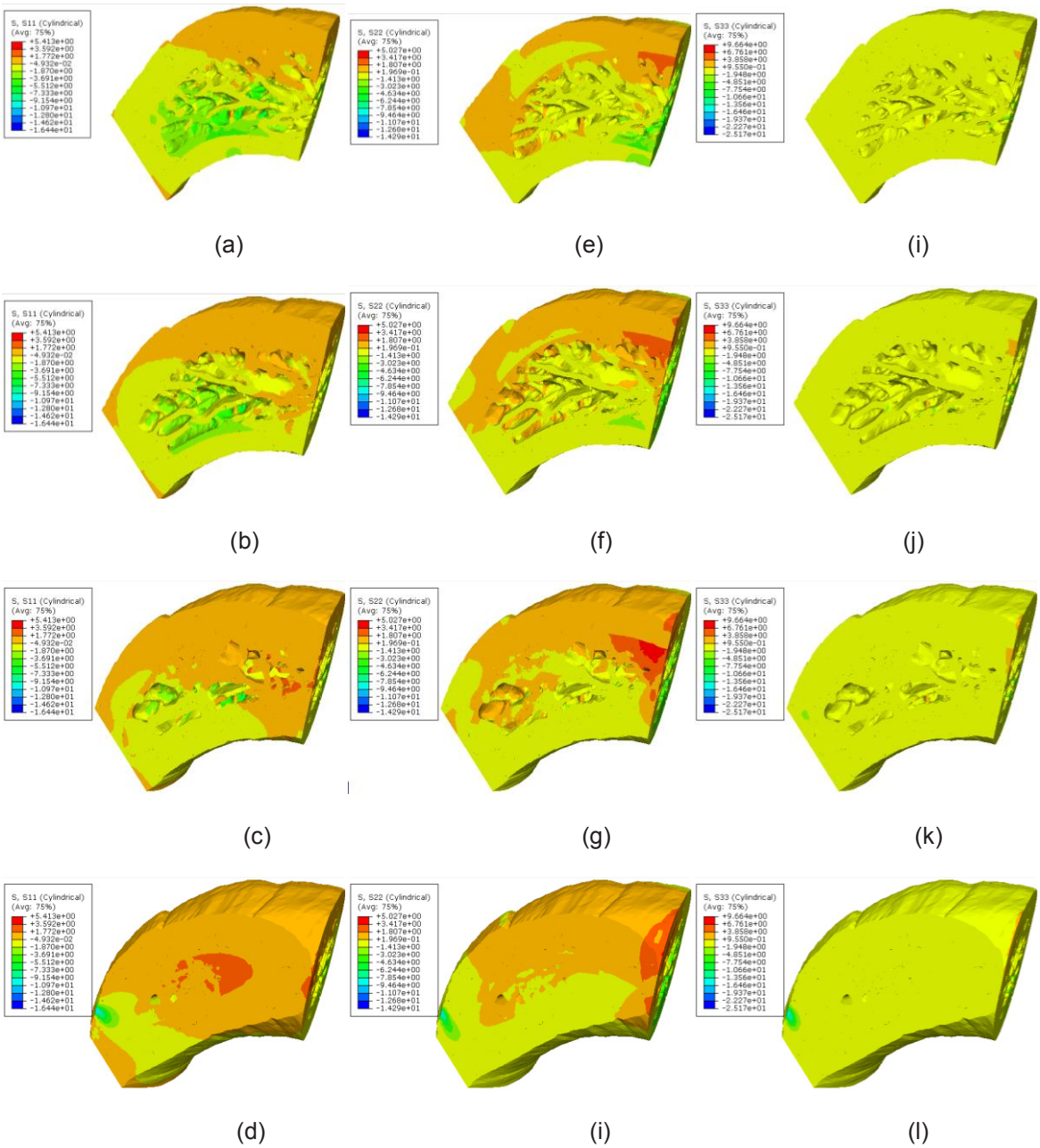

Figure 7: The computed (a)-(d) radial stress distribution, (e)-(i) circumferencial stress distribution and (j)-(l) z - direction stress distribution in a slice through the Bighorn sheep horn.

The stress components in radial, circumferential and z – direction were computed for the different structures subjected to quasi-static loading. The location of the maximum compressive and tensile stresses in radial, circumferential and z - direction can be observed in Figs. 6 and 7. The detailed maximum compressive and tensile stresses in radial, circumferential and z - direction were quoted in Table 1. The ratio of maximum compressive stress to maximum tensile stress was calculated for all the models, and was found to be 3.0, 3.01, and 2.6 for simplified horn, composite horn and complex horn structure, respectively. In contrast, it was shown in [8, 11] that the ratio varied from 3.8 to around 2.6. As it may be seen in Table 1, the difference in the maximum stress between homogeneous simplified horn and composite horn structure decreased with an increase in core stiffness. For complex horn structure, the values were found to be significantly different. This could be explained due to the presence of the sponge-like network regions in the core, these regions were stressed more during impact as compared to compact region. It can also be noticed that stresses in radial, circumferential and z – direction were not localized at a point load, but distributed throughout the structures.

Table 1: Computed maximum compressive (c) and tensile (t) stresses for different structures

Model	Maximum stresses in radial direction, σ_{rad} (MPa)		Maximum stresses in circumferential direction, σ_{cir} (MPa)		Maximum stresses in Z direction, σ_Z (MPa)	
	$(\sigma_{rad})_t$	$(\sigma_{rad})_c$	$(\sigma_{cir})_t$	$(\sigma_{cir})_c$	$(\sigma_Z)_t$	$(\sigma_Z)_c$
Homogeneous horn structure	1.222	8.969	2.982	5.603	1.251	2.947
Composite horn structure	1.222	8.96	2.992	5.432	0.951	2.664
Complex horn structure	5.431	16.44	5.027	14.29	9.664	25.17

The direction of the maximum and minimum principal stresses can be observed in Figures 8g through 8h. It can be noticed that regions of maximum and minimum principal stresses were located exactly in the same positions in the simplified homogeneous horn, composite horn and complex horn structure. The maximum principal stress direction as shown in red colour, the cyan colour refers to the minimum principal direction. For all the models, as shown in Figs. 8a through 8f, the contour plots describe how the principal stresses were uniformly distributed in the structures and directed towards the proximal end. This essentially means that the impact force is transmitted from impact point to proximal end through the structure. Additionally, porosity in the horn brings down the weight by approximately 20%. The results of the bighorn model suggested that a well designed curved composite structure should be able to absorb as much energy as possible and diffuse the remaining energy to the other systems. A few opportunities for further work in this current area were enumerated here. Firstly, the simulations were done through 3D static analyses. It was predicted that 3D dynamic will explain energy dissipation in ramming of bighorn. Secondly, if it were possible to model the bighorn sheep horn with core of spongy bone, keratinous sheath and sinuses attached next to the horn core, more accurate computations of the energy absorption and storage properties might be obtained.

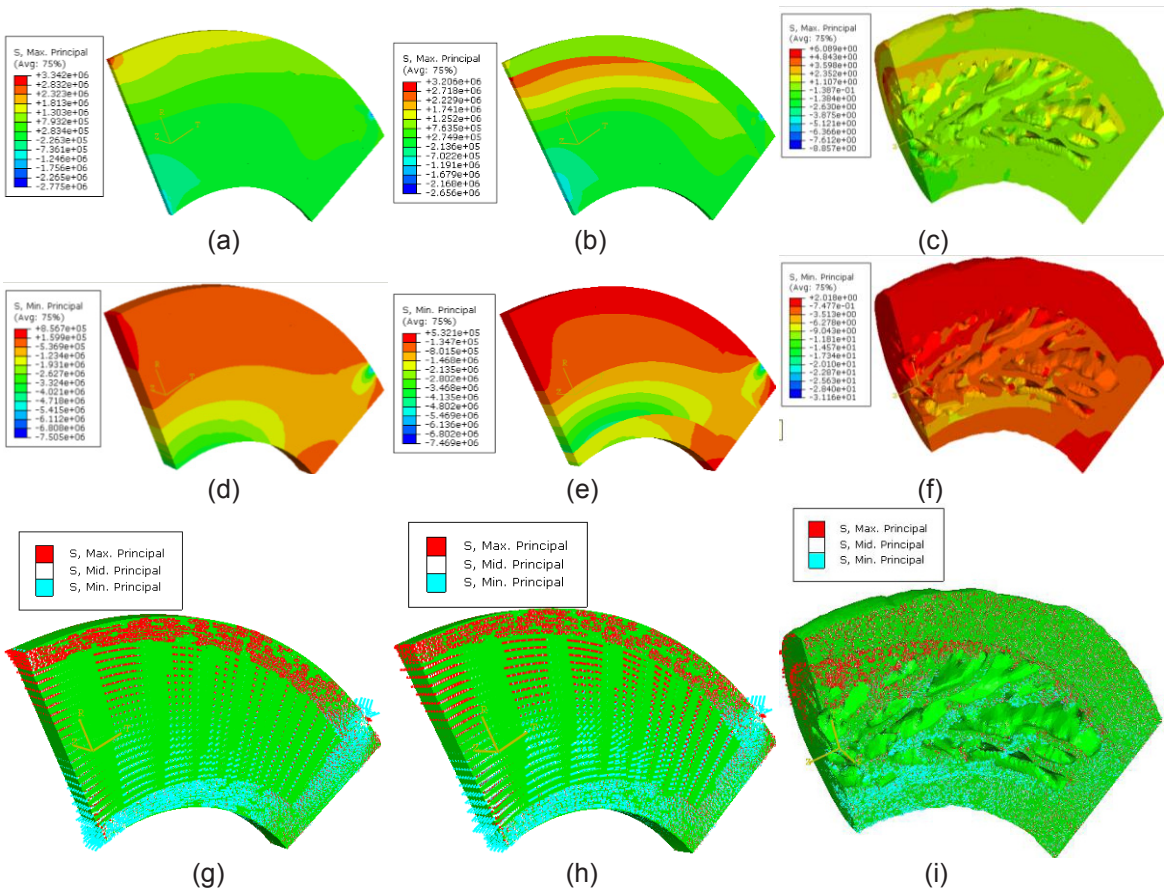

Figure 8: The distributions of (a)-(c) maximum principal stresses and (d)-(f) minimum principal stress and (g)-(i) direction of principal stresses for homogeneous horn structure, composite horn structure and complex horn structure, respectively.

Table 2: Computed maximum and minimum compressive and tensile principal stresses for different structures

Model	Maximum principal stress, σ_1 (MPa)		Minimum principal stress, σ_2 (MPa)	
	$(\sigma_1)_t$	$(\sigma_1)_c$	$(\sigma_2)_t$	$(\sigma_2)_c$
Homogeneous horn structure	3.342	2.775	0.857	7.505
Composite horn structure	3.206	2.656	0.532	7.469
Complex horn structure	6.089	8.857	2.018	31.16

CONCLUSIONS:

In this work, complex shape of the bighorn sheep horn was successfully constructed and modeled. FE model of the goat skull have been successfully analyzed to investigate the effect of varying cranial morphologies on cranial function under static load, this model mainly focused on the frontal sinuses of the horn whereas the porosity and composite nature of the horn was considered in this study. Complete stress and strain analysis in three directions were adopted to explain the ability of the load transfer in the structures. The strain energy was compared for different models under a quasi-static load of 3400 N. It has been shown that complex horns have a greater ability to store energy than other studied structures. The improvement, therefore, seems to be directly linked to the geometry of the structure and the modulus of elasticity of the layer i.e. core and sheath. It was further shown that porosity in the core of the bone was also a contributing factor to the mentioned improvement. Extensive elastic deformation in the fighting of Ovis Canadensis leading to high energy absorption is implied.

ACKNOWLEDGEMENTS:

Funding for this work was provided by TARDEC & ONR through agreement W56HZV-07-2-0001. Their support is gratefully appreciated.

REFERENCES:

1. R. L. Weber, K. V. Manning, M. W. White, College Physics, 4th Edition: McGraw-Hill, 1965.
2. W. M. Schaffer, “Intraspecific combat and the evolution of the caprini”, Evolution, Vol. 22, pp. 817-825, 1968.
3. A. A. Best and W. G. Raw, Rowland Ward’s records of big game, 15th edition, London: Rowland Ward, 1971.
4. V. Geist, Mountain sheep, A study in behaviour and evaluation, Chicago: Chicago University Press, 1971.
5. E. P. Walker, Mammals of the world, 3rd edition London: John Hopkins Press, 1975.
6. G. B. Schaller, Mountain monarchs, Chicago: Chicago University Press, 1977.
7. A. Kitchener, “An analysis of fighting of the blackbuck (Antilope cervicapra) and the bighorn sheep (Ovis canadensis) and the mechanical design of the horns of bovids”, Journal of Zoology Vol. 214, pp. 1-20, 1988.
8. W. M. Schaffer, and C. A. Reed, “The co-evolution of social behavior and cranial morphology in sheep and goats (Bovidae, Caprini)”. Fieldiana 61, pp. 1-88, 1972.
9. A. A. Farke, “Frontal sinuses and head-butting in goats: a finite element analysis”, The Journal of Experimental Biology, Vol. 211, pp. 3085-3094, 2008.
10. D. B. Burr, R. B. Martin, M. B. Schaffer, E. L. Radin. “Bone remodeling in response to in vivo fatigue microdamage”, Journal of Biomechanics, Vol. 18, No. 3, pp. 189–200, 1985.
11. A. Kitchener, “Fracture toughness of horns and a reinterpretation of the horning behaviour of bovids”, Journal of Zoology (Lond.), Vol. 213, pp. 621-639, 1987.
12. P. Frasca, “Scanning-electron microscopy studies of ‘ground substance’ in cement lines, resting lines, hypercalcified rings and reversal lines of human cortical bone”, Acta Anatomica, Vol. 109, pp. 114–121, 1981.
13. M. Linari, R. C. Woledge and N. A. Curtin, “Energy storage during stretch of active fibres from skeletal muscle”, Journal of Physiology, Vol. 548, No. 2, pp. 461-474, 2003.

Proceedings of the SEM Annual Conference
June 7-10, 2010 Indianapolis, Indiana USA

Deformation and Failure Mode Transition in Hard Biological Composites

Reza Rabiei, Sacheen Bekah and Francois Barthelat*

Department of Mechanical Engineering, McGill University, 817 Sherbrooke Street West,

Montreal, QC H3A 2K6, Canada

**corresponding author (francois.barthelat@mcgill.ca)*

ABSTRACT

Mineralized biological materials such as nacre or bone achieve remarkable combinations of stiffness and toughness, by way of staggered arrangements of stiff components (nano or microscale fibers or tablets) bonded by softer materials. Under applied stress these components slide on one another, generating inelastic deformations and toughness at the macroscale. This mechanism is prominent in nacre, a remarkable material which is now serving as model for biomimetic materials. In order to better identify which type of nacre should serve as biomimetic model, the toughness of nacre from four different mollusk species was determined in this study. Nacre from Pearl oyster was found to be toughest, and for the first time remarkable deformation and fracture patterns were observed using *in-situ* optical and atomic force microscopy. Under stress, stair-like deformation bands deform at an angle from the loading direction, forming a dense, tree-like network. This marks a clear difference from the now well documented "columnar" failure mode where deformation bands are perpendicular to the loading direction. Numerical models revealed the conditions for the transition between columnar to stair failure modes, namely large or random overlap between inclusions and local shear stress generated by inhomogeneities in the material. "Stair" failure promotes spreading of nonlinear deformation and energy dissipation, which translates into a higher toughness overall. A similar mechanism may also occur in bone, which has a microstructure in many ways similar to sheet nacre.

Introduction

Structural biological materials like seashells or mineralized skeletons are composed of relatively weak, small scale structural components, but assembled in intricate ways that lead to remarkable combinations of stiffness and toughness. In some cases the degree of "amplification" of mechanical performance from the base components is unmatched by any synthetic material [1, 2]. A well known example of this performance is nacre from mollusk shells, which is made of microscopic mineral tablets closely stacked to form a three-dimensional brick wall structure. The mineral represents 95% vol. of the material, the remaining 5% being organic materials located mostly at the interfaces between tablets [3]. Nacre is therefore a highly mineralized and stiff material, yet it is 3,000 times tougher than the brittle mineral it is made of [1]. There is therefore a great interest in understanding the mechanisms behind this remarkable performance, in order to duplicate them in artificial, biomimetic materials [2]. In fact, biomimetic materials inspired by nacre have already started to emerge [4, 5]. The staggered arrangement of the tablets in nacre dictates a specific mechanism, where applied tensile loads are transferred through tensile stress in the mineral tablets and shear stress at the softer interfaces between tablets. With sufficient applied load the tablets "slide" on one another, this "sliding" being mediated by thin layers of softer organic materials capable of accumulating large deformations while dissipating energy [6]. Resistance to shearing at the interface is provided by the organic material [6, 7], by nanoasperities [8] and by mineral bridges [9]. The tablets also show some waviness which impedes tablet sliding and generates strain hardening [10], delaying localization and propagating the sliding mechanism over large volumes. These mechanisms are now well

T. Proulx (ed.), *Time Dependent Constitutive Behavior and Fracture/Failure Processes, Volume 3*, Conference Proceedings of the Society for Experimental Mechanics Series 15, DOI 10.1007/978-1-4419-9794-4_51, © The Society for Experimental Mechanics, Inc. 2011

documented for the case of columnar nacre [10] (columnar nacre from Red Abalone is perhaps the most studied nacre). In columnar nacre the tablets are arranged in columns, with well defined core and overlap regions [10]. In this quasi-periodic structure sliding only occurs in the overlap regions, generating deformation bands perpendicular to the loading direction [8, 10]. Cracks eventually also follow the overlap regions [11].

In contrast, sheet nacre has a more random staggered arrangement, with no well defined overlap and core regions. While tablet sliding has been observed in sheet nacre [3, 8, 12], its exact deformation and cracking patterns are unclear. In term of macroscopic properties, previous studies showed that sheet nacre from Pearl oyster *Pinctada margaritifera* is slightly stiffer and stronger than other columnar nacres [3, 8] but this is not true for all sheet nacres [3]. It is also not clear which of the two types of nacres tends to be the toughest. This is a lack in the context of biomimetic materials, because fabrication procedures have now been refined to a degree allowing unprecedented control over the microstructure [4, 13]. Identifying the best natural nacre to serve as "biomimetic model material" therefore becomes increasingly important.

Nacre is part of a wider category of mineralized tissues with a "staggered arrangement" of stiff inclusions aligned along the direction of loading, and bonded by softer organic materials. Bone, for example, also follows this "universal" microstructural design over multiple length scales [14]. In particular, the sliding of the mineralized collagen fibrils along one another at the microscale was demonstrated to provide the large inelastic strains observed at the macroscale [15]. There are several analogies between nacre and bone, but the experimental study of the failure of bone at small length scales level is considerably more difficult than in nacre, because of the helicoid lamellar structure of the osteons [16]. In terms of modeling, small two-dimensional representative volume elements are typically used [17, 18] so capture the load transfer from shear at the interface to tension in the inclusions. These models provide analytical solutions for modulus and strength, and useful insights into micromechanical design and structural optimization. This type of model, however, relies on the assumptions that the structure and displacement are periodic. In consequence, the models predict that the separation of the inclusions forms a uniform network of deformation bands perpendicular to the loading direction. In reality it may not be the case because mineralized fibrils follow a random overlap, so that the failure of bone at those length scales may follow the "stair" pattern described here.

In this article a comparative study of the fracture toughness of four selected nacres is presented first. Significant differences in toughness are reported, and in addition a new "stair" type of failure mode was observed in sheet nacre. In the next section, the transition between "stair" and "columnar" failure modes is investigated by larger scale numerical simulations, where the effect of microstructure and local shear stress on failure transition is revealed. The implications on biomimetics and on our understanding of how natural composite with staggered arrangements deform and fail is finally discussed.

The fracture of sheet and columnar nacres

The nacres tested in this study consist of four species: Red Abalone (RA) and Top Shell (TS) from columnar nacre, and Pen Shell (PS) and Pearl oyster (PO) from sheet nacre. Besides different tablet arrangements, the tablets themselves showed a range of thickness and aspect ratio (Table 1). Top Shell showed the thickest tablets, followed by Pearl oyster, Red Abalone and Pen Shell. The tablet aspect ratio was the highest in Pen Shell, followed by Red Abalone, Top Shell and Pearl Oyster, which displayed the tablets with the smallest aspect ratio. These differences in mean thickness and aspect ratio between each of the four species were highly statistically significant (p-value<0.001 from an independent sample t-test with N=250).

Species	Nacre Type	tablet thickness (μm)	tablet aspect ratio	Work of Fracture (kJ/m2)
Top Shell (TS) *Trochus niloticus*	Columnar	0.74 ± 0.08	10.80 ± 3.47	0.70 ± 0.04
Red Abalone (RA) *Haliotis rufescens*	Columnar	0.45 ± 0.06	12.49 ± 7.97	0.55 ± 0.03
Pearl oyster (PO) *Pinctada margaritifera*	Sheet	0.50 ± 0.11	8.91 ± 4.68	1.44 ± 0.13
Pen Shell (PS) *Pinna nobilis*	Sheet	0.43 ± 0.10	14.37 ± 9.04	0.20 ± 0.04

Table 1. Characteristics of the nacres tested (thickness and aspect ration given as mean ± standard deviation)

Specimen preparation

Fracture specimens were prepared in shape of rectangular prisms with dimensions 20 mm in length, 0.1~1 mm in thickness and 0.2~2 mm in width. A pre-notch was next cut using a diamond saw. One side of the notched specimen was then polished, and the notch was finally deepened and sharpened with a fresh razor blade. The specimens were oriented so cracking would occur across the layers (Figure 1). Moreover, in order to comply with the ASTM requirement [19], the notch length was maintained within 0.45~0.55 of the width. Samples were kept hydrated throughout all the steps of preparation, storage and experiment.

Experimental procedure

The fracture tests were performed using on a four point bending fixture mounted on a miniature loading stage (Ernest F. Fullam, Inc, Latham, NY). Four point bending was preferred over three point bending because it generates a more uniform bending moment, enabling potential deflection of crack away from the initial crack line. The loading stage and sample were first placed under an optical microscope (BX-51M, Olympus, Markham, ON, Canada) equipped with a CCD camera (RETIGA 2000R, Qimaging, Surrey, BC, Canada), and the specimens were loaded at a rate of 0.002 mm/s up to failure.

Fracture tests results

In order to compute the fracture resistance curves, the crack length was measured from the optical images taken during the experiment. The specimens developed large inelastic regions around the crack, so that the linear elasticity-based K_{IC} toughness was not deemed appropriate. Instead, a non-linear *J* integral based approach was used following existing testing standards [19]. A data cut-off condition was applied to all curves to ensure the validity of *J* over the crack extensions [20].

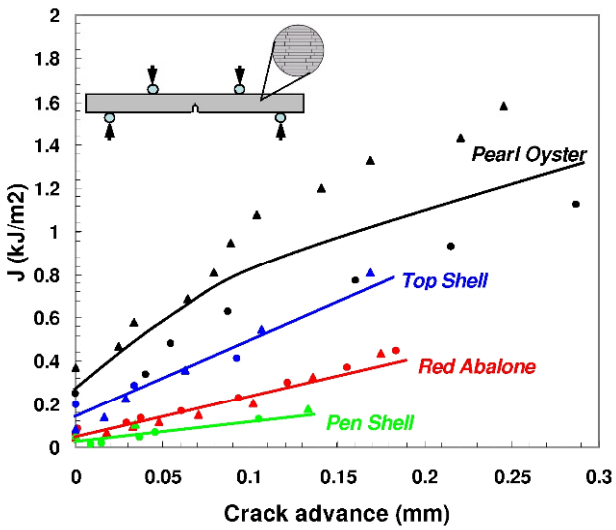

Figure 1: Fracture resistance curves for four nacres. All the shells show a raising fracture toughness attitude.

Figure 1 shows the fracture resistance curves obtained. Upon crack propagation the toughness increased with crack advance, which is consistent with the stable crack propagation observed during the experiments. A raising crack resistance curve is an indication of toughening mechanisms operating around the advancing crack. The amount of toughening was however different across species. Pearl oyster showed the most pronounced toughening, while Pen Shell showed only a modest increase. Pearl oyster also displayed the most complex crack patterns (Figure 2d), which complicated crack length measurements. For all species, the crack advance in Figure 1 was defined as the projected length of the crack along the initial crack line. The variation of crack path across pearl oyster specimens can probably explain the larger variations in the crack resistance curve compared to the other species. The data reduction also relied on assumptions typically made for metals [19] which may be questionable for a material like nacre. Therefore, another measure of toughness which does not rely on any assumption on material behavior was also used. The work of fracture, defined as the area under the load-defection curve divided by the initial surface area of the ligament [21], was computed for each experiment

(Table 1). The work of fracture was remarkably consistent across all specimens within each species, and the values were in the same range as the toughness measured on the crack resistance curves.

Optical imaging revealed that all nacres developed a white “process zone” ahead of the crack. Stress whitening is now a well documented phenomenon in nacre [3, 8, 11], it is an indication of tablets sliding, exposing organic ligaments at the ends of the separated tablets. Examples of this phenomenon are shown in Figure 2 for TS and PO. In case of TS, the whitening distribution is relatively uniform with some distinct deformation bands perpendicular to the loading direction on the front side of the process zone. The crack propagates in a relatively straight path along individual columns, remaining in an overlap region (the crack is deflected by a few microns at most, Figure 2b). In contrast, the process zone in PO consists of a tree-like network of deformation bands at about 45 degree angle from the loading direction (Figure 2c). This network is denser near the crack tip, but remains inhomogeneous. Crack deflection is significant, with deflections exceeding 10 microns (Figure 2d).

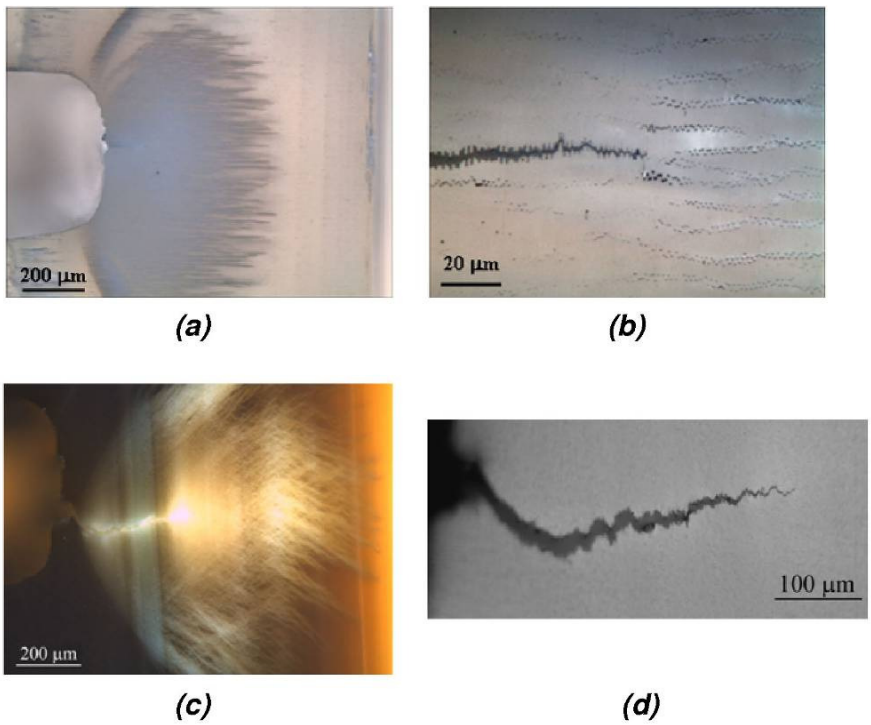

Figure 2: Optical images from fracture tests: (a) TS shows a relatively homogeneous inelastic region and, (b) a straight crack which follows tablets columns (note patial recovery behind the crack tip), (c) PO develops a network of localized inelastic branches at an angle and, (d) the crack advanced in a jagged manner.

In order to elucidate the exact micromechanisms behind the shape of the process zone additional fracture tests were performed on PO and TS, but this time under an atomic force microscope (Veeco Dimension V, Santa Barbara, CA). Surface of the samples were polished down to 0.05 micron following standard polishing procedures, and the samples were kept hydrated throughout the tests. *In-situ* imaging confirmed that for columnar nacre under tensile load all the tablets separate in a homogenous fashion (Figure 3a,b). Typical tablet separations were 100 nm, which can account for 1% tensile strain measured in tensile tests [11].

Similar images were also acquired in-situ for PO (Figure 3c,d). The AFM images indicate that tablet sliding is the only inelastic mechanism taking place ahead of the crack tip. This mechanism however appeared to be inhomogeneous, with tablets separating in some areas (i.e. area I on Figure 3) while remaining closed in others (i.e. area II). Deformation bands consisting of adjacent opened junctions are observed to be formed at an angle from the loading direction. The separation of the tablets was typically about 250 nm (Figure 3d), more than twice the separation distance observed in TS.

This marks a clear difference between columnar and sheet nacres: while columnar fails along all the overlap regions in a “columnar” type of failure, in sheet nacre a “stair” type of failure seems to prevail, leaving some tablet

junctions closed. This difference in deformation patterns of columnar and sheet nacre is further examined by means of numerical simulation in the next section.

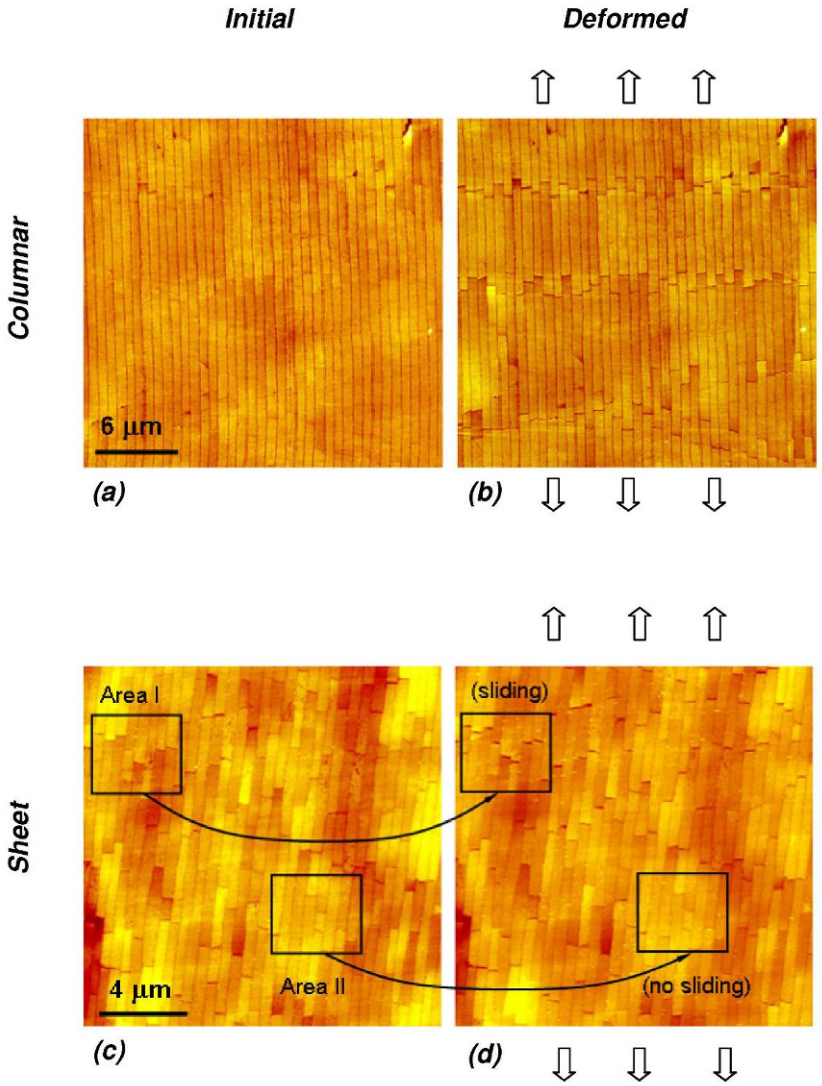

Figure 3: *In-situ* AFM imaging ahead of a propagating crack: Top Shell (a) before and (b) after deformation, showing that all the junctions open, conveying a uniform type of tablets sliding. The Pearl oyster (c) before and (d) after deformation showed that the junctions only opened in some areas while they remained closed in others.

Numerical modeling

In essence, the transition between columnar and stair failure modes can be explained based on combination of two parameters [22]: first, the applied local shear stress, and second, the microstructure through "overlap ratio" which is defined as the ratio of the tablets overlap length to the length of one tablet [10]. In particular, if the applied shear stress is sufficiently large and the overlap area is relatively large, the deformation path follows a "stair" pattern, and opposite condition triggers "columnar" failure. Local shear stresses can be induced by inhomogeneity in the material; i.e. any softer region in tension will generate shear stresses locally. For example, a crack loaded in mode I will develop local shear stresses that may trigger stair failure.

In order to examine the transition in failure modes, numerical modeling was implemented. Large plane strain finite elements models of nacre microstructures were therefore generated, with periodic geometries in both longitudinal (x) and transverse (y) directions. Each tablet was modeled as linear elastic (E=100 GPa [23, 24]) with linear plane strain elements, while the interfaces were modeled by inserting cohesive elements between the tablets. The

associated cohesive law was taken as described in [10]: A short linear elastic region was followed by a long plateau at constant strength (τ_s = 25 MPa). For all models a stretch was imposed along the longitudinal (x) direction. Simulations were performed using ABAQUS (ABAQUS Version 6.8-3, ABAQUS, inc. Providence RI).

Two large Representative Volume Elements (RVEs) were generated to model perfectly periodic columnar and sheet microstructures. Both models were composed of tablet 0.5 μm in thickness and 5 μm in length. In columnar nacre the overlap was set at 20% of the length of the tablets while in sheet nacre the overlap was set to 50% of the length of the tablets. In both models a defect was introduced in the center of the RVE by removing a few cohesive elements. The results (Figure 4) show that both models predict high shear stresses on either side of the ends of the defect, but also that the failure patterns are different. In columnar nacre, the deformation localized along a band perpendicular to the loading direction, following a columnar type of failure. In contrast, sheet nacre showed two localizations at an angle, triggered in the regions of high shear stresses and thus following a stair type of failure. These models clearly show that (i) combination of shear and microstructure can trigger stair failure (ii) stair failure enables the spreading of inelastic deformation over large volumes even in the absence of any source of hardening.

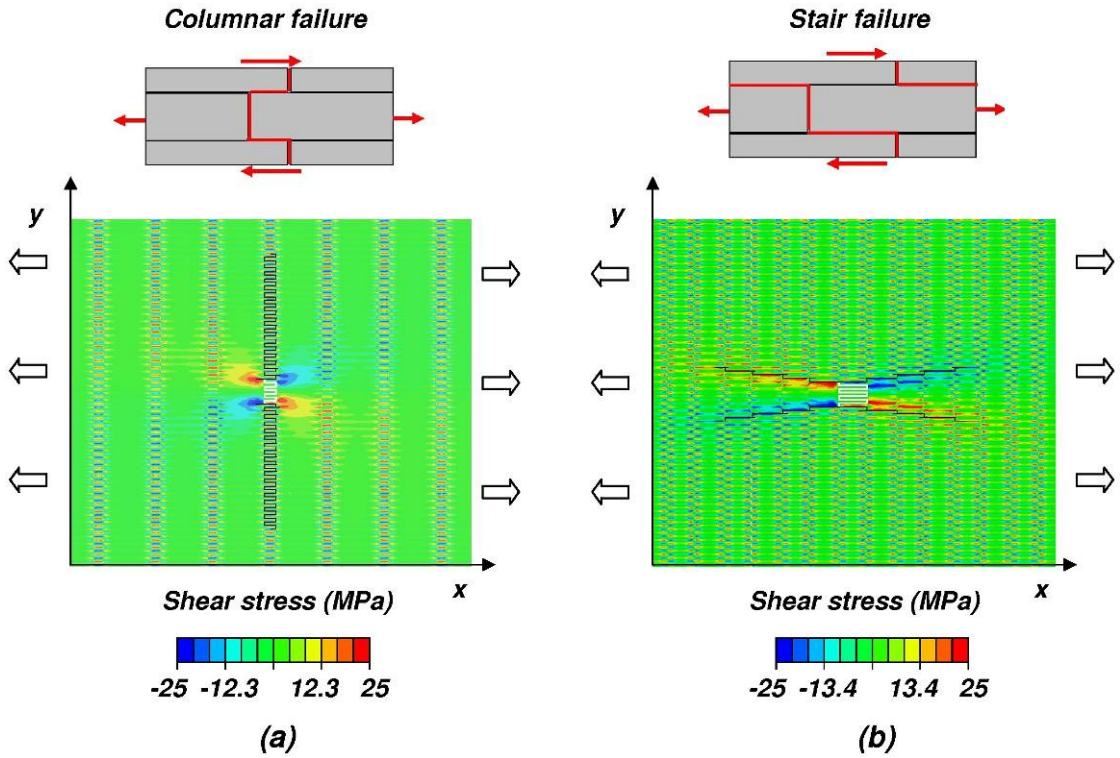

Figure 4: Shear stress contours for RVE of (a) columnar and (b) sheet nacres. The initial defect is outlined in white. The interfaces that have completely failed are highlighted in black. (Note that tablets orientation and loading direction are rotated by 90° compared to Figure 2).

Conclusions

Nacre, one of the most remarkable hard natural materials known, is increasingly serving as model for the design of biomimetic materials. In this context, this work provides new insights in the construction and mechanics of this material:

- All nacres are not equal in performance and mechanisms: within the four nacres tested in this study, sheet nacre from Pearl oyster was significantly superior in toughness, and should probably serve as model for future biomimetic materials.
- Sheet nacre from Pen Shell performed relatively poorly (Figure 1). Low fracture toughness of Pen Shell may be attributed to its higher tablet aspect ratio (Table 1), to large variations in waviness and growth defects. These features may raise the stresses in the tablets significantly, which may lead to premature fracture of the tablets before they can actually slide on one another. The toughness of nacre relies on

molecular events at the interface of the tablets [6]. Possible deficiencies in the organic materials of Pen shell could therefore also explain its lower fracture toughness.

- While columnar nacre developed well defined deformation bands following the columnar structure and perpendicular to the loading direction, sheet nacre from Pearl oyster developed a quite unusual network of deformation bands at an angle from the main crack. Analytical and numerical models demonstrated that the transition between columnar and stair failure modes is controlled by the amount of overlap between tablets, and by local shear stresses from inhomogeneities in the material. Stair failure was shown to lower the tensile strength of the material, which may be compensated by the longer overlap length in the microstructures favorable to this type of failure.
- In terms of toughness enhancement, the stair deformation mode appears to be more beneficial than columnar deformation, because it can spread over large volume even in the absence of any hardening mechanism (thereby promoting energy dissipation and toughening).

Finally, these new findings on sheet nacre and stair failure may be generalized to other natural composites with a random staggered arrangement. In particular, the conditions for the stair failure mode are met in bone at the microscale. Mineralized collagen fibrils are aligned with a random overlap, and the “ductility” of bone in tension is provided by the sliding of those fibrils along one another [15]. The models developed so far to capture this fundamental mechanism have assumed a columnar type of failure, whereas a stair type of failure may actually prevail in this case, with important implications for the strength and toughness of bone at the smallest scales.

Acknowledgment

This work was supported by the Faculty of Engineering at McGill University, the Natural Sciences and Engineering Research Council of Canada, the Canada Foundation for Innovation and the Fonds québécois de la recherche sur la nature et les technologies. The first Pearl oyster samples were generously provided by Evelyne Lopez from the Musée National d’Histoire Naturelle in Paris, France.

References

[1] Wegst UGK, Ashby MF. The mechanical efficiency of natural materials. Philosophical Magazine 2004;84:2167.

[2] Barthelat F. Biomimetics for next generation materials. Philosophical Transactions of the Royal Society a-Mathematical Physical and Engineering Sciences 2007;365:2907.

[3] Currey JD. Mechanical Properties of Mother of Pearl in Tension. Proceedings of the Royal Society of London 1977;196:443.

[4] Bonderer LJ, Studart AR, Gauckler LJ. Bioinspired design and assembly of platelet reinforced polymer films. Science 2008;319:1069.

[5] Munch E, Launey ME, Alsem DH, Saiz E, Tomsia AP, Ritchie RO. Tough, Bio-Inspired Hybrid Materials. Science 2008;322:1516.

[6] Smith BL, Schaeffer TE, Viani M, Thompson JB, Frederick NA, Kindt J, Belcher A, Stucky GD, Morse DE, Hansma PK. Molecular mechanistic origin of the toughness of natural adhesives, fibres and composites. Nature (London) 1999;399:761.

[7] Lin AYM, Meyers MA. Interfacial shear strength in abalone nacre. J. Mech. Behav. Biomed. Mater. 2009;2:607.

[8] Wang RZ, Suo Z, Evans AG, Yao N, Aksay IA. Deformation mechanisms in nacre. Journal of Materials Research 2001;16:2485.

[9] Song F, Bai YL. Effects of nanostructures on the fracture strength of the interfaces in nacre. Journal of Materials Research 2003;18:1741.

[10] Barthelat F, Tang H, Zavattieri PD, Li CM, Espinosa HD. On the mechanics of mother-of-pearl: A key feature in the material hierarchical structure. Journal of the Mechanics and Physics of Solids 2007;55:225.

[11] Barthelat F, Espinosa HD. An experimental investigation of deformation and fracture of nacre-mother of pearl. Experimental Mechanics 2007;47:311.

[12] Jackson AP, Vincent JFV, Turner RM. The Mechanical Design of Nacre. Proceedings of the Royal Society of London 1988;234:415.

[13] Deville S, Saiz E, Nalla RK, Tomsia AP. Freezing as a path to build complex composites. Science 2006;311:515.

[14] Gao HJ. Application of fracture mechanics concepts to hierarchical biomechanics of bone and bone-like materials. International Journal of Fracture 2006;138:101.

[15] Gupta HS, Seto J, Wagermaier W, Zaslansky P, Boesecke P, Fratzl P. Cooperative deformation of mineral and collagen in bone at the nanoscale. Proceedings of the National Academy of Sciences of the United States of America 2006;103:17741.

[16] Peterlik H, Roschger P, Klaushofer K, Fratzl P. From brittle to ductile fracture of bone. Nature Materials 2006;5:52.

[17] Jager I, Fratzl P. Mineralized collagen fibrils: A mechanical model with a staggered arrangement of mineral particles. Biophysical Journal 2000;79:1737.

[18] Kotha SP, Li Y, Guzelsu N. Micromechanical model of nacre tested in tension. Journal of Materials Science 2001;36:2001.

[19] ASTM. ASTM standard E 1820-01: "Standard Test Method for Measurement of Fracture Toughness", 2004.

[20] Saxena A. Nonlinear Fracture Mechanics: CRC Press, 1998.

[21] Sakai M, Bradt RC. FRACTURE-TOUGHNESS TESTING OF BRITTLE MATERIALS. International Materials Reviews 1993;38:53.

[22] Rabiei R, Bekah S, Barthelat F. Failure mode transition in nacre and bone-like materials. "in revision", 2010.

[23] Bruet BJF, Qi HJ, Boyce MC, Panas R, Tai K, Frick L, Ortiz C. Nanoscale morphology and indentation of individual nacre tablets from the gastropod mollusc Trochus niloticus. Journal of Materials Research 2005;20:2400.

[24] Barthelat F, Li CM, Comi C, Espinosa HD. Mechanical properties of nacre constituents and their impact on mechanical performance. Journal of Materials Research 2006;21:1977.

Proceedings of the SEM Annual Conference
June 7-10, 2010 Indianapolis, Indiana USA

Measurement of Structural Variations in Enamel Nanomechanical Properties using Quantitative Atomic Force Acoustic Microscopy

Wei Zhao, Changhong Cao, and Chad S. Korach*
*Corresponding author, chad.korach@stonybrook.edu
Department of Mechanical Engineering, State University of New York at Stony Brook
Stony Brook, NY, 11794-2300 USA

ABSTRACT
Quantitative Atomic force acoustic microscopy (AFAM) was used to measure the nanomechanical properties in human dental enamel associated with microstructural locations. AFAM measurements were made on samples from human molars at locations near the occlusal surface and the dentine enamel junction (DEJ). Within these locations, single point AFAM testing was performed on individual prism and sheath regions within the enamel microsctructure. Orientation changes in the enamel properties were observed by measurements in the perpendicular and parallel directions to enamel prisms. From quantitative AFAM, elastic modulus of the sample surfaces is calculated based on the measured cantilever frequency and probe tip geometry. Mean elastic modulus of the prismatic enamel was 109 ± 1 GPa and the enamel sheath was 96 ± 2 GPa, measured at the occlusal surface. Elastic modulus was found to decrease by 49% when measured in the direction normal to the prism parallel axis, and decrease by ~6.5% between the locations at the occlusal surface and those near the DEJ. The property variation of the prism and sheath is associated to the differences in the mineral to organic content, with the orientation differences due to the apatite crystal directions within the enamel microstructure.

1. Introduction

The mechanical properties of dental enamel are important for understanding the effects on restorative dental materials and the interactions of dentifrice and other objects on the enamel surface. It has been well-established that the enamel microstructure is a composite of mineralized material and bio-polymers formed in parallel rods approximately normal to the tooth surface [1]. The rods, also referred to as prisms, extend continuously from the dentine-enamel junction (DEJ) to the surface and consist of a sheath region richer in organic content surrounding the prism. The enamel microstructure is a bio-composite consisting of these two regions, each a composite of varying degrees of organic polymer (specifically enamelin) and mineralized hydroxyapaptite crystals. When observed at the macroscale, the enamel exhibits an ultrastructure consisting of disruptions in the enamel mineralization (e.g. Rentzis lines), prism twisting, and inner enamel closer to the DEJ [2].

The well-defined microstructure of the enamel (and even the dentine that lies beneath) forms a framework where an interest in the interaction and interplay at multiple scales of the microstructural materials could potentially be applied to biomimmetic materials design. To establish modeling and macroscale relationships, an understanding of the mechanical properties of the enamel is necessary. The effects of the unidirectional prism microstructure have been investigated by microindentation and demonstrated changes in the hardness in the normal (to the surface) versus longitudinal (in the cross-section) directions of enamel [3]. Indentation in the longitudinal direction has also allowed the identification of a variation in mechanical properties from the inner enamel near the DEJ towards the surface outer enamel [4].

A region of interest that potentially may play a critical role in the strength and toughness of enamel is the interplay between the sheath (also called the interrod or interprismatic enamel) and prism regions of the structure. The sheath is formed due to variations in the hydryoxyapatite crystal orientation, which are abrupt at the prism interface presenting typically towards the crown apex. This creates an often termed keyhole structure, which has a tail end in the direction away from the crown [1, 2]. In reality, the prism is more rod-like and not actually a prism, and has a horseshoe shaped sheath. Throughout the keyhole there is a continuous variation in the hydroxyapatite crystal orientation from the tail towards the keyhole head, which points in the direction of the occlusal surface, and also in the perpendicular direction to the sides of the prism centerline [5, 6]. Sharp

T. Proulx (ed.), *Time Dependent Constitutive Behavior and Fracture/Failure Processes, Volume 3*, Conference Proceedings of the Society for Experimental Mechanics Series 15, DOI 10.1007/978-1-4419-9794-4_52, © The Society for Experimental Mechanics, Inc. 2011

interfaces of hydroxyapatite orientation are present and lead to a sheath region that is less structured and high in organic content, and thus believed to be more compliant. Since the crystal orientation is strongly dissimilar (~90º in some locations) along the prism-sheath interface it would be naturally weak and prone to a high degree of failure. The presence of the higher organic content is believed to act as a natural toughening interface in the enamel, slowing down fractures and failure by absorbing energy and impeding fracture growth. Stiffness differences of the sheath and prism have been shown by AFM-based nanoindentation, at least at the scale of the indenter tip, which is on the order of 100's of nanometers [7-10]. A full understanding of the structural importance of the separate sheath and prism regions is not complete, though it has clearly been shown that fractures, which are common in enamel, preferentially occur along the prism interfaces (i.e. the sheath) [11, 3]. The sheath may act as a toughening region for slowing down and abating fracture growth by a ductile rather than brittle fracture mechanism [11]. Due to this and that enamel is a highly organized biocomposite with a defined unit cell, the material and interfaces within are of interest from the materials and engineering viewpoint.

Variations from the prism to sheath and back to prism occur at small length scales estimated to be on the order of a few 100 nanometers, which is a small percent of the prism region that is typically 5 – 7 □m in diameter. Though positive and reassuring results have been measured by nanoindentation, the extent of a plastic zone surrounding an indent could be as much as twice the indent width, affecting in turn the results due to interaction of the stress field with the neighboring prism material. Due to this, a technique with length scale resolution below 100 nm is necessary to probe mechanical properties of the enamel microstructure.

The use of atomic force microscopy (AFM) has been used to measure topography, AFM-based nanoindentation of hardness and elastic modulus [8, 10, 12], force modulation of the DEJ [13], nanoscale friction across prism and sheaths [14], and the piezo-electric response of enamel crystals [15]. Here, we utilize the high resolution of the AFM probes and scanners, combined with an ultrasonic acoustical perturbance of the sample, to measure nanomechanical properties of dental enamel spatially between the prism and sheath. Atomic force acoustic microscopy (AFAM) has been successfully applied to imaging material differences of organic thin films [16], as well as inorganic materials [17, 18], measuring features on the order of nanometer resolution, which can be applied to measuring mechanical property variations within the enamel microstructure. The advantages of AFAM are two-fold, one, the spatial resolution is on the order of the probe tip size, ~20 nm, and two, minimal to no plastic indentation is necessary. This improves the spatial accuracy and resolution of the measured mechanical properties. Here the elastic modulus between the prism and sheath regions will be compared using AFAM for the first time.

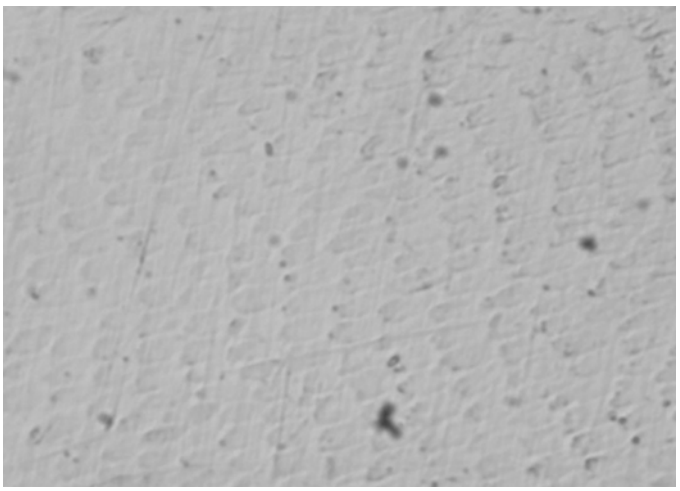

Figure 1. Optical image of the enamel surface after polishing. Differences in microstructure are observed between the prism and sheath regions of the enamel with the keyhole head pointing in the direction to the left of the image. Size of viewable area is ~100 x 135 μm.

2. Materials and Methods

2.1. Materials and Preparation

Samples were placed in a container of deionized water and refrigerated at ~ 2~3 ^{o}C, after removal from the

original biological support. A 2 mm x 1mm specimen was machined by diamond saw from the distal sides of adult human bicuspids for AFAM testing. Deionized water lubrication was provided to the specimen surface to reduce friction and heat generation during cutting. Due to the low roughness requirement to obtain results with AFAM, samples underwent metallographic polishing steps with 3 μm, 1 μm, and 0.05 μm alumina particles. Polishing was minimal to the surface and only applied long enough to obtain a flat region for testing, thus the exposed surface was outer enamel of the tooth. Water based ultrasonic cleaning was performed to remove residual polishing particles remaining on the specimen surface. After polishing, sample surfaces were examined by optical microscopy (Keyence VHX-500) to insure a smooth, flat region for testing (Figure 1) where the enamel microstructure was visible. Specimens were attached to the AFAM transducer and allowed to rest for one hour prior to starting measurements. During this period, the sample surface remained hydrated by placing deionized water drops by pipette as needed. Water was added to the surface when a visible meniscus began to disappear.

2.2. Atomic Force Acoustic Microscopy

AFAM works by insonifying a sample mounted on an ultrasonic transducer which emits longitudinal acoustic waves [19]. Combined with an AFM (NT-MDT SolverProM), an AFM cantilever is brought into contact with the sample, and resulting vibrational frequencies in the cantilever are measured with a laser-photo diode system. The AFM cantilever is modeled as a clamped beam with a distributed mass that can vibrate in different modes, such as flexural, torsional, and extensional. Analyzing flexural and torsional vibration modes for the free vibrations can result in closed form solutions of the equations of motion [20-22]. If the beam is fixed at any length L_1 and coupled to a surface through a linear spring with stiffness k^*, which represents the forces due to tip-sample contact, the equations of motion can be solved analytically using a simplified beam contact model if amplitudes are kept sufficiently small. For larger amplitudes, a non-linear representation of the surface forces would be necessary [23], though in this study, small amplitude and displacement are utilized. A representative characteristic equation for the modal flexural stiffness is given as [20]:

$$\frac{k^*}{k_c}\left[-\left(\cosh k_n L_1 \sin k_n L_1 - \sinh k_n L_1 \cos k_n L_1\right)\left(1+\cos k_n L' \cosh k_n L'\right)\right. \quad (1)$$

$$\left.+\left(\cosh k_n L' \sin k_n L' - \sinh k_n L' \cos k_n L'\right)\left(1-\cos k_n L \cosh k_n L\right)\right] = 2\frac{\left(k_n L_1\right)^3}{3}\left(1+\cos k_n L \cosh k_n L\right)$$

where k^* is the tip-sample contact stiffness, L is the total cantilever length, L_1 is the tip position along the cantilever, and $L' = L - L_1$. The modal contact stiffness, k_n, is represented by,

$$k_n = c_c\sqrt{f_n} \quad (2)$$

where f_n are the vibration frequencies ($n = 1, 2, \ldots$), and c_c is a characteristic cantilever constant,

$$c_c = \sqrt{\frac{48\pi^2\rho}{b^2 E_i}} \quad (3) \ ,$$

which is the function of the cantilever modulus E_i (=169GPa) (silicon), ρ is the cantilever mass density, and the cantilever thickness, b. The cantilever spring constant (k_c) can be calculated by the cantilever mechanical properties and geometry or a direct method as described in the following section. Typical values of cantilever spring constants used in the AFAM measurements are larger than used for contact imaging, allowing higher normal loads to be applied to the contact interface while retaining small cantilever deflections. In this study, the applied load is considered at least two orders larger than adhesive forces, which can be neglected. The resonance frequencies are sensitive to the applied normal loads and increase with applied load due to a stiffer contact created between the tip and sample, though are stable within a certain range of loads.

2.3. Cantilever Specification

The cantilever spring constant selection is based on the sensitivity of the cantilever to the materials to be measured. Incorrect cantilever selection can lead to erroneous evaluation of AFAM results, due to contact stiffness (k^*) of tip-material pairs which are out of range. Eq. (1) can be rewritten as,

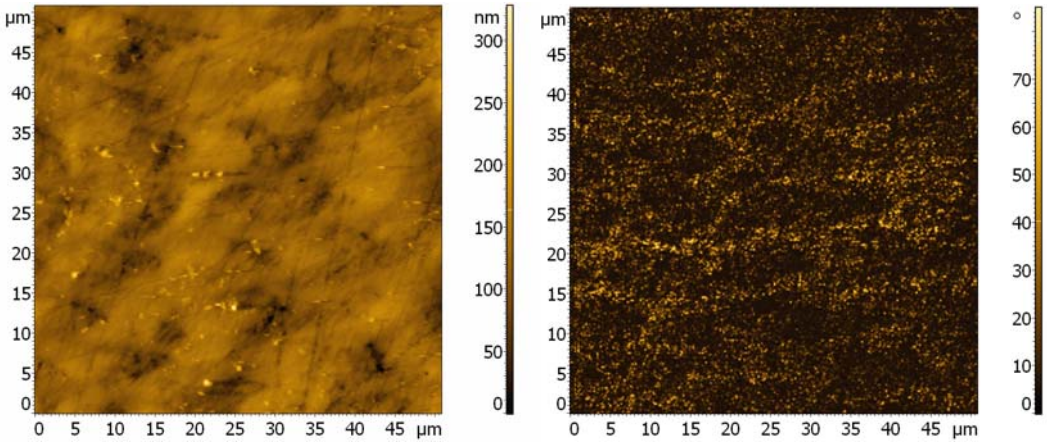

Figure 2. (a) 50 x 50µm AFM topography scan of enamel surface; (b) 50 x 50µm AFAM phase scan of enamel surface at 1493.3 kHz transducer frequency.

$$\frac{k^*}{k_c} = \frac{1+\cos(c_c\sqrt{f_n})\cosh(c_c\sqrt{f_n})}{\sinh(c_c\sqrt{f_n})\cos(c_c\sqrt{f_n})-\sin(c_c\sqrt{f_n})\cosh(c_c\sqrt{f_n})} \cdot \frac{(c_c\sqrt{f_n})^3}{3} \qquad (4)$$

By evaluating Eq. (4), at certain frequency ranges the contact stiffness may reach negative values. Also, k^* shows singularities of positive and negative infinity at the contact resonance frequencies, which could lead to sensitivity problems in calculating the sample elastic modulus, E_s. This implies that for a specific sample, cantilevers should be chosen with caution to achieve accurate results. In this study, rectangular geometry, polysilicon cantilevers (AIST fpN11S), have been used for all measurements.

Cantilever geometry was measured by combination of scanning electron and optical microscopy. Tip radius of curvature is typically in the range of 10 nm to 100 nm, and was measured for accuracy during experiments with SEM to be ~20 nm. The cantilever spring constant is the key to determine the contact force F_c, and hence to compute the elastic modulus. Though AFM cantilever manufacturers provide a typical range for k_c, for accurate nanomechanical results the direct calibration of the spring constant was determined by the thermal turning method [24] to be k_c = 22.48 N/m, and were found suitable for testing the enamel. The geometrical specifications of the fpN11s cantilevers are a length x width x thickness of 101.8 x 34.8 x 2.3 µm. Topography and AFAM phase scanning was performed at low applied loads, making radius of curvature a consistent value throughout testing. Due to the large normal loads needed for stable results using AFAM, single point testing has been performed for all the quantitative measurements to avoid tip wear and increasing the tip radius of curvature significantly by high load scanning. The applied load is controlled by varying the cantilever deflection value during measuring. AFAM results were measured under loads of 2.9, 3.4, and 3.9 µN.

3. Results

3.1. AFAM Scanning

AFAM measurements were performed on hydrated enamel specimens. Contact with the enamel surface commenced immediately after the visible water on top of the sample surface evaporated. This was done to insure the sample surface was kept in a hydrated state as long as possible prior to measurement, though it allowed that the near-surface moisture had evaporated which can affect adhesive forces. Phase angle changes in the cantilever resonance frequency while in contact with the ultrasonically perturbed enamel specimen were recorded simultaneously with the topography. This allows observation of surface topography with AFAM results, where large changes in topography can affect the measured phase changes. The enamel sheath and prism structure, which are known to have different material structure and mechanical properties, can be identified from the AFM topography images. Height variations are occurring due to the difference in the polishing rate of the sheath and

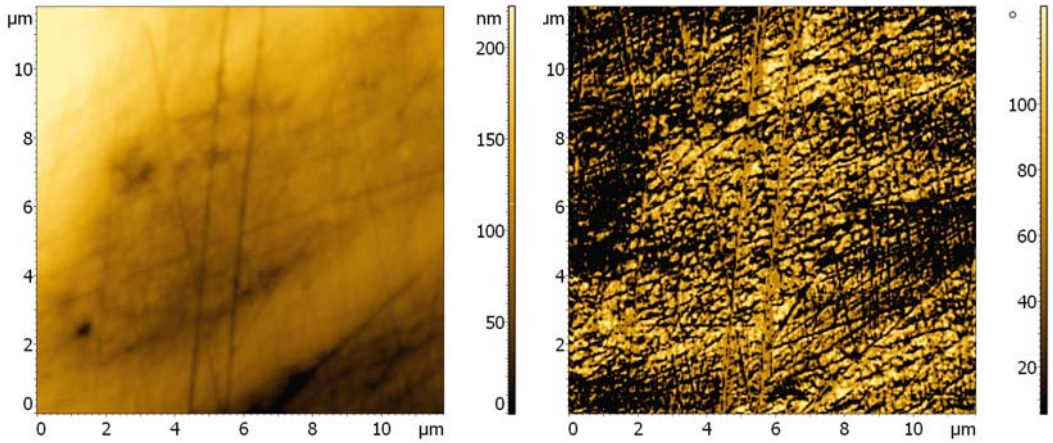

(a) (b)

Figure 3. (a) 12 x 12 µm AFM topography scan of a single prism on the enamel surface; (b) 12 x 12 µm AFAM phase scan of a single prism on enamel at 1493.3 kHz transducer frequency.

prism (see Figs. 2a and 3a). From the phase images (Figs. 2b and 3b) the sheath is observed to have a larger phase angle change in comparison with the prisms. For the 50 x 50 µm scan (Fig. 2b), due to the reference frequency point chosen, this translates to a decreased stiffness of the sheath compared with the prism. Though AFAM (and any SPM-based feedback system) is susceptible to artifacts in results created from abrupt height variations, the spatial variations of interest between the prism and sheath are large compared with the probe tip radius and sampling rate. When AFAM scanning is applied to a smaller region of the enamel, on the scale of individual prisms, the differences between prism and sheath become more evident. Figure 3 maps a phase angle variation across the prism (lighter) to sheath (darker) at a transducer excitation frequency of 1493.3 kHz. The transducer frequency was chosen after preliminary observations to provide the best possible signal strength. This change in phase angle is directly related to stiffness changes in the material surface. Here, the phase angle change indicates once again that the differences between the sheath region and the prism, with the sheath having a decreased stiffness compared with the prism based on the reference chosen. For the AFAM phase angle scanning, probe tip loads were kept at low values (~ 0.5 µN) to avoid wear of the silicon AFM probe. Variations in probe radius directly affect the sample-probe contact area which then affects the AFAM contact stiffness. The use of low contact loads is necessary to avoid the wear of the tip and to achieve the most accurate stiffness mapping, though some resolution and clarity of variations are lost and it becomes necessary to determine exact quantitative values by single point spatial testing.

3.2. AFAM Single Point Testing

To achieve quantitative stiffness measurements directly related to materials properties, AFAM single point testing was utilized [25]. For the most accurate results, a coherent contact between probe and sample is necessary. To ensure the contact of the probe to the testing surface during ultrasonic vibration, normal loads between the probe and sample are needed that are typically not used in AFM scanning (order of µN). Single point testing not only allows more accurate results, but also avoids changes in the probe tip geometry (radius of curvature), which has been observed for high load scanning. The single point testing utilizes topography images scanned in a semi-contact mode. Based on the AFM topography, regions of interest for prisms and sheaths were identified to perform the AFM point measurements. The semi-contact mode topography scanning imparts very low normal and lateral loads (order of nN) on the sample from the probe, minimizing damage during topography scanning to the sample surface which may alter stiffness measurement results. The distance between testing points were chosen to be at least 100 nm between testing locations, though spatial resolution on the order of the tip radius (~20 nm) is achievable with the technique. Three different applied loads (F_c = 2.9, 3.4, and 3.9 µN) were used to perform spatial point testing on four different locations of prisms and sheaths. When the AFM probe comes in contact with the surface, the cantilever resonance frequency will increase from the free state, as shown in Fig. 4, due to a change in the cantilever boundary conditions. The contact resonance frequency as the probe is located within different regions of the enamel surface will shift based on the sample stiffness, e.g. from the enamel sheath to the

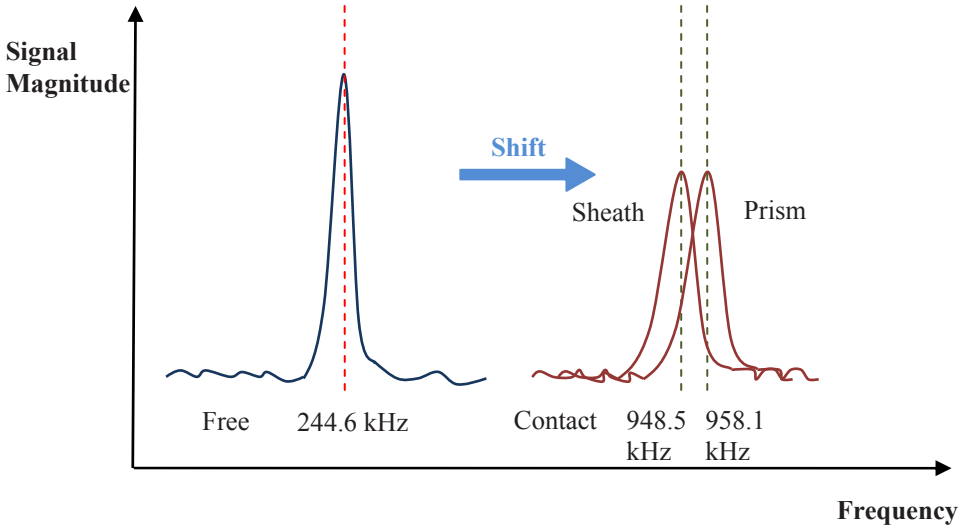

Figure 4. Resonance Frequency shift correspondent to boundary condition change from free cantilever vibration to contact resonance frequency. Further shift in frequency occurs when probe is in contact with sheath versus prism enamel (indicated on right). Note the axes are not to scale and are for comparison purposes.

Prism	**Measuring Locations**								**Average**	
	Location 1		Location 2		Location 3		Location 4		E_s	
Load	k^*	E_s	k^*	E_s	k^*	E_s	k^*	E_s	Ave	s.d.
2.88	1419.5	103.6	1139.0	68.8	1278.6	85.3	1353.8	95.1	88.2	14.9
3.38	1357.1	86.4	1595.7	118.7	1428.6	95.3	1450.9	98.2	99.7	13.7
3.87	1450.9	89.9	1749.4	130.7	1768.6	133.4	1628.1	112.7	116.7	20.1
Ave	1409.0	93.2	1494.7	106.8	1492.0	104.8	1477.6	102.0	101.7	6.0
μN	***N/m***	***GPa***	***N/m***	***GPa***	***N/m***	***GPa***	***N/m***	***GPa***	***GPa***	***GPa***
Ave	1397.5	91.5	1445.8	97.7	1373.4	88.5	1467.2	100.6	94.6	5.6
3.87	1540.9	101.1	1582.2	106.5	1470.1	92.2	1582.2	106.5	101.6	6.7
3.38	1396.4	91.2	1441.6	97.0	1396.4	91.2	1462.3	99.7	94.8	4.3
2.88	1255.3	82.4	1313.6	89.7	1253.9	82.2	1357.1	95.6	87.5	6.4
Load	k^*	E_s	k^*	E_s	k^*	E_s	k^*	E_s	Ave	s.d.
Sheath	Location 1		Location 2		Location 3		Location 4		E_s	
	Measuring Locations								**Average**	

Table 1. Contact stiffness (k^*) and elastic modulus (E_s) of prism and sheath Regions on the enamel surface.

prism, and is demonstrated on the right side of Fig. 4. From the point contact resonance frequencies for the first vibrational mode, the contact stiffness (k^*) is determined by equations (1-4) as described in section 2.2-2.3. The resulting k^* values at different locations of the enamel surface are compiled in Table 1. Contact stiffness was found to increase with applied normal load, which is expected with Hertzian contact mechanics. The values of the contact stiffness in the enamel prism region showed an overall increase versus the sheath region, and indicate that the single point testing data corresponds to the trend observed in the AFAM scanning results.

4. Discussion

After obtaining the contact stiffness from the AFAM measurements, a Hertzian contact model is used to simulate the contact conditions between the probe and surface, and calculate the elastic modulus of the sample surface. In the three dimensional Hertz analysis [26], the contact is assumed to be a parabolic indenter in contact with a flat surface. The indenter tip and the surface have elastic modulus of E_i and E_s, and Poisson's ratios of ν_i (=0.33) and

ν_s (=0.36), where *i* and *s* represent the indenter and the surface, respectively. For a statically applied force, F_c = k_c x Δz, where Δz is the cantilever deflection. In our experiments the tip-sample forces F_c are sufficiently large to overcome surface interaction forces to ensure that the elastic contact forces are the main contribution to the analysis. For small deflections, the radius of contact, a_c, and the effective elastic modulus, E^*, are given as,

$$a_c = \sqrt[3]{\frac{3F_c R}{4E^*}} \qquad (5) \qquad\qquad \frac{1}{E^*} = \frac{1-\nu_s^2}{E_s} + \frac{1-\nu_i^2}{E_i} \qquad (6)$$

where R is the radius of curvature of the indenter tip. Using equation (5) and the mutual approach between surfaces, $\delta = \frac{a^2}{R}$, the contact stiffness can be represented by,

$$k^* = \sqrt[3]{6E^{*2}RF_c} \qquad (7)$$

and relates the contact stiffness k^* to the sample surface elastic modulus (E_s), as a function of the applied contact force and the radius of curvature of the indenter tip. Using the measured contact stiffness for the enamel samples, results of elastic modulus are determined by Eqns. 5-7 and are presented in Table 1. The results point to that the average prism has a larger elastic modulus than the enamel sheath. The standard deviation in the measurements shown in Fig. 5 is observed higher in the prism region, this potentially could be due to surface roughness variation affecting the real contact area during measurement.

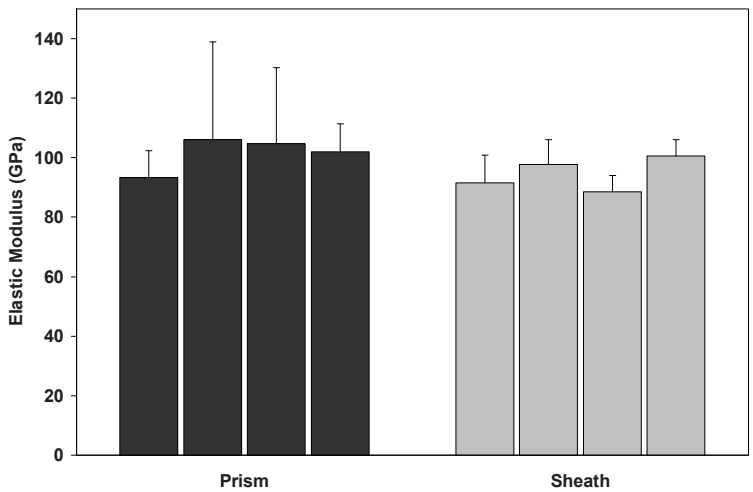

Figure 5. Elastic modulus calculated from AFAM measurements on enamel prism and sheath regions of surface. Each column represents a separate measuring position.

The enamel prism was found to have a stiffer contact and hence computed elastic modulus (E^{prism} = 101.7 GPa ± 6) than the sheath region (E^{sheath} = 94.6 GPa ± 5.6) surrounding the prism. The mechanical properties of the contact were found affected by the applied normal load, though the trend in prism modulus remaining larger than the sheath region was consistent for all loads. The dependence could be due to inaccuracy in the contact geometry assumption of the probe tip.

The larger compliance of the enamel sheath correlates with the knowledge that there exists a higher organic content and less mineral than in the prism. The higher mineral content in the prism over the sheath leads to a stiffer material. This has also been observed by nanoindentaion [8, 10] of human enamel with AFM-based diamond indenters. These results reported (all in GPa) E^{prism} = 88 +/- 8.6, 77.5 +/- 6.2; E^{sheath} = 86.4 +/- 11.7, 35.4 +/- 3.6, for ref. 8 and 10, respectively. The results compared for ref. 10 are re-computed using Eqn. 6, since the author's only presented the average reduced modulus (E_r) results of the prism and sheath. It is interesting to

note that the AFAM quantitative results of the elastic modulus reported here are larger in magnitude, though show the same trend of a stiffer prism region. The discrepancy in results could be due to the differences in spatial resolution of the techniques. Nanoindentation, even for shallow plastic indents, creates an apparent contact region on the order of 8 times the indentation depth, based on the Berkovich indenter geometry that was utilized by ref. 10. For the indentation depth of up to 80 nm used, the apparent contact width would be ~640 nm. Habelitz et al. [8] utilized a cube-corner (90º) diamond indenter to an indentation depth of 300 nm. This translates to a contact width of ~600 nm. It is clear that the contact width of both the AFM-based indentation studies were of similar value, even though the indentation depths were largely different. Due to the spatial scale of the sheath region being < ~1 μm in thickness, it may be difficult for nanoindentation to not interact with the surrounding material at that scale. Furthermore, the actual structural morphology of the organic-rich sheath region is unknown, and it is likely that some functional gradation in the structure will be present across the width. This in turn would generate a rather narrow region to perform indentation on. During nanoindentation, the plastic zone created by the indenter is estimated to be at least twice the width of contact [26], and would interact with the biomaterial interface at the intersection of the sheath and prism materials. If this is the case, then the results in the previous AFM-based indentation studies for the sheath would be affected by the stiffer prism interface or even the change in apatite crystal orientation on either side of the sheath adding additional asymmetry and complexity to the indentation mechanics. This makes the results by Ge et al. [10] more intriguing since the values of the sheath are much lower than reported here as well as in the other nanoindentation results. The AFAM technique is able to provide spatial resolution at the scale of the tip radius (~20 nm), which is within the sheath region and will not be affected by the surrounding prism stiffness or crystal orientation changes. The results here are on the same order as measured in other studies [7, 8, 10] though are trending larger. Due to the higher resolution of the AFAM technique, it is believed that the values presented here are closer to what has been measured for single apatite crystals (125 – 145 GPa depending on crystal plane [27, 28]), and less for the natural enamel nanocomposite material. Though, due to the fact that enamel is ~10% water and ~5% organic by volume [2] and the potential disorder of apatite crystals in the sheath, values are not surprising lower. The large variability observed in the results is most likely due to the sensitivity of the technique scale coming in contact with apatite and higher concentration of organic matter at different instances. Also, nanoindentation relies on the elastic recovery of the material over an unloading distance to compute the elastic modulus and since enamel is a nanocomposite of hydroxyapaptite and enamelin, there could be local variations unaccounted for. These results point to the potential size affect with the enamel microstructure. The identification of enamel mechanical properties at multiple length scales is important for not only a fundamental understanding of the microstructure of the material, but also as complimentary results used in modeling of enamel at the microstructural scale [29], which can be scaled-up to model bulk response of enamel crowns for material wear [30], trauma [31], and de- and re-mineralization effects on the enamel near-surface.

5. Conclusion

Nanomechanical characterization on the surface of human dental enamel using atomic force acoustic microscopy has been performed. The AFAM technique is shown to provide high resolution quantitative measurements on the prism and sheath regions of the enamel microstructure. The contact resonance frequency of the AFM cantilever is used to calculate the elastic modulus with a vibrational beam model in conjunction with Hertzian contact analysis. Elastic modulus was found to be consistent with different applied normal loads with a slight dependency, which may be due to inaccuracies in the probe geometry. Prism modulus was consistently found to be larger than the sheath region, and is related to the mineral and organic material content differences and the change in crystal organization from the prism to the sheath. The AFAM technique has been shown to be a promising quantitative nanomaterial technique with high lateral resolution for enamel structures.

Acknowledgements:

The authors would like to extend appreciation to NSF award CMMI-0626025 in part for support of this work, and also to Prof. Mark S. Wolff for helpful discussions.

References:

1. Tencate AR. Oral Histology: Development, Structure, and Function, 4th ed. Mosby (1994)
2. Miles AEW. Structural and Chemical Organization of Teeth, Vol. II. Academic Press (1967)
3. Xu HHK, Smith DT, Jahanmir S, Romberg E, Kelly JR, Thompson VP, Rekow ED: Indentation damage and mechanical properties of human enamel and dentin. J. of Dental Res. 1998; 77:472-480.
4. Park S, Wang DH, Zhang D, Romberg E, Arola D: Mechanical properties of human enamel as a function of age and location in the tooth. J. of Matls. Sci.: Matls. in Med. 2008; 19:2317-2324.

5. Meckel AH, Griebstein WJ, Neal RJ: Structure of mature human dental enamel as observed by electron microscopy. Arch. Oral Biol. 1965; 10:775-784.
6. Meckel AH, Griebstein WJ, Neal RJ: Ultrastructure of fully calcified human dental enamel. In Tooth enamel, its composition, properties and fundamental structure (eds. Stack MV, Fearnhead RW). John Wright (1962).
7. Willems G, Celis JP, Lambrechts P, Braem M, Vanherle G: Hardness and Young's modulus determined by nanoindentation technique of filler particles of dental restorative materials compared with human enamel. J. Biomed. Matls. Res. 1993; 27:747-755.
8. Habelitz S, Marshall SJ, Marshall GW, Balooch M: Mechanical properties of human dental enamel on the nanometer scale. Arch. Oral Biol. 2001; 46:173-183.
9. Cuy JL, Mann AB, Livi KJ, Teaford MF, Weihs TP: Nanoindentation mapping of the mechanical properties of human molar tooth enamel. Arch. Oral Biol. 2002; 47:281-291.
10. Ge J, Cui FZ, Wang XM, Feng HL: Property variations in the prism and organic sheath within enamel by nanoindentation. Biomaterials 2005; 26:3333-3339.
11. Bajaj D, Arola DD: On the R-curve behavior of human tooth enamel. Biomaterials 2009; 30:4037-4046.
12. Lippert F, Parker DM, Jandt KD: In vitro demineralization/remineralization cycles at human tooth enamel surfaces investigated by AFM and nanoindentation. J. Colloid Interf. Sci. 2004; 280:442-448.
13. Balooch G, Marshall GW, Marshall SJ, Warren OL, Asif SA, Balooch M: Evaluation of a new modulus mapping technique to investigate microstructural features of human teeth. J. Biomech. 2004; 37:1223-1232.
14. Habelitz S, Marshall SJ, Marshall GW, Balooch M: The functional width of the dentino-enamel junction determined by AFM-based nanoscratching. J. of Struct. Biol. 2001; 135:294-301.
15. Rodriguez BJ, Kalinin SV, Shin J, Jesse S, Grichko V, Thundat T, Baddorf AP, Gruverman A: Electromechanical imaging of biomaterials by scanning probe microscopy. J. Struct. Biol. 2006; 153:151-159.
16. Ngwa W, Luo W, Kamanyi A, Fomba KW, Grill W. Characterization of polymer thin films by phase-sensitive acoustic microscopy and atomic force microscopy: a comparative review. Journal of Microscopy-Oxford 2005; 218:208-218.
17. Kester E, Rabe U, Presmanes L, Tailhades P, Arnold W: Measurement of mechanical properties of nanoscaled ferrites using atomic force microscopy at ultrasonic frequencies. Nanostructured Materials 1999; 12:779-782.
18. Hurley DC, Geiss RH, Kopycinska-Muller M, Muller J, Read DT, Wright JE, Jennett NM, Maxwell AS: Anisotropic elastic properties of nanocrystalline nickel thin films. Journal of Materials Research 2005; 20:1186-1193.
19. Rabe U, Amelio S, Kester E, Scherer V, Hirsekorn S, Arnold W: Quantitative determination of contact stiffness using atomic force acoustic microscopy. Ultrasonics 2000; 38:430-437.
20. Rabe U, Janser K, Arnold W: Vibrations of free and surface-coupled atomic force microscope cantilevers: Theory and experiment. Review of Scientific Instruments 1996; 67:3281-3293.
21. Wright OB, Nishiguchi N: Vibrational dynamics of force microscopy: Effect of tip dimensions. Applied Physics Letters 1997; 71:626-628.
22. Yamanaka K, Nakano S: Quantitative elasticity evaluation by contact resonance in an atomic force microscope. Applied Physics a-Materials Science & Processing 1998; 66:313-317.
23. Hirsekorn S, Rabe U, Arnold W. Theoretical description of the transfer of vibrations from a sample to the cantilever of an atomic force microscope. Nanotechnology 1997;8(2):57-66.
24. Hutter JL, Bechhoefer J: Calibration of atomic-force microscope tips. Review of Scientific Instruments 1993; 64:1868-1873.
25. Zhao W, Singh RP, Korach CS: Effects of environmental degradation on near-fiber nanomechanical properties of carbon fiber epoxy composites. Composites: Part A 2009; 40:675-678.
26. Johnson KL. Contact Mechanics. Cambridge University Press, 1985.
27. Katz JL, Ukraincik K: On the anisotropic properties of hydroxyapatite. J. Biomech. 1971; 4:221-227.
28. Sha MC, Li Z, Bradt RC: Single-crystal elastic constants of fluorapatite. J. Appl. Phys. 1994; 75:7784-7787.
29. Spears IR: A three-dimensional finite-element model of prismatic enamel: a re-appraisal of the data on the Young's modulus of enamel. J. Dent. Res. 1997; 76:1690-1697.
30. Shimizu D, Macho GA, Spears IR: Effect of prism orientation and loading direction on contact stresses in prismatic enamel of primates: implications for interpreting wear patterns. Am. J. Phys. Anthop. 2005; 126:427-434.
31. Miura J, Maeda Y, Nakai H, Zako M: Multiscale analysis of stress distribution in teeth under applied forces. Dent. Matls. 2009; 25:67-73.

Proceedings of the SEM Annual Conference
June 7-10, 2010 Indianapolis, Indiana USA

Influence of Diamond-like Carbon Coatings on the Fatigue Behavior of Spinal Implant Rod

Yicheng Peter Pan
PhD Candidate

Jarlen Don
Associate Professor

Tsuchin Philip Chu
Professor

Department of Mechanical Engineering and Energy Process
College of Engineering, Southern Illinois University Carbondale
1230 Lincoln Drive Carbondale, Illinois 62901
Email : Panyicheng@gmail.com

Ajay Mahajan
Associate Dean for Research
College of Engineering, the University of Akron
Akron, Ohio 44325

ABSTRACT

The purpose of this paper is to discuss the influence of Diamond-Like Carbon (DLC) coatings on the fatigue behavior of Spinal implant rod. DLC exists in seven different forms of amorphous carbon materials that display some of the unique properties of diamond. They are usually applied as coatings to other materials that could benefit from some of unique diamond properties. In this work, we compared bending fatigue behavior between Stainless Ti6Al4V and DLC Coating Spinal implant rod. The positive effect has been observed by fatigue tests carried out at ASTM Standard D790. Fatigue life and endurance limit of spinal implant rod have been remarkably increased by means of thin DLC coatings. The improvement of fatigue characteristics of spinal implant rod by DLC coatings has been ascribed to the sealing of external defects which retards crack initiation.

1. INTRODUCTION

Through the use of Diamond-Like Carbon (DLC) coating it has been proven to improve the hardness, wear resistance and coefficients of friction of the material put through this processing [1]. This technology has primarily been used in automotive and tool application where friction and wear is of great concern, in a study of DLC coated piston pin there was a significant decrease of wear when tested [2]. DLC films that have hardness between 10-30 GPa result in an internal stress Young's modulus 6-10 times larger than the hardness values, this property of DLC is what limits the maximum thickness of the coating [3].

The scope of this study is to examine the fatigue behavior of DLC coated spinal implant rods, previous related work has included DLC coating for reduction of bacterial adhesion and increased corrosion and stress resistance for vascular stents. An important factor for DLC coated medical devices is to ensure the biocompatibility; the device must not have negative stimulatory effects on the cells such that it does not lead to adverse biological reactions. It is also critical that the coating meet specific mechanical properties so it may be used in the desired application, the low friction and corrosion resistance properties are proven to inhibit bacterial adhesion [4, 5]. DLC on vascular stents coats the defects on the surface of the host material thereby improving the physical properties, for this particular application the fatigue stress and elasticity of the coating are important. DLC possesses the mechanical properties to excel at this application [6].DLC coating can also enhance and improve upon a materials proportion. In one study Titanium alloys were coated with DLC. The DLC enhances the strength and anti-corrosion properties where as is drastically improved the wear resistance of the Ti [7]. DLC has the potential to improve biomedical devices and introduce new ones where they once were not available.

Currently, Titanium alloy gained more acceptances in biomedical application as surgical implants, especially Ti6AL4V. However, the lack of good resistance limits the use of Titanium alloy. As a result, DLC coating on Ti alloy would be one good solution for the above problem. Many studies have been carried out in trying to improve the mechanical properties of Titanium alloy by DLC coating and claimed that the fatigue limit of

T. Proulx (ed.), *Time Dependent Constitutive Behavior and Fracture/Failure Processes, Volume 3*, Conference Proceedings of the Society for Experimental Mechanics Series 15, DOI 10.1007/978-1-4419-9794-4_53, © The Society for Experimental Mechanics, Inc. 2011

DLC specimens were improved by about 20% in conventional Ti6AL4V [7]. Therefore, this research has focused to DLC coating on Ti6AL4V spinal implant rod and analyzed the mechanism of static and fatigue bending strength improvement between DLC coated and uncoated spinal implant rods.

2. MATERIAL AND EXPERIMENTAL PROCEDURES

2.1 Material

The material used in this study was received as commercial rods of Ti6Al4V alloy for surgical spinal implant application. Spinal implant rod is one of the original implants used in the spine. Rods are used, along with implant hooks and screws, to immobilize involved spinal levels, and to contour the spine into correct alignment. The spinal implants are shown in Figure 1. The rods are strong, yet have some flexibility so that the surgeon can shape the rod to match the contours of the patient's spine. The dimension of rods is 6 mm (0.236 inches) in diameter and length (11.811 inches) of 30 cm.

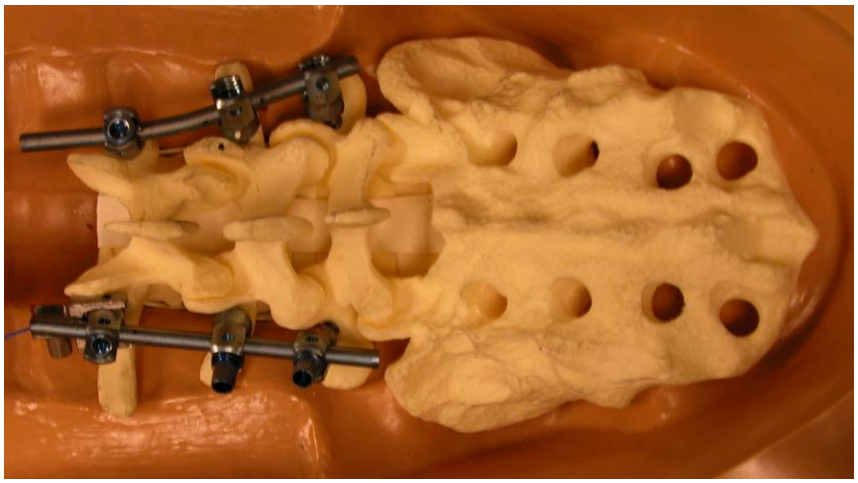

Figure 1: Image of spinal implants

The composition of commercial spinal implant rod are examined using energy dispersive X-ray spectroscopy (EDS) which is an analytical technique used for the elemental analysis or chemical characterization of a sample. The Figure 2 shows the EDS spectrum of spinal implant rod.

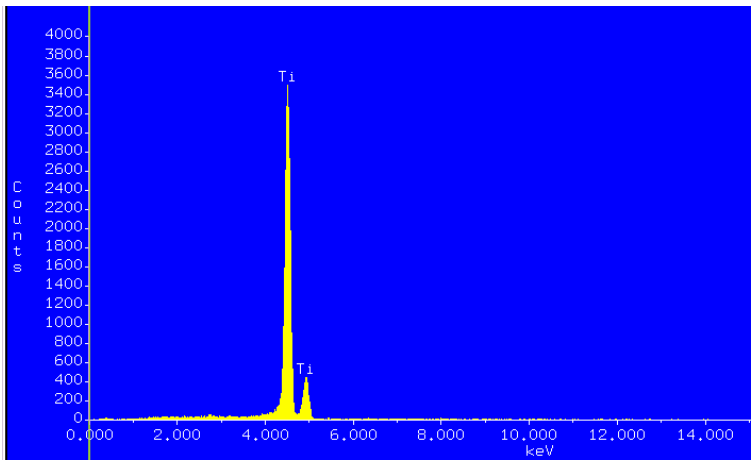

Figure 2: EDS spectrum of the commercial spinal implant rod

The samples were cleaned in an ultrasound bath before coated with DLC film to avoid crack initiation and propagation in the bending stress. DLC coating were grown from a methane/argon mixture by plasma enhanced chemical vapor deposition for 20~30minutes and thickness is 1~1.5μm. 10 uncoated and 6 DLC coated rod with similar dimensions were subjected to fatigue tests.

2.2 Experimental procedures

The schematic view of four-point-bend testing fixture is shown in Figure 3. The fixture consisted of two bottom rollers and two upper rollers with supports. The distance between the centers of the two bottom rollers was 10cm. The rod was placed on the bottom roller. The distance between the centers of the upper rollers was about 4cm. V-notches were fabricated into the top and bottom rollers. The test setup before performing the static and fatigue bending test is shown in Figure 4. An MTS testing machine of 250 KN capacity in the Civil Engineering Department of Southern Illinois University at Edwardsville (SIUE) was used for bending and fatigue testing. MTS 793 Station Manager Software was used to manually control the system and the test parameters. The static and fatigue bending tests were performed according to ASTM F2193-02 standards [8]. Low-cycle fatigue experiment was conducted in fatigue bending test. No attempt was made to monitor crack initiation or propagation in these experiments. The initial fatigue maximum moment level that is 75% of bending ultimate moment determined with the static bending test. Observations of Light Microscopy (LM) and Scanning Electron Microscopy (SEM) have been performed to study the external surfaces of specimens at different stages of fatigue life and the features of fracture surfaces.

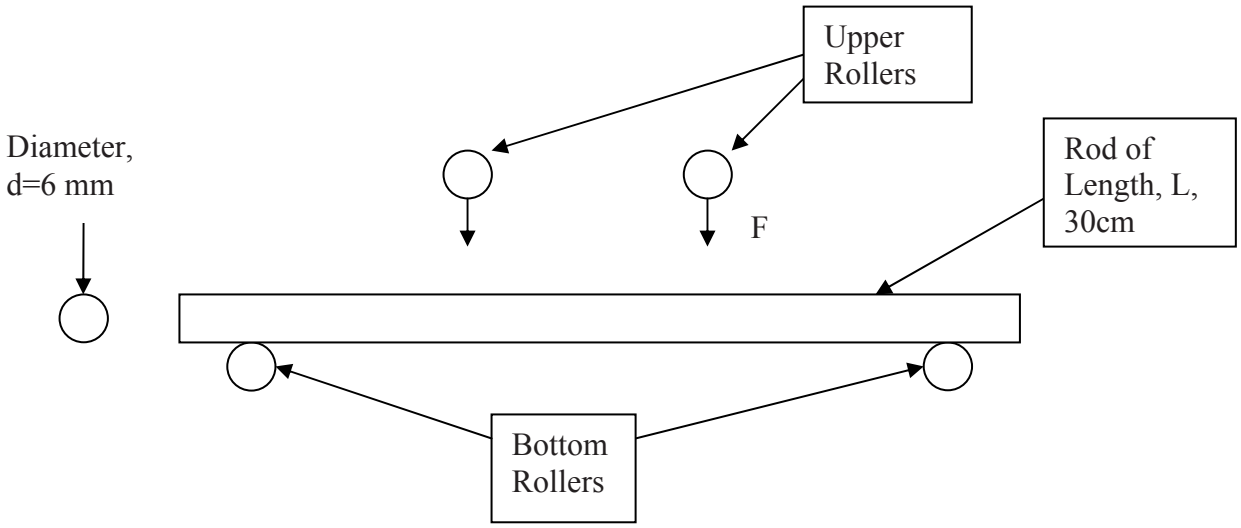

Figure 3: schematic representation of the test setup

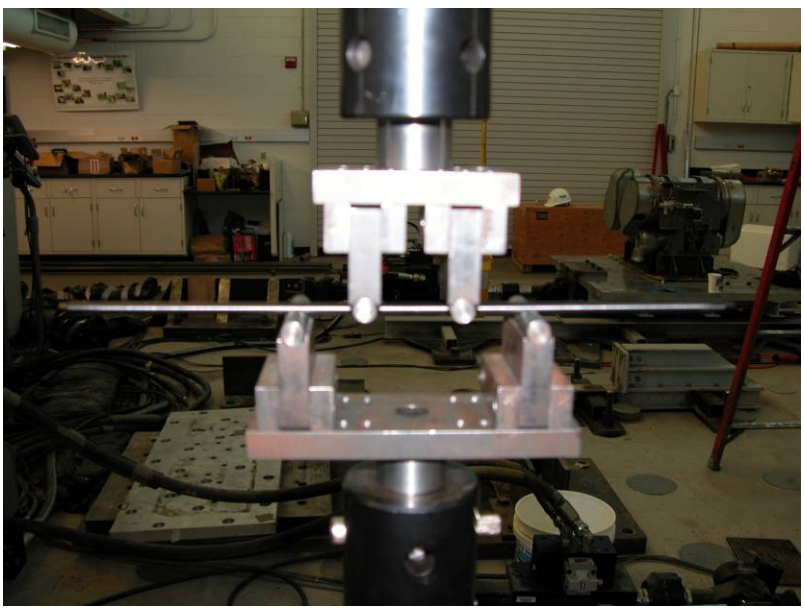

Figure 4: test setup for static and fatigue bending test

The formulas for stresses and strains according to the ASTM Standard D790 [9] were obtained for square rods and were modified for circular rods. These formulas were then defined and used in the software by changing

the Test Configuration. According to the ASTM Standard D790, the formula for calculating the stress and strain for a 4-point bending test of a rectangular rod with width 'L' is given as

STRESS, $$\sigma = \frac{(3 * F * a)}{(bL^2)} \quad (1)$$

Where σ = Stress
F = Load acting on the Rod, N
a = Support Span – Loading Span, m
b = Width of the rod cross section
L = Length of the rod cross section

Equation 1 was modified for modified for circular rod. From Equation 1, we have

STRESS, $$\sigma = \frac{3(F * a)}{\pi r^3} \quad (2)$$

Formula used in the software:

STRESS, $$\sigma = \frac{24(F * a)}{(\pi d^3)} = \frac{3(F * a)}{\pi r^3} \quad (3)$$

Where σ = Stress
F = Load acting on the Rod, N
a = Support Span – Loading Span, m
d = Diameter of the rod, m

STRAIN $$\delta = \frac{(12 * Extension * Diameter)}{3(Span - Loading \quad Span)} \quad (4)$$

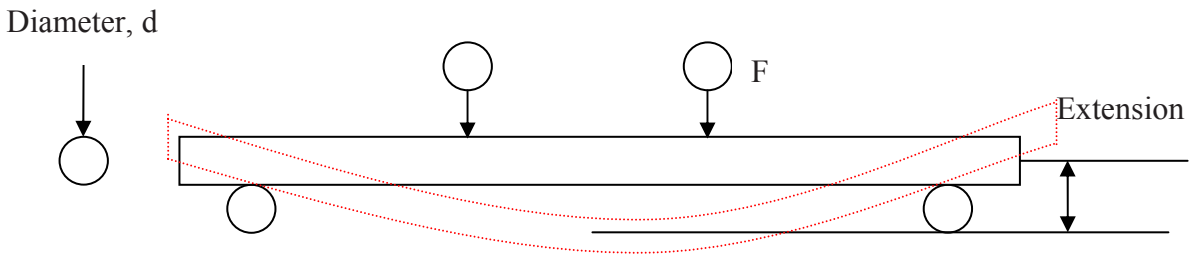

Figure 5: schematic representation of the extension

3. RESULTS AND DISCUSSION

The static bending test results are show in Figure 6. The DLC coating spinal implant rods have better bending structural stiffness, bending yield moment, and bending ultimate moment.

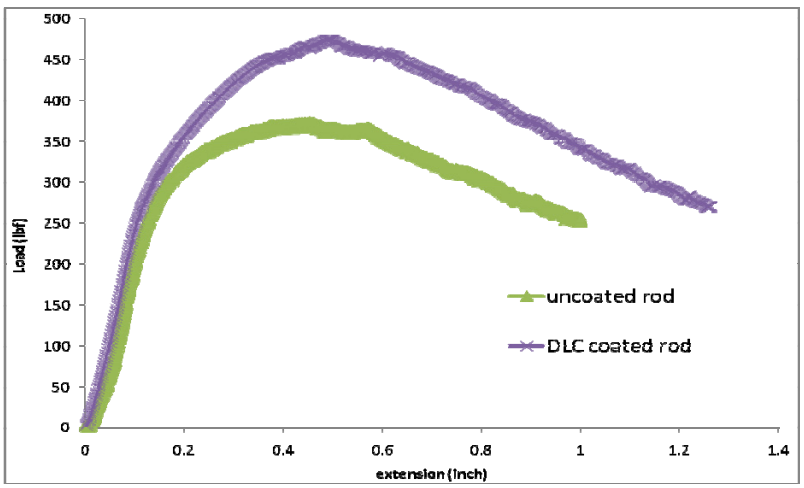

Figure 6: Static bending test of uncoated and DLC coated rods

The uncoated and DLC coated specimens were used to conduct the low cycle fatigue experiments in a laboratory air environment at room temperature. No attempt was made to monitor crack initiation or propagation in these experiments. Tests were conducted under displacement control and frequency of cycle loading is 2Hz.

Table 1: low cycle fatigue testing data

Specimen	stress range, $\Delta\sigma=\sigma max-\sigma min$, Map	Number of cycles to failure, N_f
Uncoated rod 1	549	6794
Uncoated rod 2	567	6897
Uncoated rod 3	552	6792
DLC coated rod 1	575	7634
DLC coated rod 2	586	7622
DLC coated rod 3	603	7495

The data obtained from the low cycle fatigue tests is shown in table 1. The differences between DLC coated and un-coated rods are evident. The average number of cycles to failure of un-coated rods is 6827 and the average number of cycles to failure of DLC-coated rods is 7583. Depending on the 75% of the bending ultimate moment applied to the specimens, the fatigue life can be increase by 11%.

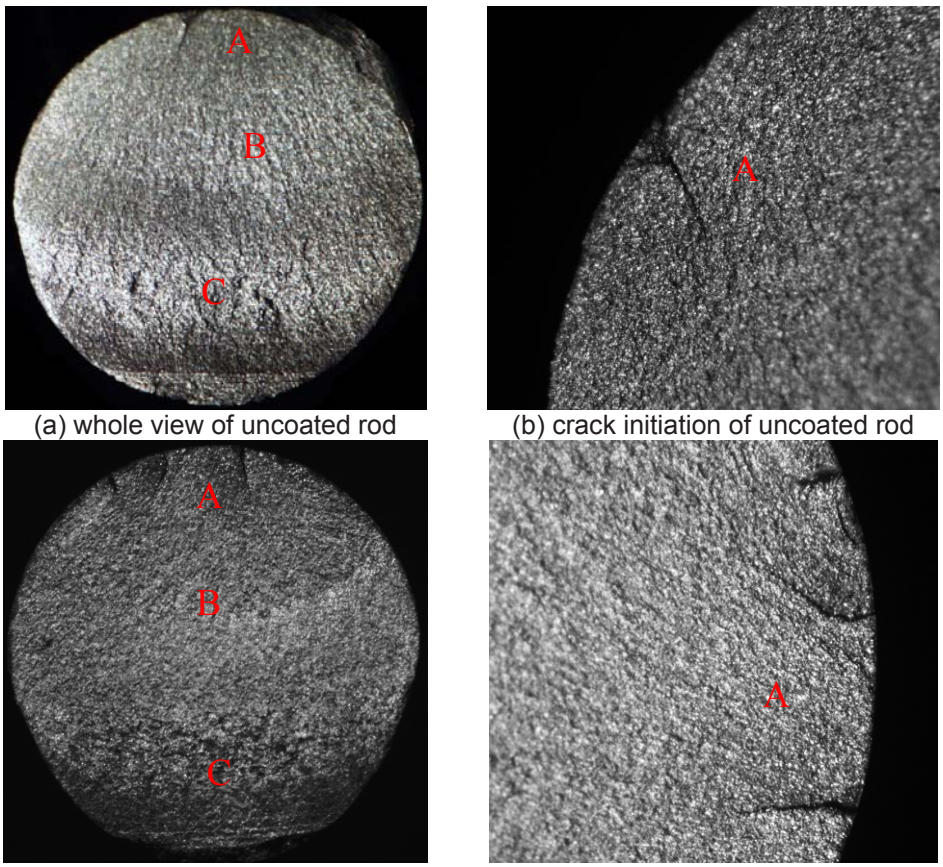

(a) whole view of uncoated rod (b) crack initiation of uncoated rod

(c) whole view of DLC coated rod (d) crack initiation of DLC coated rod

Figure 7: LM images of fracture surfaces

Figure 7 shows the whole view fracture surface of the un-coated and DLC coated Ti6AL4V spinal implant rod tested at 75% of the bending ultimate moment. In this place, a transition to common fatigue mechanism is observed in Figure 7 (a) and (c). The whole fatigue fracture surface consists of three regions: fatigue crack initiation (A), Crack propagation (B), and final fast fracture areas. Figure 7 (b) and (d) show the initiation of one or more micro-crack due to cyclic plastic deformation followed by crystallographic propagation extending from two to five grains about the region.

Representative SEM images of uncoated and DLC coated samples at whole fatigue fracture surface stage of the low cycle fatigue are shown in Figure 8. Fracture surfaces of the coated and uncoated samples have similar features: cracks start form the external surface defect and grow towards the inner part with branching and without stopping. Therefore, DLC coating do not modify the morphology of fracture surfaces.

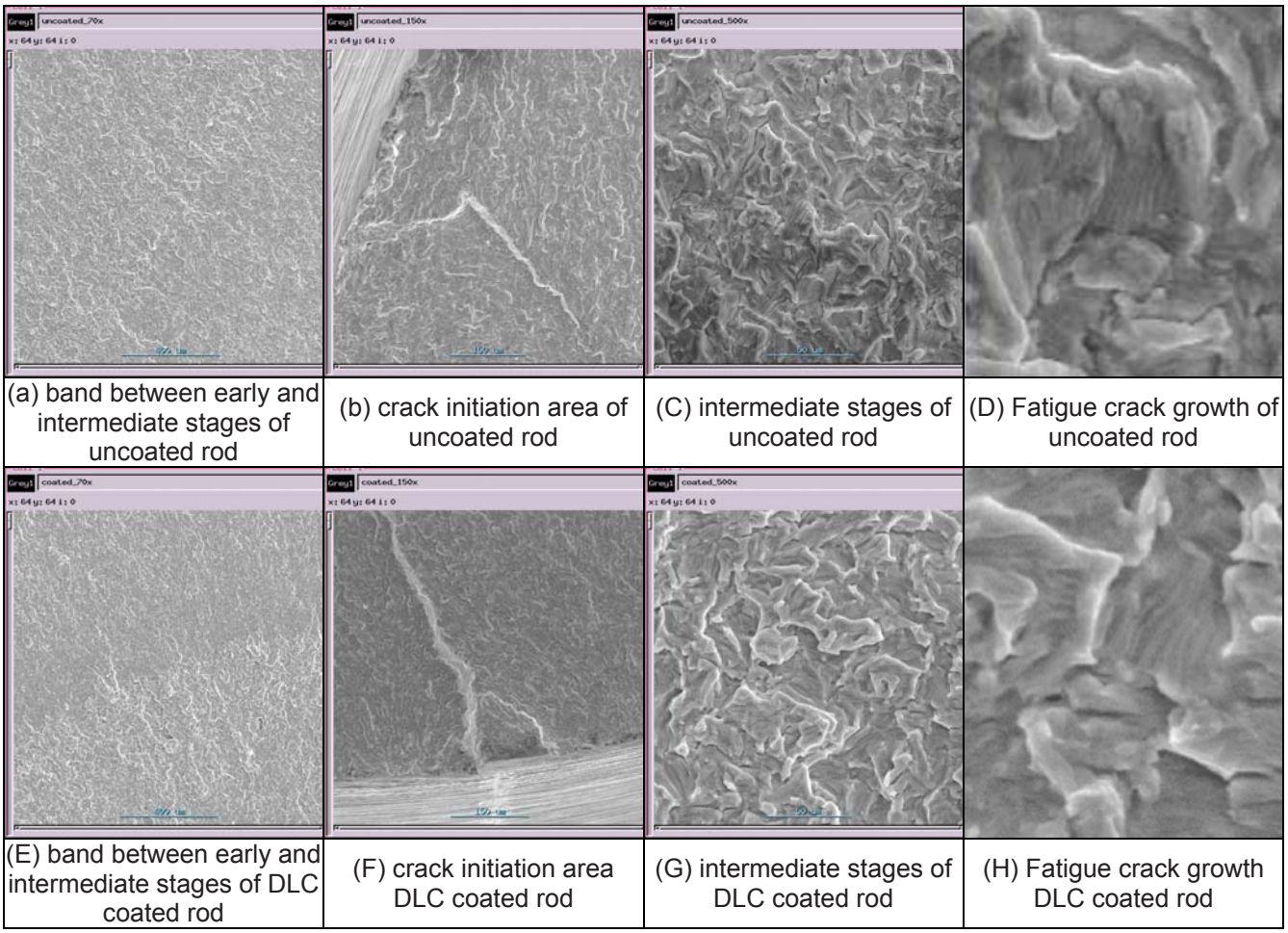

(a) band between early and intermediate stages of uncoated rod	(b) crack initiation area of uncoated rod	(C) intermediate stages of uncoated rod	(D) Fatigue crack growth of uncoated rod
(E) band between early and intermediate stages of DLC coated rod	(F) crack initiation area DLC coated rod	(G) intermediate stages of DLC coated rod	(H) Fatigue crack growth DLC coated rod

Figure 6: SEM images of fracture surfaces

SEM observations on the fracture surfaces show the same features in specimens with and without DLC coating thus crack propagation takes place in the same way. Since crack propagation is not affected by DLC coating, the improvement of fatigue behavior is associated to delayed crack initiation. To explain the reason for why coating slow down crack initiation, two reasons have been considered: (1) the quality of the surface of coated samples. In other words, it has a good adhesion of the DLC coating with the rods (2) the external surface defects sealed by DLC coating.

4. CONCLISION

With the deposition of the DLC coating, the bending structural stiffness, bending yield moment, and bending ultimate moment of Ti6AL4V spinal implant rods are improved. In addition, the fatigue life of Ti6AL4V spinal implant rod could be increased by 11%, depending on the 75% of the bending ultimate moment applied to the rods. The fatigue-resistance improvement was mainly due to the reduction of the surface roughness and the good adhesion of the DLC coating with the rods.

Acknowledgements

The Authors are grateful to Dr. Albert C. J. Luo, Southern Illinois University at Edwardsville, for the assistance in fatigue tests.

Reference

[1] Zhao, D.C.; Ren, N.; Ma, Z.J.; Xiao, G.J.; Wu, S.H., “Study on the mechanic properties of DLC films on different metal substrates” Key Engineering Materials, v 373-374, p 117-121, 2008
[2] Morgenstern, Roman; Kieling, Wolfgang; Reichstein, Simon, “Reduced friction losses and wear by DLC coating of piston pins” Proceedings of the Spring Technical Conference of the ASME Internal Combustion Engine Division, p 289-297, 2008, Proceedings of the 2008 Spring Technical Conference of the ASME Internal Combustion Engine Division
[3] Grill, Alfred, “Diamond-like carbon: State of the art” Diamond and Related Materials, v 8, n 2, p 428-434, 1999
[4] Linder, Stefan Pinkowski, Wolfhard; Aepfelbacher, Martin, “Adhesion, cytoskeletal architecture and activation status of primary human macrophages on a diamond-like carbon coated surface” Biomaterials, v 23, n 3, p 767-773, 2002
[5] Liu, C.; Zhao, Q.; Liu, Y.; Wang, S.; Abel, E.W., “Reduction of bacterial adhesion on modified DLC coatings” Colloids and Surfaces B: Biointerfaces, v 61, n 2, p 182-187, Febrary 15, 2008
[6] Nam, N.D. Lee, S.H.; Kim, J.G.; Yi, J.W.; Lee, K.R., “Effect of stress on the passivation of Si-DLC coating as stent materials in simulated body environment” Diamond and Related Materials, v 18, n 9, p 1145-1151, September 2009
[7] Hauert, R. “A review of modified DLC coatings for biological applications” Diamond and Related Materials, v 12, n 3-7, p 583-589, March/July 2003
[8] ASTM Standard F2193-02, 2007, Standard STest Method for Thermal Diffusivity by the Flash Method, ASTM International, West Conshohocken, PA, 2003, DOI: 10.1520/E1461-07, www.astm.org.
[9] ASTM Standard D790, 2007, Standard Test Method for Thermal Diffusivity by the Flash Method, ASTM International, West Conshohocken, PA, 2003, DOI: 10.1520/E1461-07, www.astm.org.

Proceedings of the SEM Annual Conference
June 7-10, 2010 Indianapolis, Indiana USA

Modeling Creep and Fatigue Properties of Bone at Nanoscale Level

Mr. Fang Yuan, Ph. D. Candidate, Department of Materials Science and Engineering, Northwestern University

Address: 2220, Campus Drive, Evanston IL 60208
Email: FangYuan2008@u.northwestern.edu

Ms. Anjali Singhal, Ph. D. Candidate, Department of Materials Science and Engineering, Northwestern University

Ms. Alix C. Deymier-Black, Ph. D. Candidate, Department of Materials Science and Engineering, Northwestern University

Dr. David C. Dunand, James N. and Margie M. Krebs Professor of Materials Science and Engineering, Department of Materials Science and Engineering, Northwestern University

Dr. L. Catherine Brinson, Jerome B. Cohen Professor of Mechanical Engineering, Department of Mechanical Engineering, Northwestern University

Extended Abstract:

Bones are important natural materials which compose the skeleton of the animals. The basic and fundamental function of bone is mechanical – to provide a frame to keep the body supported and moved, to protect internal organs, while they also serve with other important biological functions, such as blood production, mineral storage, etc. Such multifunctionality makes bone with a very complex hierarchical structure, while the millions of years' evolution makes bone have outstanding characteristics, in mechanical aspect of view, bone has a high strength and high toughness while keeping lightweight. These natural exceptional mechanical properties of bone are much better than that of the conventional artificial materials are inspiring the materials engineering community to design the novel biomimetic materials. However, on the other hand, as a natural material which lies in the body of organism, numbers of diseases infects bones and severely weakens their instinct properties, therefore, to cure the patients and recover basic functions of bone, many researches are needed to find the biological substitute of bone.

To successfully mimic the exceptional mechanical properties of bone, both as the alternative materials to restore the original function of bone and as the novel materials to fulfill outstanding performance, the understanding of the relationship between complex hierarchical structure and excellent mechanical properties of bones is necessary and extraordinarily important. However, the structure-property relationship of bone is far away from unraveled, the

T. Proulx (ed.), *Time Dependent Constitutive Behavior and Fracture/Failure Processes, Volume 3*, Conference Proceedings of the Society for Experimental Mechanics Series 15, DOI 10.1007/978-1-4419-9794-4_54, © The Society for Experimental Mechanics, Inc. 2011

fundamental part of this relationship – in the collagen fibril level (which is in the order of hundreds of nanometers or smaller) – is still unclear.

To understand the hierarchical structure and time-dependent property (such as creep and fatigue) relationships at the nanoscale level of bone, we choose to use finite element simulation technique and start from a simple composite model of bone: the weak collagen phase as the matrix filled with hard plate-like mineral phase as the reinforcement, with the consideration of the 67 nm period of the collagen assembly and the overlapping distribution of mineral plate in the axial direction as the basic geometry of bone in the collagen fibril level. This model can predict the elastic properties of both phases with a nice accuracy. Based on this basic model, we introduce the viscoelastic properties of collagen phase into the model to simulate the time-dependent properties of both phases. Since synchrotron X-ray diffraction experiments show that during the creep test, the collagen phase keeps loading while the mineral phase keeps unloading, indicating the gradual load transfer between two phases must be considered, therefore, we introduce the debonding mechanism on the collagen-mineral interface: The mineral phase and the collagen phase have different loading trends during the creep test, therefore debonding must appear on their interface to decrease the strain in the mineral phase. We create a friction-like delamination mechanism to represent the bonding-debonding-rebonding behavior of the mineral-collagen interface at nanoscale: this friction assumption is such that when the shear force on the interface is small, no sliding between the phases is allowed due to the static friction; however, when the shear force is above a critical value, sliding is initiated. Furthermore, when the shear force returns to a low value, the sliding stops and the static friction condition is restored. These three steps represent the bonding-debonding- rebonding behaviors of the collagen-HAP interface. All the results show the strain-time curves of two phases split more compared with no debonding considered, however, the strain in the mineral phase still increases as time increases until it reaches a plateau.

To explain the unusual load transfer between collagen and mineral phases, we try three different approaches:

(1) Modifying the mineral phase: a) To facilitate the debonding process and avoid artificial stress concentrators, the mineral plates are modified with smooth boundaries. b) The mineral plates are not perfectly parallel with each other, as shown in the experimental results. During the creep test, the alignment of mineral plates becomes more and more diverse, therefore, the misorientation of mineral plates is introduced into the model. The simulation results show the degree of misorientation changes the magnitude of strains in both phases, however, it is not enough to reverse the loading trend in the mineral phase.

(2) Modifying the collagen phase: a) The collagen phase is the phase with viscoelasticity which is the source of the creep behaviors. We performs a parameter research for the influence of basic viscoelastic properties on the creep behaviors of both phases. The simulation results show some specific combinations of relaxation time and debonding initiation time can influence the creep behavior in the mineral phase. b) Instead of a continuous matrix, the collagen phase is composed of lots of discrete collagen molecules. We modify the previous models with reasonable dimension parameters of collagen molecules and divide the collagen phase into several parts. To simulate the interaction between the collagen-collagen molecules, a set of springs are put between the corresponding nodes on the neighboring collagen molecules. The stiffness of springs is carefully chosen to represent a good estimate for weak bonding. The spring assumption simulates the splitting of collagen molecules as they are pulled apart by the sliding of the mineral plates and the increasing resistance as the split clearance increases.

(3) Modifying the collagen-mineral interphase contact: Based on the fact that in bone, the collagen phase is composed of discrete collagen molecules, which are about 300 nm long and 1.5 nm in diameter, and the mineral plates prefer to avoid the sharp corners, the geometry is further modified as follows. Since the length of a single collagen molecule (300 nm) in the axial direction is significantly longer than the assembly period (67 nm) and the length of mineral plate (less than 100 nm), it is improbable that the collagen fibers will terminate that the exact top or bottom of a mineral plate. Instead, small pores at the ends of the mineral plates are introduced. The release of the contact force at the top and bottom ends of mineral plates would significantly help the unloading process on the mineral plates.

By using the finite element method to simulate the response of these models, we discuss the importance of each factor on creep behaviors and compare the results with synchrotron x-ray diffraction experimental data which provide the deformation information of both the mineral plates and the connecting collagen matrix. Our simulation results match well with the experimental data qualitatively.

To further verify the assumptions in the simulation and possible explanation of creep behaviors, we also compare other time-dependent behaviors of bone at collagen fibril level between simulation results and experimental data, such as fatigue and load-unload creep. All of them confirm the underlying mechanisms of load transfer between two phases mentioned above in the creep study.

Proceedings of the SEM Annual Conference
June 7-10, 2010 Indianapolis, Indiana USA

High-energy X-ray Diffraction Measurement of Bone Deformation During Fatigue

Anjali Singhal[1], Jonathan D. Almer[2], Dean R. Haeffner[2], and David C. Dunand[1]
[1]Dept of Materials Science and Engineering, Northwestern University, Evanston IL 60208
[2] Advanced Photon Source, Argonne National Laboratory, Argonne IL 60439
Corresponding author: E-mail: a-singhal@northwestern.edu; Telephone: 1-773-290-9094

EXTENDED ABSTRACT

Hard mineralized tissues such as bone are the primary load bearing structures in the body. Its basic building block is an organic matrix – mainly type I collagen, a mineral phase – calcium hydroxyapatite and water. These three components interact to form a very complex structure hierarchically organized from the nano- to the macro-scale [1], which is capable of supporting bodily loads and resisting fracture due to its high strength and toughness. However, despite its high resistance, bone fractures occur due to both impact loads and repetitive or sustained loads exerted over larger periods of time. Cyclic loads are the most direct analog to periodic stresses and strains varying in both intensity and type seen in physiological activities like walking and running [2]. It is thus clinically important to gain a deeper understanding of the mechanisms occurring within this complicated structural hierarchy of bone to ultimately predict and prevent such failures thus leading to improved medical treatments. Fatigue damage has been shown to be characterized by cyclic property degradation [3, 4], caused by accumulation and propagation of microcracks [5, 6]. The formation of microcracks is loading mode dependent [7, 8], which in turn affects the degradation of properties during cyclic loading. The macroscopic behavior has been fairly well understood from the vast number of studies done previously. Still lacking is an understanding of the interaction between the different components of the building block and the subsequent hierarchical levels of bone during such loading, which results in the observed macroscopic behavior. The high-energy X-ray diffraction technique used in this work makes it possible to obtain through-thickness (~ 5 mm in this case) crystal lattice information from the bulk of the sample, compared to other high resolution techniques like nanoindentation which sample only surface volumes up to depths of about 1000 nm [9], or other imaging techniques like scanning and transmission electron microscopy and atomic force microscopy [10], which are good for obtaining surface structural information. With its *in situ* testing capability [11], this high-energy X-ray diffraction technique has recently found applications in probing individual components of bone [12] and dentin [13] materials. The aforementioned diffraction technique is used in the current work to determine the strains in the HAP and collagen phases of bone during cyclic loading in compression at body temperature, and study their evolution with cycles.

Fresh bovine femurs were obtained from Aurora Packing company, Inc., North Aurora, IL 60452 after about 5 hours of the death of the animal. The marrow and the attached ligaments were removed using scalpels. Samples were cut out of the cortical bone, using a low-speed diamond wafering saw (Buehler Isomet-1000), with dimensions of 5 (±0.014) x 4 (±0.009) x 3 (±0.012) mm^3. All cutting operations were done under constant irrigation with DI water to prevent the bone from drying. All the samples used in this experiment were taken from the anterio-medial or the posterio-medial sides of the femur. The samples were then stored in PBS and frozen at -20^oC until the time of the experiment. All the experiments were done at the Advanced Photon Source, Argonne National Laboratory at beamline 1-ID C. The sample was enclosed in a hydration rig made with vinyl tubing, through which Phosphate Buffered Saline was circulated, and maintained at a temperature of 37^oC. A 65 keV X-ray beam was used for the experiment, having a cross-section of 30x35 μm^2. A MAR 165 detector (2048 x 2048 pixel grid and 80 x 80 μm^2 pixel size) was used to capture the wide-angle diffraction (WAXS) rings. A Bruker CCD

T. Proulx (ed.), *Time Dependent Constitutive Behavior and Fracture/Failure Processes, Volume 3*, Conference Proceedings of the Society for Experimental Mechanics Series 15, DOI 10.1007/978-1-4419-9794-4_55, © The Society for Experimental Mechanics, Inc. 2011

detector (2048 x 2048 pixel grid and 80 x 80 μm^2 pixel size) recorded the small-angle diffraction (SAXS) rings. The x-ray exposure times used were 15 seconds for the WAXS and 5 seconds for the SAXS. The regular arrangement of atoms in the HAP lattice diffracts according to Bragg's law and produces wide angle diffraction rings [12]. The periodic arrangement of HAP crystals (~ 67 nm) in the organic (collagen) matrix produces periodic density differences [14], which diffract at much smaller angles, producing small-angle diffraction patterns. The WAXS patterns are analyzed using MATLAB^{TM} codes, to calculate the elastic lattice strains in HAP, whereas the SAXS patterns are analyzed to calculate strains due the cooperative deformation of the HAP and collagen molecules, known as fibrillar strains. These calculations are discussed in great detail in Refs. [13, 14]. Cyclic loading tests were done in uniaxial compression, investigating the effect of different parameters. Six different samples were subjected to different mean compressive stresses of -55 or -85 MPa with a constant stress amplitude of -25 MPa, each done at cycle frequencies of 0.5, 2 or 5 Hz. Next, two different samples were subject to a constant mean stress of -60 MPa with amplitudes of 35 or 45 MPa, tested at a rate of 2 Hz. All the tests were carried out to a pre-determined number of cycles. The cyclic loading was stopped after a pre-determined set of cycles, and the sample was monotonically loaded between the minimum and the maximum stress in the cycle, taking WAXS and SAXS measurements at every stress. All the experiments were done at body temperature (37^{o}C).

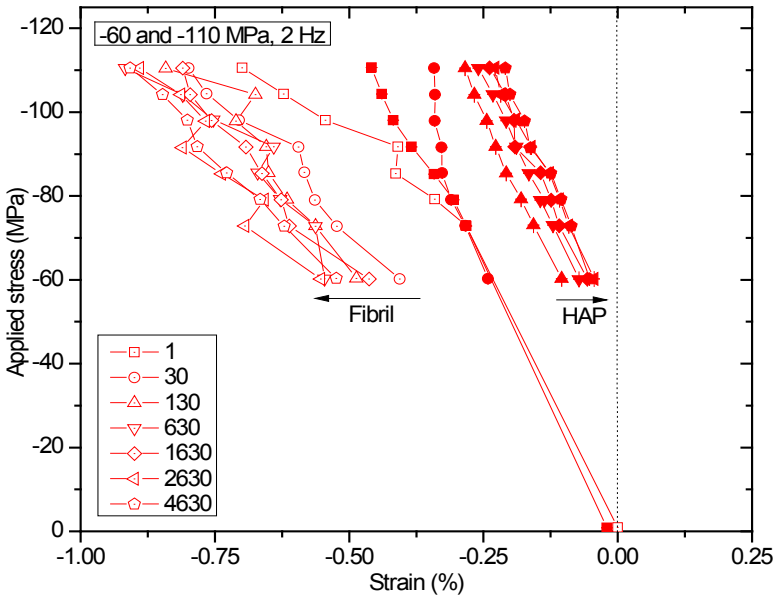

Figure 1

Shown in Figure 1 is a combined plot of longitudinal strains in HAP and fibril at different applied stresses, for the sample tested between stresses of -60 and -110 MPa, at a loading frequency of 2 Hz. This plot is an example of all the fatigue tests done in this work. The data points on every line plot have been taken after a pre-determined number of loading cycles, as indicated in the legend on the left. It can be seen that partitioning of load takes place between HAP and fibril during the first loading, with the fibrils taking up larger loads compared to HAP. After this initial partitioning, the lines begin to translate along the strain axis in opposite directions, as indicated by the arrows. Such observations have also been made for macroscopic strains in earlier studies [15, 16]. Hypothesis for this translation is that the mean stress present during the cyclic loading causes the the HAP/matrix interface to damage, resulting in a decrease of HAP strains.

The apparent modulus of HAP is calculated as the ratio of the applied stress to the HAP elastic strains (E_{app}^{HAP}). The E_{app}^{HAP} of samples in all these tests, in general, show a jump in their values after the first set of loading cycles, after which they tend to either reduce or remain constant. Comparison of E_{app}^{HAP} between samples tested at 2 and 5 Hz shows that the samples tested at 5 Hz exhibit fewer variations than those at 2 Hz. Comparison of the residual strains suggests that there is a greater decrease in the residual strains of the samples tested at 2 Hz compared to 5 Hz. Initial HAP strains have been previously reported in bone [14], and exhibit a general tendency

to reduce on unloading to zero stress. This relaxation of the pre-strains occurs probably due to the sliding of collagen molecules. The HAP strains plotted at a single load over multiple cycles tends to decrease, which is greater at 2 Hz compared to 5 Hz. Loading at a higher rate between the same stress-range would result in a smaller dwell time at each load. The deformation behavior of collagen is loading rate dependent due to its viscoelastic nature, and is found to undergo a ductile to brittle transition on increasing the loading rates [17]. Also, loading at a higher rate would reduce the response time allowed for collagen sliding to take place, thus reducing the rate at which HAP gets unloaded. These observations suggest that the fatigue behavior is indeed dependent on the loading frequency.

Comparing the samples tested at different stress ranges, the E_{app}^{HAP} of the samples tested between -60 and -110 MPa at 2 and 5 Hz show a greater change after the first set of load cycles compared to those tested between -30 and -80 MPa at the same loading rates. This would suggest that during the first few cycles, greater deformation occurs in samples being loaded to higher stresses, also resulting in plastic deformation. Beyond the first set of cycles, no specific trend can be observed between the two ranges at both the frequencies. The mean stresses of the two stress ranges are -55 and -85 MPa respectively. One would expect that cycling about the higher mean stress would result in greater damage accumulation judging from the fact that there would be greater creep at a higher mean stress. However, no such effect of damage accumulation is seen in the samples beyond the first 30 cycles. The HAP residual strain decreases with cycles for all the samples tested, but no specific dependence on mean stress is found.

The samples tested at varying stress amplitudes with a constant mean stress, on the other hand, do exhibit differences in their behaviors. The E_{app}^{HAP} clearly increases with cycles, more for the sample tested at a higher amplitude (35% vs 24%). This increase in E_{app}^{HAP} indicates that the load carried by the HAP crystals decreases continually with cycles due to the accumulation of damage at the HAP-collagen interface, causing debonding of the collagen from HAP. The residual strain of HAP in these samples also exhibits a linear decrease, which is greater for the sample tested at a lower amplitude (18% vs 13%). The deformation here is a combination of two factors – the first is that at a lower amplitude, with the same loading rate and mean stress as a higher amplitude, the dwell time at every load is higher, allowing more time for collagen sliding to take place. The second factor is that at a higher loading amplitude the sample is loaded to higher (plastic range) stresses, which would also cause sliding and plastic deformation to take place. Comparison of E_{app}^{HAP} between the above two samples suggests that more damage accumulation occurs at the higher amplitude, whereas the residual strain suggests that there is greater sliding hence relaxation of pre-strains at the lower amplitude.

In conclusion, these experiments showed that fatigue deformation in bone is essentially a fatigue-creep mechanism, which takes place by the sliding (and debonding) of the collagen molecules at the HAP-collagen interface. The residual strains in the HAP decreased with cycling due to the collagen sliding which causes relaxation of strains at the HAP-collagen interface. The deformation was found to be dependent on the frequency and stress amplitude.

REFERENCES

1. Weiner, S. and H.D. Wagner, *THE MATERIAL BONE: Structure-Mechanical Function Relations.* Annual Reviews of Materials Science, 1998. **28**(1): p. 28.
2. Evans, F.G. and M. Lebow, *Regional Differences in some of the Physical Properties of the Human Femur.* Journal of applied physiology, 1951. **3**(9).
3. Pattin, C.A., W.E. Caler, and D.R. Carter, *Cyclic mechanical property degradation during fatigue loading of cortical bone.* Journal of Biomechanics, 1996. **29**(1): p. 69-79.
4. Boyce, T.M., et al., *Damage Type and Strain Mode Associations in Human Compact Bone Bending Fatigue.* The Journal of Bone and Joint Surgery, 1998. **16**: p. 322-329.
5. Akkus, O. and C.M. Rimnac, *Cortical bone tissue resists fatigue fracture by deceleration and arrest of microcrack growth.* Journal of Biomechanics, 2001. **34**: p. 757-764.
6. Sobelman, O.S., et al., *Do microcracks decrease or increase fatigue resistance in cortical bone?* Journal of Biomechanics, 2004. **37**: p. 1295-1303.

7. George, W.T. and D. Vashishth, *Damage mechanisms and failure modes of cortical bone under components of physiological loading.* Journal of Orthopaedic Research, 2005. **23**: p. 1047-1053.
8. Carter, D.R. and W.C. Hayes, *Compact Bone Fatigue Damage.* Clinical Orthopaedics and Related Research 1977(127): p. 265-274.
9. Hengsberger, S., A. Kulik, and P. Zysset, *Nanoindentation Discriminates the Elastic Properties of Individual Human Bone Lamellae Under Dry and Physiological Conditions.* Bone, 2002. **30**(1): p. 178-184.
10. Yang, L., et al., *Micromechanical bending of single collagen fibrils using atomic force microscopy.* Journal of Biomedical Materials Research. Part A, 2007. **82**(1).
11. Haeffner, D.R., J.D. Almer, and U. Lienert, *The use of high energy X-rays from the Advanced Photon Source to study stresses in materials.* Materials Science and Engineering A, 2005. **399**.
12. Almer, J.D. and S.R. Stock, *Internal Strains and stresses measured in cortical bone via high-energy X-radiation.* Journal of Structrual Biology, 2005. **152**.
13. Deymier, A.C., et al., *Synchrotron X-ray Diffraction Study of Load Partitioning during Elastic Deformation of Bovine Dentin.* Accepted manuscript: Acta Biomaterialia, 2009.
14. Almer, J.D. and S.R. Stock, *Micromechanical responses of mineral and collagen phases in bone.* Journal of Structrual Biology, 2007. **157**.
15. Winwood, K., et al., *Strain patterns during tensile, compressive, and shear fatigue of human cortical bone and implications for bone biomechanics.* Journal of Biomedical Materials Research Part A, 2006. **79**.
16. Zioupos, P., X.T. Wong, and J.D. Currey, *Experimental and Theoretical Quantification of the Development of Damage in Fatigue Tests of Bone and Antler.* Journal of Biomechanics, 1996. **29**(8): p. 989-1002.
17. Kulin, R.M., F. Jiang, and K.S. Vecchio, *Aging and Loading Rate Effects on the Mechanical Behavior of Equine Bone.* Journal of Materials, 2008(June).

Proceedings of the SEM Annual Conference
June 7-10, 2010 Indianapolis, Indiana USA

Investigation of cyclic impact fatigue, grain-to-grain interaction, and residual stress in zirconia dental materials

Hrishikesh Bale[1,3], Nobumichi Tamura[2], Jay C. Hanan[1,*]

[1]Mechanical and Aerospace Engineering, Oklahoma State University, Tulsa, OK.
[2]Advanced Light Source. Berkeley, CA.
[3]Material Science and Engineering, University of California, Berkeley, CA.

ABSTRACT

Zirconia is widely being used as a core in all-ceramic dental restorations to provide the structural strength. In-spite of better mechanical properties, catastrophic failures of the dental crowns are frequently reported. During the service life, the dental restoration undergoes continuous mouth motion impact fatigue. An *in-situ* residual stress measurement technique using micro X-ray diffraction has been developed to understand the role of impact fatigue on damage initiation and catastrophic failure in dental restorations. Through experimental simulations of the mouth-motion impact fatigue, combined with the *in-situ* residual stress measurement capability, the various damage initiation and failure mechanisms in zirconia dental crowns were investigated. The experimental procedure and initial results of the investigation on monolithic zirconia are presented. The understanding acquired through this initial study will be extended in looking at furthermore complex layered composite dental structures. The study provides a context to address the issue of the unpredictable catastrophic failures in dental restoration.

Introduction

Zirconia core dental crowns possess better mechanical strength and damage tolerance compared to any other ceramic layered restoration system currently used. The dental crowns undergo prolonged impact fatigue in service, at impact loads much below the failure strength of the constituent materials.[1-3] The crowns are manufactured by firing a porcelain veneer on a pre-sintered and shaped zirconia core. The core materials are extremely fine grained (0.1 to 0.3 μm). Post-firing, the restorations consist of localized zones with high residual stresses, which mainly occur due to the mismatch in the coefficient of thermal expansion of the two materials. Residual stresses, especially the highly localized tensile stresses, are considered detrimental to the life of the crowns. They act as crack initiators and also accelerate crack propagation.

In-spite of the higher strength and comparatively better performance of the zirconia core crown systems, a significant number of failures have been reported, both clinically and from laboratory testing. The failures are sudden and a definitive prediction is difficult. Some earlier experimental observations using high resolution X-ray micro-diffraction have shown that there exists significant residual stresses in between neighboring grains. These extremely localized stresses are speculated to behave as crack initiators leading to catastrophic failures.[4] In order to study the stresses on a sub-micron scale, synchrotron based high resolution polychromatic diffraction (Laue diffraction) was carried out at beam-line 12.3.2 at the Advanced Light Source. Line and area scans with high spatial resolution were used to analyze local grain-to-grain interactions. Following Laue diffraction, monochromatic macro-beam diffraction averaging several grains was conducted. Analysis of both data-sets reveal details of the local and continuum residual stress states. Furthermore, the grain-to-grain interactions have been observed after load cycles simulating the *in-vivo* environment.

* Corresponding Author - Jay Hanan, Oklahoma State University, 700 N. Greenwood Ave., Tulsa, OK 74106 phone number: 918-594-8238; e-mail address: Jay.Hanan@okstate.edu

T. Proulx (ed.), *Time Dependent Constitutive Behavior and Fracture/Failure Processes, Volume 3*, Conference Proceedings of the Society for Experimental Mechanics Series 15, DOI 10.1007/978-1-4419-9794-4_56, © The Society for Experimental Mechanics, Inc. 2011

Method

The experiment aims to determine the inter-granular residual stress within zirconia. Laue diffraction was utilized to observe the stress distribution in individual grains. Experiments were carried out at beamline 12.3.2 at the Advanced Light Source, Berkeley using white beam polychromatic X-rays. High precision focusing optics allows focusing the X-ray beam to a spot of 0.7 µm x 0.8 µm dimension with very high flux (Setup shown in Figure 1). Emerging diffracted X-rays from the sample, produce spots on the CCD oriented in 90° reflection geometry as shown in Figure 2. Spots registered for every position of the beam on the sample are collected onto an X-ray CCD and analyzed using XMAS [5] (X-ray micro-diffraction analysis software), a customized indexing software. The procedure and the sample geometry is explained in the following sections.

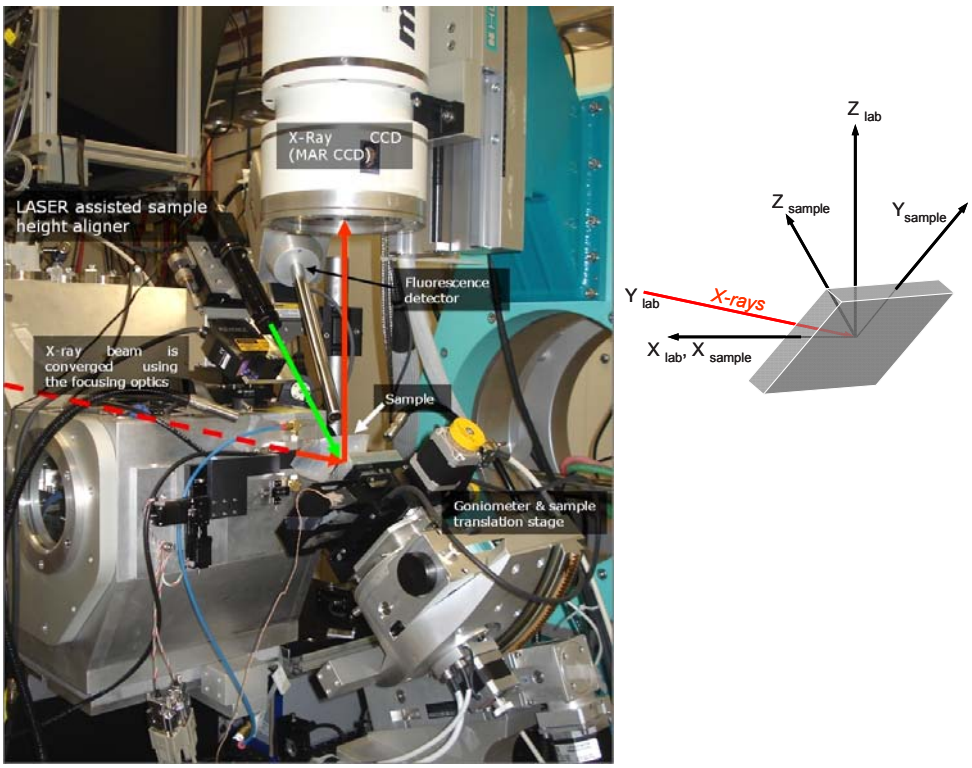

Figure 1 Experimental setup at Beamline 12.3.2, Advanced Light Source. Red dashed arrow indicates the X-ray beam incident on the sample and diffracted onto the CCD. The setup is in a 90° reflection geometry. A Laser alignment setup is used to position the sample at the focal point of the beam. A specific sample area can be registered using the fluorescence detector.

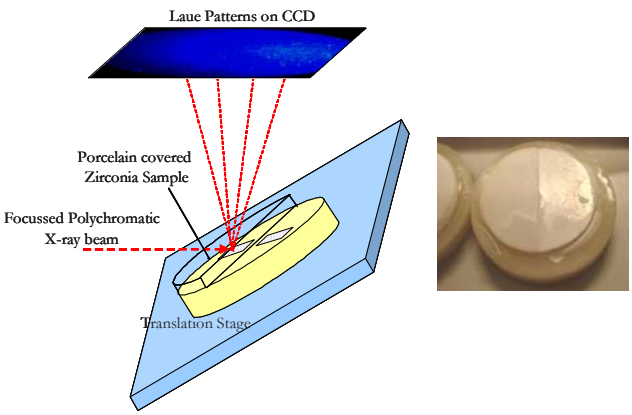

Figure 2 Schematic of the sample orientation in 90° reflection geometry. The sample consists of two semicircular zones where raster scans were obtained to study the residual stresses.

Sample Preparation

An all ceramic dental restorative crown mainly comprises of a core which provides the necessary structural strength and an exterior veneer which provides the aesthetic look of a natural tooth to the restoration. The core is veneered with porcelain to a specific contour which closely resembles the natural tooth geometry. Measurement of the in-situ residual stresses in a dental restoration such as a crown is challenging due to the complex geometry of crowns. Additionally, X-ray diffraction measurements of change in residual stresses under cyclic fatigue are difficult on the complex geometry. In the case of the micro X-ray diffraction setup, a successful experiment depends on several factors such as, the X-ray transmission through the veneer, sample displacement, the sample volume being considered, and the sample orientation. With these considerations the sample geometry was simplified to a bilayer cylindrical disk. The samples consisted of a disk, 1 mm thick made of sintered polycrystalline yttria stabilized zirconia. Half of the disk was veneered with a porcelain layer 0.5 mm thick which was ground and polished.

In-situ fatigue, Sample Positioning and Alignment

In the understanding of evolution of damage and catastrophic failures in dental crowns, investigation of the behavior of crowns under fatigue loading is important. Crowns are subject to prolonged cyclic fatigue in a patient and numerous occurrences of sudden catastrophic failures have been reported.[1, 3] A customized load frame designed for *in-situ* fatigue was utilized to subject the sample to cyclic fatigue. (Shown in Figure 3) The load frame can be operated at a maximum frequency of 5 Hz with a maximum compressive load limit of 625 N. The load frame was driven by a micro-stepping linear motor controlled by a software based tunable code.[6] The applied load feedback was obtained through a load cell incorporated within the frame. A typical cyclic load set of 40,000 cycles running at 2 Hz at 150 N took nearly 4 hours.

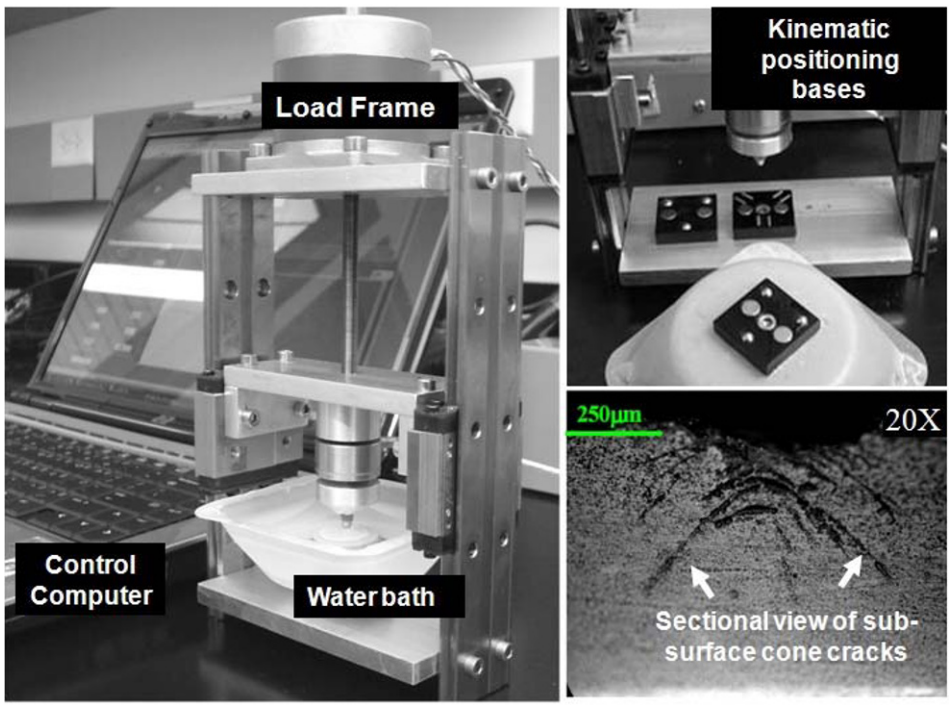

Figure 3 (Left) In-situ cyclic fatigue load frame. Top Right - Kinematic bases for easy re-positioning of sample on load frame and stage. Bottom Right - Cone cracks emerging underneath the indenter after cyclic loading

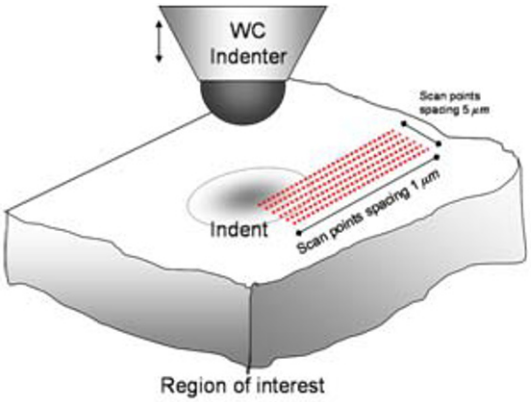

Figure 4 Schematic of scan points under the cyclic fatigue indenter. Image not to scale

Cyclic loading has to be carried out under an aqueous environment, to simulate chewing and in order to account for the crack opening phenomenon that occurs when a liquid is trapped in an already initiated crack. The kinematic bases shown in Figure 3 are fitted on both the translation stage of the diffractometer and the load frame, thus facilitating efficient sample switching with the location of the area of interest registered repeatedly. The experimental setup is designed such that the beam along with the optics is fixed. To map a diffraction scan, the sample is moved in steps to complete a 2D grid using the high precision translation stage as shown in Figure 4.

Data collection and interpretation

An automatic analysis module allows the batch analysis of an entire set of images collected from a scan on the sample. The results for each image is stored into an indexation file which further consists of information pertinent to each grain indexed at that particular spot. At the end of the automatic analysis, the software tabulates the results from the entire indexation file database into a sequential list file. Data sorting, distribution analysis was conducted on subsets of the sequential list file.

Macroscopic and microscopic stress distribution

The sequentially stored list of information related to individual images which in turn belong to a specific spatial location on the sample can be analyzed for microscopic or macroscopic stress information. Sub-grain (Type III) & grain-to-grain (Type II) stress information can be obtained when the grain size is larger than the beam.

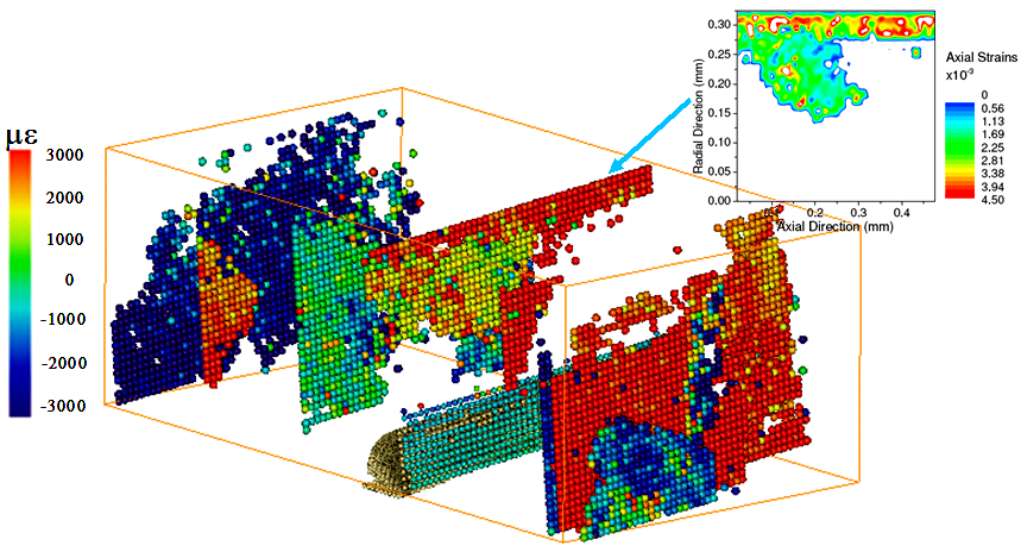

Figure 5 Micro-beam strain analysis on aluminum sapphire composite demonstrates the capability of the technique in measuring in-situ strains within individual grains. Each data point on the graphic indicates a diffraction scan point on the sample. The 3D plot indicates various grain morphologies along the X-ray beam and a portion of the sapphire fiber which is a part of the fiber-matrix composite.[7]

A microscopic grain-to-grain stress analysis has been conducted on an aluminum-sapphire metal matrix composite previously using a similar setup on beamline 7.3.3 as shown in Figure 5. [7-8] Identification of a set of scan points belonging to a particular grain, was done using orientation angle matching. A particular scan point was assigned a specific grain number based on the orientation angle within a certain range, and based on an initial histogram sort.

It is desirable to have such a result related to the grain-to-grain behavior, however in the current scenario; the grain sizes lie in the range of 0.1-0.5 micrometer, which are in the size range of the focused beam cross section. The orientations obtained over a certain area do not form a definitive histogram for the small grain size under observation. Hence mapping individual grains was not possible. The technique however gives us a good understanding of the microscopic strain over 3-10 grains averaged and macroscopic strain state when averaged over an entire scan area of many grains. It is important to have a well defined sample and laboratory coordinate system to interpret the results of the strain tensor from the experiment. Since we look at the entire result from a laboratory coordinate perspective or a global perspective, the beam which is always in a fixed position is kept as a reference. The sequential list also provides us with individual crystallographic orientation, strain and stress information. This is especially useful when analyzing bigger grain sizes as in Figure 5. The reference coordinate system is illustrated in Figure 6.

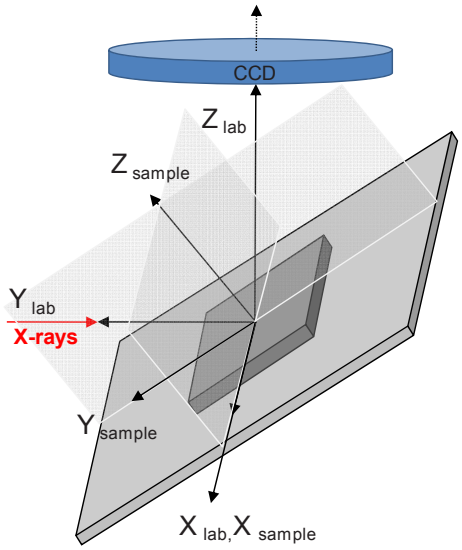

Figure 6 Laboratory and sample co-ordinate system at beamline 12.3.2. In the 90° reflection geometry, the sample is tilted at 45° to the incoming X-ray beam

Results

Analysis and extraction of interpretable results from the sequential list file was done using a data analysis and statistical software (Origin Pro 7.1). An initial sort based on the grain index was done to eliminate any ambiguous grains indexed. Ambiguous grains generally have less than 5 indexed reflections or have indexations which have erroneous peaks with low peak intensities.[9] A multiple conditional sort is implemented on a dataset related to every direction of the strain component which includes strains in the principal directions and the shear planes. Strains above the range of ± 8000 με were eliminated as outliers. Datasets acquired for monolithic zirconia, porcelain veneered zirconia and subsequent datasets related to the former two subjected to sets of fatigue cycles were refined in a similar manner as explained above. The refined dataset for every individual sample case is analyzed for an area averaged macroscopic stress/strain. This is achieved by utilizing a histogram of the probability distribution of strains from individual scan points.

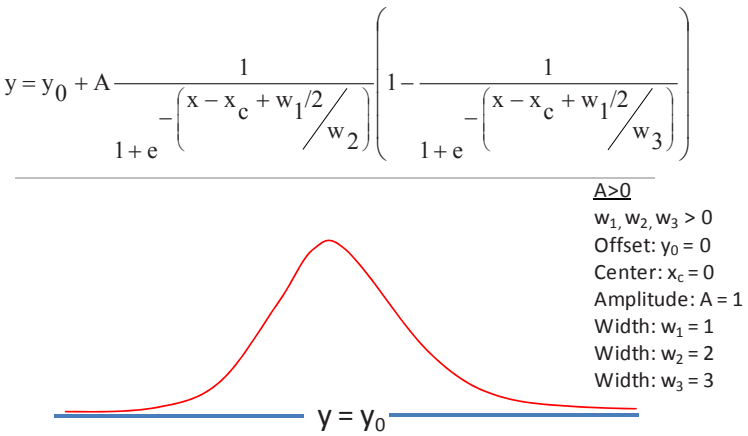

Figure 7 Asymmetric Sigma fit used to fit the stress and strain distributions

The range of ± 8000 με was binned into 100 με bins. It was found that all the data had a probability density distribution which was asymmetrically skewed around a strain value close to zero. The distributions were fit using an asymmetric sigma function as expressed in Figure 7. All the density distributions were normalized by a factor of the number of occurrences, which enables for a comparison of the residual stress/strain states of different samples.

Effect of cyclic impact loading on monolithic zirconia

Monolithic zirconia samples were subjected to 2 sets of fatigue cycles – 40,000 & 180,000 cycles, after the initial residual stress states were measured. The number of load cycles was decided based on literature values. [10-11] The monolithic disk samples were mounted on polymer bases which simulate the dentin layer. [11] The disk samples were mounted on a high precision kinematic base and fatigued in the custom built load frame at a frequency of 2 cycles/second with a load of 150 N using a 1.9 mm tungsten carbide ball indenter. The kinematic base ensures accurate alignment of samples on the translation stage after a particular cyclic loading step. Sample registration with an accuracy of 1 micron is achievable using TiO_2 marker dots. The area under the indenter and in the vicinity of the indenter was mapped for both the 40k and 180k cyclic fatigue steps. Results of the analysis of the different cyclic fatigue steps on the neat zirconia are shown in Figure 8. No significant change in the Type I residual stress was observed with increasing fatigue cycles, in any particular direction. However an in-depth observation of the grain-to-grain local stresses (Type II) at the indentation site is vital to studying damage evolution due to impact fatigue.

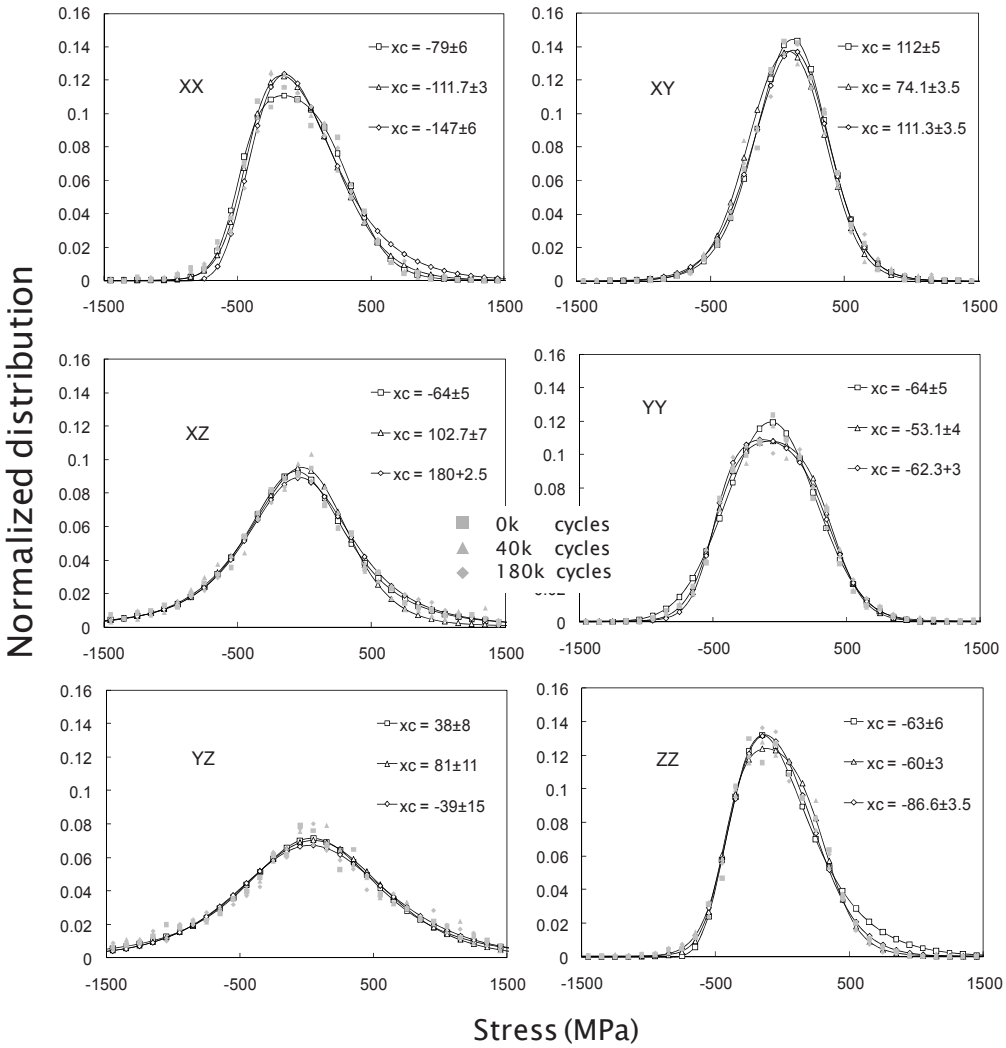

Figure 8 Influence of fatigue cycling on residual stress state in neat zirconia. The type I stress is obtained from grains averaged from a rectangular area under the indenter extending 100 micrometer away from the indenter. Solid lines with the open symbols indicate the asymmetric sigma fit to the data (solid symbols).

Discussion

With no surface treatment or presence of overlying layer, the surface stress on monolithic zirconia is anticipated to be zero. The probe cross section being very close to the size of a grain, we observed stress/strain values from individual grains. The measured stresses are far from zero locally (Type II) but zero globally (Type I). Grain-to-grain stress evaluation on zirconia has been carried out earlier. The ability to investigate the effect of cyclic fatigue on damage initiation and propagation in zirconia is important in building an understanding the failure mechanics in zirconia. Although it has a high flexural strength of 900-1200 MPa, zirconia crowns have been observed to fail at substantially lower loads in fatigue.

The residual stress measurement results of the *in-situ* cyclic fatigue test indicates that globally (Type I), considering the average over several grains, no significant change is observed. It is important to note the range of the residual stresses observed in any given direction (as seen from Figure 8) is between ± 1.5 GPa. Although a global stress, close to zero is observed, few grains roughly 10 - 25 % [9] are highly stresses and lie in the stress range anywhere greater than ±0.5 to ±1.5 GPa. To understand and observe the damage initiation at the grain level, a detailed inspection at the length scale of individual grains with higher spatial resolution would be necessary. It is important to conduct similar experiments on layered zirconia samples. With the introduction of a

compressive residual stress in zirconia due to the porcelain veneer, the behavior under cyclic fatigue would be expected to be entirely different. Such *in-situ* cyclic tests could suggest important clues in explaining the catastrophic failures seen in dental restorations.

Conclusions

An experimental procedure of measuring the residual stress state in zirconia dental restorations undergoing *in-situ* cyclic impact fatigue has been developed. Over a large area on the surface of the monolithic zirconia, roughly 10 - 25 % of the grains were observed to have highly localized residual stresses in the range of 0.5 GPa to 1.5 GPa. Multiple sets of measurements of grain averaged residual stress at various impact fatigue steps have been conducted. The impact fatigue steps ranged from pristine state, one year's service life and a four year service life. The effects of fatigue over such long durations on monolithic zirconia showed no significant changes in the global residual stress state. However the understanding of the events at the grain level are yet to be investigated. Similar investigations on the veneered bilayered zirconia were conducted and the results of the analysis will be published elsewhere.

Acknowledgements

Martin Kunz, Advanced Light Source, Berkeley, CA; and Paulo Coelho, New York University, NY provided valuable collaboration. Use of the Advanced Light Source is supported by the Director, Office of Science, Office of Basic Energy Sciences, of the U.S. Department of Energy under Contract No. DE-AC02-05CH11231. Research support provided by the Oklahoma Health Research award (project number HR07-134), from the Oklahoma Center for the Advancement of Science and Technology (OCAST). We gratefully acknowledge the assistance of Dr. V. Thompson, Dr. E. D. Rekow and M. Cabrera at NYU Dental College.

References

1. Fradeani, M. and M. Redemagni, *An 11-year clinical evaluation of leucite-reinforced glass-ceramic crowns: A retrospective study.* Quintessence International, 2002. **33**(7): p. 503-510.
2. Coelho, P.G., et al., *Laboratory Simulation of Y-TZP All-ceramic Crown Clinical Failures.* Journal of Dental Research, 2009. **88**(4): p. 382-386.
3. Zhang, Y., A. Pajares, and B.R. Lawn, *Fatigue and damage tolerance of Y-TZP ceramics in layered biomechanical systems.* Journal of Biomedical Materials Research Part B-Applied Biomaterials, 2004. **71B**(1): p. 166-171.
4. Zhang, Y. and B.R. Lawn, *Fatigue sensitivity of Y-TZP to microscale sharp-contact flaws.* Journal of Biomedical Materials Research Part B-Applied Biomaterials, 2005. **72B**(2): p. 388-392.
5. Tamura, N., et al., *Scanning X-ray microdiffraction with submicrometer white beam for strain/stress and orientation mapping in thin films.* Journal of Synchrotron Radiation, 2003. **10**: p. 137-143.
6. N. Phelps, *Local and Global Deformation from Synchrotron Imaging of Closed Cell Foams in Compression.* Master's Thesis,(Advisor) Jay Hanan, Oklahoma State University, OK, 2007.
7. Bale, H.A., J.C. Hanan, and N. Tamura, *4-D XRD for Strain in Many Grains Using Triangulation.* Powder Diffraction, 2006. **21**: p. 184.
8. Bale, H.A., N. Tamura, and J.C. Hanan. *Triangulation method for grain depth measurement using polychromatic micro-beam radiation*. in *Syncrotron Radiation for Material Science - 5*. 2006. Chicago.
9. Bale, H.A., et al., *Interface Residual Stresses in Dental Zirconia Using Laue Micro-Diffraction.* The Eighth International Conference on Residual Stresses, 2008.
10. Coelho P. G., et al., *Laboratory Simulation of Y-TZP All-Ceramic Crown Clinical Failures.* Journal of Dental Research, 2008.
11. Lawn, B.R., Y. Deng, and V.P. Thompson. *Use of contact testing in the characterization and design of all-ceramic crownlike layer structures: A review*. 2001.